ULTRASONIC STUDIES OF THE FUNDAMENTAL MECHANISMS OF RECRYSTALLIZATION AND SINTERING OF METALS

DOE GRANT NO. DE-FG02-01ER45890

Joseph A. Turner
Department of Engineering Mechanics, University of Nebraska-Lincoln
W317.4 Nebraska Hall, Lincoln, Nebraska 68588
phone: 402-472-8856 fax: 402-472-8292 e-mail: jaturner@unl.edu

Objectives

The purpose of this project was to develop a fundamental understanding of the interaction of an ultrasonic wave with complex media, with specific emphases on recrystallization and sintering of metals. A combined analytical, numerical, and experimental research program was implemented. Theoretical models of elastic wave propagation through these complex materials were developed using stochastic wave field techniques. The numerical simulations focused on finite element wave propagation solutions through complex media. The experimental efforts were focused on corroboration of the models developed and on the development of new experimental techniques. The analytical and numerical research allows the experimental results to be interpreted quantitatively.

Alteration in Collaborative Arrangement

In fall 2002, the Ames Lab partner, Dr. James C. Foley, announced that he was leaving for another position at Los Alamos National Laboratory. Dr. R. Bruce Thompson has served as the primary contact for this collaboration since Dr. Foley departed.

Accomplishments (Recrystallization)

Analytical Modeling. Expressions for the ultrasonic attenuation in media with arbitrary texture have been developed using stochastic wave propagation theory. Initial attempts at deriving simple expressions for the attenuation were unsuccessful. Therefore, a modified technique was developed that relies slightly more on numerical calculations. The method is based on a generalized function of a single scalar variable σ that characterizes the state of texture. In this case the weighting function for the individual grains is given by

$$F(\sigma,\theta)=\frac{1}{\sqrt{2\pi}\sigma}e^{-\theta^2/2\sigma^2}\ , \tag{1}$$

with θ as the grain orientation angle. Thus, when $\sigma \to 0$ all grains are aligned and the material is transversely isotropic at the macroscale. As $\sigma \to \infty$, all grains are randomly oriented and the material is isotropic at the macroscale.

In terms of attenuation, the covariance of the microstructure is the primary quantity needed for the calculation of attenuation. It is defined by

$$\Xi^{ijkl}_{\alpha\beta\gamma\delta}(\sigma) = \left\langle C_{ijkl} C_{\alpha\beta\gamma\delta} \right\rangle - \left\langle C_{ijkl} \right\rangle \left\langle C_{\alpha\beta\gamma\delta} \right\rangle,$$

and will be a function of σ. The quantities needed in this expression are defined by

$$\left\langle C_{ijkl} \right\rangle = \frac{1}{8\pi^2} \int_0^{\pi} \int_0^{2\pi} \int_0^{2\pi} C_{ijkl}(\theta,\phi,\psi) F(\sigma,\theta) \sin\theta d\theta d\phi d\psi \,, \tag{2}$$

and

$$\left\langle C_{ijkl} C_{\alpha\beta\gamma\delta} \right\rangle = \frac{1}{8\pi^2} \int_0^{\pi} \int_0^{2\pi} \int_0^{2\pi} C_{ijkl}(\theta,\phi,\psi) C_{\alpha\beta\gamma\delta}(\theta,\phi,\psi) F(\sigma,\theta) \sin\theta d\theta d\phi d\psi \,, \tag{3}$$

in which both Eqs. (2) and (3) include the grain orientation distribution function F such that <C> and <CC> are dependent on σ. Example results using Eq. (2) are shown in Fig. 1 for both the average elastic properties as well as quasilongitudinal slowness surfaces in terms of σ. The transition from transversely isotropy to complete isotropy is captured well using the grain orientation distribution function. Example results for attenuation are shown in Fig. 2. Again, the transition from transverse isotropy to complete isotropy is shown. Of particular note is the peak observed in the SH attenuation when σ is about 0.5. Such information may be useful for process monitoring.

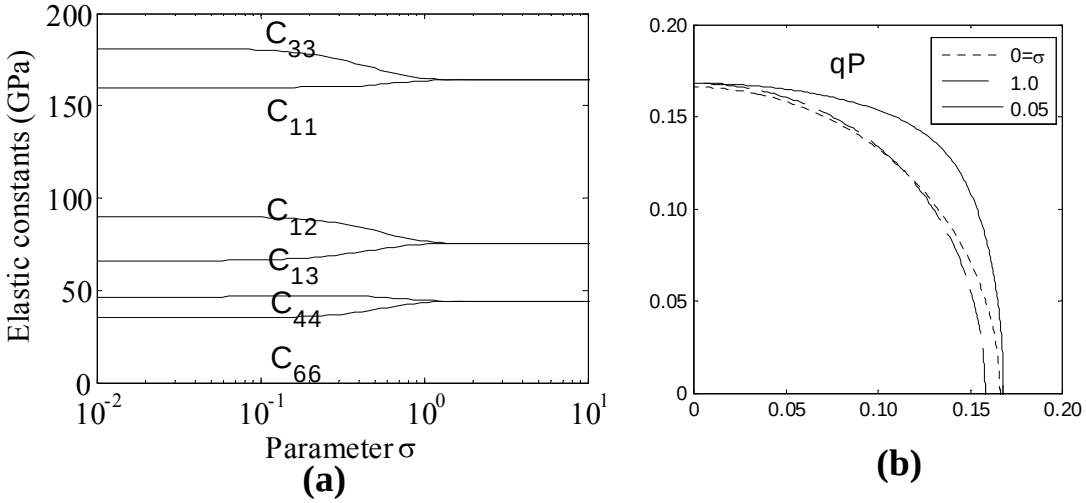

Figure 1. Example results for the average elastic properties of a material modeled using the grain orientation weighting function, Eq. (1). In (a), the average elastic moduli as calculated from Eq. (2) are shown as a function of σ. It is clear that for small σ, the material is transversely isotropic, but is isotropic for large σ. In (b), the slowness surface for the quasilongitudinal wave is shown for three values of σ. In this case, the wavespeed anisotropy is shown such that an isotropic material has a circular slowness surface.

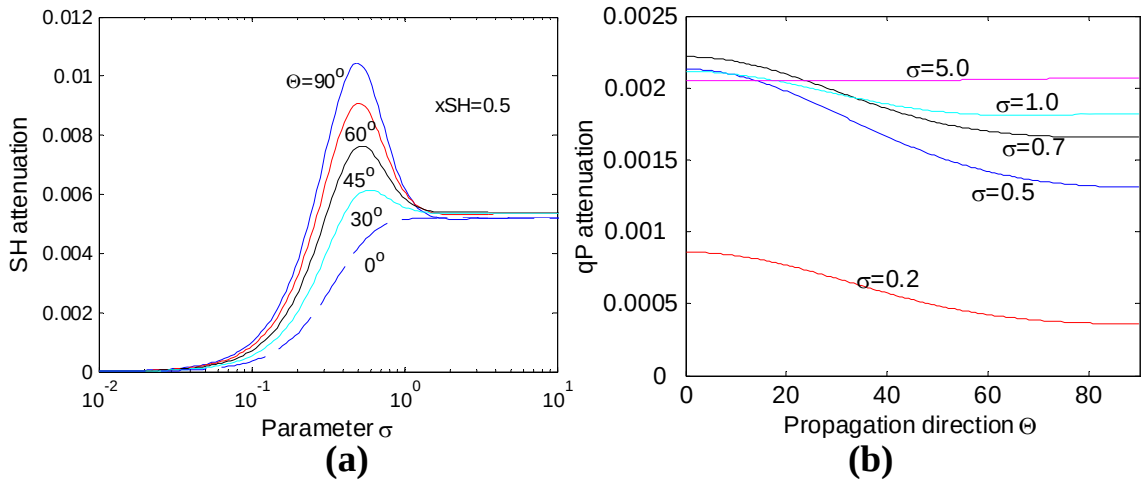

Figure 2. Example attenuation results based on the expressions in Eqs. (2) and (3) using the grain orientation distribution function *F*. In (a), the shear horizontal attenuation is shown as a function of σ. When σ is small, all grains are perfectly aligned such that the material behaves as a single crystal with no scattering attenuation. Large σ corresponds to complete isotropy with attenuation uniform with direction. In (b) the quasilongitudinal attenuation is shown as a function of direction for several values of σ.

Progress was also made in the study of multiple scattering in slab geometries. These results have applications associated with heterogeneous bonding and interface layers. Two example results are shown in Fig. 3. The layer is insonified by a plane longitudinal wave. One question in the multiple scattering regime is associated with the applicability of the diffusion limit in such geometries. For elastic waves, the diffusion limit implies that the longitudinal and transverse energies E_L and E_T, respectively, are equipartitioned. The energies ultimately achieve the relation $E_T = 2K^3 E_L$, where $K = c_L / c_T$ is the wave speed ratio. Results associated with equipartitioning are shown in Fig. 3 for (a) steady-state and (b) time-dependent cases. In 3(a), the ratio of $E_T / \left(2K^3 E_L\right)$ is plotted as a function of depth in the layer τ for several layer thickness value H. Thus, a value of unity for this ratio indicates complete equipartitioning. It is clear for the thickest layer $H = 100$ that complete equipartitioning occurs for depths of $\tau = 40 - 90$. However, near the boundaries, there is always an excess of longitudinal energy relative to the diffusion limit. It is clear that the boundary conditions dictate this result. Also, it is clear that for layers smaller than $H = 40$, that complete equipartitioning does not occur. The implications for models based on a diffusion limit are clear. In 3(b), the ratio transverse to longitudinal energy is shown as a function of time for a layer with $H = 50$ at a position $\tau = 50$. Here it is also clear that the energy does not partition according to the diffusion limit, even at late times, although a constant ratio of transverse to longitudinal energy is achieved.

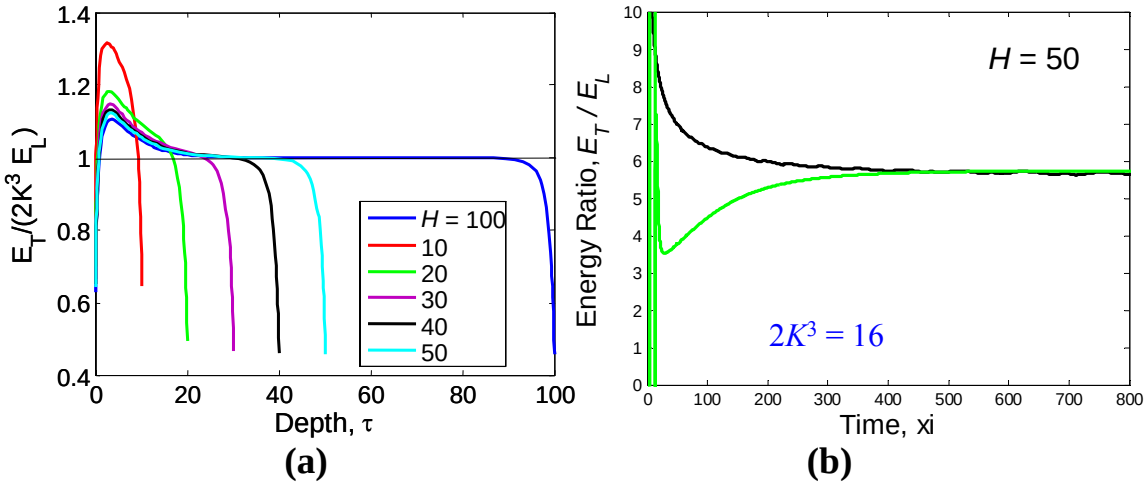

Figure 3. Multiple scattering results for a heterogeneous layer of thickness *H*. The equipartitioning of longitudinal and transverse energy in steady state is examined in (a) as a function of depth τ and layer thickness *H*. In (b), the time domain equipartitioning is examined for *H* = 50 at a position τ = 50. Both results indicate that the diffusion limit may not be fully achieved.

The applicability of the diffusion equation to model the multiple scattering of elastic waves in heterogeneous layers is examined in Fig. 4. In this case, the solution to a one-dimensional diffusion equation is used to fit to the complete multiple scattering result. Examples for two layers $H = 20$ and 50 are shown. The fit for $H = 20$ is clearly not as adequate as the fit for $H = 50$. However, in both cases the best fit was achieved for values of diffusivity and dissipation that were very different from the actual values of the medium. The use of a diffusion model for these systems is clearly not well understood.

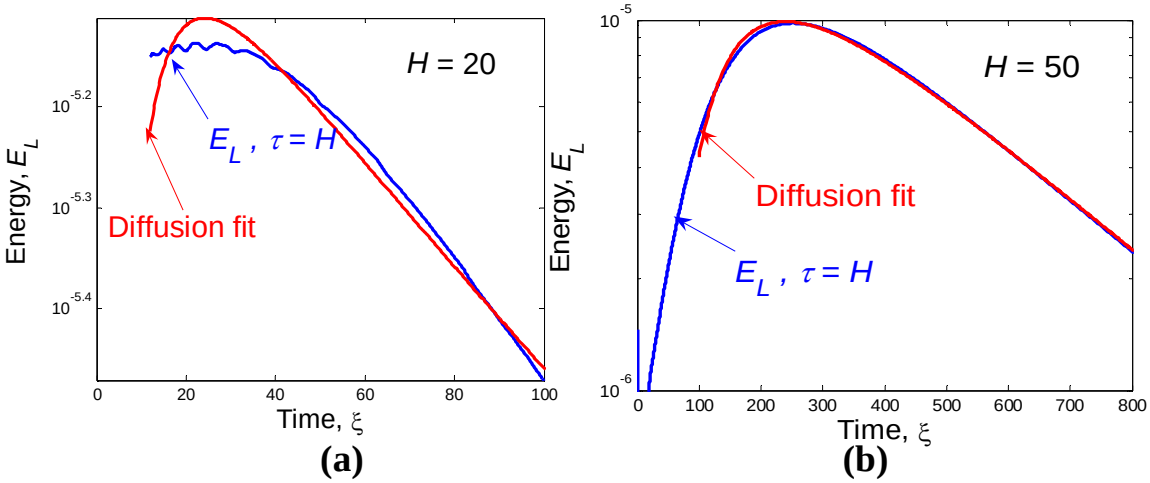

Figure 4. The use of a one-dimensional diffusion equation to fit multiple scattering solutions is examined for two layers (a) *H* = 20 and (b) 50. For (a), the fit is not very good for all times. For (b), the fit is much better. However, the fit parameters of diffusivity and dissipation do not match with the actual values of the layer. More research is needed to completely understand the diffusion limit of elastic waves.

Numerical Modeling. Numerical models of the elastic wave propagation in polycrystalline media were developed by MS student G. Ghoshal as part of his MS thesis. The first step in this process was the creation of Voronoi crystals with arbitrary elongation and orientation. Efficient algorithms were developed within Matlab using the method of virtual nuclei (MVN). Secondly, these numerical models were coupled with a finite element model (FEM). Here, a commercial code (ABAQUS-Explicit) is used. The FEM mesh, including nodal position, is overlaid on the Voronoi model and loaded into ABAQUS. An example domain for the scattering calculations is shown in Fig. 5. The Voronoi polycrystal is first determined, followed by the FEM discretization. The calculations in ABAQUS are then done. An example result of the full displacement full from ABAQUS is shown in Fig. 6 at three different time steps. The wave is excited at the top of the sample, in this case normal to the sample. Infinite elements at the edges of the sample allow the energy to leave the domain without returning. Time domain traces at the top and bottom of the specimen are used for calculating the attenuation. Examples of the multiple reflections at these locations are shown in Fig. 7. Note that the scattering from the microstructure is diminishing the wave amplitude as it travels back and forth across the specimen. These waveforms are used to determine the attenuation, such as the example shown in Fig. 8. A summary of attenuation results is shown in Fig. 9 presented in dimensionless form for a weak scattering material (aluminum) and a strong scattering material (copper). In both cases, the numerical results are compared with theory using a single correlation length. In general, the comparison is quite good for both cases. However, there are deviations from the theory particularly for the high-frequency results (small λ) for copper. These results suggest that a more complex theory is needed such that the correlation length has a frequency dependence. The development of this generalized numerical code was a major development of this grant. The code is now being used to examine attenuation and backscatter in textured materials and those with elongated grains. Results created from this code will provide a strong basis for new attenuation models under development.

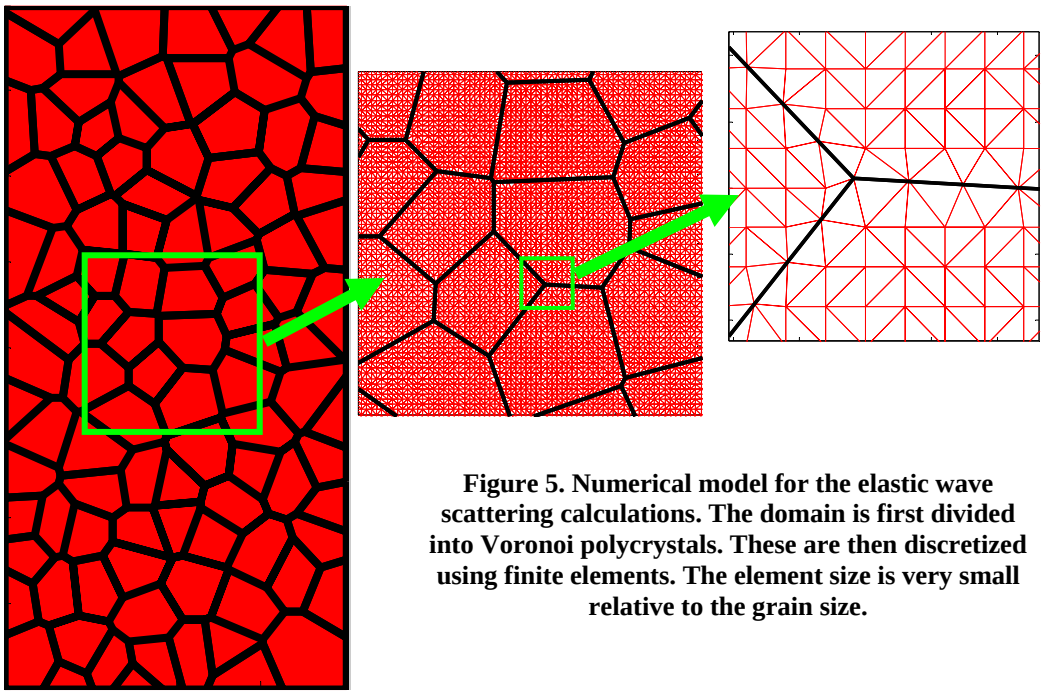

Figure 5. Numerical model for the elastic wave scattering calculations. The domain is first divided into Voronoi polycrystals. These are then discretized using finite elements. The element size is very small relative to the grain size.

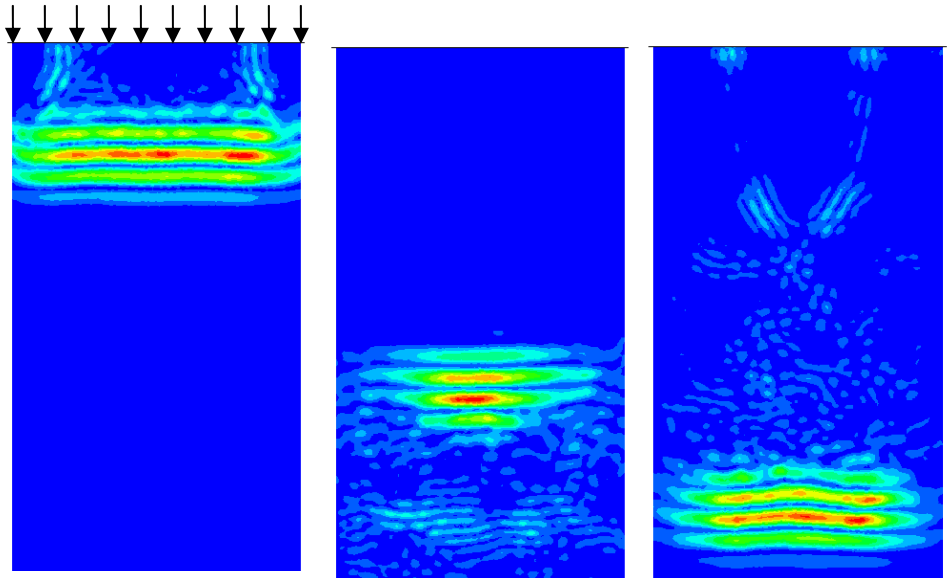

Figure 6. Example results of the full field from a finite element simulation of an elastic wave propagating in polycrystalline aluminum. At these three time steps, the wave packet has nearly propagated from the top the bottom of the domain. This calculation was done with a 14 MHz tone burst applied uniformly at the top surface with loading normal to the surface. Average grain size in the domain is 0.64 mm for this example.

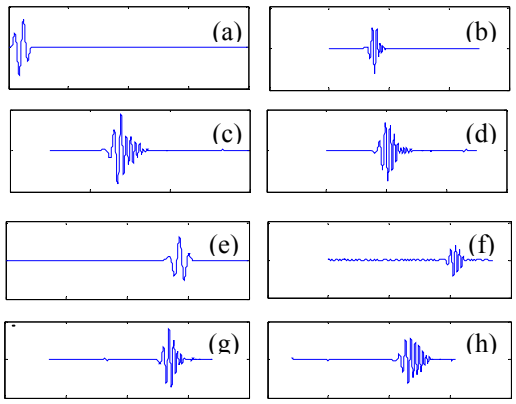

Figure 7. Example result of successive multiple reflections from the frontwall (a-d) and backwall (e-f) of the domain.

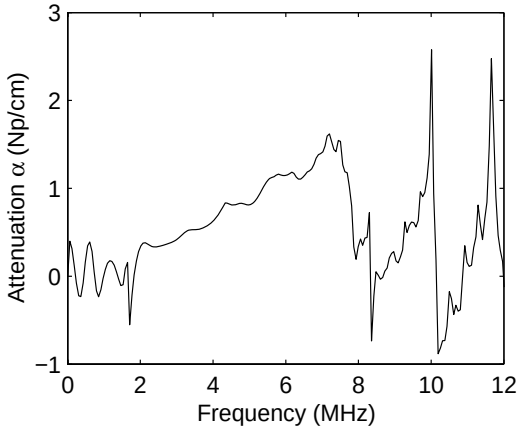

Figure 8. Example attenuation result for copper using a 5 MHz input frequency.

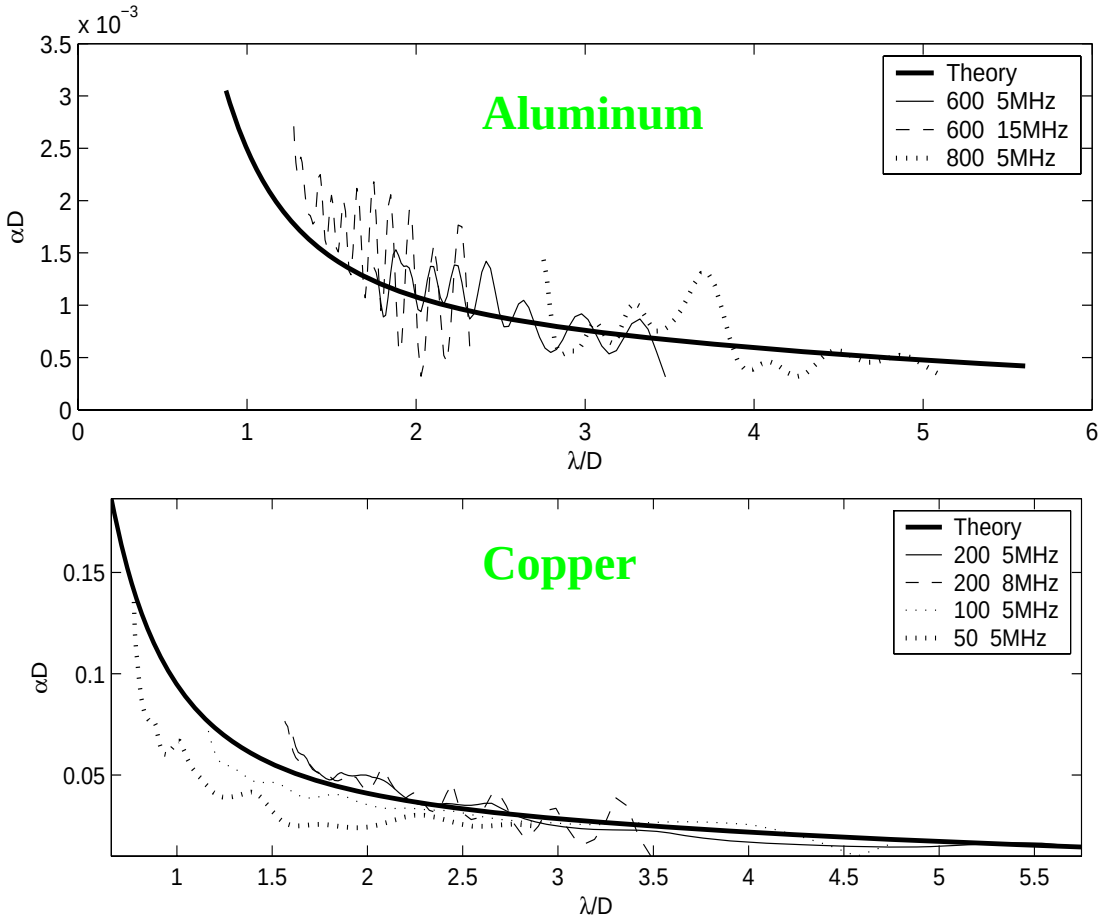

Figure 9. Comparison of numerical and theoretical attenuation for a weak-scattering material (aluminum) and a strong-scattering material (copper) over a wide range of wavelengths relative to grain diameter. The general trends are in agreement, but the locations of deviation warrant further investigation.

Experiments. The first set of specimens for recrystallization experiments were made in the summer of 2002 in collaboration with Dr. James C. Foley at Ames Laboratory. A

block of pure aluminum was cold-worked to achieve grains that are equiaxed, uniform, and of an appropriate size. This block was then rolled to a thickness about 75% of its original thickness. The rolling introduces grain elongation and material texture into the sample. From the rolled plate, several specimens were cut for the ultrasonic attenuation measurements (shown schematically in Fig. 10). One specimen (1) will be used for XRD spectroscopy from which precise microstructural information may be extracted (currently these measurements are not yet complete due to equipment problems). Specimens 2-4 are chosen with specific orientations (30°, 45°, and 0°, respectively) relative to the rolling

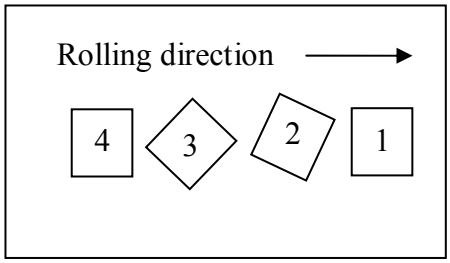

Figure 10. Schematic of the specimens cut from a rolled plate of pure aluminum.

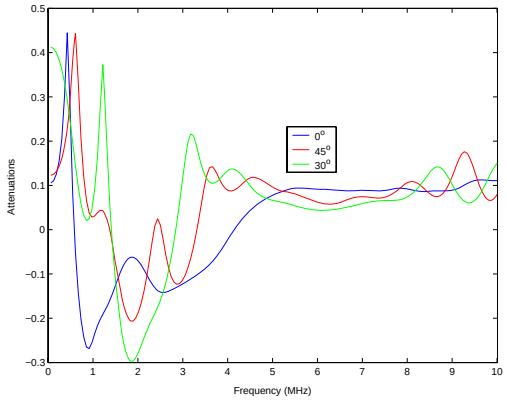

Figure 11. Example experimental result of ultrasonic attenuation (5 MHz center frequency) measured on a sample of pure aluminum that has been rolled. Propagation was normal to rolling.

direction such that the angular dependence of the attenuation may be studied. Initial longitudinal and shear wave attenuation measurements were made at Ames Lab by PhD student L. Yang. An example longitudinal attenuation measurement for the three samples is shown in Fig. 11. The propagation direction for these results was normal to the rolling plane. At this frequency (5 MHz), the attenuation is small and is similar for the three samples. Additional measurements covering higher frequencies were planned, but did not occur due to the departure of Dr. Foley from Ames Laboratory.

An additional goal of this project was for experimental expertise on ultrasonic scattering to be developed at UNL. Such expertise is critical for future research and for the infrastructure improvement of the state. Toward that ultimate goal, the experimental program at UNL resulted in the development of a Labview program for determining ultrasonic backscatter from heterogeneous specimens. A schematic of these types of experiments is shown in Fig. 12. The transducer is translated spatially and time-

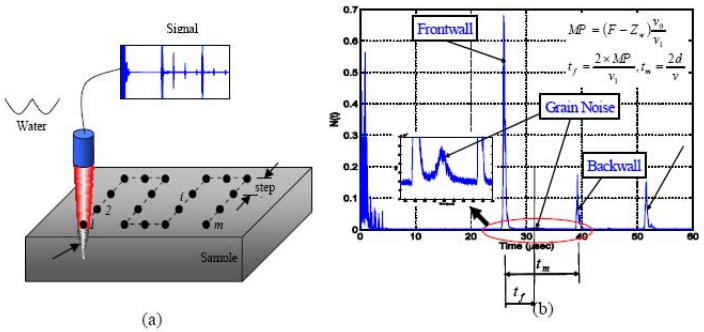

Fig. 12. (a) schematic experimental setup and (b) example measured signal acquired from 110 spatial positions.

domain signals are acquired a each position. The variance of the signals is the 'ultrasonic backscatter' that is related to the microstructure. Example results from the UNL system, compared with theory are given in Fig. 13 for two types of steel. The theoretical expressions use the single-crystal constants of iron and the grain size measured from the micrographs shown. The agreement between the theory and experiment is very good indicating that the experimental system was successfully developed.

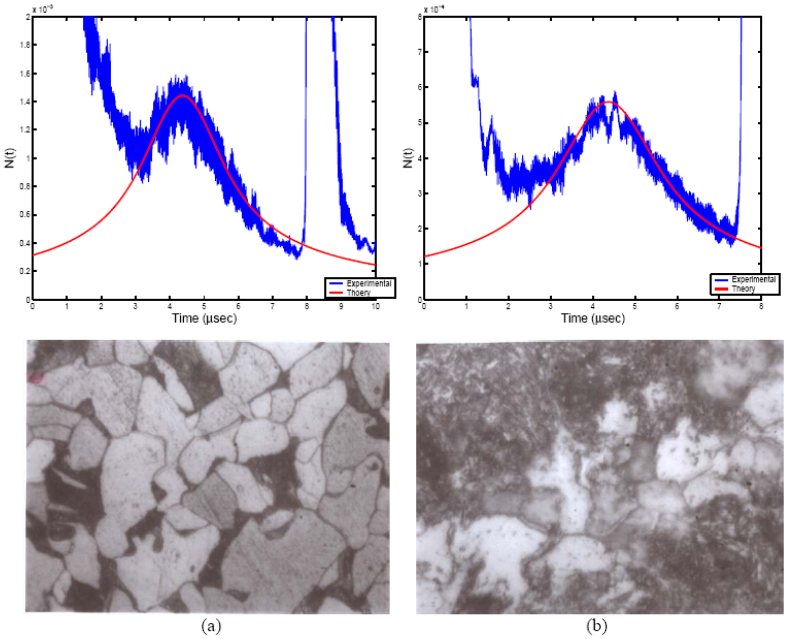

Figure 13. Comparison of experiment and theory of ultrasonic backscatter for two types of steel (a) 1080 steel and (b) 4230 steel.

Accomplishments (Sintering)

Experiments: A set of specimens of sintered aluminum powder with varying degrees of sintering were produced by Dr. Foley in December of 2002. Two types of experiments are planned for these specimens. The first set will involve measurements of ultrasonic attenuation and backscatter. These measurements will now be repeated at UNL since the development of experimental expertise at UNL.

The other experiments on the sintered specimens are focused on the use of the atomic force microscope (AFM). The experimental setup for the dynamic AFM experiments (also known as atomic force acoustic microscopy or AFAM) is shown schematically in Fig. 14. A commercial AFM (Thermomicroscopes Autoprobe CP) was

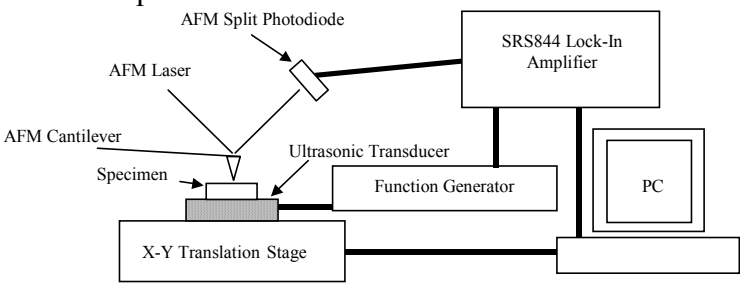

Figure 14. Experimental setup for atomic force acoustic microscopy (AFAM) in which the resonant frequencies of the AFM cantilevers are used to determine and image mechanical stiffness.

modified for these experiments. A reference specimen and an unknown specimen are placed on a broadband ultrasonic transducer (2.25 MHz center frequency). The transducer is mounted on the AFM stage and is excited by the function generator. The output from the AFM photodiode is mixed with the driving signal in the lock-in amplifier. The lock-in output and the photodiode output are both used by the AFM for imaging. The function generator is controlled by Labview software. Once the natural frequencies of the AFM beam are determined, a stiffness map may be made. The sample is excited harmonically near the resonance while the AFM topography scan is made. The resulting lock-in amplifier output is proportion to the local contact stiffness. An example result on an aluminum sinter is shown in Fig. 15. The particles in this case were 50 μm spheres cold pressed and then sintered. The topography image shows little contrast except artifacts from polishing. The AFAM image shows a clear region of higher stiffness corresponding to a particle-particle interface. It is anticipated that techniques such as AFAM will be useful for developing a better understanding the sintering process.

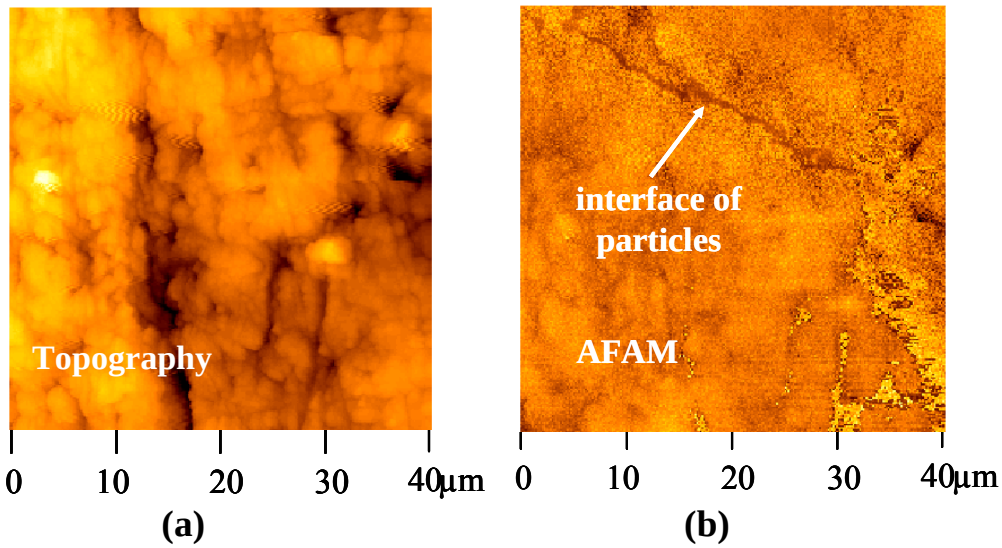

Figure 15. Example (AFAM) results on aluminum sinters: (a) surface topography of one sinter sample; (b) example AFAM scan showing stiffness variations within the sample. The particle-particle interface is clearly observed to the the impedance contrast there.

Numerical Modeling: A numerical model of the sinters was also developed based on the Voronoi polycrystal model described above for the recrystallization studies. The Voronoi model was modified such that a thin layer of elements with different material properties is concentrated at the boundaries of each particle. The material properties of the boundary layer may differ from those of primary sinter particle. An example model is shown in Fig. 16 where the geometric parameters D and d are defined as the particle diameter and interface thickness, respectively. The ultrasonic attenuation and backscatter are expected to depend on these two parameters. An example finite element simulation is shown in Fig. 17 using large density contrast. The scattering of the initial plane wave is evident in this strong-scattering example.

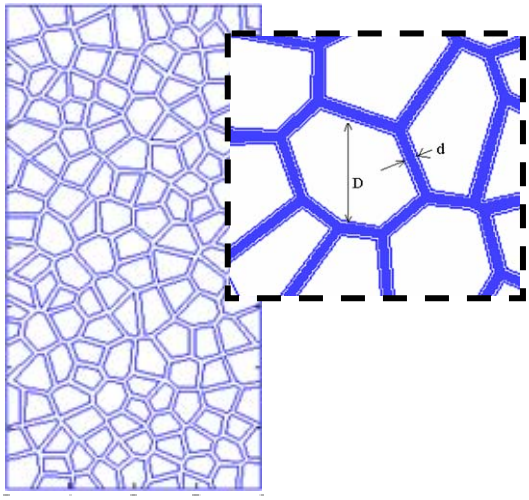

Figure 16. Model microstructure of sintered material for numerical modeling.

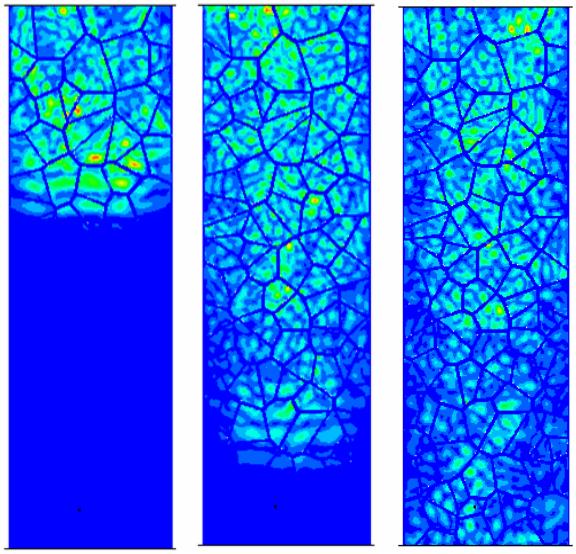

Figure 17. Example numerical simulation of wave propagation through the system.

With this model of the sintered material, the attenuation for several examples of geometry and material contrast were examined. The example shown in Fig. 17 is based on density contrast alone (λ, μ are uniform throughout). The density contrast may be characterized in terms of $s = \left[\left(\rho_1 - \rho_2\right)/\overline{\rho}\right]^2$, where ρ_1 and ρ_2 define the densities of the two constituent phases and $\overline{\rho}$ is the average density. The attenuation curves shown in Fig. 18 are for a 3 MHz incident longitudinal wave for which ρ_1 is fixed and ρ_2 is varied for two combinations of *D* and *d*.

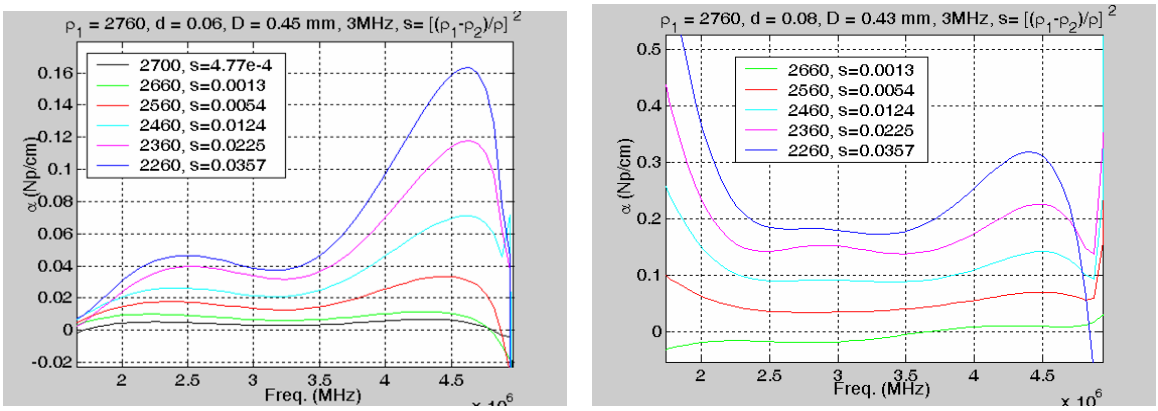

(a) **(b)**

Figure 18. Example attenuation results from numerical simulations on two-phase microstructures for: (a) *D* = 0.45 mm, *d* = 0.06 mm and (b) *D* = 0.43 mm, *d* = 0.08 mm, for several different values of density contrast *s*. The elastic properties (*λ*, *μ*) of both phases are identical.

Several simulations were conducted for 3 and 5 MHz incident waves and the attenuation results are summarized in Fig. 19 in which attenuation is plotted versus material contrast *s*. The general trend is expected in that higher values of *s* lead to higher attenuation.

However, models that invoke a weak-scattering assumption give a linear dependence of attenuation on *s*. Thus, the results in Fig. 19 suggest that the linearity may breakdown for certain combinations of material contrast and wavelength to diameter ratio. These results warrant further investigation.

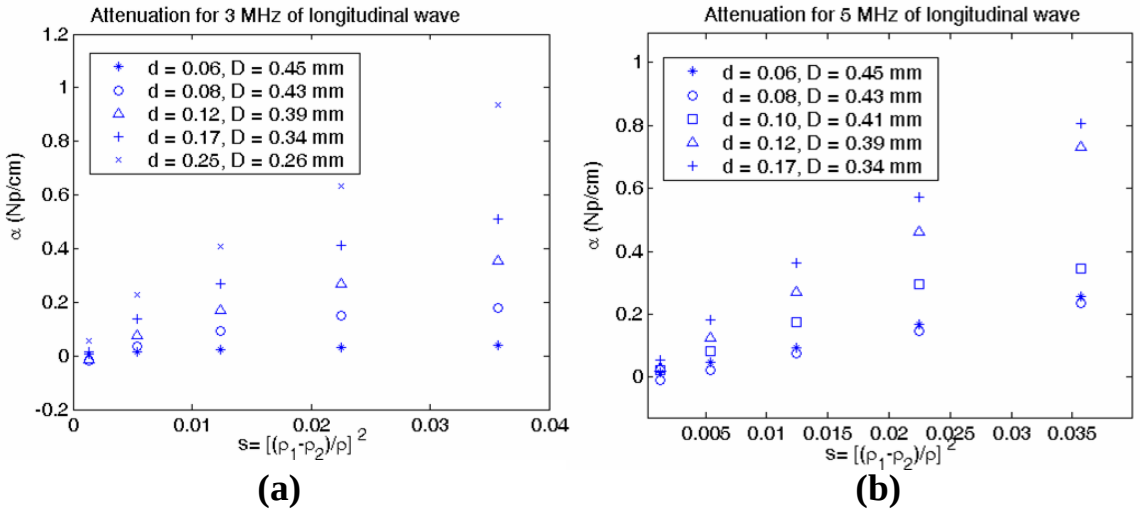

Figure 19. Summary of attenuation results for several numerical simulations on two-phase microstructures (density contrast only) for 3 MHz (a) and 5 MHz (b) input waves for several values of *D*, *d*, and *s*. The trend with *s* is not always linear as predicted by theory.

Analytical Modeling. The numerical results presented above lead to the conclusion that current attenuation models must be modified to account for the variations observed. Toward that end, spatial correlation information has been examined for the two-phase structures shown above. Attenuation models all have a dependence on the spatial correlations of the material properties. In most cases, the dependence is truncated such that only two-point correlation information is used, in the form of the correlation function $R(r)$. The attenuation is then written as a spatial convolution of the Fourier transform of R and the Green's function of the average medium. For polycrystalline materials, an exponential two-point correlation function $R(r) = e^{-r/L}$ is used with L as the spatial correlation length. Such a function was used in the examples shown above for the modeling recrystallization. For the model of the two-phase sinters, it is clear that a single correlation length will not suffice since the material has a minimum of two lengths scales D and d that must be included. In order for the appropriate correlation to be determined, numerical correlation statistics were calculated from the geometric models created (as in Fig. 16). Example correlation statistics are shown in Fig. 20 in the form of a histogram. In this case, $R(r)$ defines the probability that two points separated by a distance r lie in the same phase of the material. An appropriate function to fit the numerical histogram was then sought. The first attempts to fit the data were based on correlation functions proposed by Torquato and co-workers. Two of these examples are shown in Fig. 20(a) as the solid curves. It is clear that the fit to the data is not very good although the basic

trends are captures. The fit shown in Fig. 20(b) is a newly proposed correlation function that fits the histogram data very well. The correlation function shown has two scales that are related to *D* and *d*. This correlation function will be used in attenuation models for comparison with the numerical simulation results. The technique used for determining the correlation histogram will also be applied in the future to micrographs of two-phase materials including sinters and concrete among others.

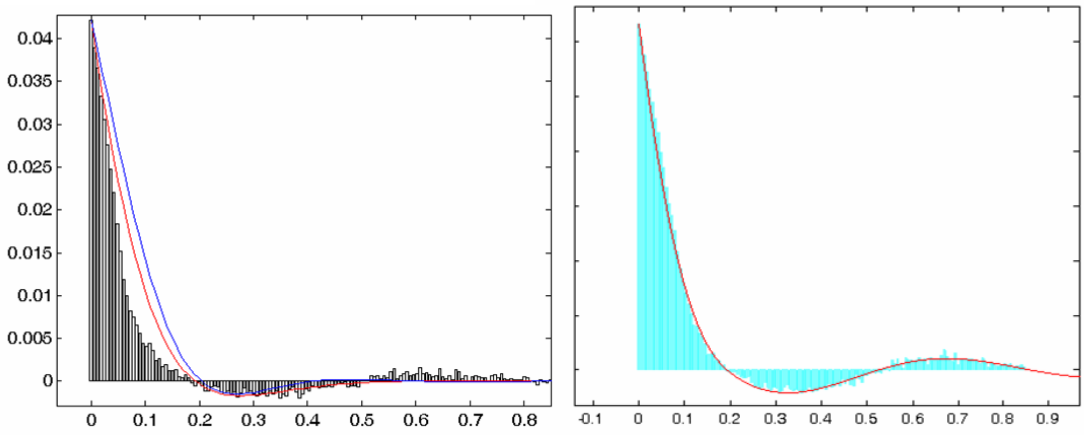

Figure 20. Spatial correlation determined numerically for Voronoi-sinter microstructure. The solid curves in (a) correspond to the models from Torquato that do not match the data sufficiently. The solid line in (b) is a new spatial correlation proposed.

Summary and Future Work

As a result of this project, several important outcomes have been achieved. These outcomes include the:

- development of a generalized polycrystal model that governs the transition from transversely isotropic to isotropic; attenuation and backscatter may be determined from the model,
- development of a generalized numerical model for polycrystalline media and sintered media using Voronoi polycrystals coupled with the finite element method,
- development of analytical models for studying ultrasound propagation through sinters,
- development of expertise at UNL for ultrasonic measurements of attenuation and backscatter for characterization of heterogeneous media, and
- development of additional AFAM research on metallic sinters.

The results presented here also lead to several new questions related to ultrasonic inspection of both the recrystallization and sintering processes. Research to be addressed in the future includes:

- understanding the influence of the two-point correlation function on the attenuation and backscatter,
- extraction of two-point spatial information from experimental measurements,

- the robustness of inversion routines associated with recrystallization of polycrystalline materials,
- the onset and influence of multiple-scattering effects in elastic media,
- the inversion of sintering parameters during processing using ultrasound,
- studies using AFAM while particles are joining (AFAM at temperature), and
- additional ultrasonic scattering phenomena associated with materials processing.

Personnel Supported

Joseph A. Turner: Associate Professor and Principal Investigator
Matthew Stagemeyer: Undergraduate student (currently an MS student at UNL)
Goutam Ghoshal: PhD student (started on this project in January 2002 and completed his MS in December 2003; his PhD research explores several new related areas)
Timothy Butler: MS student (partially supported on this project beginning May 2002)
Liyong Yang: PhD student (started on this project in October 2001 and completed his PhD in December 2003; currently a Res. Assistant Professor at UNL)
Dalie Liu: PhD student (started on this project in August 2002; partial TA match; will graduate in 2006)

Publications

The following publications include a statement acknowledging support from this grant:

(i) *Journal Publications*

G. Ghoshal and J. A. Turner, "Ultrasonic backscatter in two-dimensional domains," *in preparation*.

G. Ghoshal, J. A. Turner, and R. L. Weaver, "Radiative transfer and Wigner distributions for waves in random elastic media," *in preparation*.

D. Liu and J. A. Turner, "Spatial correlations and ultrasonic attenuation in two-phase materials," *in preparation*.

D. Liu and J. A. Turner, "Numerical models for elastic wave scattering in compact metal sinters," *in preparation*.

J. A. Turner, "Evolution of diffuse fields in heterogeneous slabs," *in preparation*.

L. Yang and J. A. Turner, "Generalized model for ultrasonic attenuation in recrystallizing media," *in preparation.*

L. Yang, G. Ghoshal, and J. A. Turner, "Ultrasonic backscatter in recrystallizing media," *in preparation.*

J. A. Turner and L. Yang, "Anisotropic diffusion of elastic waves," *in preparation*.

G. Ghoshal and J. A. Turner, "Numerical models of longitudinal wave scattering in polycrystals," *Ultrasonics* (*under revision* 2005).

L. Yang and J. A. Turner, "Attenuation of ultrasonic waves in rolled metals," *Journal of the Acoustical Society of America* **116**, 3319-3327 (2004).

J. A. Turner and D. C. Hurley, "Ultrasonic methods in contact atomic force microscopy," *Instrumentation, Mesure, Métrologie* **3,** 117-148 (2003).

(ii) *Theses and Dissertations*
Goutam Ghoshal (MS, December 2003), "Numerical simulations of elastic wave scattering in polycrystalline materials."

Liyong Yang (PhD, December 2003), "Scattering of elastic waves in statistically anisotropic media."

Goutam Ghoshal (PhD Dissertation, expected 2006)

Dalie Liu (PhD Dissertation, expected 2006)

Timothy Butler (MS Thesis, expected 2006)

Presentations/Interactions/Transitions

Presentations/Abstracts

J. A. Turner and G. Ghoshal, "Simulations of elastic wave propagation through Voronoi polycrystals," *J. Acoust. Soc. Am.* **112**, 2439 (2002).

J. A. Turner and L. Yang, "Anisotropic diffusion of elastic waves," *J. Acoust. Soc. Am*. **112**, 2296 (2002).

G. Ghoshal and J. A. Turner, "Numerical Models of Elastic Wave Scattering in Voronoi Polycrystals," proceedings of the 2003 SPIE Conference on Smart NDE and Health Monitoring of Structural and Biological Systems, March 3-7, 2003, San Diego California.

J. A. Turner and G. Ghoshal, "Simulations of Elastic Wave Propagation through Voronoi Polycrystals," presented at *Ultrasonics International*, Granada, Spain (2003).

L. Yang and J. A. Turner, "Scattering of Elastic Waves in Textured Media," presented at the 147th meeting of the Acoustical Society of America, New York, New York (2004).

J. A. Turner and G. Ghoshal, "Ultrasonic Attenuation in Voronoi Polycrystals," presented at the 147th meeting of the Acoustical Society of America, New York, New York (2004).

J. A. Turner, G. Ghoshal, P. Haldipur, F. J. Margetan, R. B. Thompson, "Influence of spatial correlation function on ultrasonic attenuation and backscatter," presented at the *Review of Progress in Quantitative NDE*, Golden, CO (2004).

G. Ghoshal and J. A. Turner, "Numerical models of ultrasonic backscatter response in polycrystals, presented at the *Review of Progress in Quantitative NDE*, Golden, CO (2004).

L. Yang and J. A. Turner, "Angular dependence of wave attenuation in textured media," presented at the *Review of Progress in Quantitative NDE*, Golden, CO (2004).

L. Yang and J. A. Turner, "Scattering of Elastic Waves in Statistically Anisotropic Media," presented at the 41st meeting of the Society of Engineering Science, October 10-13, Lincoln, Nebraska (2004).

G. Ghoshal and J. A. Turner, "Numerical Models for Ultrasonic Scattering in Polycrystals," presented at the 41st meeting of the Society of Engineering Science, October 10-13, Lincoln, Nebraska (2004).

G. Ghoshal and J. A. Turner, "Numerical Models for Ultrasonic Scattering in Polycrystals," ISNT-NDE, Pune, India (2004).

J. A. Turner and G. Ghoshal, "Evolution of diffuse fields in heterogeneous slabs," presented at Acoustical Society of America, Vancouver, Canada, *J. Acoust. Soc. Am.* **117**, 2394 (invited) (2005).

G. Ghoshal and J. A. Turner, "Ultrasonic backscatter in two-dimensional domains," presented at Acoustical Society of America, Vancouver, Canada, *J. Acoust. Soc. Am.* **117**, 2560 (2005).

J. A. Turner, "Time domain evolution of diffuse fields in heterogeneous slabs," presented presented at Acoustical Society of America, Minneapolis, *J. Acoust. Soc. Am.* **118**, 1957 (2005).

G. Ghoshal and J. A. Turner, "Monte Carlo simulations of elastic wave multiple scattering in polycrystalline media," presented at Acoustical Society of America, Minneapolis, *J. Acoust. Soc. Am.* **118**, 1957 (2005).

L. Yang and J. A. Turner, "Propagation of elastic waves in hexagonal crystals with fiber texture," presented at Acoustical Society of America, Minneapolis, *J. Acoust. Soc. Am.* **118**, 1957 (2005).

D. Liu and J. A. Turner, "Ultrasonic scattering in two-phase polycrystalline media," presented at Acoustical Society of America, Minneapolis, *J. Acoust. Soc. Am.* **118**, 1958 (2005).

Interactions. Collaborative work with Dr. Thompson of the Ames Laboratory (AL) and others continued throughout the funding period of this grant. In March 2002, the PI and PhD student (L. Yang) visited AL to complete the general training necessary for conducting experiments in AL. In addition, Mr. Yang received fundamental training for the experiments to be conducted. He returned in summer 2002 for several days to complete a series of ultrasonic attenuation experiments on pure aluminum with rolling texture. Dr. Foley produced a set of sintered aluminum samples in December 2002 with varying degrees of sintering. These are being used for attenuation, backscatter, and AFAM measurements. The PI and students made several other trips to AL and the Center for NDE for discussions of the latest accomplishments and the research directions as part of this grant.

Transitions. In conjunction with this research project, the analyses and calculations used for the research are being developed into web-based calculation tools as part of an on-line library of such tools (http://em-jaturner.unl.edu/calcs.htm). The first of these tools calculates a two-dimensional Voronoi polycrystal as a function of user input parameters. Currently, users may input the number of grains, the grain aspect ratio and grain orientation angle. The information is then passed to a MATLAB program that performs the calculations. The output is then posted in plot format in the browser frame (see example in Fig. 21). A new tool that calculates ultrasonic backscatter given specific input of material, transducer, and input wave is nearing completion. These tools will be continually expanded to include other research topics as the project progresses. All tools are included in the on-line calculation tool library.

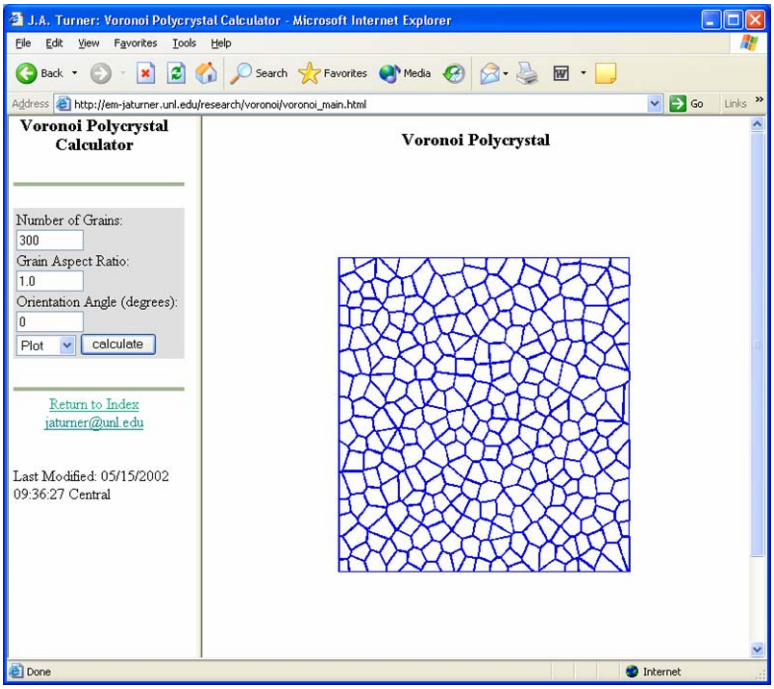

Figure 21. Output of a web-based Voronoi polycrystal calculator developed by the PI and students (see http://em-jaturner.unl.edu/calcs.htm for this and other tools).

Attenuation of ultrasonic waves in rolled metals

Liyong Yang and Joseph A. Turner[a)]
Department of Engineering Mechanics, Center for Materials Research and Analysis, W317.4 Nebraska Hall, University of Nebraska—Lincoln, Lincoln, Nebraska 68588-0526

(Received 12 March 2004; revised 31 August 2004; accepted 1 September 2004)

Scattering of ultrasonic waves in polycrystals with texture is studied in this article. The attenuations of the three wave modes are determined as a function of dimensionless frequency and propagation direction, respectively, for given orientation distribution coefficients (ODCs). The calculation is done in the case of a statistically orthorhombic sample made up of cubic crystallites. The wave propagation and scattering model is formulated by the Dyson equation using an anisotropic Green's function approach. Within the limits of the first-order smoothing approximation, the Dyson equation is solved in the spatial Fourier transform domain. The results presented are shown to be directional dependent, frequency dependent, and especially dependent on the texture coefficients (ODCs) for the quasilongitudinal and two quasishear waves. The theoretical results presented may be used to improve the understanding of the microstructure during recrystallization processes. © *2004 Acoustical Society of America.* [DOI: 10.1121/1.1810236]

PACS numbers: 43.20.Bi, 43.20.Gp, 43.35.Cg [YHB] Pages: 3319–3327

I. INTRODUCTION

Metals and alloys are made of crystallite grains whose characteristics and arrangements can be changed by the application of heat processing, such as annealing. Microstructural parameters of metals determine the macroscopic mechanical properties of a material and include the grain size, grain shape, and the orientation of the grains, or texture, and their distribution in the microstructure. Ultrasonic waves propagating in such aggregates lose energy due to scattering from the granular microstructure of these materials. This scattering is often characterized by the attenuation of the medium. In general, the attenuation and wave velocity are dependent on the grain size, shape, and on the particular orientation distributions of the grains. If the grains are randomly oriented such that the medium is statistically isotropic, these propagation properties are independent of direction. However, the scattering attenuation and wave velocity are a function of the propagation direction if the grains have a preferred orientation. The preferred orientation of grains, or texture, is best quantitatively described by the orientation distribution function (ODF) defining a probability density function, which is usually expanded in a series of generalized spherical harmonics (Roe, 1965, 1966; Bunge, 1982). Often, most metallic materials with preferred orientation of grains display anisotropy of material properties. Therefore, knowledge of the anisotropic nature of the wave propagation and scattering in textured materials such as attenuation and velocity is critical for use with ultrasonic nondestructive techniques. Such information will provide valuable insight for modeling the microstructure of such complex materials during processing.

The scattering of elastic waves by grains of polycrystals has received considerable attention. The most recent contributions for cubic symmetry with uniformly distributed orientations of grains were made by Hirsekorn (1982, 1983), Stanke (1984), and Weaver (1990). The problem of wave propagation and scattering in the case of polycrystalline grains with an aligned [001] axis has been examined by Ahmed and Thompson (1996) and Turner (1999). In that particular case, the average medium is statistically transversely isotropic. Ahmed and Thompson (1992, 1996) also studied correlations defined by both equiaxed grains and grains with elongation.

During the recrystallization process of metals, such as annealing, the microstructure may contain grains having preferred crystallographic orientations. For rolling texture, there are three orthogonal axes of symmetry which are defined as the rolling, transverse, and normal directions. Thus, the material properties of this specific case may be assumed orthorhombic due to the feature of the preferred orientation. Hirsekorn (1985) also was one of the first to investigate the wave scattering in polycrystals of cubic symmetry with rolling texture as a function of frequency by using the perturbation approach. She then extended her theory to determine the directional dependence of the phase velocities and attenuations of the three wave types under the same assumption with fiber texture (Hirsekorn, 1986). Her discussions were restricted to waves propagating in the direction of an axis of symmetry of the texture. The general formalism of the waves propagating in any direction through polycrystalline metals with rolling texture, however, has not yet been reported. The detailed wave velocities of the three wave types, inclusive of the quasilongitudinal and two quasishear waves, have been discussed elsewhere (Sayers, 1982; Johnson, 1985; Hirao *et al.*, 1987; Li and Thompson, 1990) under the assumption of orthorhombic-cubic symmetry.

In this article, the more sensitive ultrasonic parameter, scattering attenuation, is studied for waves propagating in any direction through such textured media. The wave propagation and scattering model is formulated using the Dyson

[a)]Author to whom correspondence should be addressed. Electronic mail: jaturner@unl.edu

equation studied by Frisch (1968) and Weaver (1990) which is easily solved in the spatial Fourier transform domain within the limits of the first-order smoothing approximation (FOSA) or Keller (Karal and Keller, 1964) approximation. The problem is studied here using the anisotropic Green's dyadic, an approach not used previously for textured materials. The attenuations of the three wave types are calculated numerically as a function of dimensionless frequency and propagation direction, respectively, for given orientation distribution coefficients (ODCs) using the derived expressions. The resulting attenuations are shown to be directional dependent, frequency dependent, and dependent on the texture coefficients (ODCs) for the quasilongitudinal and two quasishear waves. The theoretical results presented may be used to improve the understanding of the microstructure during the recrystallization process. In addition, the present formulation may be used to study diffuse ultrasonic problems in a straightforward manner. Although the present model is for the case of orthorhombic-cubic symmetry, the formalism can be easily modified to apply to other given symmetry cases.

In the next section, the preliminary elastodynamics of elastic wave propagation and scattering is introduced in terms of an anisotropic Green's dyadic. The formalism of the attenuation is then developed for the anisotropic case of orthorhombic-cubic symmetry.

II. WAVE PROPAGATION AND SCATTERING MODEL

The equation of motion for the elastodynamic response of an infinite, linear-elastic material to deformation is given in terms of the Green's dyadic by

$$\{-\delta_{jk}\rho\partial_t^2+\partial x_i C_{ijkl}(\mathbf{x})\partial x_l\}G_{k\alpha}(\mathbf{x},\mathbf{x}';t) = \delta_{j\alpha}\delta^3(\mathbf{x}-\mathbf{x}')\,\delta(t), \tag{1}$$

where $\delta^3(\mathbf{x}-\mathbf{x}')$ is the three-dimensional spatial Delta function. The second-order Green's dyadic, $G_{k\alpha}(\mathbf{x},\mathbf{x}';t)$, defines the response at location $\mathbf{x}$ in the kth direction to a unit impulse at location $\mathbf{x}'$ in the αth direction. The moduli are considered to vary spatially and density is assumed uniform throughout. In the case of orthorhombic-cubic symmetry, the moduli $\mathbf{C}$ are supposed to be spatially heterogeneous and have the form $C_{ijkl}(\mathbf{x})=C^0_{ijkl}+\delta C_{ijkl}(\mathbf{x})$. The material properties might have global anisotropy such that the mean moduli are not necessarily isotropic. The covariance of the moduli is characterized by an eighth-rank tensor

$$\langle \delta C_{ijkl}(\mathbf{x})\,\delta C_{\alpha\beta\gamma\delta}(\mathbf{x}')\rangle = \Xi^{\alpha\beta\gamma\delta}_{ijkl}\eta(\mathbf{x}-\mathbf{x}'). \tag{2}$$

The spatial and tensorial parts of the above covariance, Ξ and η, are assumed independent. The correlation function η is also assumed a function of the difference between two vectors, $\mathbf{x}-\mathbf{x}'$. This assumption implies that the medium is statistically homogeneous.

The mean response, $\langle\mathbf{G}\rangle$, is governed by the Dyson equation (Weaver, 1990; Frisch, 1968)

$$\langle G_{i\alpha}(\mathbf{x},\mathbf{x}')\rangle = G^0_{i\alpha}(\mathbf{x},\mathbf{x}') + \int\int G^0_{i\beta}(\mathbf{x},\mathbf{y})M_{\beta j}(\mathbf{y},\mathbf{z}) \times\langle G_{j\alpha}(\mathbf{z},\mathbf{x}')\rangle d^3y\,d^3z. \tag{3}$$

In Eq. (3), the quantity $\mathbf{G}^0$ is the bare Green's dyadic defined as the ensemble average response of the medium without fluctuations, namely, the solution to Eq. (1) when $\delta C_{ijkl}(\mathbf{x})=0$. The second order tensor $\mathbf{M}$ is the mass or self-energy operator. The Dyson equation, Eq. (3), is easily solved in the Fourier transform domain under the assumption of statistical homogeneity. The assumption of statistical homogeneity ensures that $\mathbf{G}^0$, $\mathbf{M}$, and $\langle\mathbf{G}\rangle$ are functions of a single wave vector in Fourier space. The Dyson equation is then transformed and solved to give the result for $\langle\mathbf{G}(\mathbf{p})\rangle$ of the form

$$\langle\mathbf{G}(\mathbf{p})\rangle=[\mathbf{G}^0(\mathbf{p})^{-1}-\tilde{\mathbf{M}}(\mathbf{p})]^{-1}, \tag{4}$$

where $\tilde{\mathbf{M}}$ is the spatial transform of the self-energy. The self-energy $\mathbf{M}$ can be written as an expansion in powers of moduli fluctuations. To first order (Frisch, 1968; Karal and Keller, 1964) $\mathbf{M}$ is expressed as (Weaver, 1990)

$$M_{\beta j}(\mathbf{y},\mathbf{z}) \approx\left\langle \frac{\partial}{\partial y_\alpha}\delta C_{\alpha\beta\gamma\delta}(\mathbf{y})\frac{\partial}{\partial y_\delta}G^0_{\gamma k}(\mathbf{y},\mathbf{z})\frac{\partial}{\partial z_i}\delta C_{ijkl}(\mathbf{z})\frac{\partial}{\partial z_l}\right\rangle. \tag{5}$$

Such an approximation is assumed valid if the fluctuations, $\delta\mathbf{C}$, are not too large. The components of $\tilde{\mathbf{M}}$ are employed to calculate the attenuation of the three wave modes. Further details of the scattering theory can be reviewed by the reader in the articles of Karal and Keller (1964), Frisch (1968), Stanke and Kino (1984), Weaver (1990), and Turner (1999).

The medium of oriented grains with rolling texture has orthorhombic symmetry. When ultrasonic waves propagate in such media, the phase velocity and the associated polarization vector are determined by the Christoffel equation. The dispersion relations for the mean response are then given by the solution of the Dyson equation, Eq. (4), as

$$g_\beta(\mathbf{p})=[g^0_\beta(\mathbf{p})^{-1}-m_\beta(\mathbf{p})]^{-1} =[\omega^2-p^2c_\beta^2-m_\beta(\mathbf{p})]^{-1}, \tag{6}$$

for each wave type, β, quasilongitudinal (qP) and two quasishear ($qS1$ and $qS2$) waves. The expressions for the dispersion relations of the mean response are written

$$\omega^2-p^2c_\beta^2-m_\beta(\mathbf{p})=0, \tag{7}$$

which is solved for the wave vector $\mathbf{p}$. The attenuation of each wave type is given by the imaginary part of $\mathbf{p}$. The explicit expressions of the attenuation can be determined using an approximation valid below the high-frequency geometric optics limit [$m_\beta(\mathbf{p})\approx m_\beta((\omega/c_\beta)\hat{\mathbf{p}})$] (Stanke and Kino, 1984; Weaver, 1990). This approximation allows the imaginary part of $\mathbf{p}$ to be calculated directly from Eq. (7). Thus, the attenuations of the three wave types are calculated as

$$\alpha_\beta(\hat{\mathbf{p}})=-\frac{1}{2\omega c_\beta(\hat{\mathbf{p}})}\,\mathrm{Im}\,m_\beta\left(\frac{\omega}{c_\beta}\hat{\mathbf{p}}\right). \tag{8}$$

The attenuations for the three wave types, which are each defined in Eq. (8), are finally given in the general form (Turner, 1999)

$$\alpha_\beta(\hat{\mathbf{p}})=\frac{1}{c_\beta^3(\hat{\mathbf{p}})}\left\{\frac{\pi}{4}\int d^2\hat{s}\,\frac{\omega^4}{c_{qS1}^5(\hat{\mathbf{s}})}\,\tilde{\eta}\left(\frac{\omega}{c_\beta(\hat{\mathbf{p}})}\hat{\mathbf{p}}-\frac{\omega}{c_{qS1}(\hat{\mathbf{s}})}\hat{\mathbf{s}}\right)^{\cdots\hat{\mathbf{u}}_K\hat{\mathbf{p}}\hat{\mathbf{s}}\mathbf{v}_1}_{\cdots\hat{\mathbf{u}}_K\hat{\mathbf{p}}\hat{\mathbf{s}}\mathbf{v}_1}\right.$$
$$+\frac{\pi}{4}\int d^2\hat{s}\,\frac{\omega^4}{c_{qP}^5(\hat{\mathbf{s}})}\,\tilde{\eta}\left(\frac{\omega}{c_\beta(\hat{\mathbf{p}})}\hat{\mathbf{p}}-\frac{\omega}{c_{qP}(\hat{\mathbf{s}})}\hat{\mathbf{s}}\right)\Xi^{\cdots\hat{\mathbf{u}}_K\hat{\mathbf{p}}\hat{\mathbf{s}}\mathbf{v}_2}_{\cdots\hat{\mathbf{u}}_K\hat{\mathbf{p}}\hat{\mathbf{s}}\mathbf{v}_2}$$
$$\left.+\frac{\pi}{4}\int d^2\hat{s}\,\frac{\omega^4}{c_{qS2}^5(\hat{\mathbf{s}})}\,\tilde{\eta}\left(\frac{\omega}{c_\beta(\hat{\mathbf{p}})}\hat{\mathbf{p}}-\frac{\omega}{c_{qS2}(\hat{\mathbf{s}})}\hat{\mathbf{s}}\right)\Xi^{\cdots\hat{\mathbf{u}}_K\hat{\mathbf{p}}\hat{\mathbf{s}}\mathbf{v}_3}_{\cdots\hat{\mathbf{u}}_K\hat{\mathbf{p}}\hat{\mathbf{s}}\mathbf{v}_3}\right\},\tag{9}$$

where K is defined as the polarization for the wave type β (1, 2, or 3 for wave types $qS1$, qP, and $qS2$, respectively). In the above equation, the integrals are over the unit sphere, which is defined by unit vector $\hat{\mathbf{s}}$. The direction $\hat{\mathbf{p}}$ defines the propagation direction, $\hat{\mathbf{s}}$ is the scattered direction, and $\hat{\mathbf{u}}$ and $\hat{\mathbf{v}}$ are defined as the polarization directions. The dependence of the vectors $\hat{\mathbf{u}}$ on $\hat{\mathbf{p}}$ and of $\hat{\mathbf{v}}$ on $\hat{\mathbf{s}}$ is implicit. The argument of $\tilde{\eta}$ is the difference between the incoming and outgoing propagation directions. The inner products on the covariance of the moduli fluctuations are given in terms of four unit vectors. In the next section, the correlation function is specified.

III. CORRELATION FUNCTION

As shown in Eq. (2), the tensorial and spatial contributions of the material covariance are assumed independent. The spatial correlations are characterized by η. Here, it is assumed that η has an exponential form

$$\eta(\mathbf{r})=e^{-r/L}.\tag{10}$$

The correlation length, L, is of the order of the grain radius in polycrystals. In general, a simple exponential form of the spatial correlation function is not exact for polycrystals with rolling texture for which there is grain elongation. For elongated grains, a more general spatial correlation function must be used (Ahmed and Thompson, 1992). The influence of this choice of correlation function on the attenuations is left as a subject of future investigations. In Fourier transform space, the correlation function is then given by

$$\tilde{\eta}(\mathbf{q})=\frac{L^3}{\pi^2(1+L^2q^2)^2}.\tag{11}$$

The forms of the attenuation given above contain the difference of two vectors, $\tilde{\eta}(\mathbf{q})=\tilde{\eta}([\omega/c_1(\theta)]\hat{\mathbf{p}}-[\omega/c_2(\theta')]\hat{\mathbf{s}})$ as the argument for covariance in Eq. (2). Now the correlation functions $\tilde{\eta}_{\beta-\gamma}(\hat{\mathbf{p}},\hat{\mathbf{s}})$ are considered. If the three nondimensional frequencies are then defined as $x_\beta=\omega L/c_\beta$, using the expression of the spatial Fourier transform of the correlation function in Eq. (11), the functions $\tilde{\eta}_{\beta-\gamma}(\hat{\mathbf{p}},\hat{\mathbf{s}})$ are then expressed in terms of the above dimensionless quantities as

$$\tilde{\eta}_{\beta-\gamma}(\hat{\mathbf{p}},\hat{\mathbf{s}})=\frac{L^3}{\pi^2(1+x_\beta^2(\phi)+x_\gamma^2(\phi')-2x_\beta(\phi)x_\gamma(\phi')\hat{\mathbf{p}}\cdot\hat{\mathbf{s}})^2},\tag{12}$$

for the incoming wave type β and outgoing wave type γ. The inner product, $\hat{\mathbf{p}}\cdot\hat{\mathbf{s}}=\cos\phi\cos\phi'\sin\theta\sin\theta'+\sin\phi\sin\phi'\sin\theta\sin\theta'+\cos\theta\cos\theta'$, if the unit vectors $\hat{\mathbf{p}}$ and $\hat{\mathbf{s}}$ are generally defined by $\hat{\mathbf{p}}=\mathbf{x}_1\cos\phi\sin\theta+\mathbf{x}_2\sin\phi\sin\theta+\mathbf{x}_3\cos\theta$ and $\hat{\mathbf{s}}=x_1\cos\phi'\sin\theta'+\mathbf{x}_2\sin\phi'\sin\theta'+\mathbf{x}_3\cos\theta'$. The angles θ, ϕ and θ', ϕ' are respectively defined as Euler angles in a general coordinate system. The form of the eighth-rank tensor, $\Xi_{ijkl}^{\alpha\beta\gamma\delta}$, is discussed next for rolling texture made up of cubic crystallites.

IV. COVARIANCE AND ATTENUATION

To calculate the attenuations, the relevant inner products on the covariance of the moduli fluctuations are required. The covariance of the moduli fluctuations is represented by an eighth-rank tensor which is given explicitly by

$$\Xi^{\cdots\hat{\mathbf{u}}\hat{\mathbf{p}}\hat{\mathbf{s}}\hat{\mathbf{v}}}_{\cdots\hat{\mathbf{u}}\hat{\mathbf{p}}\hat{\mathbf{s}}\hat{\mathbf{v}}}=\Xi_{\alpha\beta\gamma\delta}^{ijkl}\hat{u}_\beta\hat{u}_k\hat{p}_\alpha\hat{p}_l\hat{s}_i\hat{s}_\delta\hat{v}_\gamma\hat{v}_j.\tag{13}$$

For polycrystals of cubic symmetry, the eighth-rank covariance, $\Xi_{ijkl}^{\alpha\beta\gamma\delta}$, is written as

$$\Xi_{ijkl}^{\alpha\beta\gamma\delta}=\langle C_{ijkl}C_{\alpha\beta\gamma\delta}\rangle-\langle C_{ijkl}\rangle\langle C_{\alpha\beta\gamma\delta}\rangle$$
$$=\kappa^2\left\langle\sum_{n=1}^{3}a_{in}a_{jn}a_{kn}a_{ln}\sum_{n=1}^{3}a_{\alpha n}a_{\beta n}a_{\gamma n}a_{\delta n}\right\rangle$$
$$-\kappa^2\left\langle\sum_{n=1}^{3}a_{in}a_{jn}a_{kn}a_{ln}\right\rangle$$
$$-\left\langle\sum_{n=1}^{3}a_{\alpha n}a_{\beta n}a_{\gamma n}a_{\delta n}\right\rangle,\tag{14}$$

where the brackets, $\langle\ \rangle$, denote an ensemble average over all orientations of grains, and $\kappa=C_{11}^0-C_{12}^0-2C_{44}^0$ is the single-crystal anisotropy factor. If the polycrystal is of orthorhombic-cubic symmetry, only certain terms are nonzero. An example term necessary for calculating the attenuations is presented in the Appendix. Details of the other nonzero terms may be found elsewhere (Yang, 2003). For the second term in Eq. (14), the results are given in the details of other articles (Sayers, 1982; Johnson, 1985; Hirao *et al.*, 1987; Li and Thompson, 1990).

The forms of the attenuations presented in Eq. (9) require various inner products on the covariance tensor. These inner products have the general form of $\Xi^{\cdots\hat{\mathbf{u}}\hat{\mathbf{p}}\hat{\mathbf{s}}\hat{\mathbf{v}}}_{\cdots\hat{\mathbf{u}}\hat{\mathbf{p}}\hat{\mathbf{s}}\hat{\mathbf{v}}}$, where the vectors $\hat{\mathbf{p}}$ and $\hat{\mathbf{s}}$, respectively, represent the incoming and outgoing propagation directions. The vectors $\hat{\mathbf{u}}$ and $\hat{\mathbf{v}}$ are vectors defining the polarization directions of the particular waves. While waves propagate in arbitrary directions, the polarization vectors are found by the Christoffel equation. Substituting the correlation function, Eq. (12), and the inner products into Eq. (9), the resulting dimensionless attenuations are given in the form

$$\alpha_\beta(\hat{\mathbf{p}})L=\frac{x_\beta^4 c_\beta(\hat{\mathbf{p}})}{2\rho^2}\times\left\{\int_{4\pi}\frac{\Xi^{\cdots\hat{\mathbf{u}}_K\hat{\mathbf{p}}\hat{\mathbf{s}}\hat{\mathbf{v}}_1}_{\cdots\hat{\mathbf{u}}_K\hat{\mathbf{p}}\hat{\mathbf{s}}\hat{\mathbf{v}}_1}(\hat{\mathbf{p}},\hat{\mathbf{s}})}{(1+x_\beta^2(\hat{\mathbf{p}})+x_{qS1}^2(\hat{\mathbf{s}})-2x_\beta(\hat{\mathbf{p}})x_{qS1}(\hat{\mathbf{s}})\hat{\mathbf{p}}\cdot\hat{\mathbf{s}})^2}\frac{1}{c_{qS1}^5(\hat{\mathbf{s}})}d^2\hat{s}\right.$$
$$+\int_{4\pi}\frac{\Xi^{\cdots\hat{\mathbf{u}}_K\hat{\mathbf{p}}\hat{\mathbf{s}}\hat{\mathbf{v}}_2}_{\cdots\hat{\mathbf{u}}_K\hat{\mathbf{p}}\hat{\mathbf{s}}\hat{\mathbf{v}}_2}(\hat{\mathbf{p}},\hat{\mathbf{s}})}{(1+x_\beta^2(\hat{\mathbf{p}})+x_{qP}^2(\hat{\mathbf{s}})-2x_\beta(\hat{\mathbf{p}})x_{qP}(\hat{\mathbf{s}})\hat{\mathbf{p}}\cdot\hat{\mathbf{s}})^2}\frac{1}{c_{qP}^5(\hat{\mathbf{s}})}d^2\hat{s}$$
$$\left.+\int_{4\pi}\frac{\Xi^{\cdots\hat{\mathbf{u}}_K\hat{\mathbf{p}}\hat{\mathbf{s}}\hat{\mathbf{v}}_3}_{\cdots\hat{\mathbf{u}}_K\hat{\mathbf{p}}\hat{\mathbf{s}}\hat{\mathbf{v}}_3}(\hat{\mathbf{p}},\hat{\mathbf{s}})}{(1+x_\beta^2(\hat{\mathbf{p}})+x_{qS2}^2(\hat{\mathbf{s}})-2x_\beta(\hat{\mathbf{p}})x_{qS2}(\hat{\mathbf{s}})\hat{\mathbf{p}}\cdot\hat{\mathbf{s}})^2}\frac{1}{c_{qS2}^5(\hat{\mathbf{s}})}d^2\hat{s}\right\},\tag{15}$$

where K has the same definition as discussed in Eq. (9). It should be noted that these inner products have units of κ^2. In the long wavelength Rayleigh limit, $x_\beta \ll 1$, Eq. (15) can be simplified as

$$\alpha_\beta(\hat{\mathbf{p}})L/x_\beta^4=\frac{c_\beta(\hat{\mathbf{p}})}{2\rho^2}\times\left\{\int_{4\pi}\frac{\Xi^{\cdots\hat{\mathbf{u}}_K\hat{\mathbf{p}}\hat{\mathbf{s}}\hat{\mathbf{v}}_1}_{\cdots\hat{\mathbf{u}}_K\hat{\mathbf{p}}\hat{\mathbf{s}}\hat{\mathbf{v}}_1}}{c_{qS1}^5(\hat{\mathbf{s}})}d^2\hat{s}\right.$$
$$\left.+\int_{4\pi}\frac{\Xi^{\cdots\hat{\mathbf{u}}_K\hat{\mathbf{p}}\hat{\mathbf{s}}\hat{\mathbf{v}}_2}_{\cdots\hat{\mathbf{u}}_K\hat{\mathbf{p}}\hat{\mathbf{s}}\hat{\mathbf{v}}_2}}{c_{qP}^5(\hat{\mathbf{s}})}d^2\hat{s}+\int_{4\pi}\frac{\Xi^{\cdots\hat{\mathbf{u}}_K\hat{\mathbf{p}}\hat{\mathbf{s}}\hat{\mathbf{v}}_3}_{\cdots\hat{\mathbf{u}}_K\hat{\mathbf{p}}\hat{\mathbf{s}}\hat{\mathbf{v}}_3}}{c_{qS2}^5(\hat{\mathbf{s}})}d^2\hat{s}\right\}.\tag{16}$$

In Eq. (16), the dimensionless attenuation has been normalized by the fourth power of the dimensionless frequency for the respective wave type.

In Eqs. (15) and (16) the inner products, $\Xi^{\cdots\hat{\mathbf{u}}\hat{\mathbf{p}}\hat{\mathbf{s}}\hat{\mathbf{v}}}_{\cdots\hat{\mathbf{u}}\hat{\mathbf{p}}\hat{\mathbf{s}}\hat{\mathbf{v}}}$, do not have simple analytical forms for arbitrary propagation direction in this orthorhombic-cubic case. Thus, these results must be calculated numerically. In the next section, example numerical results and discussions are presented.

V. NUMERICAL RESULTS AND DISCUSSIONS

Numerical results are now presented for a 70% rolled steel plate. The material constants of a single crystal and the texture coefficients of the orientation distribution function with respect to the generalized spherical functions are given by (Bunge, 1982)

$$C_{11}^0=2.37\times10^{11}\ \text{Pa},\quad C_{12}^0=1.41\times10^{11}\ \text{Pa},$$
$$C_{44}^0=1.16\times10^{11}\ \text{Pa},\quad \rho=7850\ \text{kg/m}^3,\tag{17}$$

and

$$c_4^{00}=-1.47,\quad c_4^{20}=0.46,$$
$$c_4^{40}=0.50,\quad c_6^{00}=2.69,$$
$$c_6^{20}=-1.20,\quad c_6^{40}=0.46,$$
$$c_6^{60}=-0.14,\quad c_8^{00}=-0.07,\tag{18}$$
$$c_8^{20}=0.29,\quad c_8^{40}=-0.45,$$
$$c_8^{60}=-0.47,\quad c_8^{80}=-0.22.$$

The orientation distribution coefficients (ODCs) in Bunge's notation c_l^{mn} must be converted into those in Roe's notation W_{lmn}, which are used in this discussion. In order to carry out the calculations for the attenuations, Eq. (15), numerical methods are employed. The procedure of numerical methods for calculating the wave attenuations is now described.

First, using the Christoffel equation, the eigenvalue-eigenvector problem is solved for a given wave propagation direction and scattering direction. Second, the covariance of the moduli fluctuations is calculated by Eq. (14). Next, using the known covariance and eigenvectors, the inner products of each wave type are calculated numerically. Finally, the double integration is implemented numerically by the extended trapezoidal method. Here, examples are presented to describe important features of the wave attenuations for several propagation directions. The examples are generated using the methods discussed above. Since the orthorhombic symmetry has three mutually orthogonal planes of symmetry, all calculations are made for $0°\leqslant\phi\leqslant90°$ and $0°\leqslant\theta\leqslant90°$.

Convergence of the numerical integration was examined first. Wave attenuations of each wave type were examined for waves propagating in the rolling direction, that is $\phi=0°$ and $\theta=90°$, and at a dimensionless frequency $x_{qS1}=1.0$. The results show fast convergence for each wave mode in numerical integrations using the extended trapezoidal method (Yang, 2003). In order to achieve a balance between efficiency and accuracy, the number of intervals in the integra-

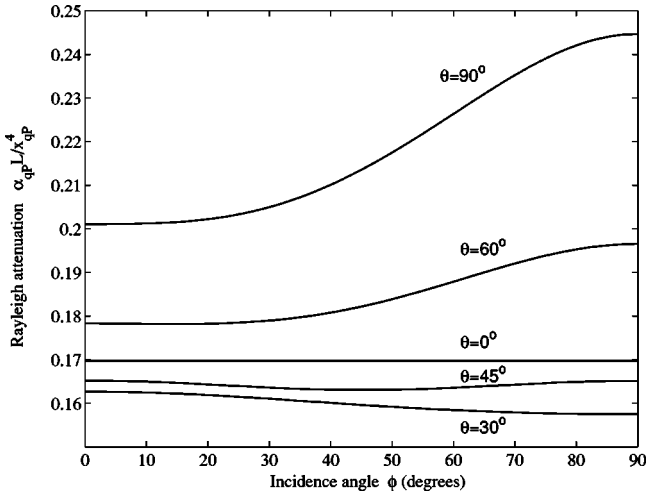

FIG. 1. Rayleigh attenuation, $\alpha_{qP}L/x_{qP}^4$, as a function of propagation direction for qP waves using the specified ODCs.

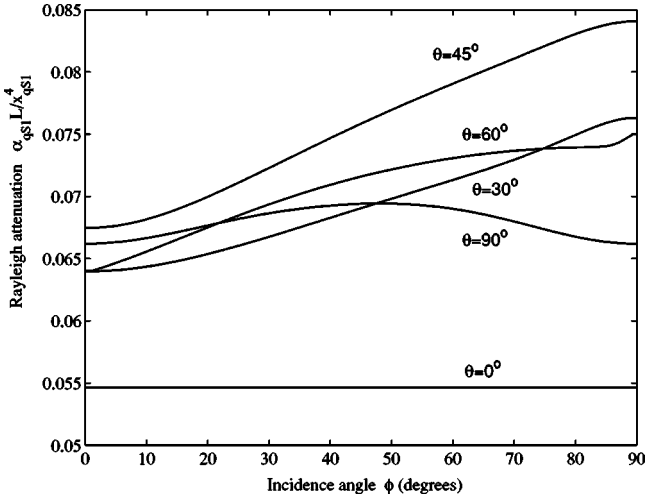

FIG. 2. Rayleigh attenuation, $\alpha_{qS1}L/x^4_{qS1}$, as a function of propagation direction for $qS1$ waves using the specified ODCs.

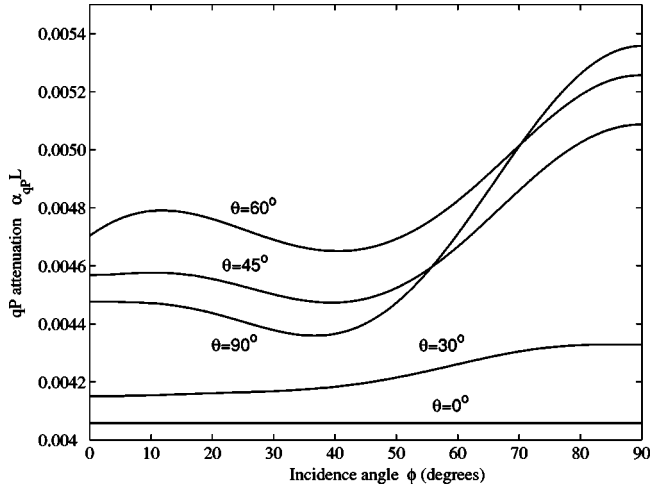

FIG. 4. Directional dependence of the normalized qP attenuation, $\alpha_{qP}L$, for frequency $x_{qS1}=1.0$.

tion $N=20$ is chosen for calculating the attenuations for each wave mode in the results shown here.

First, the attenuations within the Rayleigh limit are calculated using Eq. (16). It is known that the attenuations depend on the fourth power of frequency in the Rayleigh regime. Thus, the normalized Rayleigh attenuation $\alpha_\beta L/x^4_\beta$ of each wave mode is shown with the angular dependence in Figs. 1–3 for various propagation directions, respectively. It is observed that in this specific case the attenuations of each wave mode are considerably dependent on the wave propagation direction. For waves propagating in different directions, the curves of the attenuations have smoothly changing shapes. The percent variations of the qP, $qS1$, and $qS2$ attenuations in terms of polar angle θ shown in Figs. 1–3 are about 25–40%, 20–50%, and 15%, respectively. The variation of the $qS2$ attenuations is more uniform than that of the others.

Outside the Rayleigh regime, the attenuation results are calculated using the complete integrals, Eq. (15). The directional dependence of the attenuation is presented first for a given dimensionless frequency, $x_{qS1}=1.0$. Figure 4 shows the normalized quasilongitudinal wave (qP) attenuation, $\alpha_{qP}L$, as a function of azimuthal direction ϕ for various polar angles θ. It is seen that the attenuation is dependent on the propagation direction as expected. Here, the attenuation variation with respect to polar angle θ is around 15–30%. The results for the normalized shear wave ($qS1$ and $qS2$) attenuations are presented in Figs. 5 and 6, respectively. The directional dependence on the propagation direction for these attenuations is also significant. The percent variation of the $qS1$ and $qS2$ attenuations in terms of polar angle θ is about 10–50%. These results may be contrasted with the results in the Rayleigh limit. Comparisons of the Rayleigh attenuations with attenuations outside the Rayleigh regime show that the tendency of variation is quite different with each due to the effect of frequency. In Fig. 4, the qP wave attenuation is observed to have the maximum at $\phi=90°$ for given angles θ. In Fig. 5, the curves of the $qS1$ wave attenuations have smoothly changing shapes. Figure 6 shows that for propagation at polar angle $\theta=30°$, 45°, and 60°, the maximum attenuation is about $\phi=45°$, and at polar angle $\theta=90°$, there is a minimum attenuation approximately at $\phi=45°$. Further-

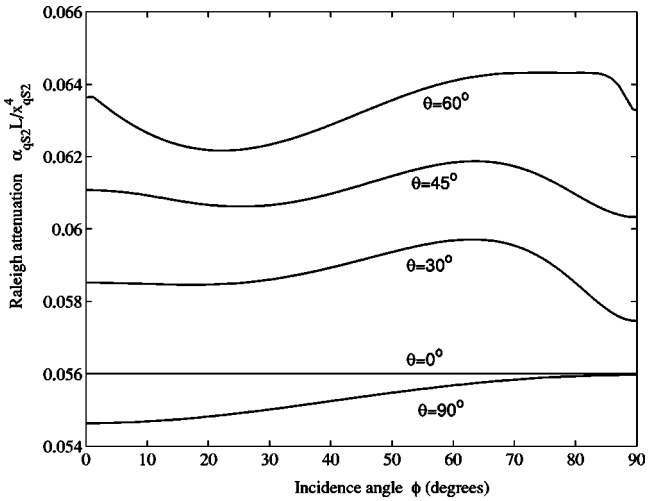

FIG. 3. Rayleigh attenuation, $\alpha_{qS2}L/x^4_{qS2}$, as a function of propagation direction for $qS2$ waves using the specified ODCs.

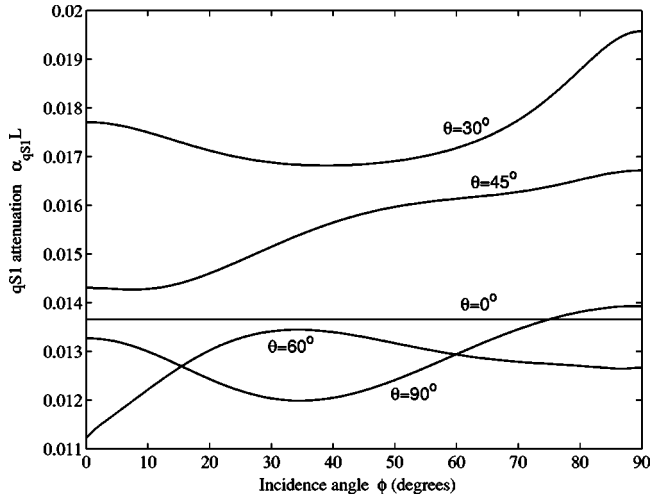

FIG. 5. Directional dependence of the normalized $qS1$ attenuation, $\alpha_{qS1}L$, for frequency $x_{qS1}=1.0$.

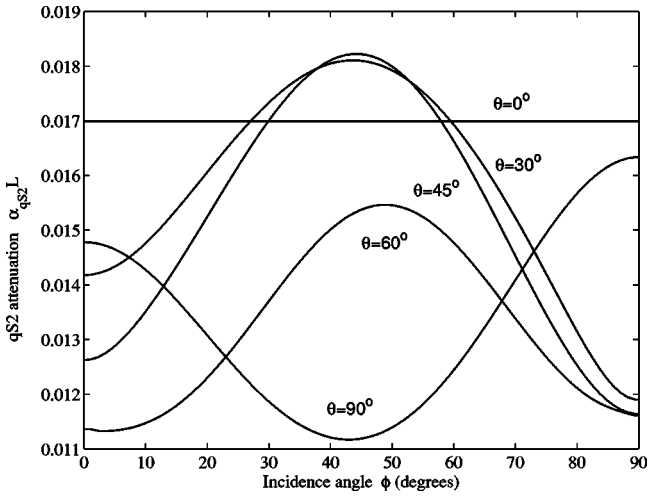

FIG. 6. Directional dependence of the normalized $qS2$ attenuation, $\alpha_{qS2}L$, for frequency $x_{qS1}=1.0$.

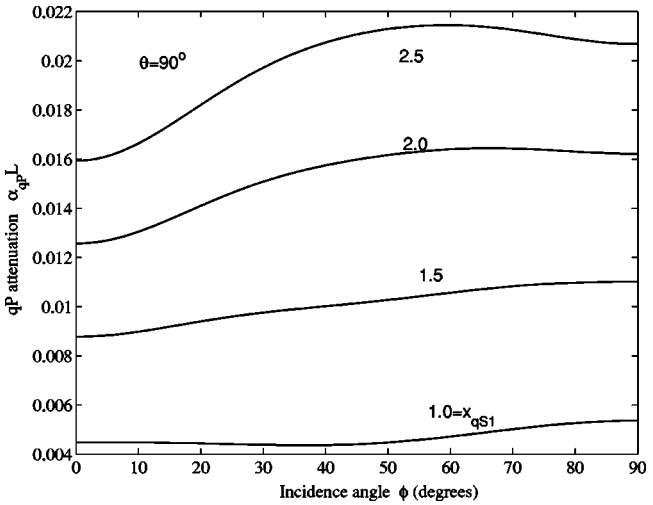

FIG. 8. Angular dependence of the normalized qP attenuation, $\alpha_{qP}L$, for various frequencies, x_{qS1}, at polar angle $\theta=90°$.

more, the asymmetry is observed in Fig. 6 for various polar angles.

Next, results are presented for the normalized attenuation as a function of aximuthal direction ϕ for four different frequencies at given polar angle $\theta=90°$. The normalized shear wave ($qS1$) attenuations, $\alpha_{qS1}L$, are shown in Fig. 7 for $\theta=90°$ for normalized frequencies $x_{qS1}=1.0$, 1.5, 2.0, and 2.5. It is seen that the attenuation curves show a similar shape with increasing frequency for the respective polar angle. The results for the normalized qP attenuations, $\alpha_{qP}L$, are shown in Fig. 8 for the same frequencies. Figure 9 shows the normalized $qS2$ attenuations, $\alpha_{qS2}L$, as a function of propagation direction for the same four frequencies. It is observed that the attenuation curves show a similar shape with increasing frequency for each wave type as well. All curves of the attenuations have smoothly changing shapes for various frequencies. Figure 9 shows that at polar angle $\theta=90°$ there is a minimum attenuation at $\phi=45°$ for various frequencies. There is no symmetry to be observed with increasing frequency as well in Fig. 9.

Finally, results are presented for the normalized attenuations as a function of frequency for several propagation directions. In Figs. 10–12, the normalized attenuations of the three wave modes are plotted versus dimensionless frequency, x_{qS1}, for propagation directions along the rolling, normal, and transverse directions, respectively. For the example considered here, Fig. 11 shows the $qS1$ wave attenuation for propagation in the rolling, normal, and transverse directions with polarization in the normal, transverse, and rolling directions, respectively. Figure 12 shows the $qS2$ wave attenuation propagated in the rolling, normal, and transverse directions and polarized in the transverse, rolling, and normal directions, respectively. It is observed that there is a transition region as the dimensionless frequency increases. Thus, the relative order of the attenuation is switched in such a transition region for the three wave modes, respectively. The attenuations increase with the fourth power of frequency in the low frequency limit. After a transition region, the attenuations scale with the square of frequency as expected. Moreover, the normalized attenuation of each wave type is plotted versus normalized frequency, x_{qS1}, for propagation within the x_1-x_2 plane for various

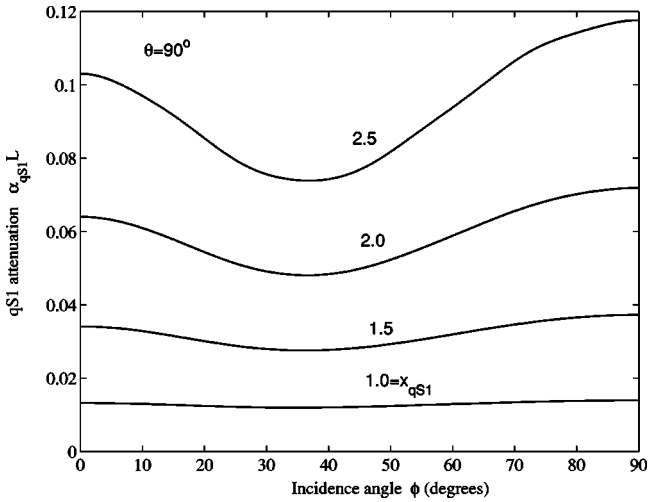

FIG. 7. Angular dependence of the normalized $qS1$ attenuation, $\alpha_{qS1}L$, for various frequencies, x_{qS1}, at polar angle $\theta=90°$.

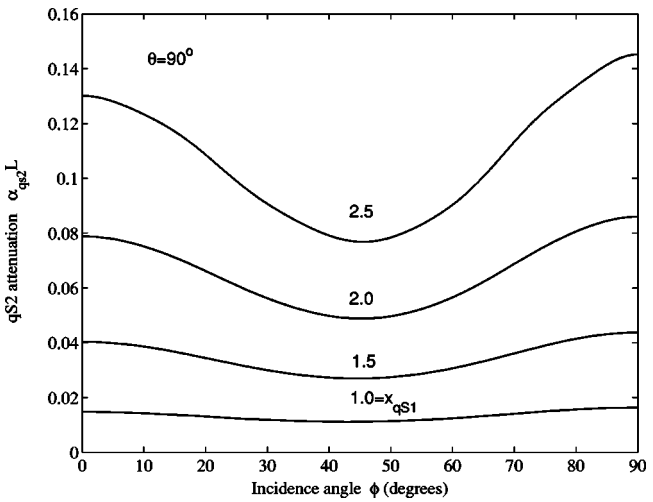

FIG. 9. Angular dependence of the normalized $qS2$ attenuation, $\alpha_{qS2}L$, for various frequencies, x_{qS1}, at polar angle $\theta=90°$.

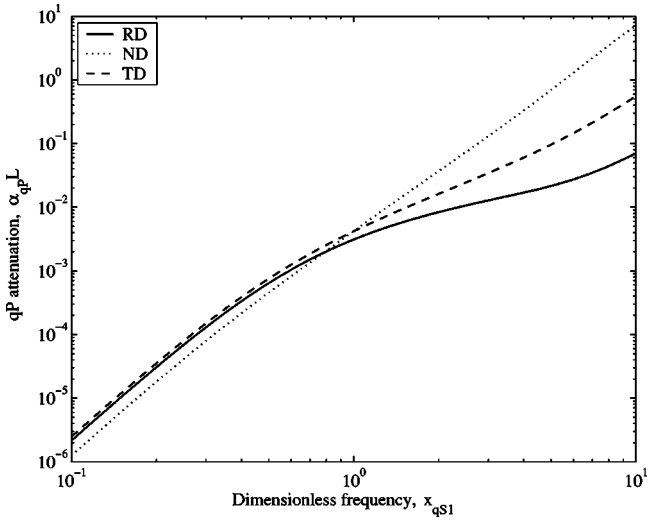

FIG. 10. Normalized qP attenuation, $\alpha_{qP}L$, as a function of dimensionless frequency, x_{qS1}, for waves propagating in the rolling (RD), normal (ND) and transverse (TD) directions.

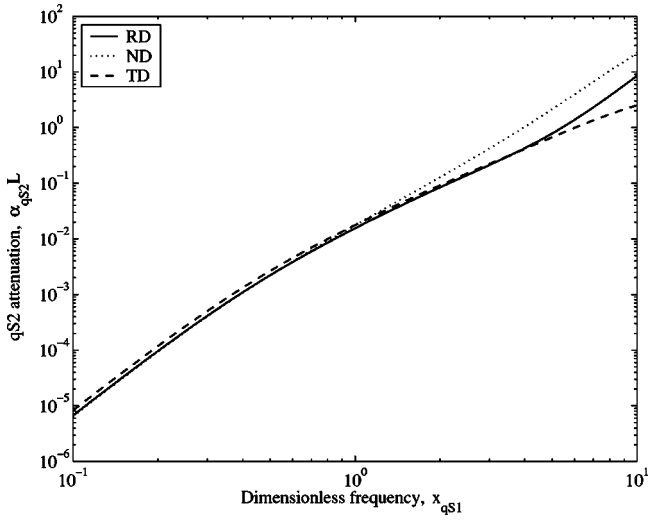

FIG. 12. Normalized $qS2$ attenuation, $\alpha_{qS2}L$, as a function of dimensionless frequency, x_{qS1}, for waves propagating in the rolling (RD), normal (ND) and transverse (TD) directions.

azimuthal angles in Figs. 13–15. In the Rayleigh regime, it is observed that the curves for each wave type mainly show the same shape. The variation of the attenuation of each wave mode is about 10%. Outside the Rayleigh regime, the attenuation of each wave mode in the rolling direction is about ten times higher than that for propagation at $\phi=30°$, 45°, and 60°. This feature is thought to be the result of the weak texture for the case discussed here.

The generalized attenuation results presented in this article for arbitrary propagation direction suggest that new ultrasonic techniques for characterization of texture coefficients may be possible. Further study is necessary to unravel the complex relations between the ODCs and the angular and frequency dependence of the attenuations. Attenuation measurements could ultimately be inverted such that the ODCs may be determined. However, such an approach must be optimized by choosing measurement directions that are the most sensitive to the desired ODC. Thus, theoretical developments such as this one will provide a firm basis for directing new experiments. Eventual process control of recrystallization that is quantitative will require modeling-directed experimental methods. In addition to theoretical research, numerical methods will also be necessary for progress to be made. This work must also be expanded to include other factors important to textured materials, such as grain size distribution and grain shape.

VI. SUMMARY

In this article, the scattering of elastic waves in polycrystalline materials with texture was discussed. The ensemble average response of the elastic waves is governed by the Dyson equation within the limits of first-order smoothing approximation. In contrast with previous work, here an anisotropic Green's dyadic approach was used. In order to calculate the attenuations, the relevant inner products on the covariance of the effective moduli fluctuations were derived

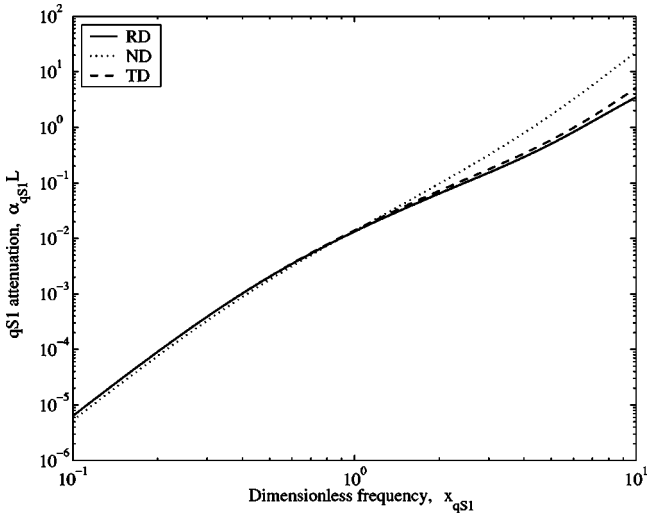

FIG. 11. Normalized $qS1$ attenuation, $\alpha_{qS1}L$, as a function of dimensionless frequency, x_{qS1}, for waves propagating in the rolling (RD), normal (ND) and transverse (TD) directions.

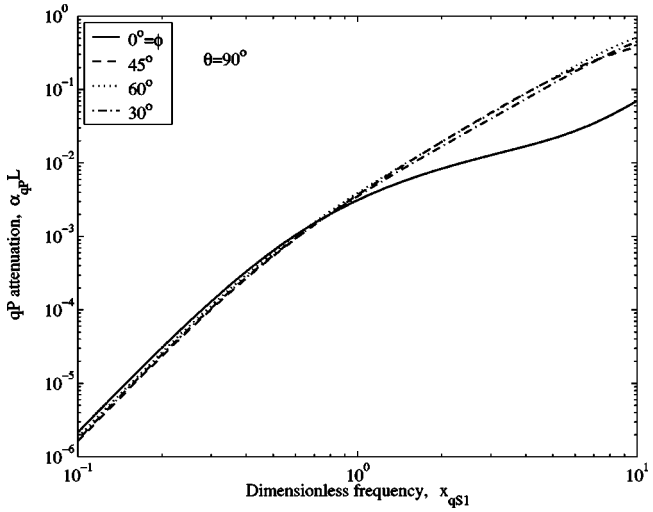

FIG. 13. Normalized qP attenuation, $\alpha_{qP}L$, as a function of dimensionless frequency, x_{qS1}, for waves propagating within the x_1-x_2 plane.

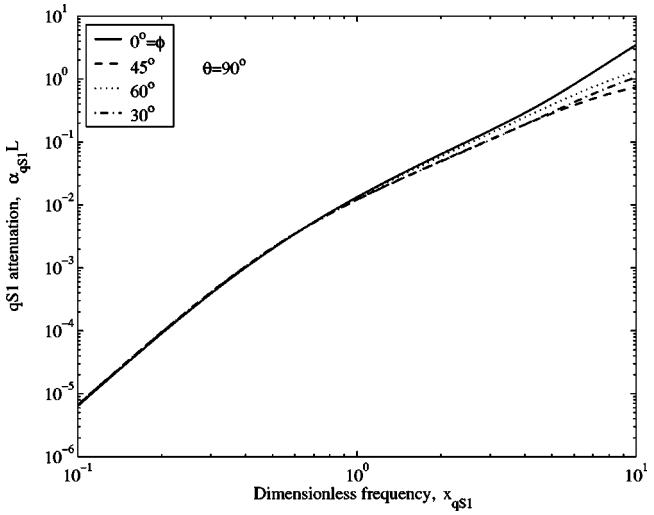

FIG. 14. Normalized $qS1$ attenuation, $\alpha_{qS1}L$, as a function of dimensionless frequency, x_{qS1}, for waves propagating within the x_1-x_2 plane.

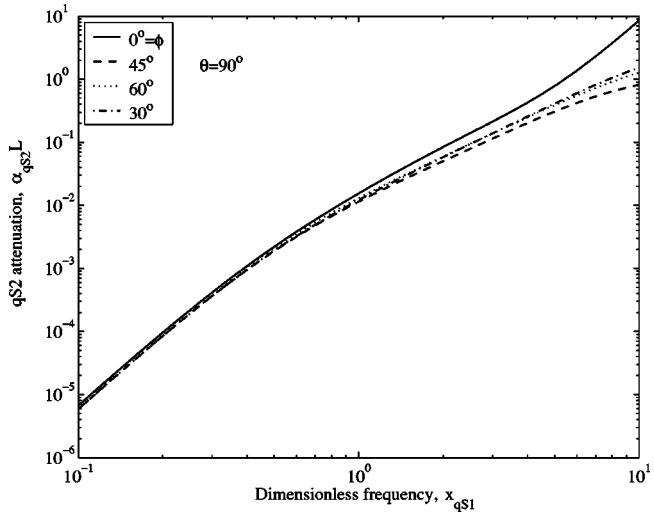

FIG. 15. Normalized $qS2$ attenuation, $\alpha_{qS2}L$, as a function of dimensionless frequency, x_{qS1}, for waves propagating within the x_1-x_2 plane.

in polycrystals of cubic symmetry with rolling texture. Compact expressions for the attenuations of the quasilongitudinal and two quasishear waves were then presented in terms of integrations over the scattered directions. In general, attenuations for each wave type are dependent on frequency, wave velocity, and wave propagation direction, as well as texture coefficients which are the expansion coefficients of the orientation function with respect to the generalized spherical functions. The results show that the attenuations of each wave type can be comprehensively affected by those parameters. The general formulation is also directly related to backscattering problems. The simple form of the results makes them particularly useful for nondestructive testing and materials characterization research. To use ultrasonic techniques for monitoring texture during processing, the relationships between ultrasonic parameters such as ultrasonic attenuation and materials texture must be investigated. If one knows the relationships between the ODCs and the ultrasonic attenuation, the texture coefficients can be inverted from ultrasonic attenuation measurements. The ultrasonic attenuations of sample specimens can then be measured during annealing such that the ODCs can be determined during processing.

ACKNOWLEDGMENTS

The financial support of the U.S. Department of Energy (Grant No. DE-FG02-01ER45890) is gratefully acknowledged. We also thank James C. Foley, R. Bruce Thompson, and David B. Rehbein at Ames Laboratory for their discussions.

APPENDIX

For polycrystals of cubic symmetry, the nonzero terms of the eighth-rank covariance, $\Xi_{ijkl}^{\alpha\beta\gamma\delta}$ in Eq. (14), are determined. The first term within the brackets is given as

$$\left\langle \sum_{n=1}^{3} a_{in}a_{jn}a_{kn}a_{ln} \sum_{n=1}^{3} a_{\alpha n}a_{\beta n}a_{\gamma n}a_{\delta n} \right\rangle$$

$$= \frac{1}{4\pi^2}\int_0^{2\pi}\int_0^{2\pi}\int_{-1}^{+1}\left(\sum_{n=1}^{3} a_{in}a_{jn}a_{kn}a_{ln} \right)\left(\sum_{n=1}^{3} a_{\alpha n}a_{\beta n}a_{\gamma n}a_{\delta n} \right) w(\xi,\psi,\varphi)\,d\xi\,d\psi\,d\varphi$$

$$= 4\pi^2\Bigg\{ W_{000}T_{000} + W_{400}\left[T_{400} + \frac{5}{\sqrt{70}}(T_{404} + T_{40\bar{4}}) \right] + W_{420}\left[T_{420} + T_{42\bar{0}} + \frac{5}{\sqrt{70}}(T_{424} + T_{42\bar{4}} + T_{424} + T_{42\bar{4}}) \right]$$

$$+ W_{440}\left[T_{440} + T_{44\bar{0}} + \frac{5}{\sqrt{70}}(T_{444} + T_{44\bar{4}} + T_{444} + T_{44\bar{4}}) \right] + W_{600}\left[T_{600} - \frac{\sqrt{14}}{2}(T_{604} + T_{60\bar{4}}) \right]$$

$$+ W_{620}\left[T_{620} + T_{62\bar{0}} - \frac{\sqrt{14}}{2}(T_{624} + T_{62\bar{4}} + T_{624} + T_{62\bar{4}}) \right] + W_{640}\left[T_{640} + T_{64\bar{0}} - \frac{\sqrt{14}}{2}(T_{644} + T_{64\bar{4}} + T_{644} + T_{64\bar{4}}) \right]$$

$$+ W_{660}\left[T_{660} + T_{66\bar{0}} - \frac{\sqrt{14}}{2}(T_{664} + T_{66\bar{4}} + T_{664} + T_{66\bar{4}}) \right] + W_{800}\left[T_{800} + \frac{\sqrt{154}}{33}(T_{804} + T_{80\bar{4}}) + \frac{\sqrt{1430}}{66}(T_{808} + T_{80\bar{8}}) \right]$$

$$+W_{820}\left[T_{820}+T_{82\bar{0}}+\frac{\sqrt{154}}{33}(T_{824}+T_{82\bar{4}}+T_{824}+T_{82\bar{4}})+\frac{\sqrt{1430}}{66}(T_{828}+T_{82\bar{8}}+T_{828}+T_{82\bar{8}})\right]$$

$$+W_{840}\left[T_{840}+T_{84\bar{0}}+\frac{\sqrt{154}}{33}(T_{844}+T_{84\bar{4}}+T_{844}+T_{84\bar{4}})+\frac{\sqrt{1430}}{66}(T_{848}+T_{84\bar{8}}+T_{848}+T_{84\bar{8}})\right]$$

$$+W_{860}\left[T_{860}+T_{86\bar{0}}+\frac{\sqrt{154}}{33}(T_{864}+T_{86\bar{4}}+T_{864}+T_{86\bar{4}})+\frac{\sqrt{1430}}{66}(T_{868}+T_{86\bar{8}}+T_{868}+T_{86\bar{8}})\right]$$

$$+W_{880}\left[T_{880}+T_{88\bar{0}}+\frac{\sqrt{154}}{33}(T_{884}+T_{88\bar{4}}+T_{884}+T_{88\bar{4}})+\frac{\sqrt{1430}}{66}(T_{888}+T_{88\bar{8}}+T_{888}+T_{88\bar{8}})\right]\Bigg\},$$

where the w is orientation distribution function (ODF). It can be expanded in a series of generalized spherical harmonics, with the coefficients W_{lmn} defining the orientation distribution coefficients (ODCs). The notations T_{lmn} are defined as

$$T_{lmn}=\frac{1}{4\pi^2}\int_0^{2\pi}\int_0^{2\pi}\int_{-1}^{+1}\left(\sum_{n=1}^{3}a_{in}a_{jn}a_{kn}a_{ln}\right)\left(\sum_{n=1}^{3}a_{\alpha n}a_{\beta n}a_{\gamma n}a_{\delta n}\right)\times Z_{lmn}(\xi)e^{-im\psi}e^{-in\varphi}\,d\xi\,d\psi\,d\varphi.$$

If the polycrystal is of orthorhombic-cubic symmetry, an example term ($i=j=k=l=1$ and $\alpha=\beta=\gamma=\delta=1$) is given as follows:

$$\left\langle\sum_{n=1}^{3}a_{n1}^4\sum_{m=1}^{3}a_{m1}^4\right\rangle=\frac{41}{105}+\frac{2232\sqrt{2}\pi^2}{5005}W_{400}-\frac{2976\sqrt{5}\pi^2}{5005}W_{420}-\frac{1448\sqrt{35}\pi^2}{5005}W_{440}-\frac{12\sqrt{26}\pi^2}{1001}W_{600}+\frac{64\sqrt{2730}\pi^2}{15015}W_{620}$$
$$-\frac{128\sqrt{91}\pi^2}{5005}W_{640}+\frac{64\sqrt{6006}\pi^2}{15015}W_{660}+\frac{56\sqrt{34}\pi^2}{7293}W_{800}-\frac{32\sqrt{1190}\pi^2}{12155}W_{820}+\frac{32\sqrt{1309}\pi^2}{12155}W_{840}-\frac{32\sqrt{14586}\pi^2}{36465}W_{860}$$
$$+\frac{16\sqrt{12155}\pi^2}{12155}W_{880}.$$

The remaining nonzero terms necessary for the calculation are given in detail elsewhere (Yang, 2003).

Ahmed, S., and Thompson, R. B. (**1992**). ''Effects of preferred grain orientation and grain elongation on ultrasonic wave propagation in stainless steel,'' in *Review of Progress in Quantitative NDE*, edited by D. O. Thompson and D. E. Chimenti (Plenum, New York), Vol. 11, pp. 1999–2006.

Ahmed, S., and Thompson, R. B. (**1996**). ''Propagation of elastic waves in equiaxed stainless-steel polycrystals with aligned [001] axes,'' J. Acoust. Soc. Am. **99**, 2086–2096.

Bunge, H. J. (**1982**). *Texture Analysis in Materials Science: Mathematical Methods* (Butterworths, London).

Frisch, U. (**1968**). ''Wave propagation in random media,'' in *Probabilistic Methods in Applied Mathematics*, edited by A. T. Barucha-Reid (Academic, New York), Vol. 1, pp. 75–198.

Hirao, M., Aoki, K., and Fukuoka, H. (**1987**). ''Texture of polycrystalline metals characterized by ultrasonic velocity measurements,'' J. Acoust. Soc. Am. **81**, 1434–1440.

Hirsekorn, S. (**1982**). ''The scattering of ultrasonic waves by polycrystals,'' J. Acoust. Soc. Am. **72**, 1021–1031.

Hirsekorn, S. (**1983**). ''The scattering of ultrasonic waves by polycrystals. II. Shear waves,'' J. Acoust. Soc. Am. **73**, 1160–1163.

Hirsekorn, S. (**1985**). ''The scattering of ultrasonic waves in polycrystalline materials with texture,'' J. Acoust. Soc. Am. **77**, 832–843.

Hirsekorn, S. (**1986**). ''Directional dependence of ultrasonic propagation in textured polycrystals,'' J. Acoust. Soc. Am. **79**, 1269–1279.

Johnson, G. C. (**1985**). ''Acoustoelastic response of a polycrystalline aggregates with orthotropic texture,'' J. Appl. Mech. **52**, 659–663.

Karal, F. C., and Keller, J. B. (**1964**). ''Elastic, electromagnetic, and other waves in a random medium,'' J. Math. Phys. **5**, 537–547.

Li, Y., and Thompson, R. B. (**1990**). ''Relations between elastic constants C_{ij} and texture parameters for hexagonal materials,'' J. Appl. Phys. **67**, 2663–2665.

Roe, R.-J. (**1965**). ''Description of crystallite orientation in polycrystalline materials. III. General solution to pole figure inversion,'' J. Appl. Phys. **36**, 2024–2031.

Roe, R.-J. (**1966**). ''Inversion of pole figures for materials having cubic crystal symmetry,'' J. Appl. Phys. **37**, 2069–2072.

Sayers, C. M. (**1982**). ''Ultrasonic velocities in anisotropic polycrystalline aggregates,'' J. Phys. D: Appl. Phys. **15**, 2157–2167.

Stanke, F. E., and Kino, G. S. (**1984**). ''A unified theory for elastic wave propagation in polycrystalline materials,'' J. Acoust. Soc. Am. **75**, 665–681.

Turner, J. A. (**1999**). ''Elastic wave propagation and scattering in heterogeneous, anisotropic media: Textured polycrystalline materials,'' J. Acoust. Soc. Am. **106**, 541–552.

Weaver, R. L. (**1990**). ''Diffusion of ultrasound in polycrystals,'' J. Mech. Phys. Solids **38**, 55–86.

Yang, L. (**2003**). ''Scattering of elastic waves in statistically anisotropic media,'' Ph.D. thesis, University of Nebraska.

Ultrasonic Methods in Contact Atomic Force Microscopy

Joseph A. Turner[1] and Donna C. Hurley[2]

[1]Department of Engineering Mechanics, W317.4 Nebraska Hall
University of Nebraska-Lincoln, Lincoln, Nebraska 68588, USA
jaturner@unl.edu

[2]National Institute of Standards and Technology,
325 Broadway, Boulder, Colorado 80305, USA
hurley@boulder.nist.gov

ABSTRACT: *In this chapter, techniques for materials characterization at the nanoscale that combine ultrasonics and atomic force microscopy (AFM) are presented. The focus is on dynamic methods in which ultrasonic excitations induce vibrations of the AFM cantilever. The methods considered are restricted to those in which the tip of the cantilever remains in contact with the specimen surface for the majority of the motion. Several aspects of coupled ultrasonic-AFM systems are examined, including the tip-sample interaction forces, the linear dynamics of the flexural and torsional modes, and the nonlinear dynamics of the flexural modes. Ways in which the dynamic behavior can be used for quantitative determination of sample stiffness and qualitative imaging of relative stiffness are then described. Both linear cantilever spectroscopy methods and nonlinear force curve methods are discussed and example results presented. Techniques such as these are expected to play a major role in nanotechnology research.*

KEY WORDS: *atomic force microscopy, AFAM, flexural and torsional vibrations, linear and nonlinear vibrations, materials characterization, UAFM, UFM, ultrasonics,*

Instrumentation, Measurement, and Metrology. Volume 3 – no 3-4/2003, pages 117 to 148

1. Introduction

The measurement of mechanical properties at small scales is motivated in part by recent efforts to develop new nanoscale materials. Many of these materials are entirely new structures such as nanotubes, nanofibers, and nanocomposites. Other nanoscale applications of interest include micro- and nano-electromechanical systems (MEMS and NEMS) that use more conventional materials (e.g., silicon). For all of these material systems, knowledge of mechanical properties is critical in order to predict their mechanical response and performance accurately. However, mechanical characterization at small scales remains an especially challenging problem. In many of these new materials, the properties can vary over nanometer (submicrometer) length scales. Even if only conventional materials are involved, the nanoscale materials properties usually cannot be predicted from bulk property measurements. Dramatic differences in mechanical properties may occur as sizes decrease and the surface-to-volume ratio increases. Thus, novel measurement techniques are needed to characterize emerging nanoscale materials and structures.

Nanoindentation [OLI92] has proven an effective technique to determine the indentation or plane strain modulus, which in isotropic materials is a combination of Young's modulus and Poisson's ratio. However, the spatial scale of nanoindentation, with contact radii typically on the order of several hundred nanometers, is still too large for many nanoscale systems. In addition, it is inherently destructive: an indent hundreds to thousands of nanometers wide is made during a force-displacement measurement. Atomic force microscopy (AFM), on the other hand, was originally developed to provide surface topography information with atomistic spatial resolution [BIN86]. The deflection of the AFM cantilever plotted as a function of surface location provides high-resolution images of surface topography. The small contact area of the AFM tip — typically a few nanometers — is ideally suited for nanoscale measurements of mechanical properties, provided that effective quantitative techniques can be developed for this purpose.

Many approaches have been taken to apply AFM to the task of mechanical characterization, including force modulation microscopy [MAI91], scanning local acceleration microscopy [BUR96], and pulsed force microscopy [ROS97]. However, in this chapter the focus is limited to methods that exploit the dynamic behavior of the AFM cantilever at *acoustic or ultrasonic* frequencies [KOL98, YAM99, RAB00, DIN00]. Work has shown that excitation frequencies in this range — at or above the first contact resonance of the beam — can be used for quantitative measurements and for stiffness imaging with little or no damage to the specimen surface. These methods rely on the relative motion between the AFM tip and the specimen surface as indicated in Fig. 1. The dynamic response of the AFM cantilever beam is usually described in terms of its flexural and torsional vibration modes. Because the frequencies of these modes range from tens of kilohertz to a few megahertz for typical cantilevers, ultrasonic transducers are often employed as the

excitation source. The appeal of these techniques lies in their potential to achieve nanometer spatial resolution, as determined by the AFM tip dimensions. However, the dynamic response of a vibrating AFM cantilever in contact with a surface is not easily described. Tip-sample interaction forces are, in general, nonlinear. When an elastic beam interacts with these surface forces, the flexural and torsional modes may be excited in a complex fashion, both linearly and nonlinearly. Thus, any quantitative technique for determining the tip-sample properties that exploits the dynamics of the AFM relies on an accurate model of this vibration system.

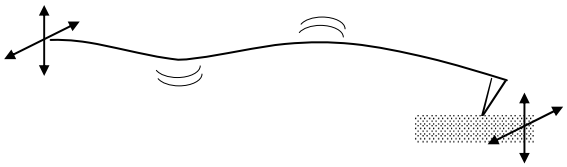

Figure 1. Schematic of the dynamic system considered here. The AFM cantilever is held in contact with the sample surface. The surface and/or cantilever holder are oscillated normal to or perpendicular to the undeformed cantilever plane, causing the cantilever to vibrate at frequencies characteristic of the coupled beam-sample system.

In this chapter, several aspects of coupled ultrasonic-AFM systems are examined, with the focus on the dynamics of AFM cantilevers and the determination of the specimen's mechanical properties. In the next section, the tip-sample interaction forces are described. Then the linear dynamics of the flexural and torsional modes are presented. A nonlinear analysis is also given for the flexural modes. In section 3, various experimental approaches are discussed in detail to illustrate how the contact mechanics models and vibration analysis may be practically implemented to determine mechanical properties. Applications involving both single-point, quantitative measurements and qualitative contrast imaging are described. Differences between the various approaches are noted. Finally, a summary is presented in section 4.

2. Dynamics of AFM Cantilevers

The dynamics of an AFM beam in contact with a vibrating surface can be very complicated. In this section, some aspects of the dynamical system are examined in detail. A critical aspect of the dynamics, and the prime nonlinearity in this system, is the tip-sample contact. The associated contact mechanics are discussed in section 2.1. In section 2.2, the linear flexural vibration theory that forms the basis for much of the AFM research under consideration is described. Section 2.3 contains a discussion of the nonlinear flexural theory with examples relevant to Hertzian contact mechanics. Finally, the potential coupling of flexural and torsional vibration modes is presented in section 2.4.

2.1. Interaction Forces/Contact Mechanics

The mechanics of the AFM tip as it interacts with a specimen are complex and generally nonlinear. Here, it is assumed that the contact is frictionless and the contact force acts normal to the tip. For simplicity, discussion is limited to elastically isotropic materials, although a similar analysis can be applied to anisotropic materials. A schematic of the contact mechanics problem is shown in Fig. 2. The goal of the contact analysis is to relate the applied force p to the penetration depth of the tip into the specimen δ. Important parameters for this problem are the radius of the contact area a, the work of adhesion at contact ω, and the stress in the cohesive zone σ_0. The reduced tip-sample radius of curvature, $1/R = 1/R_t + 1/R_s$, accounts for curvature of both tip R_t and specimen R_s. Most often, the specimen is assumed flat such that $R = R_t$. The reduced elastic modulus E^* is defined by

$$\frac{1}{E^*} = \left[\frac{1-\nu_t^2}{E_t} + \frac{1-\nu_s^2}{E_s} \right], \qquad [1]$$

where E_t, ν_t, E_s, and ν_s are Young's modulus and Poisson's ratio of the tip and sample, respectively. The general goal for materials characterization studies with AFM is to measure or image the elastic modulus of the specimen. Such a procedure involves determination of E^*. The material properties and geometry of the tip are either assumed or measured directly. In this way, the indentation or plane strain modulus of the sample, $M_s = E_s/\left(1-\nu_s^2\right)$ in the isotropic case, can be deduced from knowledge of E^*.

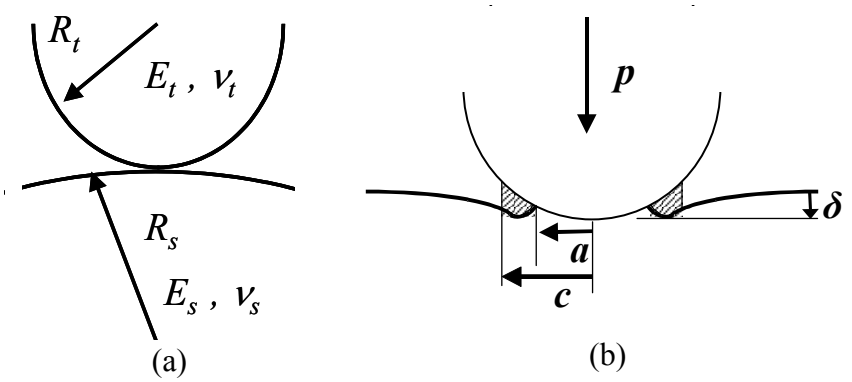

Figure 2. Contact mechanics parameters. The geometry of the contact between two spheres of different sizes is shown in (a). In (b), the contact mechanics load *p*, displacement *δ*, contact radius *a* and cohesive radius *c* are shown.

The most comprehensive tip mechanics model is that developed by Maugis [BUR99, MAU00]. The Maugis model captures many aspects of the contact

mechanics observed in AFM studies through the use of fracture mechanics concepts. Most importantly, it can account for adhesion hysteresis. The Maugis model provides a continuous functional dependence from Hertzian or Derjaguin-Muller-Toporov (DMT) mechanics without adhesion hysteresis [DER75], to the Johnson-Kendall-Roberts model (JKR) limit of maximum adhesion hysteresis [JOH71]. These limiting cases are discussed below. The following dimensionless parameters are used:

$$A = a\left(\frac{K}{\pi\omega R^2}\right)^{1/3}, \qquad P = p\left(\frac{1}{\pi\omega R}\right),$$
$$\Delta = \delta\left(\frac{K^2}{\pi^2\omega^2 R}\right)^{1/3}, \qquad \lambda = 2\sigma_0\left(\frac{R}{\pi\omega K^2}\right)^{1/3}, \qquad [2]$$

where A is the radius of contact, P is the applied force, Δ is the penetration depth, λ is the adhesion parameter, and $K = 4E^*/3$. The corresponding dimensional parameters of p, δ, and a are illustrated in Fig. 2.

In terms of these parameters, several different contact mechanics models may be described. Hertzian mechanics is given by [MAU00]

$$P_H = A^3, \qquad \Delta_H = A^2, \qquad [3]$$

which may be written $P_H = \Delta_H^{3/2}$. In the Hertz model, adhesion is neglected such that there is no attractive force associated with loss of contact. The Hertzian relation between P and Δ is shown in Fig. 3. The DMT model is a modified Hertz model [DER75]. In this case, a constant attractive force is added to the Hertzian mechanics: $P_D = A^3 - 2$. However, the tip geometry is Hertzian, $\Delta_D = A^2$. The behavior of $P_D(\Delta)$ for the DMT model is also shown in Fig. 3. The Hertz and DMT models do not include adhesion hysteresis effects. Thus, they are most applicable to AFM research for low adhesion specimens, hard materials or small radii of curvature.

In the high adhesion limit, the JKR model is appropriate. It is given by [JOH71]

$$P_J = A^3 - A\sqrt{6A}, \qquad \Delta_J = A^2 - \frac{2}{3}\sqrt{6A}. \qquad [4]$$

This model is most applicable for high adhesion specimens, soft materials or large radii of curvature.

The Maugis model is comprehensive in that it captures all types of tip-sample mechanics through the introduction of an adhesion parameter λ. Attractive (tensile) stresses are assumed to act between the tip and specimen in a cohesive zone that

surrounds the contact area. The stress σ_0 is assumed to be constant within an annulus of width d. The force and deflection are given by [MAU00]

$$P_M = A^3 - \lambda A^2 M_1, \qquad \Delta_M = A^2 - \frac{4}{3} A\lambda\sqrt{m^2 - 1}, \qquad [5]$$

where

$$M_1 = \sqrt{m^2 - 1} + m^2 \tan^{-1}\sqrt{m^2 - 1}\,. \qquad [6]$$

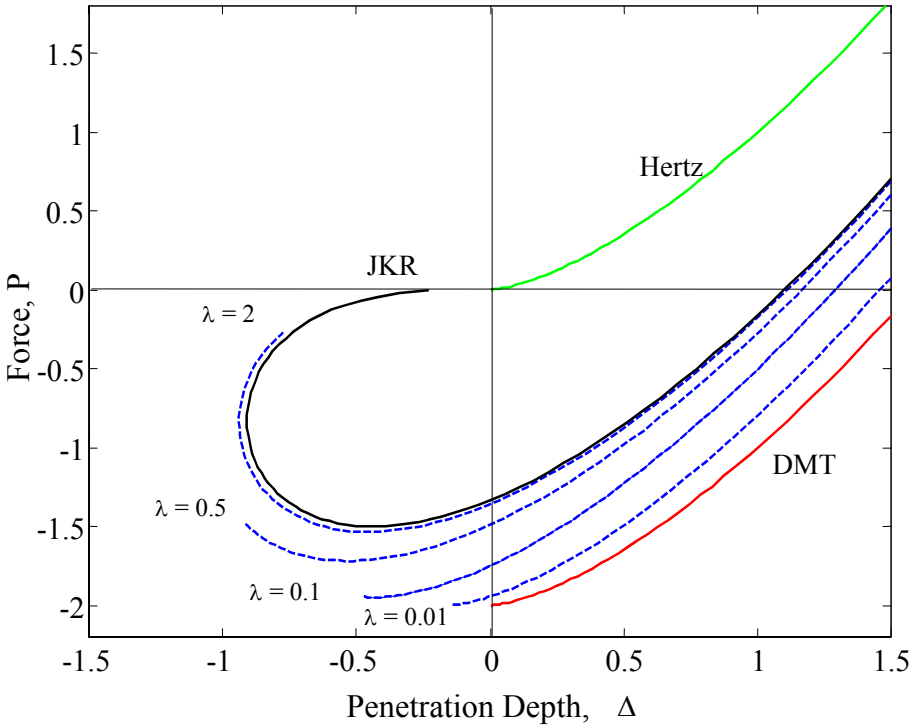

Figure 3. Force vs. penetration depth curves for several different tip-sample mechanics models. The Hertz (green), DMT (red), and JKR (black) models. The parameters λ are different values for adhesion associated with the Maugis model (blue).

In Eqs. [5] and [6], $m = c/a$ is the ratio of the radius to the edge of the cohesive zone to the radius of the contact area. The width of the cohesive zone is $d = c - a$. An additional equation is necessary for the Maugis mechanics. The Griffith equilibrium equation defines the relation between λ, m, and A:

$$\frac{\lambda A^2}{2} M_2 + \frac{4\lambda^2 A}{3} M_3 = 1, \qquad [7]$$

where

$$\begin{aligned} M_2 &= \sqrt{m^2 - 1} + \left(m^2 - 2\right)\tan^{-1}\sqrt{m^2 - 1}, \\ M_3 &= 1 - m + \sqrt{m^2 - 1}\,\tan^{-2}\sqrt{m^2 - 1}. \end{aligned} \qquad [8]$$

A comparison of the different contact models is shown in Fig. 3. The results based on the Maugis model are noted by the adhesion parameter λ. These curves require some interpretation. When Δ is positive, the sample is deflected away from the AFM tip. A negative value for Δ implies that the material bulges out from an otherwise flat surface. In the Hertz model, the AFM cantilever experiences an upward deflection ($P > 0$) as soon as contact is initiated. The DMT, JKR, and Maugis models all include some type of attractive effects, so that the cantilever deflects downward when contact is initiated. In this case, the tensile stresses in the cohesive annulus are greater than the compressive stresses in the contact area. The effect of adhesion hysteresis is also observed in Fig. 3. The curves for the JKR model and for the Maugis model with $\lambda = 2$ bend back on themselves. These curves have a section of positive slope when both P and Δ are negative. Points on this part of the curve are unstable equilibria. Thus, when moving continuously on these curves, loss of contact occurs when the slope becomes infinite. In addition, when contact is reinitiated, the tensile cohesive stresses pulls the AFM tip back into contact. This type of hysteretic behavior results when λ is slightly less than unity.

The various contact mechanics models highlight the complexity of the AFM tip-sample interaction. Moreover, the discussion here has been limited to the case of idealized surfaces; in practice, sample topography such as slope and curvature can have a critical effect on quantitative measurements. When the AFM tip is in motion, the force and penetration depth are time dependent. For small oscillations, the curves shown in Fig. 3 may be linearized about the initial static equilibrium position. The slope of this linearization is a spring stiffness that may be assumed to act at the tip location. For larger oscillations, larger portions of these curves are traversed during each period of oscillation. For sufficiently large oscillations, the tip may even lose contact with the specimen. In the following section, these vibrations are examined in more detail.

2.2. Linear Flexural Vibrations

When the tip of the AFM cantilever is in contact with a sample surface, different types of vibrations may be excited depending on the sample motion. Figure 4 shows a schematic of the cantilever-sample system. The AFM cantilever is modeled as an Euler-Bernoulli beam. It is assumed to be uniform and homogenous with constant cross-section. The beam is clamped at one end. At the opposite end of the cantilever,

a tip with a small radius of curvature is attached. The governing equation for the linearized boundary value problem for this system is given by [TUR97]

$$EI\frac{\partial^4 w(x,t)}{\partial x^4}+\rho A\frac{\partial^2 w(x,t)}{\partial t^2}=0\,, \qquad [10]$$

with boundary conditions

$$w(x,t)\big|_{x=0}=0, \qquad w'(x,t)\big|_{x=0}=0, \qquad w''(x,t)\big|_{x=L}=0, \qquad [11]$$

$$EIw'''(x,t)\big|_{x=L}=\kappa w(x,t)\big|_{x=L}. \qquad [12]$$

In Eqs. [10]-[12], $w(x,t)$ defines the cantilever position relative to its initial static deflection, $y(x)$. The cantilever is defined by its Young's modulus E, area moment of inertia I, volume density ρ, and cross-sectional area A. Here, EI and ρA are assumed uniform over the length of the cantilever. The boundary conditions given by Eq. [11] correspond to conditions of zero displacement and zero slope at $x = 0$ and zero moment at $x = L$. Equation [12] defines the force balance between the beam and the linear tip-sample stiffness. A linear spring model is used to describe the tip-sample interaction force, such that the results are restricted to small tip displacements. The relationship between the linear spring constant κ and the tip and sample parameters, especially the sample mechanical properties, depends on the interaction model used (section 2.1). The chosen contact mechanics model is linearized about the initial static applied load and the resulting slope is κ.

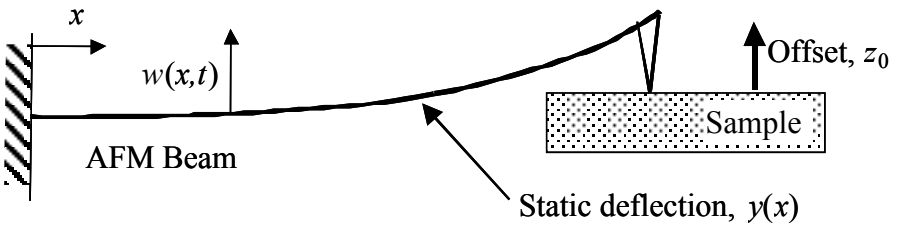

Figure 4. Schematic of the dynamic cantilever system under consideration. The AFM tip is in contact with the sample. Initial contact is made when the sample offset $z_0 = 0$. The static offset causes a static beam deflection $y(x)$. The dynamic motion $w(x,t)$ is defined relative to $y(x)$. The contact forces between the tip and the sample may be discussed using different contact models.

Equations [10]-[12] define completely the linearized flexural vibration problem. The natural frequencies of the cantilever vibrations are dependent on the linear spring constant. The solution to Eq. [10] may be written

$$w(x,t) = W(x)e^{i\omega t}. \qquad [13]$$

The mode shape $W(x)$ is found by substituting Eq. [13] into Eqs. [11]-[12] and by solving the subsequent eigenvalue problem. For the boundary conditions considered here, it may be written [TUR97]

$$W(x) = D\left(\sin kx - \sinh kx - \frac{\sin kL + \sinh kL}{\cos kL + \cosh kL}(\cos kx - \cosh kx)\right), \qquad [14]$$

where k is the flexural wave number.

The characteristic equation defines the wave numbers that admit solutions to the problem. The characteristic equation is found from the boundary condition involving the linear spring, Eq. [12], and is given by

$$\gamma^3(\cos\gamma\cosh\gamma + 1) - \frac{\kappa}{EI/L^3}(\sinh\gamma\cos\gamma - \sin\gamma\cosh\gamma) = 0, \qquad [15]$$

with $\gamma = kL$ as the dimensionless wave number. Equation [15] is solved numerically for the values of γ. The dispersion relation

$$f = \gamma^2\left(\frac{1}{4\pi^2}\right)\sqrt{\frac{EI/L^3}{\rho AL}}, \qquad [16]$$

defines the natural frequencies f in terms of the wave numbers γ.

It should be noted that in the discussion given here, the tip is assumed to be at the end of the beam, that is, $x = L$. If the tip is not located at the end, the derivation must be modified, altering the characteristic equation (Eq. [15]) and mode shape (Eq. [14]) [RAB00]. The effect of a finite tip length can also be added to the analysis described above. In this case, the boundary conditions are altered to include a bending moment at the end of the cantilever [WRI97]. Both refinements can have a substantial impact on the quantitative interpretation of resonant spectra, depending on the specific experimental conditions (contact stiffness and cantilever geometry).

2.3. Nonlinear Flexural Vibrations

The linear vibration problem described in section 2.2 is limited in the sense that the vibration amplitude must remain small over the entire period of motion. However, the inherent nonlinear response of the tip interaction with the surface as described in section 2.1 will also lead to nonlinear vibration behavior. In this section, some of the phenomena associated with these nonlinear vibrations are presented. The discussion here is focused primarily on the Hertz model. However,

more general contact theories are expected to exhibit similar nonlinear responses in the contact regime.

The boundary condition involving the tip-sample contact, Eq. [12], is first rewritten in a more general form as

$$EI\tilde{w}'''(x,t)\big|_{x=L} - 3\frac{EI}{L^3}\left(z_0/\Delta - 1\right) + K_0\Delta^{1/2}\left[1-\tilde{w}(x,t)\right]^{3/2} = 0\,, \qquad [17]$$

where $\tilde{w} = q/\Delta$ defines the beam deflection relative to the static Hertzian deformation with $K_0 = K\sqrt{R}$. (K and R were defined in section 2.1.) Note that the beam remains in contact with the surface as long as $\tilde{w}(L,t) \leq 1$. Finally, the term in Eq. [17] with the 3/2 exponent is expanded in a Taylor series expansion about the equilibrium position, $\tilde{w}(L,t) = 0$. The result is

$$EI\tilde{w}''' = \kappa\tilde{w} - \kappa_1\tilde{w}^2 - \kappa_2\tilde{w}^3\,, \qquad [18]$$

where the linear and nonlinear spring constants are given by

$$\kappa = \frac{3}{2}K_0\Delta^{1/2}, \qquad \kappa_1 = \frac{3}{8}K_0\Delta^{1/2}, \qquad \kappa_2 = \frac{1}{16}K_0\Delta^{1/2}. \qquad [19]$$

The linear spring constant κ is identical to that in section 2.2. The nonlinear spring constants κ_1 and κ_2 arise because the contact area is a function of applied load. They are not related to nonlinear elastic behavior in the tip or sample, since linear elastic behavior is assumed. The error in this type of expansion is less than 1% over the range in which the contact is not lost [TUR03]. A similar type of expansion has been successfully used to model Hertzian contact vibrations in single-degree of freedom systems [BRY85].

The nonlinear response is analyzed using the method of multiple scales. From a practical standpoint, the response of interest is that of a forced system with damping. The corresponding contact boundary condition is written as

$$EI\tilde{w}''' - \kappa\tilde{w} - \varepsilon^2 c\dot{\tilde{w}} + \varepsilon\frac{\kappa_1}{L}\tilde{w}^2 + \varepsilon^2\frac{\kappa_2}{L^2}\tilde{w}^3 = \varepsilon^2 F\cos\Omega t\,, \qquad [20]$$

where F is the forcing amplitude and ε is a dimensionless parameter introduced to order the different scales of the nonlinear problem. The forcing frequency Ω is assumed to be near to one of the natural frequencies of the system, ω_m. Thus, it is the primary resonance response that is examined here. A reduced analysis of this nonlinear vibration problem is given here. The interested reader is referred to the more complete description given in [TUR03]. The method of multiple scales is

based on the premise that multiple time scales are involved in the nonlinear vibrations. The response is expanded as

$$\tilde{w}(x;T_0,T_1,\ldots)=\tilde{w}_0(x;T_0,T_1,\ldots)+\varepsilon\tilde{w}_1(x;T_0,T_1,\ldots)+\varepsilon^2\tilde{w}_2(x;T_0,T_1,\ldots), \qquad [21]$$

where T_0, T_1, and T_2 are the different time scales of the problem, $T_n=\varepsilon^n t$ with ε defined as the scaling parameter. The expansion is substituted into Eqs. [10], [11], and [18] and like orders of ε are collected. This procedure clearly defines three different sets of partial differential equations governing the w_0, w_1, and w_2 responses referred to as the order ε^0, ε^1, and ε^2 problems, respectively. When the response near a resonance is examined, the solution to the ε^0 problem is the linear response given in section 2.2 with a time varying amplitude $\tilde{w}(x,t)=A_m(T_1,T_2)e^{i\omega_m T_0}W_m(x)$, for the mth mode. The solution to the ε^1 problem shows only that the T_1 time scale is not a part of the solution, i.e., $A_m=A_m(T_2)$. This type of result is often the case in nonlinear problems such as these [NAY00]. Finally, the ε^2 problem is solved such that the frequency shift, or detuning parameter Γ, as a function of excitation amplitude is determined. The natural frequencies shift by an amount $\varepsilon^2\Gamma$, where Γ is governed by

$$\Gamma_m=\frac{\left(\frac{\kappa_1}{EI/L^3}\right)_1^2\left[G\left(\sqrt{2\omega_m}\right)-\frac{2}{3+\kappa/(EI/L^3)}-3\frac{\kappa_2}{EI/L^3}\right]}{4P(kL)\omega_m}p^2\pm\frac{1}{P(kL)\omega_m}\sqrt{\frac{4F^2}{p^2}-c^2\omega_m^2}, \qquad [22]$$

where p is the real vibration amplitude. In Eq. [22], the functions G and P are given by

$$G(\chi)=-\frac{(\cos\chi\cosh\chi)(\sinh\chi-\sin\chi)+(\cos\chi-\cosh\chi)(\sin\chi+\sinh\chi)}{\chi^3(1+\cos\chi\cosh\chi)-(\kappa/(EI/L^3))(\sinh\chi\cos\chi-\sin\chi\cosh\chi)}, \qquad [23]$$

$$\begin{aligned}P(\gamma)=&\frac{3\gamma^2(\cos\gamma+\cosh\gamma)(1+\cos\gamma\cosh\gamma)-\gamma^3\sin\gamma\sinh\gamma(\sin\gamma+\sinh\gamma)}{\gamma^3(\cos\gamma+\cosh\gamma)^2}\\&+\frac{\kappa}{EI/L^3}\frac{\sin\gamma\sinh\gamma(\cos\gamma+\cosh\gamma)+(1+\cos\gamma\cosh\gamma)(\cosh\gamma-\cos\gamma)}{\gamma^3(\cos\gamma+\cosh\gamma)^2}.\end{aligned} \qquad [24]$$

The dependence of the nonlinear response on the different modes is included in the amplitude-frequency relation by the functions G and P.

Example results highlighting the nonlinear frequency shifts for this problem are illustrated in Figs. 5 and 6. Figure 5 shows the change in amplitude as a function of detuning parameter Γ for several values of forcing level ($\kappa = 100EI/L^3$; $c = 0.2$). Both the first and second modes are shown. The nonlinear softening behavior characterized by a decrease in frequency with amplitude is clear. For the chosen parameters, the first mode is predicted to lose contact ($p > 1$) for the highest forcing amplitudes. The second mode, however, is predicted to remain in contact for all

values of F examined and it has a maximum value of Γ of about –2. Figure 6 is an example of the modal sensitivity to the nonlinearity. The nonlinear primary response of the first and second modes is shown for two values of κ. For the two values chosen, the first mode frequency shift is similar, although the magnitude and loss of contact are different. The second mode, on the other hand, has a much stronger response to the nonlinearity when $\kappa = 400EI/L^3$. This type of sensitivity to the contact has been noted for linear vibrations as well [TUR01].

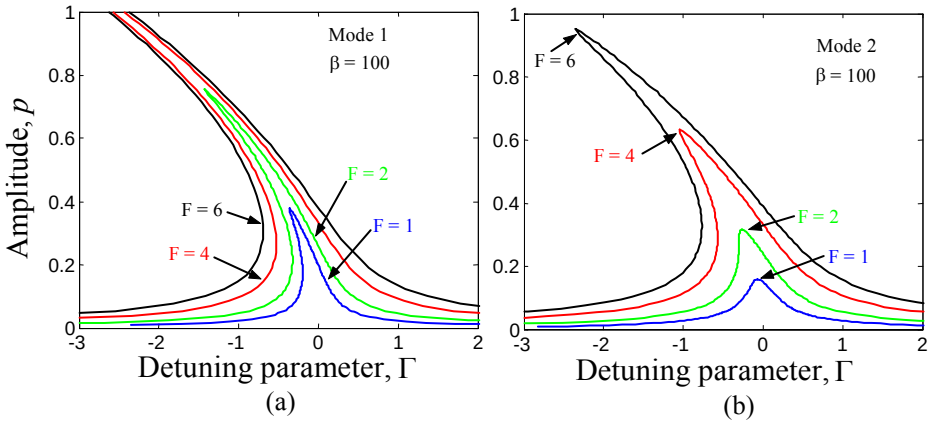

Figure 5. Example results for the primary nonlinear response for four values of forcing amplitude F with damping constant c = 0.2. The dimensionless contact stiffness $\kappa = 100EI/L^3$. The (a) first and (b) second modes are shown.

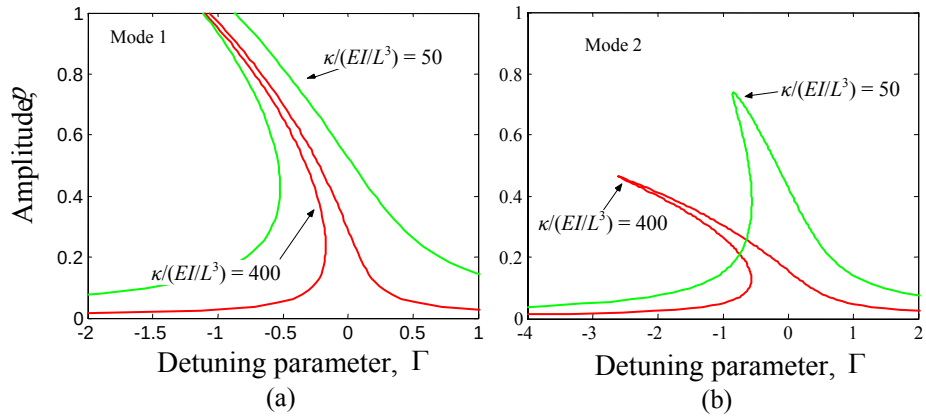

Figure 6. Nonlinear frequency shift of the (a) first and (b) second modes for two values of linear stiffness κ with c = 0.2. These plots illustrate the modal sensitivity to nonlinearity.

The expression for the detuning parameter Γ includes the linear (κ) and two nonlinear (κ_1, κ_2) spring constants used in the expansion of the Hertzian contact. The dependence on κ and κ_2 is fairly clear since these terms appear directly in Eq. [22]. The dependence on κ_1 is less clear because it is multiplied by the factor $G(\chi)$, which is dependent on the particular mode. In order to understand the nonlinear behavior in terms of the κ_1 dependence, calculations for various values of κ_1 were made. The values used for κ_1 correspond to multiples of the Hertzian value of $(\kappa_1)_H = \kappa/4$ as given above. Here, both larger and smaller values of κ_1 were examined. Figure 7 shows results for the first and third modes in which $\kappa_1 = C(\kappa_1)_H$, where the constant C is one of five values, C = 0.5, 0.75, 1.0, 1.25, 1.5. This analysis is relevant for tip mechanics models that differ from the Hertzian model. Figure 7(a) shows the dependence of the first mode on values of κ_1 for $\kappa = 50EI/L^3$, $c = 0.09$. The maximum frequency shift is seen to increase as κ_1 increases. Although this type of result may be expected, it is not guaranteed. As shown in Fig. 7(b), the nonlinear response of the third mode is much more complicated. The degree of response is not monotonic as is the first mode. Again, the modal sensitivity is expected to play a role in this complicated behavior. Such nonlinear softening has been experimentally observed [RAB99, MUR01].

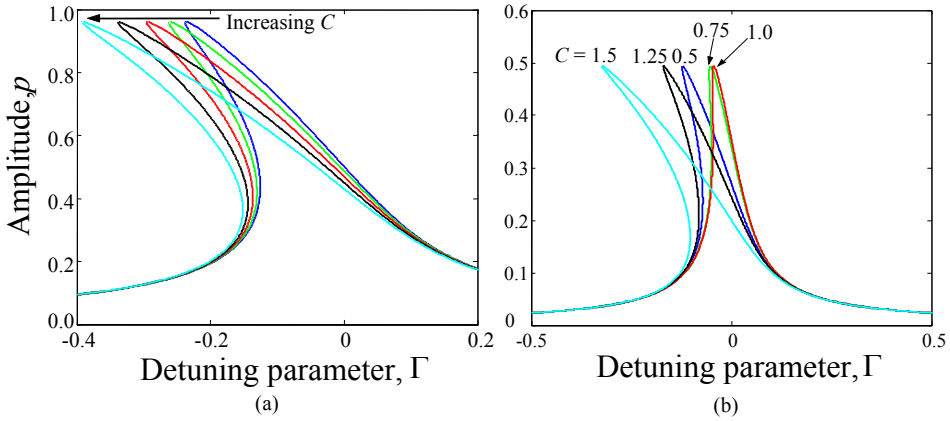

Figure 7. Change in response of the first mode (a) and third mode (b) for varying values of κ_1 relative to the Hertzian value of $(\kappa_1)_H = \kappa/4$. The curves correspond to the ratio of $C = \kappa_1/(\kappa_1)_H$ for C = 0.5, 0.75, 1.0, 1.25, 1.5. For the first mode (a), κ_1 increases from right to left ($\kappa = 50EI/L$, c = 0.09). For the third mode (b), the ordering of the nonlinear response does not follow simple heuristic arguments ($\kappa = 500EI/L$, c = 0.025).

2.4. Flexural-Torsional Mode Coupling

The flexural type of AFM response discussed thus far is important for a number of applications in which the out of plane displacements are of primary interest. In other cases, the sample is excited perpendicular to the AFM cantilever, such that torsional modes are excited. This behavior is also important for investigating the friction of the tip-sample contact. As the study of these flexural and torsional modes

has progressed, some interesting dynamics have been observed. In this section, one of those phenomena, the observed coupling between different mode types, is examined [REI03]. It is shown that the cantilever design controls this modal coupling behavior.

Consider the isotropic, elastic beam of length L shown in Fig. 4. As considered in section 2.2, it is cantilevered at $x = 0$ and has a tip at $x = L$. Here, a lateral tip-sample spring is included in the problem as shown in Fig. 8, an end view of the cantilever. The tip is assumed to have mass m_t and height h. The tip is coupled to the specimen surface through linear springs of stiffness κ_n and κ_l, which define the normal and lateral spring constants, respectively. The tip is also assumed to be offset slightly from the area center of the cross-section by an amount d.

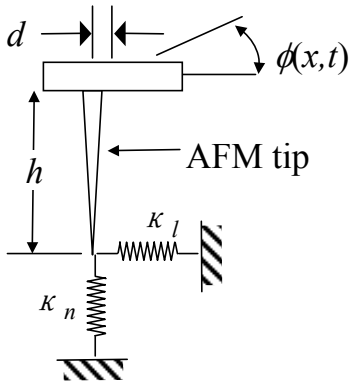

Figure 8. End-view of the AFM cantilever showing the normal and lateral springs attached to the AFM tip.

The long aspect ratio of typical AFM cantilevers lends itself to a simplified analysis. The vibrations are separated into bending and twisting motion. The motion is described by two partial differential equations (one for flexure and one for twist) in which the variable $\bar{x}$ is given in units of cantilever length L

$$\frac{EI}{L^3} w''''(\bar{x},t) + \rho A L \ddot{w}(\bar{x},t) = 0, \qquad [25]$$

$$\frac{G\xi}{L} \phi''(\bar{x},t) - \rho J L \ddot{\phi}(\bar{x},t) = 0. \qquad [26]$$

In Eqs. [25]-[26], ρ is the volumetric density, A is the area of the cross-section, J is the polar moment of area, E is the Young's modulus, and G is the shear modulus. The torsional constant ξ is used to describe the warping of the cross-section [TUR01]. The boundary conditions used here are given by

$$w(\bar{x},t) = 0, \quad w'(\bar{x},t) = 0, \quad \phi(\bar{x},t) = 0, \qquad \text{at } \bar{x} = 0, \qquad [27]$$

$$w''(\bar{x},t) = 0, \qquad \text{at } \bar{x} = 1, \qquad [28]$$

and

$$w'''(\bar{x},t) = \beta_n w(\bar{x},t) - \beta_n \frac{d}{L}\phi(\bar{x},t) + \frac{m_t}{EI/L^3}\left(\ddot{w}(\bar{x},t) - \frac{d}{L}\ddot{\phi}(\bar{x},t)\right),$$

$$\phi'(\bar{x},t) = -\beta_l \phi(\bar{x},t) - \frac{\kappa_n}{G\xi/L} dL w(\bar{x},t) + \frac{m_t}{G\xi/L}\left(dL\ddot{w}(\bar{x},t) - d^2\ddot{\phi}(\bar{x},t)\right), \qquad \text{at } \bar{x} = 1. \qquad [29]$$

The dimensionless quantities β_n and β_l are given by

$$\beta_n = \frac{\kappa_n}{EI/L^3}, \qquad \beta_l = \frac{\kappa_l h^2}{G\xi/L}. \tag{30}$$

Seeking harmonic solutions of the form $w(\bar{x},t) = W(\bar{x})e^{i\omega t}$ and $\phi(\bar{x},t) = \Phi(\bar{x})e^{i\omega t}$, and substituting into Eqs. [25]-[29] gives

$$W''''(\bar{x}) - \frac{\rho AL}{EI/L^3}\omega^2 W(\bar{x}) = 0, \tag{31}$$

$$\Phi''(\bar{x}) + \frac{\rho JL}{G\xi/L}\omega^2 \Phi(\bar{x}) = 0, \tag{32}$$

with boundary conditions

$$W(\bar{x}) = 0, \quad W'(\bar{x}) = 0, \quad \Phi(\bar{x}) = 0, \qquad \text{at } \bar{x} = 0, \tag{33}$$

$$W''(\bar{x}) = 0, \qquad \text{at } \bar{x} = 1, \tag{34}$$

$$\begin{aligned} W'''(\bar{x}) &= \beta_n W(\bar{x}) - \beta_n \frac{d}{L}\Phi(\bar{x}) - \frac{m_t\omega^2}{EI/L^3}\left(W(\bar{x}) - \frac{d}{L}\Phi(\bar{x})\right), \\ \Phi'(\bar{x}) &= -\beta_l \Phi(\bar{x}) - \frac{\kappa_n}{G\xi/L} dLW(\bar{x}) - \frac{m_t\omega^2}{G\xi/L}\left(dLW(\bar{x}) - d^2\Phi(\bar{x})\right), \end{aligned} \qquad \text{at } \bar{x} = 1. \tag{35}$$

The general solutions to Eqs. [31] and [32], Eq. [14] and $\Phi(\bar{x}) = C\sin\eta\bar{x}$, respectively, satisfy all but the coupled boundary conditions (Eqs. [35]). The flexural and torsional wave numbers, γ and η, respectively are related through the dispersion relations

$$\omega^2 = \gamma^4 \frac{EI/L^3}{\rho AL} = \eta^2 \frac{G\xi/L}{\rho JL}. \tag{36}$$

The coupled boundary conditions are now written in terms of the wave numbers as

$$\begin{aligned} W'''(\bar{x}) &= \beta_n W(\bar{x}) - \mu\gamma^4 W(\bar{x}) - \beta_n \Psi(\bar{x}) + \mu\gamma^4 \Psi(\bar{x}), \\ \Psi'(\bar{x}) &= -\beta_l \Psi(\bar{x}) + \zeta\eta^2 \Psi(\bar{x}) - \beta_n \frac{\eta^2}{\gamma^4}\frac{\zeta}{\mu} W(\bar{x}) - \zeta\eta^2 W(\bar{x}), \end{aligned} \qquad \text{at } \bar{x} = 1, \tag{37}$$

where $\mu = m_t/(\rho AL)$, $\zeta = m_t d^2/(\rho JL)$, and $\Psi(\bar{x}) = \frac{d}{L}\Phi(\bar{x})$. Substitution of the general solutions into Eqs. [37] gives a set of two equations for *C* and *D*. The determinant of the matrix of the coefficients on *C* and *D* gives the characteristic equation for the natural frequencies of the system. The zeroes of this equation are the wave numbers. The flexural and torsional wave numbers γ and η, respectively are no longer independent as seen in Eq. [36]. This relationship is given by $\eta = H\gamma^2$ where

$$H = \sqrt{\frac{EI/L^3}{\rho AL}\frac{\rho JL}{G\xi/L}}\,. \qquad [38]$$

It is this parameter *H* that determines the likelihood of modal coupling.

Modal coupling that has been observed experimentally [REI03] occurred when the cantilever was not in contact with a specimen. For this special case, $\beta_n = \beta_l = 0$ such that the final boundary conditions in Eqs. [37] reduce to

$$\begin{aligned} &W'''(\bar{x}) + \mu\gamma^4 W(\bar{x}) - \mu\gamma^4\Psi(\bar{x}) = 0\,, \\ &\Psi'(\bar{x}) - \zeta\eta^2\Psi(\bar{x}) + \zeta\eta^2 W(\bar{x}) = 0\,, \end{aligned} \qquad \text{at } \bar{x} = 1. \qquad [39]$$

The general form of the solution is substituted and the determinant of the coefficients is set to zero. The resulting characteristic equation is

$$\begin{aligned} &(\sin\gamma\cosh\gamma - \cos\gamma\sinh\gamma)\gamma\mu\cos H\gamma^2 \\ &\qquad + (\cos\gamma\cosh\gamma + 1)(\zeta H\gamma^2 \sin H\gamma^2 - \cos H\gamma^2) = 0\,. \end{aligned} \qquad [40]$$

When the tip mass is zero, $\mu = \zeta = 0$, and the characteristic equation reduces to

$$(\cos\gamma\cosh\gamma + 1)\cos H\gamma^2 = 0\,, \qquad [41]$$

giving both the flexural and torsional solutions. When the tip offset is zero, $\zeta = 0$, $\mu \neq 0$ and the characteristic equation is

$$[(\sin\gamma\cosh\gamma - \cos\gamma\sinh\gamma)\gamma\mu + (\cos\gamma\cosh\gamma + 1)]\cos H\gamma^2 = 0\,, \qquad [42]$$

corresponding to a multiplicative combination of the characteristic equations for a cantilevered beam with a mass at the end and that for a torsional cantilever. From experimental data given in [REI03], estimates on the necessary parameters may be made to find that $H = 0.025$.

The ratio of the tip mass to cantilever mass μ is estimated to be less than 0.02. The ratio of the tip inertia to cantilever inertia ζ is simplified to

$$\zeta = \frac{m_t d^2}{\rho JL} = 12\frac{m_t}{\rho AL}\frac{d^2}{\left(a^2 + t^2\right)} \approx 12\mu\frac{d^2}{a^2}, \qquad [43]$$

if $a >> t$. Thus, if $d \approx 1$ μm, $\zeta \approx 0.02\mu$. Using these values, Eq. [40] is solved for the wave numbers γ. The frequencies are then calculated. The mode shapes are a combination of the flexural and torsional solutions. The weighting of the combined solutions depends on the type of and degree of coupling as well as on the excitation method. Two modes have frequencies very near to each other. The third flexural mode (mode 3) and the first torsional mode (mode 4) lie with 5 % of each other. Thus, during forced vibrations, they are often excited simultaneously. Figure 8 shows an example of the types of mode shapes that can arise when these modes couple. In this case, the combined shape is partially flexural and partially torsional. The mode shapes shown in Fig. 9 are similar to the experimental mode shapes measured using a laser interferometer [REI03].

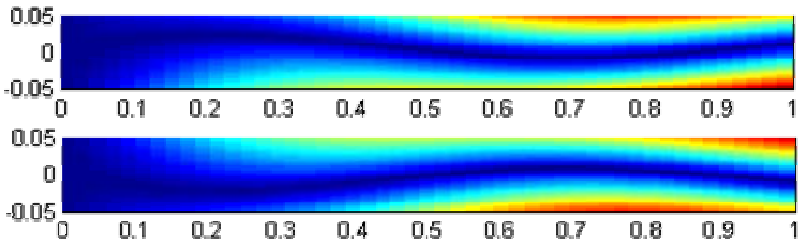

Figure 9. Profiles of the cantilever displacement for the third (top) and fourth (bottom) modes, calculated from the flexural/torsional coupling model with *H* = 0.025. When the frequencies are close together, small perturbations cause the modes to couple.

The coupling parameter H determines how close in frequency the flexural and torsional modes will be. In the example shown in Fig. 9, H was estimated to be on the order of 0.025. If this value is changed, the frequencies of these coupled modes change relative to one another. Plots of the third and fourth natural frequencies as a function of H is shown in Fig. 10(a). In the range of H plotted, the third and fourth frequencies (third flexural and first torsional modes) come close together, but never intersect. This type of *mode veering* is typical of systems with sets of orthogonal modes. A similar type of coupling is also predicted for other values of H. Figure 10(b) shows the fourth and fifth natural frequencies for this system as a function of H. Thus, in order to couple the fourth flexural with the first torsional, H must be approximately 0.013. Similar mode veering behavior is seen for these modes as well. This type of analysis is expected to be important in design of AFM cantilevers, either to avoid this type of coupling or to enhance it.

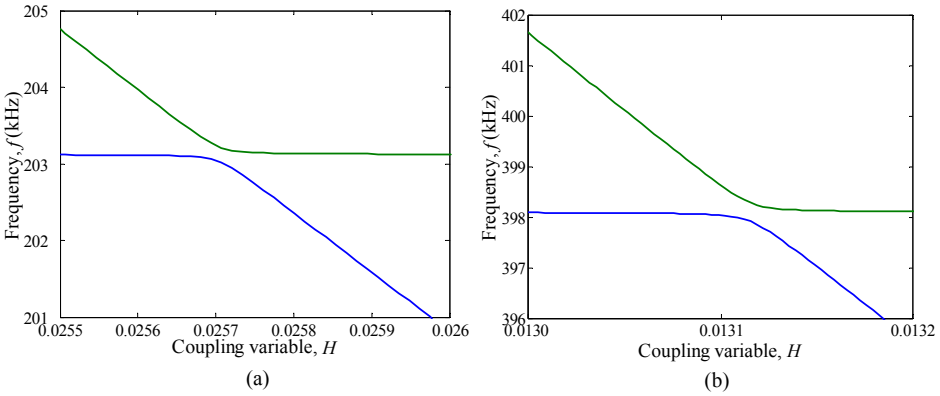

Figure 10. Natural frequencies as a function of the coupling parameter *H*. In (a), the coupling of the third flexural mode (blue) with the first torsional mode (green) is predicted. In (b), the coupling of the fourth flexural mode (green) with the first torsional mode (blue) is predicted. The phenomenon of mode veering is observed in both cases.

3. Experimental Techniques

In this section, experimental techniques are described that utilize the vibration behavior of the cantilever to characterize a sample's elastic or mechanical properties. As is often the case, different experimental approaches may be more or less suited to a given set of conditions (material class, cantilever type, etc.). The purpose here is to present each method in context with the others, such that a knowledgeable reader can determine the best technique for a given situation. All of these methods involve relatively simple modifications to standard AFM equipment. The modifications typically make use of other commercially available laboratory instruments. Access to the unprocessed output signals from the AFM apparatus is also required.

One dynamic AFM approach uses the resonant modes of the cantilever to distinguish surface and near-surface mechanical properties. This type of linear spectroscopy method has been used by several groups [RAB94, YAM99, RAB00, CRO00, HUR03]. In such experiments, the forcing amplitude is kept small enough that a linear approximation to the force-depth curves shown in Fig. 3 may be assumed. During one period of oscillation, the change in tip force and indentation depth is small. In contrast, the nonlinear techniques discussed later in this section [KOL93, YAM94, DIN00] use forcing amplitudes that are much higher. In this case, a relatively large portion of the force-depth curve is traversed during one period of excitation. For both methods, the basic physical and experimental concepts are first presented. Their use for quantitative measurements is then described and issues relevant to imaging are discussed. It is anticipated that this section provides a snapshot of the state of the art in dynamic AFM experiments.

3.1. Linear Cantilever Spectroscopy Methods

Linear cantilever spectroscopy approaches use information about the cantilever's resonant frequencies to characterize a material's mechanical properties. The technique was first developed by Rabe and coworkers [RAB94, RAB95, RAB00] and is usually called atomic force acoustic microscopy (AFAM). A very similar method, called ultrasonic atomic force microscopy (UAFM), has been developed by Yamanaka *et al*. [YAM96, YAM99].

The basic components of a typical experimental apparatus for AFAM measurements are illustrated in Fig. 11. As seen in the figure, the AFAM apparatus is based on a standard AFM instrument. The specimen under study is bonded to a commercial ultrasonic transducer or other piezoelectric element that is mounted on the AFM translation stage. A longitudinal transducer works best for exciting flexural modes, while a transverse (shear) transducer is well-suited for torsional modes. The transducer response should be optimized for the range of the cantilever's resonant frequencies; therefore, it typically has a center frequency of ~1-2 MHz. A continuous sine wave signal from a function generator is used to drive the transducer. In this way, resonances are excited in the cantilever when it is in contact with the sample. The amplitude of the cantilever deflection is monitored by the standard AFM differential (split) photodiode. Because the photodiode signal may contain several frequency components, various lock-in techniques have been implemented to isolate the signal at the excitation frequency.

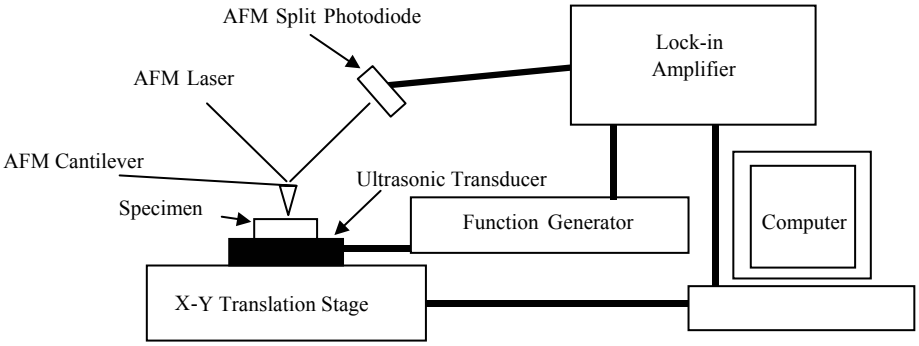

Figure 11. Schematic of apparatus for cantilever spectroscopy measurements.

In UAFM, the piezoelectric excitation element is incorporated into the clamped end of the cantilever or the cantilever holder, rather than beneath the sample. If the existing piezoelectric element of the AFM (*e.g.*, for cantilever "tuning") does not possess sufficient bandwidth for the cantilever's range of resonant frequencies, it may be necessary to introduce an additional piezoelectric element into the cantilever

holder. This modification can be difficult to implement in practice due to space constraints on the cantilever holder. However, there are certain advantages to this arrangement. For instance, access to only one side of the specimen is needed, and thick samples present fewer problems.

3.1.1. Quantitative Techniques

Quantitative measurements with spectroscopy techniques require information about the cantilever's resonant spectrum under two circumstances: when the cantilever vibrates in free space, and when it is in contact with a sample material. In this section we explain in detail how such information can be interpreted to obtain elastic properties. For clarity, we will limit the discussion to the approach used in AFAM. The specific details of the UAFM approach are somewhat different, although equally valid [YAM98, YAM99].

The following procedure has been used for quantitative measurement of the elastic modulus at a fixed sample position. First, the free-space resonances of the cantilever are measured by sweeping the function generator frequency while the cantilever remains out of contact with the sample. The transducer's vibrations are sufficiently transmitted through the air to excite the cantilever resonances. As shown below, knowledge of the free-space resonances is needed to characterize the properties of the specific cantilever in use. The cantilever tip is then brought into contact with a "reference" (calibration) sample. Resonant spectra are acquired for one or more values of sample offset. Measurements are typically made at three different offsets in the range 10–50 nm. For cantilevers used in AFAM experiments on relatively stiff materials (e.g., metals or ceramics), the corresponding applied force is in the range 0.1–3 μN. Next, the cantilever is brought into contact with the "test" (unknown) specimen. The resonances are measured for the same offset values. Finally, the measurements are repeated on the reference sample in order to check for effects such as tip wear. Examples of the resonant spectra for the first and second flexural modes during contact with a sample of single-crystal silicon are shown in Fig. 12.

From the experimental resonant frequencies, values are calculated for κ/k_c, the tip-sample contact stiffness κ relative to the cantilever spring constant k_c, for both the test and reference materials. The calculation is based on models for the tip-sample contact and cantilever dynamics such as those described in section 2. Numerical methods, such as the finite element method [HUR03], may also be used to model the cantilever response. From values of κ/k_c and knowledge of the reference material's elastic properties, the reduced Young's modulus E^* for the test material can be calculated [RAB02a]:

$$E^*_{test} = E^*_{ref}\left(\frac{\kappa_{test}}{\kappa_{ref}}\right)^n, \qquad [44]$$

where the exponent n may characterize a flat punch (n = 1) or spherical (n = 3/2) contact and the subscripts on E^* refer to the test and reference materials. The indentation modulus M_{test} of the test sample is then determined from E^*_{test} using Eq. [1] and knowledge of the cantilever tip properties.

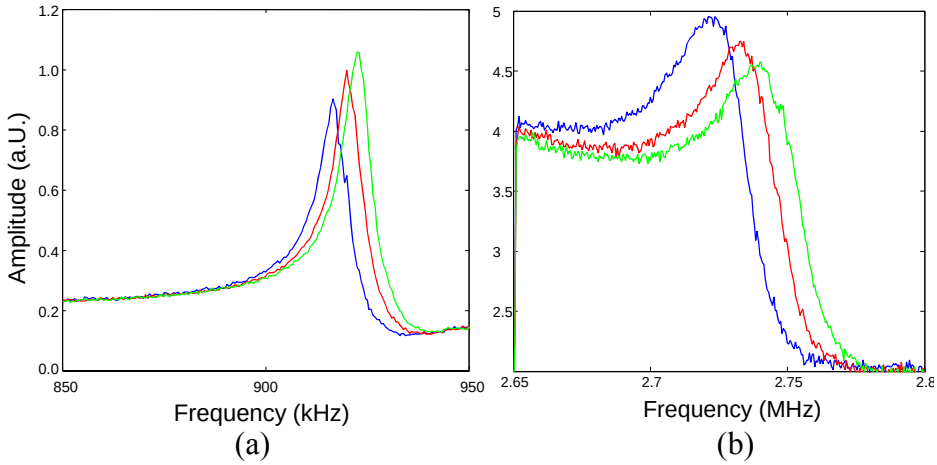

Figure 12. Spectra of the (a) first and (b) second cantilever flexural resonances on single-crystal silicon for 15, 25, and 35 nm offsets. Higher offsets cause the frequencies to shift higher due to the increased contact stiffness. The free vibration frequencies of this cantilever were 295 and 1627 kHz.

Comparison with a reference material of known elastic properties avoids the need for precise knowledge of the tip-sample contact area, which can be quite difficult to determine directly. It should be noted, however, that because κ/k_c depends on the contact area, the comparison method relies on the assumption that the contact geometry is identical for the test and reference materials. The use of multiple reference samples has been used to improve the measurement of the unknown [PRA02, HUR03]. An alternative approach that avoids this assumption using a tip shape estimation procedure has also been developed [YAM00].

In theory, the frequency of any single flexural resonance could be used to determine κ/k_c. In practice, the frequencies of two or more modes are measured and κ/k_c is calculated for each one. This practice is partially motivated by the fact that one mode is usually more sensitive than others to changes in κ/k_c [TUR01]. Moreover, the experimental values for κ/k_c obtained for different resonances typically do not exactly agree. The possible reasons for this disagreement are still under investigation. One source arises from the imprecise knowledge of the exact location of the tip. The characteristic equation, Eq. [15], was derived assuming that the tip position relative to the clamped end of the cantilever, $x = L_1$, is the very end of the cantilever (*i.e.*, $L_1 = L$). Equation [15] may be modified to include a variable tip position $L_1 < L$ [RAB00]. In this case, κ/k_c is plotted as a function of L_1 for each

flexural mode. The value of κ/k_c where the curves for different modes intersect is taken as the solution for κ/k_c. Thus, L_1 can be considered as an adjustable parameter in this approach. Typically, $L_1 = 0.91 - 0.99$ depending on the specific cantilever geometry and other experimental variables. It must be noted that this analytical model should not be applied to cantilevers whose properties are not uniform over their entire length, such as beams with a large triangular section. However, the analytical model has been shown to compare well with more geometrically accurate numerical models [HUR03], if the nonuniformity extends over a relatively small portion of the beam (< 5 %).

Comparisons of AFAM results with those from other techniques for the same sample have shown that linear spectroscopy methods can yield accurate quantitative values. In particular, measurements by Hurley *et al*. [HUR02, HUR03] on thin films have shown very good agreement with values obtained by nano- or instrumented indentation testing (IIT) and surface acoustic wave spectroscopy (SAWS). A subset of those results is given in Table 1. The stated range of AFAM values appears rather large because it includes the values calculated by different methods (analytical and numerical) from the same measurements and includes results from two different reference materials.

Table 1. Comparison of indentation modulus *M* (in GPa) for aluminum and niobium thin films obtained by different techniques [HUR03]. The values were calculated using *n* = 1 in Eq. [44].

material	literature values	SAWS	IIT	AFAM
Al	**76 – 81**	**79 ± 1**	**86 ± 4**	**55 – 81**
Nb	**116 – 133**	**121 ± 7**	**97 ± 10**	**86 – 135**

The work described above demonstrates the basic validity of AFAM techniques for quantitative determination of elastic properties. However, a comprehensive analysis of the measurement uncertainty budget has not yet been performed. To improve the precision and accuracy of quantitative AFAM methods, several sources of uncertainty should be more thoroughly examined. For instance, although quoted values usually represent an average of multiple measurements, careful estimates of measurement repeatability have not been made. Factors affecting measurement repeatability for a given system include spatial inhomogeneities in material properties (e.g., roughness, mechanical properties), variations in relative humidity that might affect tip-sample contact mechanics, and variability in contact area arising not only from tip wear but potentially also from tip nano-asperities.

As suggested above, the assumption that the tip-sample contact area is the same for both test and reference material measurements requires careful scrutiny. The accuracy with which M_{tip} and M_{ref} are known also impact the ultimate measurement accuracy. On a related note, it would be valuable to develop guidelines for choosing a suitable (that is, sensitive) cantilever for the material system under study.

3.1.2. Imaging

The spectroscopic information used to make quantitative AFAM and UAFM measurements at fixed sample position may also be used to create maps or images related to local variations in the surface elastic stiffness [RAB95, YAM96]. The spatial resolution of such images corresponds roughly to the tip-sample contact radius, which is typically in the 10-100 nm range. Images are generally obtained with a fixed excitation frequency, although a variable frequency-tracking approach has also been demonstrated [YAM01]. For fixed-frequency images, the intensity of a given image pixel represents the amplitude of the cantilever vibration detected at the corresponding position on the sample. The imaging frequency is chosen according to spectral information obtained in the manner described in section 3.1.1. The frequency is selected to fall on the shoulder of a resonant peak in a representative region of the material. During scanning, the frequency of the resonant peak shifts higher in regions of higher stiffness. Thus, if the imaging frequency is lower than the average contact frequency, higher stiffness regions correspond to lower image amplitudes. If the imaging frequency is higher than the average contact frequency, higher stiffness corresponds to higher image amplitudes. In most cases, topography and stiffness images may be obtained simultaneously.

Using such imaging techniques, the nanoscale mechanical properties of various material systems have been investigated, for instance piezoelectric ceramics [RAB02a] and carbon-fiber-reinforced polymers [YAM98]. Figures 13 and 14 contain examples of topography and AFAM images [BUT03, NIL02]. Figure 13 shows images corresponding to an interface of two aluminum particles that have been partially sintered. The sinters were formed from high-purity aluminum powder with an average particle size of 50 μm. The sample in Fig. 13 was sintered at 580 °C for 22 minutes. Although the topography is relatively smooth, the AFAM image reveals the interface of the particles. Knowledge of the AFAM excitation frequency reveals that the interface is stiffer than the particle core. Figure 14 shows topography and AFAM images for a sample of polycrystalline silicon used in microelectromechanical system (MEMS) structures. The topography reveals information about the grains. More importantly, the AFAM image indicates differences in stiffness from grain to grain. In addition, stiffness variations *within* grains due to twinning are observed, such as the grain shown in the lower-right-hand corner of the image. It should be stressed that the combination of topographic and AFAM information is needed to interpret the AFAM images appropriately.

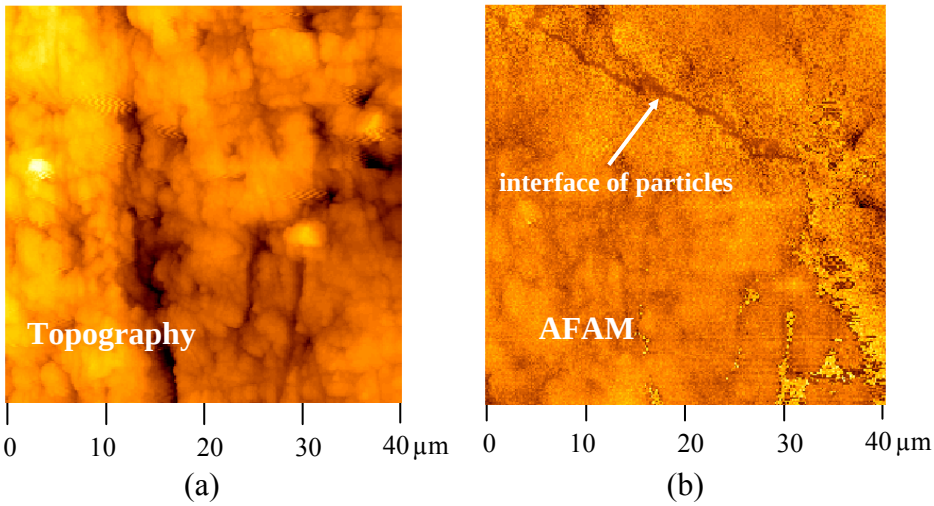

Figure 13. Topography (a) and AFAM (b) images of sintered aluminum particles [BUT03]. Although the particle interface is topographically smooth, it is stiffer than the particles themselves.

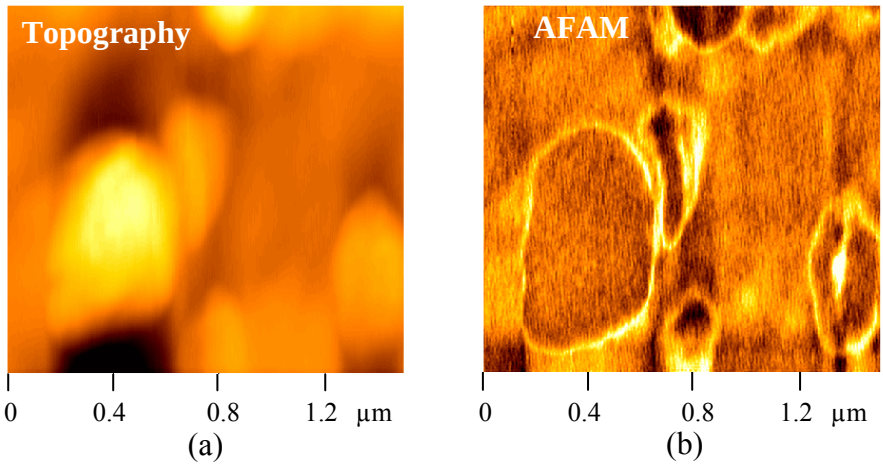

Figure 14. Topography (a) and AFAM (b) images of a polycrystalline silicon MEMS sample [NIL02]. The amplitude variations within individual grains (e.g., the lower-right-hand grain) are related to differences in stiffness from twinning.

These examples reveal the value of dynamic AFM imaging for enhanced understanding of nanoscale mechanical properties. To date, imaging techniques have

almost exclusively provided qualitative maps of relative properties only. Although simple contrast images can be invaluable, quantitative images of absolute properties is ultimately desired. This goal remains elusive. Partial progress has been made with a frequency-tracking approach [YAM01] and by time-consuming pixel-by-pixel spectrum acquisition [RAB02b]. Regardless of the specific approach, development of a tip-sample interaction model to calculate modulus values from the frequency information in each image pixel is still needed. This task is not easy, due in part to the sheer number of independent experimental parameters available that can significantly affect the final image.

3.2. Nonlinear Force Curve Methods

The cantilever spectroscopy methods described in section 3.1 rely on information about the vibration frequencies of an AFM cantilever when it is in contact with a specimen. The excitation amplitude is kept small such that linear theory may be applied. However, one can also obtain mechanical-property information using much higher excitation amplitudes. In this section, these techniques are discussed. Although the techniques are fundamentally based on cantilever dynamics, the response of the AFM cantilever is very different than that described in section 3.1.

3.2.1. Measurements and Analysis

Nonlinear force curve methods represent variations of the basic ultrasonic force microscopy (UFM) technique [KOL93, KOL98, DIN00]. The experimental apparatus is similar to that shown in Fig. 11, but involves different excitation and detection signals. Instead of the constant-amplitude excitation signal used in AFAM and UAFM experiments, in UFM the ultrasonic continuous sine wave signal is amplitude modulated. The ultrasonic oscillation frequency is typically 2 MHz or higher, while the modulation frequency is in the 1-10 kHz range and possesses a saw tooth, trapezoidal or other shape. An example of a modulation amplitude profile is shown in Fig. 15(b). The force-depth curve shown in Fig. 15(a) illustrates that as the excitation amplitude increases, the tip experiences increasingly nonlinear forces in a single cycle. For a sufficiently large excitation amplitude a_1, the cantilever tip breaks free from the surface in each cycle. At this point, the low-frequency AFM tip deflection signal exhibits a discontinuity ("tip jump") as illustrated in the upper part of Fig. 15(b). The sharpness of the discontinuity is dependent on the tip-sample contact – harder contacts have sharper discontinuities than softer contacts (depicted in Fig. 15(b)). The cantilever deflection can be detected either through direct observation with a digital oscilloscope or through lock-in techniques at the modulation frequency. It should be noted that the static forces applied in UFM experiments are typically much lower than those used for resonant methods

(approximately tens, versus hundreds, of nN). Therefore, the chances of damage to the sample are reduced.

As with linear cantilever spectroscopy methods, the most direct way to obtain quantitative information with nonlinear force curve methods requires knowledge of the measured AFM tip profile. Such information is needed to relate the measured contact stiffness to the material's elastic properties. Because it is difficult to characterize the tip directly, approaches that eliminate the need for such information have been developed. UFM methods for obtaining quantitative elastic-property information were investigated extensively using an approach called differential UFM [KOL93, DIN00]. With this method, the cantilever response was measured for two different applied forces. The corresponding threshold amplitudes, that is, the amplitudes at which force jumps occurred, were determined. The difference in applied force divided by the difference in threshold amplitudes is approximately equal to the slope of the force-depth curve between the two applied forces. This slope can be related to the contact stiffness via an appropriate contact mechanics model. Note that care should be taken in specifying absolute values of the applied force. Thus, precise knowledge of k_c is required, although accurate values are not always provided by cantilever vendors.

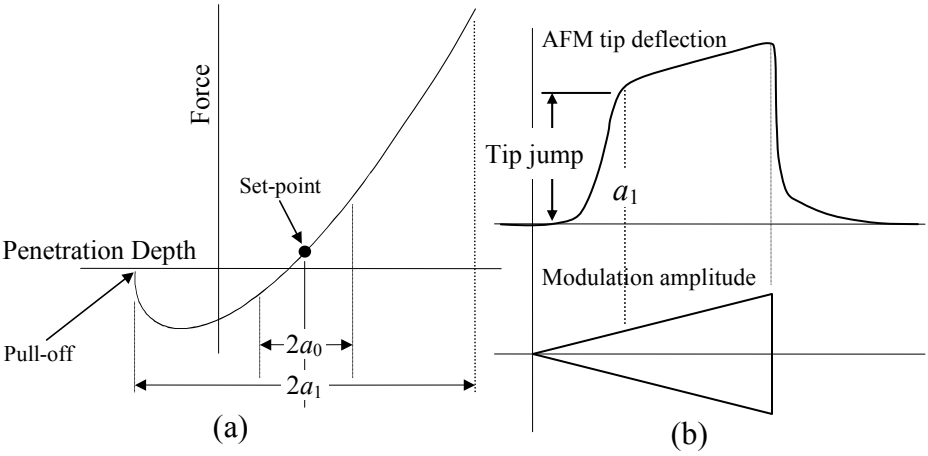

Figure 15. Schematic of nonlinear force curve principles. The force-depth curve shown in (a) illustrates that as the excitation amplitude increases, it eventually exceeds the pull-off force and the tip leaves the sample surface. At this point, a jump in the tip deflection signal is observed. The modulation amplitude and corresponding AFM tip deflection are shown in (b).

An additional assumption made in UFM measurements is related to the dynamic behavior of the AFM cantilever. The cantilever is usually regarded as a point mass with no dynamic response at high frequencies [KOL98]. For a cantilevered beam,

the linear response $w(x,t)$ to a high frequency excitation is a superposition of all modes given by

$$w(x,t) = \sum_{n=1}^{\infty} \frac{W_n^2(L)}{\omega_n^2 - \Omega^2} B(t) e^{i\Omega t}, \qquad [45]$$

where Ω is the excitation frequency, ω_n and W_n the resonance frequency and mode shape of the nth mode, and $B(t)$ is the modulation amplitude. Because $B(t)$ varies in time over a relatively large portion of the force-depth curve, the effective frequencies and mode shapes are not well defined. Their average value is related to the integrated response over one period. In addition, if Ω is close to a cantilever resonance, the response amplitude will be very large. Ω must therefore be tuned to avoid any cantilever resonances. However, if the excitation amplitude is not near a resonance, $w(x,t)$ in Eq. [45] can be very small. The specifics of the cantilever spectrum and contact behavior determine how small the linear response is and whether it is "dynamically static" [DIN00]. Thus, it is still unclear whether the response observed in UFM experiments is due to a linear response averaged over a nonlinear profile or due to more complex nonlinear behavior, such as described in section 2.3 and in [TUR03].

The application of UFM techniques for quantitative measurements of local material stiffness is inherently dependent on many factors, but is dominated by the behavior of the cantilever and the tip-sample contact mechanics. Data from nonlinear force curve techniques are more difficult to quantify and interpret than results from linear cantilever spectroscopy methods, although a value of local stiffness can be extracted. For either approach, appropriate contact mechanics models are needed to extract meaningful modulus information from the contact stiffness results. Thus, the interdependency of the experimental and modeling efforts, and the need for simultaneous development of both, cannot be overemphasized.

3.2.2. Imaging

The UFM methods described in section 3.2.1 have also been successfully used to obtain images related to local stiffness with nanoscale resolution. The low-frequency tip deflection is measured in several locations for several applied static forces. Based on this information, an applied force and excitation amplitude are chosen for imaging. The objective in imaging is to sense small changes in local properties with the AFM tip deflection. Thus, the largest changes in AFM tip deflection will occur when the excitation amplitude is chosen near the value of a_1 in Fig. 15b. As with linear methods, the local response to the chosen force and amplitude depends on both the local stiffness and adhesion. UFM imaging methods have been used to investigate applications involving a wide range of materials, including subsurface cracking in polymer/glass nanocomposites [McG02] and process-induced

mechanical variations in aluminum/polymer microelectronic test structures [GEE02]. In addition to the basic UFM approach described here, other variations have been developed and implemented for imaging. Among these are waveguide UFM [INA00] involving very high-frequency ultrasonic vibrations (50-100 MHz), and heterodyne UFM [CUB00], in which excitations at two ultrasonic frequencies are mixed and the signal at the difference frequency is detected.

4. Summary

In this chapter, atomic force microscopy (AFM) techniques for assessing mechanical properties with nanoscale resolution have been examined. Many of these techniques are dynamic methods coupling ultrasonic or acoustic vibrations with basic AFM techniques. Thus, a fundamental understanding of dynamics of the AFM cantilever beam as it interacts with the sample surface is of great importance. The cantilever dynamics have been examined in terms of linear and nonlinear flexural vibrations and flexural/torsional coupling. It was shown how the linearity of a given system is determined by the tip-sample interaction as a function of vibration amplitude. Different tip-sample interaction models were also discussed.

The practical implementation of two types of dynamic methods was also presented. Linear cantilever spectroscopy methods rely on small-amplitude excitation and high-frequency detection schemes. The resonances of the cantilever in free space and in contact with a specimen are used to deduce the local contact stiffness. Nonlinear force curve methods use a high-frequency harmonic excitation with a low-frequency amplitude modulation. The excitation amplitude is sufficiently large that the AFM tip is driven off the specimen surface during a portion of the modulation. Low-frequency detection schemes are sufficient for obtaining the tip response curve and for imaging. Both the linear and nonlinear approaches can be implemented with relatively minor adaptations to a conventional AFM. Although the basic apparatus is straightforward to implement, at present data acquisition and interpretation remains challenging.

Many of the fundamental theoretical concepts and measurement principles related to dynamic AFM methods have been presented here. From this summary, it should be clear that further research efforts are needed to continue the advancement of these promising methods. The measurement of mechanical properties at the nanoscale is essential to the development of new nanoscale materials and structures. It is anticipated that these types of dynamic AFM techniques will continue to develop and will play a crucial role in future nanotechnology efforts. Combined theoretical and experimental research is critical for the full potential of these techniques to be reached for effective characterization of new nanoscale materials and devices.

5. Acknowledgments

The support of the U.S. Air Force Office of Scientific Research (Grant No. F49620-99-1-0254), the National Science Foundation (Grant Nos. DMI-0210850 and INT-0089548) and the U.S. Department of Energy (Grant No. DE-FG02-01ER45890) is gratefully acknowledged by JAT. The authors have also greatly benefited from numerous technical discussions with several researchers (U. Rabe, W. Arnold, S. Hirsekorn, M. Kopycinska-Müller, and M. Reinstädtler) at the Fraunhofer Institut für zerstörungsfreie Prüfverfahren (IZFP) in Saarbrücken, Germany. In addition, JAT thanks current and former students (J. S. Wiehn, R. Nilchiani, B. Wei, T. Butler, P. Yuya, and K. Shen) and DCH thanks P. S. Rice for technical discussions and laboratory assistance.

6. Bibliography/References

[BIN86] G. Binning, C. F. Quate, and Ch. Gerber, "Atomic force microscope," Phys. Rev. Lett. **56**, 930-933, 1986.

[BUR96] N. A. Burnham, A. J. Kulik, G. Gremaud, P.-J. Gallo, and F. Oulevey, "Scanning local-acceleration microscopy," J. Vac. Sci. Technol. B **14**, 794-799, 1996.

[BUR99] N. A. Burnham and A. J. Kulik, "Surface forces and adhesion," *Handbook of Micro/Nanotechnology*, ed. B. Bhushan, CRC Press, Boca Raton, 1999.

[BUT03] T. P. Butler, MS Thesis, University of Nebraska-Lincoln, 2003.

[BRY85] M. D. Bryant, "Non-Linear forced oscillation of a beam coupled to an actuator via Hertzian contact," J. Sound Vib. **99**, 403–414, 1985.

[CRO00] K. B. Crozier, G. G. Yaralioglu, F. L. Degertekin, J. D. Adams, S. C. Minne, and C. F. Quate, "Thin film characterization by atomic force microscopy," Appl. Phys. Lett. **76**, 1950-1952, 2000.

[CUB00] M .T. Cuberes, H. E. Assender, G. A. D. Briggs, and O. V. Kolosov, "Heterodyne force microscopy of PMMA/rubber nanocomposites: nanomapping of viscoelastic response at ultrasonic frequencies," J. Phys. D. **33**, 2347-2355, 2000.

[DER75] B. V. Derjaguin, V. M. Muller, and Y. P. Toporov, "Effect of contact deformations on the adhesion of particles," J. Coll. Interface Sci. **53**, 314-326, 1975.

[DIN00] F. Dinelli, S. K. Biswas, G. A. D. Briggs, and O. V. Kolosov, "Measurements of stiff-material compliance on the nanoscale using ultrasonic force microscopy, Phys. Rev. B **61**, 13995-14006, 2000.

[GEE02] R. E. Geer, O. V. Kolosov, G. A. D. Briggs, and G. S. Shekhawat, "Nanometer-scale mechanical imaging of aluminum damascene interconnect structures in a low-dielectric-constant polymer," J. Appl. Phys. **91**, 4549-4555, 2002.

[HUR02] D. C. Hurley, J. S. Wiehn, J. A. Turner, and P. S. Rice, "Quantitative elastic-property information with acoustic AFM: measurements and modeling," in SPIE Symposium Proceedings Vol. 4703, eds. N. Meyendorf, G. Y. Baaklini, and B. Michel, 65-73, 2002.

[HUR03] D. C. Hurley, K. Shen, N. M. Jennett, and J. A. Turner, "Atomic force acoustic microscopy methods to determine thin-film elastic properties," J. Appl. Phys. **94**, 2347-2354, 2003.

[INA00] K. Inagaki, O. V. Kolosov, G. A. D. Briggs, and O. B. Wright, "Waveguide ultrasonic force microscopy at 60 MHz," Appl. Phys. Lett. **76**, 1836-1838, 2000.

[JOH71] K. L. Johnson, K. Kendall, and A. D. Roberts, "Surface energy and the contact of elastic solids," Proc. R. Soc. Lond. A. **324**, 301-313, 1971.

[KOL93] O. Kolosov and K. Yamanaka, "Nonlinear detection of ultrasonic vibrations in an atomic force microscope," Jpn. J. Appl. Phys. **32**, L1095-L1098, 1993.

[KOL98] O. V. Kolosov, M. R. Castell, C. D. Marsh, G. Andrew, D. Briggs, T. I. Kamins, and R. S. Williams, "Imaging the elastic nanostructure of Ge islands by ultrasonic force microscopy," Phys. Rev. Lett. **81**, 1046-1049, 1998.

[MAI91] P. Maivald, H. J. Butt, S. A. C. Gould, C. B. Prater, B. Drake, J. A. Gurley, V. B. Elings, and P. Hansma, "Using force modulation to image surface elasticities with the atomic force microscopy," Nanotechnology **2**, 103-106, 1991.

[MAU00] D. Maugis, *Contact, Adhesion and Rupture of Elastic Solids*, Springer-Verlag, Berlin, 2000.

[MUR01] M. Muraoka and W. Arnold, "A method of evaluating local elasticity and adhesion energy from the nonlinear response of AFM cantilever vibrations," JSME Int. J. Ser. A **44**, 396-405, 2001.

[McG02] A. P. McGuigan, B. D. Huey, G. A. D. Briggs, O. V. Kolosov, Y. Tsukahara, and M. Yanaka, "Measurement of debonding in cracked nanocomposite films by ultrasonic force microscopy," Appl. Phys. Lett. **80**, 1180-1182, 2002.

[NIL02] R. Nilchiani, *Atomic Force Acoustic Microscopy for Materials Characterization of Microelectromechanical Systems*, M. S. Thesis, University of Nebraska-Lincoln, 2002.

[OLI92] W. C. Oliver and G. M. Pharr, "An improved technique for determining hardness and elastic modulus using load and displacement sensing indentation experiments," J. Mater. Res. **7**, 1564-1583, 1992.

[NAY00] A. H. Nayfeh, *Nonlinear Interactions*, Wiley and Sons, New York, 2000.

[PRA02] M. Prasad, M. Kopycinska, U. Rabe, and W. Arnold, "Measurement of Young's modulus of clay minerals using AFAM," Geophys. Res. Lett. **29**, art. No. 1172, 2002.

[RAB94] U. Rabe and W. Arnold, "Acoustic microscopy by atomic force microscopy," Appl. Phys. Lett. **64**, 1493-1495, 1994.

[RAB95] U. Rabe, M. Dvorak, and W. Arnold, "The atomic force microscope as a near-field probe for ultrasound," Thin Solid Films **264**, 165-168, 1995.

[RAB99] U. Rabe, E. Kester, and W. Arnold, "Probing linear and non-linear tip-sample interaction forces by atomic force acoustic microscopy," Surf. Interface Anal. **27**, 386-391, 1999.

[RAB00] U. Rabe, S. Amelio, E. Kester, V. Scherer, S. Hirsekorn, and W. Arnold, "Quantitative determination of contact stiffness using atomic force acoustic microscopy," Ultrasonics **38**, 430-437, 2000.

[RAB02a] U. Rabe, S. Amelio, M. Kopycinska, S. Hirsekorn, M. Kempf, M. Goken, and W. Arnold, "Imaging and measurement of local mechanical material properties by atomic force acoustic microscopy," Surf. Interface Anal. **33**, 65-70, 2002.

[RAB02b] U. Rabe, M. Kopycinska, S. Hirsekorn, J. Muñoz Saldaña, G. A. Schneider, and W. Arnold, "High-resolution characterization of piezoelectric ceramics by ultrasonic scanning force microscopy techniques," J. Phys. D: Apply. Phys. **35**, 2621-2635, 2002.

[REI03] M. Reinstädler, U. Rabe, V. Scherer, J. A. Turner, and W. Arnold, "Imaging of flexural and torsional resonance modes of atomic force microscopy cantilevers using optical interferometry," Surface Science **532-535C**, 1152-1158, 2003.

[ROS97] A. Rosa-Zeiser, E. Weilandt, S. Hild, and O. Marti, "The simultaneous measurement of elastic, electrostatic and adhesive properties by scanning force microscopy: pulsed-force microscopy," Meas. Sci. Technol. **8**, 1333-1338, 1997.

[TUR97] J. A. Turner, S. Hirsekorn, U. Rabe, and W. Arnold, "High-frequency response of atomic-force microscope cantilevers," J. Appl. Phys. **82**, 966-979, 1997.

[TUR01] J. A. Turner and J. S. Wiehn, "Sensitivity of flexural and torsional modes of atomic force microscope cantilevers to surface stiffness variations," Nanotechnology, **12**, 322-330, 2001.

[TUR03] J. A. Turner, "Nonlinear vibrations of a beam with cantilever-Hertzian contact boundary conditions," J. Sound Vib., in press, 2003.

[WRI97] O. B. Wright and N. Nishiguchi, "Vibrational dynamics of force microscopy: effect of tip dimensions," Appl. Phys. Lett. **71**, 626-628, 1997.

[YAM94] K. Yamanaka, H. Ogiso, and O. Kolosov, "Ultrasonic force microscopy for nanometer resolution subsurface imaging," Appl. Phys. Lett. **64**, 178-180, 1994.

[YAM96] K. Yamanaka and S. Nakano, "Ultrasonic atomic force microscope with overtone excitation of cantilever," Jpn. J. Appl. Phys. **35**, 3787-3792, 1996.

[YAM98] K. Yamanaka and S. Nakano, "Quantitative elasticity evaluation by contact resonance in an atomic force microscope," Appl. Phys. A **66**, S313-S317, 1998.

[YAM99] K. Yamanaka, A. Noguchi, T. Tsuji, T. Koike, and T. Goto, "Quantitative material characterization by ultrasonic AFM," Surf. Interface Anal. **27**, 600-606, 1999.

[YAM00] K. Yamanaka, T. Tsuji, A. Noguchi, T. Koike, and T. Mihara, "Nanoscale elasticity measurement with *in situ* tip shape estimation in atomic force microscopy," Rev. Sci. Instr. **71**, 2403-2408, 2000.

[YAM01] K. Yamanaka, Y. Maruyama, T. Tsuji, and K. Nakamoto, "Resonance frequency and Q factor mapping by ultrasonic atomic force acoustic microscopy," Appl. Phys. Lett. **78**, 1939-1941, 2001.

Numerical models of longitudinal wave scattering in polycrystals

Goutam Ghoshal and Joseph A. Turner*

Department of Engineering Mechanics, W317.4 Nebraska Hall

University of Nebraska-Lincoln, NE 68588-0526, USA

October 8, 2004

ABSTRACT

The scattering of elastic waves in polycrystalline materials is relevant for ultrasonic materials characterization and nondestructive evaluation (NDE). Ultrasonic attenuation is used widely to extract the microstructural parameters such as grain size. Accurate interpretation of experimental data requires robust scattering models. Such models typically assume constant density, uniform grain size and ergodicity hypotheses. The accuracy and limits of applicability of these models cannot be fully tested with experiments due to practical limits of real materials processing. Here, this problem is examined in terms of numerical simulations using Voronoi polycrystals that are discretized using finite elements. Wave propagation is studied by integrating the system directly in time using a plane-strain formulation. Voronoi polycrystals with cubic symmetry and random orientations are used making the bulk material statistically isotropic. Example numerical results for materials with various degrees of scattering that are of common interest are presented. Simulations are also presented for these materials. The numerical results are

*Corresponding author. Tel: +402-472-8856. *E-mail*: jaturner@unl.edu. *URL*: www.http://em-jaturner.unl.edu

presented and compared with scattering theory for a wide range of frequencies. The numerical results show good agreement with the theory for the examples examined with evidence that the correlation function is frequency dependent. These results are anticipated to impact ultrasonic NDE of polycrystalline media.

PACS numbers : 43.20.Bi, 43.20.Gp, 43.35.Cg

I INTRODUCTION

Ultrasonic techniques are widely used to extract microstructural parameters from polycrystalline media such as grain size and grain texture. Often, these techniques rely on the scattering behavior of the waves that interact with the heterogeneous microstructure. The amplitude of the propagating wave reduces due to this scattering, a phenomenon called attenuation. Grain parameters and flaws can often be inferred if the attenuation in the material is measured. The frequency dependence of attenuation can also be related to the grain diameter. In general, there are three distinct regions of attenuation α for a given grain size D and frequency f as[1]

$$\begin{aligned} \alpha &\propto f^4 \quad \text{for} \quad \lambda > D, \\ \alpha &\propto f^2 \quad \text{for} \quad \lambda \sim D, \\ \alpha &\propto 1/D \quad \text{for} \quad \lambda \ll D, \end{aligned} \tag{1}$$

where λ is the wavelength. These scattering regimes are often denoted as the Rayleigh ($\lambda > D$), stochastic ($\lambda \sim D$), and geometric optics ($\lambda \ll D$) regimes.

Scattering theories have been developed for decades to describe the scattering attenuation. Bhatia[2,3] discussed this dependence of attenuation on these parameters and developed a model for the attenuation assuming small variations in the elastic moduli from grain to grain for the Rayleigh regime. In this theory, it was assumed that the grains were spherical with weak anisotropy and random orientation. Hirsekorn calculated the attenuation as a function of wave number and grain radius without the limitation of the Rayleigh assumption,[4,5] for different wave types in polycrystals with any symmetry. Finally, Stanke and Kino utilized stochastic operator methods to develop a unified theory of ultrasonic scattering that covers all frequency regimes.[6] This model, and equivalent models that followed,[7] provided a self-consist method for determining attenuation in polycrystalline media.

The validity of these scattering theories is often corroborated through comparison with experimental attenuation data. Ultrasonic attenuation measurements are most often made by exciting

an ultrasonic wave at one surface of the specimen using a transducer. The same transducer is then used to measure the material response that consists of successive reflections from the two parallel faces of the specimen. The measured amplitude decay can then be used to deduce the loss of energy due to scattering assuming that other factors, such as beam spreading, that may contribute to the loss of amplitude are appropriately included in the data reduction. The comparison of theoretical and experimental attenuation data is nontrivial for several reasons. Among these is the fact that the theories usually oversimplify the material microstructure, including assumptions of constant density, a single grain size and no texture. Real microstructures, however, include all of these complications to some extent such that a precise comparison is seldom possible. On the other hand, numerical models of elastic wave propagation in complex microstructures can be developed to match precisely the assumptions of the theoretical models such that their range of validity may be explored more thoroughly.

A variety of numerical methods have been used for examining wave propagation in heterogeneous media including the finite difference (FD) method,[8] the FD pseudospectral method,[9] the boundary element method,[10] and the elastodynamic finite integration technique (EFIT)[11,12] among others. Although each of these methods may be effective for certain wave problems in heterogeneous media in general, none is specifically suited to polycrystalline media. Thus, a new numerical model is needed for this important class of problems.

In this article, the finite element method (FEM) is used in conjunction with Voronoi polycrystal geometries to analyze elastic wave propagation and scattering under assumptions of plane strain. Numerical models with uniform-size grains with random crystal orientation are used for the attenuation calculations. The numerical results cover a range of frequencies and materials with various degrees of scattering, including aluminum and copper. These results are compared with the polycrystalline scattering theory. The numerical results allow observations about the dependence of the microstructural parameters on attenuation within the context of the scattering theory.[7,13] Voronoi polycrystals has been used widely for various engineering applications but

have never been used to study elastic wave scattering in polycrystalline materials.

In the next section, the important concepts of elastic wave scattering theory are reviewed. In the subsequent section, the numerical model is described and the method in which the attenuation is determined from the numerical models are discussed. Finally, the comparison between the theoretical and numerical models is made and the results discussed. These results are anticipated to impact ultrasonic NDE of polycrystalline media.

II THEORY

Elastic waves while propagating in an heterogeneous polycrystalline medium scatter at the boundaries of grains due to the mismatch in grain orientation. As a result of this scattering there is a loss of energy in the propagating wave which is termed attenuation. The elastic wave fields are composed of longitudinal and transverse components, each with its respective attenuation. Stanke and Kino used stochastic operator methods to derive the attenuation and change in phase velocity due to grain scattering for longitudinal and shear waves.[6] Their results are widely applicable for media with texture as well as for materials with elongated grains. In an alternative derivation, Weaver used diagrammatic methods to derive ultrasonic attenuations and the subsequent diffusivity for polycrystalline media.[7] His derivation was based on the discussions of Frisch[14] concerning the mathematical formulation of wave propagation in heterogeneous media. This approach is based on the Dyson and Bethe-Salpeter equations which govern the mean response and covariance of the response of the field, respectively. This approach is used here as well. In addition, the first-order smoothing (FOSA) is used to solve the Dyson equation as outlined elsewhere.[14,7]

The equation of motion for the elastodynamic response of an infinite linear elastic medium is

written in terms of the Green's dyadic as[13]

$$\left\{-\delta_{ik}\rho\frac{\partial^2}{\partial t^2}+\frac{\partial^2}{\partial x_i}C_{ijkl}(\mathbf{x})\frac{\partial^2}{\partial x_l}\right\}G_{k\alpha}(\mathbf{x},\mathbf{x}';t)=\delta_{j\alpha}\delta^3(\mathbf{x}-\mathbf{x}')\delta(t). \tag{2}$$

The second-rank Green's dyadic $G_{k\alpha}(x,x';t)$ is the response to a concentrated impulsive force. It is the response at a location x in the kth direction to a unit impulse at location x' in the αth direction. Here, the density ρ is assumed to be uniform throughout.

For the polycrystals considered here, the modulus tensor is no longer a constant but is function of position. It is assumed to be spatially varying and of the form

$$C_{ijkl}(\mathbf{x})=C^0_{ijkl}+\delta C_{ijkl}(\mathbf{x}), \tag{3}$$

where $C^0_{ijkl}=\langle C_{ijkl}(x)\rangle$ is the average modulus tensor with the angle brackets denoting an ensemble average. The fluctuation about the mean is given by δC_{ijkl} which is assumed to have zero mean $\langle\delta C_{ijkl}(x)\rangle=0$. The covariance of the moduli, an eighth rank tensor is written

$$\Lambda(|\mathbf{x}-\mathbf{y}|)^{ijkl}_{\alpha\beta\gamma\delta}=\langle\delta C_{ijkl}(\mathbf{x})\delta C_{\alpha\beta\gamma\delta}(\mathbf{y})\rangle=\Xi^{ijkl}_{\alpha\beta\gamma\delta}\eta(|\mathbf{x}-\mathbf{y}|). \tag{4}$$

The covariance Λ consists of the tensorial component Ξ and spatial component η. Here, it is assumed that η is a function of the magnitude of the difference of two vectors $|\mathbf{x}-\mathbf{y}|$ rather than x and y separately. This assumption implies that the medium is statistically homogeneous and statistically isotropic. These two assumptions are used effectively by many[6,7] and will form the basis for the numerical models outlined below. The assumption of statistical isotropy implies that the two-point correlation function $\eta(r)$ is defined as

$$\eta(r)=e^{-r/L}. \tag{5}$$

This function defines the probability that two points separated by a distance r lie within the same crystal. Here, L is the correlation length, a parameter related to the grain diameter.[6,7]

The Green's function G is a random function due to the random nature of the media. Thus, the derivation of attenuation focuses on the mean response $\langle G\rangle$ that is governed by the Dyson

equation, with the angle brackets $\langle\rangle$ denoting an ensemble average. Solution of the Dyson equation gives a dispersion equation corresponding to $\langle G \rangle$. The solution of the dispersion equation gives the wave number which will have an imaginary part that is the attenuation of the propagating wave. The final expressions for the longitudinal attenuation for a statistically isotropic material may be written[7]

$$\alpha_L = \frac{1}{2\omega c_L}\left[\frac{\pi}{2}\int \underset{\hat{\mathbf{p}}\hat{\mathbf{p}}\hat{\mathbf{s}}\hat{\mathbf{s}}\cdots\cdot}{\overset{\cdots\cdot\hat{\mathbf{p}}\hat{\mathbf{p}}\hat{\mathbf{s}}\hat{\mathbf{s}}}{\Xi}}\frac{\omega^5}{c_L^7}\hat{\eta}\left(\hat{\mathbf{p}}\frac{\omega}{c_L}-\hat{\mathbf{s}}\frac{\omega}{c_L}\right)d^2\hat{\mathbf{s}}+\frac{\pi}{2}\int \underset{\hat{\mathbf{p}}\hat{\mathbf{p}}\hat{\mathbf{s}}}{\overset{\hat{\mathbf{p}}\hat{\mathbf{p}}\hat{\mathbf{s}}}{(\mathbf{I}-\hat{\mathbf{s}}}})\cdots\cdot\Xi\frac{\omega^5}{c_L^2c_T^5}\hat{\eta}\left(\hat{\mathbf{p}}\frac{\omega}{c_L}-\hat{\mathbf{s}}\frac{\omega}{c_T}\right)d^2\hat{\mathbf{s}}\right], \qquad (6)$$

where, $\Xi_{\cdots\cdot}^{\cdots\cdot\hat{\mathbf{p}}\hat{\mathbf{p}}\hat{\mathbf{s}}\hat{\mathbf{s}}} = \Xi_{ijkl}^{\alpha\beta\gamma\delta}\hat{p}_\alpha\hat{p}_i\hat{s}_\beta\hat{s}_j\hat{p}_\gamma\hat{p}_k\hat{s}_\delta\hat{s}_l$ is the inner product on the material covariance and $\hat{\eta}$ is the spatial Fourier transform of the two-point correlation function given in Eq. 5. The integral is over a unit sphere defined by $\hat{s}$. The directions $\hat{p}$ and $\hat{s}$ define the propagation and the scattered directions, respectively. This expression for the attenuation is used for the theoretical curves presented below.

Three types of material are used for the comparison between the theoretical model with the numerical results. The properties of these material are shown in Table I. The dimensionless anisotropy factor, $\upsilon/\rho c_T^2$, introduced by Weaver,[7] is given for each material, with $\upsilon = C_{11}-C_{12}-2C_{44}$ defined for the cubic crystallite structure considered here. This factor dictates the degree of scattering for the material. From Table I, it can be seen that copper has the strongest scattering property and aluminum the weakest among the three with the factor for copper approximately 4.5 times higher than that of aluminum. The material properties of the fictitious material are chosen such that its scattering properties lie between copper and aluminum. These materials are chosen such that the numerical results may be compared with theory for weakly, moderately, and strongly scattering materials.

III NUMERICAL RESULTS

A Numerical Model

The numerical polycrystalline models used here are constructed using the Voronoi tessellation. Geometries based on the Voronoi cell are increasingly being used in the numerical analysis of many practical problems, such as the study of the microstructures of materials,[15,16,17] liquid structures,[18] biology,[19] chemistry,[20] crystallography,[21] geography,[22] and wireless communication problems.[23] As an example of the last application, given a set of x micro-cell substations, the closest substation must be chosen to carry a call. Such tessellations help in searching for the closest neighbor. Voronoi polycrystals have also been shown to represent closely the microstructures of many materials. Espinosa and Zavattieri[24,25] briefly discuss the use of Voronoi tessellation for creating a numerical model to study failure initiation in brittle materials. Ghosh, et al.[15] developed the Voronoi cell finite element method (VCFEM) for plane strain analysis of heterogeneous microstructures. Kumar, et al.[16] presented a statistical analysis of three-dimensional grains generated by a Poisson-Voronoi tessellation.

A Voronoi tessellation is used to subdivide a given region with each Voronoi cell having a nucleus. The nuclei positions are created to match the relevant application. Often they are chosen randomly. As per the definition of Voronoi diagram, any point inside a Voronoi cell V_i is nearer to the nucleus V_i than to any other nucleus V_j in the given region. Such a procedure produces convex polygons in two-dimensional and convex polyhedrons in three-dimensional domains which completely fill the given region. In the three-dimensional domain, every edge of a Voronoi cell connects three grains and two vertices and every vertex connects four edges, six faces, and four cells.[16] Readers interested in further details of Voronoi tessellations are referred to articles 25 to 36. Although Voronoi polycrystals are widely used in other polycrystal applications, they have not yet been used to study attenuation from grain scattering.

Here, Voronoi polycrystals are created inside the required finite domain using a uniform distribution. To obtain a uniform distribution of grain size, the minimum distance between Voronoi nuclei is restricted. The statistics of the grain area are shown in Fig. 2. The fit is done using the Gaussian function,

$$F(x) = \frac{1}{\sigma\sqrt{2\pi}} e^{-\frac{(x-\mu)^2}{2\sigma^2}}, \tag{7}$$

where μ is the mean area of crystals and σ is the standard deviation. A Gaussian curve fits the data of crystal area well confirming that a normal distribution of grain size is obtained.

The two-dimensional Voronoi polycrystals are constructed and discretized into finite triangular elements. Then the model is extruded by a depth approximately 1 to 1.5 times of the characteristic element size. Therefore, the two-dimensional element becomes a prism element after extrusion. The elements in the each crystal are assigned a random material orientation in the three crystal directions. Thus, the model is not completely three-dimensional, rather it is a psuedo-three-dimensional model. An example model is shown in Fig. 1. For clarity, Fig. 1 was created with large crystals and elements. Plane strain boundary conditions are chosen by restricting the displacement of all the nodes in the out-of-plane direction. Material orientation is indicated in Fig. 1 by the local coordinate axes shown for each crystal. The use of the infinite elements at the vertical boundaries of the model minimize reflections of the wave from these boundaries. The boundary conditions at the top and bottom of the model are stress free.

The loading is a pressure load applied normal to the top surface to simulate an incident longitudinal wave. A three-cycle Gaussian pulse is used as the input pressure load shown in Fig. 3. The fast Fourier transform (FFT) of the pulse is plotted in the frequency domain graph to verify the frequency content of the input wave. It should be noted that the depth of the models used here, 0.075 mm, is very small compared with the wavelength of the input wave. For example, a 5 MHz incident longitudinal wave in aluminum has a wavelength $\lambda = 1.25$ mm.

Example simulations at several time steps are shown in Figs. 4 and 5 for aluminum and copper,

respectively. Note that the original wave form is lost in a shorter time for copper compared with aluminum due to copper having a higher degree of scattering. Nodal displacements at the top and bottom surfaces of the domain are stored for use in the attenuation calculations.

B Attenuation Calculation from Numerical Results

The numerical results are obtained using the procedure outlined in the previous section. The attenuation is calculated by[26]

$$e^{-\alpha d} = \frac{|F_2(\omega)|}{|F_1(\omega)|}, \tag{8}$$

where, α is the attenuation, d is the travel length of the elastic wave, and $F_1(\omega)$ and $F_2(\omega)$ are the first and the second backwall reflections, respectively in the frequency domain. The reflections are averaged over the nodes at the surfaces for each model and the attenuation is calculated. Attenuation results are then averaged for different realizations of Voronoi polycrystals.

The materials examined here have different scattering properties as shown in Table I. The attenuation calculation can be difficult to perform as the noise in the echoes is higher when the scattering is stronger. Thus, the front and backwall echoes may be difficult to identify. When the scattering is weak, the echoes can easily be recognized. Thus, different model sizes were used according to the scattering properties of the material. Thus models for weakly scattering media have larger distance between frontwall and backwall than models for strongly scattering media. The model is made wider for strongly scattering media so that more nodal data may be obtained.

The attenuation is calculated from the backwall reflections in the model. The first two reflections are used and referred to as echo E1 and echo E2. Tapered windowing and zero padding are done on E1 and E2. Using Eq. (8), the attenuation is obtained for these responses. The attenuation is also calculated in a similar manner for the same model using homogeneous material properties. The attenuation in the homogeneous material is due to beam spreading and small

numerical scattering effects. The attenuation in the homogeneous material is deducted from that of the heterogeneous material model and the final attenuation curve obtained. An example result is shown in Fig. 6(a) and (b) for an input wave frequency of 5 MHz. The attenuation results for frequencies far from 5 MHz are primarily noise. Attenuation results are then averaged from models with different realizations of grains shown in Fig. 6(b). Similar attenuation data are obtained for the models studied by varying the grain diameter and frequency of the input wave.

IV COMPARISON OF NUMERICAL RESULTS WITH THEORY

The attenuation results are obtained for aluminum, the fictitious material and copper and are compared with the theoretical results. In the theory, a constant correlation length L is assumed. The theoretical attenuation values for the examples materials are calculated from the expression given by the Eq. (6). In contrast, the numerical model includes a distribution of grain diameters as illustrated in Fig. 2. Sixty-eight percent of the grains have diameters that fall within one σ of the mean diameter. Therefore, the results presented here are normalized to the mean diameter D_m, as well as $D_m \pm \sigma$. The numerical results are compared with the theoretical results shown in Figs. 7, 8 and 9 for aluminum, the fictitious material and copper respectively. The results cover a wide range of normalized frequency λ/D (1.5 to 6) and attenuation αD $\left(0.5 \times 10^{-3} \text{ to } 0.15\right)$. The normalized attenuation for the three materials varies by a factor of ten when compared with one another.

The model size for aluminum, a weakly scattering material, is 5x12x0.075 mm^3. Models with 600 and 800 crystals are created inside this domain. The attenuations are obtained for input wave frequencies of 5 MHz and 15 MHz as shown in Fig. 7. The normalized attenuation αD and wavelength λ/D, range from 0.0005 to 0.003 and 1.5 to 6 respectively. Here the attenuation results are obtained from fifteen realizations of Voronoi crystals. The numerical results agree well with the theory for the lower frequency range, i.e. for 5 MHz for models with 600 and 800

crystals shown in Fig. 7(a). The numerical results shown in Fig. 7(b) i.e., for attenuation and wavelength normalized by $(D_m - \sigma)$ agree well for the higher frequency results. The agreement for lower frequency results is best when attenuation and wavelength are normalized by $(D_m + \sigma)$ where D_m is the mean grain diameter, shown in Fig. 7(c).

It may be observed that the attenuation results for aluminum have relatively large variations. These variations are the result of the small amplitude drop. The amplitude drop between successive reflections must lie between two limits in order for the attenuation to be calculated accurately. If the decay is too large noise dominates the signal. On the other hand if the scattering is not very large, as is the case for aluminum, the amplitude ratio, Eq.(8) is very close to unity and may have large statistical fluctuations. This concept may be quantified by examining the amount of scattering that takes over the propagation path. The mean free path is inversely proportional to the attenuation of the material. Therefore, the inverse of αD quantifies the minimum number of crystals required along the propagation path for ultrasonic scattering that is sufficient for reduced uncertainty (i.e., the amplitude decays by e^{-1}). Therefore, the model size is adjusted to address this issue. In aluminum, for $\alpha D = 10^{-3}$ the input wave needs to travel through at least 1000 crystals to have sufficient scattering that the statistical fluctuations are reduced. Thus, the fluctuations in the attenuation results for aluminum are due to an insufficient number of crystals over the propagation path.

The models created for the fictitious material, a moderate scattering medium, are of the same size as that of the model for aluminum. Attenuations are obtained for 600 crystals for various input wave frequencies of 3 MHz, 5 MHz, 10 MHz and 15 MHz. The attenuation results are obtained for αD and λ/D ranging from 0.025 to 0.015 and 1.5 to 4.5 respectively as shown in Fig. 8. The results obtained from different frequencies follow the same trend. For $\alpha D = 0.01$, at least 100 crystals are required for sufficient scattering. Therefore, the model for this material contains enough grains for sufficient scattering such that the attenuation fluctuations are not significant.

Copper, a strongly scattering material compared with aluminum and the fictitious material, was studied using a smaller model size of $5 \times 6 \times 0.075$ mm^3. Models are created with various number of grains including 50, 100 and 200. Attenuation results for copper are shown in Fig. 9. Since copper is a strongly scattering material the noise content is the highest of the three materials considered. Therefore wave frequencies of 5 and 8 MHz were used such that the front and backwall echoes could be more easily identified. The attenuation values are the highest of all media, ranging from 0.025 to 0.15 for normalized frequency ranges from 0.75 to 5.5. For $\alpha D = 0.1$, only 10 crystals are necessary for scattering sufficient for small fluctuations in the attenuation results. For the lower frequency range the numerical results agree well with the theory, although those at higher frequency are less than adequate.

The plots shown include a theoretical curve based on the theory described above. For theoretical results, the correlation function η is an exponential form shown in Eq. 5. The numerical results show better agreement with the theory for the lower frequency ranges. Weaver[7] speculated that at higher frequency η depends on the volume density of the grain boundary rather than the grain volume. For low frequencies this relation is

$$\bar{V} = \int d^3 r e^{-\frac{r}{L}} = 8\pi L^3, \tag{9}$$

where, L is the correlation length. At higher frequency the correlation length may be half of the value calculated from Eq. 9.[7] Thus, it may be assumed that $L = cD$, with c a constant. Equation (9) implies $c = 0.28$. Here to match the numerical with the theoretical results this constant $c = 1.6$, 1.3 and 1.1 for calculating attenuation for aluminum, fictitious material and copper respectively. The constant c for the example materials are determined by minimizing the root mean square deviation of the error between the theoretical and numerical attenuation values. This constant decreases as the degree of scattering in the material increases. At higher frequency for copper, the results cannot be matched with the theory even by adjusting this value. The technical reasons for these variations in L is out of scope of this work, but the numerical model can be very useful for investigating this relation. The influence of the form of the correlation function

on the interpretation of attenuation is evident from these results.

V SUMMARY

In this article, a numerical model is constructed using Voronoi polycrystals for examining longitudinal attenuation in materials of general interest. The attenuation is calculated for polycrystalline aluminum, a fictitious material and copper which are in general weakly, moderately, and strongly scattering materials, respectively. A large range of attenuation values are obtained from the numerical results. Various models with different grains are constructed and the longitudinal attenuation is calculated for a wide range of frequencies. For each attenuation calculation fifteen realizations of Voronoi polycrystals were used. Normal pressure loading was used and infinite boundary conditions were imposed to minimize the reflections at the sides of the model.

The numerical results for attenuation show the dependence of the correlation function chosen for theoretical models. The results shows that different correlation lengths are needed depending on frequency and scattering strength as speculated by other authors.[6,7] Overall, the numerical results agree well with the theory at lower frequencies for all the materials examined. The attenuation calculated from various models and input wave specifications follow each other for any particular material tested here. The results for copper at higher frequency do not match well with the theoretical model. This result may indicate that higher-order correlations are important for strongly scattering materials, but future research is necessary to validate this hypothesis.

The numerical model can now be used efficiently to investigate the correlation function for various parameters in the model, input wave frequency and the material type which closely relate to real materials. The numerical approach developed here will be used in future work for a variety of problems, including diffuse ultrasonic scattering problems. The Voronoi polycrystal is a good model that can be used to verify theoretical models and to design new experimental methods for

characterization of microstructures.

VI ACKNOWLEDGMENTS

The support of the Department of Energy (Grant No. DE-FG02-01ER45890) for this research is gratefully acknowledged. The Matlab[27] built-in subroutine 'voronoi' has been used along with the algorithms for "Method of Virtual Nuclei"[28] above to construct the Voronoi polycrystals presented here.

References

[1] Papadakis, E. P., "Ultrasonic Attenuation Caused by Scattering in Polycrystalline Metals," *J. Acoust. Soc. Am.*, Vol. 37, No. 4, 1965, pp. 711–717.

[2] Bhatia, A. B., "Scattering of High-Frequency Sound Waves in Polycrystalline Materials," *J. Acoust. Soc. Am.*, Vol. 31, No. 1, 1959, pp. 16–23.

[3] Bhatia, A. B., *Ultrasonic Absorption*, Oxford, London, 1967.

[4] Hirsekorn, S., "The Scattering of Ultrasonic Waves by Polycrystals," *J. Acoust. Soc. Am.*, Vol. 72, No. 3, Sep. 1982, pp. 1021–1031.

[5] Hirsekorn, S., "The Scattering of Ultrasonic Waves by Polycrystals. II. Shear Waves," *J. Acoust. Soc. Am.*, Vol. 73, No. 4, 1983, pp. 1160–1163.

[6] Stanke, F. E. and Kino, G. S., "A Unified Theory for Elastic Wave Propagation in Polycrystalline Materials," *J. Acoust. Soc. Am.*, Vol. 3, 1984, pp. 665–681.

[7] Weaver, R. L., "Diffusivity of Ultrasound in Polycrystals," *J. Mech. Phys. Solids*, Vol. 38, No. 1, 1990, pp. 55–86.

[8] Alford, R. M., Kelly, K. R., and Boore, D. M., "Accuracy of Finite-Difference Modeling of the Acoustic Wave Equation," *Geophysics*, Vol. 39, No. 6, December 1974, pp. 834–842.

[9] Fornberg, B., "The Pseudospectral Method: Accurate Representation of Interface in Elastic Wave Calculations," *Geophysics*, Vol. 53, No. 5, May 1988, pp. 625–637.

[10] Liu, E. and Zhang, Z., "Numerical Study of Elastic Wave Scattering by Cracks or Inclu-

sions Using the Boundary Integral Equation Method," *J. Comp. Acoust.*, Vol. 9, No. 3, 2001, pp. 1039–1054.

[11] Fellinger, P., Marklein, R., Langenberg, K. J., and Klaholz, S., "Numerical Modeling of Elastic Wave Propagation and Scattering with EFIT - Elastodynamic Finite Integration Technique," *Wave Motion*, Vol. 21, 1995, pp. 47–66.

[12] Schubert, F., Peiffer, A., Kohler, B., and Sanderson, T., "The Elastodynamic Finite Integration Technique for Waves in Cylindrical Geometries," *J. Acoust. Soc. Am.*, Vol. 104, No. 5, November 1998, pp. 2604–2614.

[13] Turner, J. A., "Elastic Wave Propagation and Scattering in Heterogeneous, Anisotropic Media: Textured Polycrystalline Materials," *J. Acoust. Soc. Am.*, Vol. 106 (2), August 1999, pp. 541 – 552.

[14] Frisch, U., "Wave Propagation in Random Media," *Probabilistic Methods in Applied Mathematics*, edited by A. T. Barucha-Reid, Vol. 1, Academic, New York, 1968, pp. 75–198.

[15] Ghosh, S., Nowark, Z., and Lee, K., "Tessellation-Based Computational Methods for the Characterization and Analysis of Hetrogeneous Microstructures," *Composite Science and Technology*, Vol. 57, 1997, pp. 1187–1210.

[16] Kumar, S., Kurtz, S., Banavar, S., and Sharma, M., "Properties of a Three-Dimensional Poisson-Voronoi Tessellation: A Monte Carlo Study," *Journal of Statistical Physics*, Vol. 67, 1992, pp. 523–551.

[17] Zavattieri, P. D., Raghuram, P. V., and Espinosa, H., "A Computational Model of Ceramics

Microstructures Subjected to Multi-Axial Dynamic Loading," *Journal of the Mechanics and Physics of Solids*, Vol. 49, 2001, pp. 27–68.

[18] Brostow, W. and Castano, V., "Voronoi Polyhedra as a Tool for Dealing with Spatial Structures of Amorphous Solids, Liquids Ans Dense Gases," *Journal of Materials Education*, Vol. 21, 1999, pp. 297.

[19] Gerstein, M., Tsai, J., and Levitt, M., "The Volume of Atoms on the Protien Surface: Calculated from Simulation, Using Voronoi Polyhedra," *Journal of Molecular Biology*, Vol. 249, 1995, pp. 955–966.

[20] Montoro, J. C. G. and Abascal, J. L. F., "The Voronoi Polyhedra as Tools for Structure Determination," *Journal of Physical Chemistry*, Vol. 97, 1993, pp. 4211–4215.

[21] Alani, H., Jones, C., and Tudhope, D., "Voronoi-Based Region Approximation for Geographical Information Retrieval with Gazetteers," *International Journal of Geographical Information Science*, Vol. 15, 2001, pp. 287–306.

[22] Christensen, S., "Analysis of Polynuclear Aromatic Hydrocarbons Via the Voronoi Tessellation Approach: Classification of Atom Types Using Artificial Networks," *Acta Crystallographica*, Vol. A58, 2002, pp. 171–179.

[23] Baccelli, F. and Blaszczyszyn, B., "On a Coverage Process Ranging from the Boolean Model to the Poisson Voronoi Tessellation, with Application to Wireless Communications," *Advances in Applied Probability*, Vol. 33, 2001, pp. 293–323.

[24] Espinosa, H. and Zavattieri, P., "A Grain Level Model for the Study of Failure Initiation and

Evolution in Polycrystalline Brittle Materials. Part I: Theory and Numerical Implementation," *Mechanics of Materials*, Vol. 35, 2003, pp. 333–364.

[25] Espinosa, H. and Zavattieri, P., "A Grain Level Model for the Study of Failure Initiation and Evolution in Polycrystalline Brittle Materials. Part II: Numerical Examples," *Mechanics of Materials*, Vol. 35, 2003, pp. 365–394.

[26] Schmerr, L. W., *Fundamentals of Ultrasonic Nondestructive Evaluation: A Modeling Approach*, Plenum Pub. Corp., New York, 1998.

[27] Matlab, *The Language of Technical Computing*, The Math Works, Inc., Natick, MA, 2001.

[28] Ghoshal, G., *Numerical Simulations of Elastic Wave Scattering in Polycrystalline Materials*, Master's thesis, University of Nebraska-Lincoln, 2003.

VII TABLES

	Independent Elastic Constants (GPa)			**Density** (kg/m^3)	**Modulus** (GPa)	**Speed** (m/sec)		**Dimensionless**
						Longitudinal	**Shear**	**Anisotropy**
	C_{11}	C_{12}	C_{44}	ρ	E	c_L	c_T	$\upsilon/\rho c_T^2$
Aluminum	103.4	57.1	28.6	2760	70	6244	3094	-0.4127
Fictitious	200.0	130.0	65.0	5000	160	6694	3256	-1.1321
Copper	176.2	124.9	81.8	8970	110	4965	2572	-1.8931

Table 1: Single-crystal properties of materials examined.

VIII FIGURE CAPTIONS

1. Voronoi polycrystal in three-dimensional domain after extrusion in out of plane axis.
2. (a) 300 Voronoi polycrystal and (b) grain statistics for 300 Voronoi crystals inside a unit square.
3. Input Gaussian pulse wave for 5MHz.
4. Simulation for aluminum with heterogeneous material properties (600 crystals in a 5 mm by 12 mm model for 5 MHz of longitudinal wave).
5. Simulation for copper with heterogeneous material properties (200 crystals in a 5 mm by 6 mm model for 5 MHz of longitudinal wave).
6. Attenuation for copper with input wave of 5 MHz for (a) one realization and (b) average from fifteen realizations of 200 grains for a model of size 5 by 6 units.
7. Theoretical and numerical attenuation results for aluminum.
8. Theoretical and numerical attenuation results for fictitious material.
9. Theoretical and numerical attenuation results for copper.

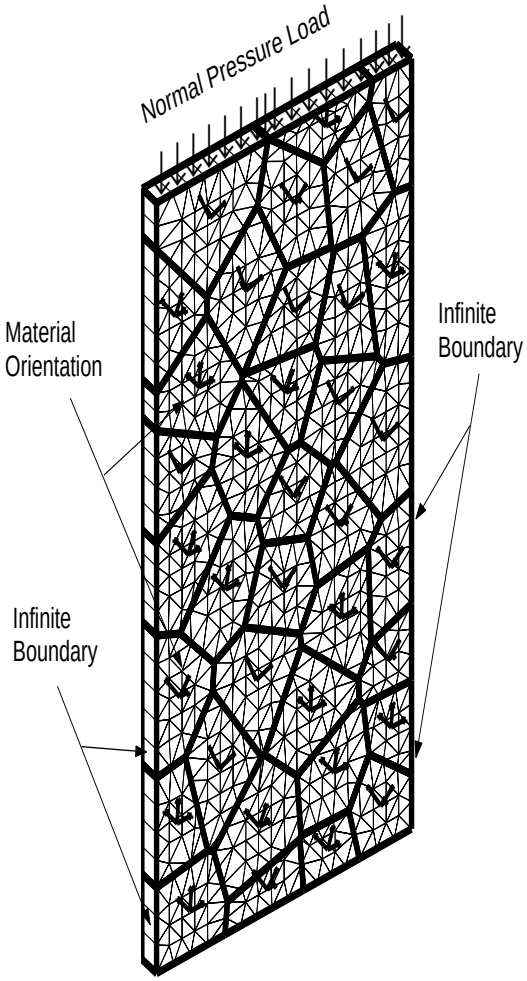

Figure 1: Voronoi polycrystal in three-dimensional domain after extrusion in out of plane axis.

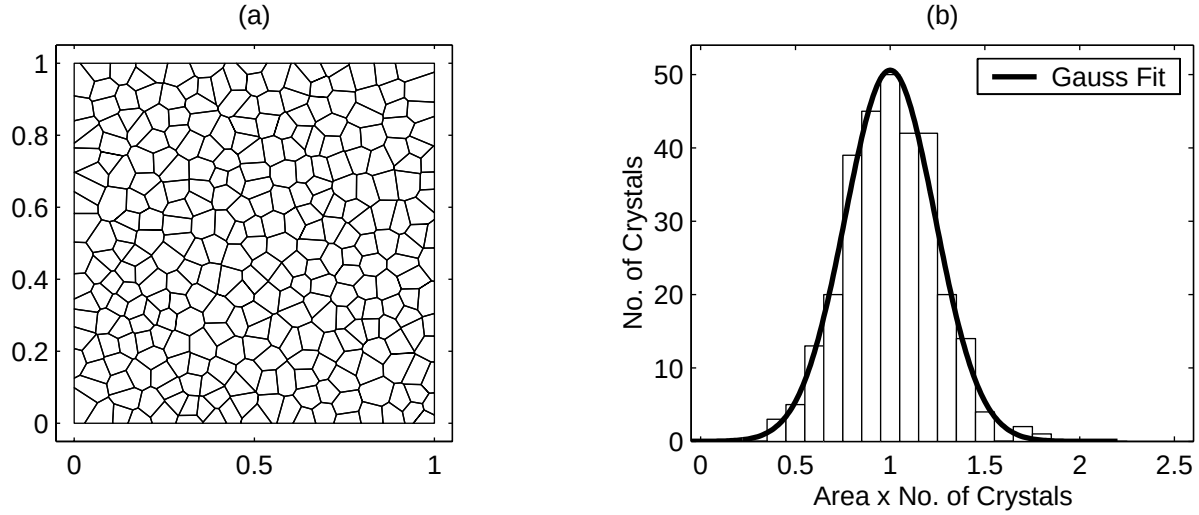

Figure 2: (a) 300 Voronoi polycrystal and (b) grain statistics for 300 Voronoi crystals inside a unit square.

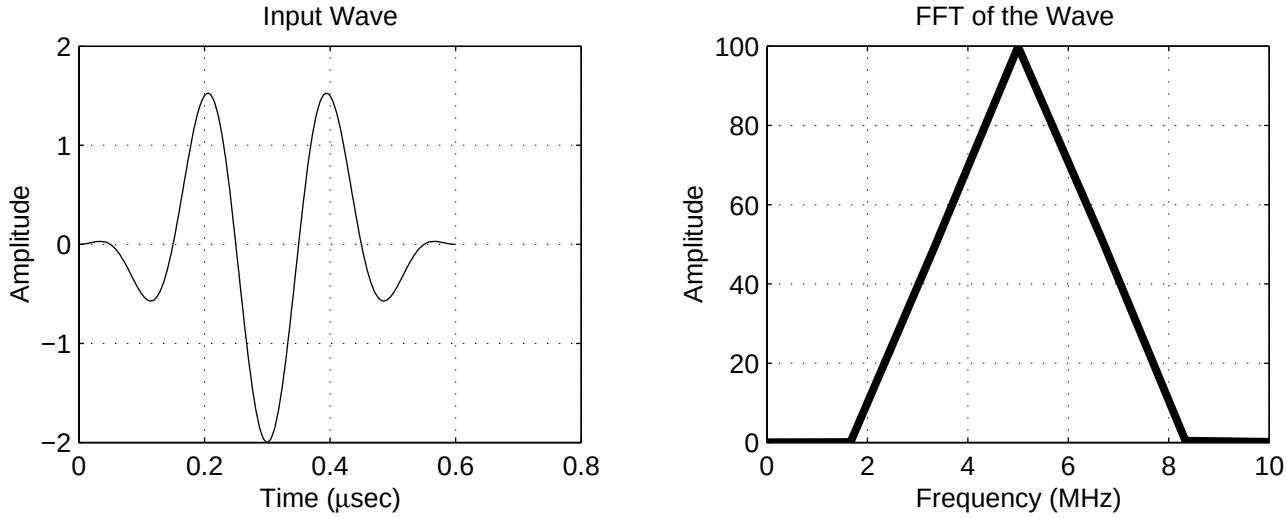

Figure 3: Input Gaussian pulse wave for 5MHz.

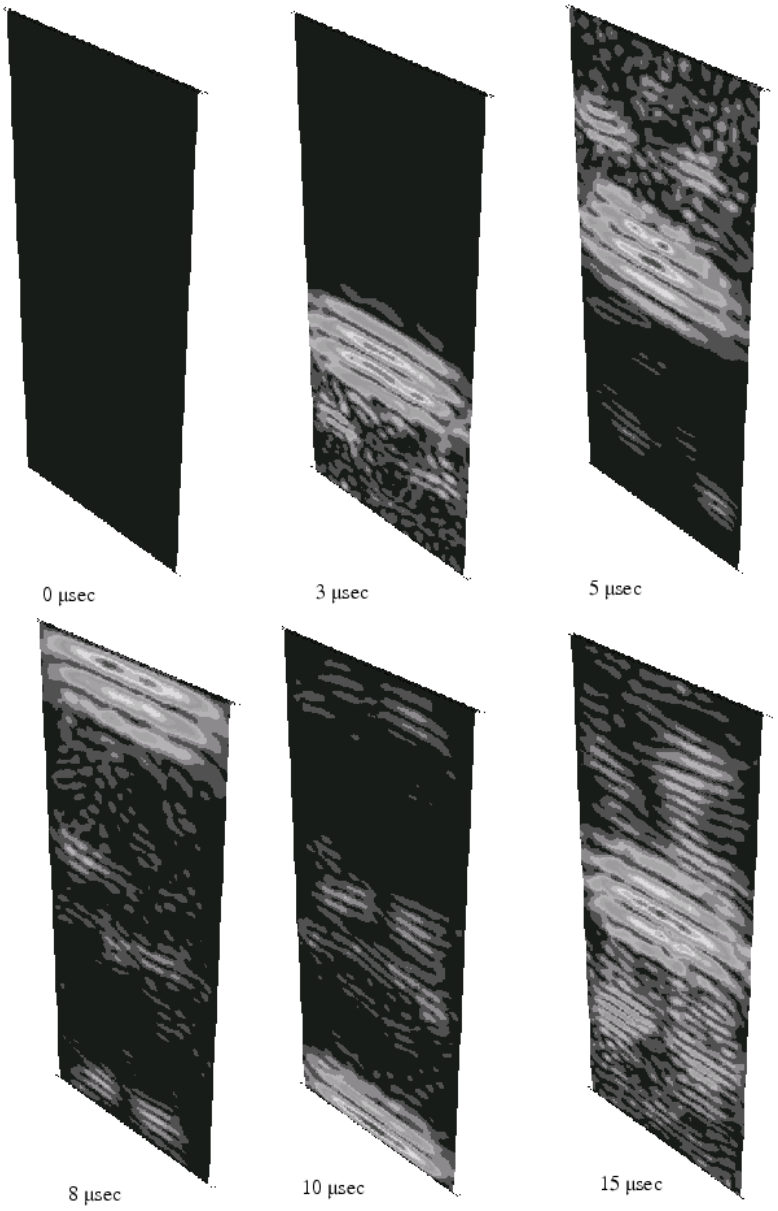

Figure 4: Simulation for aluminum with heterogeneous material properties (600 crystals in a 5 mm by 12 mm model for 5 MHz of longitudinal wave).

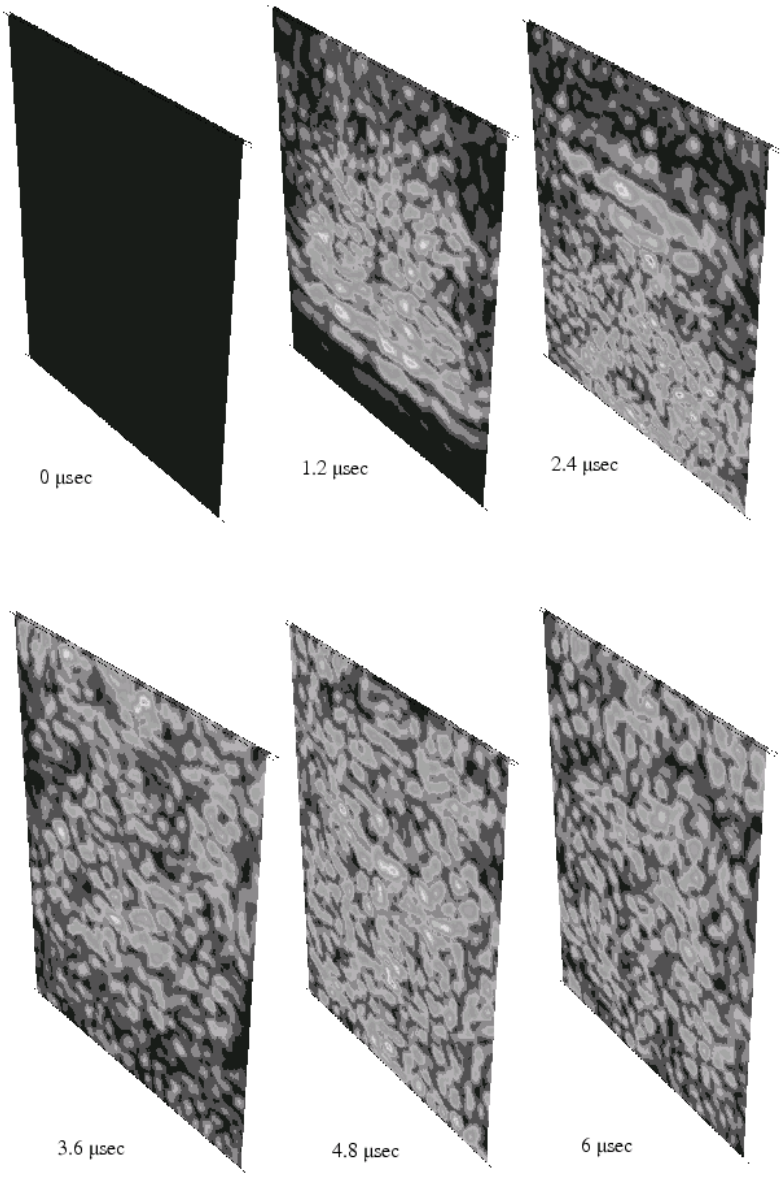

Figure 5: Simulation for copper with heterogeneous material properties (200 crystals in a 5 mm by 6 mm model for 5 MHz of longitudinal wave).

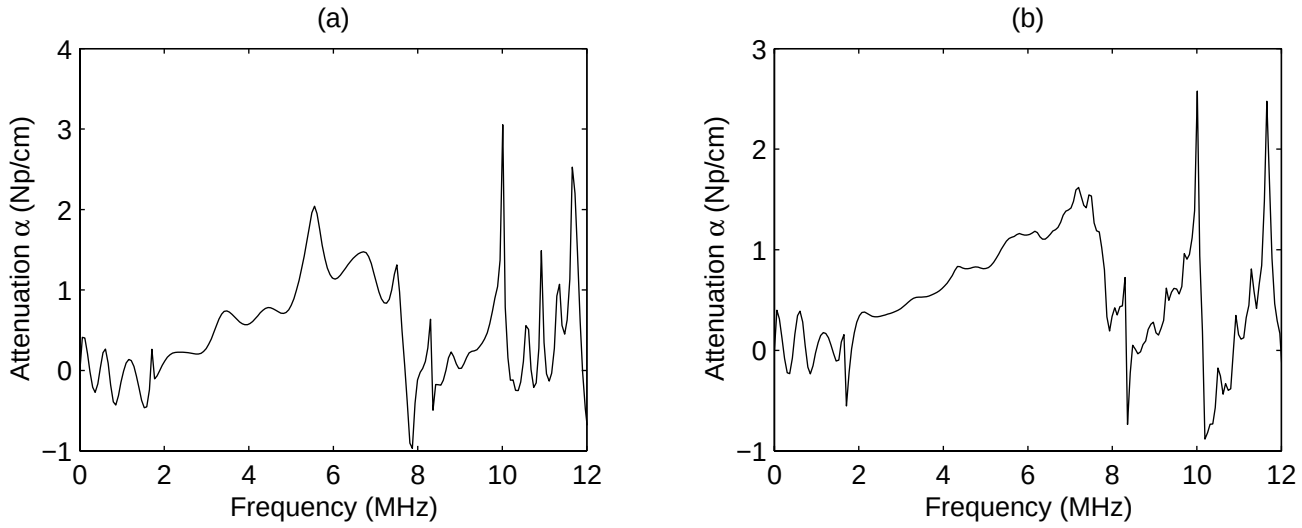

Figure 6: Attenuation for copper with input wave of 5 MHz for (a) one realization and (b) average from fifteen realizations of 200 grains for a model of size 5 by 6 units.

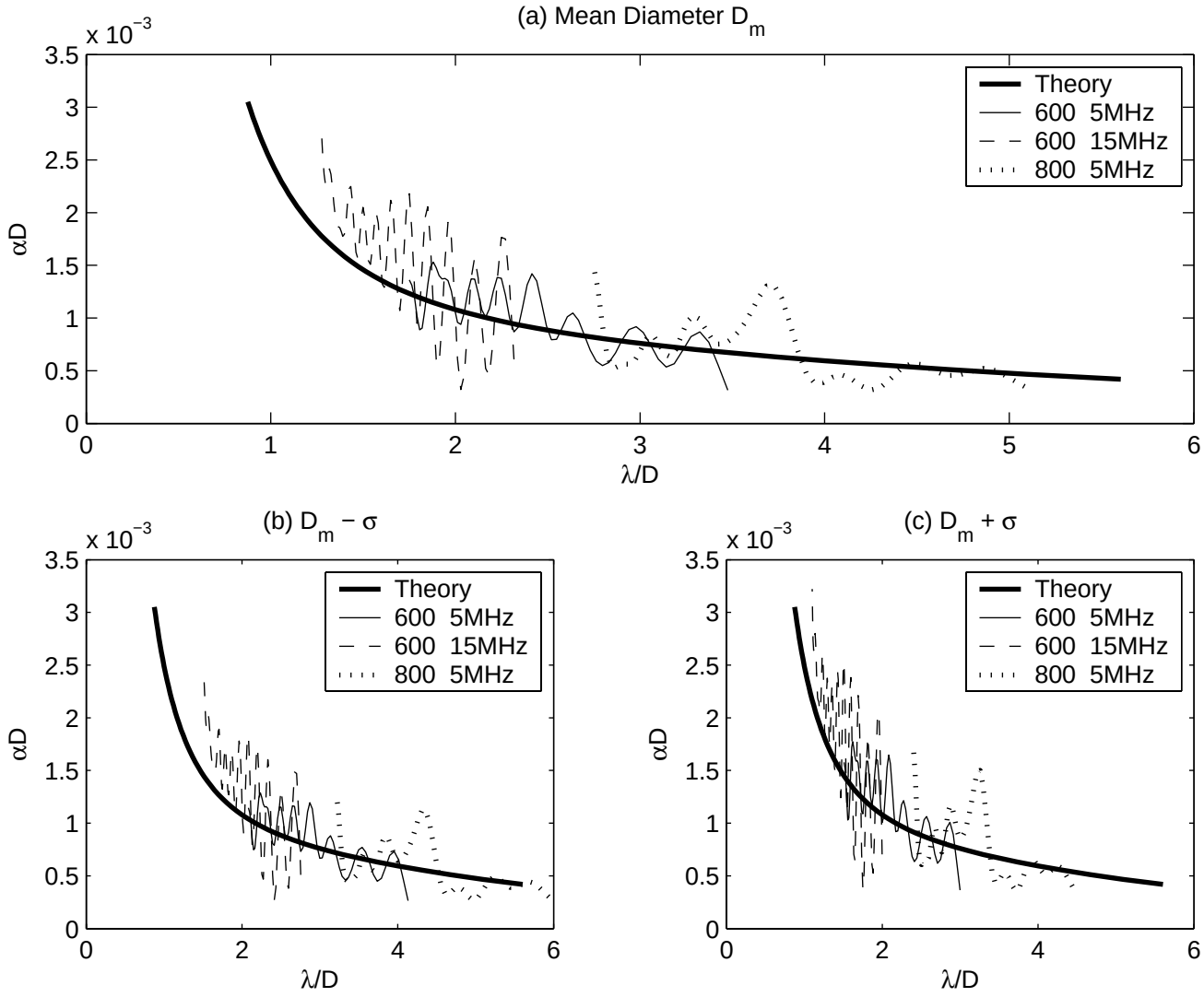

Figure 7: Theoretical and numerical attenuation results for aluminum.

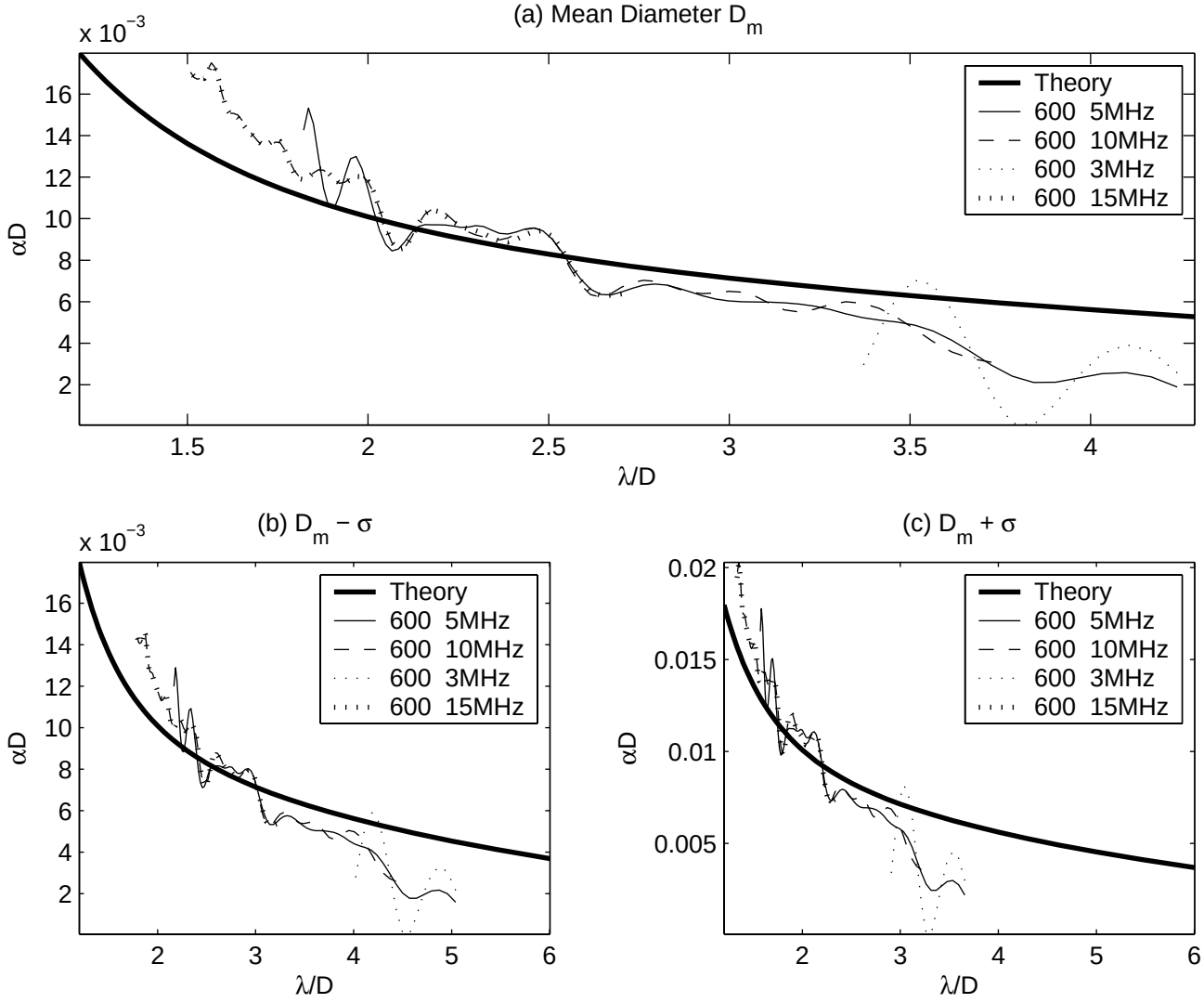

Figure 8: Theoretical and numerical attenuation results for fictitous material.

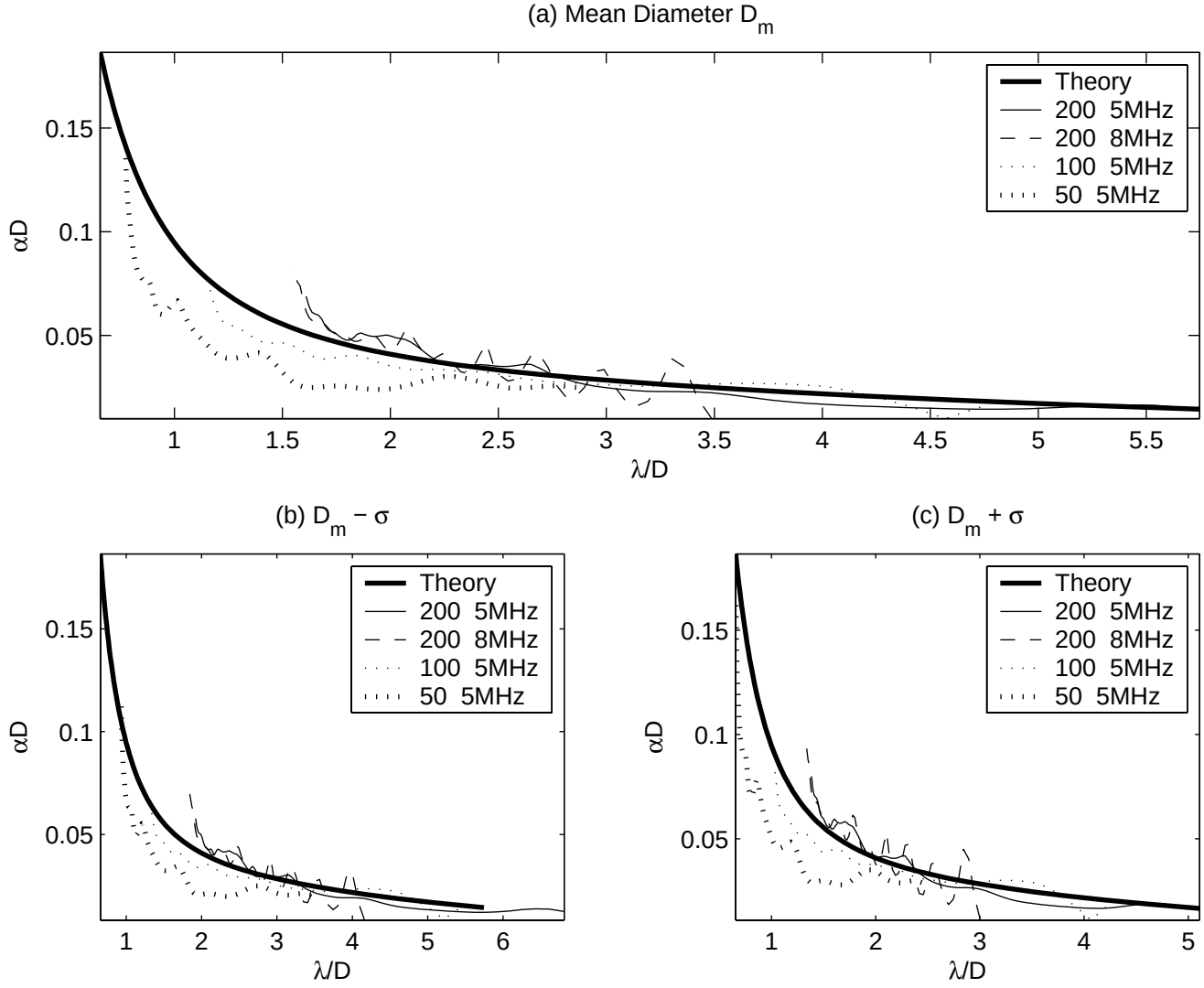

Figure 9: Theoretical and numerical attenuation results for copper.

Numerical Simulations of Elastic Wave Scattering in Polycrystalline Materials

by

Goutam Ghoshal

A THESIS

Presented to the Faculty of
The Graduate College of the University of Nebraska
In Partial Fulfillment of Requirements
For the Degree of Master of Science

Major: Engineering Mechanics

Under the Supervision of Joseph A. Turner

Lincoln, Nebraska

December, 2003

Numerical Simulations of Elastic Wave Scattering in Polycrystalline Materials

Goutam Ghoshal, M.S.

University of Nebraska, 2003

Adviser: Joseph A. Turner

The scattering of elastic waves in polycrystalline materials is relevant for ultrasonic materials characterization and nondestructive evaluation (NDE). Heterogeneity in the material ensures that ultrasonic scattering will take place, with the scattering dependent on frequency. Ultrasonic backscatter and attenuation are used widely to extract the microstructural parameters such as grain size. Accurate interpretation of experimental data requires robust ultrasonic scattering models. Such models typically assume constant density, uniform grain size and randomness hypotheses. The accuracy and limits of applicability of these models cannot be fully tested with experiments due to practical limits of real materials processing. Here, this problem is examined in terms of numerical simulations using Voronoi polycrystals.

The Voronoi diagram is used to model microstructures of polycrystalline materials. It is a method of geometric subdivision of space that is widely used in numerous science and engineering applications. The "Method of Virtual Nuclei" is presented to create Voronoi polycrystals in finite domains within any arbitrary convex geometry. Algorithms are developed to construct elongated Voronoi polycrystals with a specified aspect ratio and angle of orientation. Microstructures are presented of various processed materials such as rolled materials and functionally graded materials. The polycrystals are created for various dis-

tributions of grain size.

The Voronoi cells are discretized using finite elements. Wave propagation is studied by integrating the system directly in time. Six-noded prism elements are used for the discretization. ABAQUS/Explicit is used as the finite element software package. Voronoi polycrystals with cubic symmetry are used and given random orientations. Therefore, the bulk material is statistically isotropic. Example numerical results are presented for materials with various degrees of scattering that are of common interest. Simulations from ABAQUS/CAE are also presented for these materials. The simulations provide insight into the attenuation models relevant for polycrystalline materials. The numerical results are presented and compared with scattering theory. The theory for elastic wave attenuation is derived for a two-dimensional domain using elastodynamics and stochastic wave theory. The dependence of attenuation on the frequency of the input wave and the mean grain diameter are examined using the numerical results.

The numerical scattering results suggest that for the plane stress case the two-dimensional theory is better for weakly scattering media, while the three-dimensional is better for strongly scattering media. The results from plane strain agree well with the three-dimensional theoretical model for all materials. These results are anticipated to impact ultrasonic NDE of polycrystalline media.

Acknowledgements

The work supperted by US Department of Energy (DOE) under the Grant No. DE-FG02-01ER45890 is greatefully acknowledged.

I would like to thank my advisor Dr. Joseph A. Turner for constant guidence, inspiration, enthusiasm and support, without which this work would not have been possible. I would like to thank him for providing excellent advanced and latest computational facility and software packages in the laboratory for this work.

I would like extend my thanks to my committee members Dr. Ruqiang Feng and Dr. Florin Bobaru for providing a critical reveiw on my work.

I would like thank the University of Nebraska-Lincoln for allowing me to use the supercomputing facility at the Research Computing Facility (RCF). I would like to extend my gratitude to a number of individuals for their support and assistance in this project.

Finally, I would like to thank my parents and my brother for their never ending support, undertstanding and patience throughout my entire academic career.

Contents

List of Figures

List of Tables

Chapter 1

Introduction

Ultrasonic techniques are widely used to extract microstructural parameters such as grain size and grain structure. Heterogeneity in the material ensures that ultrasonic scattering will take place, with the scattering dependent on frequency. The amplitude of the response reduces as the wave propagates due to scattering, a phenomenon called attenuation. Grain parameters and flaws can be inferred by knowing the attenuation in the material. Attenuation is calculated by examining the reduction of amplitude of the propagating wave in the media. The frequency dependence of attenuation can be related to the grain diameter. Bhatia [1] discussed that the attenuation depends on the frequency of the propagating wave and the grain diameter. Papadakis [2] presented the three distinct regions of attenuation α for grain size D and frequency f as

$$\begin{aligned} \alpha &\propto f^4 \quad \text{for} \quad \lambda > D, \\ \alpha &\propto f^2 \quad \text{for} \quad \lambda < D, \\ \alpha &\propto 1/D \quad \text{for} \quad \lambda \ll D. \end{aligned} \tag{1.1}$$

where λ is the wavelength.

Bhatia [3] discussed the dependence of the parameters assuming negligible variation in the elastic moduli from grain to grain for a wavelength that is large compared with the grain diameter. He also showed the attenuation due to thermal agitation resulting in local fluctuations in the density in the material. The theory presented by Bhatia assumes spherical grains and polycrystals that are weakly anisotropic with grains that are randomly oriented. Hirsekorn [4] calculated the attenuation as a function of wave number and grain radius without limitation of the Rayleigh region. She presented the theory to calculate the velocity and attenuation of different wave types in polycrystals with any symmetry. She also presented the theory for plane shear waves in polycrystals [5] with cubic symmetry and randomly oriented grains.

Evans, et al. [6] presented a different approach for the attenuation expression for the Rayleigh and stochastic regions. His approach is based on the numerical computation of the cross section and extreme-value size distributions of the predominant scatterers assuming each scatterer is small compared with the wavelength.

The theory for attenuation in a two-dimensional domain is derived using the three-dimensional model presented previously by Weaver [7] and Turner [8] using the elastodynamic, stochastic theory of scattering. Their model for the attenuation includes the assumption of grains with random orientation. Therefore, the bulk material is assumed to be statistically isotropic. This assumption is also made by Weaver [7].

Analysis of experimental data is made using assumptions such as constant density, single grain size and randomness hypotheses. These measurements are made by sending ultrasonic waves through the media using transducers. In experiments there are also limi-

tations on the frequency ranges of the available transducers. Analytical methods cannot be used for very complex problems. Numerical study eliminates the limitations of the experiments and helps in modeling such that the material behavior at higher frequency ranges and for complex media may be understood. These models help to understand how waves interact and propagate in the media and the different mode conversions. Numerical models also allow the microstructural parameters to be controlled precisely by the user. Here a numerical model is presented for studying ultrasonic attenuation.

Different numerical methods have been used previously for modeling wave propagation in complex media. One of the methods developed is the finite difference (FD) method. FD can be used to model the wave equation as shown by Alford, et al.[9] with fine grids. Alford used an explicit second order difference scheme to approximate the governing wave equation in a homogeneous region due to a line source distribution. Fornberg [10] pointed out the errors in FD methods and improved the method. He introduced the pseudospectral method to solve the elastic wave equation in discontinuous media with smoothing at the interface.

Scalerandi, et al. [11] presented a new simulation method known as the Local Interaction Simulation Approach (LISA). This method is very convenient for utilizing parallel computing to solve the problem. Each processor is mapped one-to-one with cells of the discretized model. Each cell can be given different material properties since the processors are mutually independent and the boundary nodes can be given the interface properties. The computational time is greatly reduced since each cell is treated as homogeneous. The problem is based on a local interaction simulation approach and Preisach-Mayergoyz (PM)

space model of Guyer and McCall [12],[13]. The PM space is a density space consisting the mesoscopic structural features and their elastic properties. This space describes the elastic properties of the materials.

Fellinger, et al. [14] introduced a new method known as Elastodynamic Finite Integration Technique (EFIT) to model the elastic wave scattering in homogeneous and heterogeneous, isotropic and anisotropic linear elastic media. EFIT uses the finite integration technique to discretize Maxwell's equation. Schubert, et al. [15] extended EFIT in cylindrical coordinates for cylindrical geometries system which helps to reduce it from a three-dimensional problem to a two-dimensional one.

Lui, et al. [16] used the boundary element method (BEM) for a two-dimensional domain for detecting cracks or inclusions in the material. A two-dimensional elastodynamic boundary integral equation is used to solve the multiple scattering problem due to cracks and inclusions. The computational cost increases as the number of inclusions to be discretized increases. In this method he also pointed out that as the scattering increases the difficulties in analyzing the results due to background noise in the signals also increase. The method includes multiple scattering without any difficulties.

The finite element method (FEM) is used here as the numerical method to analyze elastic wave propagation in heterogenous media. FEM is very widely used for static and dynamic analysis. The Voronoi polycrystal is used as the basis geometry for the finite element analysis. FEM is used to discretize the partial differential equation to obtain the solution. Barbe, et al. [17] used a network of cubes for meshing Voronoi polycrystals and distributed the material parameters at the Gauss points. Here prism elements are used

to mesh the Voronoi polycrystals. A MATLAB [18] code is generated to construct and mesh the numerical model. The "Method of Virtual Nuclei" is developed to construct Voronoi polycrystals in finite domain for any arbitrary convex geometry. The algorithms for constructing Voronoi polycrystals are explained in detail in Chapter 2. ABAQUS is used to obtain the FEM solutions of wave propagation in Voronoi polycrystals. ABAQUS can formulate the plane stress model with infinite boundary conditions. These infinite boundaries absorb the energy such that reflection is prevented. The model with plain strain boundary conditions is also formulated by constraining the out of plane displacement of all the nodes in the model. The FEM modeling using ABAQUS is explained in detail in Chapter 3.

Models with various grain diameters over a range of frequencies are used here for the attenuation calculation. The procedure for obtaining the attenuation of the material from the numerical results is explained in detail in Chapter 4. ABAQUS simulations are presented for visualization of the wave propagating in the model. Numerical calculations are shown for materials with various degree of scattering. Examples results are obtained for four materials, namely aluminum, fictitious, nickel and copper. Copper has the highest degree of scattering and aluminum the least among the four materials. The material parameters of the fictitious material are set to have scattering properties between aluminum and copper.

The scattering theory in two- and three-dimensional domains is explained in Chapter 5. The numerical results are then compared with two-and three-dimensional theories to verify the authenticity of the numerical model for the plane stress and plane strain cases. The numerical results obtained are used to observe the dependence of parameters for atten-

uation and the scattering theory, authenticity and the robustness of the numerical model. To verify the model for different boundary conditions, plane stress and plane strain analyses are both done.

Chapter 2

Voronoi Polycrystal

2.1 Introduction

Geometries based on the Voronoi cell are increasingly being used in the numerical analysis of many practical problems, such as the study of the microstructures of materials [19][20][21], liquid structures [22], biology [23], chemistry [24], crystallography [25], geography [26], and wireless communication problems [27]. As an example of the last application, given a set of x micro-cell substations, the closest substation must be chosen to carry a call. Such tessellations help in searching for the closest neighbor. Voronoi polycrystals have also been shown to represent closely the microstructures of many materials. Construction of numerical models of such microstructures for relevant materials should be done with efficiency. Espinosa and Zavattieri [28][29], briefly discuss the use of Voronoi tessellation for creating a numerical model to study the failure initiation in brittle materials. Ghosh, et al. [19] developed the Voronoi cell finite element method (VCFEM) for plane strain analysis of heterogeneous microstructures. Kumar, et al. [20] show a statistical analysis

of three-dimensional grains generated by a Poisson-Voronoi tessellation. In many of these applications, the polycrystalline geometry is needed in a finite domain.

A Voronoi tessellation is a method to subdivide a given region. Each Voronoi cell has a nucleus. The nuclei positions are created to match the relevant applications. Often they are chosen randomly. As per the definition of the Voronoi diagram, any point inside a Voronoi cell V is nearer to the nucleus V than to any other nucleus in the given region. Such a procedure produces convex polygons in two-dimensional and convex polyhedrons in three-dimensional domains which completely fill the given region. In three-dimensional domain, every edge of a Voronoi cell connects three grains and two vertices and every vertex connects four edges, six faces, and four cells [20].

In this chapter, the creation of uniform Voronoi polycrystals in arbitrary domains is discussed. The focus here is on creating microstructures with elongated and oriented grains in arbitrary domains. In the next section, the Voronoi polycrystal is discussed. In section 3, the general algorithm, called the Method of Virtual Nuclei (MVN) is introduced. This method is used for creating the prescribed microstructures including two-dimensional examples for grain elongation and grain orientation. In section 4, the three-dimensional extension of MVN is used for additional examples.

2.2 Voronoi Polycrystals

A Voronoi polycrystal is created by generating a set of points, which represent the Voronoi nuclei. Perpendicular bisectors are drawn between neighboring pairs of nuclei in a given space. The intersection of these perpendicular bisectors gives the vertices of each

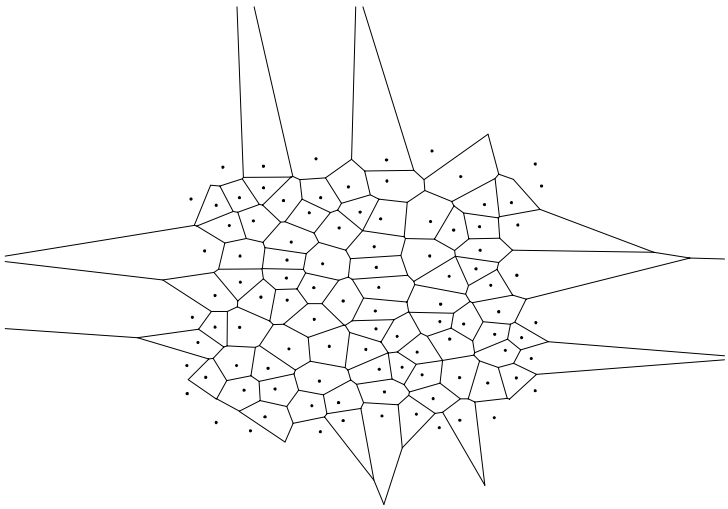

Figure 2.1: 2-D Voronoi diagram for a set of 100 random points.

Voronoi cell. In general, nuclei at the outer edges of the space will not have neighboring nuclei in all directions. Therefore, some of the vertices of theses cells may lie very far away, even at infinity. Fig 2.1 shows a Voronoi diagram with 100 nuclei generated by the above method. The dots represent the Voronoi nuclei of each cell. Generation of a Voronoi diagram by this method does not guarantee a closed figure without vertices at infinity. Many applications involving polycrystalline materials require finite domains.

To overcome the difficulty associated with the infinite vertices, the required geometry inside which a Voronoi diagram is to be created can be extracted from Fig. 2.1 as shown in Fig. 2.2. One drawback with this method is that the number of Voronoi cells in the extracted portion is not known a priori. To determine the exact number of cells inside the chosen domain a count must be made. In addition, the boundary cells may not have the appropriate Voronoi properties. Finally, not all polycrystals may contain nuclei. To improve upon these limitations, a method is described in the next section that allows a

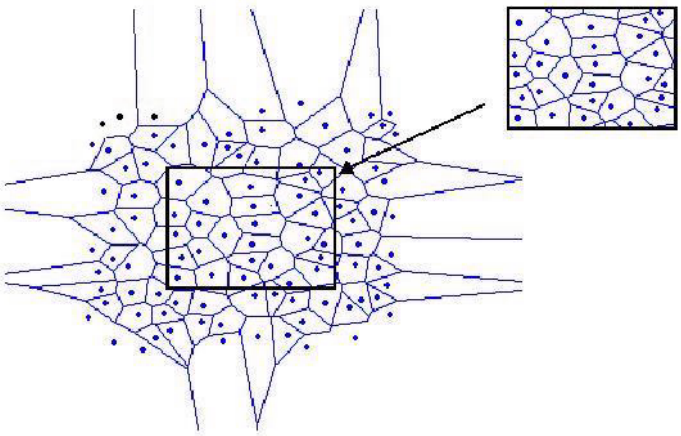

Figure 2.2: Voronoi plot obtained by extracting a subspace from the main diagram.

Voronoi polycrystal to be created efficiently in an arbitrary domain.

2.3 Method of Virtual Nuclei

The general description for easily creating the desired Voronoi polycrystals is discussed using a two-dimensional format such that the explanation is clearer. Results using the three-dimensional extension of this method are given in section 4. This algorithm eliminates the use of any other method of cutting the required domain from a Voronoi diagram.

Consider a unit square domain in which the Voronoi polycrystal is to be created. Coordinates of Voronoi nuclei are selected within this domain. The position of these nuclei may be chosen using any type of distribution, such as a Poisson distribution. For the case of interest here, the nuclei positions are chosen such that the grain size is as uniform as possible in the domain. For this example, 100 random Voronoi nuclei are selected. These nuclei are referred as "real nuclei." After the positions of the 100 real nuclei have been

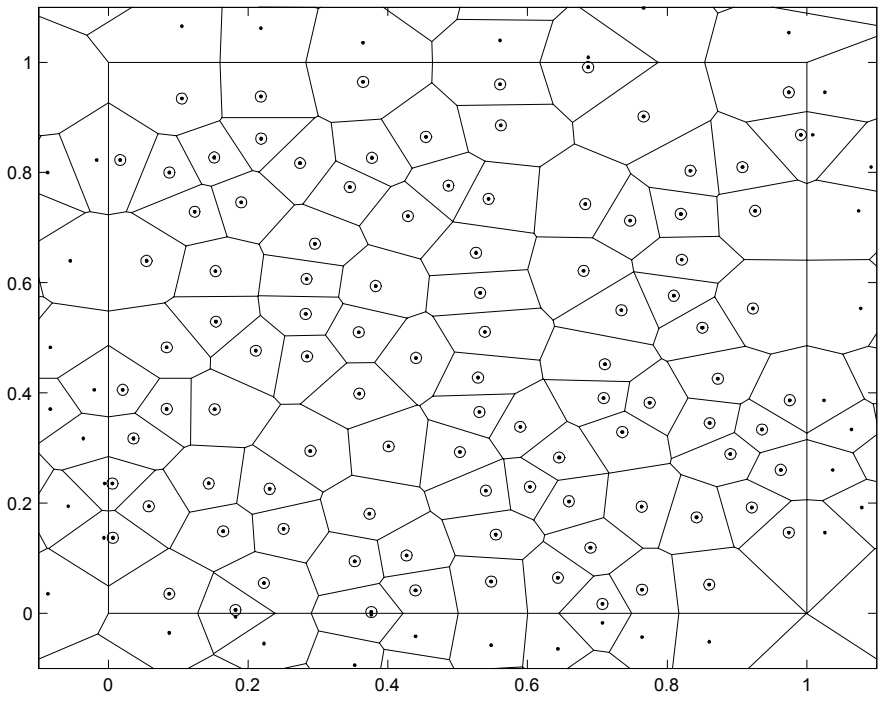

Figure 2.3: Voronoi plot with real and virtual nuclei.

determined, "virtual nuclei" are created. These nuclei are reflections in the space of the nuclei closest to the borders of the area of interest about the respective sides of the domain. The nuclei closest to the boundaries are the ones when joined forms a closed polygon and all the real nuclei falls inside or on the boundary of this polygon. Perpendicular bisectors between real and virtual nuclei are, by definition, the boundaries of the domain of interest. Fig. 2.3 illustrates this method with 100 Voronoi nuclei inside a unit square region.

The vertices of the Voronoi cells contained inside the region (cells associated with the real nuclei) are extracted and become the needed final polycrystal, as shown in Fig. 2.4. Thus, a Voronoi polycrystal constructed using the method of virtual nuclei will have cells at the boundaries containing nuclei and having appropriate properties, i.e., every edge of a

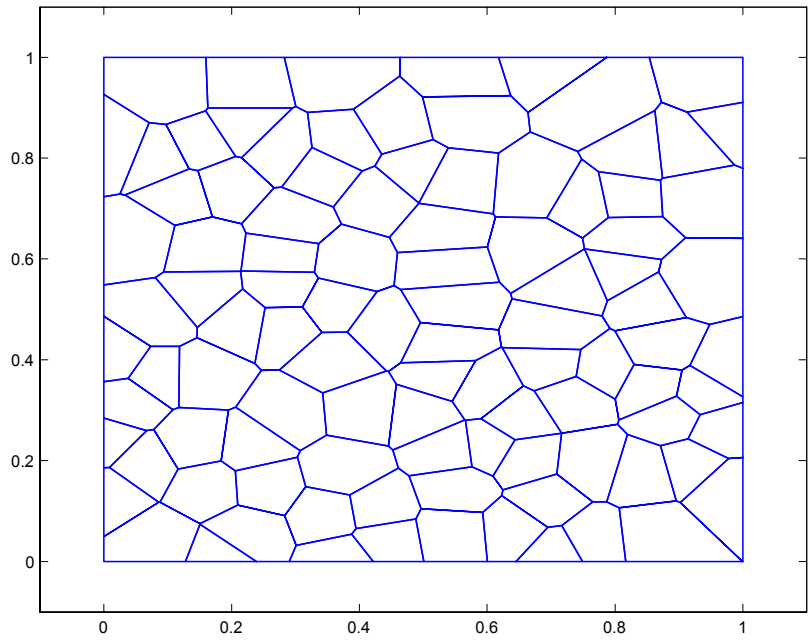

Figure 2.4: Extracted Voronoi plot with 100 real nuclei.

Voronoi cell connects three grains and two vertices and every vertex connects four edges, six faces, and four cells [20]. Here the exact number of cells in the unit square is also known. The algorithm for the Method of Virtual Nuclei is given as *Algorithm 1.*

Algorithm 1 *The Method of Virtual Nuclei*

1. *Construct the geometry of the chosen domain.*

2. *Obtain the coordinates of all "real" Voronoi nucleus within the chosen domain.*

3. *Reflect these points about the boundaries of the chosen domain. These are the "virtual" Voronoi nuclei.*

4. *Plot the Voronoi diagram for all the nuclei, both real and virtual.*

5. Extract the vertices of the Voronoi cells associated with the real nuclei.

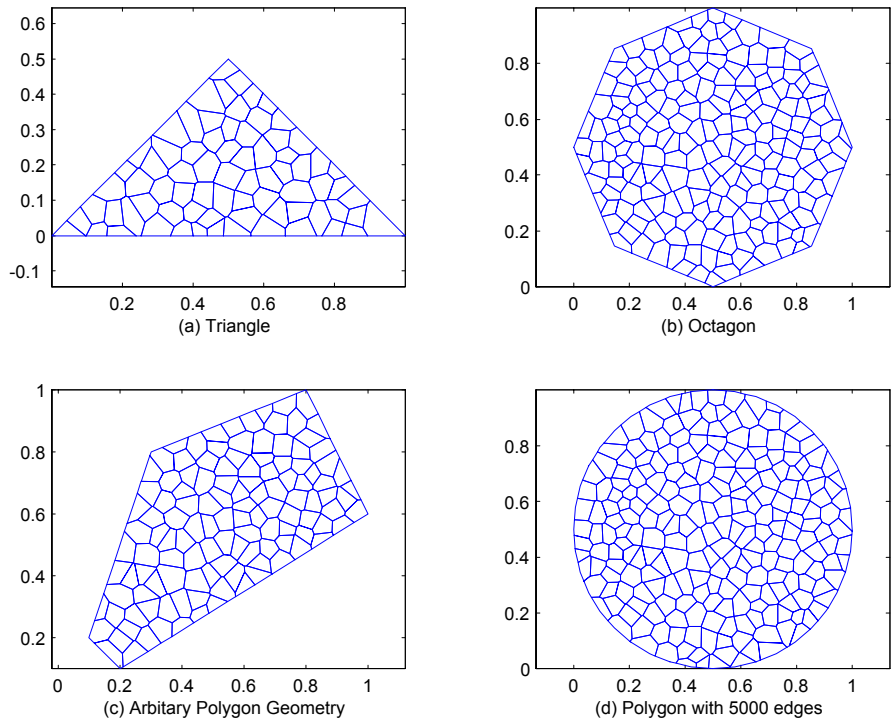

Figure 2.5: Voronoi diagram within different shapes.

A Voronoi polycrystal for an arbitrary geometry can also be obtained with this method easily. The required geometry inside which the Voronoi polycrystal is to be created should be closed and a convex polygon of any number of sides. The restriction to polygons is due to the linear boundaries of the Voronoi cells. In Fig.2.5, four example Voronoi polycrystals of different shapes are shown using *Algorithm 1.* Fig. 2.5(a) is a Voronoi polycrystal within a triangle; 2.55(b) is for an octagon; 2.55(c) shows the Voronoi polycrystal for an arbitrary polygon. Fig. 2.5(d) is the Voronoi polycrystal within a polygon of 5000

sides - an approximation of a circle. In general, Voronoi diagram has the complexity of the order $O(n^3)$. The computational time increases with the number of edges. The Method of Virtual Nuclei also provides the framework for construction of more complex microstructures relevant to many engineering problems. During the processes of rolling, extruding and pressing the grains in materials change shape and may elongate. In some cases, the elongated crystals may have an angle of orientation relative to the boundaries. The Method of Virtual Nuclei is now exploited to create polycrystalline structures of interest in science and engineering: elongated grains with an arbitrary orientation. This technique widens the areas of applicability of the Voronoi polycrystal.

2.4 Grain Elongation

The procedure for creating a Voronoi polycrystal with elongated grains essentially involves a mapping from a stretched domain. An example is presented here for grains with a 3 to 1 aspect ratio within a unit square. The unit square is first elongated in the direction perpendicular to the desired major grain axis. The Voronoi polycrystal is constructed and the rectangular box is then compressed. The resulting microstructure is that of elongated grains. The elongated grain will not be true Voronoi cells as their boundaries no longer remain perpendicular bisectors between the Voronoi nuclei after compression. The size of the rectangular box depends upon the required aspect ratio.

Therefore, the required rectangle size for an aspect ratio 3 is of 1 unit by 3 units. The Voronoi diagram is obtained as shown in Fig. 2.6. The domain shown in Fig. 2.6 is then compressed horizontally resulting in the microstructure shown in Fig. 2.7.

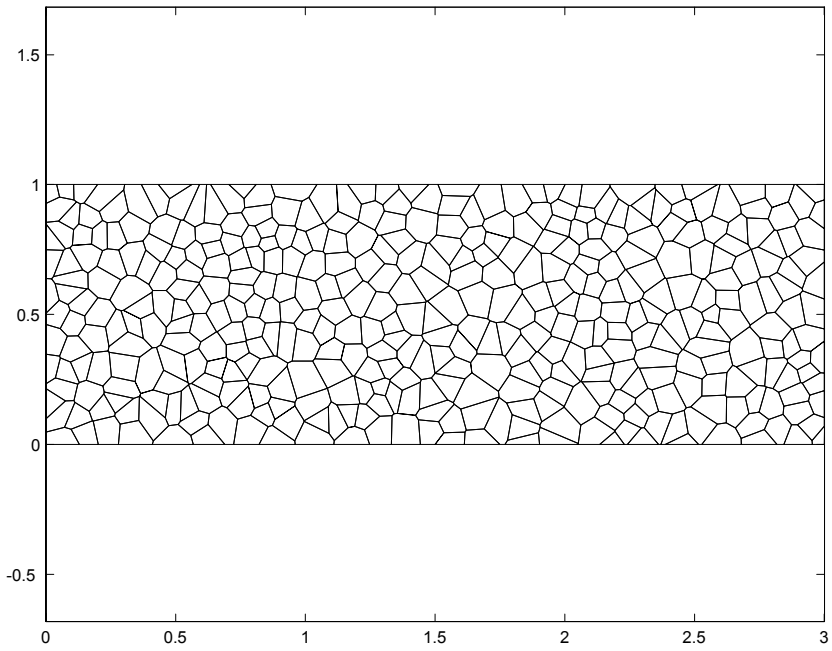

Figure 2.6: Voronoi plot within a rectangle so that when compressed the required ratio is obtained.

Since it is compressed horizontally the horizontal coordinates of all the vertices of the Voronoi cells are divided by the required aspect ratio. In Fig. 2.7, the aspect ratio of 3 is chosen for the Voronoi polycrystal within a unit square. *Algorithm 2* summarizes the method.

Algorithm 2 *Construction of Voronoi polycrystals with elongated grains*

1. *Determine the geometry inside which Voronoi polycrystal is to be created.*

2. *Multiply the respective coordinates of the geometry by the desired grain aspect ratio.*

3. *Choose the Voronoi nuclei inside the elongated geometry.*

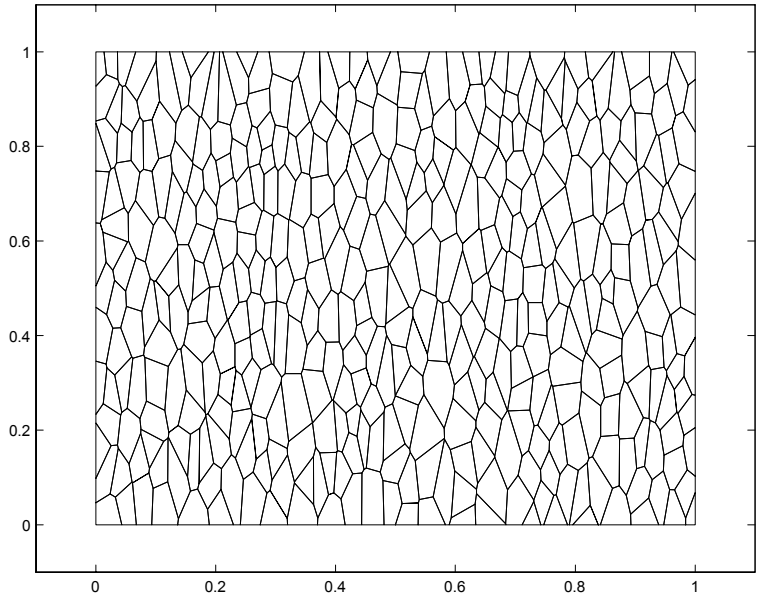

Figure 2.7: Voronoi plot of 400 elongated grains with aspect ratio of 3, obtained by compressing the domain shown in Fig. 2.6.

4. *Reflect the "real" nuclei about the boundaries of the elongated geometry. These are the "virtual" Voronoi nuclei.*

5. *Plot the voronoi diagram inside the elongated geometry.*

6. *Extract all Voronoi cells corresponding to the "real" nuclei.*

7. *Create Voronoi polycrystal in the elongated geometry.*

8. *Divide all respective coordinates of the extracted Voronoi vertices by the aspect ratio.*

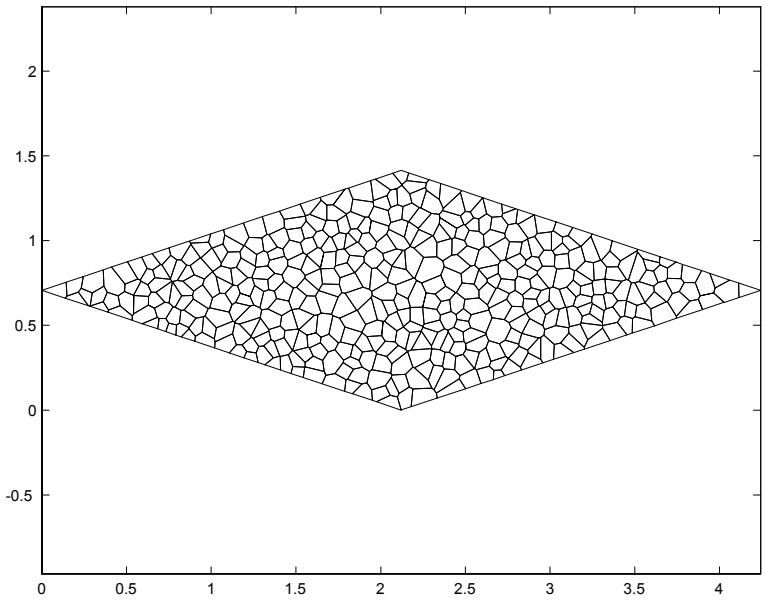

Figure 2.8: Voronoi plot inside the geometry determined.

2.5 Grain Orientation

Voronoi polycrystals with specified angles of orientation can also be obtained using the Method of Virtual Nuclei as a framework. First, the unit square is rotated to the required angle θ. Then the Voronoi nuclei are selected inside the parallelogram and the Voronoi polycrystal is constructed. Finally the geometry is rotated back resulting in a Voronoi polycrystal that has the required angle of orientation inside the unit square.

When both elongated and tilted Voronoi polycrystals are required, the geometry is rotated and elongated simultaneously before depositing the Voronoi nuclei. The rotated geometry is obtained such that when it compressed and rotated back, the required Voronoi polycrystal is created for the required geometry. The general algorithm is outlined in *Algorithm 3*.

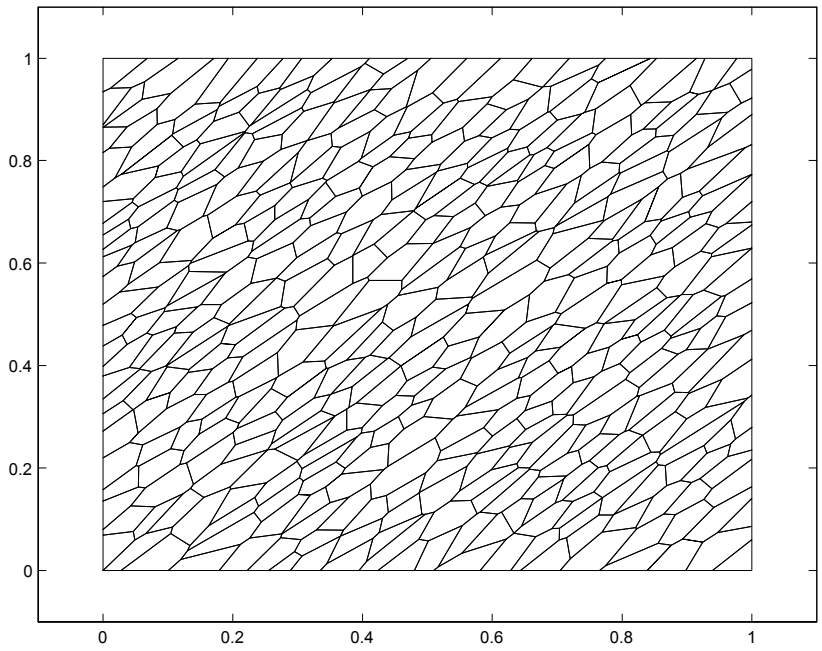

Figure 2.9: Voronoi plot of 400 elongated grains with aspect ratio 3 and angle of orientation 45°.

The required dimensions of the domain in Fig. 2.8 are determined such that the compressed and tilted geometry gives the required geometry as shown in Fig. 2.9. Figure 2.8 is an example for 400 Voronoi cells within a unit square, with a grain aspect ratio of 3 and an angle of orientation of the cells of 45° relative to the domain boundary using this method, as described in *Algorithm 3*. This procedure can be implemented for any arbitrary geometry as well.

Algorithm 3 *Construction of Voronoi polycrystals with orientated grains*

1. *Determine the geometry inside which Voronoi polycrystal is to be created*

2. *Tilt the geometry at an angle equal to the angle of orientation of the cells required.*

3. *Choose the Voronoi nuclei inside the tilted geometry.*

4. *Reflect the "real" nuclei about the boundaries of the elongated geometry. These are "virtual nuclei" Voronoi nuclei.*

5. *Plot the Voronoi diagram inside the tilted geometry.*

6. *Extract all Voronoi cells corresponding to the "real" nuclei.*

7. *Create Voronoi polycrystal in the tilted geometry.*

8. *Tilt back all the voronoi vertices by the angel of orientation required.*

Some more examples are shown in Fig. 2.10 for different orientation angles in a triangular domain with an aspect ratio of the crystals of 3. Similarly, elongated and orientated Voronoi crystals can be obtained inside any closed convex polygon using the algorithms given above.

A model for Functionally Graded Materials (FGM) is developed as shown in the Fig. 2.11. The model is made to have variable material and grain size distribution in a two-dimensional domain. A uniform grain size and variable material distribution is shown in Fig. 2.11(a). Figures 2.11(b)-(d) show quadratic grain size distribution in the horizontal, vertical, and 45° line, respectively. Any axis can be made n^{th} order depending on the variation in the model required and the direction of variation.

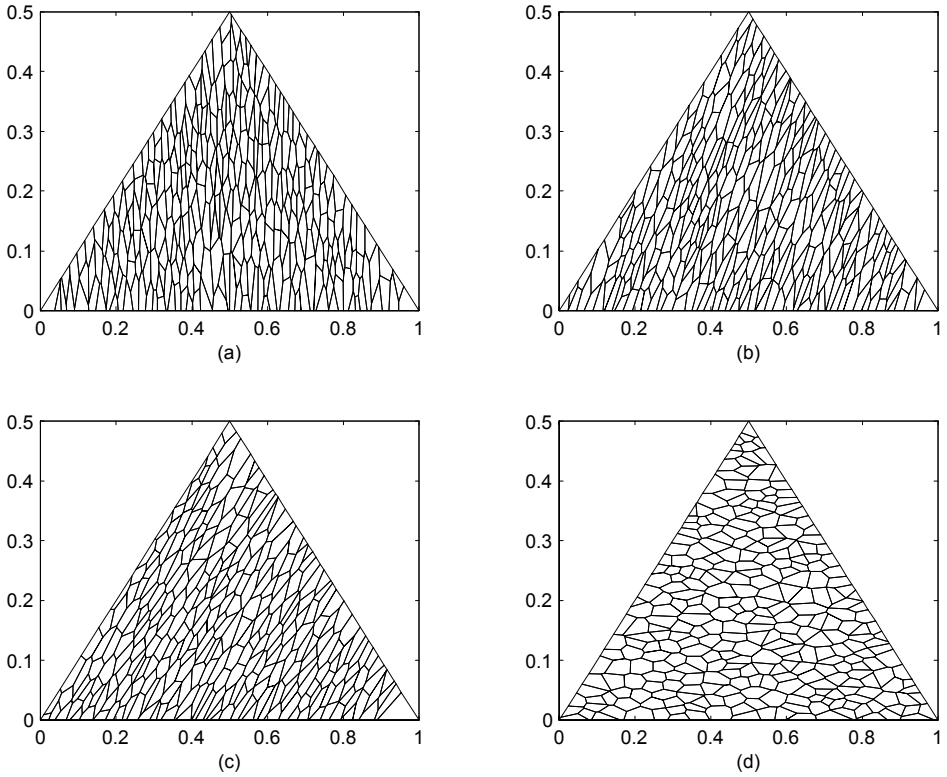

Figure 2.10: Elongated and tilted Voronoi crystals inside a triangular domiain. The aspect ratio is 3 and tilt angles of the vornoi crystals are (a) 0° (b) 30° (c) 45° (d) 90° with vertical axis.

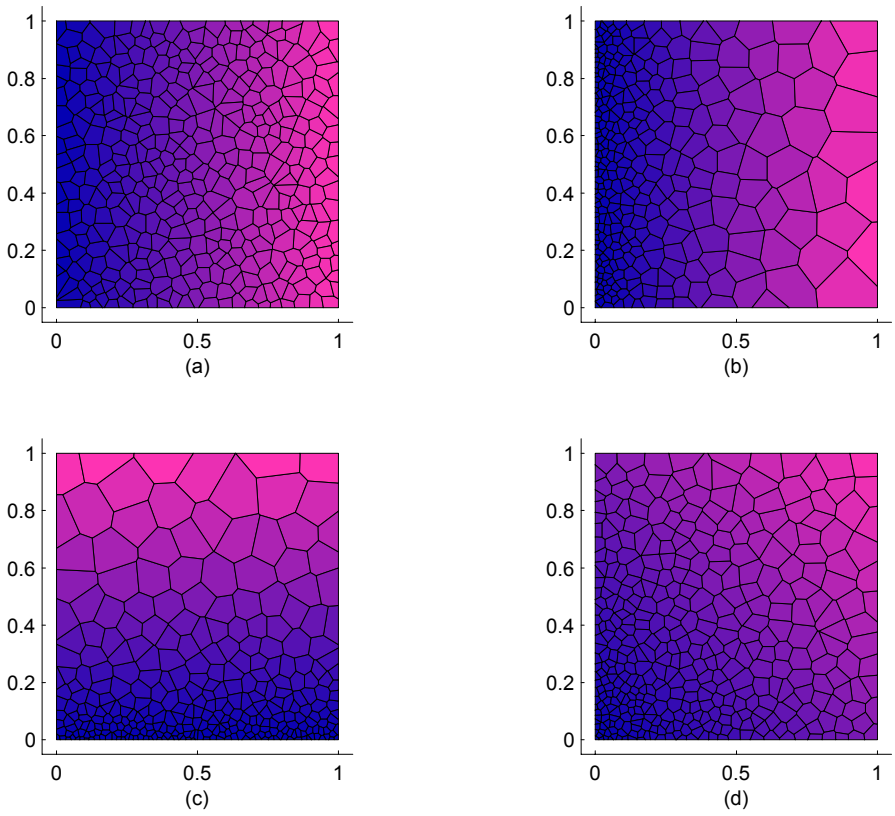

Figure 2.11: Numerical model for FGM (a) uniform (b) quardradic vertical axis (c) quadratic horizontal axis (d) quadratic vertical and horizontal axis.

2.6 Three-Dimensional Models

The same procedures for two–dimensional domains may be extended to three–dimensional Voronoi polycrystals as well. Figure 2.12 shows a three-dimensional Voronoi polycrystal within four different geometries. The algorithms used to construct them are identical as described above with an addition of one more axis.

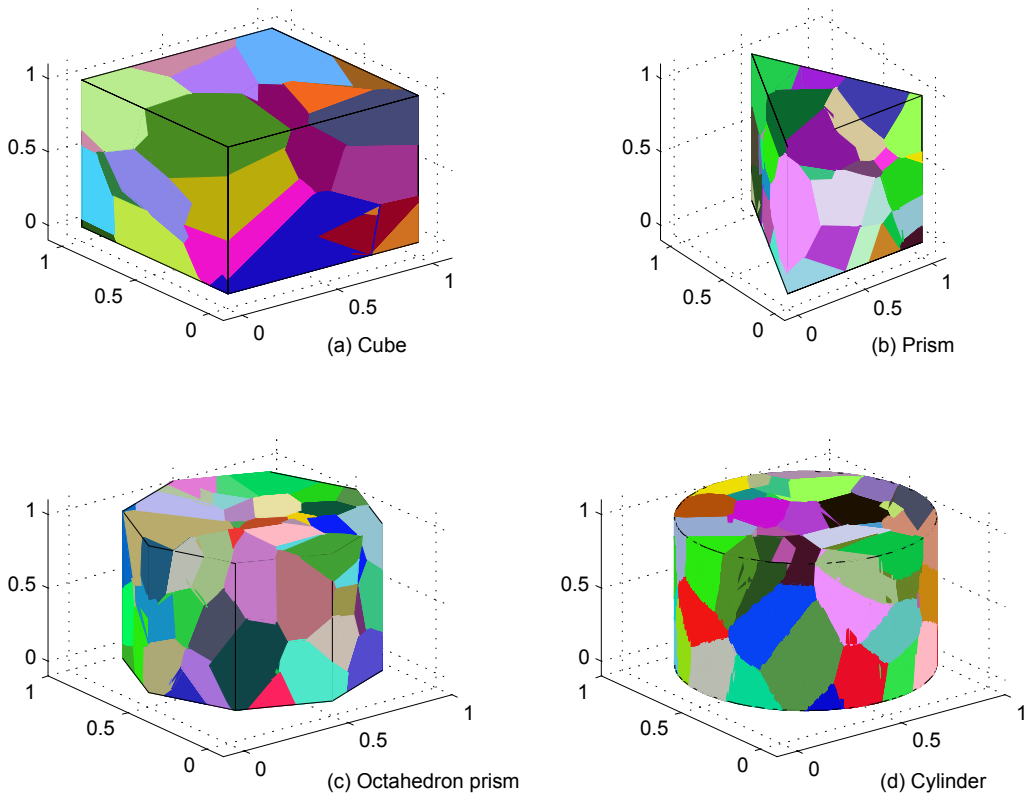

Figure 2.12: 3D Voronoi polycrystals within different geometry.

In three-dimensional domains, the geometric orientation of the Voronoi polycrystals can be made with respect to any or all three coordinate axes. The orientation angle can

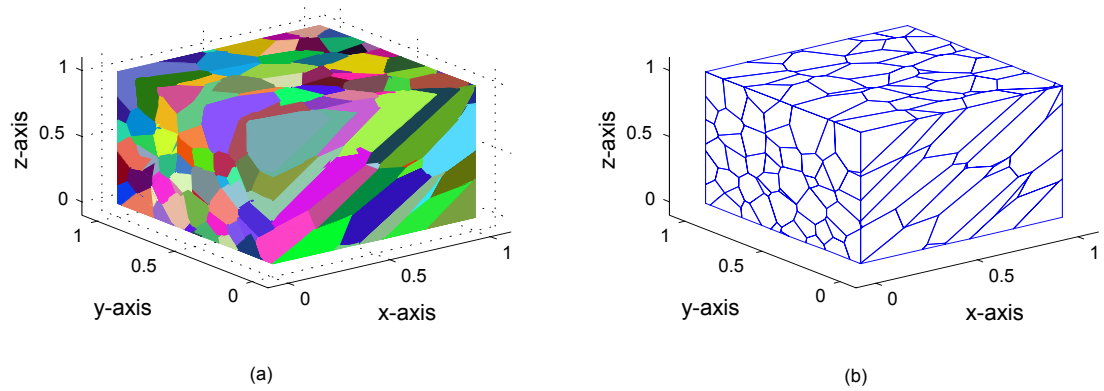

Figure 2.13: Tilted and elongated Voronoi polycrystals inside an unit cube (a) Solid plot (b) Contour plot of the surfaces.

also be different with respect to the respective axes. In Fig. 2.13, 200 elongated Voronoi polycrystals with an aspect ratio 3 and oriented at 45°with respect to x-axis is shown.

2.7 Grain Statistics

In this section, statistical analysis is done for Voronoi polycrystals in a two-dimensional domain. 300 voronoi polycrystals inside an unit square for two different random realizations are shown in Fig 2.14. Statistics for the grain area and the number of edges are studied. Restricting a minimum distance between any two crystals, a normal distribution of Voronoi nuclei is obtained. The fit is done by using the Gaussian function,

$$F(x) = \frac{1}{\sigma\sqrt{2\pi}} e^{-\frac{(x-\mu)^2}{2\sigma^2}}, \tag{2.1}$$

where μ is the mean area of crystals and σ is the standard deviation. A Gaussian curve fits the data of crystal area well confirming that a normal distribution of grain size is obtained.

Kumar, et al. [20] presented the statistical analysis for a Poisson distribution of three-dimensional Voronoi polycrystals for different parameters. Two examples of a Poisson

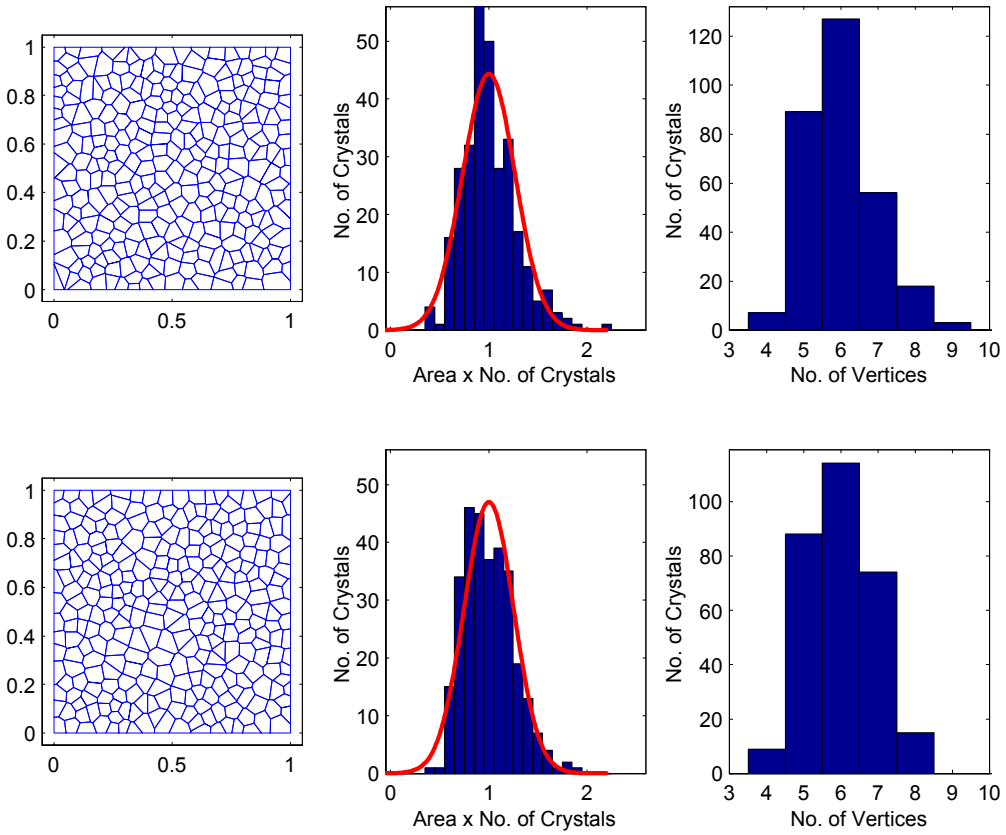

Figure 2.14: Grain statistics for 300 Voronoi crystals inside a unit square.

distribution of two-dimensional Voronoi polycrystals are shown in Fig. 2.15 for two different random realizations. The Poisson fit to the distribution is given by,

$$F(x) = \frac{e^{-\mu}\mu^{x}}{x!}, \tag{2.2}$$

where μ is the mean area of crystals and $\sqrt{\mu}$ is the standard deviation.

A Poisson distribution of Voronoi nuclei is made by removing the minimum distance requirement as discussed for Gaussian distribution between any two crystals and randomly select the Voronoi nuclei. Matlab [18] function *rand,* which generates uniformly distributed random numbers in the interval [0,1], is used to generate random Voronoi nuclei.

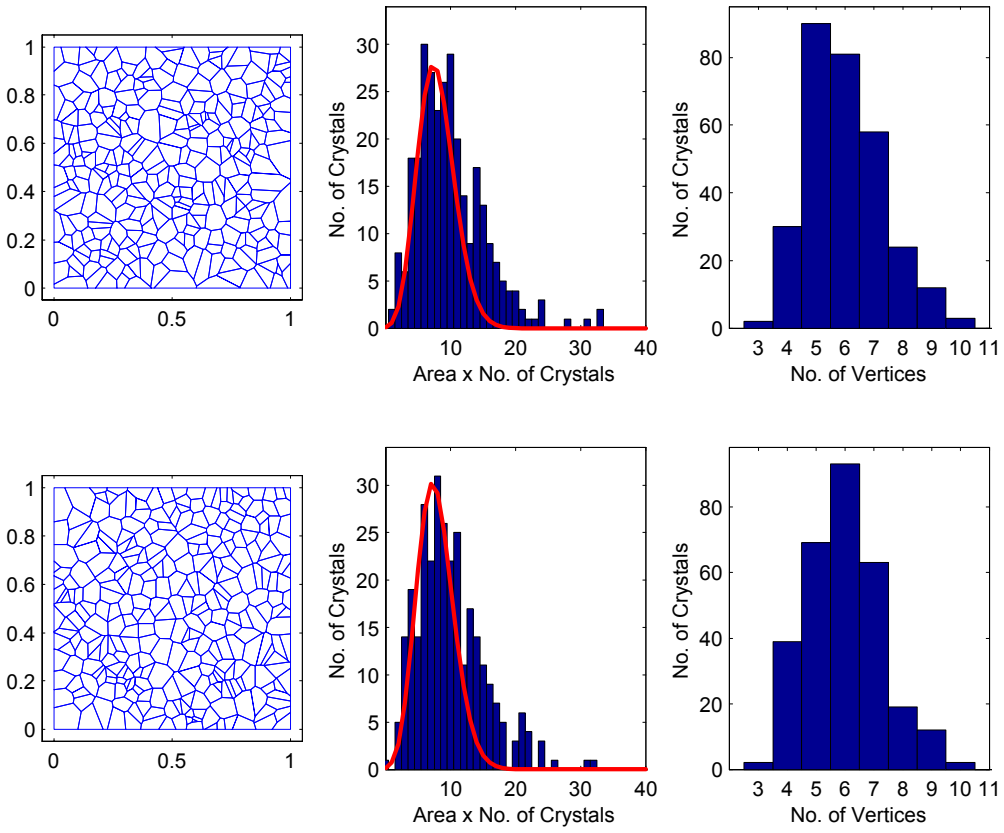

Figure 2.15: Grain statistics for 300 Voronoi polycrystals in a unit square with Poisson distribution.

A normal distribution of Voronoi nuclei is used to obtain the results shown in the following chapters. This type of distribution is used since the scattering theories typically assume uniform grain size.

The probability distribution of edges is shown in Fig. 2.16 for varying number of realizations with 200 crystals. The results are obtained by creating random numbers of normally distributed 200 crystals inside a unit square of 1mm by 1mm. The probability distribution of the number of edges for a two-dimensional Voronoi polycrystal is obtained for 5, 15, 500, 10000 realizations. Voronoi polycrystals with other types of distributions can

also be obtained with ease. Figure 2.16 shows consistent probability for a different number of realizations of the grains.

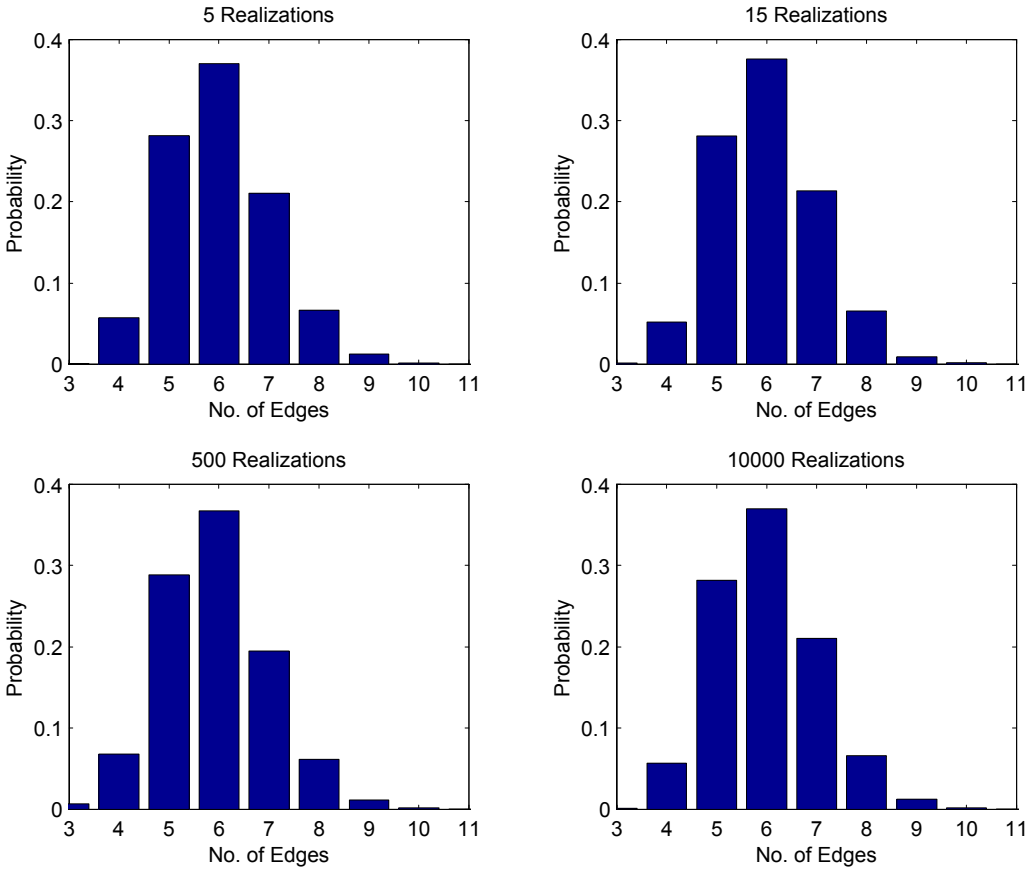

Figure 2.16: Probability distribution of edges of 200 two-dimensional Voronoi polycrystals obtained based on a different number of realizations.

2.8 Summary

In this chapter, the Method of Virtual Nuclei (MVN) has been discussed with applications to creation of Voronoi polycrystals within arbitrary domains. Examples have been presented for two- and three-dimensional domains. The MVN allows the creation of

elongated grains with arbitrary orientations to be done with ease. The applications for science and engineering problems are expected to be numerous. The general technique may be used for two or three-dimensional domains. Statistical analysis was presented for the two-dimensional Voronoi polycrystals.

Chapter 3

Finite Element Modeling

The finite element method (FEM) is a numerical method for solving partial differential equations for complicated geometries and boundary conditions. It is one of the most powerful numerical methods used to model complex mathematical problems. In Chapter 1 other numerical methods have been discussed in brief. FEM can produce an approximate solution to a problem and the accuracy can be generally increased as desired. The general three steps for any finite element analysis are governed by:

- Pre-processing of input data to discretization functions and equations,
- Solution of the matrix equation, and,
- Post-processing of output results, to retrieve the solution from the discretization.

Today, with supercomputers, FEM is used to solve large problems with ease and efficiency. There are also numerous FEM commercial software packages available today to solve complex problems, as well as softwares to mesh very complex shaped models for finite

element analysis.

Espinosa, et al. [28] showed the implementation of finite element methods for static analysis of microstructures using the Voronoi polycrystal. In this thesis, the finite element method is used to model the dynamic response problem in the time domain. A model to simulate elastic wave propagation in polycrystalline materials is constructed using the Voronoi polycrystal as the basis for the polycrystalline geometry. ABAQUS/Explicit [30], a commercial finite element software package is used for the numerical analysis of elastic wave propagation in Voronoi polycrystals. The finite element method is used to monitor the nodal displacements at the boundaries for an applied pulse pressure load. A Matlab [18] code is developed to create and mesh the model for the finite element analysis.

3.1 Mathematical Formulation

ABAQUS was used for all FEM analyses. Here the basic equations for the mathematical formulation for FEM are stated for clarity. The ABAQUS [30] manuals may be consulted for more details. The equation of motion for the dynamic response in the time domain is given by

$$\sigma_{ij,i}(x,t) + b_j(x,t) = \rho(x)\ddot{u}_j(x,t), \tag{3.1}$$

where ρ is the density, σ_{ij} is the stress, $\ddot{u}_j$is the acceleration of the body and b_j is the body force. Wave propagation in a perfectly linearly elastic solid obeys Hooke's law which states that the stress tensor σ_{ij} is proportional to the strain tensor ε_{kl},

$$\sigma_{ij} = c_{ijkl}\varepsilon_{kl}, \tag{3.2}$$

where

$$\varepsilon_{kl} = \frac{1}{2}(u_{k,l} + u_{l,k}) \ (k, l = 1, 2, 3), \tag{3.3}$$

and c_{ijkl} is the elastic stiffness tensor. Symmetry indicates that $c_{ijkl} = c_{jikl} = c_{klij}$ for σ_{ij} and ε_{kl} symmetric tensors. There are 21 independent elastic stiffness constants which refer to a crystal which possesses no rotational symmetry. These materials are known as general anisotropic materials. For crystal systems of higher symmetry this number is considerably reduced. The values of the elastic constants depend on the orientation of these axes relative to the crystal lattice. ABAQUS/Explicit [30] uses explicit integration with diagonal lumped element mass matrices to solve dynamic problems. The equation of motion is integrated using the explicit central difference integration rule,

$$\begin{aligned} \dot{u}^{(i+\frac{1}{2})} &= \dot{u}^{(i-\frac{1}{2})} + \frac{\triangle\, t^{(i+1)} + t^{(i)}}{2}\ddot{u}^{(i)}, \\ u^{(i+1)} &= u^{(i)} + \triangle\, t^{(i+1)}\dot{u}^{(i+\frac{1}{2})}, \end{aligned} \tag{3.4}$$

where u, $\dot{u}$ and $\ddot{u}$ are displacement, velocity and acceleration respectively. The superscripts (i) are the increment number and $(i \pm \frac{1}{2})$ are the midincrement values. From the principle of virtual work, the basic equations for dynamic equilibrium at time t is,

$$\ddot{\mathbf{u}}^{(i)} = \mathbf{M}^{-1}(\mathbf{F}^{(i)} - \mathbf{I}^{(i)}), \tag{3.5}$$

where $\mathbf{M}$ is the diagonal lumped mass matrix, $\mathbf{F}$ is force vector and $\mathbf{I}$ is the internal force vector. The initial inversion of the lumped mass matrix, which is tridiagonal, for calculating the acceleration makes the calculation inexpensive. Thus, the explicit method does not require any iterations or stiffness matrix. The initial conditions of velocity and

acceleration can be defined by the user. Otherwise, zero is taken as the default value. For computing the acceleration $\ddot{u}$, n operations are required where n is the degrees of freedom of the model. This method uses a large number of small increments of time step efficiently. The computational cost of this procedure is directly proportional to the size of the finite element model.

3.2 Meshing

Meshing is a critical part for finite element analysis. The mesh size is proportional to the size of the displacement vector **u**. The step time is proportional to the smallest transit time of a longitudinal wave across any element in the mesh,

$$\Delta t \approx \frac{L_{\min}}{c_L}, \tag{3.6}$$

where $L_{\min}$ is the size of the smallest element and c_L is the longitudinal wave speed. This is known as the Courant-Friedrichs-Lewy condition for stability. Thus the time step must be reduced as the size of the element decreases. The time step will also decrease if there are only a few number of small elements compared with the whole model mesh. Therefore, care should be taken to obtain a mesh with uniform size of elements as much as possible. Six-noded triangular prism elements are used here to mesh the domain. The depth of the domain is equal to the depth of the prism element. First, the model is constructed in a two-dimensional domain and meshed using Delaunay triangulation. Then the triangular elements are extruded to form prism elements. Therefore, the model can be approximated as a two-dimensional as there is no scattering of elastic waves in the out of plane direction.

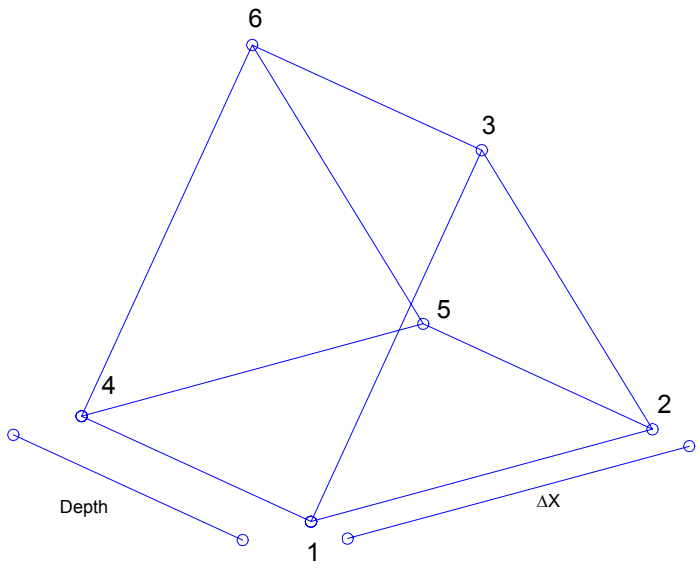

Figure 3.1: Six noded triangular prism element.

The six noded triangular prism element is shown in Fig. 3.1. The depth of the prism is generally $1.25-1.50$ times the length of one of the side of the equilateral triangular face denoted by Δx. The meshing is done crystal by crystal in the following way:

- The nodes are deposited at the boundaries of each crystals such that distance between any two nodes is equal to the element size Δx. When the length of the boundaries are not multiples of Δx, then some of the elements are of different size which is unavoidable and acceptable.

- A uniform grid of points is created inside the domain such that the particular Voronoi polycrystal fits into the domain. The distance between any two points is made such that a uniform mesh is obtained with element size equal to Δx.

- Each Voronoi crystal is reduced by a very small percentage and the uniform grid is

laid over it such that they overlap each other. The points common to each Voronoi crystal and the uniform grid are taken as the nodes inside the Voronoi polycrystal. The uniform grid is laid over the reduced crystal so that points inside the crystal are not too close to the boundaries of the actual crystal. Generally, the reduction ratio is chosen in such a way, that the perpendicular distance between a reduced side and its actual side is approximately the size of the element Δx. Therefore, the crystal has nodes on the boundaries and inside.

- These nodes are then used to form Delaunay triangulation using MATLAB. All the crystals are meshed by looping over the number of crystals in the model.

Using this method, each crystal is meshed and assembled to form the complete mesh of the model. Here each crystal is meshed separately to avoid errors such as one element being shared by two or more crystals making an irregular surface for these crystals. The procedure is shown schematically in Fig. 3.2. In Fig. 3.2(a) the crystal marked in black is used to show the above procedure. The nodes on the boundary of a crystal are shown in Fig. 3.2(b). Figure 3.2(c) is plotted to show the overlapping of a uniform grid in blue dots over the reduced crystal denoted by the red polygon. The polygon in black is the actual crystal. Figure 3.2(d) shows all the nodes used for meshing the crystal. The meshed crystal is shown in Fig. 3.2(e). All the crystals are meshed and assembled as shown in the Fig. 3.2(f).

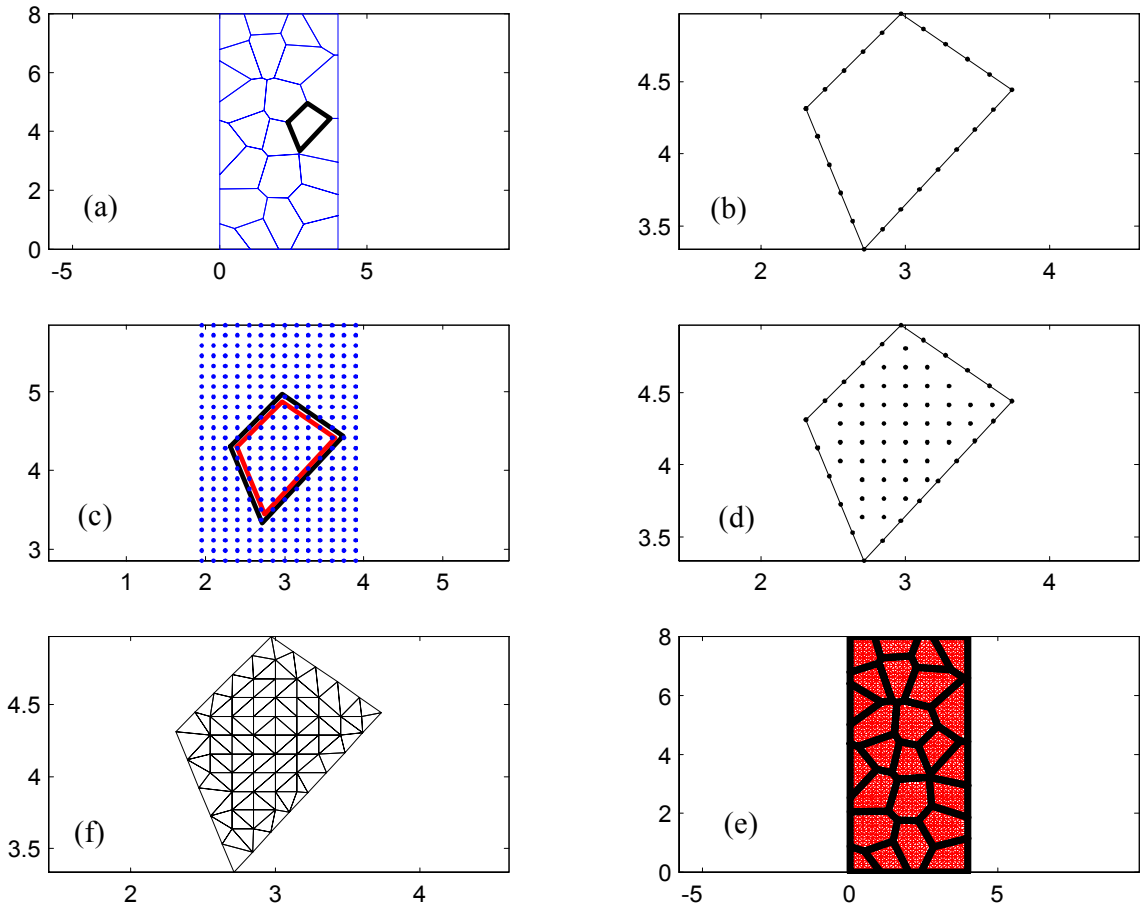

Figure 3.2: Steps to mesh the model (a)Voronoi plot (b) Nodes on the boundaries of a grain (c) Unifrom grid over a grain (d) Nodes obtained from the unifrom grid (e) Mesh the grain (f) Completed mesh of the model.

3.2.1 Infinite element

Infinite elements reduce the reflections from the side wall. These elements are often known as "quiet" boundaries. These elements have some damping properties to absorb the wave such that little energy is reflected. The material properties are isotropic which is the requirement of ABAQUS. The software decides the damping values also to prevent maximum reflections from the boundaries. There are some reflections due to numerical errors. The infinite element is shown in the Fig. 3.3. The procedure for node numbering

of an infinite element required by ABAQUS is shown in the figure. The theory of "quiet" boundaries is explained in detail in the ABAQUS/Explicit [30] manuals.

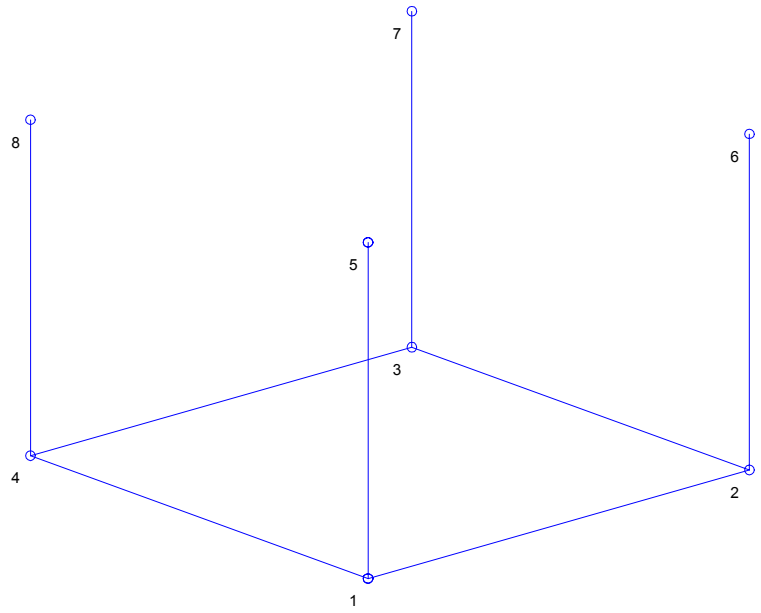

Figure 3.3: Infinite element node numbering.

3.3 Material Properties

For the attenuation calculations two types of models are created. The first one with homogeneous material properties and the second with crystal-specific heterogeneous material properties. The infinite elements for both types have isotropic material properties. For the heterogeneous case, the elements within each crystal are given orthotropic material symmetry. The orthotropic elements for a given crystal have random material orientation in all the three directions. Models are created for four types of material, namely aluminum, fictitious, nickel and copper.

Table 3.1: Single-crystal properties of materials examined.

	Independent Elastic Constants			**Density**	**Young's Modulus**
	C_{11} **(GPa)**	C_{12} **(GPa)**	C_{44} **(GPa)**	ρ**(Kg/m^3)**	E **(GPa)**
Aluminum	103.4	57.1	28.6	2760	70
Fictitious	200.0	130.0	65.0	5000	160
Nickel	243.6	149.4	119.6	8908	200
Copper	176.2	124.9	81.8	8970	110

Table 3.2: Material characteristics.

	c_L	c_T	$\upsilon/\rho c_T^2$
Aluminum	6244	3094	-0.4127
Fictitious	6694	3256	-1.1321
Nickel	5889	3163	-1.6498
Copper	4965	2572	-1.8931

The material properties for the materials used are shown in Table. 3.1. In Table 3.2 the longitudinal and shear wave speeds for the material are given and a dimensionless anisotropy factor $\upsilon/\rho c_T^2$, introduced by Weaver [7], is given for the materials, where $\upsilon = C_{11} - C_{12} - 2C_{44}$. The dimensionless anisotropy factor dictates the degree of scattering for the material. From Table. 3.2, it can be seen that copper has the strongest scattering properties and aluminum the weakest among the four. All of the materials have cubic crystallite structure. From the Table 3.2 the dimensionless anisotropy factor for copper is approximately 4.5 times higher than aluminum. The material properties of the fictitious material are chosen such that its scattering properties are between copper and aluminum. These materials are chosen such that the numerical results can be compared with strong, weak and moderate scattering material.

3.4 Boundary Conditions

The plane stress formulation is constructed and the boundary conditions are applied to avoid reflections from the side of the model as much as possible. The displacements in the x-axis and y-axis at the corners are set to zero while they are free everywhere else in the model. The model is free in the out of plane direction. The use of the infinite elements minimizes reflections of the wave from the boundaries. The loading is a pressure load normal to the surface to simulate longitudinal waves. The boundary conditions are shown in Fig. 3.4. This plot is obtained from the ABAQUS/Explicit CAE. For simplicity, the model shown in Fig. 3.4 has ten crystals and the element size is 200 μm. The loading is shown in the figure by the arrows perpendicular to the top surface of the model. The infinite elements are shown at both the sides of the model. At the bottom left-hand corner the material orientation is shown by the yellow lines. The boundary conditions are marked by arrow heads at the bottom right and left corner of the model in orange. For the plane strain boundary condition the model has zero displacements in the out of plane direction as shown in Fig. 3.5.

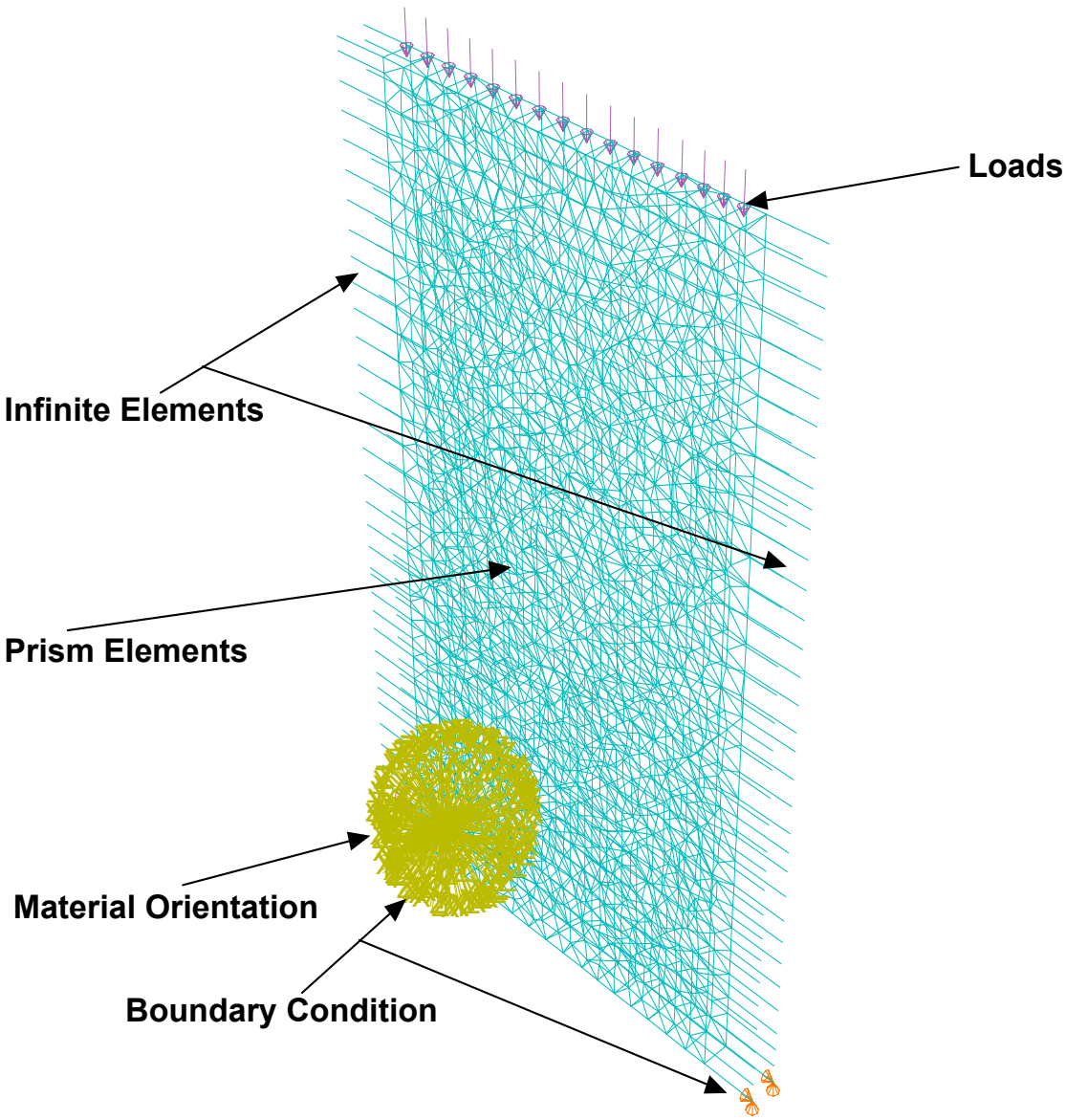

Figure 3.4: Model with incident longitudinal wave and plane stress boundary conditions.

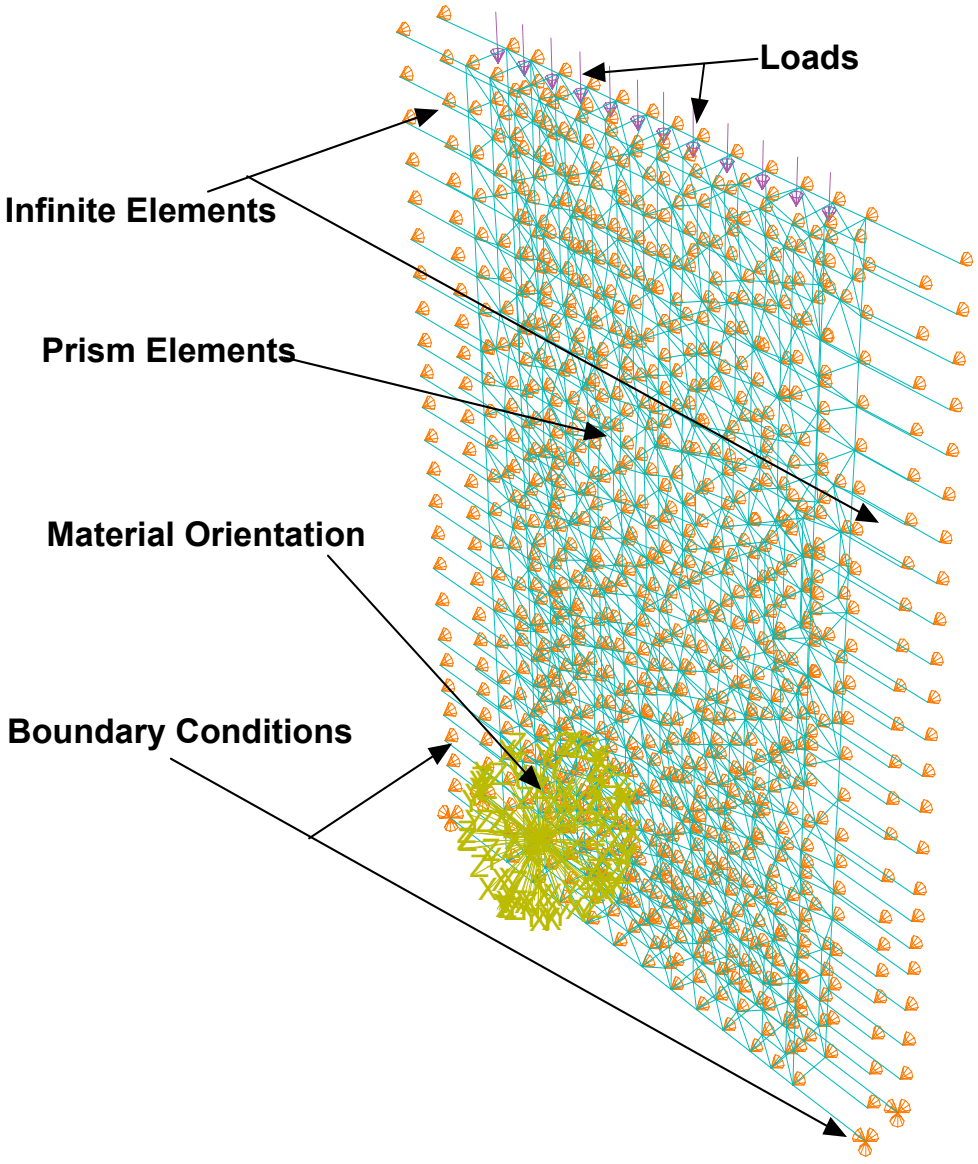

Figure 3.5: Model with incident longitudinal wave and plane strain boundary conditions.

The loading is done using a Gaussian pulse at the required frequency as shown in Fig. 3.6. The y-axis of the plot is shown as LOAD for the model. The fast Fourier transform (FFT) of the pulse is plotted in the frequency domain graph to verify the frequency of the input wave. The depth of the model is 0.075 mm is very small compared with the wavelength of the input wave. Typically, for a 5 MHz incident longitudinal wave the wavelength λ is 1.2488 mm. Therefore, the scattering is expected to be independent of the depth of this model with plane stress boundary conditions.

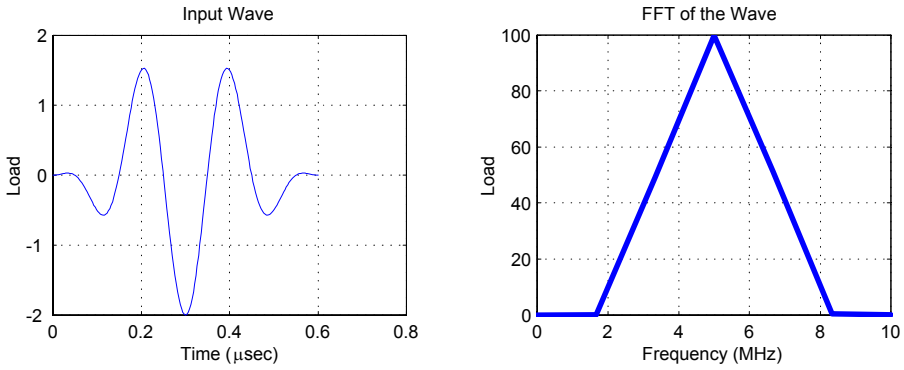

Figure 3.6: Input Gaussian pulse wave.

3.5 Convergence

The convergence in the explicit method is guaranteed as long as the problem is stable. As the element size decreases the computational time also increases. The convergence is checked for the optimum element size to obtain accurate attenuation results. Convergence is checked for aluminum for an incident longitudinal wave.

Example backwall reflections are shown in Fig. 3.7 for a model with a different

element sizes using the same distribution of grains. At the top of each subplot the element size, Δx is noted in μm. A parameter $\lambda/\Delta x$ is computed for each element size to define the number of elements in a wavelength, where λ is the wavelength of the input wave.

The difference of each backwall reflection is compared with that of the model with 40 μm as the element size as shown in Fig. 3.8. The x-axis of each subplot is the time in μsec and the y-axis is the displacement in μm. The displacements for the backwall reflection are substracted from the backwall results for the model with element size 40 μm. The absolute value of the error is shown. The final subplot is the backwall response for 40 μm.

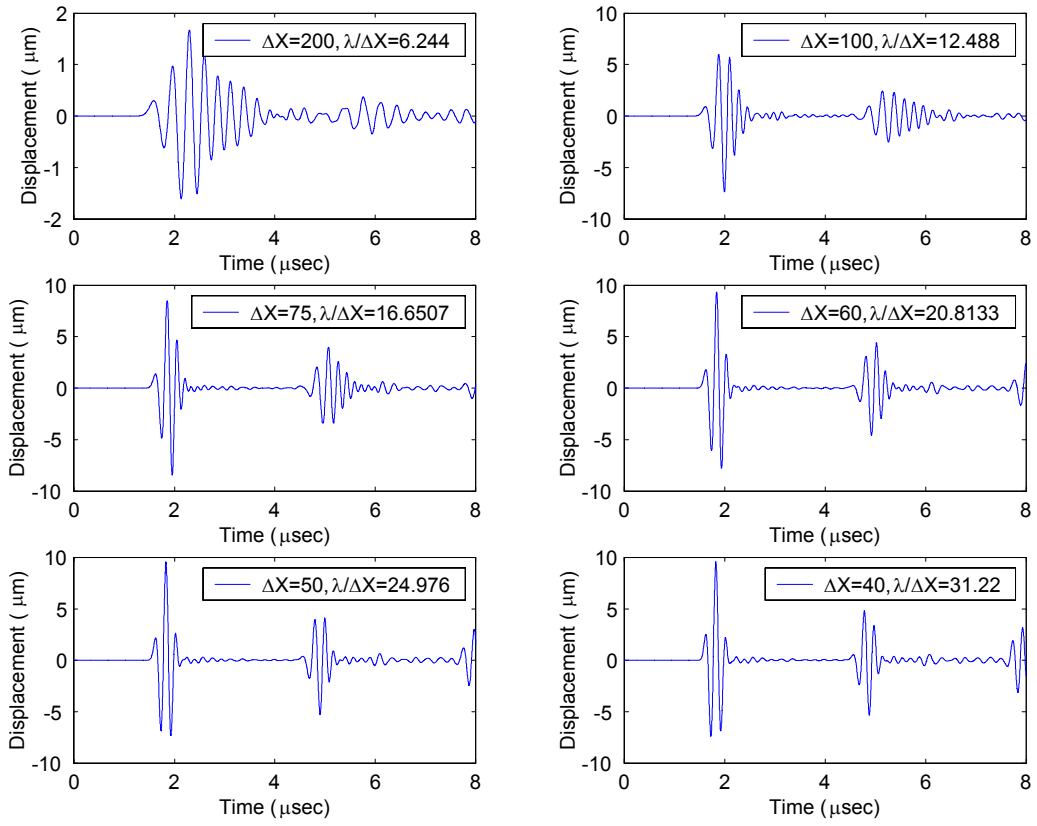

Figure 3.7: Backwall response for heterogeneous aluminum cubic crystal.

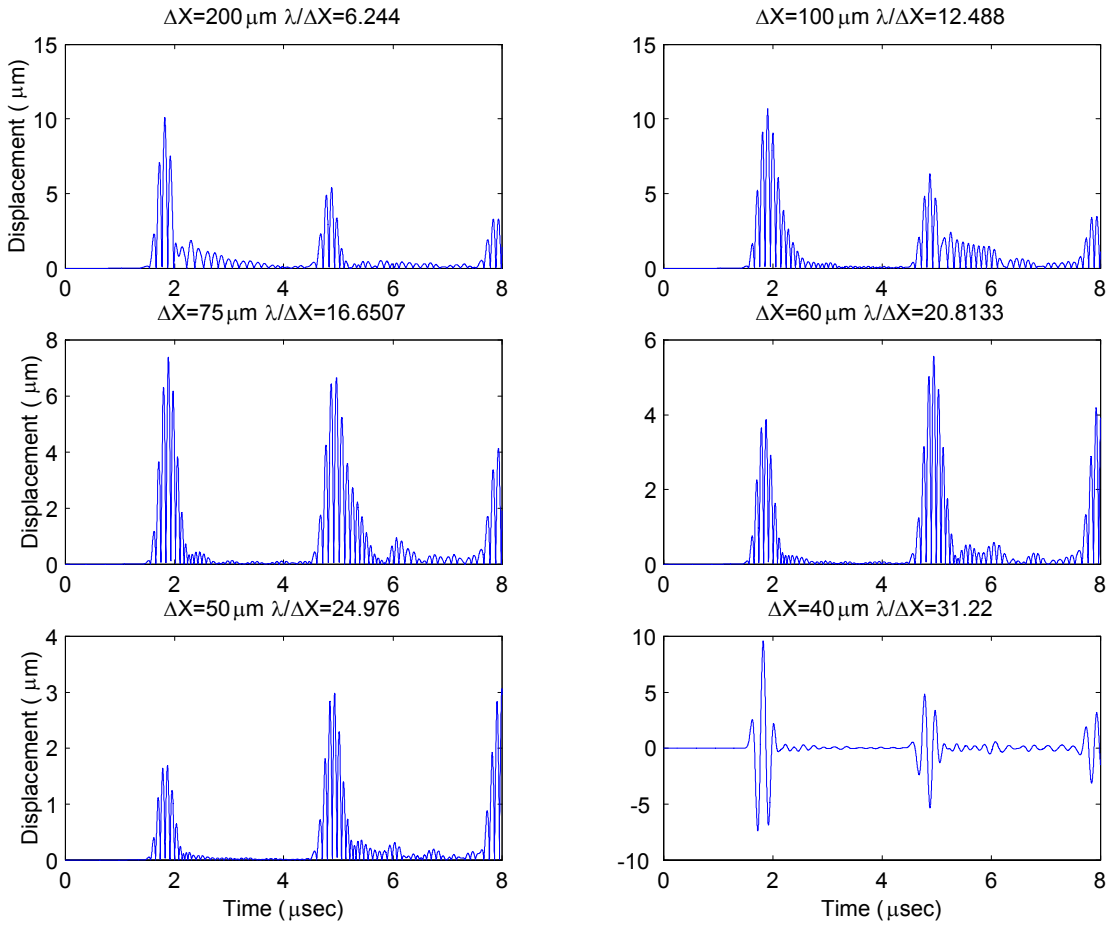

Figure 3.8: Error in backwall response relative to the 40 μm elements for different element size.

The backwall results for 40 μm and 50 μm element size are shown together in Fig. 3.9. As seen from the figure there is still a small time shift. Therefore, this error may not infer convergence with respect to the backwall of the model. The error is due to the time shift in the echoes but the amplitude difference may be small. Calculation of the attenuation is the main concern here, so the attenuation must be compared to confirm convergence of the model. For calculating attenuation the amplitude is of the main concern. The attenuation calculation involves the FFT of the backwall reflection, which is in the frequency domain. Here, the time shift does not matter much.

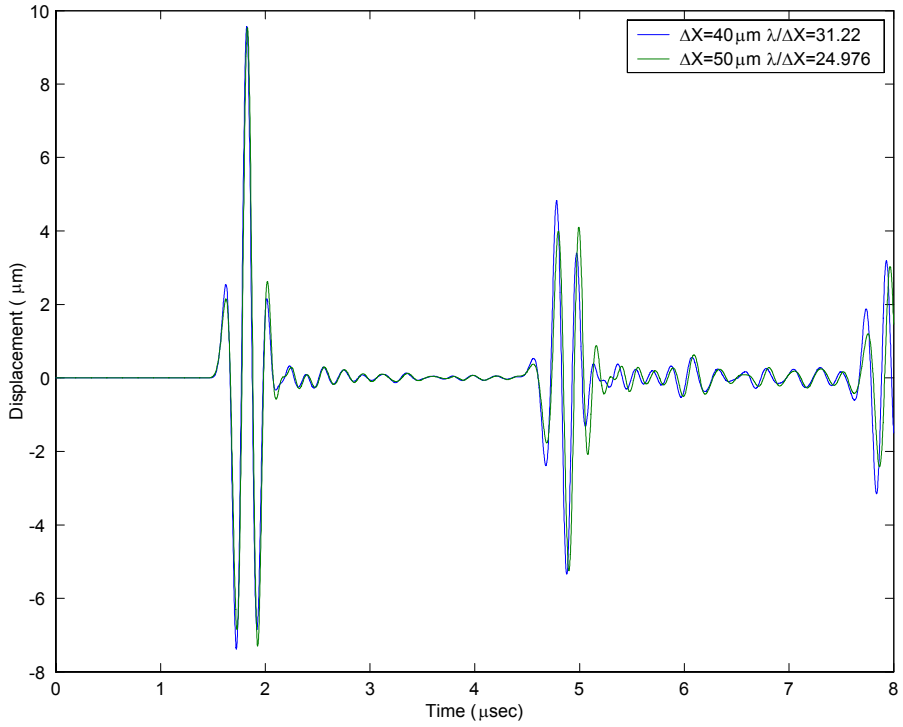

Figure 3.9: Comparison of backwall response for model with element size 40 μm and 50 μm.

The attenuation for a 5 MHz longitudinal incident wave is shown in Fig. 3.10 as a function of element size. Each plot is expanded in the range of interest as there is noise before and after this frequency range. This acceptable region varies, generally taken as the area under $A/\sqrt{2}$ of the FFT of the wave with A as the peak value of the FFT. Most of the energy is concentrated within this region. The attenuation coefficient can be extracted for this region easily. The x-axis is the frequency in MHz and the y-axis is attenuation coefficient in Np/cm for all the subplots in Fig. 3.10. The backwall reflections cannot be differentiated from each other for the model with element size $\Delta x = 200$ μm due to the large element size because the whole signal is just noise. Therefore, attenuation cannot be calculated and hence not plotted for the model with element size $\Delta x = 200$ μm.

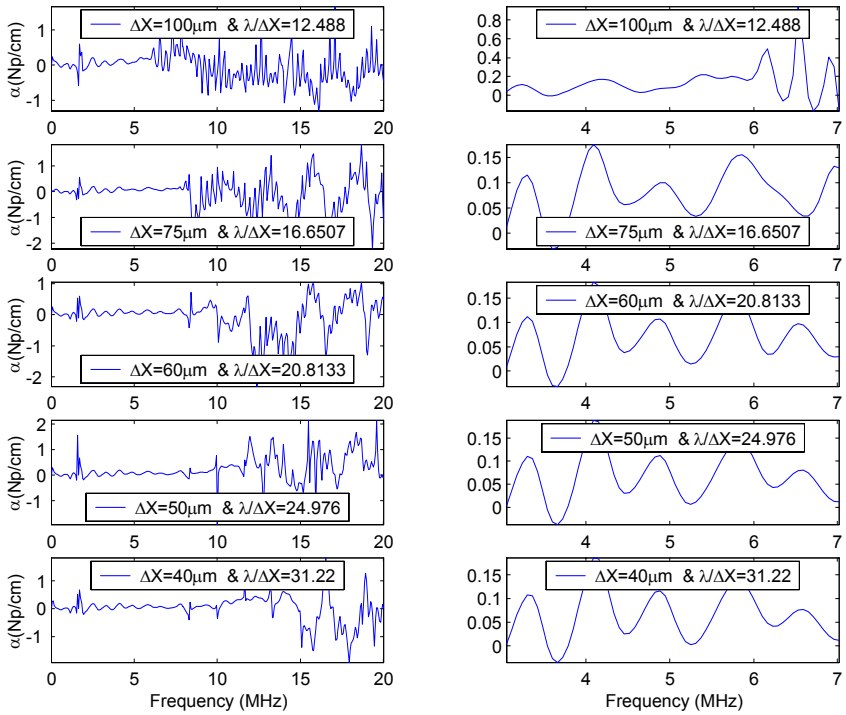

Figure 3.10: Attenuation for different element size.

The attenuation for each model at each point is now substracted from the model with element size $\Delta x = 40$ μm at the same points as done before for the backwall reflection comparison. The attenuation comparison is shown in Fig. 3.11 for the region of interest neglecting the noise region. The absolute value of the difference is plotted. The error decreases as the element size decreases as expected. From the graph the error also oscillates in between the bounds. These bounds are of main interest here. The element size can now be chosen as per the acceptable error bounds.

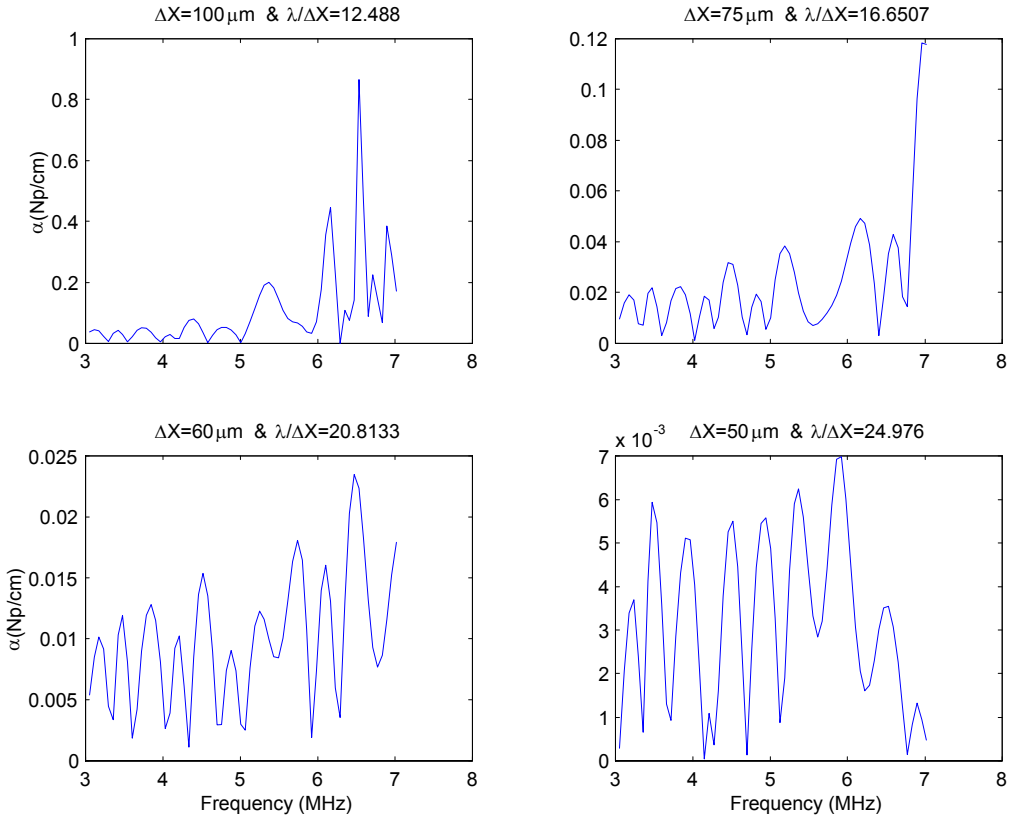

Figure 3.11: Comparison of attenuation with the 40 μm element results for different element sizes.

The attenuation results for 40 μm and 50 μm elements are plotted together in

Fig. 3.12. The error for 50 μm elements is very small when compared with results 40 μm elements. For calculating attenuation, models are created with different distributions of grains and then the backwall reflections from all the models are used for averaging. This averaging is required for the attenuation calculation as the model is very small and there are few nodes at the boundaries. Here the above results are only for one realization of grains. The error also decreases when compared with the theory if averaged over different random realizations of grains. Thus, convergence in attenuation is achieved with $\Delta x = 50$ μm with an acceptable range of error.

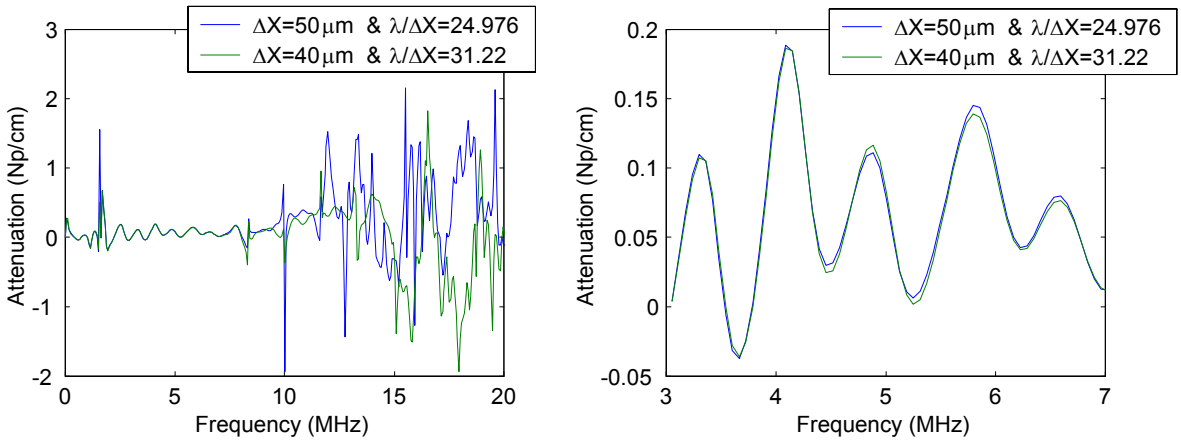

Figure 3.12: Comparison of attenuation coefficient for element size 40 μm and 50 μm.

From the backwall reflection results for the homogeneous material, attenuation has been observed which should not be there as per the scattering theory, since there is no scattering in a homogeneous material. This reduction in amplitude is due to geometric spreading of the input beam as well as small numerical attenuation due to the discretization. The difference in attenuation between homogeneous and heterogeneous material is the

attenuation for the material. For any attenuation, fifteen realizations are considered when calculating the attenuation coefficient.

3.6 Summary

In this chapter the basic equations for the mathematical formulation of the wave propagation in polycrystalline materials for finite element analysis was presented as referred in the ABAQUS [30] manuals. The meshing procedure is explained in this chapter in detail. Sometimes some Voronoi polycrystals have very small edges which are smaller than the element size. These elements make the computational time costly. Different realizations have been used to overcome this problem and eliminate the models with very small edges. The attenuation coefficient is used for a convergence check. The error is deemed acceptable for the attenuation calculation for an element size $\Delta x = 50$ μm and this size has been used to mesh all the models used in this thesis. The triangles created from the uniform grid may not be exactly equilateral but can be approximated to have the same length for all three sides of the triangles. Therefore, the element size mentioned here is determined with this assumption. Also, the triangles near the edges are not equilateral most of the time. This assumption is made to refer to the element size with which other parameters can be related easily like number of elements in a wavelength or in a crystals. Matlab codes described in Appendix A and B, have been developed to create the input file for ABAQUS. A pressure load at the surface of the element is introduced to simulate a longitudinal wave. In the next chapter, the data acquisition and method to obtain the numerical attenuation results are explained in detail.

Chapter 4

Example Numerical Results (Plane Stress)

The numerical results are obtained for the material of general interest with plain stress boundary conditions. The attenuation calculated numerically is given by [31],

$$e^{-\alpha d} = \frac{|F_2(\omega)|}{|F_1(\omega)|} \tag{4.1}$$

where, α is the attenuation, d is the travel length of the elastic wave, and $F_1(\omega)$ and $F_2(\omega)$ are the first and the second backwall reflections, respectively in the frequency domain. The backwall reflections are averaged over the nodes at the surfaces for each model and the attenuation is calculated. Attenuation results are then averaged for different realizations of Voronoi polycrystals. To obtain a normal distribution of crystals in a domain a minimum distance restriction between any two Voronoi nuclei is used. The minimum distance data for different models for a specific number of crystals is obtained. Any kind of interpolation

can be used to fit the data. Here a spline is used to fit to the data. Figure 4.1 shows the spline fit to the data obtained from a unit square domain which is used as a reference domain. For different model sizes, a linear transformation is done by considering the total area of the reference and the current domain.

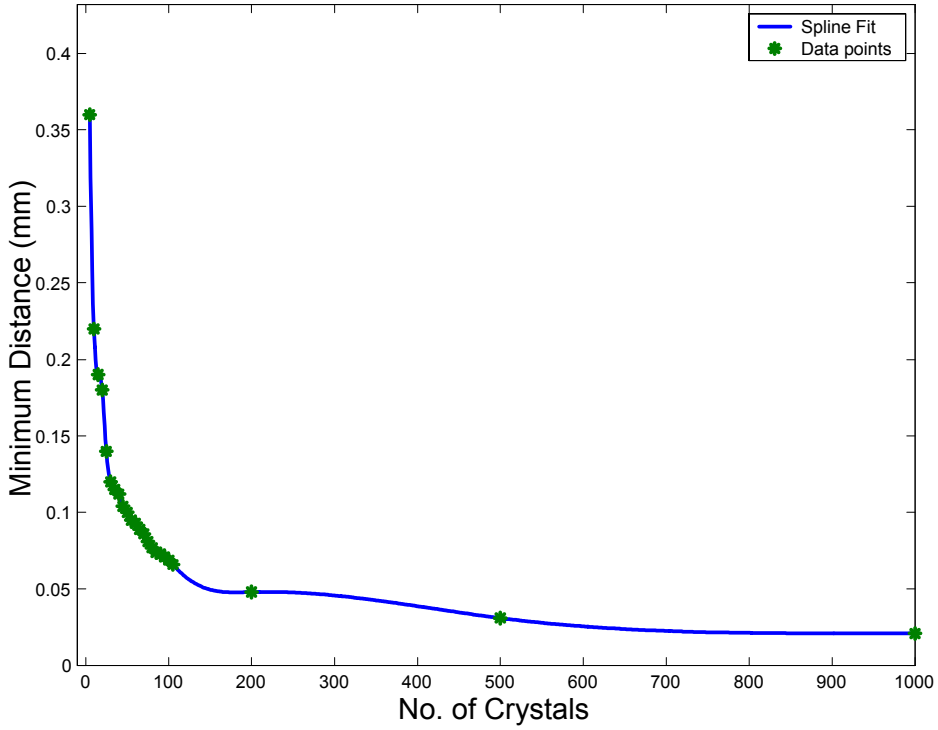

Figure 4.1: Minimum distance required between any two crystals inside an unit square for a normal distribution of grain size.

The materials examined here have different scattering properties as shown in Tables 3.1 and 3.2. Due to this scattering the attenuation calculation can be difficult as the noise in the echoes increases with increase in anisotropy factor of the material. The noise in the output signal makes the reflections of the backwall and frontwall hard to differentiate. The frontwall displacement data for aluminum and copper are shown in Fig. 4.2. The reflection echoes can easily be recognized for aluminum by looking at the figure. However, for

copper the noise is higher so the reflections cannot be differentiated from each other. This noise is directly proportional to the length of travel of the wave. To obtain a clear waveform with less noise different model sizes were used according to the scattering property of the material. The models for weak scattering media are longer and for strong scattering media they are shorter. The model is made wider for strong scattering so that more nodal data may be obtained. Example results are shown in this chapter for models with plane stress boundary conditions.

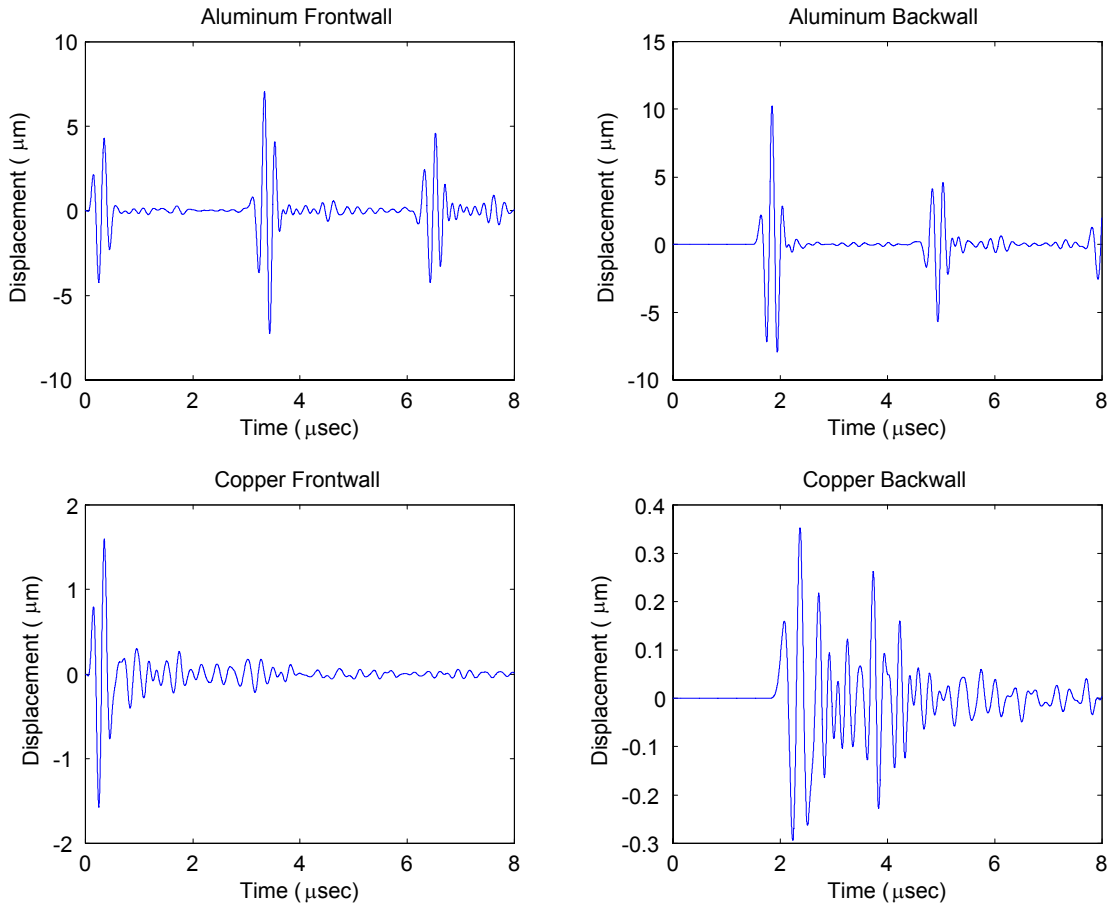

Figure 4.2: Frontwall and backwall responses for aluminum and copper.

4.1 Aluminum

Aluminum is the weakest scattering media among the four materials studied here. The model domain used for aluminum is the longest. Due to a low anisotropy factor, the same size model with a different number of crystals with different input frequency are constructed as shown in Table 4.1.

Table 4.1: Model specification for aluminum

No. of	**Model Size**	**Diameter** (μm)		**Input Frequency**	$\frac{\lambda}{D_m}$
Crystals	(mm^3)	**Mean** (D_m)	**Std Deviation**	(MHz)	
150	$4 \times 8 \times 0.075$	512	95	3	4.0651
150	$4 \times 8 \times 0.075$	512	95	5	2.4391
150	$4 \times 8 \times 0.075$	512	95	8	1.5244
200	$4 \times 8 \times 0.075$	446	71	5	2.8001

The procedure for calculating attenuation is now explained using an example of 150 crystals for 5 MHz as the input wave frequency for a single realization of crystals. The attenuation is calculated from the backwall reflections in the model. The backwall responses for the homogeneous and heterogeneous cases are shown in Fig. 4.3. The attenuation is less for the homogeneous case. Due to geometric spreading there is a small reduction in amplitude. The backwall response shown was determined by averaging over the nodes on the backwall. For this model there are 20 nodes over which the averaging is done. Only nodes near the center of the wall are chosen. The nodes near the corners are avoided since they are outside the coherent wave profile.

The first two reflections are used and referred to as Echo E1 and Echo E2 as shown in Fig. 4.4(a) and (b), respectively. Tapered windowing and zero padding is done on E1 and E2 as shown in Fig. 4.4(c) and (d) respectively. Figure 4.4(e) shows the FFT of the

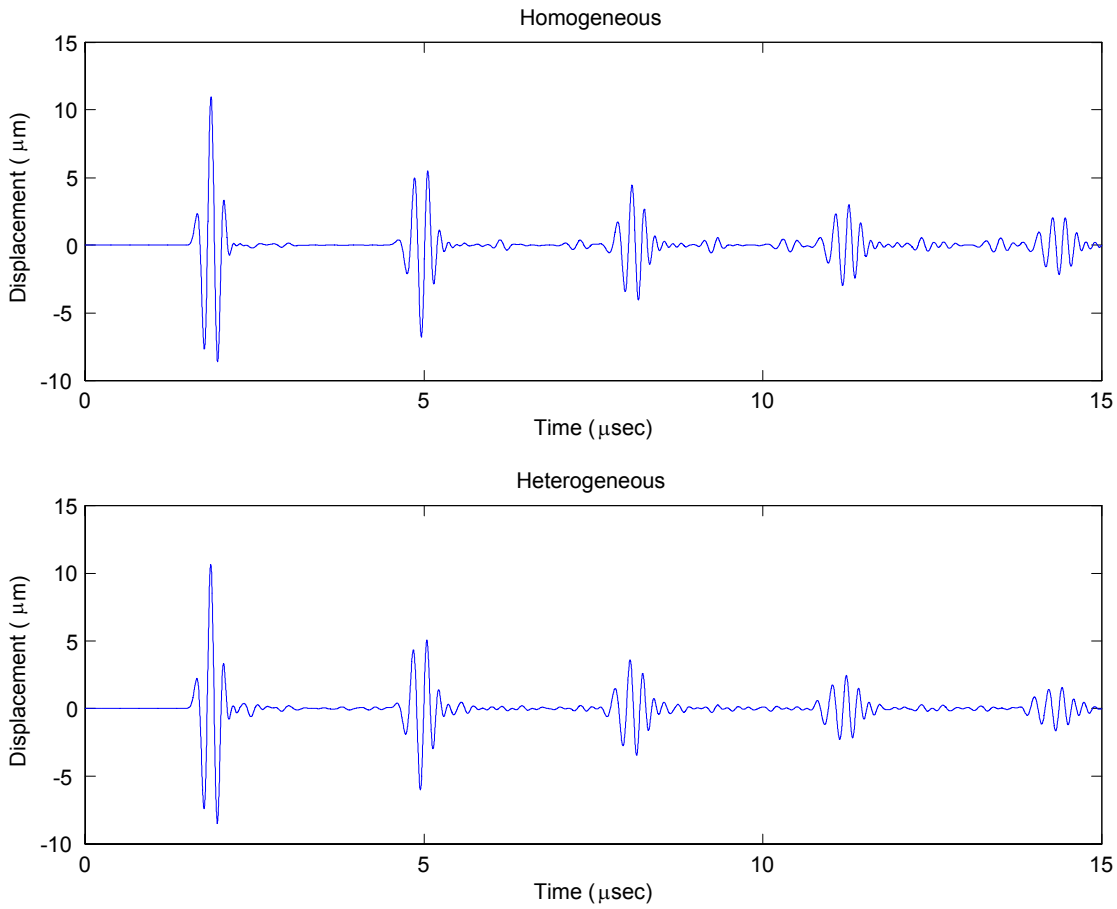

Figure 4.3: Backwall reflection for 150 aluminum crystals at 5 MHz.

windowed data. Using Eq. 4.1, the attenuation is obtained for these responses as shown in Fig. 4.4(f). The attenuation in the homogeneous material is due to beam spreading and numerical scattering. In the Fig. 4.4(e) the FFT is very smooth and the attenuation for a region around 5 MHz is constant. Attenuation results for frequencies far from 5 MHz are primarily noise.

The same procedure is followed for the heterogeneous case. Example results are shown in Fig. 4.5(a)-(f). The scattering is seen to be higher in the heterogeneous case which

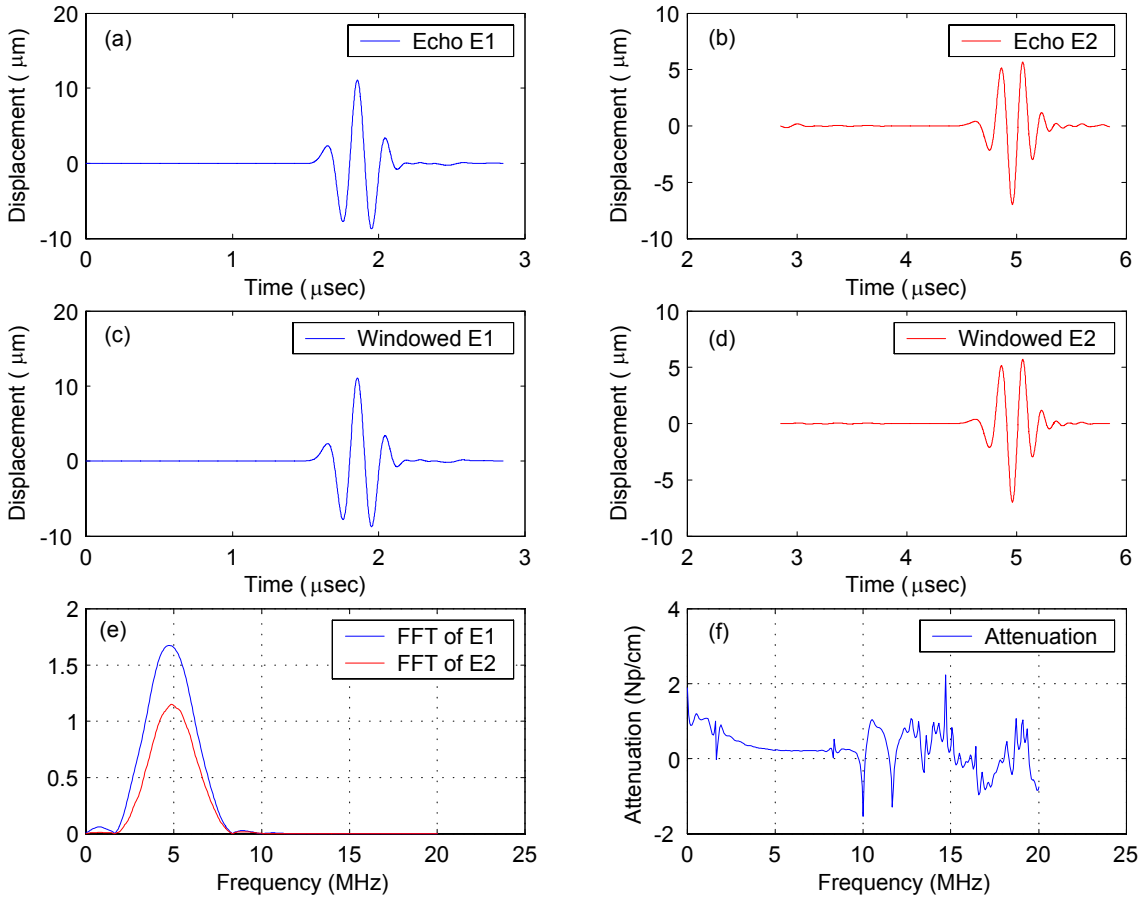

Figure 4.4: Calculation of attenuation for one realization of homogeneous crystals.

is expected. The FFT is not as smooth as that of homogeneous case, shown in Fig. 4.5(e). The echoes contain more noise from scattering than that of the homogeneous material. This noise increases as scattering introduces more noise into the echo signals. Eq. 4.1 is used to calculate the attenuation from the FFT data.

The attenuation for the homogeneous material is due to beam spreading and numerical scattering. The same effects are also included in the results for the heterogeneous case. The attenuation is found by substracting the homogeneous results from the heteroge-

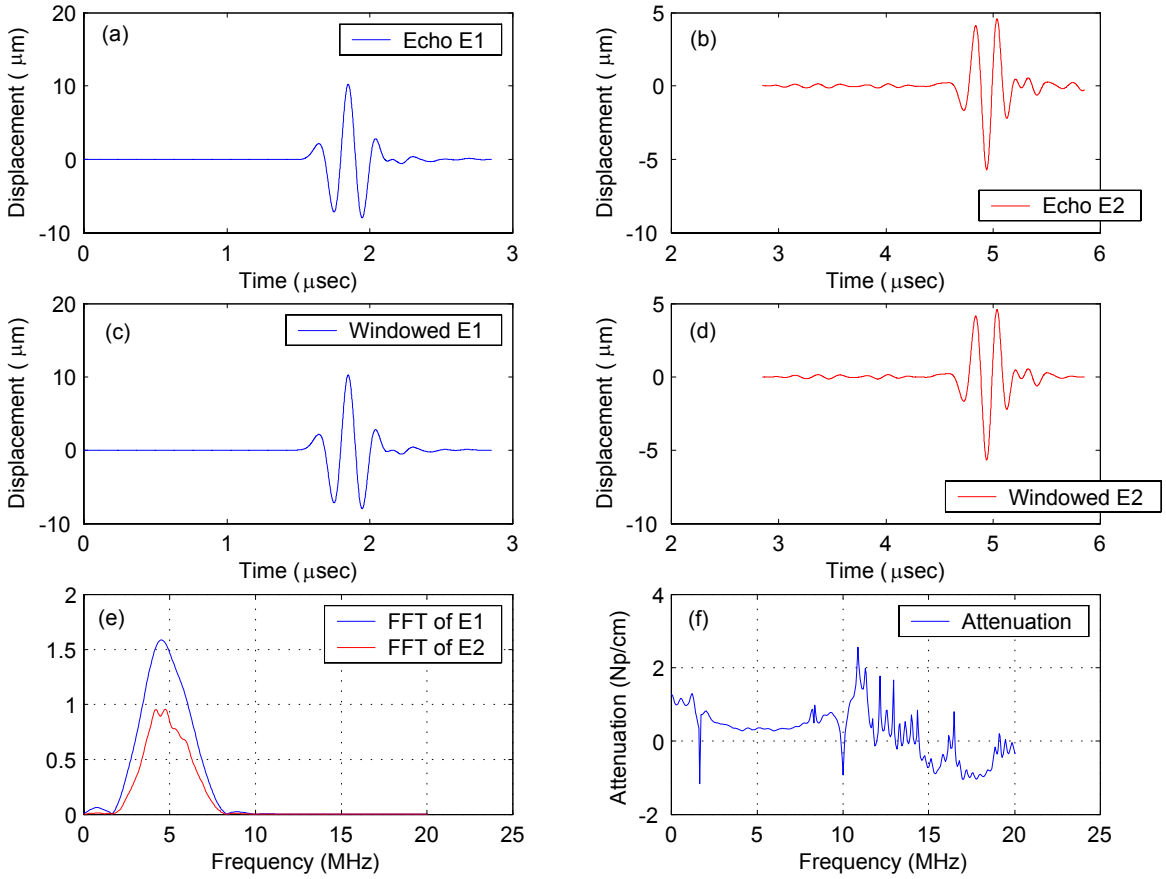

Figure 4.5: Attenuation calculation for one realization of randomly oriented cubic crystals.

neous results. The attenuation obtained after subtraction is shown in Fig. 4.6. This result is the attenuation from one realization of a Voronoi polycrystal.

The attenuation for different realizations are compared so that the minimum number of realizations required to obtain accurate attenuation results may be understood. These results are shown in Fig. 4.7(a)-(f). One of the main purposes of having different realizations is that more nodal displacement data may be used for averaging. As seen from Fig. 4.7(a), relevant frequency range without noise is 5±2 MHz. Figure 4.7(b) shows the average attenuation values from 10, 11, 12, 13 and 14 realizations. These attenuation values are

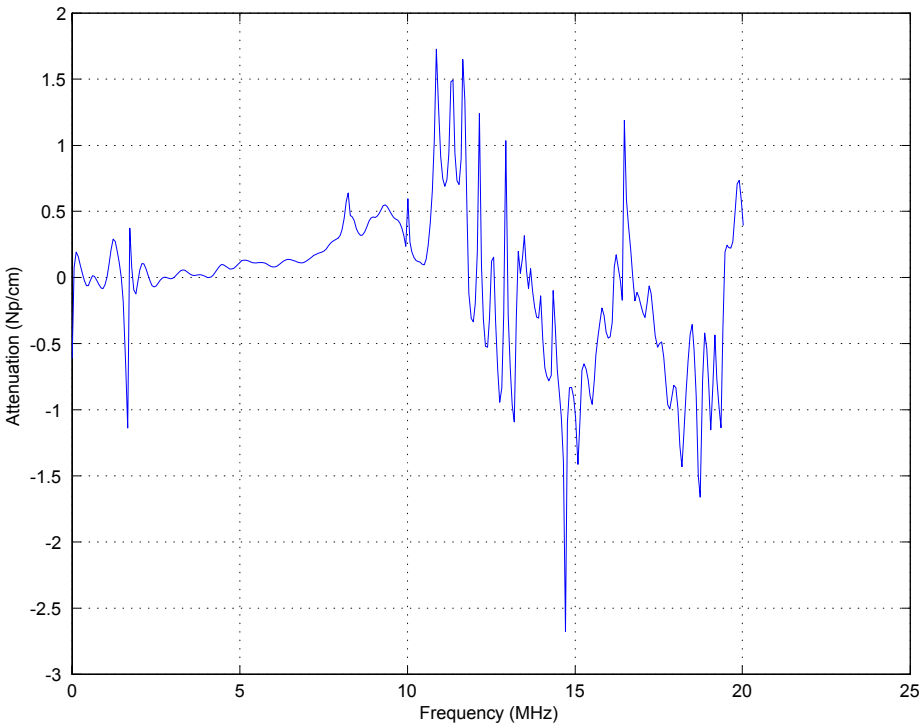

Figure 4.6: Attenution for one realization of aluminum crystal.

compared with 15 averaged values. The difference decreases as the number of realizations increases as shown in Fig. 4.7(c). In Fig. 4.7(d) the average from 14 and 15 realizations is shown. Thus, it is concluded that 15 realizations are sufficient to obtain the attenuation values for aluminum.

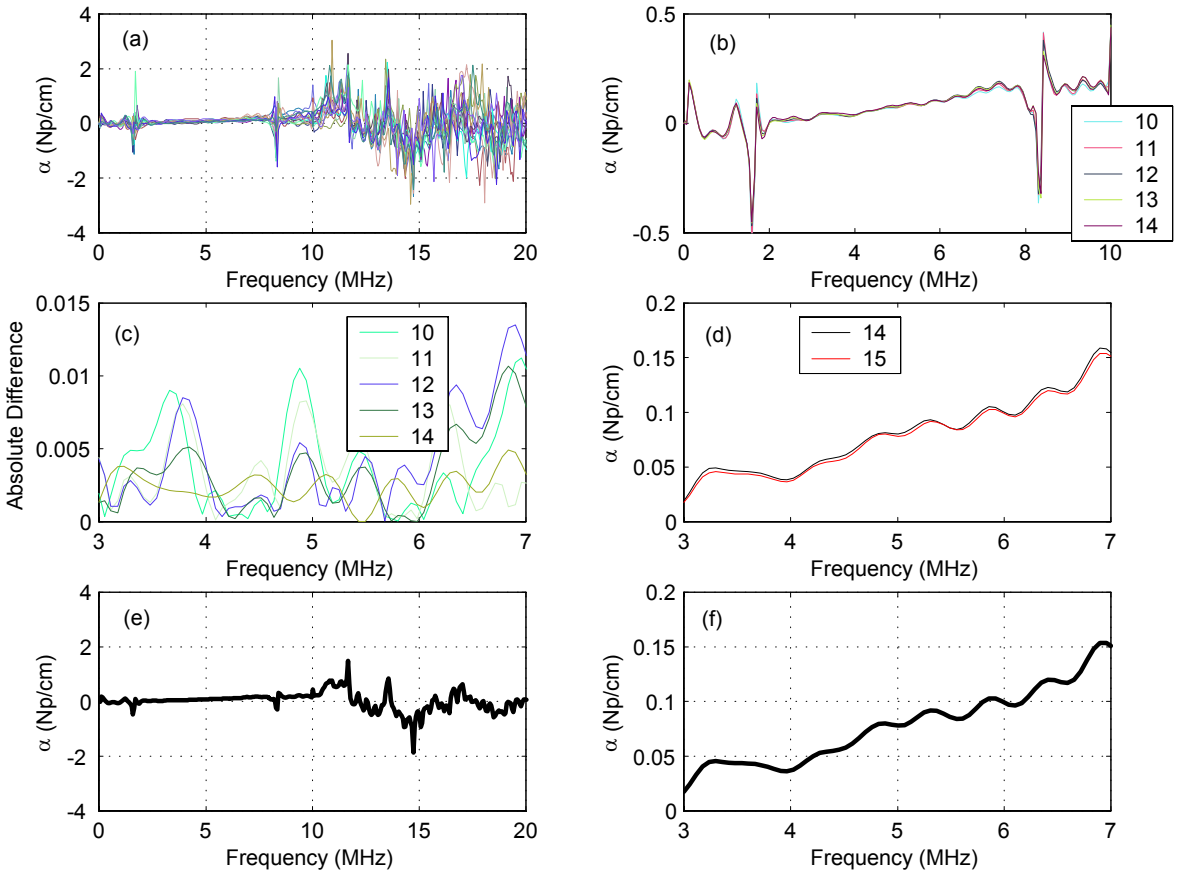

Figure 4.7: Attenuation comparison for different realizations of crystals for 150 aluminum crystals in a 4 mm by 8 mm model for 5 MHz (a) attenuation from a 15 realizations (b) average attenuation from 10, 11, 12, 13 and 14 realizations (c) differences the different average attenuation (d) average attenuation from 14 and 15 realizations (e) average attenuation for 15 realization (f) average attenuation from 15 realization for the region of concern.

Attenuation from different realizations of crystals at different frequencies are obtained as shown in Fig. 4.8. The color lines in the plot are attenuation for each realization of the crystals. Fifteen realizations are used for the attenuation calculation. The average from all the 15 realizations is marked in black. Thus, the longitudinal attenuation for aluminum is obtained for values of frequency over the range of λ/D.

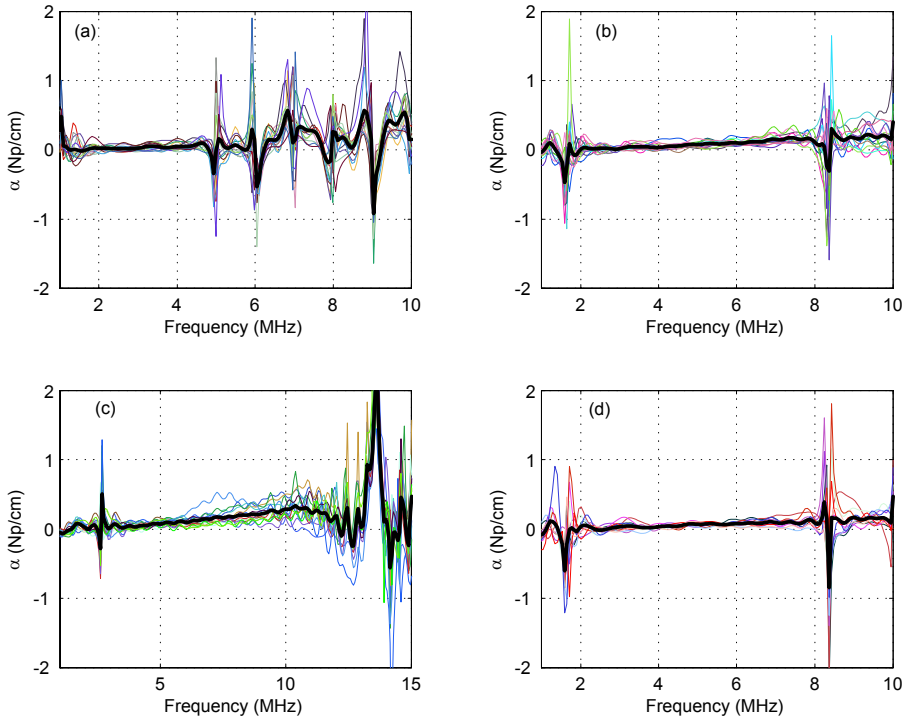

Figure 4.8: Longitudinal attenuation from different realization of crystal for model size of 4 mm by 8 mm and input frequency of the wave (a) 150 crystals for 3 MHz (b) 150 crystals for 5 MHz (c) 150 crystals for 8 MHz (d)200 crystals for 5 MHz.

Simulations for the homogeneous and heterogeneous material properties models are shown in Figs. 4.9 and 4.10. The figure shows the stress waves propagating through the model at various times. Less attenuation is seen in the homogeneous case than the heterogenous case.

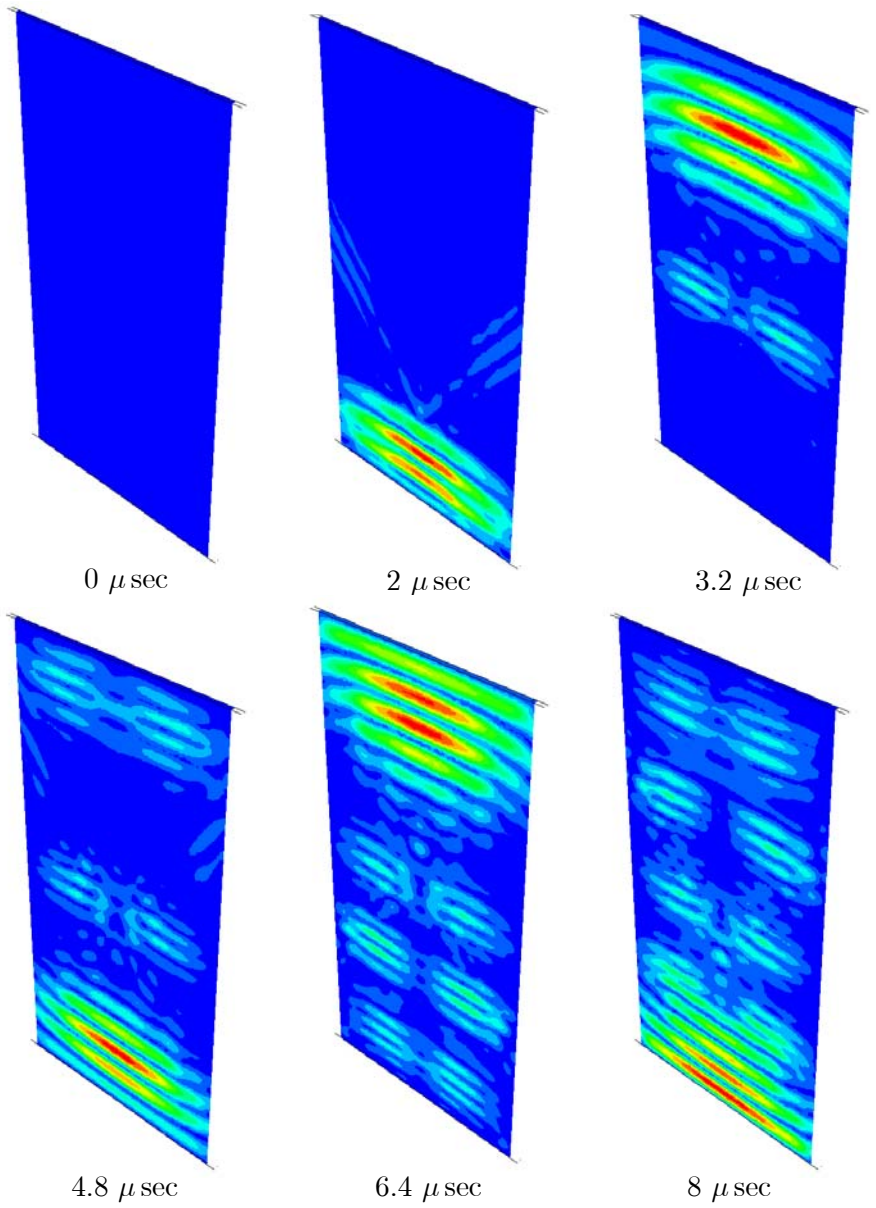

Figure 4.9: Simulation for aluminum with homogeneous material properties. 150 crystals in a 4 mm by 8 mm model for 5 MHz of longitudinal wave.

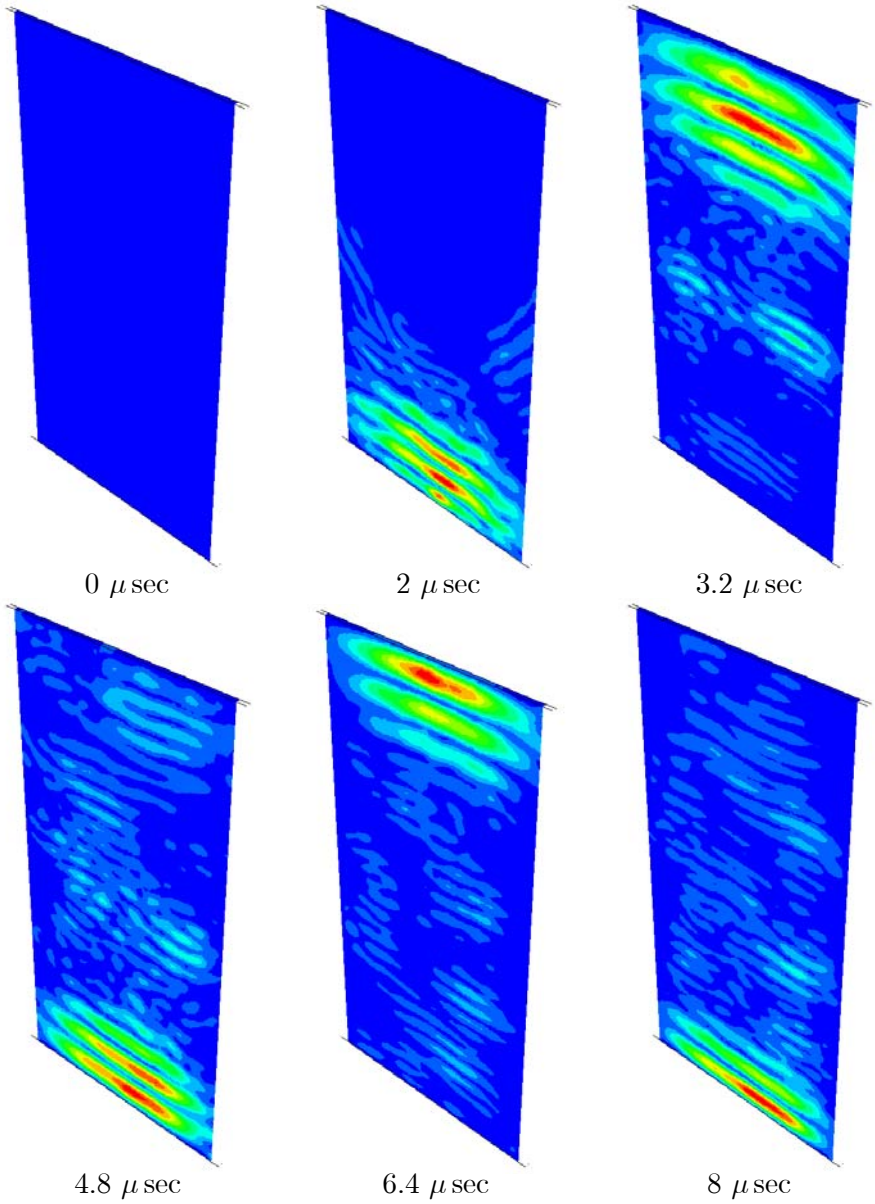

Figure 4.10: Simulation for aluminum with heterogeneous material properties. 150 crystals in a 4 mm by 8 mm model for 5 MHz of longitudinal wave.

4.2 Fictitious Material

Three models for the fictitious material have been created as shown in Tables 4.2 for incident longitudinal waves. For this material different frequencies of incident longitudinal wave have been used. The model size used is 8 mm by 6 mm with 0.075 mm depth with 512 μm as the mean grain diameter and 95 μm as the standard deviation of the mean grain diameter. Therefore, by keeping the mean grain diameter constant for all the models, λ/D is varied. The results for attenuation are shown in Fig. 4.11 for an incident longitudinal. As seen in the figure the scattering is higher than aluminum which is expected from theory. Fifteen realizations of Voronoi polycrystals have been constructed. The average attenuation from all the realizations are also shown in the figures. The numerical attenuation has a negative region as seen in the Fig. 4.11 due to the noise in the response signal for very low and very high frequency ranges compared with the input frequency for the model. The negative region is outside the main frequency band of the incident wave and is thus neglected. The attenuation values obtained are approximately in the range of 0.5 to 1.0 Np/cm for the incident longitudinal wave. The averaged attenuation curve is smoother than a curve from any particular realization.

Table 4.2: Model specification for fictious material

No. of	Model Size	Diameter (μm)		Input Frequency	$\frac{\lambda}{D_m}$
Crystals	(mm^3)	Mean (D_m)	Std Deviation	(MHz)	
150	$4 \times 8 \times 0.075$	512	95	3	4.0651
150	$4 \times 8 \times 0.075$	512	95	5	1.5244
150	$4 \times 8 \times 0.075$	512	95	8	2.8001

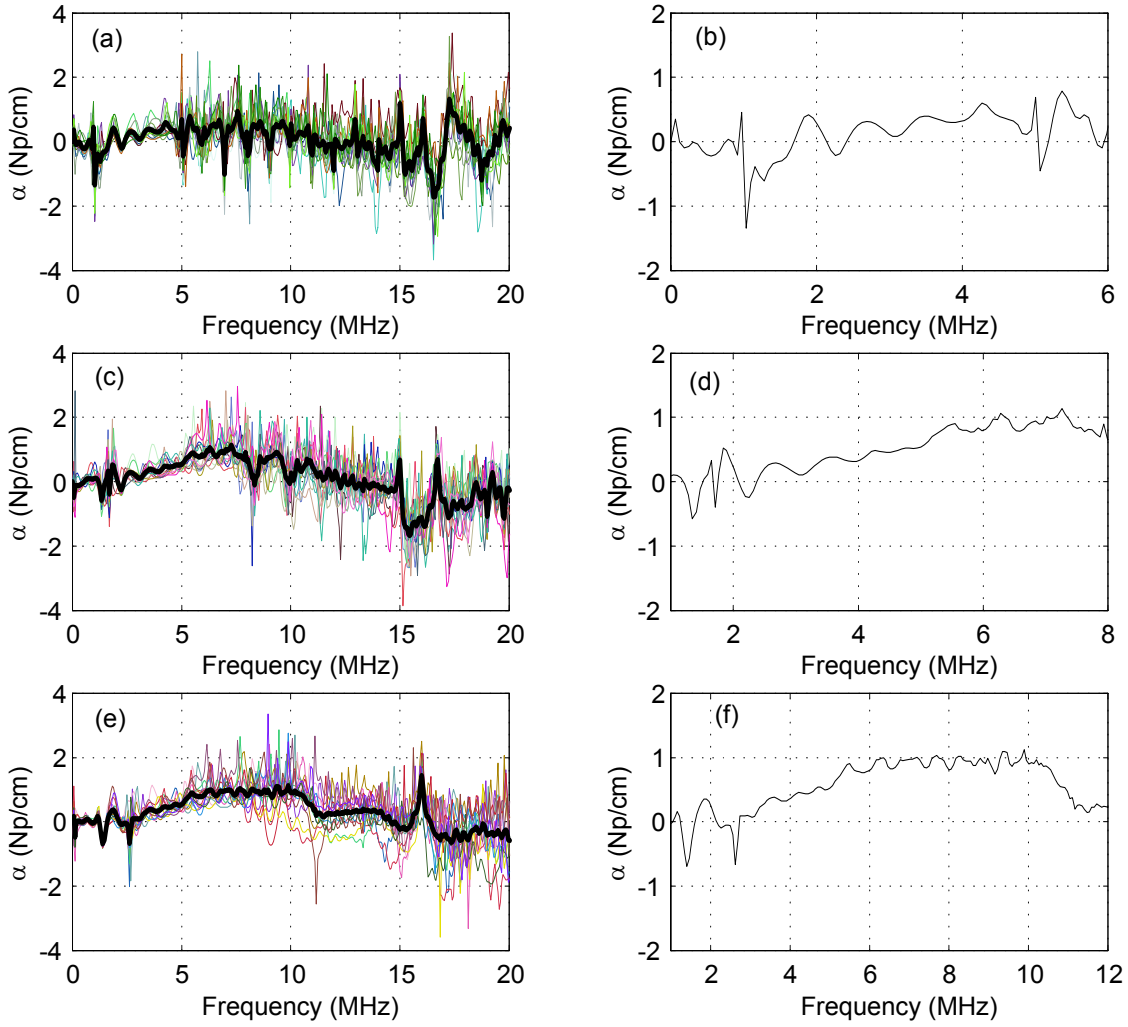

Figure 4.11: Attenuation for fictious material (a) 3 MHz (b) average attenuation for 3 MHz (c) 5 MHz (d) average attenuation for 3 MHz (e) 8 MHz (f) average attenuation for 8 MHz.

4.3 Nickel

Nickel has a higher degree of scattering than aluminum and fictitious material. The anisotropy factor is approximately four times more than that of aluminum. Three models have been created of same size of 5 mm by 6 mm with 0.075 mm as the depth. The model is made shorter such that the wave travels a lesser distance. The model is wider than the model used for aluminum and fictitious material in order for more nodes at the surface to be included in the response data. Twenty realizations have been created for each model to have more data for averaging the attenuation results. Different numbers of crystals are created. The input frequency is constant for all the models. The model specifications are shown in Table 4.3. The λ/D obtained is approximately in the range of 1.44 to 2.89. The numerical attenuation results from different models are shown in Fig. 4.12. The scattering is higher than what is observed for aluminum and fictitious material due to nickel having higher anisotropy factor. The negative attenuation values of are again out of the relevant frequency range, which is due to the noise. Figure 4.12 shows the smooth attenuation curve near the input frequency for the models. The attenuation values for a wide range of frequencies can be considered leaving out the noise region shown in Fig. 4.12 (b), (d) and (f) averaged for the values obtained from twenty different realizations of each model.

Table 4.3: Model specification for nickel for longitudinal wave

No. of Crystals	Model Size (mm^3)	Diameter (μm)		Input Frequency (MHz)	$\frac{\lambda}{D_m}$
		Mean (D_m)	Std Deviation		
50	$5 \times 6 \times 0.075$	862	147	5	1.4487
100	$5 \times 6 \times 0.075$	614	76	5	2.0339
200	$5 \times 6 \times 0.075$	432	70	5	2.8907

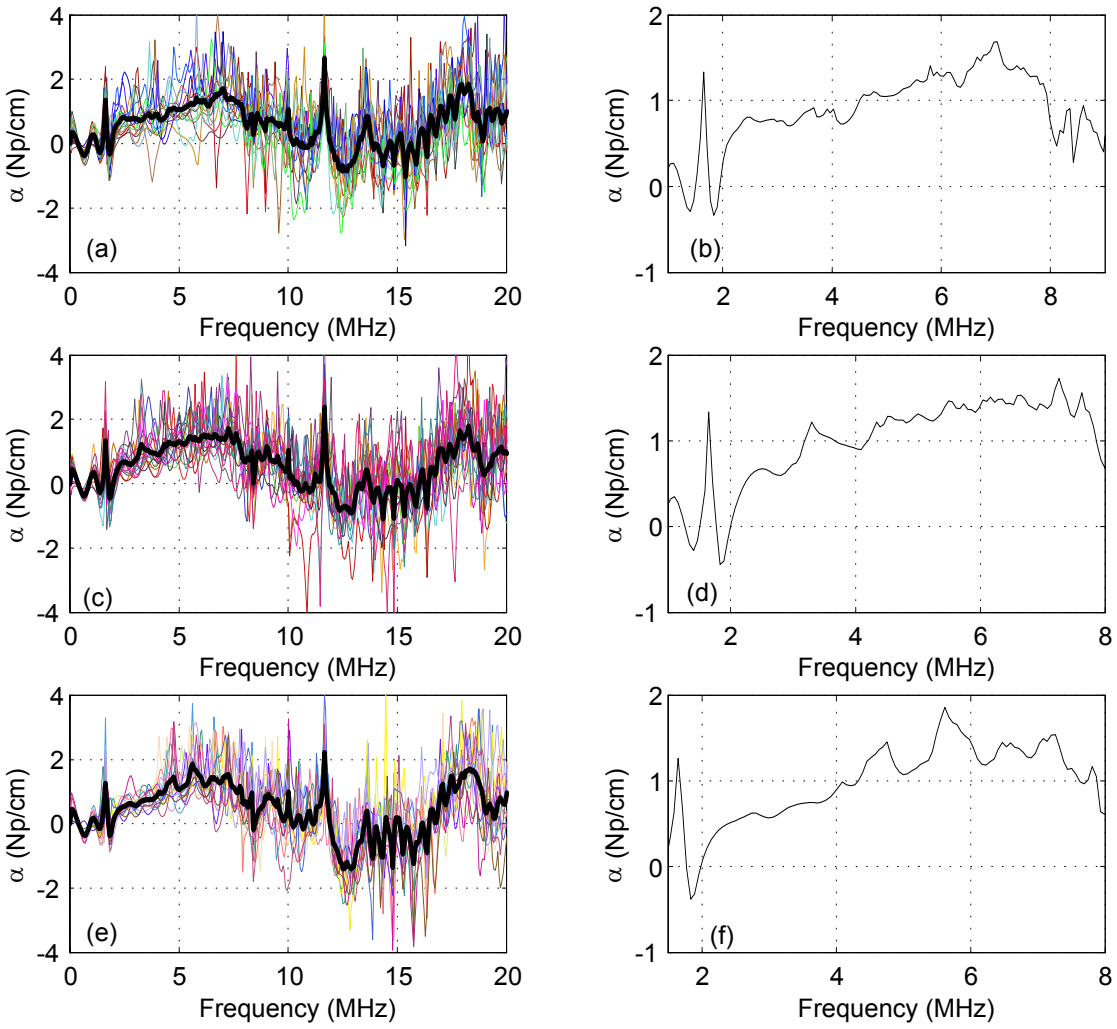

Figure 4.12: Attenuation for nickel for different crystals. (a) & (b) 50 crystals (c) & (d) 100 crystals (e) & (f) 200 crystals.

4.4 Copper

Copper is the strongest scattering media among the four materials examined. Two different sizes of model are used with 10 and 20 crystals only. Table 4.4 shows the model specifications used for copper for a longitudinal wave. The model has fewer crystals and is smaller in length to reduce the amplitude reduction as it depends on these parameters. The shorter length makes the wave travel a shorter distance and also scatter less. The bigger crystal makes the mean diameter high ranging from 1.396 mm to 1.995 mm.

The input wave propagates through approximately two to three crystals in each model. This model is chosen such that response signal has less noise and the analysis is possible. Here λ/D ranges from 0.6260 to 0.8946. Even though the λ/D is low, which implies high attenuation is high, the response signal contains less noise than for the same model containing more grains making the mean diameter lower and λ/D high. The frequency of the input wave is kept constant at 5 MHz. The number of realizations is increased with the variations in the scattering properties of the material. Twenty five realizations of Voronoi polycrystals have been constructed to have more data for averaging the attenuation results for copper. The attenuation for copper is observed to be higher than nickel as shown in Fig. 4.13. The figure also shows that the average attenuation curve becomes smoother.

The simulation from ABAQUS/CAE is shown in Fig. 4.14 for one model. The figure shows high scattering as the original input wave form vanishes after few number of time step and noise becomes more dominant. Also as the original form of input wave starts distorting and the noise content also increases.

Table 4.4: Model specification for copper

No. of Crystals	Model Size (mm^3)	Diameter (μm)		Input Frequency (MHz)	$\frac{\lambda}{D_m}$
		Mean (D_m)	Std Deviation		
10	$8 \times 4 \times 0.075$	1995	323	5	0.6260
20	$8 \times 4 \times 0.075$	1396	304	5	0.8946
10	$8 \times 6 \times 0.075$	2443	396	5	0.6285

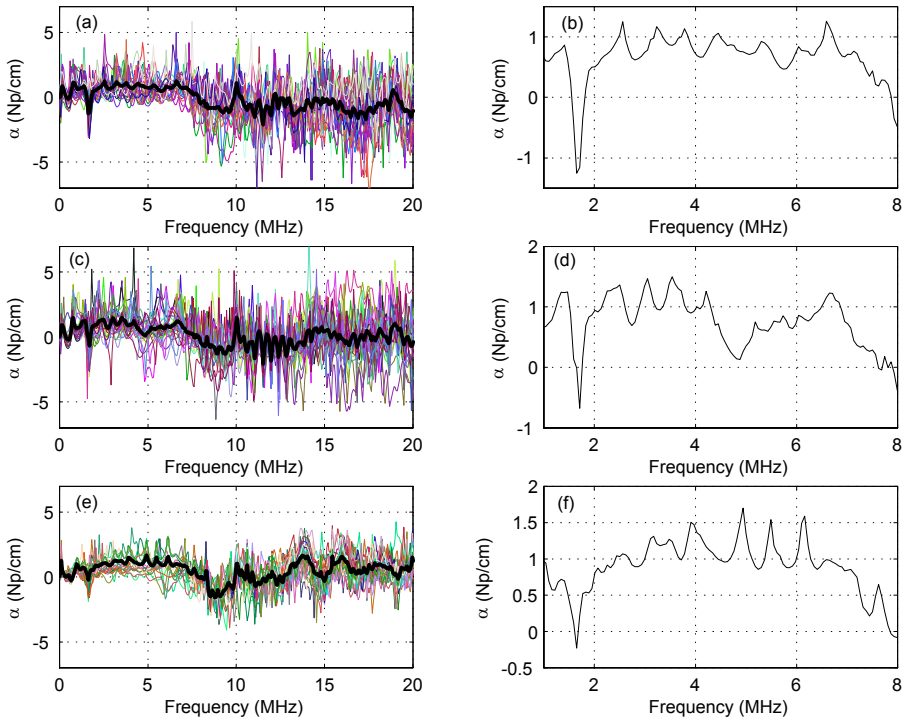

Figure 4.13: Longitudinal attenuation for copper for different domains for 5 MHz as input frequency (a) & (b) 8 mm by 4 mm model with 10 grains (c) & (d) 8 mm by 4 mm model with 20 grains (e) & (f) 8 mm by 6 mm model with 10 grains.

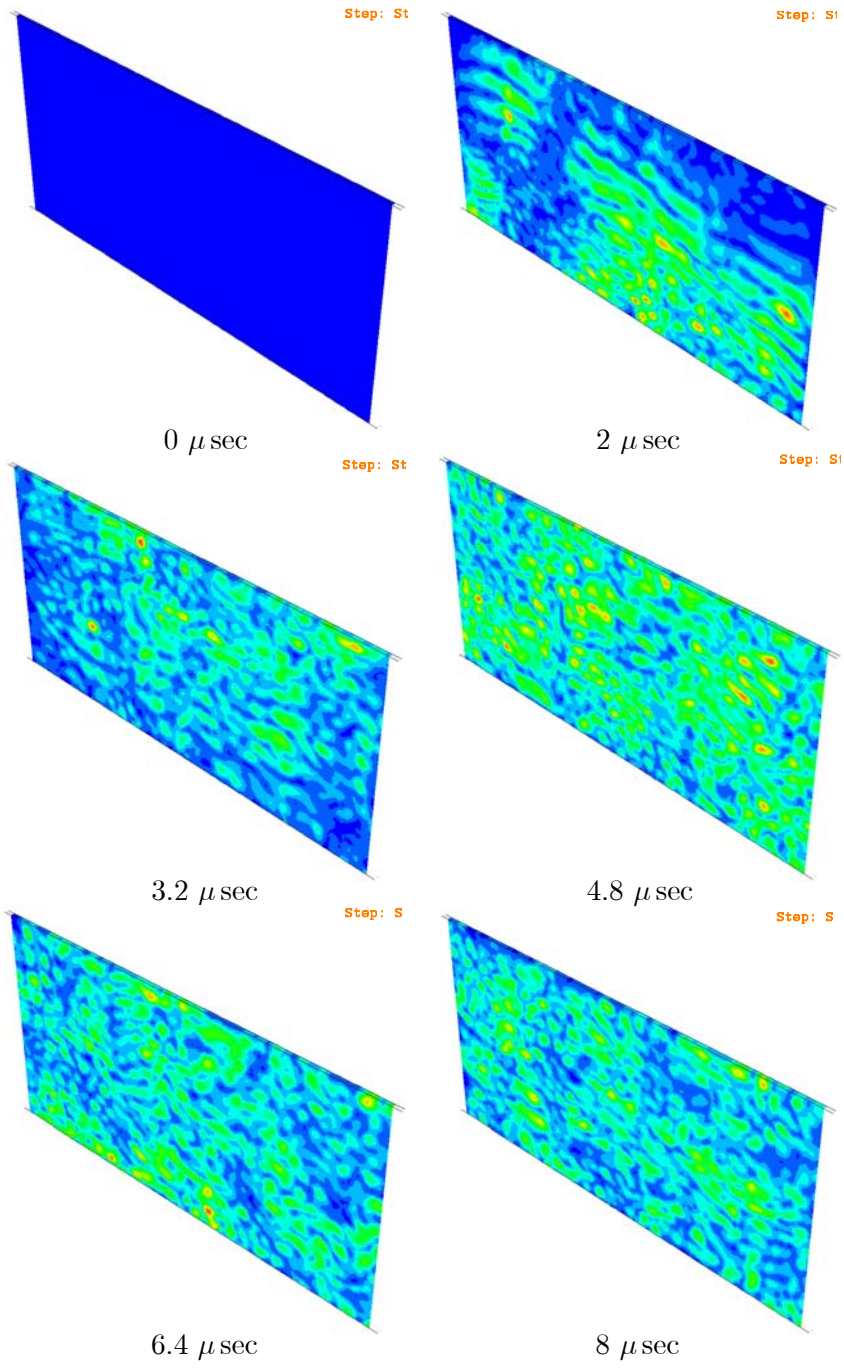

Figure 4.14: Simulation for copper with heterogeneous material properties. 20 crystals in a 8 mm by 4 mm model for 5 MHz of longitudinal wave.

4.5 Summary

In this chapter, example numerical attenuation results for four materials have been presented for plane stress boundary conditions. The attenuation calculation for aluminum is the simplest as it is a weakly scattering material. The fictitious material is an imaginary material having material properties such that its scattering properties lie in between aluminum and copper. The numerical methods allow any material properties to verify theories for fictitious material parameters which is not possible in laboratories. Obtaining the attenuation for copper is the hardest since it is the strongest scattering media among the four. The simulations shows that the wave scatters more for copper. The simulation for aluminum shows the weak scattering nature expected. The simulation figures are the output from ABAQUS/CAE. In the next chapter, the theoretical values of attenuation are discussed in detail. The numerical results obtained here are then compared with these theories.

Chapter 5

Comparison of Theoretical and Numerical Results

Elastic waves while propagating in an heterogeneous polycrystalline medium scatter at the boundaries of grains due to the mismatch in grain orientation. As a result of this scattering there is a loss of energy in the propagating wave which is termed attenuation. The loss of energy from the main beam is governed by the length of travel of the wave in the media.

Bhatia [1] discussed the dependence of the attenuation on λ compared with the average diameter D of the grains. He showed the attenuation scales with the fourth power of frequency for $\lambda \gg D$, a result analogous to light scattering by Rayleigh [32] and scales with the square of frequency for $\lambda < D$. At very high frequencies, i.e. $\lambda \ll D$, the attenuation becomes constant. This limit is the so-called geometric optics limit. Pao [33] presented the integral formulas for elastic waves in isotropic and anisotropic media using the Green's

displacement dyadic and a second rank Green's tensor. He derived Helmholtz and Kirchoff type integrals for both transient and steady-state waves. Elastic wave fields are composed of longitudinal and transverse parts that propagate at different speeds. The attenuation is a function of propagation direction for a statistically anisotropic media. Stanke and Kino [34] used a second-order multiple-scattering theory to determine the attenuation and change in phase velocity due to grain scattering. Their results are applicable for media with texture and for materials with elongated grains. Hirsekorn [35] presented the theory for calculating the velocities and attenuation of longitudinal and shear waves in weakly anisotropic medium which is dependent on frequency. Frisch[36] has given the mathematical formulation for waves propagating in heterogeneous media. He has also given the basic Dyson [37][38] equation in terms of the Green's dyadic which governs the mean response of the field. He introduced the first-order smoothing (FOSA) that may be used to solve the Dyson equation.

Weaver [7] introduced the Ultrasonic Radiative Transfer Equation (URTE) to model wave propagation in heterogeneous media. Turner [8] has presented the expression for attenuation for shear horizontal, quasicompressional and quasishear wave using the Green's dyadic for transversely isotropic materials. The attenuation expressions for different wave types are given as a function of direction and frequency of the propagating wave in the media. The three-dimensional model created by Turner [8] and Weaver [7] using elastodynamic theory and the URTE are used to model the attenuation expression in two-dimensional domain with material orientation in three directions. Numerical results are obtained to verify the theoretical model of attenuation.

5.1 General Three-Dimensional Model

The three-dimensional theoretical model was developed by Weaver [7] and Turner [8]. For completeness of this thesis and to understand the mathematical derivations for attenuation expression given by them, their work is reviewed in this section. The equation of motion for an elastic medium is given by

$$\sigma_{ij,j} + f_i = \rho \ddot{u}_i, \tag{5.1}$$

where σ_{ij} is the stress tensor, f_i the body force and ρ is the mass density of the material, with $\ddot{u}_i$ the acceleration. Waves propagating in a linearly elastic solid obey Hooke's law which states that each stress component σ_{ij} is proportional to the strain component ε_{kl}

$$\sigma_{ij} = C_{ijkl}\varepsilon_{kl}, \tag{5.2}$$

where $\varepsilon_{kl} = \frac{1}{2}(u_{k,l} + u_{l,k})$ with $k, l = 1, 2, 3$. C_{ijkl} is the elastic stiffness tensor with symmetric conditions $C_{ijkl} = C_{jikl} = C_{klij}$. Thus there are 21 independent elastic stiffness constants which refer to a crystal which possesses no rotational symmetry. For crystal systems of higher symmetry this number is considerably reduced. The values of the elastic constants depend on the orientation of these axes relative to the crystal lattice.

Substituting Eq. (5.2) in Eq. (5.1) gives

$$C_{ijkl}u_{k,lj} + f_i = \rho \ddot{u}_i, \tag{5.3}$$

or

$$-\rho \ddot{u}_i + C_{ijkl}u_{k,lj} = -f_i, \quad \text{where,} \quad f_i = (f_1, f_2, f_3). \tag{5.4}$$

For a compressive load

$$f_i = -\delta_{ik}\delta^3(\mathbf{x} - \mathbf{x}')\delta(t), \tag{5.5}$$

where, $\delta^3(x-x') = \delta(x-x')\delta(y-y')\delta(z-z')$. Substituting Eq. (5.5) in Eq. (5.4) gives

$$-\rho\ddot{u}_i + C_{ijkl}u_{k,lj} = \delta_{ik}\delta^3(\mathbf{x}-\mathbf{x}')\delta(t). \tag{5.6}$$

The equation of motion is now written for the elastodynamic response in terms of the Green's dyadic as,

$$\left\{-\delta_{ik}\frac{\partial^2}{\partial t^2} + \frac{\partial^2}{\partial x_i}C_{ijkl}(\mathbf{x})\frac{\partial^2}{\partial x_l}\right\}G_{k\alpha}(\mathbf{x},\mathbf{x}';t) = \delta_{j\alpha}\delta^3(\mathbf{x}-\mathbf{x}')\delta(t). \tag{5.7}$$

The second-rank Green's dyadic $G_{k\alpha}(\mathbf{x},\mathbf{x}';t)$ is the response to a concentrated impulsive force. It is the response at a location $\mathbf{x}$ in the kth direction to a unit impulse at location $\mathbf{x}'$ in the αth direction. That is, $G_{k\alpha}(\mathbf{x},\mathbf{x}';t)$ is the solution for $u_k(\mathbf{x},;t)$ when the body force density is $f_\alpha(\mathbf{x}')$. Here, the density is assumed to be uniform throughout. For Eq. (5.7) the units are chosen in such a way that the density is unity.

For the polycrystals considered, the modulus tensor is no longer a constant but is function of position. It is assumed to be spatially heterogeneous and of the form

$$C_{ijkl}(\mathbf{x}) = C^0_{ijkl} + \delta C_{ijkl}(\mathbf{x}). \tag{5.8}$$

where $C^0_{ijkl} = \langle C_{ijkl}(x)\rangle$ is the average moduli and δC_{ijkl} is the fluctuation about the mean. The fluctuation is assumed to have a zero mean $\langle \delta C_{ijkl}(x)\rangle = 0$. The covariance of the moduli, an eighth rank tensor is written

$$\Lambda(|\mathbf{x}-\mathbf{y}|)^{ijkl}_{\alpha\beta\gamma\delta} = \langle \delta C_{ijkl}(\mathbf{x})\delta C_{\alpha\beta\gamma\delta}(\mathbf{y})\rangle = \Xi^{ijkl}_{\alpha\beta\gamma\delta}\eta(|\mathbf{x}-\mathbf{y}|). \tag{5.9}$$

Here, the covariance Λ is a function of the magnitude of the difference of two vectors $|\mathbf{x}-\mathbf{y}|$ rather than $\mathbf{x}$ and $\mathbf{y}$ separately. This assumption states that the second order statistics are homogeneous and isotropic. Therefore, the medium is assumed statistically

homogeneous and statistically isotropic. Additionally, the grains are assumed equiaxed. These two assumptions are made by many people [7], [8], [34]. In this case a two-point correlation function $\eta(r)$ may be defined as [34]

$$\eta(\mathbf{r}) = e^{-\frac{r}{L}}, \tag{5.10}$$

where $\eta(r)$ is a two-points correlation function which states the probability of any two points separated by a distance r lie on the same crystal.

For cubic symmetry the fourth-rank elastic modulus tensor is given by [7],

$$\begin{aligned} C_{ijkl} &= \lambda^I \delta_{ij}\delta_{kl} + \mu^I(\delta_{ik}\delta_{jl} + \delta_{il}\delta_{jk}) + \nu\delta_{ijkl}, \\ &= C^I_{ijkl} + \nu\delta_{ijkl}, \end{aligned} \tag{5.11}$$

with δ_{ijkl} is equal to one for $i = j = k = l$ and to zero otherwise. λ^I, μ^I and ν are the crystal properties for cubic symmetry given by

$$\begin{aligned} \lambda^I &= C_{1122}, \\ \mu^I &= C_{1212}, \\ \nu &= C_{1111} - C_{1122} - 2C_{1212}. \end{aligned} \tag{5.12}$$

The elastic modulus tensor may be represented with respect to the laboratory axes by

$$C_{ijkl} = C^I_{ijkl} + \nu \sum_{n=1}^{3} a^n_i a^n_j a^n_k a^n_l, \tag{5.13}$$

where a^n_i represents the elements in a transformation matrix between crystallite and laboratory axes. The rotation between these two axes is represented by three Euler angles ϕ, Θ

and ζ. The matrix is given by

$$\mathbf{a} = \begin{bmatrix} -\cos\Theta\sin\phi\sin\zeta + \cos\phi\cos\zeta & \cos\Theta\cos\phi\sin\zeta + \sin\phi\cos\zeta & \sin\zeta\sin\Theta \\ -\cos\Theta\sin\phi\sin\zeta - \cos\phi\cos\zeta & \cos\Theta\cos\phi\sin\zeta - \sin\phi\cos\zeta & \cos\zeta\sin\Theta \\ \sin\Theta\sin\phi & -\cos\Theta\cos\phi\sin\zeta & \cos\Theta \end{bmatrix}. \tag{5.14}$$

The ensemble average modulus is thus defined by

$$\langle C_{ijkl}\rangle \equiv C^0_{ijkl} = C^I + \nu \sum_{n=1}^{3} \int a_i^n a_j^n a_k^n a_l^n \frac{\sin\Theta d\Theta d\phi d\zeta}{8\pi^2}. \tag{5.15}$$

The Voigt-average and the isotropic stiffness C^0_{ijkl} given by Weaver [7]

$$C^0_{ijkl} \equiv (c_L^2 - 2c_T^2)\delta_{ij}\delta_{kl} + c_T^2[\delta_{ik}\delta_{jl} + \delta_{il}\delta_{jk}]. \tag{5.16}$$

where c_L and c_T represents the longitudinal and shear wave speeds respectively are written in terms of the crystal properties as

$$\begin{aligned} c_L^2 &= \lambda + 2\mu + \nu/5, \\ c_T^2 &= \mu + \nu/5. \end{aligned} \tag{5.17}$$

The covariance, Eq. (5.9), is an eighth-rank tensor,

$$\mathbf{\Lambda}^{\alpha\beta\gamma\delta}_{ijkl} \equiv \langle C_{\alpha\beta\gamma\delta}(\mathbf{x}) C_{ijkl}(\mathbf{y})\rangle - \langle C_{\alpha\beta\gamma\delta}(\mathbf{x})\rangle\langle C_{ijkl}(\mathbf{y})\rangle \tag{5.18}$$

The inner products given by Weaver [7] are derived in terms of two unit vectors $\hat{\mathbf{p}}$ and $\hat{\mathbf{s}}$ which will be used in deriving the attenuation coefficients. Three relevant functions

are given by

$$\begin{aligned} L(\theta_{ps}) &= \Xi_{ijkl}^{\alpha\beta\gamma\delta}\hat{p}_\alpha\hat{p}_i\hat{s}_\beta\hat{s}_j\hat{p}_\gamma\hat{p}_k\hat{s}_\delta\hat{s}_l = \mathbf{\Xi}_{\cdots\hat{\mathbf{p}}\hat{\mathbf{p}}\hat{\mathbf{s}}\hat{\mathbf{s}}}^{\cdots\hat{\mathbf{p}}\hat{\mathbf{p}}\hat{\mathbf{s}}\hat{\mathbf{s}}}, \\ &= (\frac{6}{105}-\frac{1}{25})+(\hat{\mathbf{p}}\cdot\hat{\mathbf{s}})^2(\frac{18}{105}-\frac{4}{25})+(\hat{\mathbf{p}}\cdot\hat{\mathbf{s}})^4(\frac{17}{105}-\frac{4}{25}), \\ &= \frac{9}{525}+\frac{6}{525}\cos^2\theta_{ps}+\frac{1}{525}\cos^4\theta_{ps}, \\ M(\theta_{ps}) &= \Xi_{ijkl}^{\alpha\beta\gamma\delta}\hat{p}_\alpha\hat{p}_i\hat{s}_\beta\hat{s}_j\hat{p}_\gamma\hat{p}_k\hat{s}_\delta\hat{s}_l = \mathbf{\Xi}_{\cdots\hat{\mathbf{p}}\hat{\mathbf{p}}\hat{\mathbf{s}}}^{\cdots\hat{\mathbf{p}}\hat{\mathbf{p}}\hat{\mathbf{s}}}I = \mathbf{\Xi}_{\cdots}^{\cdots}\mathbf{I}_{\hat{\mathbf{p}}\hat{\mathbf{p}}\hat{\mathbf{s}}}^{\hat{\mathbf{p}}\hat{\mathbf{p}}\hat{\mathbf{s}}} = \frac{24}{525}+\frac{12}{525}\cos^2\theta_{ps}, \\ N(\theta_{ps}) &= \Xi_{ijkl}^{\alpha\beta\gamma\delta}\hat{p}_\alpha\hat{p}_i\hat{s}_\beta\hat{s}_j\hat{p}_\gamma\hat{p}_k\hat{s}_\delta\hat{s}_l = \mathbf{\Xi}_{\cdots}^{\cdots}\mathbf{I}_{\hat{\mathbf{p}}\hat{\mathbf{s}}}^{\hat{\mathbf{p}}\hat{\mathbf{s}}}\mathbf{I} = \frac{63}{525}+\frac{21}{525}\cos^2\theta_{ps}, \end{aligned} \tag{5.19}$$

where θ_{ps} is the angle between $\hat{\mathbf{p}}$ and $\hat{\mathbf{s}}$.

Using the spatial Fourier transform of $\mathbf{\Lambda}$ gives,

$$\widetilde{\Lambda}(\mathbf{p})_{\alpha\beta\gamma\delta}^{ijkl} = \int \Lambda(\mathbf{r})_{\alpha\beta\gamma\delta}^{ijkl} e^{-i\mathbf{r}\cdot\mathbf{p}} d^3\mathbf{r}. \tag{5.20}$$

The correlation length L is of the order of the radius and proportional to the volume of the grain. The Fourier transform of the correlation function,

$$\widetilde{\eta}(\mathbf{q}) = \int \eta(\mathbf{r}) e^{-i\mathbf{r}\cdot\mathbf{p}} d^3\mathbf{r}. \tag{5.21}$$

The direction $\hat{\mathbf{p}}$ defines the propagation direction and $\hat{\mathbf{s}}$ is the scattered direction and θ_{ps} is the angle between the two vectors. The two-point correlation function is defined in the wave vector domain as

$$\begin{aligned} \widetilde{\eta}(\mathbf{q}) &= \frac{1}{(2\pi)^3}\int_0^{2\pi}\int_0^{\theta}\int_0^{\pi} e^{-\frac{r}{L}} e^{-ipr\cos\theta}\sin\theta r^2 d\theta dr d\phi, \\ &= \frac{L^3}{\pi^2(1+L^2q^2)^2}. \end{aligned} \tag{5.22}$$

The above expression is integrated most conveniently with respect to θ first and then to r. Weaver [7] showed that the main microstructural quantity at low frequency is the mean

grain volume. At higher frequencies the correlation length may vary and may need to be multiplied by a constant. Thus the correlation function may be related to the mean grain volume as

$$V = \int d^3 r e^{-\frac{r}{L}}, \tag{5.23}$$

such that

$$\frac{\pi}{6} D^3 = (2\pi)^3 \widetilde{\eta}(\mathbf{0}). \tag{5.24}$$

Therefore, the correlation length may be related to grain diameter by,

$$L = \frac{1}{2\sqrt[3]{6}} D. \tag{5.25}$$

The Green's function $\mathbf{G}$ is a random function due to the random nature of the media. Therefore, the statistics of $\mathbf{G}$ are of main concern. The statistics includes the mean response $\langle \mathbf{G} \rangle$ and the covariance of the response $\langle \mathbf{G}\mathbf{G}^* \rangle$ where $\mathbf{G}^*$ is the complex conjugate. The angular brackets represents the ensemble averages of the quantity. Frisch [36] used diagrammatic methods for solution of the mean response. The integral equation for the mean response is governed by the Dyson equation [7],[8],[36],

$$\langle G_{i\alpha}(\mathbf{x}, \mathbf{x}') \rangle = G^0_{i\alpha}(\mathbf{x}, \mathbf{x}') + \iint G^0_{i\beta}(\mathbf{x}, \mathbf{y}) M_{\beta j}(\mathbf{y}, \mathbf{z}) \langle G_{j\alpha}(\mathbf{z}, \acute{\mathbf{x}}) \rangle d^3 y d^3 z, \tag{5.26}$$

where $\mathbf{M}$ is the mass or self-energy operator and $\mathbf{G}^0$ is Green's dyadic for the bare Voigt-average, medium, i.e., the solution to Eq. (5.33) when $\delta C_{ijkl}(\mathbf{x}) = 0$. The Dyson equation is exact. Equation (5.26) may be solved in the spatial Fourier transform domain. The spatial Fourier transform pair of $\mathbf{G}^0$ is given by

$$G^0_{i\alpha}(\mathbf{p}) \delta^3(\mathbf{p} - \mathbf{q}) = \frac{1}{(2\pi)^3} \iint G^0_{i\alpha}(\mathbf{x}, \acute{\mathbf{x}}) e^{-i\mathbf{p}.\mathbf{x}} e^{-i\mathbf{q}.\acute{\mathbf{x}}} d^3 x d^3 \acute{x}, \tag{5.27}$$

$$G^0_{i\alpha}(\mathbf{x},\mathbf{x}') = \frac{1}{(2\pi)^3}\iint G^0_{i\alpha}(\mathbf{p})\delta^3(\mathbf{p}-\mathbf{q})e^{-i\mathbf{p}.\mathbf{x}}e^{-i\mathbf{q}.\hat{\mathbf{x}}}d^3pd^3q. \tag{5.28}$$

An approximation is necessary for the equation of **M**. The simplest approximation which can be based on the Dyson equation retains only the lowest order term. Frisch [36] used a diagrammatic method to approximate **M** by its lowest order term and called it the first-order smoothing approximation (FOSA). The FOSA expression for **M** is given by [7], [8]

$$M_{\beta j}(\mathbf{y},\mathbf{z}) \approx \langle \frac{\partial}{\partial y_\alpha}\delta C_{\alpha\beta\gamma\delta}(\mathbf{y})\frac{\partial}{\partial y_\delta}G^0_{\gamma k}(\mathbf{y},\mathbf{z})\frac{\partial}{\partial z_i}\delta C_{ijkl}(\mathbf{z})\frac{\partial}{\partial z_l}\rangle. \tag{5.29}$$

It is assumed the fluctuations δC are small. The spatial Fourier transform of **M** is given by [7] as a convolution of Green's dyadic and Fourier transform of the covariance of the moduli fluctuation. It is written

$$\tilde{M}_{\beta j}(\mathbf{p}) = \int d^3s G^0_{\gamma k}(\mathbf{s})p_\alpha p_l s_\delta s_i \widetilde{\Lambda}(\mathbf{p}-\mathbf{s})^{ijkl}_{\alpha\beta\gamma\delta}. \tag{5.30}$$

The Fourier transform pair for the function $f(t)$ and $\tilde{f}(\omega)$ are defined by

$$\tilde{f}(\omega) = \int f(t)e^{i\omega t}dt, \tag{5.31}$$

$$f(t) = \frac{1}{2\pi}\int \tilde{f}(\omega)e^{-i\omega t}d\omega. \tag{5.32}$$

Using the Fourier transform and substituting from equation(5.8) allows Eq. (5.7) to be written in frequency domain,

$$\left\{-(-i\omega)^2\delta_{jk} + C^0_{ijkl}\frac{\partial}{\partial x_i}\frac{\partial}{\partial x_l} + \frac{\partial}{\partial x_i}\delta C_{ijkl}(\mathbf{x})\frac{\partial}{\partial x_l}\right\}G_{k\alpha}(\mathbf{x},\hat{\mathbf{x}};\omega) = \delta_{j\alpha}\delta^3(\mathbf{x}-\hat{\mathbf{x}}),$$

$$\left\{\omega^2\delta_{jk} + C^0_{ijkl}\frac{\partial}{\partial x_i}\frac{\partial}{\partial x_l} + \frac{\partial}{\partial x_i}\delta C_{ijkl}(\mathbf{x})\frac{\partial}{\partial x_l}\right\}G_{k\alpha}(\mathbf{x},\hat{\mathbf{x}};\omega) = \delta_{j\alpha}\delta^3(\mathbf{x}-\hat{\mathbf{x}}). \tag{5.33}$$

Using Eq. (5.33) with $\delta C_{ijkl}(\mathbf{x})$ set to zero and using the Fourier transformed $\mathbf{G^0}(\mathbf{p})$ allows Eq. (5.16) to be written as

$$\left\{\omega^2\delta_{li} + p_k p_j C^0_{klij}\right\} G^0_{i\alpha}(\mathbf{p}) = \delta_{l\alpha}. \tag{5.34}$$

The equation is written in direct notation as,

$$(\hat{\mathbf{p}}\hat{\mathbf{p}}\left\{\omega^2 - p^2c_L^2\right\} + (\mathbf{I} - \hat{\mathbf{p}}\hat{\mathbf{p}})\left\{\omega^2 - p^2c_T^2\right\}) \cdot \mathbf{G^0} = \mathbf{I}. \tag{5.35}$$

The solution to Eq. (5.35) is given by [7]

$$\mathbf{G^0}(\mathbf{p}) = \hat{\mathbf{p}}\hat{\mathbf{p}}g^{0L}(p) + (\mathbf{I} - \hat{\mathbf{p}}\hat{\mathbf{p}})g^{0T}(p), \tag{5.36}$$

where the $g^{0L}(p)$ and $g^{0T}(p)$ are termed the bare longitudinal and shear propagators given by

$$g^{0L}(\mathbf{p}) = [\omega^2 - p^2c_L^2]^{-1}, \tag{5.37}$$

$$g^{0T}(\mathbf{p}) = [\omega^2 - p^2c_T^2]^{-1}. \tag{5.38}$$

The imaginary parts of the bare propagators, used for deriving the attenuation expressions, are given by

$$\begin{aligned} \mathrm{Im}\, g^{0L}(\mathbf{p}) &= -\pi sgn(\omega)\delta(\omega^2 - p^2c_L^2), \\ \mathrm{Im}\, g^{0T}(\mathbf{p}) &= -\pi sgn(\omega)\delta(\omega^2 - p^2c_T^2). \end{aligned} \tag{5.39}$$

The spatial Fourier transform for $\mathbf{G}$ and $\mathbf{M}$ are given above. To solve for $\langle G(\mathbf{p})\rangle$ the Dyson equation can be spatially Fourier transformed, giving

$$\langle \mathbf{G}(\mathbf{p})\rangle = [\mathbf{G}^0(\mathbf{p})^{-1} - \tilde{\mathbf{M}}(\mathbf{p})]^{-1}. \tag{5.40}$$

The mean response and the self-energy is expressed in terms of unit vectors $\hat{\mathbf{p}}$,

$$\begin{aligned} \langle \mathbf{G}(\mathbf{p}) \rangle &= g_L(p)\hat{\mathbf{p}}\hat{\mathbf{p}} + g_T(p)(\mathbf{I} - \hat{\mathbf{p}}\hat{\mathbf{p}}), \qquad (5.41) \\ \tilde{\mathbf{M}}(\mathbf{p}) &= m_L(p)\hat{\mathbf{p}}\hat{\mathbf{p}} + m_T(p)(\mathbf{I} - \hat{\mathbf{p}}\hat{\mathbf{p}}). \qquad (5.42) \end{aligned}$$

The solution of the Dyson Eq. (5.40) gives the dispersion relation for the mean response as

$$\begin{aligned} g_L(\mathbf{p}) &= [g^{oL}(\mathbf{p})^{-1} - m_L(\mathbf{p})]^{-1} = [\omega^2 - p^2 c_L^2 - m_L(\mathbf{p})]^{-1}, \qquad (5.43) \\ g_T(\mathbf{p}) &= [g^{oT}(\mathbf{p})^{-1} - m_T(\mathbf{p})]^{-1} = [\omega^2 - p^2 c_T^2 - m_T(\mathbf{p})]^{-1}, \end{aligned}$$

which gives the phase velocity and attenuation of each wave type. The real part of $\hat{\mathbf{p}}$ defines the phase velocity and the imaginary part defines the attenuation. The solution is generally obtained using the root finding techniques [39]. It is an iterative procedure which starts with an estimate of the root and produces successively better approximations. The explicit attenuation can be obtained by using an assumption valid below the high frequency geometric optic limits. Such an approximation is sometimes known as a Born approximation [7] [34], where the wave vector $\mathbf{p}$ is close to bare wave vector $(\omega/c_\gamma)\hat{\mathbf{p}}$. Therefore, by this assumption $m_\gamma(\mathbf{p}) \approx m_\gamma[(\omega/c)\hat{\mathbf{p}}]$, where γ is the wave type. The expression for attenuation is then given by

$$\begin{aligned} \alpha_L &= \frac{1}{2\omega c_L} \operatorname{Im} m_L(\omega/c_L), \qquad (5.44) \\ \alpha_T &= \frac{1}{2\omega c_T} \operatorname{Im} m_T(\omega/c_L), \end{aligned}$$

where

$$\begin{aligned}
\operatorname{Im} m_L(\omega/c_L) &= \frac{\pi}{2}\int \hat{\mathbf{p}}\hat{\mathbf{p}}\hat{\mathbf{s}}\hat{\mathbf{s}}\cdots\Xi\frac{\omega^5}{c_L^7}\hat{\eta}\left(\hat{\mathbf{p}}\frac{\omega}{c_L}-\hat{\mathbf{s}}\frac{\omega}{c_L}\right)d^2\hat{\mathbf{s}} \\
&\quad +\frac{\pi}{2}\int \hat{\mathbf{p}}\hat{\mathbf{p}}\hat{\mathbf{s}}(\mathbf{I}-\hat{\mathbf{s}})\cdots\Xi\frac{\omega^5}{c_L^2c_T^5}\hat{\eta}\left(\hat{\mathbf{p}}\frac{\omega}{c_L}-\hat{\mathbf{s}}\frac{\omega}{c_T}\right)d^2\hat{\mathbf{s}}, \\
\operatorname{Im} m_T(\omega/c_T) &= \frac{\pi}{4}\int (\mathbf{I}-\hat{\mathbf{p}})\hat{\mathbf{p}}\hat{\mathbf{s}}\hat{\mathbf{s}}\cdots\Xi\frac{\omega^5}{c_L^5c_T^2}\hat{\eta}\left(\hat{\mathbf{p}}\frac{\omega}{c_T}-\hat{\mathbf{s}}\frac{\omega}{c_L}\right)d^2\hat{\mathbf{s}} \\
&\quad +\frac{\pi}{4}\int (\mathbf{I}-\hat{\mathbf{p}})\hat{\mathbf{p}}\hat{\mathbf{s}}(\mathbf{I}-\hat{\mathbf{s}})\cdots\Xi\frac{\omega^5}{c_T^7}\hat{\eta}\left(\hat{\mathbf{p}}\frac{\omega}{c_T}-\hat{\mathbf{s}}\frac{\omega}{c_T}\right)d^2\hat{\mathbf{s}}.
\end{aligned}$$

Three functions have been defined in terms of θ_{ps}, the angle between the two unit vectors $\hat{\mathbf{p}}$ and $\hat{\mathbf{s}}$,

$$\begin{aligned}
\eta_{LL}(\theta_{ps}) &= \hat{\eta}\left(\hat{\mathbf{p}}\frac{\omega}{c_L}-\hat{\mathbf{s}}\frac{\omega}{c_L}\right), \\
\eta_{LT}(\theta_{ps}) &= \eta_{TL}(\theta_{ps}) = \hat{\eta}\left(\hat{\mathbf{p}}\frac{\omega}{c_L}-\hat{\mathbf{s}}\frac{\omega}{c_T}\right), \\
\eta_{TT}(\theta_{ps}) &= \hat{\eta}\left(\hat{\mathbf{p}}\frac{\omega}{c_T}-\hat{\mathbf{s}}\frac{\omega}{c_T}\right).
\end{aligned} \tag{5.45}$$

The final expressions for the attenuations are given by [7]

$$\alpha_L = \alpha_{LL}+\alpha_{LT}, \tag{5.46}$$

$$\alpha_T = \alpha_{TT}+\alpha_{TL}, \tag{5.47}$$

where

$$\begin{aligned}
\alpha_{LL} &= \frac{\pi^2\omega^4}{2c_L^8}\int_{-1}^{+1}\eta_{LL}(\theta)L(\theta)d\mu, \\
\alpha_{LT} &= \frac{\pi^2\omega^4}{2c_L^3c_T^5}\int_{-1}^{+1}\eta_{LT}(\theta)(M(\theta)-L(\theta))d\mu, \\
\alpha_{TL} &= \frac{1}{2}(c_T/c_L)^2\alpha_{LT}, \\
\alpha_{TT} &= \frac{\pi^2\omega^4}{4c_T^8}\int_{-1}^{+1}\eta_{TT}(\theta)(N(\theta)-2M(\theta)+L(\theta))d\mu,
\end{aligned} \tag{5.48}$$

with $\mu = \cos\theta$. Based on this three-dimensional model the attenuation expressions are derived for two-dimensional domains in the next section of the chapter.

5.2 Two-Dimensional Model

The numerical model described in Chapters 3 and 4 is not truly three-dimensional. Thus the theory described in section 5.1 must be modified. Since the numerical model has material orientation in all three directions the elastic modulus and the covariance remains the same as that of the three-dimensional model. The two-point correlation function in the two-dimensional domain is defined by,

$$\begin{aligned}\widetilde{\eta}(\mathbf{q}) &= \int_0^{2\pi}\int_0^{\infty} e^{-\frac{r}{L}} e^{-ipr\cos\phi} r dr d\phi, \\ &= -\int_0^{2\pi} \frac{L^2}{-1+p^2L^2\cos^2\phi - 2ipL\cos\phi} d\phi, \\ &= \frac{2\pi L^2}{(1+q^2L^2)^{3/2}}.\end{aligned} \tag{5.49}$$

In the low frequency limit $\widetilde{\eta}(\mathbf{q})$ scales with L^2 as shown in Eq. (5.49). The longitudinal to longitudinal attenuation expression is now given by

$$\begin{aligned}\alpha_{LL} &= -\frac{1}{2\omega c_L}\int d^2s \, \begin{smallmatrix}\hat{\mathbf{p}}\hat{\mathbf{p}}\hat{\mathbf{s}}\cdots\cdot \\ \hat{\mathbf{p}}\hat{\mathbf{p}}\hat{\mathbf{s}}\cdots\cdot\end{smallmatrix} \Xi_{\cdot}^{\cdot} \left\{ \begin{smallmatrix}\hat{\mathbf{s}} \\ \hat{\mathbf{s}}\end{smallmatrix} g^{oL}(\mathbf{s}) \right\} \hat{\eta}\left(\mathbf{p}-\mathbf{s}\right), \\ &= -\frac{1}{2\omega c_L}\int s ds d\hat{\mathbf{s}} \begin{smallmatrix}\hat{\mathbf{p}}\hat{\mathbf{p}}\hat{\mathbf{s}}\cdots\cdot \\ \hat{\mathbf{p}}\hat{\mathbf{p}}\hat{\mathbf{s}}\cdots\cdot\end{smallmatrix} \Xi_{\cdot}^{\cdot} \left\{ \begin{smallmatrix}\hat{\mathbf{s}} \\ \hat{\mathbf{s}}\end{smallmatrix} - \frac{\pi}{2\omega c_L}\delta\left(\omega-\omega/c_L\right) \right\} \hat{\eta}\left(\mathbf{p}-\mathbf{s}\right), \\ &= \frac{1}{2\omega c_L}\frac{\pi}{2}\int \begin{smallmatrix}\hat{\mathbf{p}}\hat{\mathbf{p}}\hat{\mathbf{s}}\hat{\mathbf{s}}\cdots\cdot \\ \hat{\mathbf{p}}\hat{\mathbf{p}}\hat{\mathbf{s}}\hat{\mathbf{s}}\cdots\cdot\end{smallmatrix} \Xi \frac{1}{\omega c_L}\frac{\omega}{c_L}\frac{\omega^2}{c_L^2}\frac{\omega^2}{c_L^2}\hat{\eta}\left(\hat{\mathbf{p}}\frac{\omega}{c_L}-\hat{\mathbf{s}}\frac{\omega}{c_L}\right) d\hat{\mathbf{s}}, \\ &= \frac{\pi\omega^3}{4c_L^7}\int \hat{\eta}\left(\hat{\mathbf{p}}\frac{\omega}{c_L}-\hat{\mathbf{s}}\frac{\omega}{c_L}\right) L(\theta) d\hat{\mathbf{s}}, \\ &= \frac{\pi\omega^3}{4c_L^7}\int_{-1}^{+1} \hat{\eta}_{LL}(\theta) L(\theta) d\mu.\end{aligned} \tag{5.50}$$

Similarly,

$$\begin{aligned}\alpha_{LT} &= \frac{\pi\omega^3}{2c_L^3c_T^4}\int_{-1}^{+1} \eta_{LT}(\theta)(M(\theta)-L(\theta)) d\mu, \\ \alpha_{TT} &= \frac{\pi\omega^3}{4c_T^7}\int_{-1}^{+1} \eta_{TT}(\theta)(N(\theta)-2M(\theta)+L(\theta)) d\mu.\end{aligned} \tag{5.51}$$

The correlation length L is related to the mean grain area in the two-dimensional domain as

$$A = \int d^2 r e^{-\frac{r}{L}}, \tag{5.52}$$

such that

$$\frac{\pi}{4} D^2 = (2\pi)^2 \widetilde{\eta}(\mathbf{0}), \tag{5.53}$$

Thus, for the two-dimensional case, the correlation length is related to grain diameter by

$$L = \frac{1}{4\pi\sqrt{2}} D$$

where D is the mean diameter of grains.

Using the expressions for attenuation given above the theoretical attenuations for aluminum, copper, nickel and the fictitious material are shown in Fig. 5.1 with 600 μm as the mean diameter of the grains. The attenuation and wavelength are normalized by the mean diameter of the grains. The longitudinal and shear attenuation for the two-dimensional model is higher than the three-dimensional. Schubert, et al. [40] showed that the attenuation for the two-dimensional case is higher than for a three-dimensional case using a numerical model of concrete.

The attenuation for the fictitious material lies in between aluminum and copper as shown in Fig. 5.1. Copper has the highest and aluminum the lowest attenuation values among the four materials. The longitudinal attenuation for the two-dimensional model is approximately 8 to 10 times higher than in the three-dimensional model and about 1.2 to 1.5 times higher for the shear attenuation. The numerical results from these models are discussed in detail in the next section.

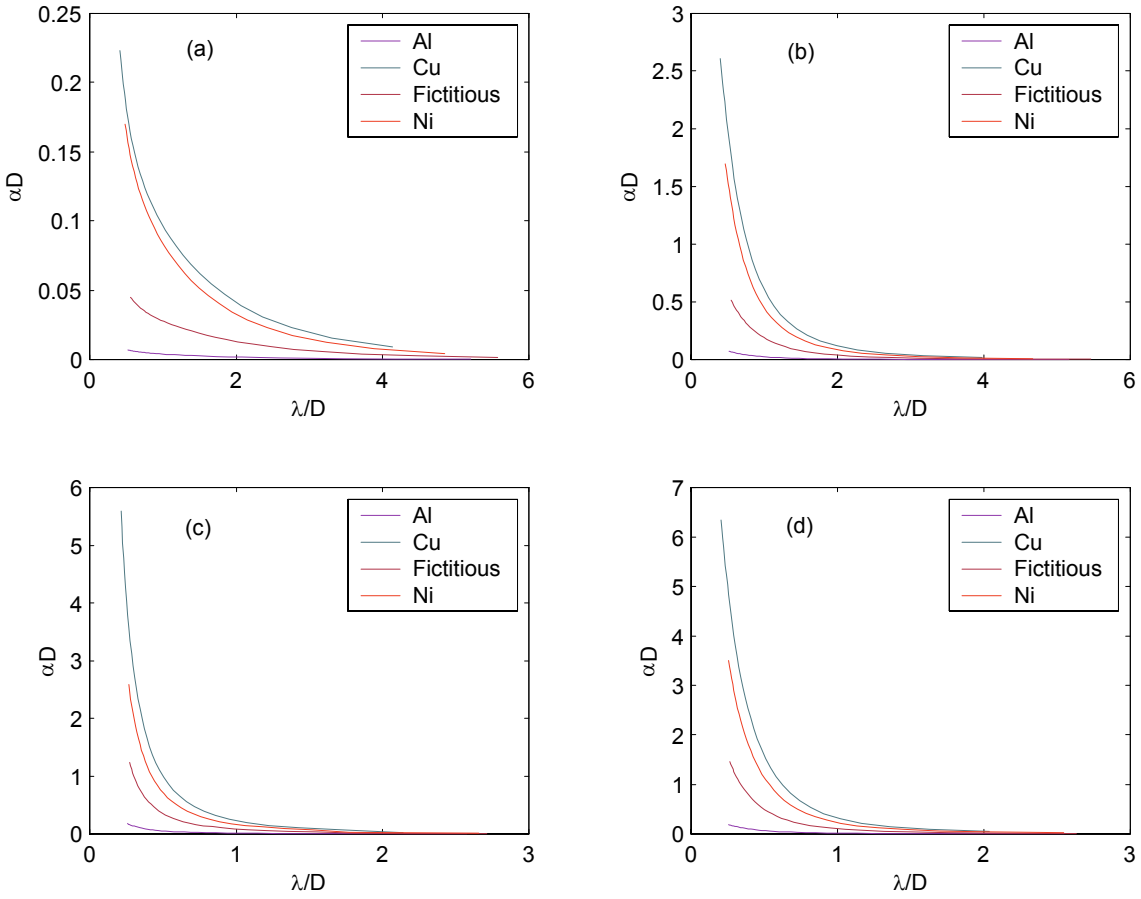

Figure 5.1: Theoretical attenuation normalized by the mean grain diameter for (a) 3D longitudinal attenuation (b) 2D longitudinal attenuation (c) 3D shear attenuation (d) 2D shear attenuation.

5.3 Plane Stress

The numerical results for plane stress boundary conditions are compared both with two- and three-dimensional theoretical models. The theoretical attenuations are computed for the mean diameter and for the standard deviation of the mean grain diameter. The numerical and theoretical attenuations are normalized by the mean grain diameter. The theoretical attenuation scales with the correlation length L. Therefore, theoretical atten-

uation is first normalized by the correlation length and then multiplied by the D/L ratio so that it can be compared with the numerical results which are normalized by the grain diameter, in the same scale.

5.3.1 Aluminum

The numerical attenuation results normalized by the mean grain diameter are shown in Fig. 5.2 for a longitudinal wave in aluminum. The numerical results agree well with the theory for a wide range of λ/D. The λ/D ratio ranges approximately from 1.2 to 4. The consistency of the numerical results is observed as the numerical attenuation curves follows each other from the different models. Frequencies ranging from 2 MHz to 8 MHz could be used due to the low scattering in aluminum. The models have material orientation in three directions but there is no scattering from the z-axis. Therefore, the scattering properties should lie in between the two-dimensional and three-dimensional theoretical model.

The numerical attenuation normalized by the mean grain diameter plus and minus one standard deviation of the diameter are shown in Figs. 5.3(a) and (b). For one standard deviation of mean grain diameter the numerical results fits well with the theory. For $3\sigma, 5\sigma$ the length of the error bars will increase and a higher range of error bars will be obtained. Therefore, if the results fit well for 1σ it will also fit for 3σ and 5σ. Thus, 1σ is used here. The numerical attenuation curves shift when normalized by the positive and negative standard deviation of the grain diameter. The shifting of the numerical attenuation towards the theoretical three-dimensional curve is observed for attenuation normalized by the positive standard deviation of the mean grain diameter shown in Fig. 5.3 (b).

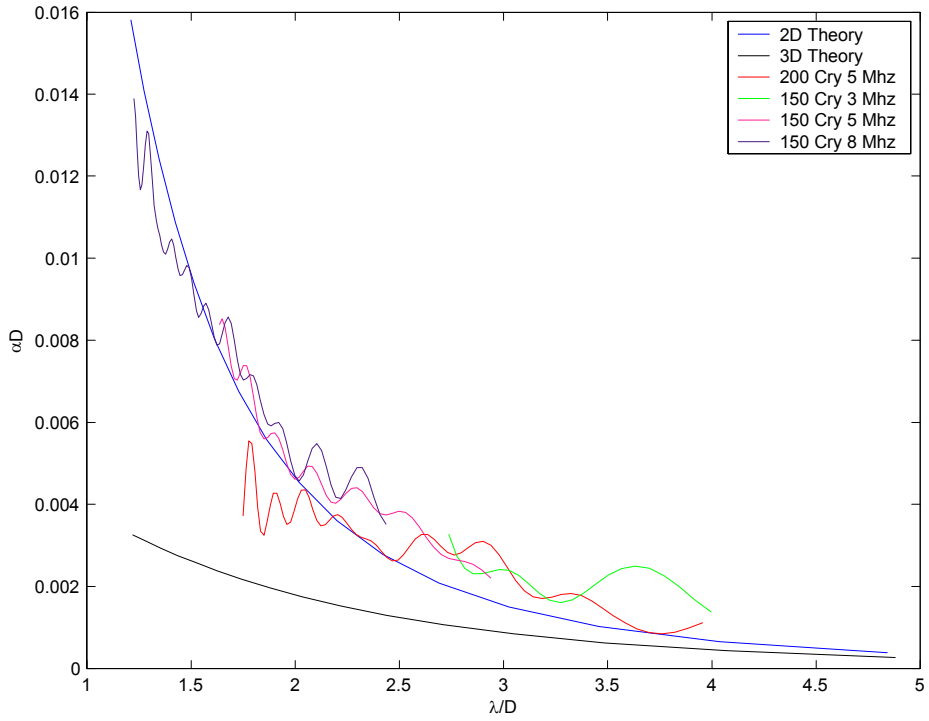

Figure 5.2: Normalized longitudinal theoretical and numerical attenuation for mean diameter of aluminum for model size 4 mm by 8 mm.

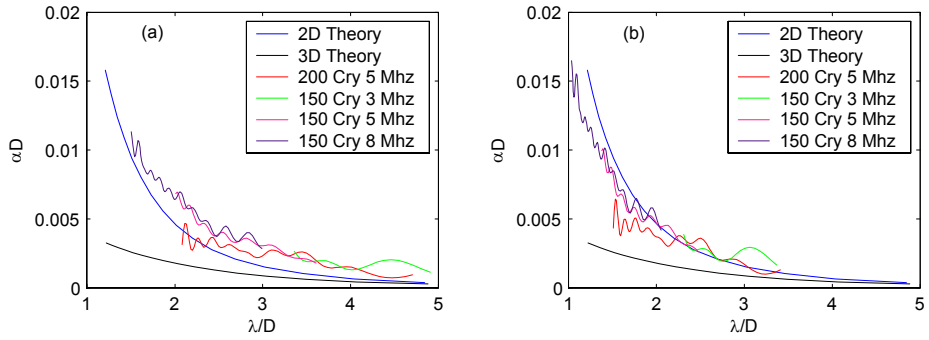

Figure 5.3: Normalized longitudinal attenuation for aluminum for standard deviation of the grain diameter (a) negative deviation (b) positive deviation.

The numerical attenuation results shows good agreement with the theoretical model for longitudinal waves. The numerical results obtained from different models are shown in different colors in the figures.

5.3.2 Fictitious material

The model size of 4 mm by 8 mm with 0.075 mm as depth is used for the fictitious material with same number of crystals and input frequencies of 3 MHz, 5 MHz and 8 MHz. All the models have 150 crystals. The numerical longitudinal attenuation normalized by the mean grain diameter is shown Fig. 5.4. The λ/D ratio obtained ranges approximately from 2 to 5. The numerical attenuation normalized by the positive and negative standard deviation of the mean grain diameter is shown in Figure 5.5(a) and (b). The results fit well within the standard deviation of the numerical results. Thus, the two-dimensional model appears well-suited for these numerical results.

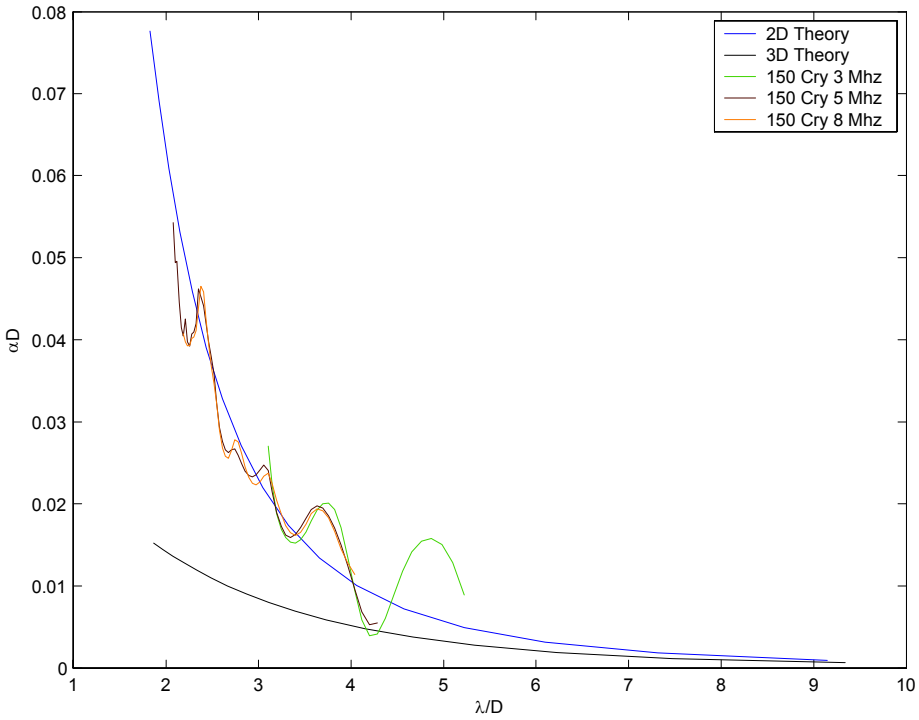

Figure 5.4: Normalized longitudinal theoretical and numerical attenuation for mean diameter of fictitious material for model size 4 mm by 8 mm.

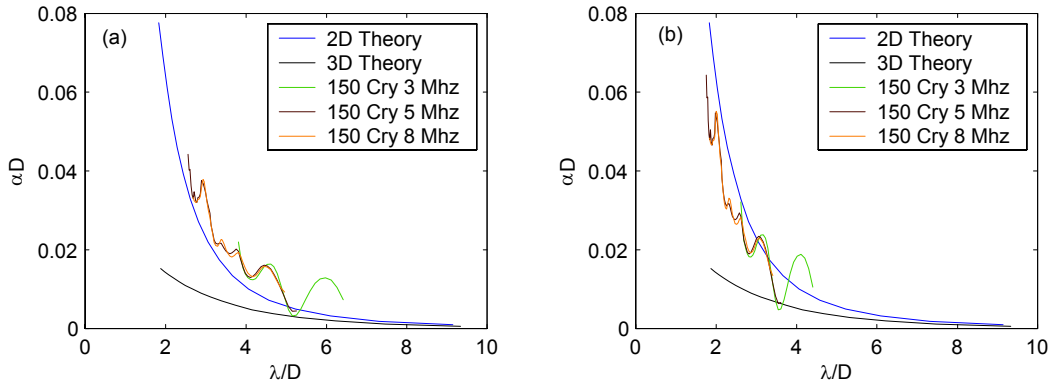

Figure 5.5: Normalized longitudinal attenuation for fictitious material for standard deviation of the grain diameter (a) negative deviation (b) positive deviation.

The quality of the numerical results obtained for the fictitious material shows the same nature as seen for aluminum. The numerical attenuation results increase as the λ/D decreases as expected from the theory. The model shows agreement with the two-dimensional theory for this material.

5.3.3 Nickel

Nickel has higher a degree of scattering than either aluminum or the fictitious material. Therefore, the model used is made wider and shorter than the model used for the longitudinal attenuation calculation for aluminum and fictitious material. The model used is 5 mm wide and 6 mm long. Three models with 50, 100 and 200 crystals are constructed. The input frequency for all the models is 5 MHz. The numerical attenuation normalized by the mean grain diameter is shown in Fig. 5.6. The range of λ/D obtained is approximately between 1 and 6.5. A wide range of λ/D ratio is obtained for attenuation results for the model with 200 crystals due to reduced amplitude reduction as the mean diameter decreases. In this case the noise content in the response signal is reduced. The numerical attenuation curve is between the two-and three-dimensional theoretical models. The attenuation normalized by the mean diameter plus minus the standard deviation of the mean grain diameter is shown in Figs. 5.7 (a) and (b). Twenty realizations of grains have been used for nickel.

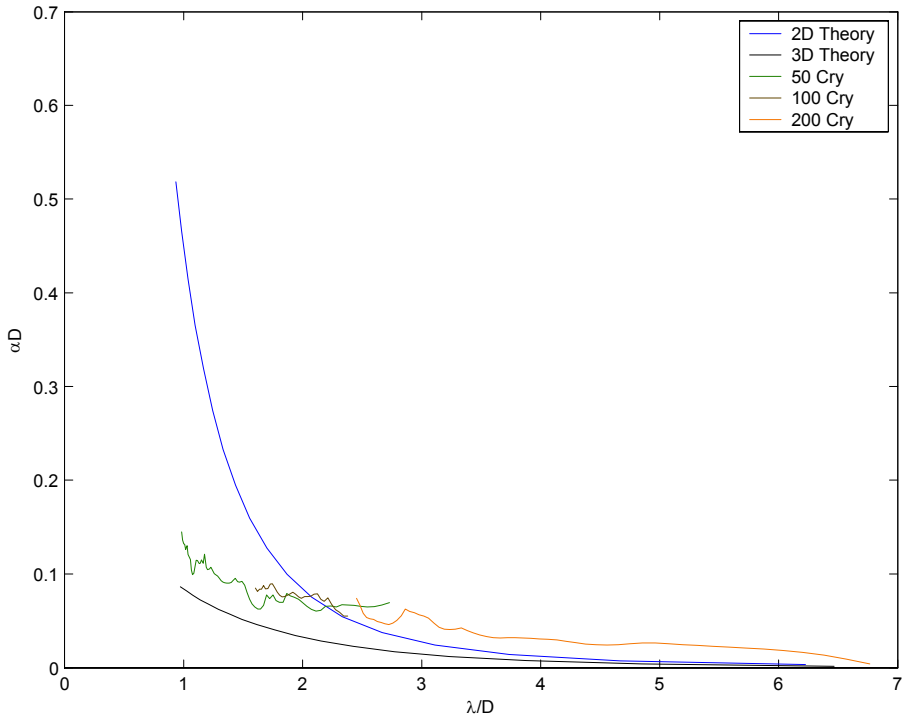

Figure 5.6: Normalized longitudinal theoretical and numerical attenuation for mean diameter of nickel for model size 5 mm by 6 mm for 5 MHz of input frequency.

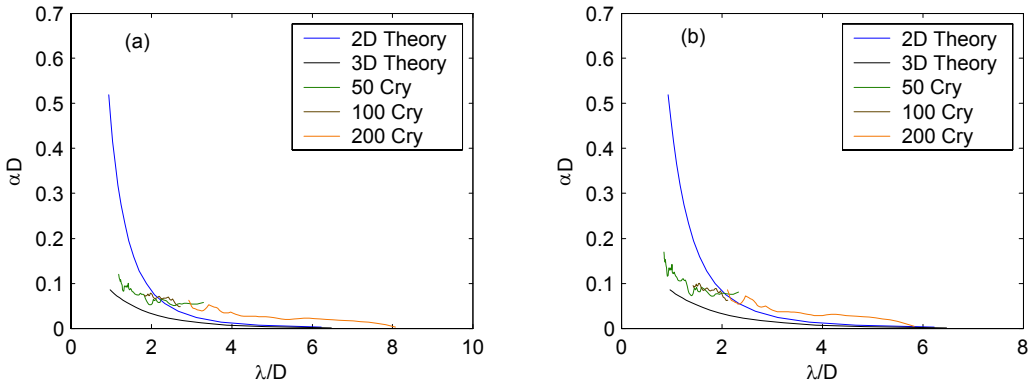

Figure 5.7: Normalized longitudinal attenuation for fictitious material for standard deviation of the grain diameter (a) negative deviation (b) positive deviation.

The numerical results for the longitudinal attenuation of nickel are obtained for a wide range of frequencies. Due to high scattering the slope of the numerical attenuation curve shows more similarity with the three-dimensional theoretical model.

5.3.4 Copper

Copper shows the highest degree of scattering among the four materials from theory. The numerical results also verify the same. Therefore, the model is made wider and shorter as compared with the models used for the other three materials. Three different models with two different sizes, 8 mm by 4 mm and 8 mm by 6 mm, are constructed for copper. The input frequency is kept constant at 5 MHz for all the models. Twenty five realizations of grains are used for averaging the attenuation results. The model has fewer grains to minimize the noise content in the response signal. The results are shown in Figs. 5.8 and 5.9. The numerical attenuation curves lie between the two-and three-dimensional models. The slope of the numerical attenuation curves is closer to the theoretical three-dimensional model than to the two-dimensional model. The numerical attenuation normalized by the mean grain diameter plus minus the standard deviation also lies between the two and three-dimensional models as shown in Fig. 5.9 (a) and (b). The λ/D ratio obtained from the numerical results ranges approximately from 0.6 to 1.7.

Copper being a strong scattering media the consistency in the numerical results is observed from Figs. 5.8 and 5.9. Therefore, the numerical results for copper also shows good agreement with the theory.

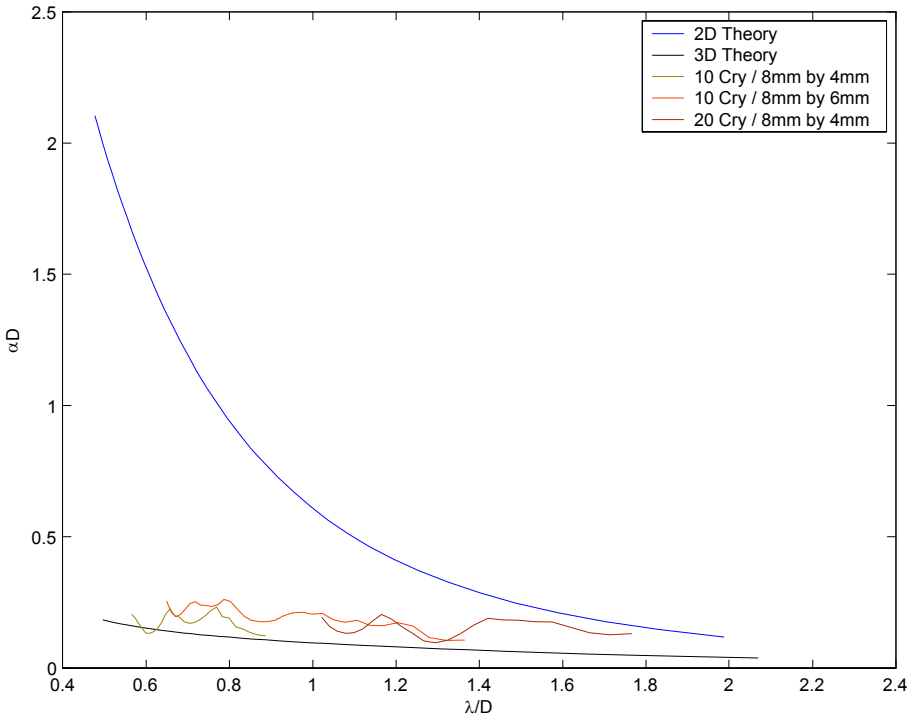

Figure 5.8: Normalized longitudinal theoretical and numerical attenuation for mean diameter of copper for 5 MHz of input frequency.

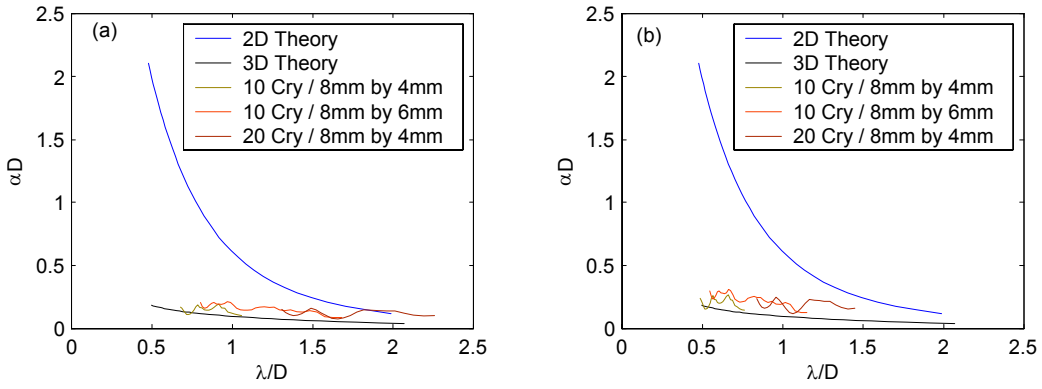

Figure 5.9: Normalized longitudinal attenuation for copper for standard deviation of the grain diameter (a) negative deviation (b) positive deviation.

5.4 Plane Strain

The model is created with plane strain boundary conditions by constraining the out of plane displacements of all the nodes in the finite element model. The rest of the boundary conditions remains the same as the plane stress case such as the loading and infinite elements. The data are analyzed in the same manner as explained in Chapter 4. In this section the final attenuation results are presented and compared with the theoretical models. Results for an incident longitudinal wave are obtained for aluminum, nickel and copper. All of the models used in the plane stress analysis are used for the plane strain boundary conditions. Therefore, the realization and the crystal geometry remains the same as the models discussed in Chapter 4.

5.4.1 Aluminum

The attenuation results with plane strain boundary conditions for aluminum are shown in Fig. 5.10. The attenuation values obtained here have large fluctuations and some of the data are in the negative region i.e. data obtained for 3 MHz of input wave. Since the model has zero displacement in the out of plane direction the wave scatters only in between the crystals. The mean free path is inversely proportional to the attenuation of the material. Therefore, the inverse of αD gives the minimum number of crystals required in a material for sufficient ultrasonic scattering. The model has 150 and 200 crystals which is not sufficient for enough scattering. From the Fig. 5.10 the highest value of αD is approximately 0.0002 and its inverse is 500. Therefore, a least 500 crystals are required for sufficient scattering. Thus the data for a 3 MHz pulse may not be representative results.

The slope of the numerical curve is closer to the three-dimensional theoretical model. Therefore, the two-dimensional theoretical curves are not used for comparison for the plane strain results. The numerical attenuation results normalized by the mean grain diameter minus the standard deviation of the diameter fits well with the three-dimensional theoretical curve shown in Fig. 5.11.

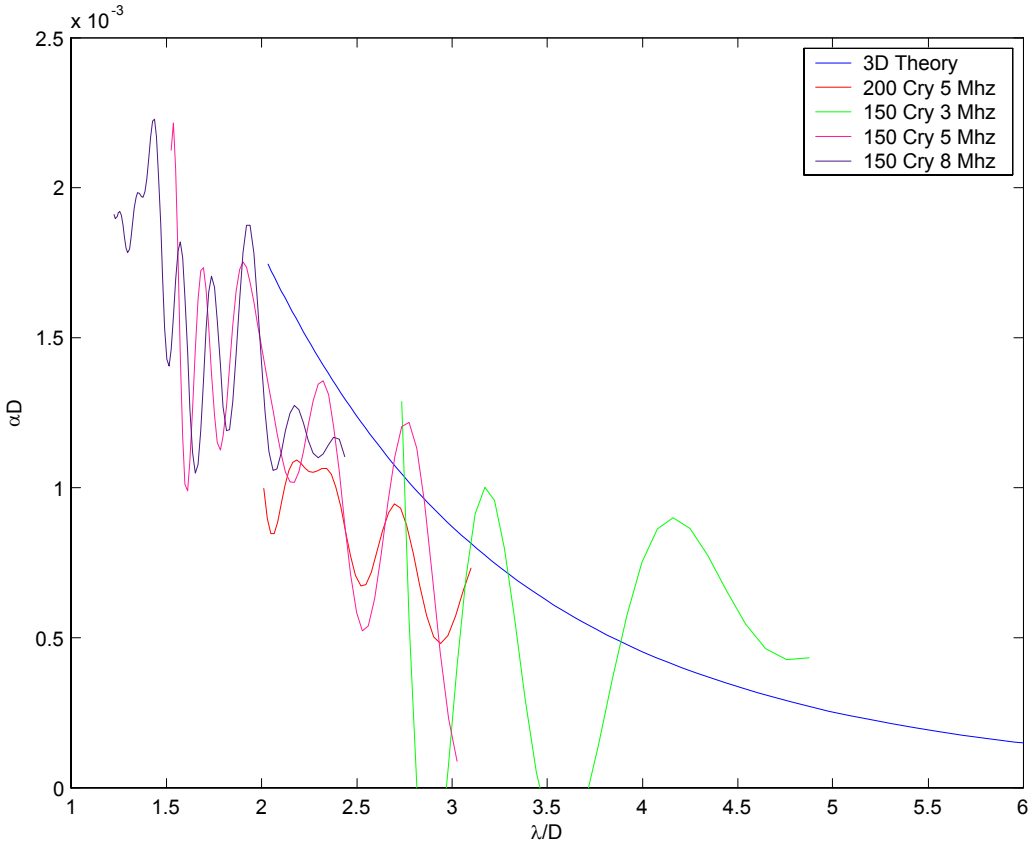

Figure 5.10: Normalized longitudinal theoretical and numerical attenuation for mean diameter of aluminum.

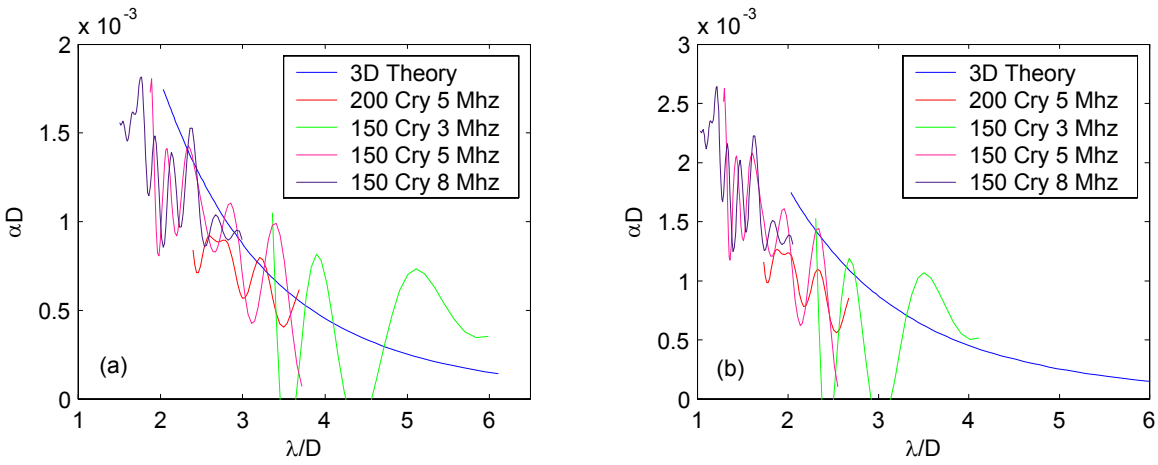

Figure 5.11: Normalized longitudinal attenuation for aluminum for mean diameter plus (a) negative deviation (b) positive deviation.

5.4.2 Nickel

The attenuation results for nickel normalized by the mean grain diameter are shown in Fig. 5.12 and by the variation of the mean grain diameter, i.e. $D_m \pm \sigma$ are shown in Fig. 5.13. For the minimum value of αD, 0.005 approximately 200 crystals are required. Therefore, for higher values of αD the model has enough crystals for sufficient scattering. The numerical results fit well with the theoretical curves for this material for all the models. Figure 5.13(b) shows very good agreement with the theory. It is also seen that as the number of crystals increases, the numerical results show better agreement with the theory. In addition, the data can be obtained for a wide range of frequencies.

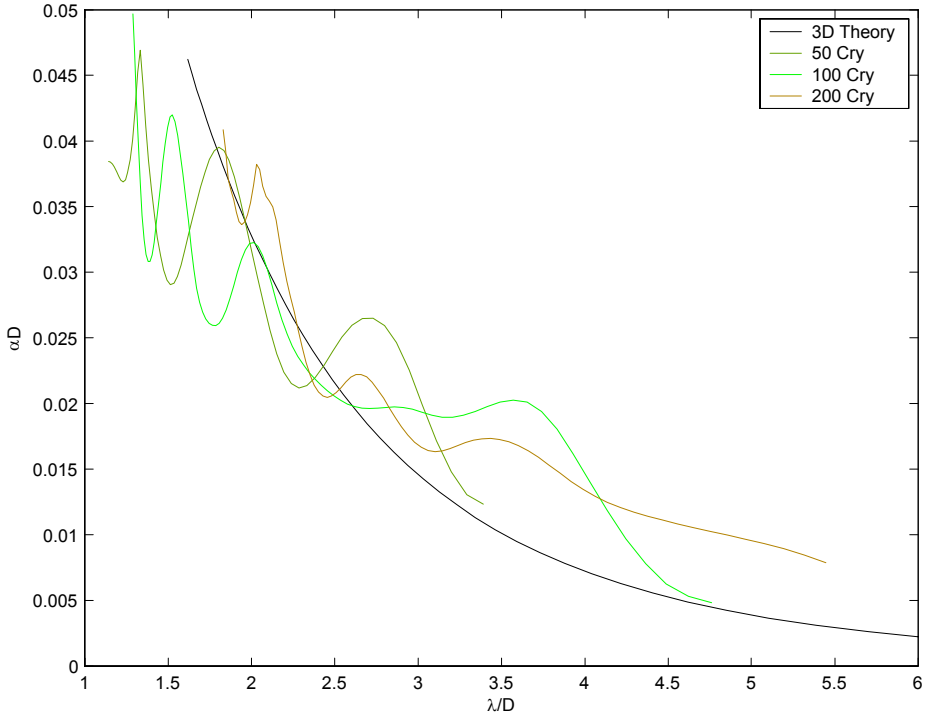

Figure 5.12: Normalized longitudinal theoretical and numerical attenuation for mean diameter of nickel for 5 MHz of input frequency with various crystals.

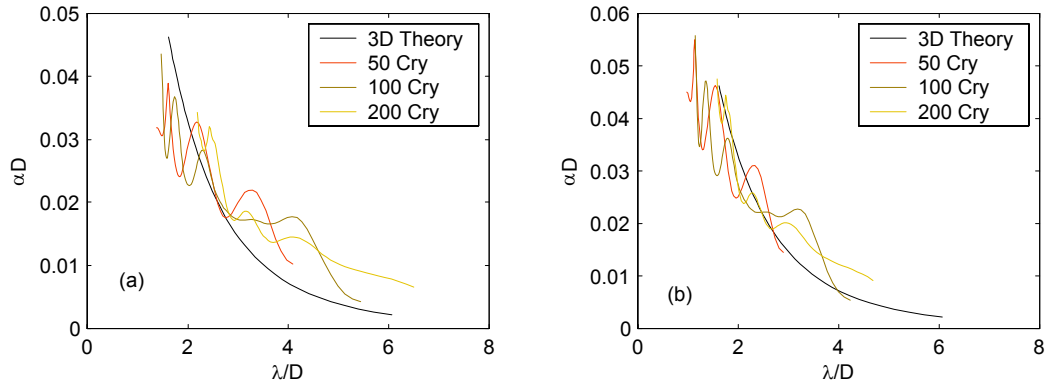

Figure 5.13: Normalized longitudinal attenuation for nickel for mean diameter plus (a) negative deviation (b) positive deviation.

5.4.3 Copper

Copper is the strongest scattering material among the four materials. The numerical curve lies below the three-dimensional theoretical curve as shown in Fig. 5.14. Only the results for the model with 20 crystals show better agreement with the theory than the other two models for copper. This result may be due to the fact that the other two models have fewer crystals. The attenuation results for the mean diameter plus and minus the standard deviation are shown in Fig. 5.15.

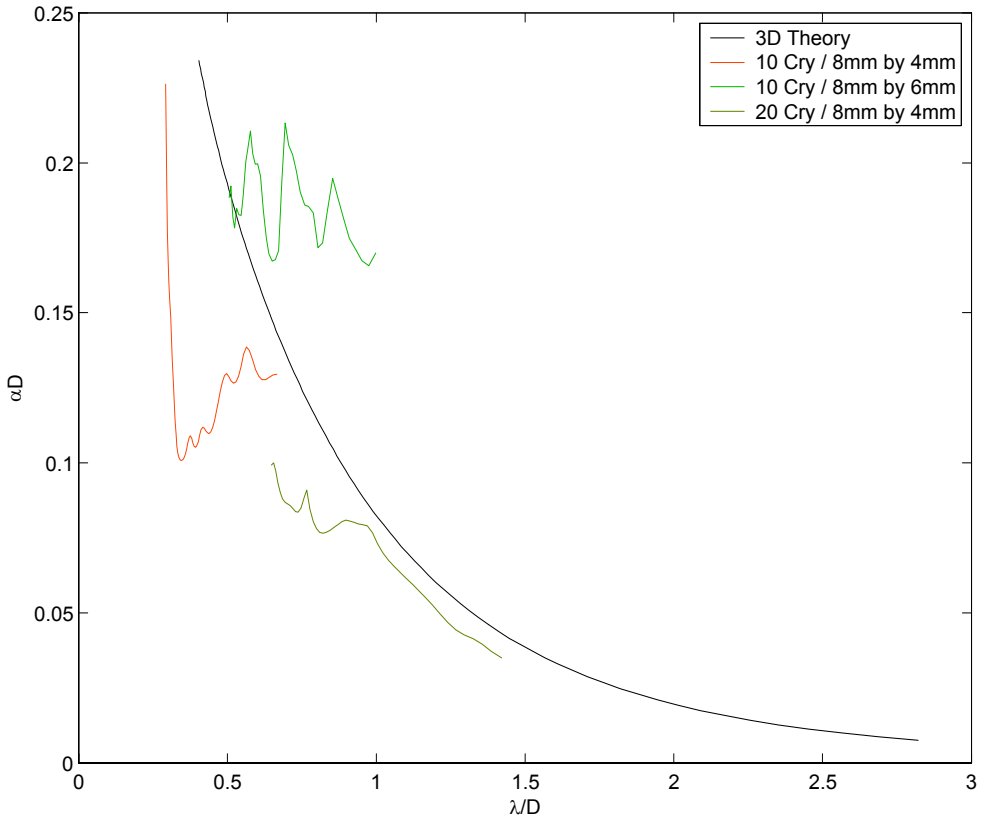

Figure 5.14: Normalized longitudinal theoretical and numerical attenuation for mean diameter of copper for various grain size and 5 MHz of input frequency.

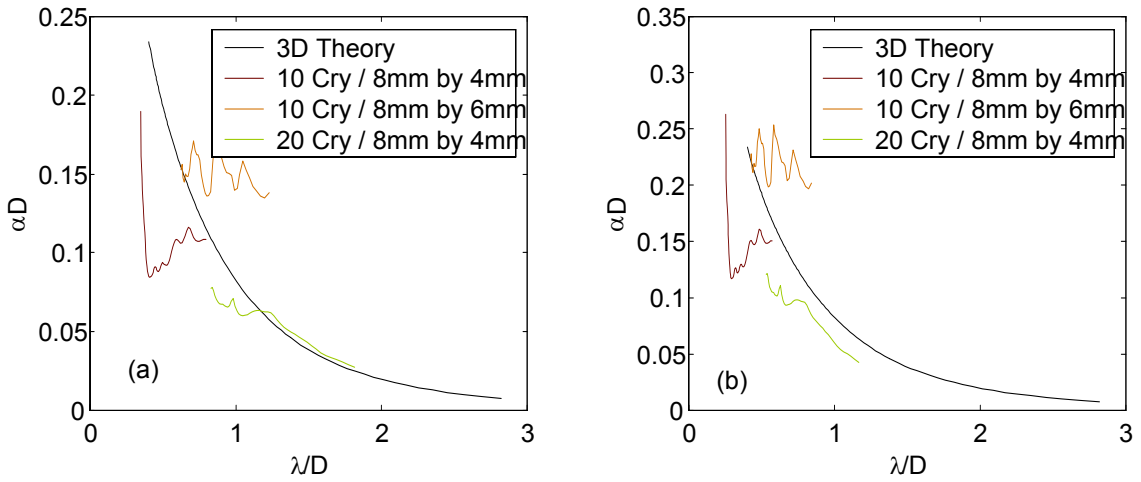

Figure 5.15: Normalized longitudinal attenuation for aluminum for mean diameter plus (a) negative deviation (b) positive deviation.

5.5 Summary

The numerical attenuation results are normalized by the mean grain diameter, and mean grain diameter plus and minus the standard deviation of the mean grain diameter to observe the range of the numerical attenuation curves for all the models with respect to the theoretical attenuation curves. The numerical curves for plane stress consistently lie between the two- and three-dimensional theoretical curves which verifies the authenticity of the numerical models. The numerical results show the λ/D ratio dependence on the attenuation. Various ratios are obtained by varying λ and D. The noise content in the response signal increases as the input frequency increases. The slope of the numerical attenuation curve starts to follow the slope of the three-dimensional model as the degree of scattering increases. This nature is observed for nickel and copper more prominently compared with aluminum and nickel which have lesser anisotropy factor.

The numerical results agree well for the plane strain case with the three-dimensional theoretical model. In the plane strain analysis it is also observed that the model should have enough crystals for sufficient scattering. Therefore, better results are obtained for nickel for the plane strain case.

Chapter 6

Summary of Thesis

The propagation of elastic waves in polycrystalline materials have been simulated using a numerical model of the microstructures of polycrystalline materials using Voronoi polycrystals. The Method of Virtual Nuclei was be used to create Voronoi polycrystals in a domain with arbitrary geometry with ease. This method also ensures the Voronoi properties of each Voronoi polygons as seen from the statistical analysis in Chapter 2. The statistical analysis also shows that various types of distributions of Voronoi nuclei can be modeled. Voronoi polycrystals in three-dimensional domains were also shown in Chapter 2. Numerical models for microstructure for different processed materials such as rolled materials were shown in both two-and three dimensional domains. By using MVN the creation of Voronoi polycrystals for any arbitrary domain can be obtained easily in three-dimensions as well. Elongated and oriented grains in the model with different aspect ratio and angle of orientation were shown. The models used for the attenuation calculations represent materials with long grains which can be approximated as a two-

dimensional problem.

The meshing is done by using six-noded prism element which allows the material orientation to be in three directions even though there are no scattering in the third axis. Each crystal is meshed separately to avoid any delinquencies of more than one crystal sharing the same elements which might occur if the whole model is meshed at once. ABAQUS/Explicit is used as the FE software package. The simulations from the finite element analysis help to visualize the scattering in the material.

Numerical models were obtained with a uniform distribution of grain diameter. However, in order to fill the domain, the grains had a distribution of sizes with mean and a standard deviation. The theoretical modeling assumes a uniform diameter in a model. Therefore, the numerical results are computed for mean grain diameter and standard deviation of the mean grain diameter. The attenuation for the two-dimensional domain is also derived using the three-dimensional model derived previously.

The plane stress finite element results using Voronoi polycrystals showed good agreement with attenuation from theory. The averaged attenuation from different realizations of Voronoi polycrystals made the results more accurate. Four materials of common interest with various anisotropy factors were used to study the accuracy of the numerical results. The model for copper had fewer grains, i.e. larger mean diameter, due to its high anisotropy factor. The numerical results for these material agreed well with the theory. Using the numerical methods, attenuation for a wide range of λ/D values were obtained and verified with the theory. The attenuation results agreed well for all the four materials namely aluminum, fictitious, nickel and copper with a wide range of scattering degree for

an incident longitudinal wave. The numerical results also showed the increase in scattering as the λ/D decreases as observed in the theory.

It was also observed that averaging over different realizations of grains reduced the fluctuations in the numerical attenuation results. The number of realizations required also increases with increasing degree of scattering in the materials. Therefore, the maximum number of realization were constructed for copper and the least for aluminum. The averaged attenuation curve was smoother and more consistent compared with results from any one realization. The model was verified for various range of λ/D for different materials. The attenuation governed by the frequency and diameter of the grain is observed for all the numerical results.

The results for the models with plane strain boundary conditions show good agreement with the three-dimensional theoretical longitudinal attenuation values. Nickel shows the best results among the materials tested with the plane strain boundary condition, as there are enough crystals for ultrasonic scattering in the model. The aluminum model has fewer crystals than that required for sufficient scattering. Therefore, it can be easily observed that for the plane strain case the model should have enough crystals for scattering. Copper showed good results for a model with 20 crystals.

The work contained here has been focused on the construction of a robust and efficient numerical model for attenuation due to scattering in polycrystals. The Voronoi polycrystal is observed to be a good numerical model for the attenuation calculation in polycrystalline materials. Such an analysis has not been used before for the dynamic case. The Voronoi polycrystal can be used efficiently to model microstructures of various types.

The distribution of the grains can also be controlled numerically with ease.

Various ultrasonic theories can be examined using the Voronoi model for various kinds of microstructures such as grains with preferred orientations and textured media. In this work the results are obtained for plane stress and plane strain boundary conditions. For plane stress boundary conditions the numerical scattering results suggest that the two-dimensional theory is better for weakly scattering media, while the three-dimensional is better for strongly scattering media. The results from plane strain agree well with the three-dimensional theoretical model for all the materials.

This work forms the basis for many more studies in the future. Some of these ideas are discussed in the next chapter. The model is used for initial work on ultrasonic backscatter which is explained briefly in the next chapter.

Chapter 7

Future Work

A numerical model for wave propagation in polycrystalline material has been constructed successfully. The models can now be used to study several aspects of ultrasonic theories in polycrystalline materials. There is much work to do both theoretically and numerically. Voronoi polycrystals can now be used to model a wide range of microstructure types for ultrasonic parameters in them which may not be easily studied analytically or experimentally.

7.1 Three-Dimensional Model

The three-dimensional model was shown in Chapter 2 for various domains. The meshing of a Voronoi polycrystal in a three-dimensional domain is computationally challenging. It is necessary to find the vertices of all the surfaces of a Voronoi polygon for surface meshing. Theoretically the vertices of any particular surface lie on the same plane. Due to numerical error and precision of the computer the vertices of any particular surface

may lie on the same plane with small errors. These error bounds have to be kept in mind for assuming points lying in the same plane. Convex hull concepts can be used to extract the faces of each crystal. The vertices of the Voronoi polygon can be obtained from the MATLAB output but the surfaces of each polygon must be found.

The second problem arises due to many very small edges for each Voronoi polygon as it is in a three-dimensional domain. These small edges makes elongated surfaces. These surfaces can be so elongated that they cannot be further subdivided into triangles. The step time increases drastically due to these elongated elements because one of its side is very small compared with the other elements in the model.

Two points which are very close to each other can be collapsed to one point which will prevent the formulation of small edges. Overcoming the above difficulties will create a Voronoi polycrystal in a three-dimensional domain meshed with tetrahedrons. Each crystals in the three-dimensional model should also be meshed separately and then assembled to avoid any delinquencies. The three-dimensional model will make the numerical results more accurate and realistic for cases that cannot be verified in two-dimensional domains. The theory for the three-dimensional model can then be compared directly with the numerical results.

7.2 Backscatter

The heterogenenity in the material ensures that incident wave fields will be scattered. This scattering will be wavelength dependent. The scattered energy can be used for probing microstructural parameters and flaws in the materials. While the wave propagates

through the medium, it scatters at the grain boundaries due to the inhomogeneity as illustrated in Fig. 7.1. The grains have random material orientation making it a heterogeneous material. A portion of this scattered energy reaches the frontwall before the reflection of the wave from the backwall. During scattering at the grain boundaries mode conversion of the wave also takes place. In Fig. 7.1, the black arrows represent the scattering from longitudinal to longitudinal and the red arrows represent mode conversion of longitudinal to shear waves for a longitudinal incident pulse. The scattered energy can be quantified to infer the microstructural parameters and flaws in the material. The nodal displacements from the finite element analysis are used to calculate the background rms grain noise of the model numerically. Experiments can also be carried out for backscatter measurements but collecting data for mode conversion will be difficult due to transducer restrictions.

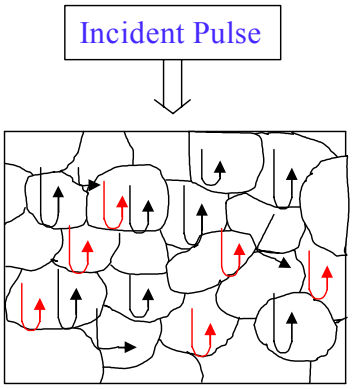

Figure 7.1: Scattering at the grain boundaries due to inhomogeneity for an longitudinal incident wave.

Backscatter measurements can be used for flaw detection in the material. For example one grain can be modeled as a harder phase to study the probability of detection. A crack could also be introduced in the model to study the effects of cracks on backscatter.

Margetan, et al. [41], presented the theoretical model for rms grain noise in polycrystalline materials. The average nodal displacement for M nodes is

$$b(t) = \frac{1}{M}\sum_{i=1}^{M} V_i(t), \tag{7.1}$$

where $V_i(t)$ is the displacement of the ith node at time t. The root-mean squared deviation of the grain noise from the background is then [41],[42]

$$n(t) = \left[\frac{1}{M}\sum_{i=1}^{M}[V_i(t) - b(t)]^2\right]^2. \tag{7.2}$$

The region of interest for backscatter measurement is shown in Fig.7.2. The region in red indicates the arrival of grain noise before the backwall echo.

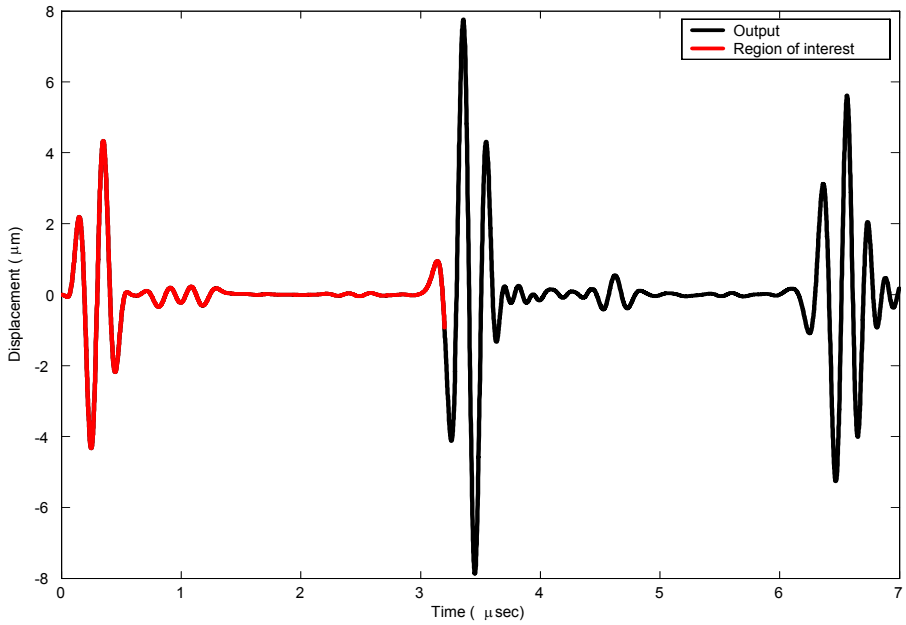

Figure 7.2: Average nodal displacement for aluminum at 5 MHz.

The rms grain noise can also be computed for mode conversion of the wave by using the finite element method. Backscatter results for aluminum and copper are given as examples. The rms grain noise for aluminum is shown in Fig. 7.3. From the figure, the rms grain noise increases as the λ/D decreases which is expected from the theory. The rms grain noise can be compared with the theoretical model for verification of the numerical model.

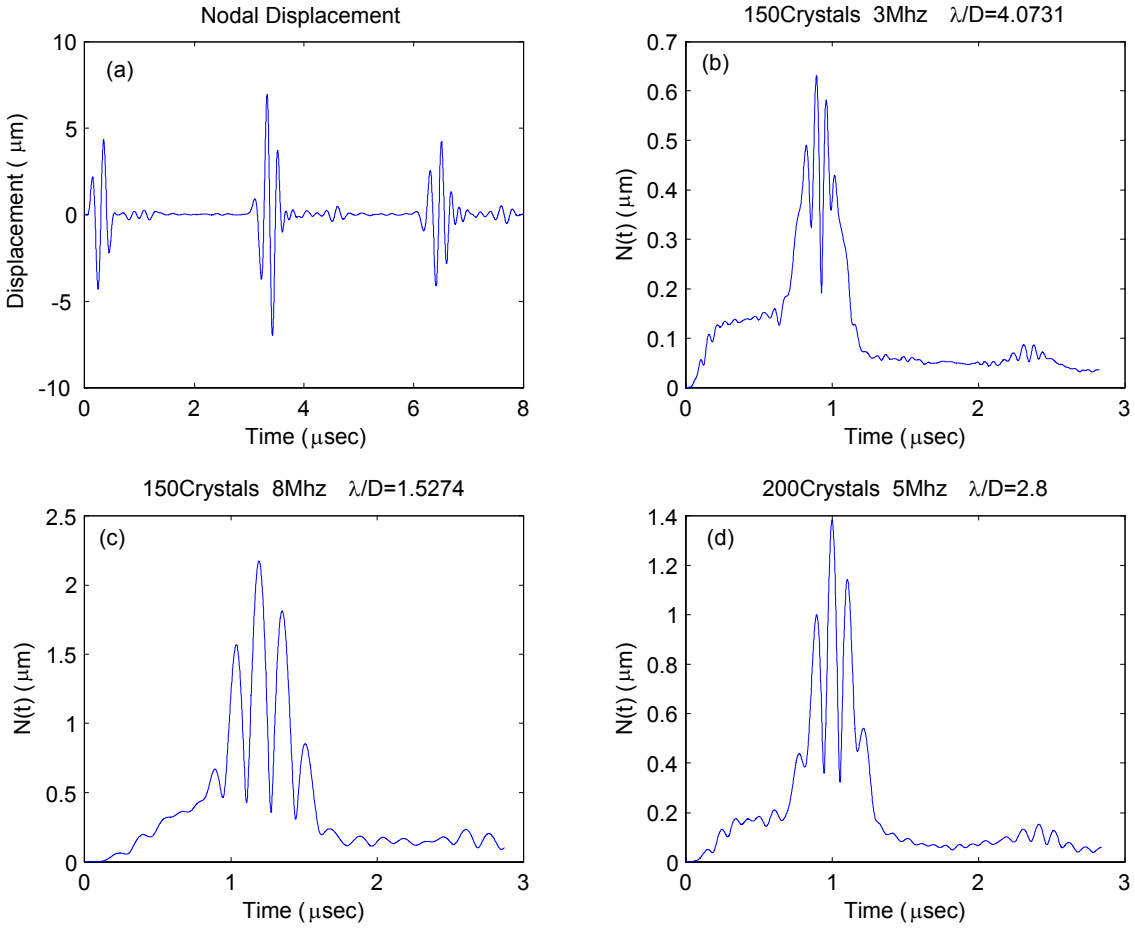

Figure 7.3: Longitudinal to longitudinal rms grain noise for aluminum.

The backscatter results for copper are shown in Fig. 7.4. The mode conversion of longitudinal to shear has also been computed numerically for copper. The multiple scattering effect is greater in copper than aluminum as seen in the rms grain noise plot due to copper being a stronger scattering medium than aluminum. The rms grain noise is plotted with respect to λ/D. The rms grain noise is higher for mode conversion as shown in Fig. 7.4.

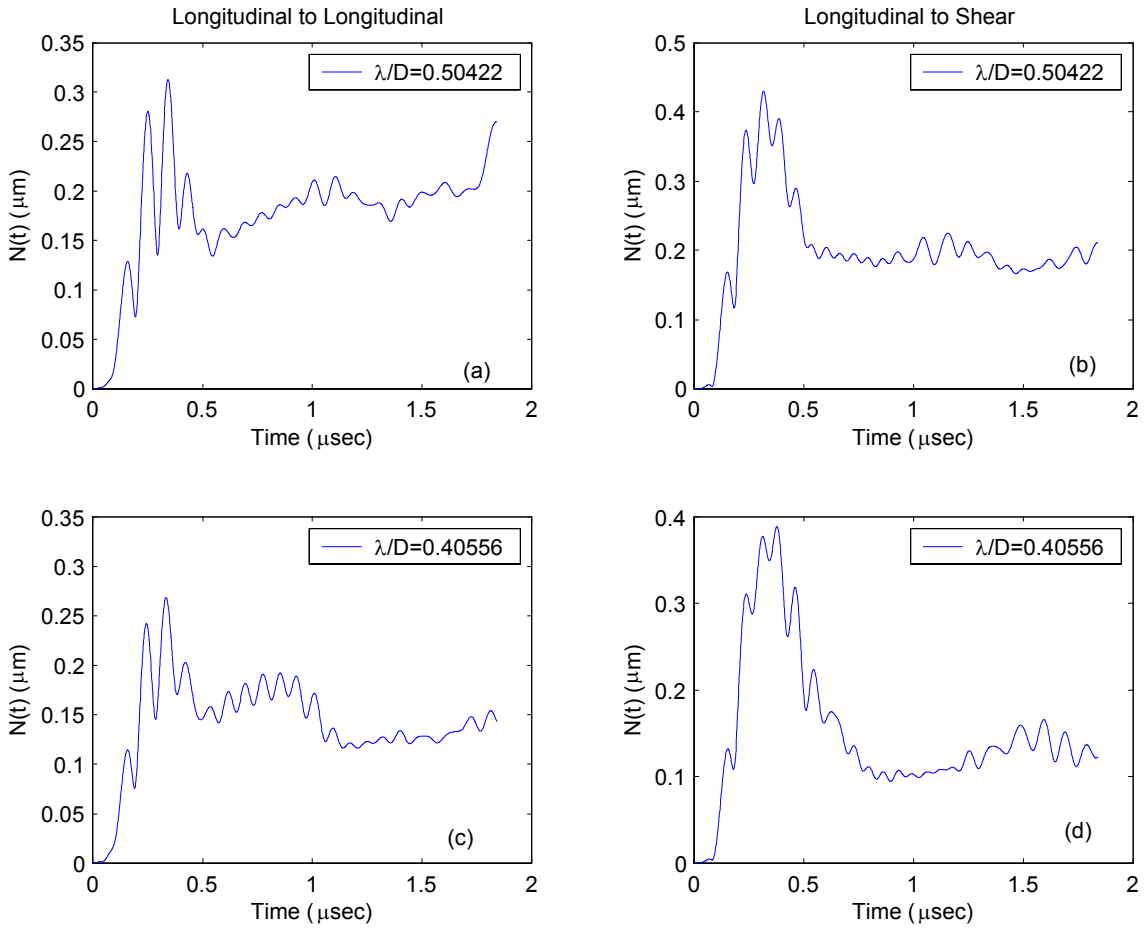

Figure 7.4: Longitudinal to longitudinal and longitudinal to shear rms grain noise for copper.

The grain noise can be modelled theoretically and verified numerical. The numer-

ical method will help in verifying the theory for mode conversion of waves as such data cannot be easily acquired experimentally. It is expected that Ultrasonic Radiative Transfer (URT) theory can be used for modelling the rms grain noise and multiple scattering effects observed. Theories for mode conversion scattering have not yet been developed but can be modeled using URT. A numerical model can be very useful for computing backscatter results for mode conversion of waves.

7.3 Shear Attenuation

Initial work has been done for shear attenuation calculations for plane stress boundary conditions. Nodal displacements parallel to the surface are used to simulate a shear wave. The nodal displacements are given using the same type of pulse wave used for an incident longitudinal wave. Different model sizes are also used for longitudinal and shear waves for the same material, since the shear wave attenuation is much higher. The boundary conditions for the plane stress analysis are shown in Fig. 7.5, which is taken from ABAQUS/CAE. For simplicity of visualization, the elements are made larger in the model. For the shear attenuation calculation all the models have the element size of 50 μm. The shear attenuation results are obtained for aluminum and fictitious materials for plane stress boundary conditions. Two models are created and the same model is used for both aluminum and fictitious material.

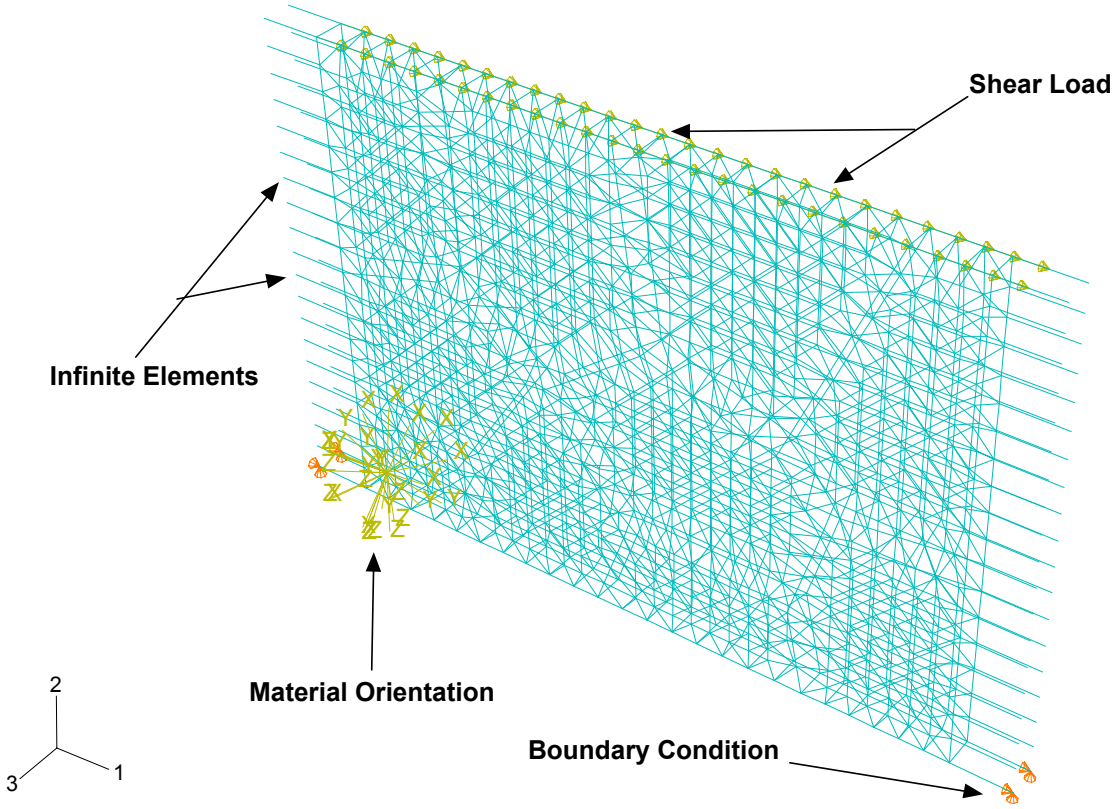

Figure 7.5: Model with shear wave loading condition.

7.3.1 Aluminum

A model smaller in length but wider is used for the shear wave such that more data points at the backwall may be used for averaging. In addition, the wave travels a shorter distance when the model is shorter. This information is shown in Table 7.1.

Table 7.1: Model specification for aluminum for shear wave

No. of Crystals	Model Size (mm^3)	Diameter (μm)		Input Frequency (MHz)	$\frac{\lambda}{D_m}$
		Mean (D_m)	Std Deviation		
50	$8 \times 6 \times 0.075$	1092	174	5	0.5667
100	$8 \times 6 \times 0.075$	774	112	5	0.7995

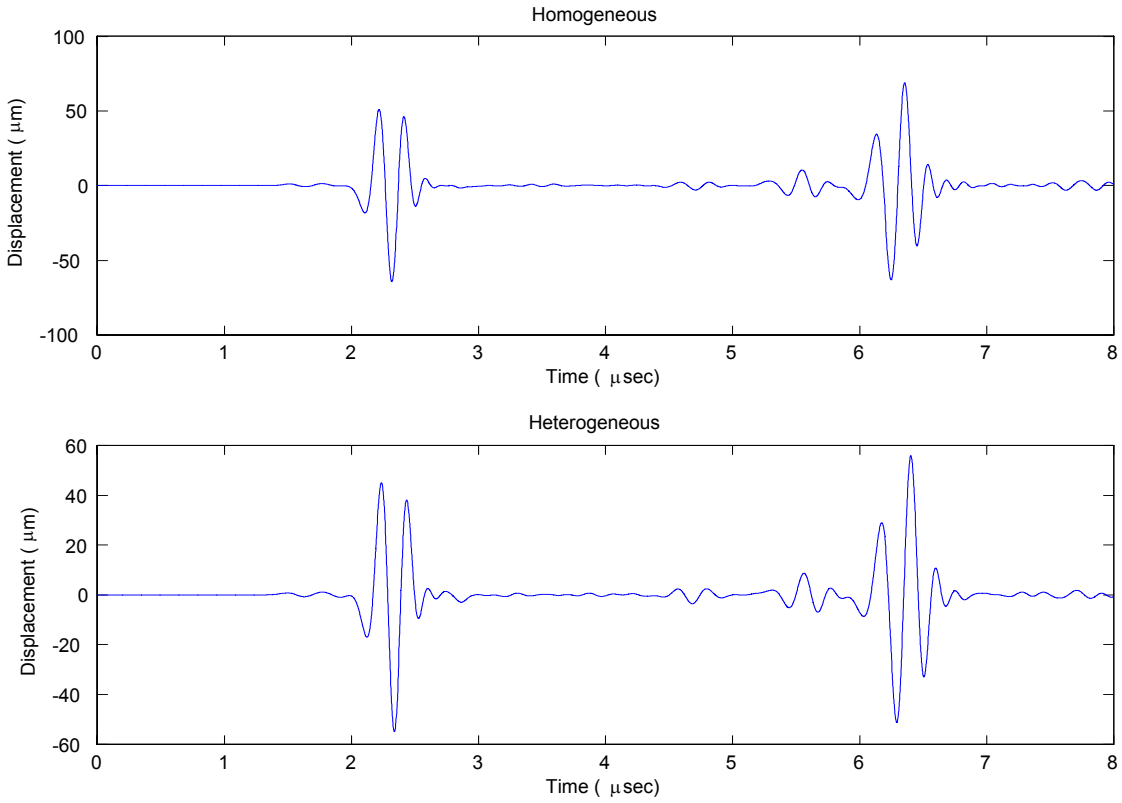

Figure 7.6: Backwall reflection for 50 aluminum crystals at 5 MHz for incident shear wave. The model size is 8 mm by 6 mm and the depth is 0.075 mm.

The shear wave is more difficult to analyze than the longitudinal wave due to the higher attenuation. The procedure for determining attenuation remains the same, only the wave speed differs. The backwall response for a shear wave is shown in Fig. 7.6. The same procedure is applied to obtain the attenuation as outlined above. For the shear wave, 15 realizations are also used to obtain the attenuation values. The attenuation for the models is described in Table 7.1. Two models are used to obtain the attenuation results. The length of the model is smaller than that of longitudinal model due to higher attenuation for the shear wave. The attenuation for the models described in Table 7.1 is shown in Fig. 7.7.

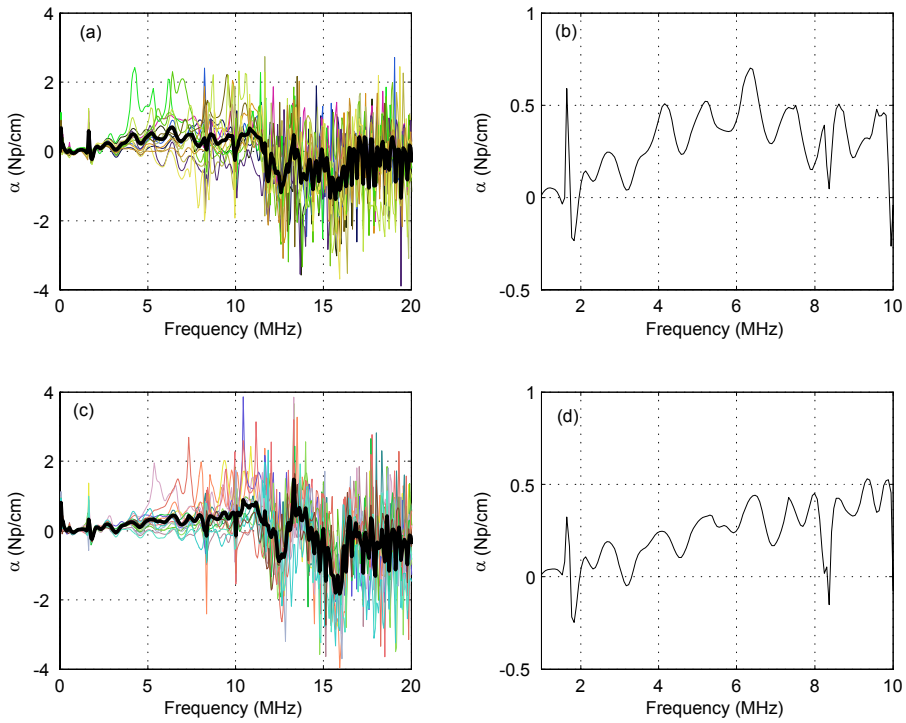

Figure 7.7: Shear attenuation for aluminum (a) 50 crystals (b) average attenuation for 50 crystals (c) 100 crystals (d) average attenuation for 100 crystals.

The simulation for the incident shear wave is shown in Fig. 7.8. The simulation for an incident shear wave shows more scattering. Since aluminum is a weakly scattering medium the coherent wave does not vanish and the noise content is small.

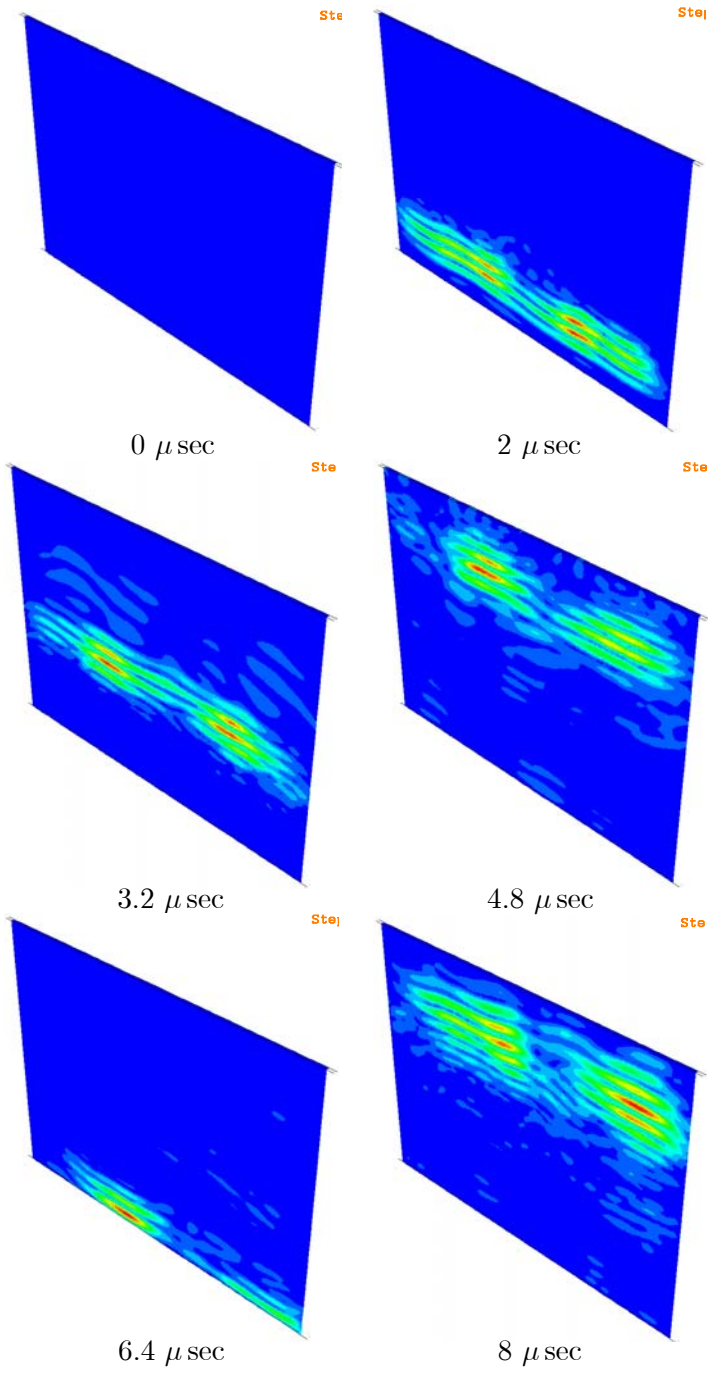

Figure 7.8: Simulation for aluminum with heterogeneous material properties. 100 crystals in a 8 mm by 6 mm model for 5 MHz of shear wave.

The numerical results can also be compared with the theoretical model. The numerical results for shear attenuation show fluctuations as seen in Fig. 7.9. The input frequency used for both models is 5 MHz. The results obtained for such a λ/D ratio make it difficult to comment on the slope of the numerical attenuation curve compared with the theoretical models. At these values of λ/D the difference in slope between the two-dimensional and the three-dimensional attenuation curves is very small. It is possible that these fluctuations may be minimized by having more realizations. The attenuation normalized by the standard deviation of the mean grain diameter is shown in Fig. 7.10. The normalized numerical attenuation curves by the standard deviation of the mean grain diameter shifts left and right when compared with the attenuation normalized by the mean grain diameter.

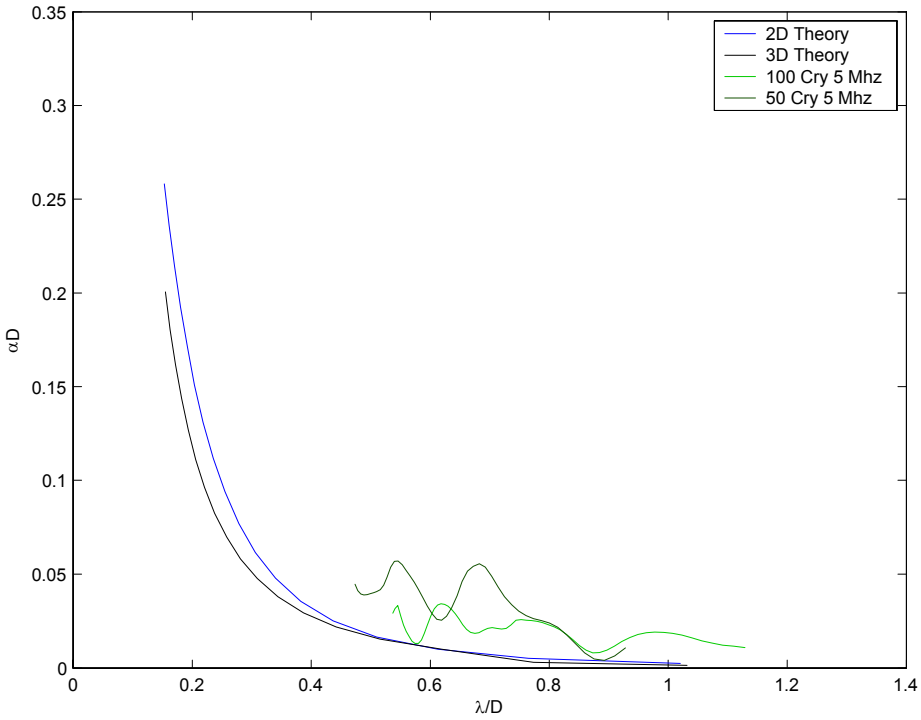

Figure 7.9: Normalized shear theoretical and numerical attenuation for mean diameter of aluminum for model size 8 mm by 6 mm.

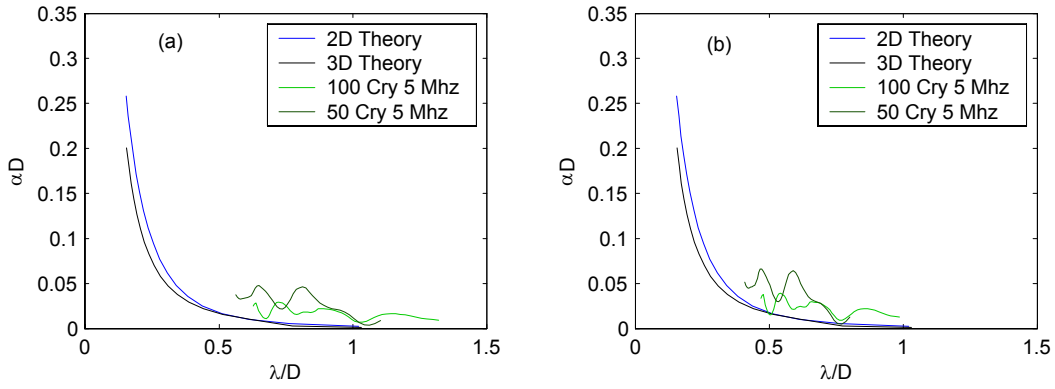

Figure 7.10: Normalized shear attenuation for aluminum by the standard deviation of the grain diameter (a) negative deviation (b) positive deviation.

7.3.2 Fictitious Material

The attenuation results for the fictitious material are shown in Fig. 7.11 for an incident shear wave. The numerical attenuation goes to a negative region as seen in the Fig. 7.11 due to the noise in the response signal for very low and very high frequency ranges compared with the input frequency for the model. The model specifications are given in Table 7.2. For the shear wave different mean grain diameters are used keeping the frequency constants such that λ/D is varied.

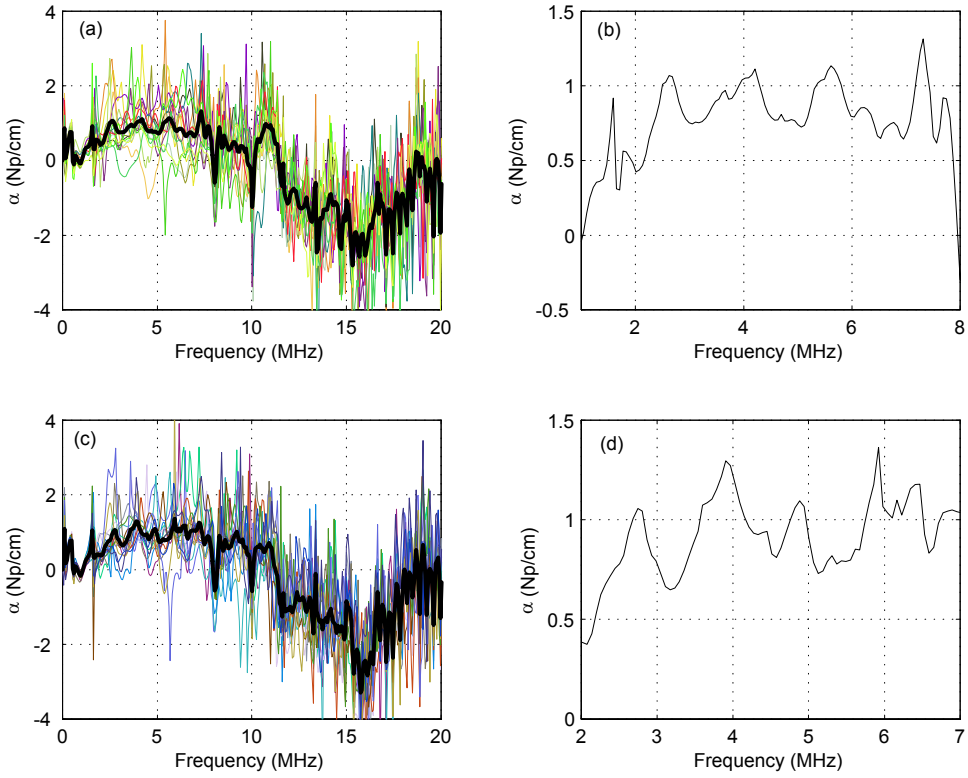

Figure 7.11: Attenuation for shear wave for (a) & (b) 50 crystals (c) & (d) 100 crystals.

The numerical shear attenuation results normalized by the mean grain diameter,

Table 7.2: Model specification for fictious material for shear wave

No. of Crystals	Model Size (mm^3)	Diameter (μm)		Input Frequency (MHz)	$\frac{\lambda}{D_m}$
		Mean (D_m)	Std Deviation		
50	$8 \times 6 \times 0.075$	1092	174	5	0.5667
100	$8 \times 6 \times 0.075$	774	112	5	0.7995

and mean diameter plus and minus the standard deviation of the mean grain diameter are shown in Figs. 7.12, and 7.13 respectively. The same models used for aluminum are used here for the fictitious material. The input frequency of 5 MHz is used. The numerical results show fluctuations as seen for the shear attenuation in aluminum.

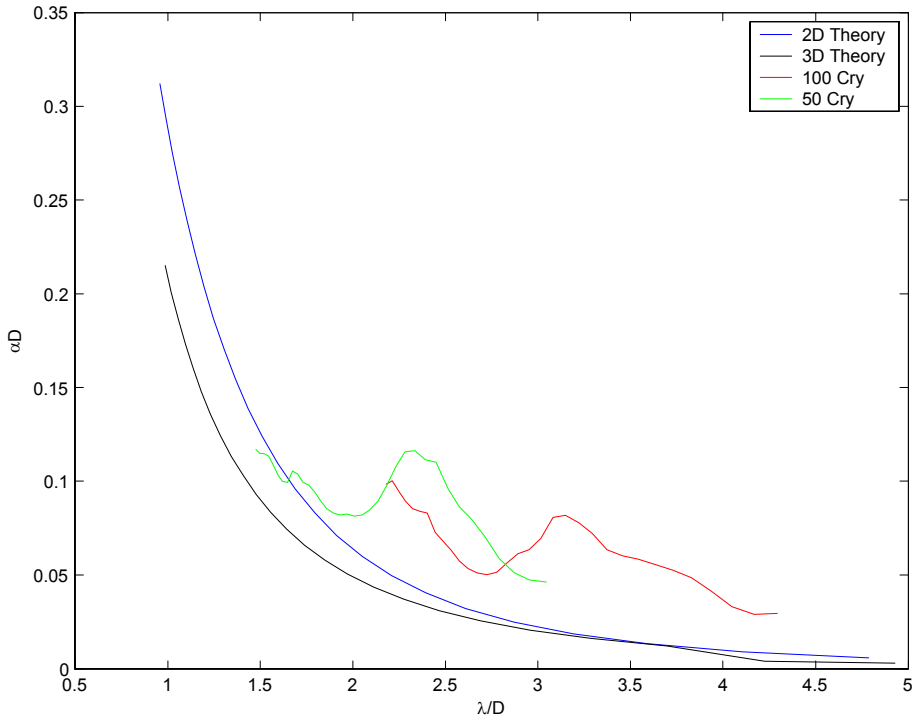

Figure 7.12: Normalized shear theoretical and numerical attenuation by mean diameter of fictitious material for model size 8 mm by 6 mm.

The shear attenuation is high compared with the longitudinal attenuation of aluminum and fictitious material. The high attenuation increases the degree of scattering such

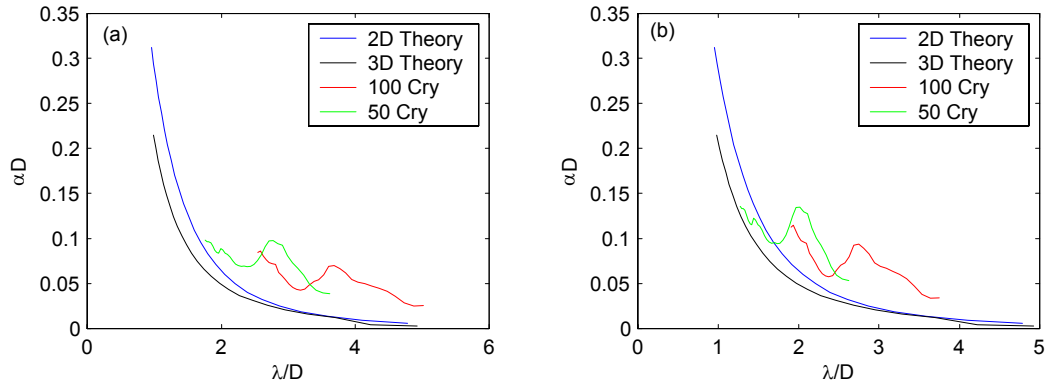

Figure 7.13: Normalized shear attenuation for fictitious material for standard deviation of the mean grain diameter (a) negative deviation (b) positive deviation.

that the response contains more noise. As the noise content in the signal increases the level of difficulty in analyzing the signal also increases. Analysis can also be done for plane strain formulations for an incident shear wave. The results can be obtained for a model with more crystals and more realizations to check if the fluctuations in the numerical results decrease.

Bibliography

[1] Bhatia, A. B., *Ultrasonic Absorption*, Oxford, London, 1967.

[2] Papadakis, E. P., "Ultrasonic Attenuation Caused by Scattering in Polycrystalline Metals," *J. Acoust. Soc. Am.*, Vol. 37, No. 4, 1965, pp. 711–717.

[3] Bhatia, A. B., "Scattering of High-Frequency Sound Waves in Polycrystalline Materials," *J. Acoust. Soc. Am.*, Vol. 31, No. 1, 1959, pp. 16–23.

[4] Hirsekorn, S., "The Scattering of Ultrasonic Waves by Polycrystals," *J. Acoust. Soc. Am.*, Vol. 72, No. 3, Sep. 1982, pp. 1021–1031.

[5] Hirsekorn, S., "The Scattering of Ultrasonic Waves by Polycrystals. II. Shear Waves," *J. Acoust. Soc. Am.*, Vol. 73, No. 4, 1983, pp. 1160–1163.

[6] Evans, A. G., Tittmann, B. R., Ahlberg, L., Khuri-Yakub, B. T., and Kino, G. S., "Ultrasonic Attenuation in Ceramics," *J. Appl. Phys.*, Vol. 49, No. 5, May 1978, pp. 2669–2679.

[7] Weaver, R. L., "Diffusivity of Ultrasound in Polycrystals," *J. Mech. Phys. Solids*, Vol. 38, No. 1, 1990, pp. 55–86.

[8] Turner, J. A., "Elastic Wave Propagation and Scattering in Hetrogeneous, Anisotropic Media: Textured Polycrystalline Materials," *J. Acoust. Soc. Am.*, Vol. 106 (2), August 1999, pp. 541 – 552.

[9] Alford, R. M., Kelly, K. R., and Boore, D. M., "Accuracy of Finite-Difference Modeling of the Acoustic Wave Equation," *Geophysics*, Vol. 39, No. 6, December 1974, pp. 834–842.

[10] Fornberg, B., "The Pseudospectral Method: Accurate Representation of Interface in Elastic Wave Calculations," *Geophysics*, Vol. 53, No. 5, May 1988, pp. 625–637.

[11] Scalerandi, M., Ruffino, E., Delsanto, P. P., Johnson, P. A., and Abeele, K. V. D., "Non-Linear Techniques for Ultrasonic Micro-Damage Diagnostics: A Simulation Approach," *Review in Progress in Quantitative NDE*, edited by D. O. Thompson and D. E. Chimenti, Vol. 19B, Plenum Press, New York, 1999, pp. 1393–1399.

[12] Guyer, R. A., McCall, K. R., and Boitnott, G. N., "Hysteresis, Discrete Memory, and Nonlinear Wave Propagation in Rock: A New Paradigm," *Physical Review Letters*, Vol. 74, No. 17, April 1995, pp. 3491–3494.

[13] Guyer, R. A. and Johnson, P., "Nonlinear Mesoscopic Elasticity: Evidence For A New Class of Materials," *Physics Today*, April 1999, pp. 30–36.

[14] Fellinger, P., Marklein, R., Langenberg, K. J., and Klaholz, S., "Numerical Modeling of Elastic Wave Propagation and Scattering with EFIT - Elastodynamic Finite Integration Technique," *Wave Motion*, Vol. 21, 1995, pp. 47–66.

[15] Schubert, F., Peiffer, A., Kohler, B., and Sanderson, T., "The Elastodynamic Finite Integration Technique for Waves in Cylindrical Geometries," *J. Acoust. Soc. Am.*, Vol. 104, No. 5, November 1998, pp. 2604–2614.

[16] Liu, E. and Zhang, Z., "Numerical Study of Elastic Wave Scattering by Cracks or Inclusions Using the Boundary Integral Equation Method," *J. Comp. Acoust.*, Vol. 9, No. 3, 2001, pp. 1039–1054.

[17] Barbe, F., Decker, L., Jeulin, D., and Cailletaud, G., "Intergranular and Intragranular Behavior of Polycrystalline Aggregates. Part 1: F.E. Model," *International Journal of Plasticity*, Vol. 17, 2001, pp. 513–536.

[18] Matlab, *The Language of Technical Computing*, The Math Works, Inc., Natick, MA, 2001.

[19] Ghosh, S., Nowark, Z., and Lee, K., "Tessellation-Based Computational Methods for the Characterization and Analysis of Hetrogeneous Microstructures," *Composite Science and Technology*, Vol. 57, 1997, pp. 1187–1210.

[20] Kumar, S., Kurtz, S., Banavar, S., and Sharma, M., "Properties of a Three-Dimensional Poisson-Voronoi Tessellation: A Monte Carlo Study," *Journal of Statistical Physics*, Vol. 67, 1992, pp. 523–551.

[21] Zavattieri, P. D., Raghuram, P. V., and Espinosa, H., "A Computational Model of Ceramics Microstructures Subjected to Multi-Axial Dynamic Loading," *Journal of the Mechanics and Physics of Solids*, Vol. 49, 2001, pp. 27–68.

[22] Brostow, W. and Castano, V., "Voronoi Polyhedra as a Tool for Dealing with Spatial Structures of Amorphous Solids, Liquids Ans Dense Gases," *Journal of Materials Education*, Vol. 21, 1999, pp. 297.

[23] Gerstein, M., Tsai, J., and Levitt, M., "The Volume of Atoms on the Protien Surface: Calculated from Simulation, Using Voronoi Polyhedra," *Journal of Molecular Biology*, Vol. 249, 1995, pp. 955–966.

[24] Montoro, J. C. G. and Abascal, J. L. F., "The Voronoi Polyhedra as Tools for Structure Determination," *Journal of Physical Chemistry*, Vol. 97, 1993, pp. 4211–4215.

[25] Alani, H., Jones, C., and Tudhope, D., "Voronoi-Based Region Approximation for Geographical Information Retrieval with Gazetteers," *International Journal of Geographical Information Science*, Vol. 15, 2001, pp. 287–306.

[26] Christensen, S., "Analysis of Polynuclear Aromatic Hydrocarbons Via the Voronoi Tessellation Approach: Classification of Atom Types Using Artificial Networks," *Acta Crystallographica*, Vol. A58, 2002, pp. 171–179.

[27] Baccelli, F. and Blaszczyszyn, B., "On a Coverage Process Ranging from the Boolean Model to the Poisson Voronoi Tessellation, with Application to Wireless Communications," *Advances in Applied Probability*, Vol. 33, 2001, pp. 293–323.

[28] Espinosa, H. and Zavattieri, P., "A Grani Level Model for the Study of Failure Initiation and Evolution in Polycrystalline Brittle Materials. Part I: Theory and Numerical Implementation," *Mechanics of Materials*, Vol. 35, 2003, pp. 333–364.

[29] Espinosa, H. and Zavattieri, P., "A Grain Level Model for the Study of Failure Initiation and Evolution in Polycrystalline Brittle Materials. Part II: Numerical Examples," *Mechanics of Materials*, Vol. 35, 2003, pp. 365–394.

[30] ABAQUS, *ABAQUS: Finite Element Analysis Solutions*, ABAQUS, Inc., Pawtucket, RI, 2001.

[31] Schmerr, L. W., *Fundamentals of Ultrasonic Nondestructive Evaluation: A Modeling Approach*, Plenum Pub. Corp., New York, 1998.

[32] Rayleigh, L., *Theory of Sound*, Dover Publications, New York, 1945.

[33] Pao, Y. P. and Varatharajulu, V., "Huygen's principle, radiation conditions, and integral formulas for the scattering of elastic waves," *J. Acoust. Soc. Am.*, Vol. 59 (6), June 1976, pp. 136–1371.

[34] Stanke, F. E. and Kino, G. S., "A Unified Theory for Elastic Wave Propagation in Polycrystalline Materials," *J. Acoust. Soc. Am.*, Vol. 3, 1984, pp. 665–681.

[35] Hirsekorn, S., "The Scattering of Ultrasonic Waves in Polycrystalline Materials with Texture," *J. Acoust. Soc. Am.*, Vol. 77, No. 3, 1985, pp. 832–843.

[36] Frisch, U., "Wave Propagation in Random Media," *Probabilistic Methods in Applied Mathematics*, edited by A. T. Barucha-Reid, Vol. 1, Academic, New York, 1968, pp. 75–198.

[37] Dyson, F. J., "The Radiation Theory of Tomonaga, Schwinger, and Feynman," *Phys. Rev.*, Vol. 75, 1949, pp. 486–502.

[38] Dyson, F. J., "The S Matrix in Quantum Electrodynamics," *Phys. Rev.*, Vol. 75, 1949, pp. 1736–1755.

[39] Ahmed, S. and Thompson, R. B., "Propagation of Elastic Wave in Equiaxed Stainless-Steel Polycrystals with Aligned [001] Axes," *J. Acoust. Soc. Am*, Vol. 99, 1996, pp. 2086–2096.

[40] Shubert, F. and Koehler, B., "Three-Dimensional Time Domain Modeling of Ultrasonic Wave Propagation in Concrete in Explicit Consideration of Aggregates and Porosity," *J. Comp. Acoust.*, Vol. 9, No. 4, 2001, pp. 1543–1560.

[41] Margetan, F. J., Gray, T. A., and Thompson, R. B., "A Technique for Quantitative Measuring Microstructurally Induced Ultrasonic Noise," *Review of Progress in Quantitative NDE*, edited by D. O. Thompson and D. E. Chimenti, Vol. 10, Plenum Press, New York, 1991, pp. 1721 – 1728.

[42] Thompsom, R. B., "Elastic Wave Propagation in Random Polycrystals: Fundamentals and Application to Nondestructive Evaluation," *Topics Appl. Phys*, Vol. 84, 2002, pp. 233–257.

Appendix A

Voronoi Model

A.1 VoronoiPoly2D.m

This program constructs the Voronoi polycrystal inside a regular polygon of n sides. Uniformly distributed grains are created. The user can enter the aspect ratio and angle of orientation for the grains.

Input Parameters

- side : the length of each side of the regular polygon.
- crys : number of crystal to be constructed.
- asp_ratio : aspect ratio.
- orien : geometric orientation angle for each crystal.

Output Data

- x : x-axis coordinates of the Voronoi polycrystals.
- y : y-axis coordinates of the Voronoi polycrystals.

Appendix B

Finite Element

B.1 VorPrismABQ.m

This file constructs the Voronoi polycrystals inside a two-dimensional rectangular domain. Subroutine similar to VoronoiPoly2D.m is written to construct Voronoi polycrystals inside a rectangular domain only, without any elongation and geometric orientation of the grains, and this subroutine is called to obtain the vertices of the Voronoi polycrystals. The meshing and the extrusion of the model to obtain prism elements are done in this program. Then the infinite elements are created. The connectivity table for all the elements are created. At the end the input file for ABAQUS is created for homogeneous and heterogeneous case as the output of this program. This code returns 1 if all the procedures are performed successfully. The directory and the input file name for ABAQUS with the file extension are entered by the user. Subroutines are written to perform the particular task such as to construct infinite elements, to write the input file for ABAQUS. This is the main program within which all the subroutines are called. Batch files are created to run the all the models one after another.

Input Parameters

- xlen : the length of the rectangle.
- ylen : the width of the rectangle.
- points : number of grains.
- elem_len : characteristic element size.
- files : number of realizations to be created.
- dirname : the directory and the filename with extension in an string array.
- density : density of the material in kg/m^3.
- E : Young's modulus in Pa.
- cmat : elastic constants in an 1 by 3 array in Pa. $\left(\text{i.e. } \begin{bmatrix} C_{11} & C_{12} & C_{44} \end{bmatrix}\right)$

Output Data

- 1 : if all the processes are successfully completed.
- .inp : the input file for ABAQUS.

Appendix C

Attenuation Calculation

C.1 AttenCal.m

This program calculates attenuation for each realization of grains. The data is acquired by running a Fortran code (the sample code is given in ABAQUS manuals). The output data file obtained by running the Fortran code, contains the displacement information for the nodes requested by the user. These displacement data are read and used for attenuation calculation by the MATLAB code AttenCal.m.

Input Parameters

- wave_speed : the sound wave speed in the material.
- freq : frequency of the input wave.
- temp : number of files i.e. number of realizations.
- cry : number of crystals.
- xlen : width of the model.
- ylen : length of the model.
- filename : output data file name.

Output Data

- .txt : output file is created which contains attenuation data for different realizations. The first column contains the frequency values in MHz and then each column for attenuation in Np/cm for different realizations.

Scattering of Elastic Waves in Statistically Anisotropic Media

by

Liyong Yang

A DISSERTATION

Presented to the Faculty of
The Graduate College of the University of Nebraska
In Partial Fulfillment of Requirements
For the Degree of Doctor of Philosophy

Major: Engineering (Engineering Mechanics)

Under the Supervision of Professor Joseph A. Turner

Lincoln, Nebraska

December, 2003

Scattering of Elastic Waves in Statistically Anisotropic Media

Liyong Yang, Ph.D.

University of Nebraska, 2003

Adviser: Professor Joseph A. Turner

The investigation of wave propagation and scattering of ultrasonic waves in heterogeneous, anisotropic media is of substantial interest to quantitative nondestructive evaluation and materials characterization, particularly for ultrasonic techniques. In this dissertation, models for wave propagation and scattering in statistically anisotropic media, such as cracked media and textured media are developed. These models provide insightful information about the wave propagation parameters and can also be used to guide experimental design for determining the microstructure properties for nondestructive evaluation techniques. Compact expressions are derived for attenuations and wave velocities of the quasilongitudinal and two quasishear waves using stochastic wave theory in a generalized dyadic approach. Those derivations are based upon the diagrammatic approach, in which the mean response is governed by the Dyson equation. The Dyson equation is then solved in the Fourier transform domain within the limits of the first-order smoothing approximation (FOSA).

In cracked media, the derivation of explicit expressions of wave attenuations and velocities in a medium with damage from randomly distributed penny-shaped microcracks is first discussed. Under the same framework, wave propagation and scattering in a solid medium permeated by uniaxially aligned and perfectly aligned penny-shaped cracks are then studied, respectively. The resulting attenuations are investigated in terms of the directional,

frequency, and damage dependence.

In the case of polycrystalline media with texture, attenuations and wave velocities are developed in a general orthorhombic material made up of cubic crystallites. The attenuations of each wave type are calculated numerically as a function of dimensionless frequency and wave propagation direction, respectively, for given orientation distribution coefficients (ODCs). The ODCs are, in essence, the coefficients of an expansion of crystallite of orientation distribution function (ODF) in terms of a series of generalized spherical harmonics. The relationship between the phase velocity and recrystallization variables, such as annealing time, is also investigated for specific examples. Finally, numerical results are presented and discussed in terms of the relevant dependent parameters. It is anticipated that these models will improve the understanding of the microstructure characterization for both cracked and textured media. Moreover, the present formulation allows the study of backscattering problems to be examined in a straightforward manner.

Acknowledgements

This work was sponsored by the National Science Foundation under Grant Nos. CMS-9978707 and INT-0089548 and the Department of Energy under Grant No. DE-FG02-01ER45890. The National Bridge Research Organization and Ames Laboratory are also greatly acknowledged for supporting this research.

I would like first to thank my kind advisor Professor Joseph A. Turner for his much-needed direction and warmly support which provided substantial help throughout the whole work. I am greatly indebted to my committee members Professor Ruqiang Feng, Professor Mehrdad Negahban, Professor Barry Rosson and Professor Mao See Wu for their critical comments and input during my Ph.D. study. I also appreciated the effort of my fellow graduate students and departmental faculty and staff who provided me with assistance when needed and for many useful discussions.

I would like to thank my parents and brothers for their great support and for encouraging me to pursue my doctorate abroad. Most importantly, I would like to thank my pretty wife Rong Wang for her love, understanding, patience and emotional support over the course of this research work.

Contents

List of Figures

List of Tables

Chapter 1

Introduction

Elastic wave propagation in solid media is a very broad, interesting and complicated research subject. The investigation of wave propagation and scattering of elastic waves in heterogeneous, anisotropic media is of substantial interest to quantitative nondestructive evaluation (QNDE) and materials characterization, particularly for ultrasonic techniques. The corresponding results of this field have considerable and wide-ranging engineering applications such as in material science, in-situ safety and reliability control of complex structural components by acoustic emission, industrial and medical ultrasonics, quantitative nondestructive materials testing, dynamic fracture mechanics, seismology and geophysics.

Wave propagation in solids with cracks or texture, unlike in purely homogeneous solids, is generally associated with diffraction, scattering, attenuation, dispersion, and local dynamic stress concentrations. While ultrasonic waves propagate through those media, the incident energy is dispersed in many directions due to interaction with the heterogeneities

(cracks or crystallites) within the medium. If there are a large number of scatterers in the medium, the wave propagation will become very complicated due to multiple scattering effects. In general, diffraction refers to the wave deviation from its original path, while scattering may be regarded as the wave radiation from the scatterers. During the diffraction and scattering process, a part of the incident wave energy is transformed into the energy of diffracted and scattered waves. Although the energy of the whole system is conserved, a heterogeneous solid is observed by an incident wave as an attenuative and dispersive medium.

Engineering materials often contain dispersed scatterers such as microcracks in cracked media and oriented crystallites in polycrystalline media. In the case of structural materials such as concrete, polycrystalline metals and most composites, these scatterers are typically induced by mechanical loading, materials processing, manufacturing, aging, temperature variation and other conditions. The presence of cracks or texture in complex media may significantly affect material properties, for example the stiffness and the strength as well as the integrity of the materials. Changes in material response due to scattering are typically inferred ultrasonically by the variation in wave velocity and the changes in ultrasonic attenuation. In particular, distributed microcracks often give rise to a decrease in wave velocity and an increase in attenuation. The definition of attenuation refers to the intensity or the amplitude of the incident wave that decreases through the complex media. In addition, the energy disturbance causes a shape distortion of the incident wave, which is referred as dispersion, due to the frequency dependence of the effective velocity. Techniques of quantitative nondestructive evaluation using ultrasonic waves are especially appealing

because of the direct connection between the changes of wave propagation characteristics and microstructure properties such as crack density, crystallite distribution, location, size and orientation. In particular, it gives a physical feeling for the process, it is easy to perform parametric studies, and it is a good tool for the development of testing procedures and signal processing. Thus, quantitative nondestructive evaluation by ultrasonic techniques provides a realistic approach to the detection of microcracks and characterization of microstructures of materials.

The basic principle of quantitative nondestructive evaluation and acoustic emission relies on elastic wave propagation and scattering in complex solids. Besides experimental techniques, quantitative comparisons with experimental results require a well-developed model of the effects of the microstructure on the wave behavior. Theoretical models may provide the direct information to design the experiment configurations and to explain the measured data correctly. Once the microstructures have been detected and characterized, mechanics concepts can be applied for assessing the safety and stability of existing complex materials. Therefore, understanding how waves propagate and multiply scatter as they go through complex media is of considerable importance to practical structural applications.

Because of the complexity of microstructures in complex media, statistical approaches are often employed to study the wave propagation and scattering through the complex media. The scattering of elastic waves by cracks or crystallites has been studied by a number of methods from purely numerical ones to more analytically oriented approaches. Traditional approaches to model the randomly fluctuating field quantities, such as stress field or strain field, are replaced by modeling certain statistical quantities, such as the sta-

tistical mean fields of the corresponding fields. It is known that these statistical approaches do not give solutions in terms of the field quantities, but present an essential understanding of the statistical nature of the material responses. The statistical characterization must emphasize the universal aspects and simultaneously ignore the inconsequential details. The precision and rigor of the selected statistical characterization of microstructure depend on the purpose of the analysis and the required resolution of the model.

In this dissertation, the theory of elastic wave propagation and scattering using stochastic wave field techniques in which the mean field is governed by the Dyson equation is applied to model the attenuation phenomena in two types of statistically anisotropic media, that is the cracked media and textured media. For cracked media, the discussion is first focused on an isotropic, homogeneous medium with damage from distributed penny-shaped microcracks which are assumed to be randomly oriented and uniformly distributed. In the succeeding discussions, within the same framework wave propagation and scattering in a solid medium permeated by uniaxially aligned penny-shaped cracks and perfectly aligned penny-shaped cracks are then studied, respectively. It is always assumed that the microcracks are noninteracting throughout the discussions. This assumption allows the effective stiffness to be determined by integration over a continuous distribution of crack sizes and orientations. Moreover, it is acceptable only for a dilute distribution or for weak scatterers. It may not be good enough for a dense distribution or for strong scatterers.

The second medium is a polycrystalline medium with texture, which is defined as the preferred orientation of grains. All grains to be considered are assumed to have the same sizes and shapes, and each grain is assumed to have a different orientation. The orientation

of a given crystallite with the sample axes may then be defined uniquely by the three Euler angles θ, ψ and φ. The crystallite orientation distribution is represented by the orientation distribution function (ODF). In the harmonic method, which was given first by Roe [1],[2] and Bunge [3], the ODF is expanded in generalized spherical harmonic functions. Still, there is no correlation between material properties from grain to grain. In this case, the differences in elastic constants from grain to grain result only from differences in orientation. Thus, the elastic constants of a grain with arbitrary orientation can be described by the single crystal constants with a rotation. The ensemble average elastic constants are given by averaging over the orientation distribution function (ODF). Integrals over a grain volume are approximately equal to the corresponding integrals over a sphere of the same volume.

In this presentation, the Voigt type averaging approximation method is employed. Within the method of Voigt [4], uniformity of strain across the media is assumed, while in the method of Reuss [5] uniformity of stress is assumed. As shown by Hill [6], the Voigt and Reuss average methods provide the upper and lower bounds on the elastic constants, respectively. Rigorous bounds have been given by Kröner [7], and these bounds usually lie close to the average of the Voigt and Reuss values.

1.1 Previous Work

The increased complexity of the elastic wave reflection phenomena, due to mode conversion effects, yields scattering problems in imperfect solids more complicated than in purely homogeneous solids as elastic waves move through the media. Studies of elastic wave propagation in cracked solid media have been continuous for at least thirty years due

to their significance. This subject of research began in the late 1960s with Mal [8],[9], [10],[11]. He first examined the response of a penny-shaped crack embedded in an infinite isotropic, elastic medium to an incident plane harmonic wave and demonstrated that at low frequencies the stress intensity factors are always greater than those of the corresponding static cases [8],[9]. In [10] and [11], Mal studied the problems of the diffraction of normally incident longitudinal and shear elastic waves by a crack, for example a penny-shaped crack and a Griffith crack, located in an infinite isotropic elastic medium. Meanwhile, Robertson [12] also examined the diffraction of a plane longitudinal wave by a penny-shaped crack. Piau [13],[14] then presented the attenuation of plane compressional waves in cracked media with randomly distributed cracks and oriented cracks. Chatterjee and coworkers [15] gave the results of attenuation in a cracked, fluid-saturated solid. Martin [16] obtained the scattered displacement fields as the harmonic elastic waves move through an infinite elastic solid containing a penny-shaped crack. Krenk and Schmidt [17] discussed the elastic wave scattering by a circular crack. Martin and Wickham [18] presented the numerical results of the scattered displacement fields. Sayers and Smith [19] gave the results of wave velocity and attenuation in an epoxy matrix containing lead inclusions. It was noted that all of the above solutions may be finally transformed into Fredholm integral equations of the second kind, which are suitable for iteration at low frequencies.

Thereafter, the coherent wave scattering through cracked solids had been more thoroughly investigated. Budreck and Achenbach [20] introduced the scattering results induced from three-dimensional planar cracks by the boundary integral equation method. Wave scattering from an interface crack was discussed by Yang and Bogy [21], Boström

[22] and Qu [23]. Sotiropoulos and Achenbach [24] presented the reflection results of elastic waves by a distribution of coplanar cracks. Zhang and Achenbach [25] then presented an improved approach to develop the effective phase velocity and the attenuation of ultrasonic waves in a material containing distributed penny-shaped cracks. Extensive reviews were presented further by Zhang and Gross [26],[27],[28]. They finally demonstrated the numerical results of wave attenuations and dispersion relations in randomly cracked solids, such as penny-shaped cracks and slit cracks with several propagation directions. More importantly, they presented numerically the relationships between the effective wave velocity and attenuation and damage density. Smyshlyaev and Willis [29] discussed the linear and nonlinear scattering phenomena as waves propagate through cracked media. Eriksson, Boström and Datta [30] also examined the problem of ultrasonic wave propagation through a cracked solid. However, they considered the medium with a crack distribution as an effective viscoelastic medium and presented the attenuation results for both open and fluid-filled crack cases. For most of those results, the Foldy [31] theory of multiple scattering had been employed to calculate the effective wave velocity and the coefficients of attenuation. Foldy in 1945 first introduced the concept of ensemble averaging and obtained a closed form expression for the complex wave number governing the coherent intensity due to an assemblage of isotropic point scatterers (Foldy's equation) [31]. Recently, Boström in 2003 presented a review of the hypersingular integral equation method for crack scattering and applications. In particular, he described how the integral equation approach to crack scattering can be used as the most important part for the modeling of ultrasonic nondestructive testing [32]. It can be seen that although some important results had been obtained, the general exact

results of the wave propagation and scattering through cracked solids such as aligned cracks are still less well developed.

Studies of elastic wave propagation in polycrystalline materials began in the late 1940s. Quantitative evaluations of material properties in polycrystalline media had relied mostly upon the use of the coherent field, through the examinations of either wave speed or attenuation or both. Mason and McSkimm in 1947 [33] first studied the coherent propagation of ultrasound in polycrystals and demonstrated that in the Rayleigh frequency limit the scattering attenuations are proportional to the fourth power of the frequency. During this time period, many others [34],[35],[36],[37],[38] conducted similar research on ultrasonic scattering. Mason and McSkimm also theorized that in the Rayleigh frequency limit the grains would scatter energy as spherical scatterers. Bhatia [39] then improved upon this theory by assuming the grains were isotropic with elastic properties varying slightly from the elastic properties of the bulk medium. In the meantime, Bhatia and Moore [40] used a perturbation approach to obtained accurate expressions for the scattered energy due to variations in elastic constants for a general orthorhombic crystallite in the Rayleigh limit. They demonstrated that those anisotropic results are 3.5 times larger than the isotropic results obtained, and their expressions agreed with the results of attenuation presented by Mason and McSkimm. Papadakis [41] also discussed many of the ultrasonic techniques available for nondestructive evaluation with coherent fields. Correlations between the ultrasonic properties of wave speed and attenuation and material properties, such as yield strength, fracture toughness, and so on, had been discovered. The general summaries were presented in Vary's review paper [42].

Beginning in the 1980s, the theoretical work for frequencies outside the Rayleigh limit was studied by Hirsekorn [43],[44] first in untextured polycrystalline materials. She assumed the grains were individual scatterers which scattered like a sphere and demonstrated that the general attenuation and wave speed were a function of its wavenumber multiplied by grain radius without the frequency limitation to the Rayleigh region using the Born approximation. Because of the assumption of single-sized spheres, her results showed oscillatory behavior with respect to frequency in the transition between the Rayleigh and stochastic regions. It is known that this behavior is not physical for real polycrystalline materials. Finally, Hirsekorn [45],[46] used the identical approach to examine the ultrasonic scattering in textured polycrystals. Frequency dependence and directional dependence of scattering coefficients were respectively investigated. The calculation was restricted to waves propagating in the direction of an axis of symmetry of the texture. In particular, the directional dependence was discussed for the polycrystalline media with fiber texture. So far her results were only found to demonstrate the ultrasonic scattering completely in polycrystals of cubic symmetry with rolling texture. Stanke and Kino [47] developed a unified approach to derive the attenuation and phase velocity for different kinds of elastic waves due to grain scattering in single-phase, polycrystalline media. Their results were valid in the Rayleigh, stochastic and geometric regions and showed the transition phenomena between these regions. By the use of the Keller approximation [48], their derivation was done for a particular inhomogeneous medium that is weakly heterogeneous, and without the assumption of spherical scattering made by Hirsekorn [43],[44]. The general operator notation as discussed by Keller [48] allowed the results to be applied to various physical problems in a straightforward man-

ner. Hirsekorn in 1988 [49] then used the perturbation method to investigate the ultrasonic scattering by multiphase polycrystals.

Because of the relevance to nondestructive characterization of microstructures, the investigation of ultrasonic scattering in polycrystals continued. In the recent two decades, ultrasonic inspection of random media has been expanded to use diffuse fields methods. Coherent methods and diffuse fields methods are very different. In particular, diffuse fields can be investigated at higher frequencies than coherent fields. Weaver in 1990 [50] presented a multiple scattering formulation using a mean Green's dyadic function based on the method of first-order smoothing approximation. He also employed a Born approximation which limited the validity of the results to frequencies below the geometrical optics regime, and obtained the exact diffusivity for randomly distributed orientation of all crystallites. Turner and Weaver [51],[52],[53],[54],[55] proposed to model ultrasonic multiple scattering effects in a medium containing randomly located discrete scatterers using radiative transfer theory and applied that theory to polycrystalline media as well. They demonstrated that the scattered intensity is angularly dependent as expected. Ahmed and Thompson [56] studied the wave scattering in equiaxed stainless-steel polycrystals with aligned [001] axes, transversely polycrystalline media, based on the Stanke and Kino unified approach. They showed various results of attenuation and phase velocity with direction of propagation and frequency for quasilongitudinal, shear horizontal, and quasishear waves. Turner [57] presented a general wave propagation and scattering method by using an anisotropic Green's function for modeling the attenuation in statistically anisotropic media. He finally specified the formalism for particular problem of equiaxed cubic polycrystalline media with texture. His attenu-

ation results agreed well with the attenuation calculations of Ahmed and Thompson [56]. Many others [58],[59], [60],[61] conducted research on wave propagation phenomena during this time period.

Experimental studies of microstructural characterization had accompanied much of the above theoretical work. Experiments with coherent ultrasonic inspection on polycrystalline specimens are typically performed in a water tank using reflection and transmission techniques. If two transducers are used, one transducer sends a wave with known amplitude into the specimen which is received by the other transducer located on the opposite side of the specimen. The change in amplitude of the received signal after passing through the medium is attributed to the exponential decay caused by attenuation. If one transducer is used, it acts as both transmitter and receiver. The wave reflects from the opposite face and returns to the transducer. In this situation, the amplitude will be reduced due to two specimen crossings. Coherent ultrasound experiments have many limitations. Particularly absorption and scattering attenuations cannot be distinguished in these types of experiments. Diffuse field experiments are usually conducted using backscattered techniques. Because the coherent field continues to propagate in the forward direction, the backscattered field contains only diffuse energy until the coherent pulse returns after reflecting from the opposite face. A number of researchers have discussed the use of the incoherently backscattered field for the characterization of microstructure [62],[63],[64],[65],[66],[67],[68],[69]. Other previous references are cited in their work.

It is the above literature review that shows that models of elastic wave propagation and scattering through polycrystalline media with texture had typically focused on

special cases of texture. For example, the attenuation through cubic polycrystalline materials with one aligned axis had been studied using several different techniques. However, the propagation and scattering through polycrystalline media with texture, which may be applied to any state of texture, have not been undertaken. Consequently an effort will be taken to understand the behavior of the attenuation and phase velocity in polycrystalline materials with general texture in Chapters 6 and 7 of this dissertation. It is anticipated that this research may provide a few useful insights to this challenging research subject on microstructural characterization.

1.2 Objective

The objective of this research is to develop a more comprehensive, general theoretical model for wave propagation and scattering in statistically anisotropic media, one of cracked media and one of textured media, that is expected to provide insightful information about the propagation constants and can also be used for guiding experimental design and for determining the materials properties for nondestructive evaluation techniques. Compact expressions will be derived for attenuations and wave velocities of the quasilongitudinal and two quasishear waves using stochastic wave theory in a generalized dyadic approach. The coordinate-free approach allows for nonrandom ensembles of properties to be studied with relative ease. The analysis of expressions is limited to frequencies below the geometric optics limit. The derivations are based upon the diagrammatic approach, in which the mean response is governed by the Dyson equation. The Dyson equation is then solved in the Fourier transform domain within the limits of the first-order smoothing approximation

(FOSA), or Keller approximation [48].

For cracked media, explicit expressions of wave attenuations and velocities in a medium with damage from randomly distributed penny-shaped microcracks will be first discussed. Under this assumption, the average effective medium is assumed statistically isotropic. The explicit results for the attenuations and wave velocities of longitudinal and shear elastic waves in the isotropic case show a good comparison with previous results developed. More importantly, this isotropic case provides the fundamentals for studying the statistically anisotropic cases. Next, the same framework is then extended to study the attenuation of elastic waves in solids with aligned cracks that are statistically homogeneous. In the uniaxially aligned crack situation, the crack alignment refers the case in which the unit normals of all cracks are randomly oriented within a plane of isotropy. Whereas, in the perfectly aligned crack case the unit normals of all cracks to be considered are perpendicular to the plane of isotropy. As such, the overall responses of the cracked solids are transversely isotropic with the plane that is perpendicular to the unit normals defining the plane of isotropy. Therefore, the attenuation is not only a function of frequency but also a function of propagation direction. In the presentation, both exact expressions of attenuations and wave speeds of the shear horizontal, quasilongitudinal, and quasishear vertical waves are presented. The resulting attenuations are investigated in terms of the directional, frequency, and damage dependence. The generalized anisotropic cases such as the orthorhombic symmetry could be the subject of future research in this direction.

In the case of polycrystalline materials with texture, attenuations and wave velocities will be developed in a general orthorhombic material made up of cubic crystallites.

The texture, preferred orientation of grains, is best quantitatively described by the orientation distribution function (ODF) defined as a probability density function, which is often expanded in a series generalized spherical harmonics [1],[2],[3]. In this dissertation, explicit attenuations of each wave type are derived as the function of dimensionless frequency and wave propagation directions, respectively, for given orientation distribution coefficients (ODCs). A relationship between the phase velocity and recrystallization characteristic variables, such as annealing time, is also investigated for specific examples. Finally, numerical results are presented and discussed in terms of the relevant dependent parameters. The theoretical results might be used to improve the understanding of the microstructure of polycrystals during the recrystallization process. Moreover, although the present application is for the case of orthohombic-cubic symmetry, the formalism can be easily modified to apply to other given symmetry cases.

This dissertation is organized in the following manner. Chapter 2 provides the preliminary elastodynamics of the wave propagation and scattering model for statistically anisotropic media. In Chapter 3, wave propagation and scattering in an isotropic, homogeneous medium with embedded microcracks which are randomly oriented are first investigated. Next, wave propagation and scattering in solids with uniaxially aligned cracks that are transverse isotropy and statistical homogeneity are examined in Chapter 4. In Chapter 5, wave attenuations in solids with perfectly aligned cracks are discussed. The exact results of attenuations are derived and example numerical results are presented to aid in a comparison with results presented by Hudson [70]. In Chapter 6, the phenomena of wave velocity and polarization of elastic waves moving through the textured polycrystals are examined.

The compact results of attenuations are formulated in terms of the orientation distribution coefficients (W_{lmn}) in Chapter 7. For both Chapter 6 and Chapter 7, numerical results are presented and discussed. Chapter 8 is the conclusion chapter, in which the results of the whole dissertation are summarized and discussed. In Chapter 9, future research subjects are addressed. The present formulation allows the study of backscattering problems to be examined in a straightforward manner. It is anticipated that this research work will be a valuable theoretical tool for use in ultrasonic nondestructive techniques to improve the understanding of the microstructure for both cracked and textured media in related research areas.

Chapter 2

Preliminary Elastodynamics

2.1 Introduction

Waves in solids are significantly important to engineering applications. Waves are a disturbance propagating in a medium. In order to understand wave behavior, mathematical and numerical tools are required to analyze and simulate the phenomena of waves in solids. Using these tools can also help us construct virtual views of waves in a medium. Solids are stressed when they are subjected to external forces or loads. Forces can be static or dynamic. Statics deal with the mechanics of solids and structures subject to the static loads. Solids that will experience dynamic motion under the action of dynamic forces which vary with time must apply the principles and theories of dynamics. The dynamic motion is often observed and noted as vibration and wave motion. It is not easy to draw exactly a clear line between vibration and wave motion, however, in general we can say that a wave is a localized vibration and a vibration is a motion of waves with very long wavelength. When talking about waves, one usually pays special attenuation to the motion or propagation

of a localized mechanical disturbance. When discussing vibration, one is concerned more with the global motion of the entire structure. Mathematically, both vibration and wave motion are governed by the same dynamic equations of motion, which may be derived using Newton's law. In this chapter, these principles and theories dealing with wave motion in solids are discussed, especially focusing on statistically anisotropic materials.

Depending on the material properties and loading conditions, solids can be treated as elastic meaning that the deformation in the solids disappears completely after it is unloaded. There are also solids that are plastic, which means that the deformation in the solids cannot be fully recovered when unloaded. Elasticity deals with solids and structures of elastic materials, while plasticity deals with those of plastic materials. This dissertation is focused on the solids of elastic materials. Waves propagating in elastic materials are termed elastic waves. One of the major applications of elastic waves is in the area of nondestructive evaluation. In such an application, ultrasonic waves are usually used and one can always keep the response level of materials within the elastic range. Otherwise, it could be destructive. Therefore, the topics in this dissertation are fully applicable in areas relating to nondestructive evaluation.

Materials can be regarded as isotropic or anisotropic. Isotropy means that material property does not vary with direction, while anisotropy means that material property is a function of direction. Deformation in an anisotropic material caused by a force applied in a direction may be significantly different from that resulted from the same force applied in another direction. Engineering materials such as cracked materials and polycrystalline materials are often regarded as anisotropic. The number of material constants necessary to

define the linear elastic response of anisotropic materials decreases with degree of anisotropy or increasing symmetry. At the limit, isotropic materials have only two independent elastic material constants, traditionally known as Young's modulus and Poisson's ratio. This chapter is focused on the theory of wave propagation and scattering in general anisotropic materials. All the formulations are, however, applicable to isotropic materials as a special case. Waves in an anisotropic material exhibit anisotropic characteristics, which means that their properties such as velocity and attenuation have direction dependence.

2.2 Ensemble Average Response

The equation of motion for the elastodynamic response of an infinite, linear-elastic material to deformation is given in terms of the Green's dyadic by

$$\left\{-\delta_{jk}\rho\partial_t^2 + \partial x_i C_{ijkl}\left(\mathbf{x}\right)\partial x_l\right\} G_{k\alpha}\left(\mathbf{x},\mathbf{x}';t\right) = \delta_{j\alpha}\delta^3\left(\mathbf{x}-\mathbf{x}'\right)\delta\left(t\right). \tag{2.1}$$

where $\delta^3\left(\mathbf{x}-\mathbf{x}'\right)$ is the three-dimensional spatial Delta function. The second order Green's dyadic, $G_{k\alpha}\left(\mathbf{x},\mathbf{x}';t\right)$, defines the response at location $\mathbf{x}$ in the kth direction to a unit impulse at location $\mathbf{x}'$ in the αth direction. The notation ∂_t^2 is defined as $\partial^2/\partial t^2$, and ∂x_i is defined as $\partial/\partial x_i$. The moduli are considered to vary spatially and density is assumed uniform throughout with units chosen such that density is unity [$\rho = 1$]. The moduli $\mathbf{C}$ are assumed to be spatially heterogeneous and have the form $C_{ijkl}(\mathbf{x}) = C^0_{ijkl} + \delta C_{ijkl}(\mathbf{x})$. Thus, the moduli have the form of average moduli, that is $C^0_{ijkl} = \langle C_{ijkl}(\mathbf{x})\rangle$, plus a fluctuation about this mean, $\delta C_{ijkl}(\mathbf{x})$. The fluctuations are assumed to have zero mean $\langle \delta C_{ijkl}(\mathbf{x})\rangle = 0$. The brackets, $\langle\rangle$, denote the ensemble average. The material properties might have global anisotropy, such that the mean moduli are not necessarily isotropic. The covariance of the

moduli is characterized by an eighth-rank tensor

$$\left\langle \delta C_{ijkl}\left(\mathbf{x}\right)\delta C_{\alpha\beta\gamma\delta}\left(\mathbf{x}'\right)\right\rangle = \mathbf{\Xi}_{ijkl}^{\alpha\beta\gamma\delta}\eta\left(\mathbf{x}-\mathbf{x}'\right) \ . \tag{2.2}$$

The spatial and tensorial parts of the above covariance, Ξ and η, are assumed independent. The correlation function η is also assumed as a function of the difference between two vectors, $\mathbf{x}-\mathbf{x}'$. This assumption implies that the medium is statistically homogeneous. For statistically isotropic materials, however, an additional assumption must be made such that η is a function of $|\mathbf{x}-\mathbf{x}'|$.

The spatio-temporal Fourier transform pair for the function $f(\mathbf{x},t)$ and $\widetilde{f}(\mathbf{p},\omega)$ is defined as

$$\begin{aligned} \tilde{f}\left(\mathbf{p},\omega\right) &= \int_{-\infty}^{+\infty}\int_{-\infty}^{+\infty} f\left(\mathbf{x},t\right)e^{i\omega t}e^{-i\mathbf{x}\cdot\mathbf{p}}d^3xdt, \\ f\left(\mathbf{x},t\right) &= \frac{1}{\left(2\pi\right)^4}\int_{-\infty}^{+\infty}\int_{-\infty}^{+\infty}\tilde{f}\left(\mathbf{p},\omega\right)e^{-i\omega t}e^{i\mathbf{x}\cdot\mathbf{p}}d^3pd\omega. \end{aligned} \tag{2.3}$$

These definitions allow Eq. (2.1) to be temporally transformed to the following form

$$\{\omega^2\delta_{jk}+C_{ijkl}^0\partial_i\partial_l+\partial_i\delta C_{ijkl}(\mathbf{x})\partial_l\}\mathbf{G}_{k\alpha}\left(\mathbf{x},\mathbf{x}';\omega\right)=\delta_{j\alpha}\delta^3\left(\mathbf{x}-\mathbf{x}'\right). \tag{2.4}$$

The random nature of the medium suggests that the Green's function, $\mathbf{G}$, is of little value as it will also be a random function. The interesting quantities are instead those related to the statistics of the response. These statistics include the mean response, $\langle\mathbf{G}\rangle$, and the covariance of the response, $\langle\mathbf{G}\mathbf{G}^*\rangle$, with the $*$ denoting a complex conjugate. This dissertation is devoted to examination of the mean response with corresponding phase velocities and attenuations.

Wave propagation and scattering problems of this sort do not lend themselves to solution by perturbation methods. As Frisch discussed, these solutions do not converge

[71]. Instead, Frisch used diagrammatic methods for solution of the mean response [71]. The mean response, $\langle \mathbf{G} \rangle$, is governed by the Dyson equation [50],[71]

$$\left\langle G_{i\alpha}\left(\mathbf{x},\mathbf{x}'\right)\right\rangle = G^0_{i\alpha}\left(\mathbf{x},\mathbf{x}'\right) + \int\int G^0_{i\beta}\left(\mathbf{x},\mathbf{y}\right) M_{\beta j}\left(\mathbf{y},\mathbf{z}\right)\left\langle G_{j\alpha}\left(\mathbf{z},\mathbf{x}'\right)\right\rangle d^3y d^3z. \tag{2.5}$$

The notation $G^0_{i\alpha}(\mathbf{x},\mathbf{x}')$ is the bare Green's dyadic defined as the ensemble average response of the medium (without fluctuations), namely, the solution to Eq. (2.1) when $\delta C_{ijkl}(\mathbf{x}) = 0$. The second order tensor $\mathbf{M}$ is the mass or self-energy operator. Equation (2.5) is easily solved in the Fourier transform domain under the assumption of statistical homogeneity. The spatial Fourier transform pair for $\mathbf{G}^0$ is given by

$$\begin{aligned} G^0_{i\alpha}\left(\mathbf{p}\right)\delta^3\left(\mathbf{p}-\mathbf{q}\right) &= \frac{1}{\left(2\pi\right)^3}\int\int G^0_{i\alpha}\left(\mathbf{x},\mathbf{x}'\right) e^{-i\mathbf{p}\cdot\mathbf{x}} e^{i\mathbf{q}\cdot\mathbf{x}'} d^3x d^3x', \\ G^0_{i\alpha}\left(\mathbf{x},\mathbf{x}'\right) &= \frac{1}{\left(2\pi\right)^3}\int\int G^0_{i\alpha}\left(\mathbf{p}\right)\delta^3\left(\mathbf{p}-\mathbf{q}\right) e^{i\mathbf{p}\cdot\mathbf{x}} e^{-i\mathbf{q}\cdot\mathbf{x}'} d^3p d^3q. \end{aligned} \tag{2.6}$$

The Fourier transforms which define $\langle \mathbf{G}(\mathbf{p}) \rangle$ and $\tilde{\mathbf{M}}(\mathbf{p})$ are given by expressions similar to that defining $\mathbf{G}^0(\mathbf{p})$. The assumption of statistical homogeneity ensures that $\mathbf{G}^0$, $\mathbf{M}$ and $\langle \mathbf{G} \rangle$ are functions of a single wave vector in Fourier space. The Dyson equation is then transformed and solved to give the result for $\langle \mathbf{G}\left(\mathbf{p}\right) \rangle$ of the form

$$\left\langle \mathbf{G}\left(\mathbf{p}\right)\right\rangle = \left[\mathbf{G}^0\left(\mathbf{p}\right)^{-1} - \tilde{\mathbf{M}}\left(\mathbf{p}\right)\right]^{-1}, \tag{2.7}$$

where $\tilde{\mathbf{M}}$ is the spatial transform of the self-energy. The Dyson equation is exact and describes the mean response of the medium. The main difficulty in the solution of Eq. (2.7) is the representation of $\mathbf{M}$. An approximation of the self-energy $\mathbf{M}$ can be written as an expansion in powers of moduli fluctuations. To first order [71],[48] $\mathbf{M}$ is expressed as [50]

$$M_{\beta j}\left(\mathbf{y},\mathbf{z}\right) \approx \left\langle \frac{\partial}{\partial y_\alpha}\delta C_{\alpha\beta\gamma\delta}\left(\mathbf{y}\right)\frac{\partial}{\partial y_\delta}G^0_{\gamma k}\left(\mathbf{y},\mathbf{z}\right)\frac{\partial}{\partial z_i}\delta C_{ijkl}\left(\mathbf{z}\right)\frac{\partial}{\partial z_l}\right\rangle. \tag{2.8}$$

Such an approximation is assumed valid if the fluctuations, $\delta\mathbf{C}$, are not too large. The spatial Fourier transform, as defined by Eq. (2.3), of the self-energy, $\mathbf{M}$, is then formulated. Manipulation of this integration allows it to be reduced to [50]

$$\tilde{M}_{\beta j}\left(\mathbf{p}\right) = \int d^3 s G^0_{\gamma k}(\mathbf{s}) p_\alpha p_l s_\delta s_i \mathbf{\Xi}^{\alpha\beta\gamma\delta}_{ijkl} \widetilde{\eta}(\mathbf{p}-\mathbf{s}). \tag{2.9}$$

Thus, the transform of the self-energy can be written as a convolution between the bare Green's dyadic and the Fourier transform of the covariance of the moduli fluctuations. The components of $\tilde{\mathbf{M}}$, Eq. (2.9) and the Dyson equation, Eq. (2.7), will be employed to calculate the phase velocity and attenuation of the wave modes next. Further details of the scattering theory can be found in the articles of Karal and Keller [48], Frisch [71], Stanke and Kino [47], Weaver [50], and Turner [57].

When ultrasonic waves propagate in anisotropic materials, the phase velocity and the associated polarization vector are generally determined by the Christoffel equation, which has been discussed in the literature [72],[73]. In this approach, the dispersion relations for the mean response are then given by the solution of the Dyson equation, Eq. (2.7), as

$$g_\beta\left(\mathbf{p}\right) = \left[g^0_\beta\left(\mathbf{p}\right)^{-1} - m_\beta\left(\mathbf{p}\right)\right]^{-1} = \left[\omega^2 - p^2 c^2_\beta - m_\beta\left(\mathbf{p}\right)\right]^{-1}, \tag{2.10}$$

for each wave type, β, inclusive of the quasilongitudinal (qP) and two quasishear ($qS1$ and $qS2$) waves. For the transversely isotropic case, the two quasishear waves are generally called the shear horizontal (SH) and quasishear vertical (qSV) waves. These are the expressions for the dispersion relation of the mean response, which defines the phase velocity and attenuation of each wave type from solution of

$$\omega^2 - p^2 c^2_\beta - m_\beta\left(\mathbf{p}\right) = 0, \tag{2.11}$$

for the wave vector $\mathbf{p}$. The phase velocity is given by the real part of $\mathbf{p}$ and the attenuation of each wave type is given by the imaginary part of $\mathbf{p}$. Such solutions of Eq. (2.10) are usually done numerically using root finding techniques [56]. However, explicit expressions of the attenuation can be determined using an approximation valid below the high-frequency geometric optics limit. In this case, the wave vector $\mathbf{p}$ within the self-energy is approximated as being equal to the bare wave vector. Such an approximation, $m_\beta(\mathbf{p}) \approx m_\beta\left(\frac{\omega}{c_\beta}\hat{\mathbf{p}}\right)$, is sometimes called a Born approximation [47],[50]. This approximation allows the imaginary part of $\mathbf{p}$ to be calculated directly from Eq. (2.11). Thus, the attenuations of each wave type are given by

$$\alpha_\beta(\hat{\mathbf{p}}) = -\frac{1}{2\omega c_\beta(\hat{\mathbf{p}})}\operatorname{Im} m_\beta\left(\frac{\omega}{c_\beta}\hat{\mathbf{p}}\right). \tag{2.12}$$

The final step in this derivation now lies in the expression for the imaginary part of the self-energy. The definition of the self-energy is given by Eq. (2.9). Approximate inner products allow each component of the self-energy to be determined independently. The wave numbers which appear in Eq. (2.9) are approximated to the same degree of the Born approximation discussed above. The integration over the magnitude of the wave vector is easily done due to the delta-function form of $\mathbf{G}^0(\mathbf{s})$. The attenuations for the three wave types, which are each defined in Eq. (2.12), are finally given in the general form [57],[74]

$$\begin{aligned}\alpha_\beta(\hat{\mathbf{p}}) \;=\; & \frac{1}{c_\beta^3(\hat{\mathbf{p}})}\left\{\frac{\pi}{4}\int d^2\hat{s}\,\frac{\omega^4}{c_{qS1}^5(\hat{\mathbf{s}})}\tilde{\tilde{\Xi}}\left(\frac{\omega}{c_\beta(\hat{\mathbf{p}})}\hat{\mathbf{p}}-\frac{\omega}{c_{qS1}(\hat{\mathbf{s}})}\hat{\mathbf{s}}\right)_{\cdots\hat{\mathbf{u}}_K\hat{\mathbf{p}}\hat{\mathbf{s}}\hat{\mathbf{v}}_1}^{\cdots\hat{\mathbf{u}}_K\hat{\mathbf{p}}\hat{\mathbf{s}}\hat{\mathbf{v}}_1}\right. \\ & +\frac{\pi}{4}\int d^2\hat{s}\,\frac{\omega^4}{c_{qP}^5(\hat{\mathbf{s}})}\tilde{\tilde{\Xi}}\left(\frac{\omega}{c_\beta(\hat{\mathbf{p}})}\hat{\mathbf{p}}-\frac{\omega}{c_{qP}(\hat{\mathbf{s}})}\hat{\mathbf{s}}\right)_{\cdots\hat{\mathbf{u}}_K\hat{\mathbf{p}}\hat{\mathbf{s}}\hat{\mathbf{v}}_2}^{\cdots\hat{\mathbf{u}}_K\hat{\mathbf{p}}\hat{\mathbf{s}}\hat{\mathbf{v}}_2} \\ & \left.+\frac{\pi}{4}\int d^2\hat{s}\,\frac{\omega^4}{c_{qS2}^5(\hat{\mathbf{s}})}\tilde{\tilde{\Xi}}\left(\frac{\omega}{c_\beta(\hat{\mathbf{p}})}\hat{\mathbf{p}}-\frac{\omega}{c_{qS2}(\hat{\mathbf{s}})}\hat{\mathbf{s}}\right)_{\cdots\hat{\mathbf{u}}_K\hat{\mathbf{p}}\hat{\mathbf{s}}\hat{\mathbf{v}}_3}^{\cdots\hat{\mathbf{u}}_K\hat{\mathbf{p}}\hat{\mathbf{s}}\hat{\mathbf{v}}_3}\right\},\end{aligned} \tag{2.13}$$

where K is defined as the polarization for the wave type β ($1, 2$ or 3 for wave types $qS1, qP$

and $qS2$, respectively). In the above equation, it is shown that the integrals are over the unit sphere, which is defined by unit vector $\hat{\mathbf{s}}$. The direction $\hat{\mathbf{p}}$ defines the propagation direction, $\hat{\mathbf{s}}$ is the scattered direction, and $\hat{\mathbf{u}}$ and $\hat{\mathbf{v}}$ are defined as the polarization directions. The dependence of the vectors $\hat{\mathbf{u}}$ on $\hat{\mathbf{p}}$ and of $\hat{\mathbf{v}}$ on $\hat{\mathbf{s}}$ is implicit. The argument of the correlation is the difference between the incoming and outgoing propagation directions. The inner products on the covariance of the moduli fluctuations are given in terms of four unit vectors. In the next section, the correlation function is discussed.

2.3 Correlation Function

The heterogeneous internal structure of almost all natural and man-made materials requires that any adequate theory concerning their macroscopic behavior should start with modeling them as random media. In the most general sense, a random medium consists of domains of different materials (phases) or the same materials in different states. In most situations, however, the details of the microstructure are not completely known. This knowledge naturally leads one to attempt to estimate the effective properties from partially statistical information on the sample in the form of a spatial correlation function. This presentation focuses attention on the instances in which the microscopic length scale is much larger than the molecular dimensions but much smaller than the characteristic length or correlation length of the macroscopic sample. In such circumstances, the random media such as fiber composites, cracked media, polycrystals, cements, rocks, and so on, can be viewed as a continuum on the microscopic scale. In order to study the statistical properties such as attenuation, it is necessary to introduce the spatial correlation function between the

different phases or different states in random media. Next the simplest correlation function is introduced, particularly focusing the applications on wave scattering problems.

As discussed in Eq. (2.2), the tensorial and spatial contributions of the material covariance are assumed independent. The spatial correlations are characterized by η and it is assumed that the simplest case of η has an exponential form

$$\eta(\mathbf{r}) = e^{-r/L}. \tag{2.14}$$

The correlation length, L, is of the order of the crack radius in cracked media or grain radius in polycrystals. As discussed by Stanke [75] an exponential function describes the correlation of continuous and discrete materials reasonably well. Such a model, with a single length scale, is perhaps oversimplified for materials containing a wide range of crack sizes for example. However, for many materials, such a model is expected to describe the statistics of the material properties well. Other correlation functions, such as that discussed by Markov and Willis [76], are thought to give similar results for the frequency range considered here. The influence of this choice of correlation function on the attenuations exists to some extent, but is left as a subject of future investigations. In Fourier transform space, the correlation function is then given by

$$\tilde{\eta}(\mathbf{q}) = \frac{L^3}{\pi^2(1 + L^2q^2)^2}. \tag{2.15}$$

The forms of the attenuation given above contain the difference of two vectors, $\tilde{\eta}(\mathbf{q}) = \tilde{\eta}([\omega/c_1(\Theta)]\,\hat{\mathbf{p}} - [\omega/c_2(\Theta')]\,\hat{\mathbf{s}})$ as the argument for the covariance in Eq. (2.2). Now the correlation functions $\tilde{W}_{\beta-\gamma}\,(\hat{\mathbf{p}}, \hat{\mathbf{s}})$ is considered. If the three nondimensional frequencies are then defined as $x_\beta = \omega L/c_\beta = kL$, using the expression of the spatial Fourier transform of the correlation function in Eq. (2.15), the functions $\tilde{W}_{\beta-\gamma}\,(\hat{\mathbf{p}}, \hat{\mathbf{s}})$ are then expressed in

terms of the above dimensionless quantities as

$$\tilde{W}_{\beta-\gamma}\left(\hat{\mathbf{p}},\hat{\mathbf{s}}\right)=\frac{L^3}{\pi^2\left(1+x_\beta^2\left(\hat{\mathbf{p}}\right)+x_\gamma^2\left(\hat{\mathbf{s}}\right)-2x_\beta\left(\hat{\mathbf{p}}\right)x_\gamma\left(\hat{\mathbf{s}}\right)\hat{\mathbf{p}}\cdot\hat{\mathbf{s}}\right)^2}, \tag{2.16}$$

for the incoming wave type β and outgoing wave type γ. The inner product, $\hat{\mathbf{p}}\cdot\hat{\mathbf{s}}=\cos\Theta\cos\Theta'\sin\phi\sin\phi'+\sin\Theta\sin\Theta'\sin\phi\sin\phi'+\cos\phi\cos\phi'$, if the unit vectors $\hat{\mathbf{p}}$ and $\hat{\mathbf{s}}$ are generally defined by $\hat{\mathbf{p}}=\mathbf{x}_1\cos\Theta\sin\phi+\mathbf{x}_2\sin\Theta\sin\phi+\mathbf{x}_3\cos\phi$ and $\hat{\mathbf{s}}=\mathbf{x}_1\cos\Theta'\sin\phi'+\mathbf{x}_2\sin\Theta'\sin\phi'+\mathbf{x}_3\cos\phi'$. The angles Θ, ϕ, and Θ', ϕ' are, respectively, defined as Euler angles in a general coordinate system. The form of the eighth-rank tensor, $\Xi_{ijkl}^{\alpha\beta\gamma\delta}$, is discussed next, respectively, for different cases in this presentation.

Chapter 3

Scattering in Damaged Solids

3.1 Introduction

The scattering of elastic waves in complex media, particularly at ultrasonic frequencies, is of importance to nondestructive testing, materials characterization and other research areas. Information about the decay in the coherent field due to scattering attenuation may often be used to infer information about the microstructure of the material [77]. The incoherent field also contains microstructural information. Quantitative comparisons with experimental results require a well-developed model of the effects of the microstructure on the wave behavior. If the microstructure is modified, such as through the development of microcracks within the medium, this change in microstructure would manifest itself in the scattered wave fields as well. In the case of structural materials such as concrete, polycrystalline metals and most composites, these microcracks are typically induced by loading, materials processing, manufacturing, aging and other in-service conditions. Changes in material response due to microcracking are typically inferred ultrasonically by the decrease

in wave velocity or the increase in ultrasonic attenuation, both of which indicate a stiffness degradation or loss of strength of the material [25]. The limits of detecting these changes in wave behavior depend on the amount of increased scattering due to the system of microcracks.

Damage is a continuous concept which is intuitively related to the microcracks. It is measured by the cumulative effect which these microcracks and other microdefects have on the macroscopic response [78],[79]. The effect of many microcracks can be described analytically by a damage parameter only when the material is statistically homogeneous in the neighborhood of the observed material point of the configuration. If a material is neither statistically homogeneous nor statistically self similar, a single tensor parameter may be used to represent the effect of many microcracks. In general, the damage may become a cause of or lead to fracture, but it is, by no means, synonymous with it.

In this chapter, a generalized tensor-based approach is used to examine the attenuation of elastic waves in an isotropic, homogeneous medium with embedded microcracks. The microcracks are assumed to be noninteracting, penny-shaped cracks that are randomly oriented. However, the coordinate-free approach allows for nonrandom ensembles of microcracks to be studied with relative ease. The topic of aligned cracks will be presented in the subsequent two chapters. It is assumed that the constitutive behavior of the stiffness matrix or compliance matrix in the pristine state is sufficiently characterized at the local level by a linear elastic relation between the average stresses and average strains of the traditional form. In standard damage mechanics theory [78],[79], the continuum model is described by a macroscopic damage parameter attributed to the microcracks. The effective

elastic moduli of the medium that contains many penny-shaped cracks is first presented using techniques discussed by Nemat-Nasser and Hori [80], Kachanov et al. [81] and Krajcinovic [79]. These techniques have been used to estimate the upper and lower bounds of the material properties with distributed damage. The general inequality was presented by Hashin and Shtrikman [82] using a variational approach. Similar ideas have been used to estimate the effective conductivity of such media [83]. The effective Lamé constants derived here are in agreement with previous analyses. Next, expressions for the moduli fluctuations are derived in terms of the single crack compliance and stiffness. The fluctuations and corresponding covariance of the moduli, which are necessary for the attenuation derivation, are then presented.

3.2 Effective Elastic Properties

A solid is considered to be damaged if some of the bonds connecting parts of its microstructure are missing. Bonds between the molecules in a crystallite lattice may be ruptured and the cohesion at the fiber-matrix interface may be lost. However, this type of damage cannot be measured *in situ* by nondestructive testing. Damage must, therefore, be measured indirectly by the effect it has on the effective material properties. Damage is a continuum concept which is intuitively related to the microcracks. It is measured by the cumulative effect which these microcracks have on the macroscopic response. As suggested in damage mechanics [78],[79], the rate of damage accumulation may be conveniently measured by the rate of change of the effective stiffness or compliance tensor. The present focus is on the elastic properties weakened by a large number of microcracks which are randomly

positioned throughout a large part of the representative volume element (RVE).

3.2.1 Linear Elastic Fracture Mechanics

Methods which make use of estimating the effective elastic properties of the statistically homogeneous elastic solids which contain a large number of microcracks were investigated by Nemat-Nasser and Hori [80], Kachanov et al. [81] and others. The first step in determining the effective properties of the damaged elastic solid involves consideration of a single penny-shaped crack, which is located within an infinite, homogeneous, isotropic and elastic continuum. In accordance with linear elastic fracture mechanics, the total, local and average stress $\overline{\boldsymbol{\sigma}}$ and strain $\overline{\boldsymbol{\gamma}}$ fields hold for superposition [84]. The average stress and strain are related by

$$\overline{\boldsymbol{\gamma}} = \overline{\mathbf{S}}\overline{\boldsymbol{\sigma}}, \qquad \text{or} \qquad \overline{\boldsymbol{\sigma}}=\overline{\mathbf{C}}\overline{\boldsymbol{\gamma}}, \tag{3.1}$$

where

$$\begin{aligned} \overline{\mathbf{S}} &= \mathbf{S} + \mathbf{S}^*, \\ \overline{\mathbf{C}} &= \mathbf{C} - \mathbf{C}^*. \end{aligned} \tag{3.2}$$

In Eqs. (3.1)-(3.2), $\overline{\boldsymbol{\gamma}} = \langle \boldsymbol{\gamma}(\mathbf{x}) \rangle$ and $\overline{\boldsymbol{\sigma}} = \langle \boldsymbol{\sigma}(\mathbf{x}) \rangle$ are the ensemble average strain and average stress, respectively. Here $\overline{\mathbf{S}}$ and $\overline{\mathbf{C}}$ are the effective compliance and effective stiffness, respectively, of the elastic solid which contains the cracks. $\mathbf{S}^*$ is defined as the effective compliance contributed by all cracks within the elastic solid and $\mathbf{C}^*$ is defined as the effective stiffness contributed by all cracks within the elastic solid. It should be noted that $(\mathbf{C}^*)^{-1} \neq \mathbf{S}^*$. The tensors $\mathbf{S}$ and $\mathbf{C}$ are the compliance and stiffness, respectively, of the pristine material.

The components of the effective compliance tensor $\mathbf{S}^*$ can be estimated from the contribution by the microcracks. The contributions are calculated by the complementary strain energy in terms of the path independent integral of fracture mechanics. The strain energy is expressed as

$$\psi^* = \int_0^a \frac{M}{a} da, \tag{3.3}$$

where ψ^* is the Gibb's energy and a is the crack radius. The factor M in the integrand is written as the line integral of the J integral (energy release rate) along the crack perimeter L

$$M = \oint_L aJdL. \tag{3.4}$$

The energy release rate J is expressed in terms of the stress intensity factors K_m ($m = \mathrm{I}, \mathrm{II}, \mathrm{III}$) corresponding to the three fundamental crack modes as

$$J = \frac{1-\nu}{2\mu}(K_{\mathrm{I}}^2 + K_{\mathrm{II}}^2) + \frac{1}{2\mu}K_{\mathrm{III}}^2, \tag{3.5}$$

where ν and μ are the Poisson's ratio and shear modulus, respectively, of the surrounding material. Thus, the final Gibbs' energy is derived in compact form as

$$\psi^* = \int_0^a \left[\oint \overline{M}_{mn} K_m K_n dL \right] da. \tag{3.6}$$

The tensor $\bar{\mathbf{M}}$ is given by

$$\overline{M}_{mn} = \frac{1}{2\mu}\left[(1-\nu)\delta_{mn} + \nu\delta_{m\mathrm{III}}\delta_{n\mathrm{III}}\right], \tag{3.7}$$

where δ_{mn} is the Kronecker delta, and the subscript n also represents the three fundamental cracks modes I, II, or III.

The symmetric forms of the expressions for the stress intensity factors of a penny-shaped crack embedded in a homogeneous, isotropic and elastic material are [85]

$$\begin{aligned} K_{\mathrm{I}} &= \frac{2}{\pi}\widetilde{\sigma}_{11}\sqrt{\pi a}, \\ K_{\mathrm{II}} &= \frac{2}{\pi}\frac{1}{2-\nu}\sqrt{\pi a}\left[(\widetilde{\sigma}_{12}+\widetilde{\sigma}_{21})\cos\alpha+(\widetilde{\sigma}_{13}+\widetilde{\sigma}_{31})\sin\alpha\right], \\ K_{\mathrm{III}} &= \frac{2}{\pi}\frac{1-\nu}{2-\nu}\sqrt{\pi a}\left[(\widetilde{\sigma}_{12}+\widetilde{\sigma}_{21})\sin\alpha-(\widetilde{\sigma}_{13}+\widetilde{\sigma}_{31})\cos\alpha\right], \end{aligned} \tag{3.8}$$

where $\widetilde{\sigma}_{ij}$ are the stress components in the crack coordinate system and α is the angle defined by the orientation of a penny-shaped crack. Expressions (3.8) are valid only if the stress component $\widetilde{\sigma}_{11}$ normal to the crack surface is tensile. Differentiating Eq. (3.8) with respect to the stresses leads to the following expressions

$$\begin{aligned} \frac{\partial K_{\mathrm{I}}}{\partial\widetilde{\sigma}_{ij}} &= \frac{2}{\pi}\sqrt{\pi a}\delta_{i1}\delta_{j1}, \\ \frac{\partial K_{\mathrm{II}}}{\partial\widetilde{\sigma}_{ij}} &= \frac{2}{\pi}\frac{1}{2-\nu}\sqrt{\pi a}\left[(\delta_{i1}\delta_{j2}+\delta_{i2}\delta_{j1})\cos\alpha+(\delta_{i1}\delta_{j3}+\delta_{i3}\delta_{j1})\sin\alpha\right], \\ \frac{\partial K_{\mathrm{III}}}{\partial\widetilde{\sigma}_{ij}} &= \frac{2}{\pi}\frac{1-\nu}{2-\nu}\sqrt{\pi a}\left[(\delta_{i1}\delta_{j2}+\delta_{i2}\delta_{j1})\sin\alpha-(\delta_{i1}\delta_{j3}+\delta_{i3}\delta_{j1})\cos\alpha\right]. \end{aligned} \tag{3.9}$$

The stress intensity factor associated with the pure mode vanishes ($K_{\mathrm{I}}=0$) when the stress component $\widetilde{\sigma}_{11}$ normal to the crack surface is compressive.

3.2.2 Compliance Tensor Attributable to a Single Crack

The components of the compliance tensor are related to the Gibb's energy through $\widetilde{S}^{(s)}_{ijkl}=\partial^2\psi^*/\partial\widetilde{\sigma}_{ij}\partial\widetilde{\sigma}_{kl}$ (in the local coordinate system, the notation ($\tilde{}$) is used). Thus, the compliance attributed to the presence of a single penny-shaped active crack in a representative volume V is then

$$\widetilde{S}^{(s)}_{ijkl}=\frac{2}{V}\int_0^a\left[\oint\overline{M}_{mn}\frac{\partial K_m}{\partial\widetilde{\sigma}_{ij}}\frac{\partial K_n}{\partial\widetilde{\sigma}_{kl}}dL\right]da. \tag{3.10}$$

Substituting K_m into Eq. (3.10) and integrating gives the compact form [79]

$$\widetilde{S}^{(s)}_{ijkl} = \frac{16}{3V}\frac{1-\widetilde{\nu}}{2-\widetilde{\nu}}\frac{1}{2\widetilde{\mu}}a^3\{2\widetilde{I}^5_{ijkl} - \widetilde{\nu}\widetilde{I}^6_{ijkl}\}. \tag{3.11}$$

In the global coordinate system, using a coordinate transformation and assuming the normal stress at the crack surface is tensile, the effective compliance attributable to a single, planar, penny-shaped crack of radius a is written in the simple form

$$S^{(s)}_{ijkl} = \frac{16}{3V}\frac{1-\nu}{2-\nu}\frac{1}{2\mu}a^3\{2I^5_{ijkl} - \nu I^6_{ijkl}\}. \tag{3.12}$$

The compliance of a single crack is dependent on the unit normal $\hat{\mathbf{m}}$, which defines the crack orientation. This orientation is implicit in the tensors $\mathbf{I}^5, \mathbf{I}^6$. These tensors and other necessary basis tensors are given in terms of unit normal vector $\hat{\mathbf{m}}$ and Kronecker delta δ_{ij} as [86]

$$\begin{gathered} I^1_{ijkl} = \frac{1}{2}(\delta_{ik}\delta_{jl} + \delta_{il}\delta_{jk}), \qquad I^2_{ijkl} = \delta_{ij}\delta_{kl}, \\ I^3_{ijkl} = \delta_{ij}\hat{m}_k\hat{m}_l, \quad I^4_{ijkl} = \hat{m}_i\hat{m}_j\delta_{kl}, \quad I^6_{ijkl} = \hat{m}_i\hat{m}_j\hat{m}_k\hat{m}_l, \\ I^5_{ijkl} = \frac{1}{4}(\hat{m}_i\hat{m}_k\delta_{jl} + \hat{m}_i\hat{m}_l\delta_{jk} + \hat{m}_j\hat{m}_k\delta_{il} + \hat{m}_j\hat{m}_l\delta_{ik}). \end{gathered} \tag{3.13}$$

3.2.3 Stiffness Tensor Attributable to a Single Crack

If it is assumed that the damaged medium is statistically homogeneous and statistically isotropic, the effective compliance attributable to one single crack is approximately the inverse of the effective stiffness. It is convenient to derive the attenuation in terms of the effective stiffness attributable to one penny-shaped crack. The compliance tensor of the pristine, undamaged elastic matrix is

$$S^0_{ijkl} = \frac{1}{2\mu}(I^1_{ijkl} - \frac{\nu}{1+\nu}\ I^2_{ijkl}). \tag{3.14}$$

Then the effective compliance expression for a simple crack in a matrix can be written

$$\widehat{\mathbf{S}} = \mathbf{S}^{(s)} + \mathbf{S}^{0} = \frac{1}{2\mu} e_i \mathbf{I}^i, \tag{3.15}$$

in which

$$\begin{aligned} e_1 = 1, \qquad e_2 = -\frac{\nu}{1-\nu}, \qquad e_3 = e_4 = 0, \\ e_5 = \frac{32}{3}\frac{1-\nu}{2-\nu}a^3, \qquad e_6 = -\frac{16}{3}\frac{\nu(1-\nu)}{2-\nu}a^3, \end{aligned} \tag{3.16}$$

where the repeated index i denotes the summation convention over the range of $i = 1 - 6$. It should be noted that this summation convention and range are used throughout the dissertation. To calculate the stiffness tensor, the other irreducible tensor basis $\mathbf{J}$ ($J^i, i = 1, 2, ...6$) is used [86]. These basis tensors may be formed from the tensors $\mathbf{I}$ using a linear transformation. The effective compliance tensor expressed in terms of the $\mathbf{J}$ basis tensors is given by

$$\widehat{\mathbf{S}} = \frac{1}{2\mu} f_i \mathbf{J}^i, \tag{3.17}$$

where

$$\begin{aligned} f_1 &= \frac{2-\nu}{2(1+\nu)} + \frac{8}{3}(1-\nu)a^3, \quad f_2 = \frac{\nu}{2(1+\nu)} + \frac{8}{3}(1-\nu)a^3, \\ f_3 &= -\frac{3\nu}{2(1+\nu)}, \qquad f_4 = -\frac{\nu}{2(1+\nu)}, \\ f_5 &= 1 + \frac{16}{3}\frac{1-\nu}{2-\nu}a^3, \qquad f_6 = 1. \end{aligned} \tag{3.18}$$

The effective stiffness tensor may also be expanded in a similar way as

$$\widehat{\mathbf{C}} = \widehat{\mathbf{S}}^{-1} = 2\mu b_i \mathbf{J}^i, \tag{3.19}$$

where the scalar coefficients b_i are related to the scalar coefficients f_i,

$$\{b_1, b_2, b_3, b_4, b_5, b_6\} = \Delta \left\{ f_1, -f_2, -f_3, -f_4, \frac{1}{f_5\Delta}, \frac{1}{f_6\Delta} \right\}, \tag{3.20}$$

with

$$\Delta^{-1} = f_1^2 - f_2^2 - f_3^2 + f_4^2. \tag{3.21}$$

If the penny-shaped crack volume is much smaller than the representative volume, the higher order terms in the coefficients may be neglected. This truncation is used to simplify the form of the derivation that follows and places some limits on the resulting attenuations. In this case, the corresponding coefficients are

$$\begin{aligned}
b_1 &= \frac{2-\nu}{2(1-2\nu)} + \frac{8}{3}\frac{(1-\nu)(-3\nu^2+2\nu-1)}{(1-2\nu)^2}a^3, \\
b_2 &= -\frac{\nu}{2(1-2\nu)} - \frac{8}{3}\frac{(1-\nu)(-\nu^2-2\nu+1)}{(1-2\nu)^2}a^3, \\
b_3 &= \frac{3\nu}{2(1-2\nu)} - \frac{8}{3}\frac{3\nu(1-\nu)^2}{(1-2\nu)^2}a^3, \\
b_4 &= \frac{\nu}{2(1-2\nu)} - \frac{8}{3}\frac{\nu(1-\nu)^2}{(1-2\nu)^2}a^3, \\
b_5 &= 1 - \frac{16}{3}\frac{1-\nu}{2-\nu}a^3, \qquad b_6 = 1.
\end{aligned} \tag{3.22}$$

Again the effective stiffness is represented in terms of the six fourth order tensors $\mathbf{I}$,

$$\widehat{\mathbf{C}} = 2\mu c_i \mathbf{I}^i, \tag{3.23}$$

where the coefficients c_i are

$$\begin{aligned}
c_1 = 1, \quad c_2 &= \frac{\nu}{1-\nu} - \frac{16}{3}\frac{\nu^2(1-\nu)}{(1-2\nu)^2}a^3 \\
c_3 = c_4 &= -\frac{16}{3}\frac{\nu(1-\nu)}{1-2\nu}a^3, \\
c_5 = -\frac{32}{3}\frac{1-\nu}{2-\nu}a^3, \quad c_6 &= \frac{16}{3}\frac{\nu(1-\nu)}{2-\nu}a^3.
\end{aligned} \tag{3.24}$$

The single crack stiffness reduces the stiffness of the pristine, undamaged elastic matrix with stiffness $\mathbf{C}^0 = 2\mu(\mathbf{I}^1 + \frac{\nu}{1-\nu}\mathbf{I}^2)$. Thus, the effective stiffness of the crack in a unit volume of

matrix is

$$\mathbf{C}^{(s)} = \mathbf{C}^0 - \widehat{\mathbf{C}} = 2\mu d_i \mathbf{I}^i, \tag{3.25}$$

where the coefficients d_i are

$$\begin{aligned} d_1 = 0, \quad d_2 = \frac{16}{3}\frac{\nu^2(1-\nu)}{(1-2\nu)^2}a^3, \\ d_3 = d_4 = \frac{16}{3}\frac{\nu(1-\nu)}{1-2\nu}a^3, \\ d_5 = \frac{32}{3}\frac{1-\nu}{2-\nu}a^3, \quad d_6 = -\frac{16}{3}\frac{\nu(1-\nu)}{2-\nu}a^3. \end{aligned} \tag{3.26}$$

3.2.4 Ensemble Average Stiffness

To estimate the ensemble average properties, an infinitely extended, homogeneous, isotropic and elastic three-dimensional continuum is considered. The medium is assumed to contain a large number of microcracks which do not interact with each other. The effective compliance or stiffness may be determined by the superposition of the contributions of individual microcracks. In the case of a large number of microcracks, the summation can be replaced by an integration over a continuous distribution of crack sizes and orientations. The penny-shaped crack is characterized by its radius a and two Euler angles θ and φ that define the orientation of the unit normal $\hat{\mathbf{m}}$ as shown in Fig. 3.1. The specific distribution of the crack radii and orientations is expressed by the probability density function $W(a, \theta, \varphi)$. In some situations, the microcrack radii, shapes and orientations may be correlated. The density function is then replaced by the probability density function $P(a, \theta, \varphi) = P^{\theta\varphi}(\theta, \varphi) P^a(a|\theta, \varphi)$. Here, however, it is assumed that the microcrack radii and orientations are not correlated. In this case, the density function is expressed as

$$W(a, \theta, \varphi) = A(a)\, \zeta(\theta, \varphi). \tag{3.27}$$

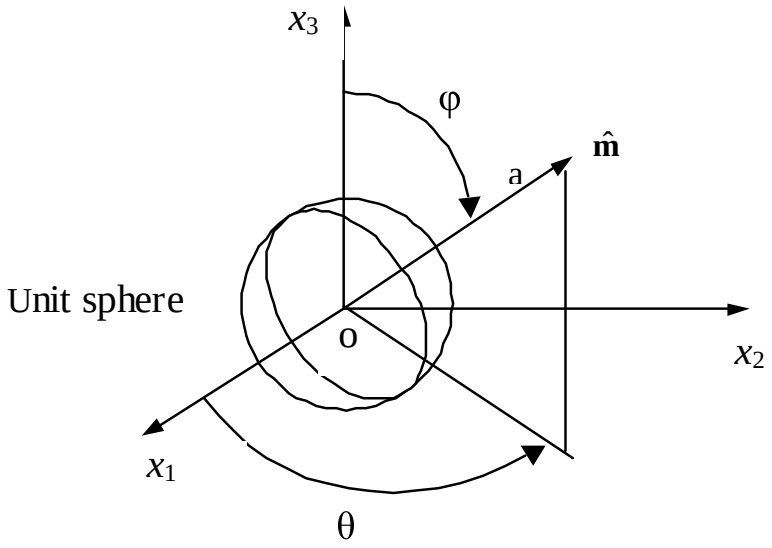

Figure 3.1: Geometry of a penny-shaped crack.

The effective continuum properties per unit volume are expressed in terms of an ensemble average utilizing the density function (3.27) and Eq. (3.25) such that

$$C^*_{ijkl} = \frac{\varepsilon}{4\pi} \int_0^{2\pi} \int_{-\pi/2}^{\pi/2} C^{(s)}_{ijkl} \zeta\left(\theta, \varphi\right) d\theta \sin\varphi d\varphi. \tag{3.28}$$

In Eq. (3.28), the non-dimensional microcrack density per unit volume is defined by

$$\varepsilon = N \left\langle a^3 \right\rangle = \int_{a^-}^{a^+} A(a) a^3 da, \tag{3.29}$$

where N is number of cracks per unit volume and the angular brackets represent the ensemble average. This damage density was introduced by Walsh [87] for the case of an isotropic distribution of the penny-shaped microcracks. A more general form of the damage factor in terms of elliptical microcracks was given by Budiansky and O'Connell [88]

$$\varepsilon = \frac{2N}{\pi} \left\langle \frac{\Gamma^2}{P} \right\rangle, \tag{3.30}$$

where Γ and P are the crack surface area and the perimeter length, respectively.

The simplest model of the microcrack distribution is assumed when their orientations are random. In this case, the normal to the microcrack plane takes every direction with equal probability, such that the effective compliance or stiffness tensor attributable to the presence of microcracks is isotropic. In this case, the density function in Eq. (3.27) is given by

$$\zeta(\theta, \varphi) = 1. \tag{3.31}$$

The effective stiffness attributable to the presence of N active microcracks per unit volume is then derived from the Eq. (3.28)

$$C^*_{ijkl} = \frac{\varepsilon}{4\pi} \int_0^{2\pi} \int_{-\pi/2}^{\pi/2} C^{(s)}_{ijkl}(\theta, \varphi) \sin\varphi d\theta d\varphi, \tag{3.32}$$

where $C^{(s)}_{ijkl}$ is given by Eqs. (3.25) and (3.26). Carrying out the integration in Eq. (3.32) gives the effective stiffness due to an isotropic distribution of penny shaped microcracks as

$$C^*_{ijkl} = \frac{16}{45} \frac{1-\nu}{2-\nu} 2\mu\varepsilon \left\{ 2(5-\nu) I^1_{ijkl} + \frac{\nu(\nu^2 - 16\nu + 19)}{(1-2\nu)^2} I^2_{ijkl} \right\}. \tag{3.33}$$

The stiffness tensor of the homogeneous, isotropic and elastic solids in its pristine, undamaged state is

$$C^0_{ijkl} = \lambda I^2_{ijkl} + 2\mu I^1_{ijkl}. \tag{3.34}$$

Here, the ensemble average stiffness is redefined such that the average fluctuations are zero. Such a procedure, while not necessary, is convenient for the calculation of material covariance and attenuation. The moduli are assumed to be spatially varying and of the form

$$\overline{C}_{ijkl}(\mathbf{x}) = \overline{C}^0_{ijkl} + \delta\overline{C}_{ijkl}(\mathbf{x}), \tag{3.35}$$

where

$$\overline{C}^0_{ijkl} = C^0_{ijkl} - C^*_{ijkl}. \tag{3.36}$$

Thus, the moduli have the form of the average moduli

$$\overline{C}^0_{ijkl} = \left\langle \overline{C}_{ijkl}(\mathbf{x}) \right\rangle = \overline{\lambda} I^2_{ijkl} + 2\overline{\mu} I^1_{ijkl}. \tag{3.37}$$

plus the fluctuation about the mean $\delta\overline{C}_{ijkl}$. Hence, $\overline{C}_{ijkl}$ has the average value of $\overline{C}^0_{ijkl}$ and $\delta\overline{C}_{ijkl}$ represents the modulus fluctuation. The effective constants are

$$\begin{aligned} \overline{\mu} &= \mu\left[1 - \frac{32}{45}\frac{(1-\nu)(5-\nu)}{2-\nu}\varepsilon\right], \\ \overline{\lambda} &= \lambda\left[1 - \frac{16}{45}\frac{(1-\nu)(\nu^2-16\nu+19)}{(2-\nu)(1-2\nu)}\varepsilon\right]. \end{aligned} \tag{3.38}$$

These results are identical with the results obtained by Krajcinovic [79], Kachanov et al. [89], Budiansky and O'Connell [88] and Zimmerman [90]. The effective properties of the damaged material are shown by Eqs. (3.38) to be linearly related to the damage parameter ε. Thus, wave speed changes that are the result of damage will scale linearly with ε as well.

The fluctuations, which are defined here to have zero average, $\left\langle \delta\overline{C} \right\rangle = 0$, are given by

$$\delta\overline{C}_{ijkl}(\mathbf{x}) = C^*_{ijkl} - C^{(s)}_{ijkl} H(\mathbf{x}), \tag{3.39}$$

The function $H(\mathbf{x})$ is defined as

$$H(\mathbf{x}) = \begin{cases} 1 & \text{if } \mathbf{x} \in \mathbf{S} \\ 0 & \text{otherwise} \end{cases}, \tag{3.40}$$

where $\mathbf{S}$ is the space occupied by the crack phase.

3.3 Mean Response

The mean response, $\langle \mathbf{G}(\mathbf{p}) \rangle$, is given by the solution of the Dyson equation, Eq.(2.7), above. The solution of $\langle \mathbf{G}(\mathbf{p}) \rangle$ is expressed in terms of $\mathbf{G}^0(\mathbf{p})$ and $\tilde{\mathbf{M}}(\mathbf{p})$. For the statistically isotropic case, the bare Green's dyadic, $\mathbf{G}^0$, is the solution of Eq. (2.4) with the modulus fluctuation equal to zero. Hence

$$\mathbf{G}^0(\mathbf{p}) = \hat{\mathbf{p}}\hat{\mathbf{p}} g_L^0(p) + (\mathbf{I} - \hat{\mathbf{p}}\hat{\mathbf{p}}) g_T^0(p), \tag{3.41}$$

for propagation in the $\hat{\mathbf{p}}$ direction. The bare longitudinal wave $g_L^0(p)$ and transverse wave $g_T^0(p)$ propagators are denoted

$$\begin{aligned} g_L^0(p) &= \left[\omega^2 - p^2 c_L^2\right]^{-1}, \\ g_T^0(p) &= \left[\omega^2 - p^2 c_T^2\right]^{-1}, \end{aligned} \tag{3.42}$$

where the c_L and c_T are the average longitudinal and transverse wave speeds, respectively. The Fourier transforms which define $\langle \mathbf{G}(\mathbf{p}) \rangle$ and $\tilde{\mathbf{M}}(\mathbf{p})$ are given by expressions similar to those defining $\mathbf{G}^0(\mathbf{p})$. The spatial transform of the self-energy and the mean Green's dyadic have the same form as the bare Green's dyadic. Hence, one may write

$$\begin{aligned} \tilde{\mathbf{M}}(\mathbf{p}) &= \hat{\mathbf{p}}\hat{\mathbf{p}} m_L(p) + (\mathbf{I} - \hat{\mathbf{p}}\hat{\mathbf{p}}) m_T(p), \\ \left\langle \tilde{\mathbf{G}}(\mathbf{p}) \right\rangle &= \hat{\mathbf{p}}\hat{\mathbf{p}} g_L(p) + (\mathbf{I} - \hat{\mathbf{p}}\hat{\mathbf{p}}) g_T(p), \end{aligned} \tag{3.43}$$

where

$$\begin{aligned} m_L(\mathbf{p}) &= -\int d^3 s \; \begin{matrix} \hat{\mathbf{p}}\hat{\mathbf{p}}\hat{\mathbf{s}}\cdots \\ \hat{\mathbf{p}}\hat{\mathbf{p}}\hat{\mathbf{p}}\cdots \end{matrix} \Xi_{\cdot\cdot} \{ \begin{matrix} \hat{\mathbf{s}} \\ \hat{\mathbf{s}} \end{matrix} g_L^0(\mathbf{s}) + (\mathbf{I} - \begin{matrix} \hat{\mathbf{s}} \\ \hat{\mathbf{s}} \end{matrix}) g_T^0(\mathbf{s}) \} \tilde{\eta}(\mathbf{p} - \mathbf{s}), \\ m_T(\mathbf{p}) &= -\frac{1}{2} \int d^3 s \; (\mathbf{I} - \begin{matrix} \hat{\mathbf{p}} \\ \hat{\mathbf{p}} \end{matrix}) \; \begin{matrix} \hat{\mathbf{p}}\hat{\mathbf{s}}\cdots \\ \hat{\mathbf{p}}\hat{\mathbf{p}}\cdots \end{matrix} \Xi_{\cdot\cdot} \{ \begin{matrix} \hat{\mathbf{s}} \\ \hat{\mathbf{s}} \end{matrix} g_L^0(\mathbf{s}) + (\mathbf{I} - \begin{matrix} \hat{\mathbf{s}} \\ \hat{\mathbf{s}} \end{matrix}) g_T^0(\mathbf{s}) \} \tilde{\eta}(\mathbf{p} - \mathbf{s}). \end{aligned} \tag{3.44}$$

and

$$\begin{aligned} g_L(p) &= [\omega^2 - p^2 c_L^2 + m_L(p)]^{-1}, \\ g_T(p) &= [\omega^2 - p^2 c_T^2 + m_T(p)]^{-1}. \end{aligned} \tag{3.45}$$

These are the expressions for the mean response. They define the phase velocity and the attenuation of longitudinal and transverse wave types in statistically isotropic media. Using Eqs. (2.11) and (2.12), the attenuations in statistically isotropic media, which are the imaginary part for each wave type, can be derived. The imaginary parts of m_β (where $\beta = L$ or T) are determined from Eqs. (3.44) such that the attenuations are given by

$$\begin{aligned} \alpha_L(\hat{\mathbf{p}}) = \frac{\pi}{4\omega c_L} \int & \hat{\mathbf{p}}\hat{\mathbf{p}}\hat{\mathbf{s}}\hat{\mathbf{s}}\cdots\cdot \Xi \widetilde{\eta}\left(\hat{\mathbf{p}}\frac{\omega}{c_L} - \hat{\mathbf{s}}\frac{\omega}{c_L}\right)\frac{\omega^5}{c_L^7} d^2\hat{\mathbf{s}} \\ + \frac{\pi}{4\omega c_T} \int & \hat{\mathbf{p}}\hat{\mathbf{p}}\hat{\mathbf{s}}(\mathbf{I}-\hat{\mathbf{s}})\cdots\cdot \Xi\, \widetilde{\eta}\left(\hat{\mathbf{p}}\frac{\omega}{c_L} - \hat{\mathbf{s}}\frac{\omega}{c_T}\right)\frac{\omega^5}{c_T^5 c_L^2} d^2\hat{\mathbf{s}}, \end{aligned} \tag{3.46}$$

and

$$\begin{aligned} \alpha_T(\hat{\mathbf{p}}) = \frac{\pi}{8\omega c_L} \int & \left(\mathbf{I}-\hat{\mathbf{p}}\right)_{\hat{\mathbf{p}}\hat{\mathbf{s}}\hat{\mathbf{s}}\cdots\cdot}^{\hat{\mathbf{p}}\hat{\mathbf{s}}\hat{\mathbf{s}}\cdots\cdot} \Xi\, \widetilde{\eta}\left(\hat{\mathbf{p}}\frac{\omega}{c_T} - \hat{\mathbf{s}}\frac{\omega}{c_L}\right)\frac{\omega^5}{c_L^5 c_T^2} d^2\hat{\mathbf{s}} \\ + \frac{\pi}{8\omega c_T} \int & (\mathbf{I}-\hat{\mathbf{p}})_{\hat{\mathbf{p}}\hat{\mathbf{s}}}^{\hat{\mathbf{p}}\hat{\mathbf{s}}}(\mathbf{I}-\hat{\mathbf{s}})\cdots\cdot \Xi\, \widetilde{\eta}(\hat{\mathbf{p}}\frac{\omega}{c_T} - \hat{\mathbf{s}}\frac{\omega}{c_T})\frac{\omega^5}{c_T^7} d^2\hat{\mathbf{s}}, \end{aligned} \tag{3.47}$$

where the integrals are over the unit sphere $\hat{\mathbf{s}}$. Three additional functions are defined as

$$\begin{aligned} \eta_{LL}(\theta_{ps}) &= \widetilde{\eta}(\hat{\mathbf{p}}\frac{\omega}{c_L} - \hat{\mathbf{s}}\frac{\omega}{c_L}), \\ \eta_{TT}(\theta_{ps}) &= \widetilde{\eta}(\hat{\mathbf{p}}\frac{\omega}{c_T} - \hat{\mathbf{s}}\frac{\omega}{c_T}), \\ \eta_{LT}(\theta_{ps}) &= \eta_{TL}(\theta_{ps}) = \widetilde{\eta}(\hat{\mathbf{p}}\frac{\omega}{c_L} - \hat{\mathbf{s}}\frac{\omega}{c_T}), \end{aligned} \tag{3.48}$$

where the direction $\hat{\mathbf{p}}$ defines the propagation direction, $\hat{\mathbf{s}}$ defines the scattered direction, and θ_{ps} is the angle between these directions (i.e., $\cos\theta_{ps} = \hat{\mathbf{p}} \cdot \hat{\mathbf{s}}$).

3.4 Attenuations

To derive the attenuations, the relevant inner products on the covariance of the effective moduli fluctuations are required. The covariance of the moduli fluctuations is represented by an eight-order tensor which is given in Eq. (2.2). The inner product is given explicitly by

$$\Xi^{\cdots\hat{\mathbf{u}}\hat{\mathbf{p}}\hat{\mathbf{s}}\hat{\mathbf{v}}}_{\cdots\hat{\mathbf{u}}\hat{\mathbf{p}}\hat{\mathbf{s}}\hat{\mathbf{v}}} = \Xi^{\alpha\beta\gamma\delta}_{ijkl}\hat{u}_\beta\hat{u}_k\hat{p}_\alpha\hat{p}_l\hat{s}_i\hat{s}_\delta\hat{v}_\gamma\hat{v}_j \tag{3.49}$$

The covariance here is given in terms of an average over all crack orientations. Thus, the crack normal $\hat{\mathbf{m}}$ may vary over all possible directions. In this case, the following identities are needed

$$\begin{aligned}
\langle\hat{m}_i\hat{m}_j\rangle &= \frac{1}{3}\delta_{ij},\\
\langle\hat{m}_i\hat{m}_j\hat{m}_k\hat{m}_l\rangle &= \frac{1}{15}\left(\delta_{ij}\delta_{kl}+\delta_{ik}\delta_{jl}+\delta_{il}\delta_{jk}\right),\\
\langle\hat{m}_i\hat{m}_j\hat{m}_k\hat{m}_l\hat{m}_\alpha\hat{m}_\beta\rangle &= \frac{1}{105}(\delta_{ij}\delta_{kl}\delta_{\alpha\beta}\\
&\quad + \text{all permutations} - 15 \text{ terms in all}),\\
\langle\hat{m}_i\hat{m}_j\hat{m}_k\hat{m}_l\hat{m}_\alpha\hat{m}_\beta\hat{m}_\gamma\hat{m}_\delta\rangle &= \frac{1}{945}(\delta_{ij}\delta_{kl}\delta_{\alpha\beta}\delta_{\gamma\delta}\\
&\quad + \text{all permutations} - 105 \text{ terms in all }),
\end{aligned} \tag{3.50}$$

where the brackets, $\langle\rangle$, denote the ensemble average. All averages of odd numbers of $\hat{\mathbf{m}}$'s are zero. The average of the tensorial part of the covariance over all orientations of crack normal is defined by

$$\Xi^{\alpha\beta\gamma\delta}_{ijkl} = \frac{1}{4\pi}\int_0^{2\pi}\int_{-\pi/2}^{\pi/2}\overline{C}^{(s)}_{ijkl}\overline{C}^{(s)}_{\alpha\beta\gamma\delta}\sin\varphi d\varphi d\theta. \tag{3.51}$$

Here we use the relation $\langle H(\mathbf{x})H(\mathbf{y})\rangle = \varepsilon\Pr(r|0)$, where $\Pr(r|0) = (1-\varepsilon)\eta(r)+\varepsilon$ is defined as the conditional probability [76]. The notation r is the magnitude of the difference between

two vectors. Here, the second order terms in ε are neglected under the assumption that the damage density is small. Thus, $\langle \delta C_{ijkl}(\mathbf{x}) \delta C_{\alpha\beta\gamma\delta}(\mathbf{y}) \rangle = \varepsilon \eta(r) \, \Xi_{ijkl}^{\alpha\beta\gamma\delta}$. It is noted that

$$\overline{\mathbf{C}}^{(s)} = 2\mu \overline{d}_i \mathbf{I}^i, \tag{3.52}$$

with

$$\begin{aligned} \overline{d}_1 &= 0, \quad \overline{d}_2 = \frac{16}{3} \frac{\nu^2(1-\nu)}{(1-2\nu)^2}, \quad \overline{d}_5 = \frac{32}{3} \frac{1-\nu}{2-\nu}, \\ \overline{d}_3 &= \overline{d}_4 = \frac{16}{3} \frac{\nu(1-\nu)}{1-2\nu}, \quad \overline{d}_6 = -\frac{16}{3} \frac{\nu(1-\nu)}{2-\nu}. \end{aligned} \tag{3.53}$$

Using the identities in Eqs. (3.50), the general form of $\mathbf{\Xi}$ is given in terms of Kronecker deltas. Thus, the general compact form of $\mathbf{\Xi}$ is expressed as

$$\begin{aligned} \Xi_{ijkl}^{\alpha\beta\gamma\delta} &= T_1 \delta_{ij}\delta_{kl}\delta_{\alpha\beta}\delta_{\gamma\delta} \\ &+ T_2 \left[\delta_{ij}\delta_{kl} \left(\delta_{\alpha\gamma}\delta_{\beta\delta} + \delta_{\alpha\delta}\delta_{\beta\gamma} \right) + \delta_{\alpha\beta}\delta_{\gamma\delta} \left(\delta_{ik}\delta_{jl} + \delta_{il}\delta_{jk} \right) \right] \\ &+ T_3 \left(\delta_{ik}\delta_{jl} + \delta_{il}\delta_{jk} \right) \left(\delta_{\alpha\gamma}\delta_{\beta\delta} + \delta_{\alpha\delta}\delta_{\beta\gamma} \right) \\ &+ T_4 \left[\delta_{ij}\delta_{\alpha\beta} \left(\delta_{\gamma k}\delta_{\delta l} + \delta_{\gamma l}\delta_{\delta k} \right) + \delta_{kl}\delta_{\alpha\beta} \left(\delta_{\gamma i}\delta_{\delta j} + \delta_{\gamma j}\delta_{\delta i} \right) \right. \\ &\quad \left. + \delta_{ij}\delta_{\gamma\delta} \left(\delta_{\alpha k}\delta_{\beta l} + \delta_{\alpha l}\delta_{\beta k} \right) + \delta_{kl}\delta_{\gamma\delta} \left(\delta_{\alpha i}\delta_{\beta j} + \delta_{\alpha j}\delta_{\beta i} \right) \right] \\ &+ T_5 \left[\delta_{\alpha\beta}\delta_{ik} \left(\delta_{\gamma j}\delta_{\delta l} + \delta_{\gamma l}\delta_{\delta j} \right) + \delta_{\alpha\beta}\delta_{il} \left(\delta_{\gamma j}\delta_{\delta k} + \delta_{\gamma k}\delta_{\delta j} \right) \right. \\ &\quad + \delta_{\alpha\beta}\delta_{jk} \left(\delta_{\gamma i}\delta_{\delta l} + \delta_{\gamma l}\delta_{\delta i} \right) + \delta_{\alpha\beta}\delta_{jl} \left(\delta_{\gamma i}\delta_{\delta k} + \delta_{\gamma k}\delta_{\delta i} \right) \\ &\quad + \delta_{\gamma\delta}\delta_{ik} \left(\delta_{\alpha j}\delta_{\beta l} + \delta_{\alpha l}\delta_{\beta j} \right) + \delta_{\gamma\delta}\delta_{il} \left(\delta_{\alpha j}\delta_{\beta k} + \delta_{\alpha k}\delta_{\beta j} \right) \\ &\quad + \delta_{\gamma\delta}\delta_{jk} \left(\delta_{\alpha i}\delta_{\beta l} + \delta_{\alpha l}\delta_{\beta i} \right) + \delta_{\gamma\delta}\delta_{jl} \left(\delta_{\alpha i}\delta_{\beta k} + \delta_{\alpha k}\delta_{\beta i} \right) \\ &\quad + \delta_{\alpha\gamma}\delta_{ij} \left(\delta_{\beta k}\delta_{\delta l} + \delta_{\beta l}\delta_{\delta k} \right) + \delta_{\alpha\gamma}\delta_{kl} \left(\delta_{\beta i}\delta_{\delta j} + \delta_{\beta j}\delta_{\delta i} \right) \\ &\quad + \delta_{\alpha\delta}\delta_{ij} \left(\delta_{\beta k}\delta_{\gamma l} + \delta_{\beta l}\delta_{\gamma k} \right) + \delta_{\alpha\delta}\delta_{kl} \left(\delta_{\beta i}\delta_{\gamma j} + \delta_{\beta j}\delta_{\gamma i} \right) \\ &\quad \left. + \delta_{\beta\gamma}\delta_{ij} \left(\delta_{\alpha k}\delta_{\delta l} + \delta_{\alpha l}\delta_{\delta k} \right) + \delta_{\beta\gamma}\delta_{kl} \left(\delta_{\alpha i}\delta_{\delta j} + \delta_{\alpha j}\delta_{\delta i} \right) \right. \end{aligned} \tag{3.54}$$

$$
\begin{aligned}
&+\delta_{\beta\delta}\delta_{ij}\left(\delta_{\alpha k}\delta_{\gamma l}+\delta_{\alpha l}\delta_{\gamma k}\right)+\delta_{\beta\delta}\delta_{kl}\left(\delta_{\alpha i}\delta_{\gamma j}+\delta_{\alpha j}\delta_{\gamma i}\right)]\\
&+T_6\left[\delta_{\alpha\gamma}\delta_{ik}\left(\delta_{\beta j}\delta_{\delta l}+\delta_{\beta l}\delta_{\delta j}\right)+\delta_{\alpha\gamma}\delta_{il}\left(\delta_{\beta j}\delta_{\delta k}+\delta_{\beta k}\delta_{\delta j}\right)\right.\\
&+\delta_{\alpha\gamma}\delta_{jk}\left(\delta_{\beta i}\delta_{\delta l}+\delta_{\beta l}\delta_{\delta i}\right)+\delta_{\alpha\gamma}\delta_{jl}\left(\delta_{\beta i}\delta_{\delta k}+\delta_{\beta k}\delta_{\delta i}\right)\\
&+\delta_{\alpha\delta}\delta_{ik}\left(\delta_{\beta j}\delta_{\gamma l}+\delta_{\beta l}\delta_{\gamma j}\right)+\delta_{\alpha\delta}\delta_{il}\left(\delta_{\beta j}\delta_{\gamma k}+\delta_{\beta k}\delta_{\gamma j}\right)\\
&+\delta_{\alpha\delta}\delta_{jk}\left(\delta_{\beta i}\delta_{\gamma l}+\delta_{\beta l}\delta_{\gamma i}\right)+\delta_{\alpha\delta}\delta_{jl}\left(\delta_{\beta i}\delta_{\gamma k}+\delta_{\beta k}\delta_{\gamma i}\right)\\
&+\delta_{\beta\gamma}\delta_{ik}\left(\delta_{\alpha j}\delta_{\delta l}+\delta_{\alpha l}\delta_{\delta j}\right)+\delta_{\beta\gamma}\delta_{il}\left(\delta_{\alpha j}\delta_{\delta k}+\delta_{\alpha k}\delta_{\delta j}\right)\\
&+\delta_{\beta\gamma}\delta_{jk}\left(\delta_{\alpha i}\delta_{\delta l}+\delta_{\alpha l}\delta_{\delta i}\right)+\delta_{\beta\gamma}\delta_{jl}\left(\delta_{\alpha i}\delta_{\delta k}+\delta_{\alpha k}\delta_{\delta i}\right)\\
&+\delta_{\beta\delta}\delta_{ik}\left(\delta_{\alpha j}\delta_{\gamma l}+\delta_{\alpha l}\delta_{\gamma j}\right)+\delta_{\beta\delta}\delta_{il}\left(\delta_{\alpha j}\delta_{\gamma k}+\delta_{\alpha k}\delta_{\gamma j}\right)\\
&+\delta_{\beta\delta}\delta_{jk}\left(\delta_{\alpha i}\delta_{\gamma l}+\delta_{\alpha l}\delta_{\gamma i}\right)+\delta_{\beta\delta}\delta_{jl}\left(\delta_{\alpha i}\delta_{\gamma k}+\delta_{\alpha k}\delta_{\gamma i}\right)]\\
&+T_7\left[\delta_{\alpha i}\delta_{\beta j}\delta_{\gamma k}\delta_{\delta l}+\delta_{\alpha i}\delta_{\beta l}\delta_{\gamma j}\delta_{\delta k}+\delta_{\alpha i}\delta_{\beta k}\delta_{\gamma j}\delta_{\delta l}\right.\\
&+\delta_{\alpha i}\delta_{\beta k}\delta_{\gamma l}\delta_{\delta j}+\delta_{\alpha i}\delta_{\beta l}\delta_{\gamma j}\delta_{\delta k}+\delta_{\alpha i}\delta_{\beta l}\delta_{\gamma k}\delta_{\delta j}\\
&+\delta_{\alpha j}\delta_{\beta i}\delta_{\gamma k}\delta_{\delta l}+\delta_{\alpha j}\delta_{\beta i}\delta_{\gamma l}\delta_{\delta k}+\delta_{\alpha j}\delta_{\beta k}\delta_{\gamma i}\delta_{\delta l}\\
&+\delta_{\alpha j}\delta_{\beta k}\delta_{\gamma l}\delta_{\delta i}+\delta_{\alpha j}\delta_{\beta l}\delta_{\gamma k}\delta_{\delta i}+\delta_{\alpha j}\delta_{\beta l}\delta_{\gamma i}\delta_{\delta k}\\
&+\delta_{\alpha k}\delta_{\beta i}\delta_{\gamma j}\delta_{\delta l}+\delta_{\alpha k}\delta_{\beta i}\delta_{\gamma l}\delta_{\delta j}+\delta_{\alpha k}\delta_{\beta j}\delta_{\gamma i}\delta_{\delta l}\\
&+\delta_{\alpha k}\delta_{\beta j}\delta_{\gamma l}\delta_{\delta i}+\delta_{\alpha k}\delta_{\beta l}\delta_{\gamma i}\delta_{\delta j}+\delta_{\alpha k}\delta_{\beta l}\delta_{\gamma j}\delta_{\delta i}\\
&+\delta_{\alpha l}\delta_{\beta i}\delta_{\gamma j}\delta_{\delta k}+\delta_{\alpha l}\delta_{\beta i}\delta_{\gamma k}\delta_{\delta j}+\delta_{\alpha l}\delta_{\beta j}\delta_{\gamma i}\delta_{\delta k}\\
&\left.+\delta_{\alpha l}\delta_{\beta j}\delta_{\gamma k}\delta_{\delta i}+\delta_{\alpha l}\delta_{\beta k}\delta_{\gamma i}\delta_{\delta j}+\delta_{\alpha l}\delta_{\beta k}\delta_{\gamma j}\delta_{\delta i}\right].
\end{aligned}
$$

The expressions for the attenuations, in turn, involve certain inner products of $\boldsymbol{\Xi}$ with incoming and outgoing wave vectors. In terms of the angle between $\hat{\mathbf{p}}$ and $\hat{\mathbf{s}}$, these necessary

inner products reduce to

$$
\begin{aligned}
\Xi^{\cdots\hat{\mathbf{p}}\hat{\mathbf{p}}\hat{\mathbf{s}}\hat{\mathbf{s}}}_{\cdots\hat{\mathbf{p}}\hat{\mathbf{p}}\hat{\mathbf{s}}\hat{\mathbf{s}}} &= [T_1 + 4T_4 + 4T_7] + [4T_2 + 4T_4 + 32T_5 + 16T_6 + 16T_7]\cos^2\theta_{ps} \\
&\quad + [4T_3 + 16T_6 + 4T_7]\cos^4\theta_{ps}, \\
\Xi^{\cdots\hat{\mathbf{p}}\hat{\mathbf{p}}\hat{\mathbf{s}}\hat{\mathbf{s}}_2}_{\cdots\hat{\mathbf{p}}\hat{\mathbf{p}}\hat{\mathbf{s}}\hat{\mathbf{s}}_2} &= \Xi^{\cdots\hat{\mathbf{p}}_2\hat{\mathbf{p}}\hat{\mathbf{s}}\hat{\mathbf{s}}}_{\cdots\hat{\mathbf{p}}_2\hat{\mathbf{p}}\hat{\mathbf{s}}\hat{\mathbf{s}}} = [T_4 + 2T_7] + [4T_5 + 4T_6 + 4T_7]\cos^2\theta_{ps}, \\
\Xi^{\cdots\hat{\mathbf{p}}\hat{\mathbf{p}}\hat{\mathbf{s}}\hat{\mathbf{s}}_3}_{\cdots\hat{\mathbf{p}}\hat{\mathbf{p}}\hat{\mathbf{s}}\hat{\mathbf{s}}_3} &= \Xi^{\cdots\hat{\mathbf{p}}_3\hat{\mathbf{p}}\hat{\mathbf{s}}\hat{\mathbf{s}}}_{\cdots\hat{\mathbf{p}}_3\hat{\mathbf{p}}\hat{\mathbf{s}}\hat{\mathbf{s}}} = [T_4 + 4T_5 + 4T_6 + 6T_7] + [4T_3 + 16T_6 + 4T_7]\cos^2\theta_{ps} \\
&\quad - [4T_3 + 16T_6 + 4T_7]\cos^4\theta_{ps}, \\
\Xi^{\cdots\hat{\mathbf{p}}_2\hat{\mathbf{p}}\hat{\mathbf{s}}\hat{\mathbf{s}}_2}_{\cdots\hat{\mathbf{p}}_2\hat{\mathbf{p}}\hat{\mathbf{s}}\hat{\mathbf{s}}_2} &= [T_6 + 2T_7] + [T_3 + 3T_6 + 2T_7]\cos^2\theta_{ps}, \\
\Xi^{\cdots\hat{\mathbf{p}}_3\hat{\mathbf{p}}\hat{\mathbf{s}}\hat{\mathbf{s}}_3}_{\cdots\hat{\mathbf{p}}_3\hat{\mathbf{p}}\hat{\mathbf{s}}\hat{\mathbf{s}}_3} &= [T_3 + 4T_6 + 4T_7] + [-4T_3 - 16T_6 - 4T_7]\cos^2\theta_{ps} \\
&\quad + [4T_3 + 16T_6 + 4T_7]\cos^4\theta_{ps}, \qquad (3.55) \\
\Xi^{\cdots\hat{\mathbf{p}}_2\hat{\mathbf{p}}\hat{\mathbf{s}}\hat{\mathbf{s}}_3}_{\cdots\hat{\mathbf{p}}_2\hat{\mathbf{p}}\hat{\mathbf{s}}\hat{\mathbf{s}}_3} &= \Xi^{\cdots\hat{\mathbf{p}}_3\hat{\mathbf{p}}\hat{\mathbf{s}}\hat{\mathbf{s}}_2}_{\cdots\hat{\mathbf{p}}_3\hat{\mathbf{p}}\hat{\mathbf{s}}\hat{\mathbf{s}}_2} = [T_6 + 2T_7], \\
\Xi^{\cdots\hat{\mathbf{p}}_2\hat{\mathbf{p}}\hat{\mathbf{s}}\hat{\mathbf{s}}_2}_{\cdots\hat{\mathbf{p}}_3\hat{\mathbf{p}}\hat{\mathbf{s}}\hat{\mathbf{s}}_3} &= \Xi^{\cdots\hat{\mathbf{p}}_3\hat{\mathbf{p}}\hat{\mathbf{s}}\hat{\mathbf{s}}_3}_{\cdots\hat{\mathbf{p}}_2\hat{\mathbf{p}}\hat{\mathbf{s}}\hat{\mathbf{s}}_2} = [-T_3 - 2T_6]\cos\theta_{ps} + [2T_3 + 4T_6]\cos^3\theta_{ps}, \\
\Xi^{\cdots\hat{\mathbf{p}}_2\hat{\mathbf{p}}\hat{\mathbf{s}}\hat{\mathbf{s}}_3}_{\cdots\hat{\mathbf{p}}_3\hat{\mathbf{p}}\hat{\mathbf{s}}\hat{\mathbf{s}}_2} &= \Xi^{\cdots\hat{\mathbf{p}}_3\hat{\mathbf{p}}\hat{\mathbf{s}}\hat{\mathbf{s}}_2}_{\cdots\hat{\mathbf{p}}_2\hat{\mathbf{p}}\hat{\mathbf{s}}\hat{\mathbf{s}}_3} = -3T_6\cos\theta_{ps} + [4T_6 + 2T_7]\cos^3\theta_{ps}, \\
\Xi^{\cdots\hat{\mathbf{p}}_2\hat{\mathbf{p}}\hat{\mathbf{s}}\hat{\mathbf{s}}_2}_{\cdots\hat{\mathbf{p}}_2\hat{\mathbf{p}}\hat{\mathbf{s}}\hat{\mathbf{s}}_3} &= \Xi^{\cdots\hat{\mathbf{p}}_2\hat{\mathbf{p}}\hat{\mathbf{s}}\hat{\mathbf{s}}_2}_{\cdots\hat{\mathbf{p}}_3\hat{\mathbf{p}}\hat{\mathbf{s}}\hat{\mathbf{s}}_2} = \Xi^{\cdots\hat{\mathbf{p}}_2\hat{\mathbf{p}}\hat{\mathbf{s}}\hat{\mathbf{s}}_3}_{\cdots\hat{\mathbf{p}}_2\hat{\mathbf{p}}\hat{\mathbf{s}}\hat{\mathbf{s}}_2} = \Xi^{\cdots\hat{\mathbf{p}}_3\hat{\mathbf{p}}\hat{\mathbf{s}}\hat{\mathbf{s}}_2}_{\cdots\hat{\mathbf{p}}_2\hat{\mathbf{p}}\hat{\mathbf{s}}\hat{\mathbf{s}}_2} = 0, \\
\Xi^{\cdots\hat{\mathbf{p}}_3\hat{\mathbf{p}}\hat{\mathbf{s}}\hat{\mathbf{s}}_3}_{\cdots\hat{\mathbf{p}}_3\hat{\mathbf{p}}\hat{\mathbf{s}}\hat{\mathbf{s}}_2} &= \Xi^{\cdots\hat{\mathbf{p}}_2\hat{\mathbf{p}}\hat{\mathbf{s}}\hat{\mathbf{s}}_3}_{\cdots\hat{\mathbf{p}}_3\hat{\mathbf{p}}\hat{\mathbf{s}}\hat{\mathbf{s}}_3} = \Xi^{\cdots\hat{\mathbf{p}}_3\hat{\mathbf{p}}\hat{\mathbf{s}}\hat{\mathbf{s}}_3}_{\cdots\hat{\mathbf{p}}_2\hat{\mathbf{p}}\hat{\mathbf{s}}\hat{\mathbf{s}}_3} = \Xi^{\cdots\hat{\mathbf{p}}_3\hat{\mathbf{p}}\hat{\mathbf{s}}\hat{\mathbf{s}}_2}_{\cdots\hat{\mathbf{p}}_3\hat{\mathbf{p}}\hat{\mathbf{s}}\hat{\mathbf{s}}_3} = 0, \\
\Xi^{\cdots\hat{\mathbf{p}}\hat{\mathbf{p}}\hat{\mathbf{s}}\hat{\mathbf{s}}_3}_{\cdots\hat{\mathbf{p}}\hat{\mathbf{p}}\hat{\mathbf{s}}\hat{\mathbf{s}}_2} &= \Xi^{\cdots\hat{\mathbf{p}}_2\hat{\mathbf{p}}\hat{\mathbf{s}}\hat{\mathbf{s}}}_{\cdots\hat{\mathbf{p}}_3\hat{\mathbf{p}}\hat{\mathbf{s}}\hat{\mathbf{s}}} = \Xi^{\cdots\hat{\mathbf{p}}_3\hat{\mathbf{p}}\hat{\mathbf{s}}\hat{\mathbf{s}}}_{\cdots\hat{\mathbf{p}}_2\hat{\mathbf{p}}\hat{\mathbf{s}}\hat{\mathbf{s}}} = \Xi^{\cdots\hat{\mathbf{p}}\hat{\mathbf{p}}\hat{\mathbf{s}}\hat{\mathbf{s}}_2}_{\cdots\hat{\mathbf{p}}\hat{\mathbf{p}}\hat{\mathbf{s}}\hat{\mathbf{s}}_3} = 0.
\end{aligned}
$$

The coefficients T_i are given by

$$
\begin{aligned}
T_1 &= -\frac{D^2\nu^2}{945}\frac{335\nu^4 - 1984\nu^3 + 2946\nu^2 - 208\nu - 937}{(1-2\nu)^2}, \\
T_2 &= \frac{D^2\nu}{4725}\frac{31\nu^3 - 139\nu^2 + \nu + 243}{1-2\nu}, \qquad T_7 = \frac{D^2\nu^2(1-2\nu)^2}{945}, \\
T_3 &= \frac{D^2}{945}(1-2\nu)^2(\nu^2 - 18\nu + 63),\ T_4 = \frac{D^2\nu^2}{945}(31\nu^2 - 166\nu + 217), \qquad (3.56) \\
T_5 &= \frac{D^2\nu}{1890}(1-2\nu)(14\nu^2 - 79\nu + 117),\quad T_6 = \frac{D^2}{420}(1-2\nu)^2(7-4\nu),
\end{aligned}
$$

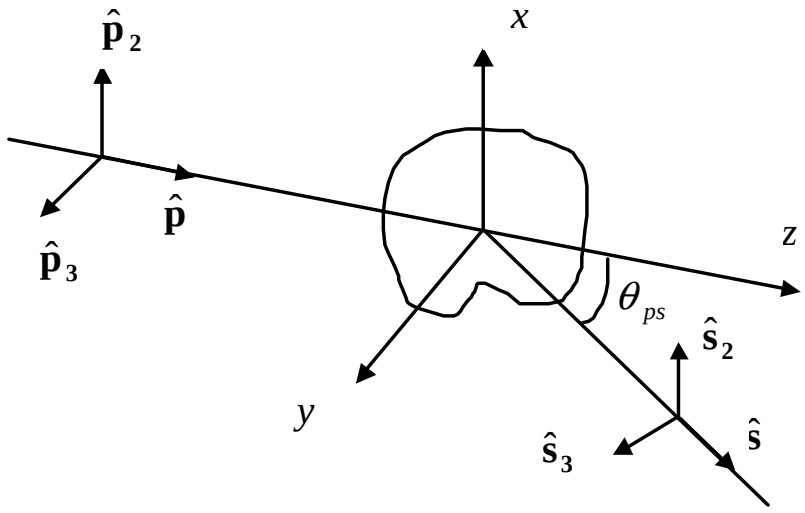

Figure 3.2: Geometry for scattering in the local coordinate system

with the constant $D = \frac{16}{3}\frac{1-\nu}{(2-\nu)(1-2\nu)}2\mu$. The unit vectors $\hat{\mathbf{p}}$, $\hat{\mathbf{p}}_2$, $\hat{\mathbf{p}}_3$ and $\hat{\mathbf{s}}$, $\hat{\mathbf{s}}_2$, $\hat{\mathbf{s}}_3$ used in Eq. (3.55) are defined as orthonormal triads, respectively as shown in Fig 3.2.

Using the notation

$$\begin{aligned} F(\theta_{ps}) &= \Xi^{\cdots\hat{\mathbf{p}}\hat{\mathbf{p}}\hat{\mathbf{s}}\hat{\mathbf{s}}}_{\cdots\hat{\mathbf{p}}\hat{\mathbf{p}}\hat{\mathbf{s}}\hat{\mathbf{s}}}, \\ M(\theta_{ps}) &= \Xi^{\cdots\hat{\mathbf{p}}\hat{\mathbf{p}}\hat{\mathbf{s}}\hat{\mathbf{s}}_2}_{\cdots\hat{\mathbf{p}}\hat{\mathbf{p}}\hat{\mathbf{s}}\hat{\mathbf{s}}_2} + \Xi^{\cdots\hat{\mathbf{p}}\hat{\mathbf{p}}\hat{\mathbf{s}}\hat{\mathbf{s}}_3}_{\cdots\hat{\mathbf{p}}\hat{\mathbf{p}}\hat{\mathbf{s}}\hat{\mathbf{s}}_3} = \Xi^{\cdots\hat{\mathbf{p}}_2\hat{\mathbf{p}}\hat{\mathbf{s}}\hat{\mathbf{s}}}_{\cdots\hat{\mathbf{p}}_2\hat{\mathbf{p}}\hat{\mathbf{s}}\hat{\mathbf{s}}} + \Xi^{\cdots\hat{\mathbf{p}}_3\hat{\mathbf{p}}\hat{\mathbf{s}}\hat{\mathbf{s}}}_{\cdots\hat{\mathbf{p}}_3\hat{\mathbf{p}}\hat{\mathbf{s}}\hat{\mathbf{s}}}, \\ N(\theta_{ps}) &= \Xi^{\cdots\hat{\mathbf{p}}_2\hat{\mathbf{p}}\hat{\mathbf{s}}\hat{\mathbf{s}}_2}_{\cdots\hat{\mathbf{p}}_2\hat{\mathbf{p}}\hat{\mathbf{s}}\hat{\mathbf{s}}_2} + \Xi^{\cdots\hat{\mathbf{p}}_3\hat{\mathbf{p}}\hat{\mathbf{s}}\hat{\mathbf{s}}_3}_{\cdots\hat{\mathbf{p}}_3\hat{\mathbf{p}}\hat{\mathbf{s}}\hat{\mathbf{s}}_3} + \Xi^{\cdots\hat{\mathbf{p}}_2\hat{\mathbf{p}}\hat{\mathbf{s}}\hat{\mathbf{s}}_3}_{\cdots\hat{\mathbf{p}}_2\hat{\mathbf{p}}\hat{\mathbf{s}}\hat{\mathbf{s}}_3} + \Xi^{\cdots\hat{\mathbf{p}}_3\hat{\mathbf{p}}\hat{\mathbf{s}}\hat{\mathbf{s}}_2}_{\cdots\hat{\mathbf{p}}_3\hat{\mathbf{p}}\hat{\mathbf{s}}\hat{\mathbf{s}}_2}, \end{aligned} \tag{3.57}$$

allows the attenuations to be reduced to the form

$$\begin{aligned} \alpha_{LL} &= \frac{1}{4}\frac{\pi\omega^4\varepsilon}{c_L^8}\int \eta_{LL}(\theta_{ps})\, F(\theta_{ps})\, d^2\hat{\mathbf{s}} = \frac{1}{2}\frac{\pi^2\omega^4\varepsilon}{c_L^8}\int_{-1}^{+1} \eta_{LL}(\theta)\, F(\theta)\, d\cos\theta, \\ \alpha_{LT} &= \frac{1}{4}\frac{\pi\omega^4\varepsilon}{c_L^3 c_T^5}\int \eta_{LT}(\theta_{ps})\, M(\theta_{ps})\, d^2\hat{\mathbf{s}} = \frac{1}{2}\frac{\pi^2\omega^4\varepsilon}{c_L^3 c_T^5}\int_{-1}^{+1} \eta_{LT}(\theta)\, M(\theta)\, d\cos\theta, \\ \alpha_{TL} &= \frac{1}{2}\left(\frac{c_T}{c_L}\right)^2 \alpha_{LT}, \\ \alpha_{TT} &= \frac{1}{8}\frac{\pi\omega^4\varepsilon}{c_T^8}\int \eta_{TT}(\theta_{ps})\, N(\theta_{ps})\, d^2\hat{\mathbf{s}} = \frac{1}{4}\frac{\pi^2\omega^4\varepsilon}{c_T^8}\int_{-1}^{+1} \eta_{TT}(\theta)\, N(\theta)\, d\cos\theta, \end{aligned} \tag{3.58}$$

The total attenuations for the longitudinal and transverse waves are given by

$$\alpha_L = \alpha_{LL} + \alpha_{LT}, \qquad \alpha_T = \alpha_{TT} + \alpha_{TL.} \tag{3.59}$$

The appropriate expressions for the tensorial part of the covariance, Eq. (3.55), and the final expressions for attenuation, Eqs. (3.58)-(3.59) are the main results of this chapter. The attenuations are expressed as integrations on the unit circle in terms of the spatial transform of the spatial correlation function. Most importantly, the results are expressed in terms of the damage density ε. It is seen that the attenuations scale with damage factor ε. In the next section, using the correlation function η given in Eq. (2.14), example results are presented.

3.5 Example Results

In this section, example results are presented in terms of the nondimensional damage density ε for an assumed spatial correlation function. For the example case, the material properties of the uncracked medium used are Young's modulus $E = 2.0 \times 10^7$Pa, Poisson's ratio $\nu = 0.16$. As discussed in Eqs. (2.14) and (2.15), the spatial correlation is assumed to have an exponential form. An exponential function describes the correlation of continuous and discrete materials reasonably well. For the isotropic case, the transform of the difference between two wave vectors is expressed as

$$\eta_{\alpha\beta}(\chi) = \frac{L^3}{\pi^2(1 + x_\alpha^2 + x_\beta^2 - 2x_\alpha x_\beta \chi)^2}. \tag{3.60}$$

where L is the spatial correlation length, $L = 2\langle a \rangle$. The scripts, α, β denote the wave types L or T, and $\chi = \cos\theta_{ps}$. The dimensionless longitudinal and transverse frequencies

are defined as $x_L = \omega L/c_L$ and $x_T = \omega L/c_T$. In dimensionless form, the attenuations in Eqs. (3.58) simplify to

$$\alpha_{LL}L = \frac{x_L^4 B^4 \varepsilon}{2\mu^2} \int_{-1}^{+1} \frac{h_1 + h_2\chi^2 + h_3\chi^4}{\left(1 + 2x_L^2\left(1-\chi\right)\right)^2} d\chi, \tag{3.61}$$

$$\alpha_{LT}L = \frac{x_L^4 \varepsilon}{2B\mu^2} \int_{-1}^{+1} \frac{m_1 + m_2\chi^2 + m_3\chi^4}{\left(1 + x_L^2 + x_T^2 - 2x_L x_T \chi\right)^2} d\chi, \tag{3.62}$$

$$\alpha_{TT}L = \frac{x_T^4 \varepsilon}{4\mu^2} \int_{-1}^{+1} \frac{n_1 + n_2\chi^2 + n_3\chi^4}{\left(1 + 2x_T^2\left(1-\chi\right)\right)^2} d\chi, \tag{3.63}$$

where $B = c_T/c_L$ is the wave speed ratio. The coefficients $h_i, m_i, n_i (i = 1, 2, 3)$ are given as

$$\begin{aligned} h_1 &= T_1 + 4T_4 + 4T_7, \\ h_2 &= 4T_2 + 4T_4 + 32T_5 + 16T_6 + 16T_7, \\ h_3 &= 4T_3 + 16T_6 + 4T_7, \end{aligned} \tag{3.64}$$

$$\begin{aligned} m_1 &= 2T_4 + 4T_5 + 4T_6 + 8T_7, \\ m_2 &= 4T_3 + 4T_5 + 20T_6 + 8T_7, \\ m_3 &= -4T_3 - 16T_6 - 4T_7, \end{aligned} \tag{3.65}$$

$$\begin{aligned} n_1 &= T_3 + 7T_6 + 10T_7, \\ n_2 &= -3T_3 - 13T_6 - 2T_7, \\ n_3 &= 4T_3 + 16T_6 + 4T_7. \end{aligned} \tag{3.66}$$

Example calculations using Eqs. (3.61)-(3.63) are shown in Fig. 3.3. The dimensionless longitudinal and transverse attenuations, $\alpha_L L$ and $\alpha_T L$, respectively, are plotted as a function of dimensionless frequency, x_L, for two values of the damage parameter ε. Equations (3.61)-(3.63) are shown to scale with the linearity of ε such that other values of ε

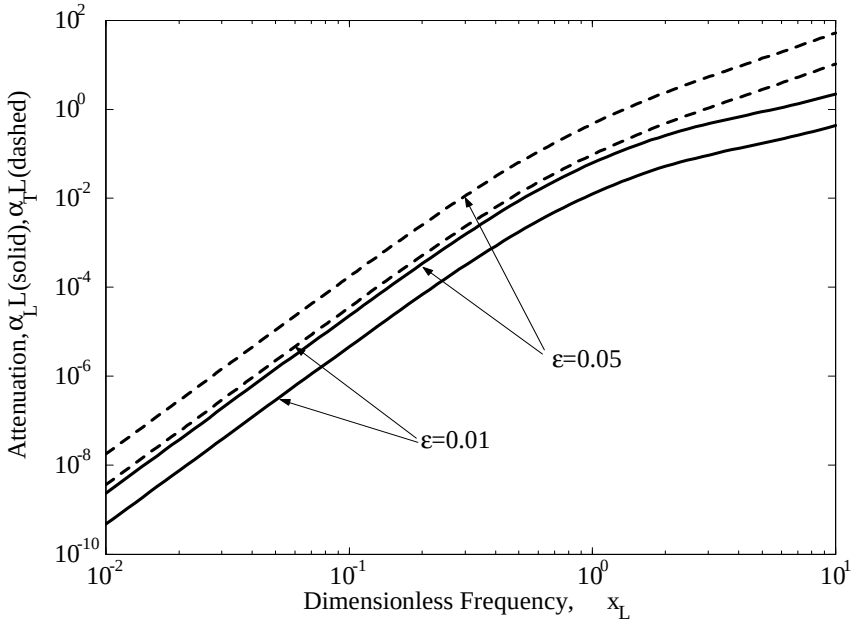

Figure 3.3: Dimensionless longitudinal and transverse attenuations, $\alpha_L L$ (solid) and $\alpha_T L$ (dashed), as a function of dimensionless frequency, x_L, for damage density $\varepsilon = 0.01$ and $\varepsilon = 0.05$.

lead to constant shifts in these curves. The attenuations increase with the fourth power of frequency in the low frequency limit as expected. After a transition region, the attenuations increase with the square of frequency. However, it should be noted that the results at higher frequencies are less accurate than those at lower frequencies. This inaccuracy is the result of the truncation of the expansion in Eqs. (3.22). The longitudinal attenuation is smaller than the transverse attenuation in part due to the wavelengths of the respective waves. However, when the attenuations are plotted in terms of their respective dimensionless frequency as shown in Fig. 3.4, the transverse attenuations remained larger than the longitudinal. Thus, the higher transverse attenuation is a combination of effects of wavelength and interaction with the cracks. As shown in Fig. 3.3, the ratio of the longitudinal and transverse attenuations is a constant at low frequencies, but changes at higher frequencies. Figure 3.5 is a

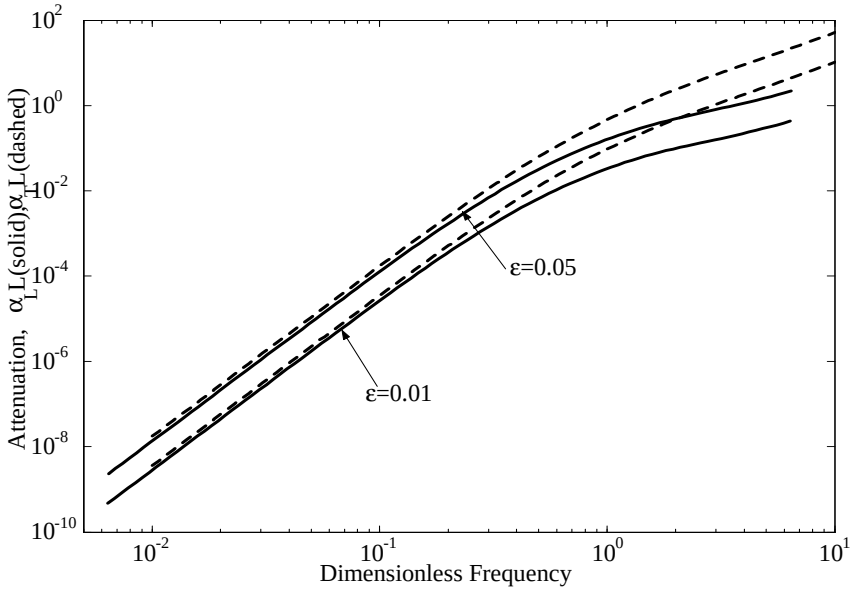

Figure 3.4: Dimensionless longitudinal attenuation, $\alpha_L L$ (solid), as a function of dimensionless frequency, x_L, and dimensionless transverse attenuation, $\alpha_T L$ (dashed), as a function of dimensionless frequency, x_T, for damage density $\varepsilon = 0.01$ and $\varepsilon = 0.05$.

plot of the wave speed ratio $B^e = \overline{C}_T/\overline{C}_L$ and $C = (\overline{C}_T/C_T)/(\overline{C}_L/C_L)$, as a function of damage density ε. As has been observed experimentally, the wave speed changes much less than the attenuation for a given damage level [91]. Thus, the result shown in Fig. 3.5 is not unexpected.

3.6 Conclusions

The propagation and scattering of elastic waves in a homogeneous, isotropic medium with damage from microcracking has been investigated in this chapter. A generalized tensor-based approach was used such that the results are coordinate free. The effective compliance and stiffness in terms of the damage parameter was discussed. Initially, effective compliance due to a single penny-shaped crack embedded in an infinite elastic solids was examined. The

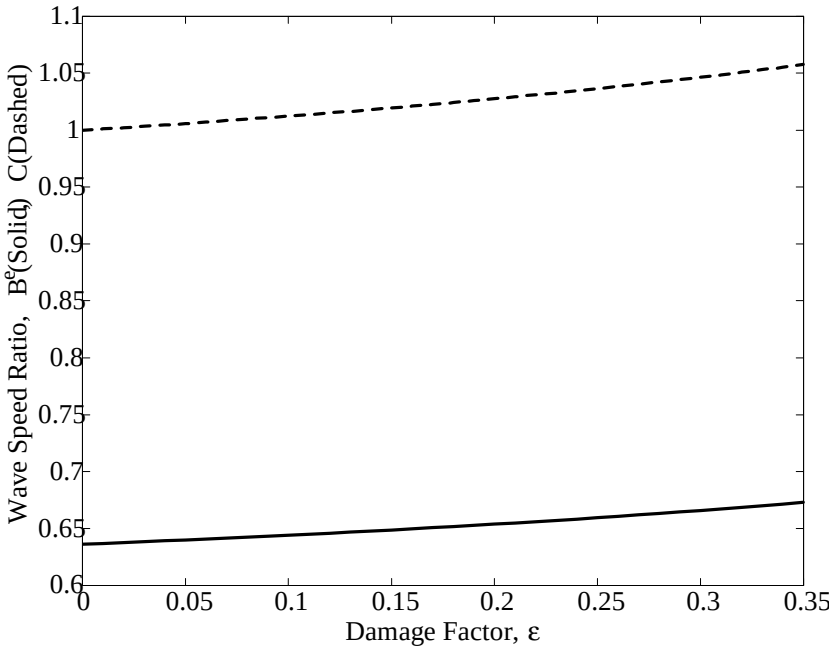

Figure 3.5: Wave speed ratio $B^e = \bar{C}_T/\bar{C}_L$ and $C = \left(\bar{C}_T/C_T\right) / \left(\bar{C}_L/C_L\right)$, as a function of damage density ε.

effective properties of a homogenous, isotropic solid in which a large number of microcracks is embedded were then determined by superposition. The modulus fluctuations were then derived relative to the average moduli. The ensemble average covariance of the moduli fluctuations was then derived for randomly oriented cracks. The expressions for the longitudinal and transverse attenuations were derived by considering the Dyson equation, which governs the mean elastodynamic response of the medium. The Dyson equation was solved within the limits of first-order smoothing approximation (FOSA). The final forms of the attenuations have a linear dependency on the damage parameter, which is expected to be valid for low damage densities. The use of the tensor-based approach presented here for studying elastic wave scattering in media with microcracks allowed the attenuation expressions to be reduced to simple form. These results should be very useful for nondestructive

testing and material characterization research. In particular, the study of wave interactions with aligned cracks will be much more direct. The topic of aligned cracks is examined in the subsequent two chapters. The general formulation is also convenient for considering other problems such as studies of backscatter phenomena.

Chapter 4

Uniaxially Aligned Crack Scattering

4.1 Introduction

Analytical and experimental examinations of attenuation and wave speeds of ultrasonic waves in cracked solids provide a direct approach for the detection of material damage. Material responses, which are typically evaluated ultrasonically by the decrease in wave velocity or increase in wave attenuation, vary with microcracking changes. Both of these phenomena are caused by the stiffness degradation of the material by the cracks. In Chapter 3, explicit general expressions of wave attenuations and wave speeds in a medium with damage from randomly distributed penny-shaped microcracks were derived. Under the assumption of statistical isotropy used in that work, the attenuation is independent of propagation direction. However, in the case of structural materials such as concrete, poly-

crystalline metals, fiber-reinforced composites, and many others, those microcracks induced by directional loading or temperature are typically parallel to some direction. In this case, the effective media may acquire an anisotropy essentially due to the presence of such uniaxially aligned cracks. Thus, the scattering attenuation is a function of propagation direction. The analysis of this scattering attenuation is, therefore, more complicated than that of the isotropic case.

In this chapter, the framework used in the previous chapter is extended to study the attenuation of elastic waves in solids with uniaxially aligned cracks that are statistically homogeneous. Again, the microcracks are assumed to be noninteracting, penny-shaped cracks. Here, the unit normals of all cracks are assumed to be coplanar, but random within this plane of isotropy. Thus, the uniaxial symmetry direction is perpendicular to this plane. It should be noted that this case is different from the case of perfect crack alignment by all cracks, as discussed by Hudson [70] for example, which will be presented in the next chapter within the same framework. The use of an anisotropic Green's function for modeling the scattering in anisotropic media was investigated by Turner [57]. Here, this approach is employed as well to formulate the uniaxially aligned crack problem. In this way, the mean response is written in terms of the Dyson equation as discussed by Frisch [71] and Weaver [50]. The Dyson equation is solved in the spatial Fourier transform domain within the limits of the first-order smoothing approximation (FOSA), or Keller [48] approximation. A further approximation is also made which restricts the results to frequencies below the high-frequency geometric optics limit. The resulting attenuations are shown to be directional dependent, frequency dependent, and damage dependent for the shear horizontal,

quasilongitudinal, and quasishear vertical waves. In particular, the angular dependence of the attenuations in the Rayleigh limit is obtained explicitly. Outside the Rayleigh limit, simple expressions of the attenuations of the shear horizontal, quasilongitudinal, and quasishear vertical waves are derived in terms of integrations on the unit circle. Quantitative and qualitative comparisons with previous results by Zhang and Gross [26],[27], Zhang and Achenbach [25], Eriksson and Datta [30], Ahmed and Thompson [56] and Turner [57] show that the more general, direct expressions derived here are reliable and comprehensive for practical applications of detecting damage from microcracks.

4.2 Effective Elastic Properties

The effective stiffness attributed to a single penny-shaped crack, which is located within an infinite, homogeneous, isotropic and elastic continuum has to be considered in order to calculate the ensemble average stiffness. As discussed in Chapter 3, the effective stiffness attributable to a single, penny-shaped crack of radius a in a unit volume, called the crack basis Green's function, is given by Eq. (3.25) [92]. The stiffness of a single crack is dependent on the unit normal $\hat{\mathbf{m}}$, which defines the crack orientation. This orientation is implicit in the tensors $\mathbf{I}$. These basis tensors are given in terms of unit vector $\hat{\mathbf{m}}$ and Kronecker delta function as shown in Eq. (3.13).

Next, the ensemble average properties contributed by all cracks are considered. The cracks are assumed to be embedded in an infinitely extended, homogeneous, isotropic and elastic three-dimensional continuum. The penny-shaped crack is characterized by its radius a and two Euler angles θ and φ, which define the direction of the unit normal $\hat{\mathbf{m}}$ as

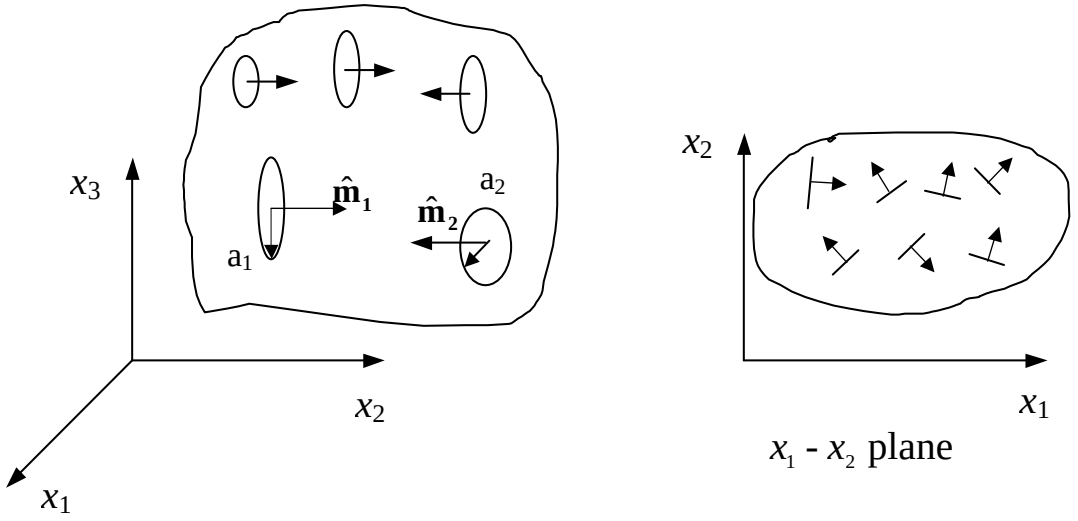

Figure 4.1: The distribution of microcracks parallel to the x_3-axis.

shown in Fig. 3.1. It is also assumed that the microcracks do not interact with each other. As discussed previously, the density function may be separated into independent radius and orientation functions of the form as shown in Eq. (3.27).

It is also assumed that all microcracks are parallel to the x_3 axis ($\hat{\mathbf{n}}$ direction) with their unit normals (lying in the $x_1 - x_2$ plane), having a random distribution, as shown in Fig. 4.1. In this situation, due to the symmetry about the $x_1 - x_2$ plane, the average elastic properties are those of transverse isotropy, with the x_3 axis as the uniaxial symmetry axis. Here, the distribution of the microcracks is supposed to be dilute, and the distribution of the crack sizes is also assumed to be independent of their orientations. The crack orientation distribution function in Eq. (3.27), which implies that the orientation function $\zeta(\theta, \varphi)$ is independent of the angle θ, is then given by

$$\zeta(\theta, \varphi) = 2\delta\left(\varphi - \frac{\pi}{2}\right). \tag{4.1}$$

Therefore, the effective continuum material properties caused by all microcracks per unit volume are weighted by the density function, Eq. (3.27), over the crack Green's function, Eq. (3.25), and are then given by

$$C^*_{ijkl} = \frac{\varepsilon}{2\pi} \int_0^{2\pi} \int_{-\pi/2}^{\pi/2} \delta\left(\varphi - \frac{\pi}{2}\right) C^{(s)}_{ijkl}(\theta, \varphi) \sin\varphi d\theta d\varphi. \tag{4.2}$$

In Eq. (4.2), the non-dimensional microcrack density per unit volume is again defined by

$$\varepsilon = N \left\langle a^3 \right\rangle = \int_{a^-}^{a^+} A(a) a^3 da, \tag{4.3}$$

where N is the number of cracks per unit volume and the angular brackets denote the ensemble average. This damage density definition was introduced first by Walsh [87] for the case of a statistically isotropic distribution of penny-shaped microcracks. A more general form of the damage density is discussed by Budiansky [88]. The basis function $C^{(s)}_{ijkl}$ is specified in Eq. (3.25). By integrating over the Euler angles in Eq. (4.2), the effective stiffness due to the distribution of uniaxially aligned penny-shaped microcracks is derived as

$$C^*_{ijkl} = D a_i \mathbf{I}^i, \tag{4.4}$$

where the coefficients D and a_i are

$$\begin{gathered} D = 2\varepsilon\mu \frac{16}{3} \frac{1-\nu}{2-\nu}, \qquad a_1 = 1 - \frac{\nu}{4}, \\ a_2 = \frac{\nu(15 - 20\nu + 4\nu^2)}{8(1-2\nu)^2}, \quad a_3 = a_4 = \frac{\nu(-7+2\nu)}{8(1-2\nu)}, \\ a_5 = 1 - \frac{\nu}{2}, \qquad a_6 = -\frac{3\nu}{8}. \end{gathered} \tag{4.5}$$

In the tensors $\mathbf{I}$ used in Eq. (4.4), the orientation is that of the symmetry direction $\hat{\mathbf{n}}$, rather than the direction $\hat{\mathbf{m}}$. It is hoped that this notation is not confusing to the reader.

If the original undamaged state of the material is homogeneous and isotropic, the stiffness tensor is given in the standard form $\mathbf{C}^0 = \lambda \mathbf{I}^2 + 2\mu \mathbf{I}^1$.

The ensemble effective stiffness is now redefined such that the average fluctuations are zero as done in the previous chapter for the convenience of calculating the material covariance and attenuation. The moduli are assumed to be spatially varying and of the form

$$\overline{\mathbf{C}}(\mathbf{x}) = \overline{\mathbf{C}}^0 + \delta\overline{\mathbf{C}}(\mathbf{x}), \tag{4.6}$$

where

$$\overline{\mathbf{C}}^0 = \mathbf{C}^0 - \mathbf{C}^*. \tag{4.7}$$

Thus, the average moduli have the form

$$\overline{\mathbf{C}}^0 = \left\langle \overline{\mathbf{C}}(\mathbf{x}) \right\rangle = \lambda_\perp \mathbf{I}^2 + \mu_\perp \mathbf{I}^1 + \Gamma_1(\mathbf{I}^3 + \mathbf{I}^4) + \Gamma_2 \mathbf{I}^5 + \Gamma_3 \mathbf{I}^6, \tag{4.8}$$

where the effective elastic constants are

$$\begin{aligned} \lambda_\perp &= \lambda - \frac{D\nu(15 - 20\nu + 4\nu^2)}{8(1-2\nu)^2}, \quad \mu_\perp = \mu - \frac{D(4-\nu)}{8}, \\ \Gamma_1 &= \frac{D\nu(7-2\nu)}{8(1-2\nu)}, \quad \Gamma_2 = D(-1 + \frac{\nu}{2}), \quad \Gamma_3 = \frac{3D\nu}{8}. \end{aligned} \tag{4.9}$$

The moduli fluctuations, which have zero mean, $\left\langle \delta\overline{C} \right\rangle = 0$, are given by

$$\delta\overline{\mathbf{C}} = \mathbf{C}^* - \mathbf{C}^{(s)} H(\mathbf{x}), \tag{4.10}$$

where the function $H(\mathbf{x})$ is defined in Eq. (3.40).

In the next section, a Green's dyadic approach is developed for a transversely isotropic medium. The elastic modulus tensor is specified for the transversely isotropic case and expressions of the attenuation for each wave type are determined.

4.3 Green's Dyadic for Transversely Isotropic Media

The solution of the Dyson equation, Eq. (2.7), for the mean response requires the Green's dyadic for the bare medium. The bare Green's dyadic, $\mathbf{G}^0$, is defined as the solution of the equation of motion, Eq. (2.4), without heterogeneities ($\delta\overline{C}_{ijkl}(\mathbf{x}) = 0$). The emphasis here is on anisotropic media with heterogeneities. Thus, the $\mathbf{G}^0$ required is that for an anisotropic medium. The lowest possible anisotropic symmetry class to be considered is that of a medium with a single symmetry axis, that is transversely isotropic. The medium of uniaxially aligned cracks is considered to be transversely isotropic, a medium with a single symmetry axis defined here by the unit vector $\hat{\mathbf{n}}$. The fourth-rank elastic moduli tensor, $\overline{\mathbf{C}}$, given in Eq. (4.8) for a transversely isotropic medium, may be written in terms of $\hat{\mathbf{n}}$ as

$$\overline{C}_{ijkl} = \lambda_\perp \delta_{ij}\delta_{kl} + \mu_\perp (\delta_{ik}\delta_{jl} + \delta_{il}\delta_{jk}) + \Gamma_1 (\delta_{ij}\hat{n}_k\hat{n}_l + \delta_{ij}\hat{n}_i\hat{n}_j) +$$
$$\Gamma_2 (\delta_{ik}\hat{n}_j\hat{n}_l + \delta_{il}\hat{n}_j\hat{n}_k + \delta_{jk}\hat{n}_i\hat{n}_l + \delta_{jl}\hat{n}_i\hat{n}_k) + \Gamma_3\ \hat{n}_i\hat{n}_j\hat{n}_k\hat{n}_l. \tag{4.11}$$

The above elastic constants are defined in Eqs. (4.9).

For propagation in the $\hat{\mathbf{p}}$ direction as shown in Fig. 4.2, the shear horizontal wave (SH) in a transversely isotropic medium is polarized in direction $\hat{\mathbf{u}}_1$, that is perpendicular to the plane defined by $\hat{\mathbf{p}}$ and $\hat{\mathbf{n}}$. The angle between the $\hat{\mathbf{p}}$ and $\hat{\mathbf{n}}$ is defined as Θ. The quasi-P and quasi-SV waves are polarized in directions defined by $\hat{\mathbf{u}}_2$ and $\hat{\mathbf{u}}_3$, respectively, both of which lie in the $\hat{\mathbf{p}}$-$\hat{\mathbf{n}}$ plane. It is noted that $\hat{\mathbf{u}}_1$, $\hat{\mathbf{u}}_2$ and $\hat{\mathbf{u}}_3$ form an orthonormal basis such that $\hat{\mathbf{u}}_3 = \hat{\mathbf{u}}_1 \times \hat{\mathbf{u}}_2$. The vector $\hat{\mathbf{u}}_2$ is directed at an angle ψ from the propagation direction $\hat{\mathbf{p}}$. The bare Green's dyadic $\mathbf{G}^0$ may be diagonalized by using the directions $\hat{\mathbf{u}}_2$ and $\hat{\mathbf{u}}_3$, such that $\mathbf{I} - \hat{\mathbf{u}}_1\hat{\mathbf{u}}_1 = \hat{\mathbf{u}}_2\hat{\mathbf{u}}_2 + \hat{\mathbf{u}}_3\hat{\mathbf{u}}_3$.

Substituting the elastic stiffness tensor $\overline{\mathbf{C}}$ into the transformed equation of motion,

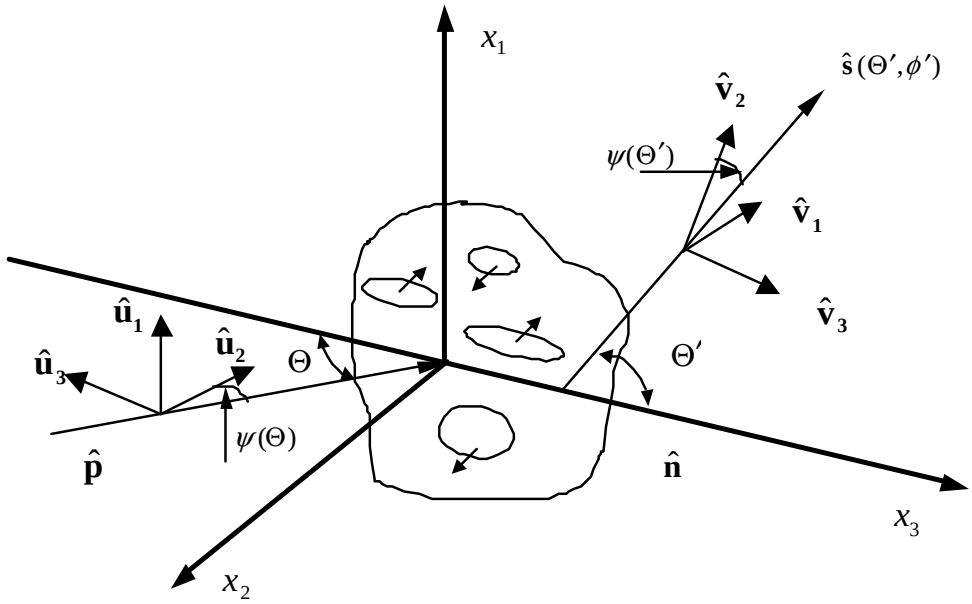

Figure 4.2: Geometry for the propagation direction $\hat{\mathbf{p}}$, the scattered direction $\hat{\mathbf{s}}$, and the respective polarization direction $\hat{\mathbf{u}}$ and $\hat{\mathbf{v}}$ in the local coordinate system.

Eq. (2.4), gives in direct notation [57]

$$\begin{aligned}
&\left\{\hat{\mathbf{u}}_1\hat{\mathbf{u}}_1\left[\omega^2 - p^2\left(\mu_\perp + \Gamma_2\cos^2\Theta\right)\right]\right. \\
&+\hat{\mathbf{u}}_2\hat{\mathbf{u}}_2\left[\omega^2 - p^2\left(Q + P\cos^2\psi + R\cos^2\left(\Theta+\psi\right)\right)\right] \\
&\left.+\hat{\mathbf{u}}_3\hat{\mathbf{u}}_3\left[\omega^2 - p^2\left(Q + P\sin^2\psi + R\sin^2\left(\Theta+\psi\right)\right)\right]\right\}\cdot\mathbf{G}^0\left(\mathbf{p}\right) = \mathbf{I}.
\end{aligned} \tag{4.12}$$

The quantities Q, P, and R in Eq. (4.12) are defined by

$$\begin{aligned}
Q &= \mu_\perp + \Gamma_2\left(\hat{\mathbf{p}}\cdot\hat{\mathbf{n}}\right)^2 - \left(\Gamma_1+\Gamma_2\right)\left(1-\left(\hat{\mathbf{p}}\cdot\hat{\mathbf{n}}\right)^2\right), \\
P &= \lambda_\perp + \mu_\perp + \Gamma_1 + \Gamma_2, \\
R &= \Gamma_1 + 2\Gamma_2 + \Gamma_3\left(\hat{\mathbf{p}}\cdot\hat{\mathbf{n}}\right)^2.
\end{aligned} \tag{4.13}$$

It should also be kept in mind that the vectors $\hat{\mathbf{u}}_2$ and $\hat{\mathbf{u}}_3$ are functions of the direction of propagation, $\hat{\mathbf{p}}$, relative to the material symmetry axis, $\hat{\mathbf{n}}$. This dependence, $\psi = \psi\left(\Theta\right)$ will

remain implicit throughout.

The bare Green's dyadic may then be written in the form

$$\mathbf{G}^0(\mathbf{p}) = g^0_{SH}(\mathbf{p})\,\hat{\mathbf{u}}_1\hat{\mathbf{u}}_1 + g^0_{qP}(\mathbf{p})\,\hat{\mathbf{u}}_2\hat{\mathbf{u}}_2 + g^0_{qSV}(\mathbf{p})\,\hat{\mathbf{u}}_3\hat{\mathbf{u}}_3, \tag{4.14}$$

where the dispersion relations for the bare response of the SH, qP, and qSV waves are given by

$$\begin{aligned}
g^0_{SH}(\mathbf{p}) &= \left[\omega^2 - p^2\left(\mu_\perp + \Gamma_2\cos^2\Theta\right)\right]^{-1} \\
&= \left[\omega^2 - p^2 c^2_{SH}\right]^{-1}, \\
g^0_{qP}(\mathbf{p}) &= \left[\omega^2 - p^2\left(Q + P\cos^2\psi + R\cos^2(\Theta+\psi)\right)\right]^{-1} \\
&= \left[\omega^2 - p^2 c^2_{qP}\right]^{-1}, \\
g^0_{qSV}(\mathbf{p}) &= \left[\omega^2 - p^2\left(Q + P\sin^2\psi + R\sin^2(\Theta+\psi)\right)\right]^{-1} \\
&= \left[\omega^2 - p^2 c^2_{qSV}\right]^{-1},
\end{aligned} \tag{4.15}$$

with Q, P, and R defined in Eqs. (4.13).

The mean response, $\langle\mathbf{G}(\mathbf{p})\rangle$, is governed by the Dyson equation, Eq. (2.7). The solution of $\langle\mathbf{G}(\mathbf{p})\rangle$ is expressed in terms of $\mathbf{G}^0(\mathbf{p})$ and $\tilde{\mathbf{M}}(\mathbf{p})$. Similar to $\mathbf{G}^0$, the mean response $\langle\mathbf{G}(\mathbf{p})\rangle$ and self-energy $\tilde{\mathbf{M}}(\mathbf{p})$ may be written in terms of the orthonormal basis defined by $\hat{\mathbf{u}}_1$, $\hat{\mathbf{u}}_2$, and $\hat{\mathbf{u}}_3$ in the form

$$\begin{aligned}
\langle\mathbf{G}(\mathbf{p})\rangle &= g_{SH}(\mathbf{p})\,\hat{\mathbf{u}}_1\hat{\mathbf{u}}_1 + g_{qP}(\mathbf{p})\,\hat{\mathbf{u}}_2\hat{\mathbf{u}}_2 + g_{qSV}(\mathbf{p})\,\hat{\mathbf{u}}_3\hat{\mathbf{u}}_3, \\
\tilde{\mathbf{M}}(\mathbf{p}) &= m_{SH}(\mathbf{p})\,\hat{\mathbf{u}}_1\hat{\mathbf{u}}_1 + m_{qP}(\mathbf{p})\,\hat{\mathbf{u}}_2\hat{\mathbf{u}}_2 + m_{qSV}(\mathbf{p})\,\hat{\mathbf{u}}_3\hat{\mathbf{u}}_3,
\end{aligned} \tag{4.16}$$

where it is again noted that the propagation direction $\hat{\mathbf{p}}$ is implicit within the directions $\hat{\mathbf{u}}_1$, $\hat{\mathbf{u}}_2$, and $\hat{\mathbf{u}}_3$. The attenuations for the three wave types are given in the general form,

Eq. (2.13). In this transversely isotropic case, the notation K is defined as the polarization for the wave type β ($1, 2$ or 3 for wave types SH, qP and qSV, respectively). It is clear that the above expressions of the attenuation for uniaxially aligned crack distributions are more complicated than those for a distribution of randomly oriented cracks as discussed in Chapter 3. In the next section, the covariance and attenuation are specified.

4.4 Attenuations

The relevant inner products on the covariance of the effective moduli fluctuations are necessary for calculating the attenuations. The tensorial part of the covariance is represented by an eighth-rank tensor which is given explicitly by

$$\Xi\left(\mathbf{q}\right)^{\cdots\cdot\mathbf{\hat{u}\hat{p}\hat{s}\hat{v}}}_{\cdots\cdot\mathbf{\hat{u}\hat{p}\hat{s}\hat{v}}} = \Xi\left(\mathbf{q}\right)^{ijkl}_{\alpha\beta\gamma\delta}\,\hat{u}_\beta\hat{u}_k\hat{p}_\alpha\hat{p}_l\hat{s}_i\hat{s}_\delta\hat{v}_\gamma\hat{v}_j. \tag{4.17}$$

For the case of uniaxially aligned cracks, the covariance is dependent on the crack orientations $\hat{\mathbf{m}}$. To calculate the covariance, the following identities are needed

$$\begin{aligned}
\langle\hat{m}_i\hat{m}_j\rangle &= \frac{1}{2}\Delta_{ij},\\
\langle\hat{m}_i\hat{m}_j\hat{m}_k\hat{m}_l\rangle &= \frac{1}{8}\left(\Delta_{ij}\Delta_{kl}+\Delta_{ik}\Delta_{jl}+\Delta_{il}\Delta_{jk}\right),\\
\langle\hat{m}_i\hat{m}_j\hat{m}_k\hat{m}_l\hat{m}_\alpha\hat{m}_\beta\rangle &= \frac{1}{48}\left[\Delta_{ij}\Delta_{kl}\Delta_{\alpha\beta}\right.\\
&\quad \left.+\text{all permutations -15 terms in all }\right],\\
\langle\hat{m}_i\hat{m}_j\hat{m}_k\hat{m}_l\hat{m}_\alpha\hat{m}_\beta\hat{m}_\gamma\hat{m}_\delta\rangle &= \frac{1}{384}\left[\Delta_{ij}\Delta_{kl}\Delta_{\alpha\beta}\Delta_{\gamma\delta}\right.\\
&\quad \left.+\text{all permutations -105 terms in all }\right],
\end{aligned} \tag{4.18}$$

where the brackets, $\langle\rangle$, denote an ensemble average, and $\Delta_{MN} = (\delta_{MN} - \hat{n}_M\hat{n}_N)$. The unit vector $\hat{\mathbf{n}}$ is the uniaxial symmetry axis. All averages of odd numbers of $\hat{\mathbf{m}}$'s are zero.

In addition to these tensorial averages, the average of the spatial part of the covariance must be determined. As discussed in Chapter 3, the necessary relation is given by $\langle H(\mathbf{x})H(\mathbf{y})\rangle = \varepsilon \Pr(r|0)$, where $\Pr(r|0) = (1-\varepsilon)W(r) + \varepsilon$, is defined as the conditional probability [76]. Due to the assumption of small damage density, the higher order terms in ε may be neglected. Therefore, $\langle \delta C_{ijkl}(\mathbf{x}) \delta C_{\alpha\beta\gamma\delta}(\mathbf{y})\rangle = \varepsilon W(r)\, \Xi_{ijkl}^{\alpha\beta\gamma\delta}$. Averaging over all crack orientations, the covariance is thus defined by

$$\Xi_{ijkl}^{\alpha\beta\gamma\delta} = \frac{1}{2\pi}\int_0^{2\pi}\int_{-\pi/2}^{\pi/2}\left(\overline{C}_{ijkl}^{(s)}\overline{C}_{\alpha\beta\gamma\delta}^{(s)}\right)\delta(\varphi - \frac{\pi}{2})\sin\varphi d\varphi d\theta, \tag{4.19}$$

where the definition of $\overline{\mathbf{C}}^{(s)}$ is given by Eq. (3.53) in the previous chapter. Substituting the identities of Eqs. (4.18) into Eq.(4.19), the generally compact form of $\boldsymbol{\Xi}$ is constructed in terms of Kronecker deltas and pairs of $\hat{\mathbf{n}}$'s. The general compact form of $\boldsymbol{\Xi}$ is given by

$$\begin{aligned}
\Xi_{ijkl}^{\alpha\beta\gamma\delta} &= T_1(\delta_{ij} - n_i n_j)(\delta_{kl} - n_k n_l)(\delta_{\alpha\beta} - n_\alpha n_\beta)(\delta_{\gamma\delta} - n_\gamma n_\delta) \\
&+ T_2\{(\delta_{ij} - n_i n_j)(\delta_{kl} - n_k n_l)[(\delta_{\alpha\gamma} - n_\alpha n_\gamma)(\delta_{\beta\delta} - n_\beta n_\delta) + (\delta_{\alpha\delta} - n_\alpha n_\delta)(\delta_{\beta\gamma} - n_\beta n_\gamma)] \\
&+ (\delta_{\alpha\beta} - n_\alpha n_\beta)(\delta_{\gamma\delta} - n_\gamma n_\delta)[(\delta_{ik} - n_i n_k)(\delta_{jl} - n_j n_l) + (\delta_{il} - n_i n_l)(\delta_{jk} - n_j n_k)]\} \\
&+ T_3[(\delta_{ik} - n_i n_k)(\delta_{jl} - n_j n_l) + (\delta_{il} - n_i n_l)(\delta_{jk} - n_j n_k)] \\
&\quad \cdot [(\delta_{\alpha\gamma} - n_\alpha n_\gamma)(\delta_{\beta\delta} - n_\beta n_\delta) + (\delta_{\alpha\delta} - n_\alpha n_\delta)(\delta_{\beta\gamma} - n_\beta n_\gamma)] \\
&+ T_4\{(\delta_{ij} - n_i n_j)(\delta_{\alpha\beta} - n_\alpha n_\beta)[(\delta_{\gamma k} - n_\gamma n_k)(\delta_{\delta l} - n_\delta n_l) + (\delta_{\gamma l} - n_\gamma n_l)(\delta_{\delta k} - n_\delta n_k)] \\
&+ (\delta_{kl} - n_k n_l)(\delta_{\alpha\beta} - n_\alpha n_\beta)[(\delta_{\gamma i} - n_\gamma n_i)(\delta_{\delta j} - n_\delta n_j) + (\delta_{\gamma j} - n_\gamma n_j)(\delta_{\delta i} - n_\delta n_i)]
\end{aligned} \tag{4.20}$$

$$\begin{aligned}
&+ (\delta_{ij} - n_i n_j)(\delta_{\gamma\delta} - n_\gamma n_\delta)[(\delta_{\alpha k} - n_\alpha n_k)(\delta_{\beta l} - n_\beta n_l) + (\delta_{\alpha l} - n_\alpha n_l)(\delta_{\beta k} - n_\beta n_k)] \\
&+ (\delta_{kl} - n_k n_l)(\delta_{\gamma\delta} - n_\gamma n_\delta)[(\delta_{\alpha i} - n_\alpha n_i)(\delta_{\beta j} - n_\beta n_j) + (\delta_{\alpha j} - n_\alpha n_j)(\delta_{\beta i} - n_\beta n_i)] \\
&+ T_5\{(\delta_{\alpha\beta} - n_\alpha n_\beta)(\delta_{ik} - n_i n_k)[(\delta_{\gamma j} - n_\gamma n_j)(\delta_{\delta l} - n_\delta n_l) + (\delta_{\gamma l} - n_\gamma n_l)(\delta_{\delta j} - n_\delta n_j)]
\end{aligned}$$

$$+(\delta_{\alpha\beta}-n_\alpha n_\beta)(\delta_{il}-n_i n_l)[(\delta_{\gamma j}-n_\gamma n_j)(\delta_{\delta k}-n_\delta n_k)+(\delta_{\gamma k}-n_\gamma n_k)(\delta_{\delta j}-n_\delta n_j)]$$

$$+(\delta_{\alpha\beta}-n_\alpha n_\beta)(\delta_{jk}-n_j n_k)[(\delta_{\gamma i}-n_\gamma n_i)(\delta_{\delta l}-n_\delta n_l)+(\delta_{\gamma l}-n_\gamma n_l)(\delta_{\delta i}-n_\delta n_i)]$$

$$+(\delta_{\alpha\beta}-n_\alpha n_\beta)(\delta_{jl}-n_j n_l)[(\delta_{\gamma i}-n_\gamma n_i)(\delta_{\delta k}-n_\delta n_k)+(\delta_{\gamma k}-n_\gamma n_k)(\delta_{\delta i}-n_\delta n_i)]$$

$$+(\delta_{\gamma\delta}-n_\gamma n_\delta)(\delta_{ik}-n_i n_k)[(\delta_{\alpha j}-n_\alpha n_j)(\delta_{\beta l}-n_\beta n_l)+(\delta_{\alpha l}-n_\alpha n_l)(\delta_{\beta j}-n_\beta n_j)]$$

$$+(\delta_{\gamma\delta}-n_\gamma n_\delta)(\delta_{il}-n_i n_l)[(\delta_{\alpha j}-n_\alpha n_j)(\delta_{\beta k}-n_\beta n_k)+(\delta_{\alpha k}-n_\alpha n_k)(\delta_{\beta j}-n_\beta n_j)]$$

$$+(\delta_{\gamma\delta}-n_\gamma n_\delta)(\delta_{jk}-n_j n_k)[(\delta_{\alpha i}-n_\alpha n_i)(\delta_{\beta l}-n_\beta n_l)+(\delta_{\alpha l}-n_\alpha n_l)(\delta_{\beta i}-n_\beta n_i)]$$

$$+(\delta_{\gamma\delta}-n_\gamma n_\delta)(\delta_{jl}-n_j n_l)[(\delta_{\alpha i}-n_\alpha n_i)(\delta_{\beta k}-n_\beta n_k)+(\delta_{\alpha k}-n_\alpha n_k)(\delta_{\beta i}-n_\beta n_i)]$$

$$+(\delta_{\alpha\gamma}-n_\alpha n_\gamma)(\delta_{ij}-n_i n_j)[(\delta_{\beta k}-n_\beta n_k)(\delta_{\delta l}-n_\delta n_l)+(\delta_{\beta l}-n_\beta n_l)(\delta_{\delta k}-n_\delta n_k)]$$

$$+(\delta_{\alpha\gamma}-n_\alpha n_\gamma)(\delta_{kl}-n_k n_l)[(\delta_{\beta i}-n_\beta n_i)(\delta_{\delta j}-n_\delta n_j)+(\delta_{\beta j}-n_\beta n_j)(\delta_{\delta i}-n_\delta n_i)]$$

$$+(\delta_{\alpha\delta}-n_\alpha n_\delta)(\delta_{ij}-n_i n_j)[(\delta_{\beta k}-n_\beta n_k)(\delta_{\gamma l}-n_\gamma n_l)+(\delta_{\beta l}-n_\beta n_l)(\delta_{\gamma k}-n_\gamma n_k)]$$

$$+(\delta_{\alpha\delta}-n_\alpha n_\delta)(\delta_{kl}-n_k n_l)[(\delta_{\beta i}-n_\beta n_i)(\delta_{\gamma j}-n_\gamma n_j)+(\delta_{\beta j}-n_\beta n_j)(\delta_{\gamma i}-n_\gamma n_i)]$$

$$+(\delta_{\beta\gamma}-n_\beta n_\gamma)(\delta_{ij}-n_i n_j)[(\delta_{\alpha k}-n_\alpha n_k)(\delta_{\delta l}-n_\delta n_l)+(\delta_{\alpha l}-n_\alpha n_l)(\delta_{\delta k}-n_\delta n_k)]$$

$$+(\delta_{\beta\gamma}-n_\beta n_\gamma)(\delta_{kl}-n_k n_l)[(\delta_{\alpha i}-n_\alpha n_i)(\delta_{\delta j}-n_\delta n_j)+(\delta_{\alpha j}-n_\alpha n_j)(\delta_{\delta i}-n_\delta n_i)]$$

$$+(\delta_{\beta\delta}-n_\beta n_\delta)(\delta_{ij}-n_i n_j)[(\delta_{\alpha k}-n_\alpha n_k)(\delta_{\gamma l}-n_\gamma n_l)+(\delta_{\alpha l}-n_\alpha n_l)(\delta_{\gamma k}-n_\gamma n_k)]$$

$$+(\delta_{\beta\delta}-n_\beta n_\delta)(\delta_{kl}-n_k n_l)[(\delta_{\alpha i}-n_\alpha n_i)(\delta_{\gamma j}-n_\gamma n_j)+(\delta_{\alpha j}-n_\alpha n_j)(\delta_{\gamma i}-n_\gamma n_i)]\}$$

$$+T_6\{(\delta_{\alpha\gamma}-n_\alpha n_\gamma)(\delta_{ik}-n_i n_k)[(\delta_{\beta j}-n_\beta n_j)(\delta_{\delta l}-n_\delta n_l)+(\delta_{\beta l}-n_\beta n_l)(\delta_{\delta j}-n_\delta n_j)]$$

$$+(\delta_{\alpha\gamma}-n_\alpha n_\gamma)(\delta_{il}-n_i n_l)[(\delta_{\beta j}-n_\beta n_j)(\delta_{\delta k}-n_\delta n_k)+(\delta_{\beta k}-n_\beta n_k)(\delta_{\delta j}-n_\delta n_j)]$$

$$+(\delta_{\alpha\gamma}-n_\alpha n_\gamma)(\delta_{jk}-n_j n_k)[(\delta_{\beta i}-n_\beta n_i)(\delta_{\delta l}-n_\delta n_l)+(\delta_{\beta l}-n_\beta n_l)(\delta_{\delta i}-n_\delta n_i)]$$

$$+(\delta_{\alpha\gamma}-n_\alpha n_\gamma)(\delta_{jl}-n_j n_l)[(\delta_{\beta i}-n_\beta n_i)(\delta_{\delta k}-n_\delta n_k)+(\delta_{\beta k}-n_\beta n_k)(\delta_{\delta i}-n_\delta n_i)]$$

$$+(\delta_{\alpha\delta}-n_\alpha n_\delta)(\delta_{ik}-n_i n_k)[(\delta_{\beta j}-n_\beta n_j)(\delta_{\gamma l}-n_\gamma n_l)+(\delta_{\beta l}-n_\beta n_l)(\delta_{\gamma j}-n_\gamma n_j)]$$

$$+(\delta_{\alpha\delta}-n_\alpha n_\delta)(\delta_{il}-n_i n_l)[(\delta_{\beta j}-n_\beta n_j)(\delta_{\gamma k}-n_\gamma n_k)+(\delta_{\beta k}-n_\beta n_k)(\delta_{\gamma j}-n_\gamma n_j)]$$

$$+(\delta_{\alpha\delta}-n_\alpha n_\delta)(\delta_{jk}-n_j n_k)[(\delta_{\beta i}-n_\beta n_i)(\delta_{\gamma l}-n_\gamma n_l)+(\delta_{\beta l}-n_\beta n_l)(\delta_{\gamma i}-n_\gamma n_i)]$$

$$+(\delta_{\alpha\delta}-n_\alpha n_\delta)(\delta_{jl}-n_j n_l)[(\delta_{\beta i}-n_\beta n_i)(\delta_{\gamma k}-n_\gamma n_k)+(\delta_{\beta k}-n_\beta n_k)(\delta_{\gamma i}-n_\gamma n_i)]$$

$$+(\delta_{\beta\gamma}-n_\beta n_\gamma)(\delta_{ik}-n_i n_k)[(\delta_{\alpha j}-n_\alpha n_j)(\delta_{\delta l}-n_\delta n_l)+(\delta_{\alpha l}-n_\alpha n_l)(\delta_{\delta j}-n_\delta n_j)]$$

$$+(\delta_{\beta\gamma}-n_\beta n_\gamma)(\delta_{il}-n_i n_l)[(\delta_{\alpha j}-n_\alpha n_j)(\delta_{\delta k}-n_\delta n_k)+(\delta_{\alpha k}-n_\alpha n_k)(\delta_{\delta j}-n_\delta n_j)]$$

$$+(\delta_{\beta\gamma}-n_\beta n_\gamma)(\delta_{jk}-n_j n_k)[(\delta_{\alpha i}-n_\alpha n_i)(\delta_{\delta l}-n_\delta n_l)+(\delta_{\alpha l}-n_\alpha n_l)(\delta_{\delta i}-n_\delta n_i)]$$

$$+(\delta_{\beta\gamma}-n_\beta n_\gamma)(\delta_{jl}-n_j n_l)[(\delta_{\alpha i}-n_\alpha n_i)(\delta_{\delta k}-n_\delta n_k)+(\delta_{\alpha k}-n_\alpha n_k)(\delta_{\delta i}-n_\delta n_i)]$$

$$+(\delta_{\beta\delta}-n_\beta n_\delta)(\delta_{ik}-n_i n_k)[(\delta_{\alpha j}-n_\alpha n_j)(\delta_{\gamma l}-n_\gamma n_l)+(\delta_{\alpha l}-n_\alpha n_l)(\delta_{\gamma j}-n_\gamma n_j)]$$

$$+(\delta_{\beta\delta}-n_\beta n_\delta)(\delta_{il}-n_i n_l)[(\delta_{\alpha j}-n_\alpha n_j)(\delta_{\gamma k}-n_\gamma n_k)+(\delta_{\alpha k}-n_\alpha n_k)(\delta_{\gamma j}-n_\gamma n_j)]$$

$$+(\delta_{\beta\delta}-n_\beta n_\delta)(\delta_{jk}-n_j n_k)[(\delta_{\alpha i}-n_\alpha n_i)(\delta_{\gamma l}-n_\gamma n_l)+(\delta_{\alpha l}-n_\alpha n_l)(\delta_{\gamma i}-n_\gamma n_i)]$$

$$+(\delta_{\beta\delta}-n_\beta n_\delta)(\delta_{jl}-n_j n_l)[(\delta_{\alpha i}-n_\alpha n_i)(\delta_{\gamma k}-n_\gamma n_k)+(\delta_{\alpha k}-n_\alpha n_k)(\delta_{\gamma i}-n_\gamma n_i)]\}$$

$$+T_7[(\delta_{\alpha i}-n_\alpha n_i)(\delta_{\beta j}-n_\beta n_j)(\delta_{\gamma k}-n_\gamma n_k)(\delta_{\delta l}-n_\delta n_l)$$

$$+(\delta_{\alpha i}-n_\alpha n_i)(\delta_{\beta l}-n_\beta n_l)(\delta_{\gamma j}-n_\gamma n_j)(\delta_{\delta k}-n_\delta n_k)$$

$$+(\delta_{\alpha i}-n_\alpha n_i)(\delta_{\beta k}-n_\beta n_k)(\delta_{\gamma j}-n_\gamma n_j)(\delta_{\delta l}-n_\delta n_l)$$

$$+(\delta_{\alpha i}-n_\alpha n_i)(\delta_{\beta k}-n_\beta n_k)(\delta_{\gamma l}-n_\gamma n_l)(\delta_{\delta j}-n_\delta n_j)$$

$$+(\delta_{\alpha i}-n_\alpha n_i)(\delta_{\beta l}-n_\beta n_l)(\delta_{\gamma j}-n_\gamma n_j)(\delta_{\delta k}-n_\delta n_k)$$

$$+(\delta_{\alpha i}-n_\alpha n_i)(\delta_{\beta l}-n_\beta n_l)(\delta_{\gamma k}-n_\gamma n_k)(\delta_{\delta j}-n_\delta n_j)$$

$$+(\delta_{\alpha j}-n_\alpha n_j)(\delta_{\beta i}-n_\beta n_i)(\delta_{\gamma k}-n_\gamma n_k)(\delta_{\delta l}-n_\delta n_l)$$

$$+(\delta_{\alpha j}-n_\alpha n_j)(\delta_{\beta i}-n_\beta n_i)(\delta_{\gamma l}-n_\gamma n_l)(\delta_{\delta k}-n_\delta n_k)$$

$$+(\delta_{\alpha j}-n_\alpha n_j)(\delta_{\beta k}-n_\beta n_k)(\delta_{\gamma i}-n_\gamma n_i)(\delta_{\delta l}-n_\delta n_l)$$

$$+(\delta_{\alpha j}-n_\alpha n_j)(\delta_{\beta k}-n_\beta n_k)(\delta_{\gamma l}-n_\gamma n_l)(\delta_{\delta i}-n_\delta n_i)$$

$$+(\delta_{\alpha j}-n_\alpha n_j)(\delta_{\beta l}-n_\beta n_l)(\delta_{\gamma k}-n_\gamma n_k)(\delta_{\delta i}-n_\delta n_i)$$

$$+(\delta_{\alpha j}-n_\alpha n_j)(\delta_{\beta l}-n_\beta n_l)(\delta_{\gamma i}-n_\gamma n_i)(\delta_{\delta k}-n_\delta n_k)$$

$$+(\delta_{\alpha k}-n_\alpha n_k)(\delta_{\beta i}-n_\beta n_i)(\delta_{\gamma j}-n_\gamma n_j)(\delta_{\delta l}-n_\delta n_l)$$

$$+(\delta_{\alpha k}-n_\alpha n_k)(\delta_{\beta i}-n_\beta n_i)(\delta_{\gamma l}-n_\gamma n_l)(\delta_{\delta j}-n_\delta n_j)$$

$$+(\delta_{\alpha k}-n_\alpha n_k)(\delta_{\beta j}-n_\beta n_j)(\delta_{\gamma i}-n_\gamma n_i)(\delta_{\delta l}-n_\delta n_l)$$

$$+(\delta_{\alpha k}-n_\alpha n_k)(\delta_{\beta j}-n_\beta n_j)(\delta_{\gamma l}-n_\gamma n_l)(\delta_{\delta i}-n_\delta n_i)$$

$$+(\delta_{\alpha k}-n_\alpha n_k)(\delta_{\beta l}-n_\beta n_l)(\delta_{\gamma i}-n_\gamma n_i)(\delta_{\delta j}-n_\delta n_j)$$

$$+(\delta_{\alpha k}-n_\alpha n_k)(\delta_{\beta l}-n_\beta n_l)(\delta_{\gamma j}-n_\gamma n_j)(\delta_{\delta i}-n_\delta n_i)$$

$$+(\delta_{\alpha l}-n_\alpha n_l)(\delta_{\beta i}-n_\beta n_i)(\delta_{\gamma j}-n_\gamma n_j)(\delta_{\delta k}-n_\delta n_k)$$

$$+(\delta_{\alpha l}-n_\alpha n_l)(\delta_{\beta i}-n_\beta n_i)(\delta_{\gamma k}-n_\gamma n_k)(\delta_{\delta j}-n_\delta n_j)$$

$$+(\delta_{\alpha l}-n_\alpha n_l)(\delta_{\beta j}-n_\beta n_j)(\delta_{\gamma i}-n_\gamma n_i)(\delta_{\delta k}-n_\delta n_k)$$

$$+(\delta_{\alpha l}-n_\alpha n_l)(\delta_{\beta j}-n_\beta n_j)(\delta_{\gamma k}-n_\gamma n_k)(\delta_{\delta i}-n_\delta n_i)$$

$$+(\delta_{\alpha l}-n_\alpha n_l)(\delta_{\beta k}-n_\beta n_k)(\delta_{\gamma i}-n_\gamma n_i)(\delta_{\delta j}-n_\delta n_j)$$

$$+(\delta_{\alpha l}-n_\alpha n_l)(\delta_{\beta k}-n_\beta n_k)(\delta_{\gamma j}-n_\gamma n_j)(\delta_{\delta i}-n_\delta n_i)].$$

The form of the attenuations given in Eqs. (2.13) is dependent on various inner products on the covariance tensor. The vectors $\hat{\mathbf{p}}$ and $\hat{\mathbf{s}}$, respectively, represent the incoming and outgoing propagation directions. The vectors $\hat{\mathbf{u}}$ and $\hat{\mathbf{v}}$ are vectors defining the polarization directions of the particular waves. These vectors are perpendicular to the plane defined by $\hat{\mathbf{s}}$ or $\hat{\mathbf{p}}$ and $\hat{\mathbf{n}}$ (for SH waves) or they lie in this plane (for qP and qSV).

Now the necessary inner products involved in determining the attenuations are

calculated. The attenuations will vary angularly only within the plane defined by the propagation direction $\hat{\mathbf{p}}$ and the crack alignment direction $\hat{\mathbf{n}}$. Therefore, without loss of generality, a reference plane is defined as the $\hat{\mathbf{p}}$-$\hat{\mathbf{n}}$ plane as shown in Fig. 4.2). The following vectors are then defined with respect to a general $x_1x_2x_3$ coordinate system as

$$\begin{aligned} \hat{\mathbf{n}} &= \hat{\mathbf{x}}_3, \\ \hat{\mathbf{p}} &= \hat{\mathbf{x}}_2 \sin\Theta + \hat{\mathbf{x}}_3 \cos\Theta, \\ \hat{\mathbf{s}} &= \hat{\mathbf{x}}_1 \sin\Theta' \cos\phi' + \hat{\mathbf{x}}_2 \sin\Theta' \sin\phi' + \hat{\mathbf{x}}_3 \cos\Theta'. \end{aligned} \tag{4.21}$$

The polarization vectors $\hat{\mathbf{u}}$ and $\hat{\mathbf{v}}$ are then defined with respect to these angles and ψ as

$$\begin{aligned} \hat{\mathbf{u}}_1 &= \hat{\mathbf{x}}_1, \\ \hat{\mathbf{u}}_2 &= \hat{\mathbf{x}}_2 \sin\gamma + \hat{\mathbf{x}}_3 \cos\gamma, \\ \hat{\mathbf{u}}_3 &= -\hat{\mathbf{x}}_2 \cos\gamma + \hat{\mathbf{x}}_3 \sin\gamma, \end{aligned} \tag{4.22}$$

and

$$\begin{aligned} \hat{\mathbf{v}}_1 &= \hat{\mathbf{x}}_1 \sin\phi' - \hat{\mathbf{x}}_2 \cos\phi', \\ \hat{\mathbf{v}}_2 &= \hat{\mathbf{x}}_1 \sin\gamma' \cos\phi' + \hat{\mathbf{x}}_2 \sin\gamma' \sin\phi' + \hat{\mathbf{x}}_3 \cos\gamma', \\ \hat{\mathbf{v}}_3 &= -\hat{\mathbf{x}}_1 \cos\gamma' \cos\phi' - \hat{\mathbf{x}}_2 \cos\gamma' \sin\phi' + \hat{\mathbf{x}}_3 \sin\gamma', \end{aligned} \tag{4.23}$$

where the angles γ and γ' used hereafter are defined by

$$\gamma = \Theta + \psi(\Theta), \qquad \gamma' = \Theta' + \psi\left(\Theta'\right). \tag{4.24}$$

These angles, γ and γ', define the orientation angle of the qP wave with respect to the $\hat{\mathbf{n}}$ direction, for the $\hat{\mathbf{p}}$ and $\hat{\mathbf{s}}$ directions, respectively.

Inserting these definitions of the relevant unit vectors into Eq. (4.19), the required inner products are reduced to a simple form. The inner products are:

for α_{SH}

$$\begin{aligned}
\Xi^{\cdots\hat{\mathbf{u}}_1\hat{\mathbf{p}}\hat{\mathbf{s}}\hat{\mathbf{v}}_1}_{\cdots\hat{\mathbf{u}}_1\hat{\mathbf{p}}\hat{\mathbf{s}}\hat{\mathbf{v}}_1} &= \sin^2\Theta\sin^2\Theta'\left[-\eta_1\cos^2\phi'\sin^2\phi'+\eta_2\right], \\
\Xi^{\cdots\hat{\mathbf{u}}_1\hat{\mathbf{p}}\hat{\mathbf{s}}\hat{\mathbf{v}}_2}_{\cdots\hat{\mathbf{u}}_1\hat{\mathbf{p}}\hat{\mathbf{s}}\hat{\mathbf{v}}_2} &= \sin^2\Theta\sin^2\Theta'\sin^2\gamma'\left[\eta_1\cos^2\phi'\sin^2\phi'+\eta_3\right], \\
\Xi^{\cdots\hat{\mathbf{u}}_1\hat{\mathbf{p}}\hat{\mathbf{s}}\hat{\mathbf{v}}_3}_{\cdots\hat{\mathbf{u}}_1\hat{\mathbf{p}}\hat{\mathbf{s}}\hat{\mathbf{v}}_3} &= \sin^2\Theta\sin^2\Theta'\cos^2\gamma'\left[\eta_1\cos^2\phi'\sin^2\phi'+\eta_3\right],
\end{aligned} \tag{4.25}$$

for α_{qP}

$$\begin{aligned}
\Xi^{\cdots\hat{\mathbf{u}}_2\hat{\mathbf{p}}\hat{\mathbf{s}}\hat{\mathbf{v}}_1}_{\cdots\hat{\mathbf{u}}_2\hat{\mathbf{p}}\hat{\mathbf{s}}\hat{\mathbf{v}}_1} &= \sin^2\Theta\sin^2\Theta'\sin^2\gamma\left[\eta_1\cos^2\phi'\sin^2\phi'+\eta_3\right], \\
\Xi^{\cdots\hat{\mathbf{u}}_2\hat{\mathbf{p}}\hat{\mathbf{s}}\hat{\mathbf{v}}_2}_{\cdots\hat{\mathbf{u}}_2\hat{\mathbf{p}}\hat{\mathbf{s}}\hat{\mathbf{v}}_2} &= \sin^2\Theta\sin^2\Theta'\sin^2\gamma\sin^2\gamma'\left[\eta_1\sin^4\phi'+\eta_4\sin^2\phi'+\eta_5\right], \\
\Xi^{\cdots\hat{\mathbf{u}}_2\hat{\mathbf{p}}\hat{\mathbf{s}}\hat{\mathbf{v}}_3}_{\cdots\hat{\mathbf{u}}_2\hat{\mathbf{p}}\hat{\mathbf{s}}\hat{\mathbf{v}}_3} &= \sin^2\Theta\sin^2\Theta'\sin^2\gamma\cos^2\gamma'\left[\eta_1\sin^4\phi'+\eta_4\sin^2\phi'+\eta_5\right],
\end{aligned} \tag{4.26}$$

and for α_{qSV}

$$\begin{aligned}
\Xi^{\cdots\hat{\mathbf{u}}_3\hat{\mathbf{p}}\hat{\mathbf{s}}\hat{\mathbf{v}}_1}_{\cdots\hat{\mathbf{u}}_3\hat{\mathbf{p}}\hat{\mathbf{s}}\hat{\mathbf{v}}_1} &= \sin^2\Theta\sin^2\Theta'\cos^2\gamma\left[\eta_1\cos^2\phi'\sin^2\phi'+\eta_3\right], \\
\Xi^{\cdots\hat{\mathbf{u}}_3\hat{\mathbf{p}}\hat{\mathbf{s}}\hat{\mathbf{v}}_2}_{\cdots\hat{\mathbf{u}}_3\hat{\mathbf{p}}\hat{\mathbf{s}}\hat{\mathbf{v}}_2} &= \sin^2\Theta\sin^2\Theta'\cos^2\gamma\sin^2\gamma'\left[\eta_1\sin^4\phi'+\eta_4\sin^2\phi'+\eta_5\right], \\
\Xi^{\cdots\hat{\mathbf{u}}_3\hat{\mathbf{p}}\hat{\mathbf{s}}\hat{\mathbf{v}}_3}_{\cdots\hat{\mathbf{u}}_3\hat{\mathbf{p}}\hat{\mathbf{s}}\hat{\mathbf{v}}_3} &= \sin^2\Theta\sin^2\Theta'\cos^2\gamma\cos^2\gamma'\left[\eta_1\sin^4\phi'+\eta_4\sin^2\phi'+\eta_5\right],
\end{aligned} \tag{4.27}$$

where γ and γ' are defined in Eq. (4.24). The coefficients η_i $(i = 1...5)$ and T_j $(j = 1...7)$, are given by

$$\begin{gathered}
\eta_1 = 4T_3 + 16T_6 + 4T_7, \quad \eta_2 = T_3 + 4T_6 + 4T_7, \\
\eta_3 = T_4 + 4T_5 + 4T_6 + 6T_7, \\
\eta_4 = 4T_2 + 4T_4 + 32T_5 + 16T_6 + 16T_7, \quad \eta_5 = T_1 + 4T_4 + 4T_7,
\end{gathered} \tag{4.28}$$

and

$$
\begin{aligned}
T_1 &= -\frac{\nu^2(80\nu^4 - 416\nu^3 + 472\nu^2 + 184\nu - 235)M^2}{128(1-2\nu)^2}, \\
T_2 &= -\frac{\nu(12\nu^3 - 28\nu^2 + 127\nu - 184)M^2}{384}, \quad T_7 = \frac{\nu^2(1-2\nu)^2M^2}{384}, \\
T_3 &= \frac{(\nu-4)(\nu-12)(1-2\nu)^2M^2}{384}, \quad T_4 = \frac{\nu^2(10\nu-23)(2\nu-7)M^2}{384}, \\
T_5 &= \frac{\nu(1-2\nu)(6\nu^2 - 31\nu + 44)M^2}{384}, \quad T_6 = \frac{(3-2\nu)(1-2\nu)^2M^2}{96},
\end{aligned}
\tag{4.29}
$$

where the constant M is defined as $M = \mu\frac{32}{3}\frac{1-\nu}{(2-\nu)(1-2\nu)}$. The expressions given by Eqs. (4.25)-(4.27) are also directly related to the diffuse energy propagation, including backscatter [52],[53],[54].

As discussed previously, the tensorial and spatial components of the covariance are assumed to be independent and the correlation function η is assumed to have an exponential form $\eta(\mathbf{r}) = e^{-r/L}$, where L is the spatial correlation length, $L = 2\langle a \rangle$. Substituting the above inner products into Eqs. (2.13) and integrating over the azimuthal angle ϕ', the attenuations finally reduce to dimensionless forms

$$
\begin{aligned}
\alpha_{SH}(\Theta) L &= x_{SH}^4 \frac{\varepsilon}{2\rho^2 \bar{c}_{SH}^4} r_{SH}^3(\Theta) \sin^2\Theta \left[I_{SH-SH} \right. \\
&\quad \left. + I_{SH-qP} \left(\frac{\bar{c}_{SH}}{\bar{c}_{qP}} \right)^5 + I_{SH-qSV} \left(\frac{\bar{c}_{SH}}{\bar{c}_{qSV}} \right)^5 \right],
\end{aligned}
\tag{4.30}
$$

$$
\begin{aligned}
\alpha_{qP}(\Theta) L &= x_{qP}^4 \frac{\varepsilon}{2\rho^2 \bar{c}_{qP}^4} r_{qP}^3(\Theta) \sin^2\Theta \sin^2\gamma \left[I_{qP-SH} \left(\frac{\bar{c}_{qP}}{\bar{c}_{SH}} \right)^5 \right. \\
&\quad \left. + I_{qP-qP} + I_{qP-qSV} \left(\frac{\bar{c}_{qP}}{\bar{c}_{qSV}} \right)^5 \right],
\end{aligned}
\tag{4.31}
$$

$$
\begin{aligned}
\alpha_{qSV}(\Theta) L &= x_{qSV}^4 \frac{\varepsilon}{2\rho^2 \bar{c}_{qSV}^4} r_{qSV}^3(\Theta) \sin^2\Theta \cos^2\gamma \left[I_{qSV-SH} \left(\frac{\bar{c}_{qSV}}{\bar{c}_{SH}} \right)^5 \right. \\
&\quad \left. + I_{qSV-qP} \left(\frac{\bar{c}_{qSV}}{\bar{c}_{qP}} \right)^5 + I_{qSV-qSV} \right],
\end{aligned}
\tag{4.32}
$$

with the density, ρ, now included in the general form. The terms denoted by $I_{\beta-\gamma}$ within the square brackets represent integrals defined by

$$\begin{aligned}
I_{SH-SH} &= \int_0^{\pi} \left[\frac{\eta_1 \left(6X_{SH-SH}^2 - Y_{SH-SH}^2\right)}{2Y_{SH-SH}^2} + \frac{\eta_1 \left(2X_{SH-SH}Y_{SH-SH}^2 - 3X_{SH-SH}^2\right)}{Y_{SH-SH}^4 \left(X_{SH-SH}^2 - Y_{SH-SH}^2\right)^{1/2}} \right. \\
&\quad \left. \frac{\eta_2 X_{SH-SH}}{\left(X_{SH-SH}^2 - Y_{SH-SH}^2\right)^{3/2}} \right] r_{SH}^5 \left(\Theta'\right) \sin^3 \Theta' d\Theta', \\
I_{SH-\alpha} &= \int_0^{\pi} \left[\frac{\eta_1 \left(Y_{SH-\alpha}^2 - 6X_{SH-\alpha}^2\right)}{2Y_{SH-\alpha}^2} + \frac{\eta_1 \left(3X_{SH-\alpha}^2 - 2X_{SH-\alpha}Y_{SH-\alpha}^2\right)}{Y_{SH-\alpha}^4 \left(X_{SH-\alpha}^2 - Y_{SH-\alpha}^2\right)^{1/2}} \right. \\
&\quad \left. \frac{\eta_3 X_{SH-\alpha}}{\left(X_{SH-\alpha}^2 - Y_{SH-\alpha}^2\right)^{3/2}} \right] r_{\alpha}^5 \left(\Theta'\right) \Pi_{\alpha} \sin^3 \Theta' d\Theta',
\end{aligned} \tag{4.33}$$

and

$$\begin{aligned}
I_{\alpha-SH} &= \int_0^{\pi} \left[\frac{\eta_1 \left(Y_{\alpha-SH}^2 - 6X_{\alpha-SH}^2\right)}{2Y_{\alpha-SH}^2} + \frac{\eta_1 \left(3X_{\alpha-SH}^2 - 2X_{\alpha-SH}Y_{\alpha-SH}^2\right)}{Y_{\alpha-SH}^4 \left(X_{\alpha-SH}^2 - Y_{\alpha-SH}^2\right)^{1/2}} \right. \\
&\quad \left. \frac{\eta_2 X_{\alpha-SH}}{\left(X_{\alpha-SH}^2 - Y_{\alpha-SH}^2\right)^{3/2}} \right] r_{SH}^5 \left(\Theta'\right) \sin^3 \Theta' d\Theta', \\
I_{\delta-\alpha} &= \int_0^{\pi} \left[\frac{\eta_1 \left(6X_{\delta-\alpha}^2 + Y_{\delta-\alpha}^2\right) + 2\eta_4 Y_{\delta-\alpha}^2}{2Y_{\delta-\alpha}^4} \right. \\
&\quad + \frac{\eta_1 \left(4X_{\delta-\alpha}^3 Y_{\delta-\alpha}^2 - 3X_{\delta-\alpha}^5\right) + \eta_4 Y_{\delta-\alpha}^2 \left(2X_{\delta-\alpha}Y_{\delta-\alpha}^2 - X_{\delta-\alpha}^3\right)}{Y_{\delta-\alpha}^4 \left(X_{\delta-\alpha}^2 - Y_{\delta-\alpha}^2\right)^{3/2}} \\
&\quad \left. + \frac{\eta_5 X_{\delta-\alpha} Y_{\delta-\alpha}^4}{Y_{\delta-\alpha}^4 \left(X_{\delta-\alpha}^2 - Y_{\delta-\alpha}^2\right)^{3/2}} \right] r_{\alpha}^5 \left(\Theta'\right) \Pi_{\alpha} \sin^3 \Theta' d\Theta',
\end{aligned} \tag{4.34}$$

with

$$\begin{aligned}
X_{\beta-\gamma} &= 1 + x_{\beta}^2 r_{\beta}^2 \left(\Theta\right) + x_{\gamma}^2 r_{\gamma}^2 \left(\Theta'\right) - 2x_{\beta}x_{\gamma} r_{\beta}\left(\Theta\right) r_{\gamma}\left(\Theta'\right) \cos\Theta \cos\Theta', \\
Y_{\beta-\gamma} &= 2x_{\beta}x_{\gamma} r_{\beta}\left(\Theta\right) r_{\gamma}\left(\Theta'\right) \sin\Theta \sin\Theta',
\end{aligned} \tag{4.35}$$

for the different wave types, β and γ. The subscripts δ and α denote either the qP or qSV wave type, and the notation $\Pi_{qP} = \sin^2\left(\Theta' + \psi\left(\Theta'\right)\right)$, $\Pi_{qSV} = \cos^2\left(\Theta' + \psi\left(\Theta'\right)\right)$ is used. In Eqs. (4.30)-(4.35), the angular averaged wave speeds are defined as $\bar{c}_{\beta} =$

$\frac{1}{2}\int_0^{\pi} c_\beta(\Theta)\sin\Theta d\Theta$, for each wave type, β. Three nondimensional frequencies are then defined as $x_\beta = \omega L/\bar{c}_\beta$ and the slowness surface for each wave type is defined by the dimensionless quantity $r_\beta(\Theta) = \bar{c}_\beta/c_\beta(\Theta)$. Equations (4.30)-(4.34) are the primary results of this section.

In the long wavelength Rayleigh limit, $x_\beta << 1$ and these integrals become independent of incident direction and frequency. Therefore, they reduce to a much simpler form as

$$\begin{aligned} I_{SH-SH} &= \int_0^{\pi} \left(-\frac{\eta_1}{8} + \eta_2\right) r_{SH}^5(\Theta') \sin^3\Theta' d\Theta', \\ I_{SH-\alpha} &= \int_0^{\pi} \left(\frac{\eta_1}{8} + \eta_3\right) r_\alpha^5(\Theta') \Pi_\alpha \sin^3\Theta' d\Theta', \end{aligned} \tag{4.36}$$

and

$$\begin{aligned} I_{\alpha-SH} &= \int_0^{\pi} \left(\frac{\eta_1}{8} + \eta_3\right) r_{SH}^5(\Theta') \sin^3\Theta' d\Theta', \\ I_{\delta-\alpha} &= \int_0^{\pi} \left(\frac{3\eta_1}{8} + \frac{\eta_4}{2} + \eta_5\right) r_\alpha^5(\Theta') \Pi_\alpha \sin^3\Theta' d\Theta'. \end{aligned} \tag{4.37}$$

for all outgoing wave types. In the Rayleigh limit, the angular dependence of the attenuation is explicitly seen. In the subsequent section, example numerical results and discussion are presented.

4.5 Example Results

Numerical results are now presented for a specific case, in which the observed anisotropy of the cracked material is essentially due to the presence of the uniaxially aligned cracks. The material properties of the uncracked medium used are Young's modulus $E = 2.0 \times 10^{11}$Pa, Poisson's ratio $\nu = 0.30$, and density $\rho = 7850\,\mathrm{kg}\,/\,\mathrm{m}^3$. Using the dispersion

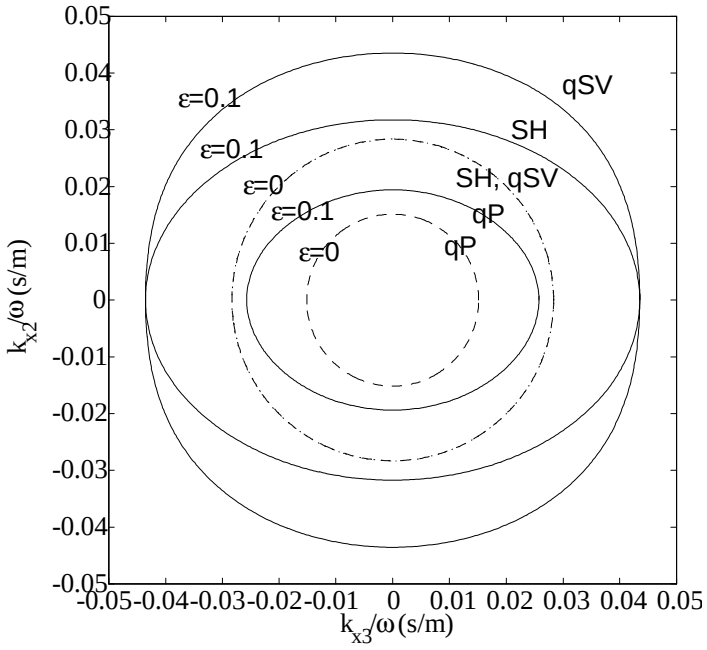

Figure 4.3: Slowness surfaces for damage densities $\varepsilon = 0$, 0.1.

relations given in Eqs. (4.15), the slowness surfaces calculated for different damage densities, $\varepsilon = 0$ and 0.1, are shown in Fig. 4.3. The normalized effective wave velocity, $c_\beta(\varepsilon)/c_\beta(\varepsilon = 0)$, of each wave type is presented in Fig. 4.4. The effective velocities decrease with increasing damage density ε within the considered frequency range. The reduction of velocity of the SH and qP waves due to the presence of the uniaxially aligned cracks is a maximum at $\Theta = 90°$, it becomes smaller as Θ decreases, and the reduction reaches a minimum at $\Theta = 0°$, though the changes are not substantial. These results are in basic agreement with those of Zhang and Gross [26] and Eriksson and Datta [30]. The qSV wave velocity is seen to have a greater reduction at $\Theta = 45°$ than at $\Theta = 0°$ and 90°.

In the Rayleigh limit, the attenuations simplify considerably since the integrals reduce to those given by Eqs. (4.36) and (4.37). The attenuation depends on the fourth

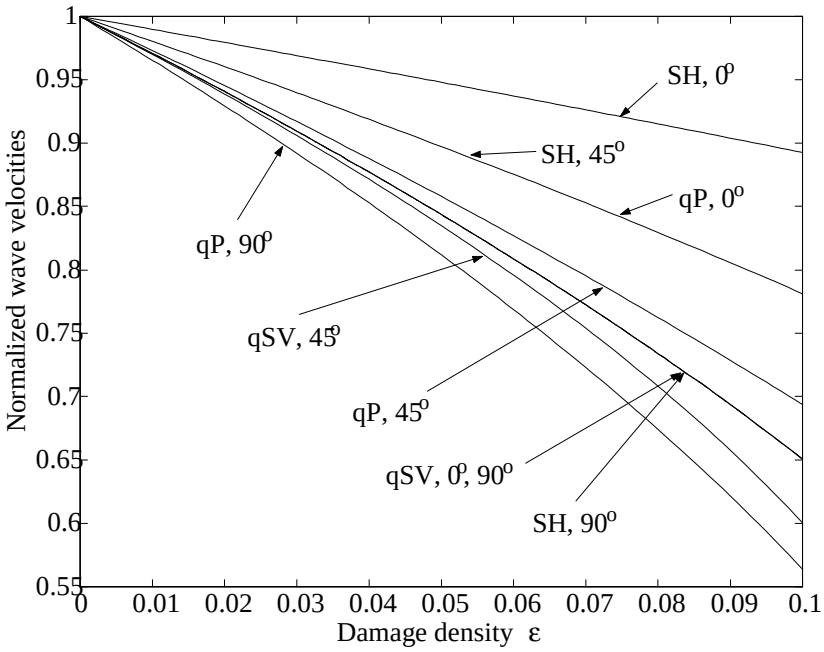

Figure 4.4: Normalized wave velocity of each wave type, $c_\beta(\varepsilon)/c_\beta(\varepsilon = 0)$, versus damage density ε at $\Theta = 0°, 45°$ and $90°$.

power of frequency in the Rayleigh regime. Thus, the angular Rayleigh attenuation results shown in Fig. 4.5 are given in a general form of, $\alpha L/(x^4\varepsilon)$, for each wave type. In Fig. 4.5, the SH and qP waves are observed to have their maxima at $\Theta = 90°$ — perpendicular to the crack alignment direction $\hat{\mathbf{n}}$. The qSV wave is observed to have zero attenuation for propagation along the symmetry axis ($\Theta = 0°$) and perpendicular to it ($\Theta = 90°$). All wave types have zero attenuation along the symmetry axis, because the material properties do not vary in that direction. Those results are qualitatively the same as previous work [56],[46],[57]. Zhang and Gross [26] comment that their attenuation results are not zero for propagation along the symmetry axis. They speculate that the attenuation arises from Poisson effects. However, such a comparison is difficult to make since the focus of their work was at much higher frequencies. An additional feature observed for the qSV wave in

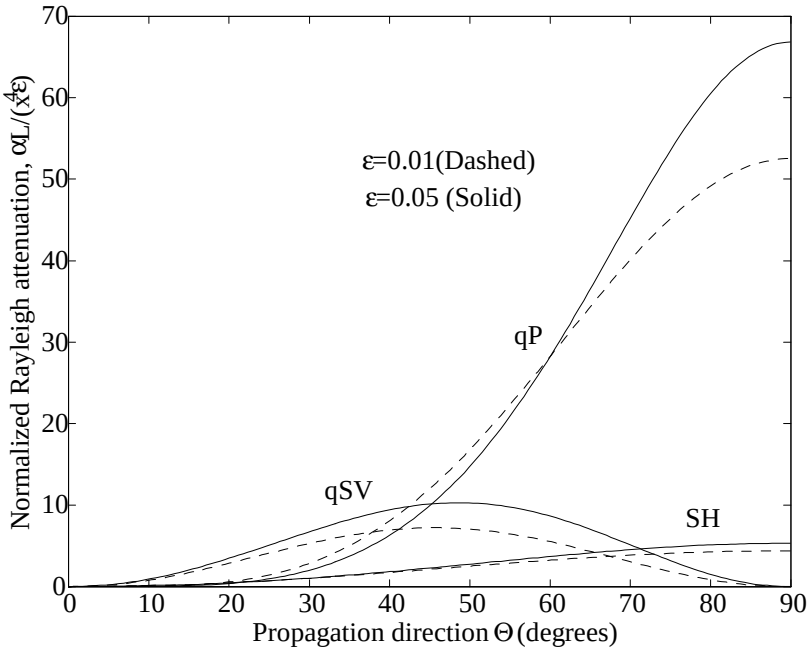

Figure 4.5: Rayleigh limit as a function of direction for the SH, qP, and qSV waves for damage density $\varepsilon = 0.01$(dashed) and $\varepsilon = 0.05$(solid). The dimensionless attenuation αL has been normalized by the fourth power of the dimensionless frequency and damage density for the respective wave type: $\alpha_{SH}L/(x_{SH}^4\epsilon)$, $\alpha_{qP}L/(x_{qP}^4\epsilon)$, and $\alpha_{qSV}L/(x_{qSV}^4\epsilon)$.

Fig. 4.5, is the asymmetry that develops as ε increases. This peak is around $\Theta = 45°$, but shifts slightly higher as ε increases from 0.01 to 0.05.

Using Eqs. (4.30)-(4.32), attenuation results are given in terms of the single dimensionless frequency $x_{SH} = \omega L/\bar{c}_{SH}$. Outside the Rayleigh regime, the attenuations were calculated using the complete integrals, Eqs. (4.33) and (4.34), by numerical integration. In Fig. 4.6, the normalized SH wave attenuation, α_{SH}/k_{SH}, is presented as a function of propagation direction for three different damage densities at frequency $x_{SH} = 1.0$. The attenuation for propagation perpendicular to the crack alignment direction is seen to increase more quickly than for other directions as the damage increases. The results for the normalized qP attenuation, α_{qP}/k_{qP}, are shown in Fig. 4.7. These results display similar behavior

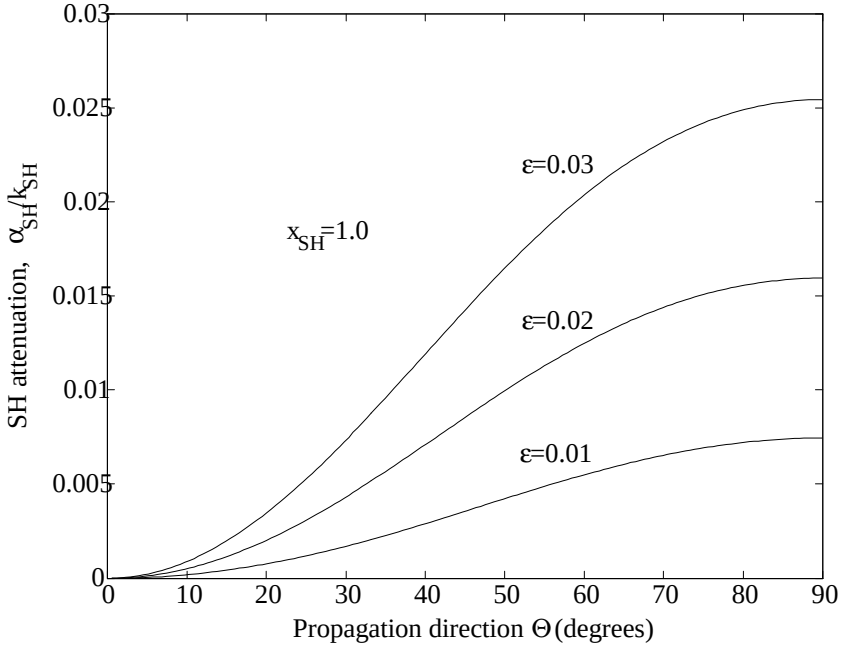

Figure 4.6: Angular dependence of the normalized SH attenuation, α_{SH}/k_{SH} for various damage densities ε at frequency $x_{SH} = 1.0$.

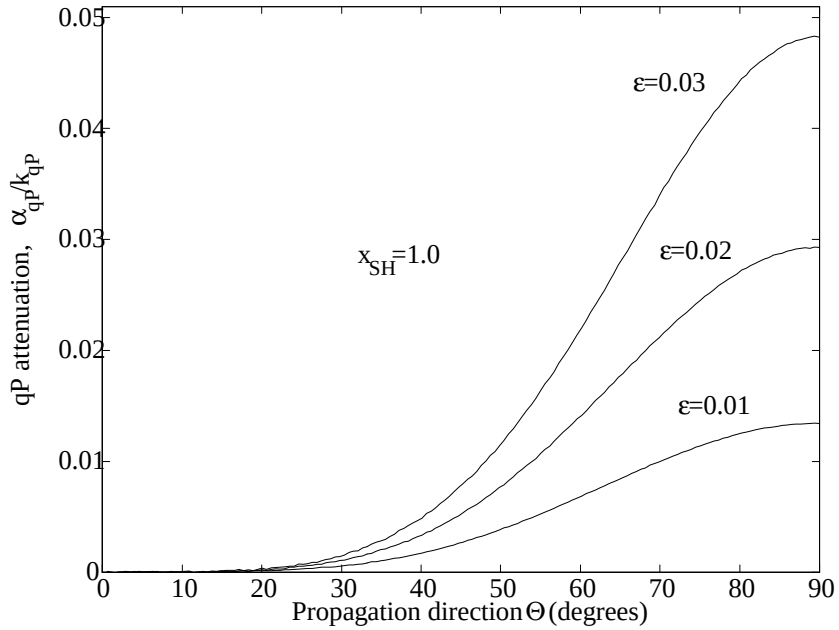

Figure 4.7: Angular dependence of the normalized qP attenuation, α_{qP}/k_{qP} for various damage densities ε at frequency $x_{SH} = 1.0$.

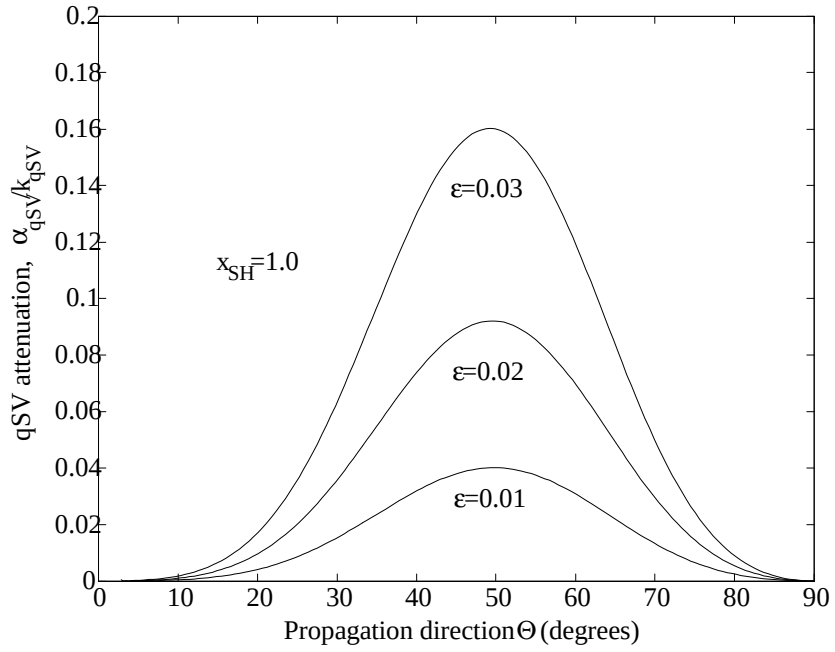

Figure 4.8: Angular dependence of the normalized qSV attenuation, α_{qSV}/k_{qSV} for various damage densities ε at frequency $x_{SH} = 1.0$.

as the SH attenuation in terms of the change with angle and damage. Analogous results have been observed in textured polycrystals by Hirsekorn [46], Ahmed and Thompson [56], and Turner [57]. In Fig. 4.8, the normalized qSV attenuation, α_{qSV}/k_{qSV}, is presented at various damage densities for frequency $x_{SH} = 1.0$. The attenuation for propagation at $\Theta = 0°$ and $90°$ is zero as discussed above. For propagation at $\Theta = 45°$, the attenuation is the largest. In addition, it is seen that the peak of maximum attenuation shifts as the damage increases, although this shift is not significant. The direction of maximum α_{qSV} is dependent upon both frequency and damage. This shift is thought to be the result of the induced anisotropy from the cracks as shown in the slowness plots in Fig. 4.3 as speculated elsewhere [57]. However, further investigation is necessary to determine the precise reason for this peak shift.

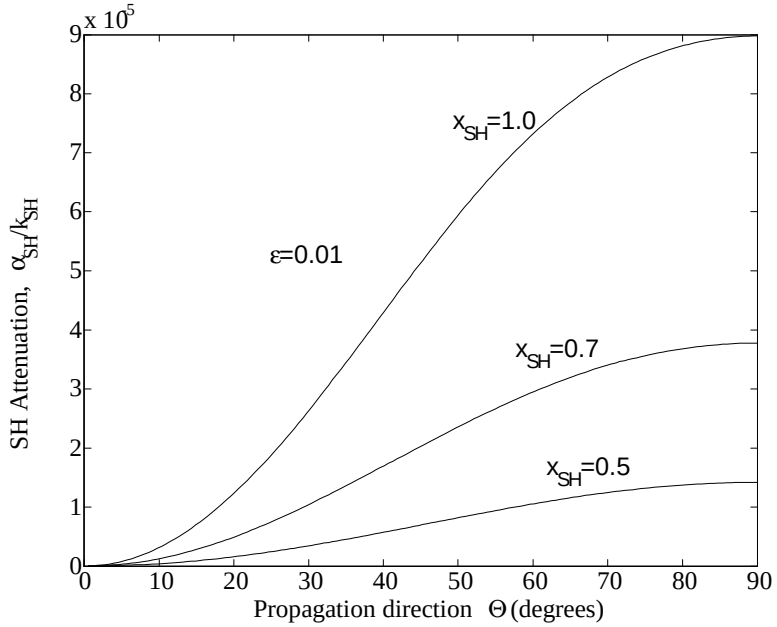

Figure 4.9: Angular dependence of the normalized SH attenuation, α_{SH}/k_{SH} for various frequencies, x_{SH}, at damage density $\varepsilon = 0.01$.

In Fig. 4.9, the normalized SH wave attenuation, α_{SH}/k_{SH}, is presented as a function of propagation direction for three different frequencies, x_{SH}, at damage density $\varepsilon = 0.01$. The attenuation for propagation perpendicular to the crack alignment direction is seen to increase more rapidly than for other directions as the frequency increases. The results for the normalized qP attenuation, α_{qP}/k_{qP}, are shown in Fig. 4.10. These results demonstrate similar behavior as the SH attenuation in terms of the change with angle and frequency. Analogous results have been observed in textured polycrystals by Ahmed and Thompson [56] and Turner [57]. In Fig. 4.11, the normalized qSV attenuation, α_{qSV}/k_{qSV}, is presented at various frequencies for damage density $\varepsilon = 0.01$. The attenuation for propagation at $\Theta = 0°$ and $90°$ is zero as discussed above. For propagation at $\Theta = 45°$, the attenuation is the largest. In addition, it is seen that the peak of maximum attenuation shifts slightly higher

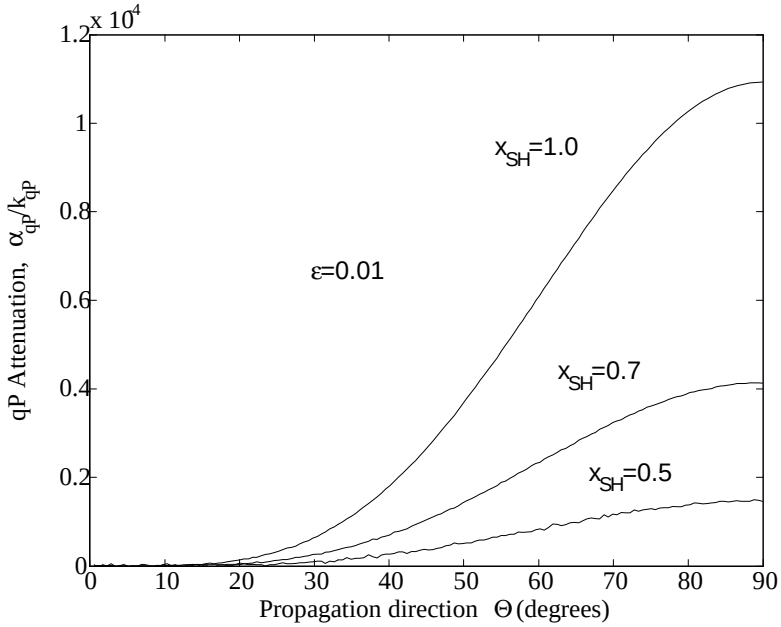

Figure 4.10: Angular dependence of the normalized qP attenuation, α_{qP}/k_{qP} for various frequencies, x_{SH}, at damage density $\varepsilon = 0.01$.

as the frequency increases, although this shift is not significant. The direction of maximum α_{qSV} is dependent upon both frequency and damage. This shift is thought to be the result of the induced anisotropy from the cracks as shown in the slowness plots in Fig. 4.3 as speculated elsewhere [57].

Finally, results are presented for the normalized attenuations as a function of frequency for several propagation directions at damage density $\varepsilon = 0.01$. In Figs. 4.12 and 4.13, the normalized SH and qP attenuations are plotted versus dimensionless frequency, x_{SH}, for propagation $45°, 60°$ and $90°$. The attenuations for propagation perpendicular to the crack alignment direction are seen to increase more rapidly than for other directions as the frequency increases. The normalized qSV attenuation is plotted versus, x_{SH}, for propagation $45°, 60°$ and $30°$ in Fig. 4.14. The attenuations for propagation direction at

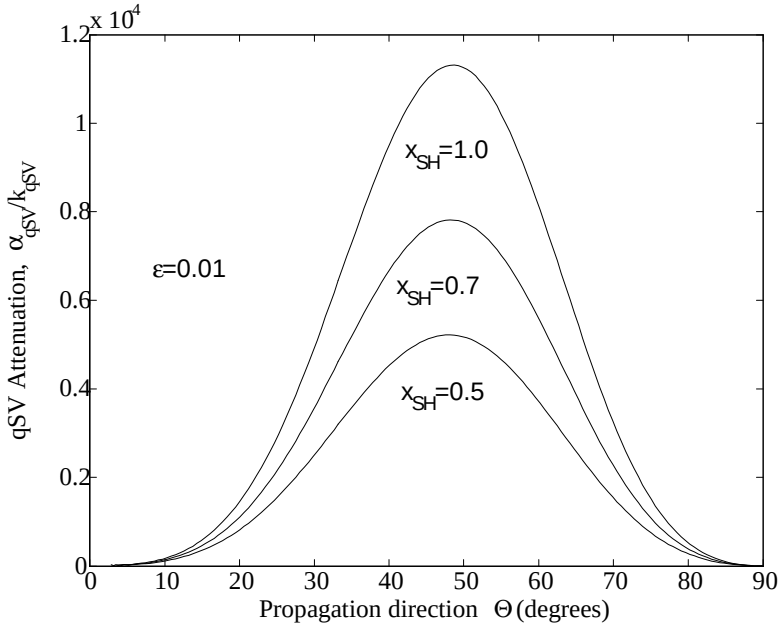

Figure 4.11: Angular dependence of the normalized qSV attenuation, α_{qSV}/k_{qSV} for various frequencies, x_{SH}, at damage density $\varepsilon = 0.01$.

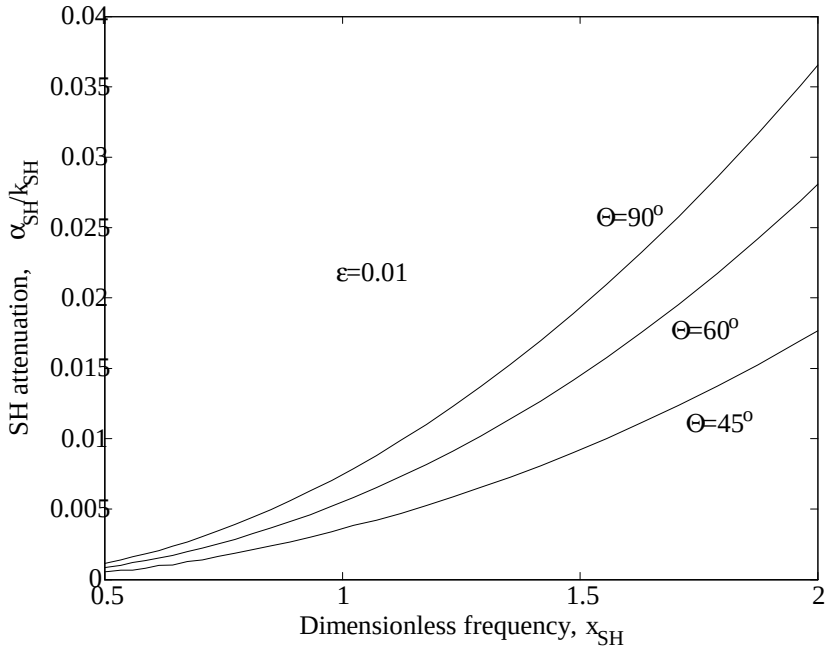

Figure 4.12: Normalized SH attenuation, α_{SH}/k_{SH}, as a function of dimensionless frequency, x_{SH}, at damage density $\varepsilon = 0.01$, for propagation directions of $45°, 60°, 90°$.

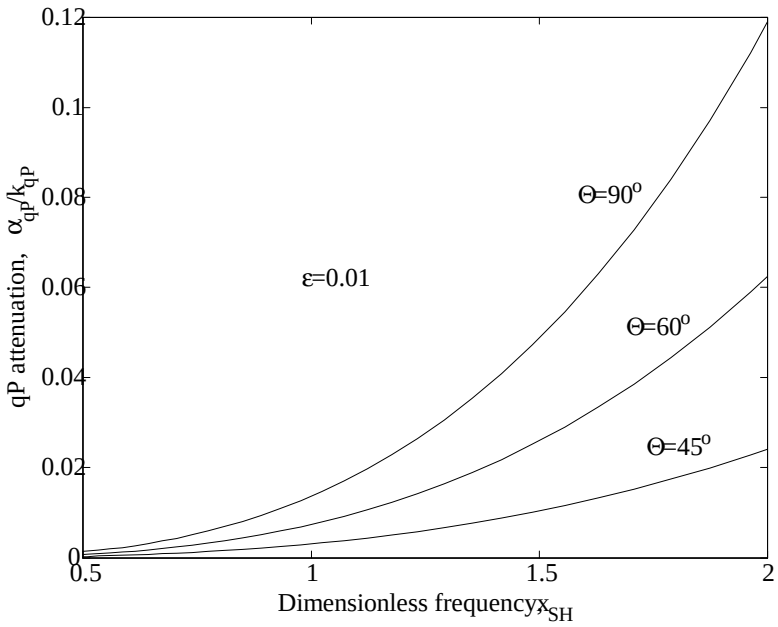

Figure 4.13: Normalized qP attenuation, α_{qP}/k_{qP}, as a function of dimensionless frequency, x_{SH}, at damage density $\varepsilon = 0.01$, for propagation directions of $45°, 60°, 90°$.

$\Theta = 60°$ and $30°$ are not identical such that the maximum peak is not located at $\Theta = 45°$ within the frequency limits considered here. This result implies that the feature of the asymmetry is developed as frequency increases as discussed above.

4.6 Conclusions

In this chapter, wave propagation and scattering have been examined for media with uniaxially aligned cracks. These cracks have unit normals that are randomly oriented within a plane of isotropy. The ensemble average elastic wave response is governed by the Dyson equation which is solved within the limits of the first-order smoothing approximation. The general Green's dyadic for a transversely isotropic medium was employed to derive expressions of the attenuation of the shear horizontal, quasilongitudinal and quasishear ver-

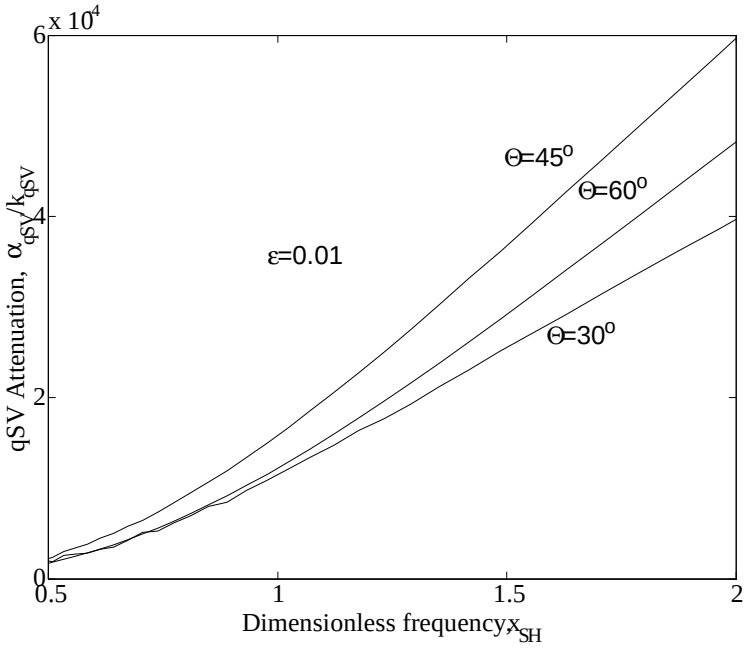

Figure 4.14: Normalized qSV attenuation, α_{qSV}/k_{qSV}, as a function of dimensionless frequency, x_{SH}, at damage density $\varepsilon = 0.01$, for propagation directions of $45°, 60°, 30°$.

tical waves. This dyadic approach is convenient to make the results coordinate free. Thus, the final forms of the attenuations for the three wave types were given directly by simple compact expressions involving integrations over the unit circle. In particular, the integrals are simplified considerably in the Rayleigh regime. The general attenuations for each wave type are dependent on frequency, wave velocity, wave direction and damage density. Finally, numerical results show how the attenuations and the effective wave velocity of each wave type are affected by those parameters. The general formulation is also directly related to other types of elastic wave scattering such as backscatter. The simple form of the results makes them particularly useful for nondestructive testing and materials characterization research. However, the neglect of mutual interactions among the microcracks may have a large influence for the scattering effects. This analysis may be investigated in future work.

Chapter 5

Perfectly Aligned Crack Scattering

5.1 Introduction

The scattering of elastic waves by cracks in elastic media has important applications in various areas of engineering and geophysics, in particular to ultrasonic nondestructive evaluation and materials characterization. Quantitative assessment of damage using nondestructive methods is essential for determining the structural integrity of structures and for predicting the remaining usable life. Changes of material responses due to the strength reduction or effective elastic stiffness drop with damage from microcracking have a significant influence on the physical properties of the materials, e.g., on the velocities of elastic waves and especially on the attenuation. Distributed microcracks often give rise to a decrease in wave velocity and an increase in attenuation. Precise knowledge of attenuation and wave velocities of ultrasonic waves in cracked media provides a direct approach for detecting the material damage.

In the previous chapter, a theory was developed which describes the scattering of

elastic waves by uniaxially aligned penny-shaped cracks, which often result from uniaxial compressive loading. In that case, the unit normals of all cracks were assumed to be coplanar, but random within the plane of isotropy. Under the assumption of transverse isotropy used in that work, explicit general expressions of attenuations were obtained in the limit of frequencies below the geometric optics limit. However, in the case of structural materials subjected to uniaxial tension, the status of damage is generally defined as that of perfectly aligned cracks. In this case, the unit normals of all cracks are perpendicular to the plane of isotropy as studied by Hudson [70]. His investigations of wave attenuation in cracked solids were restricted to the Rayleigh regime where the wavelength is much larger than the characteristic length of the cracks. Outside the Rayleigh limit, wave examinations of attenuation for this situation have not been examined. With this motivation, a detailed analysis in solids with perfectly aligned penny-shaped cracks is examined here.

In this chapter, the analysis procedure used previously is applied to study the attenuation of elastic waves by perfectly aligned cracks. Again, the interactions between individual microcracks are not considered, such that the present analysis is appropriate only for small crack densities. The effective elastic properties of a solid containing the perfectly aligned cracks are presented in section 5.2. Explicit expressions of attenuations of the shear horizontal, quasilongitudinal, and quasishear vertical waves are presented in section 5.3. In particular, the angular dependence of the attenuations in the Rayleigh limit is given explicitly. Numerical results are presented and discussed in section 5.4. Special attention is paid to the exploration of the effects of the crack density and wave frequency on the attenuation. In the Rayleigh limit, comparisons of numerical results obtained here

and those presented by Hudson [70] are particularly addressed. Finally, conclusions are presented.

5.2 Effective Elastic Properties

The ensemble average stiffness in an initially isotropic solid weakened by an ensemble of perfectly aligned penny-shaped microcracks is dependent on the properties of single cracks. The effective stiffness attributable to a single, penny-shaped crack of radius in a unit volume, which was derived under the framework discussed by Nemat-Nasser and Hori [80], Kachanov [89], and Krajcinovic [79], is given by the Eq. (3.25). The stiffness of a single crack is dependent on the unit normal $\hat{\mathbf{m}}$, which defines the crack unit normal. This orientation is implicit in the tensors $\mathbf{I}$. These basis tensors are given in terms of unit vector $\hat{\mathbf{m}}$ and Kronecker delta function as shown in Eq. (3.13).

The ensemble average properties contributed by all cracks are considered. The cracks are assumed to be embedded in an infinitely extended, homogeneous, isotropic and elastic three-dimensional continuum. The penny-shaped crack is characterized by its radius a and two Euler angles θ and φ, which define the direction of the unit normal $\hat{\mathbf{m}}$ as shown in Fig. 3.1. It is also assumed that the microcracks do not interact with each other. As previously discussed, the density function may be separated into independent radius and orientation functions of the form as presented in Eq. (3.27).

For perfectly aligned cracks, it is assumed that the unit normals of all microcracks are perpendicular to the plane of isotropy as shown in Fig. 5.1. As such, the overall properties of the cracked solid are transversely isotropic with symmetry axis in the x_3

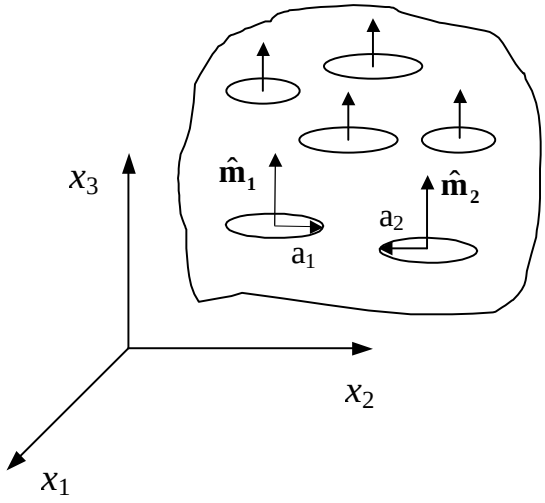

Figure 5.1: The distribution of microcracks aligned with the axis.

axis ($\hat{\mathbf{n}}$ direction). Therefore, the unit normals of all perfectly aligned cracks are defined by the unit vector $\hat{\mathbf{m}} = (\sin\varphi_0 \cos\theta_0, \sin\varphi_0 \sin\theta_0, \cos\varphi_0)$, where the value of φ_0 is equal to zero under the above assumption. To make the analysis as simple as possible, the distribution of the microcracks is assumed to be dilute, and the distribution of the crack sizes is also assumed to be independent of their orientations. Given $\varphi = 0$, a unit vector $\hat{\mathbf{n}} = (\sin\varphi\cos\theta, \sin\varphi\sin\theta, \cos\varphi)$ denotes the x_3 direction, which defines the normal of the plane of isotropy and the symmetry axis. The considered microcrack density distribution in Eq. (3.27) is then given by

$$\zeta(\theta, \varphi) = 2\pi \left[\delta\left(\hat{\mathbf{n}} - \hat{\mathbf{m}}\right) + \delta\left(\hat{\mathbf{n}} + \hat{\mathbf{m}}\right)\right]. \tag{5.1}$$

Therefore, the effective continuum material properties caused by all microcracks per unit volume are weighted by the density function, Eq. (3.27), over the crack Green's function,

Eq. (3.25), and is then given by

$$C^*_{ijkl} = \frac{\varepsilon}{4\pi}\int_\Omega C^{(s)}_{ijkl}(\hat{\mathbf{m}})\zeta(\hat{\mathbf{n}},\hat{\mathbf{m}})d\Omega. \tag{5.2}$$

In the above equation, the non-dimensional microcrack density per unit volume is defined in Eq. (4.3). The basis function $C^{(s)}_{ijkl}$ is specified in Eq. (3.25). By performing the integration over all orientations in Eq. (5.2), the effective stiffness due to the distribution of perfectly aligned penny-shaped microcracks is derived as

$$C^*_{ijkl} = \varepsilon b_i \mathbf{I}^i, \tag{5.3}$$

where the coefficients b_i are

$$\begin{aligned} b_1 = 0, \quad b_2 = 2\mu\frac{16\nu^2(1-\nu)}{3(1-2\nu)^2}, \\ b_3 = b_4 = 2\mu\frac{16\nu(1-\nu)}{3(1-2\nu)}, \\ b_5 = 2\mu\frac{32(1-\nu)}{3(2-\nu)}, \qquad b_6 = -2\mu\frac{16\nu(1-\nu)}{3(2-\nu)}. \end{aligned} \tag{5.4}$$

It should be mentioned that in the tenors used in Eq. (5.3), the symmetry orientation $\hat{\mathbf{n}}$, rather than the direction $\hat{\mathbf{m}}$, is implicit although these are the same from the mathematical point of view. This implication should be kept in mind throughout this chapter. In Eq. (5.4), the effective constants can be defined alternatively as $C^*_{11}, C^*_{33}, C^*_{44}, C^*_{66}$ and C^*_{13}, respectively and are expressed as

$$\begin{aligned} C^*_{11} &= b_1 + b_2, \quad C^*_{33} = b_1 + b_2 + 2b_3 + b_5 + b_6, \\ C^*_{44} &= \frac{1}{2}b_1 + \frac{1}{4}b_5, \quad C^*_{66} = \frac{1}{2}b_1, \quad C^*_{13} = b_2 + b_3. \end{aligned} \tag{5.5}$$

Substituting Eq. (5.4) into Eq. (5.5), the given results are identical with those obtained by Hudson [70] in Eq. (21). In addition the stiffness tensor of the homogeneous, isotropic and

elastic matrix in the uncracked state is written in the standard form

$$\mathbf{C}^0 = \lambda \mathbf{I}^2 + 2\mu \mathbf{I}^1. \tag{5.6}$$

Thus, the ensemble average stiffness is assumed to be spatially varying and may be represented by

$$\overline{\mathbf{C}}(\mathbf{x}) = \overline{\mathbf{C}}^0 + \delta\overline{\mathbf{C}}(\mathbf{x}), \tag{5.7}$$

where $\overline{\mathbf{C}}^0 = \left\langle \overline{\mathbf{C}}(\mathbf{x}) \right\rangle = \mathbf{C}^0 - \mathbf{C}^*$ is the ensemble average modulus tensor for a transversely isotropic medium. It is written in the form

$$\overline{\mathbf{C}}^0 = \lambda_\perp \mathbf{I}^2 + \mu_\perp \mathbf{I}^1 + \Gamma_1(\mathbf{I}^3 + \mathbf{I}^4) + \Gamma_2 \mathbf{I}^5 + \Gamma_3 \mathbf{I}^6, \tag{5.8}$$

where the five effective elastic constants are

$$\begin{aligned} \mu_\perp &= 2\mu, \quad \lambda_\perp = \lambda - 2\mu \frac{16\nu^2(1-\nu)}{3(1-2\nu)^2}, \quad \Gamma_1 = -2\mu \frac{16\nu(1-\nu)}{3(1-2\nu)} \\ \Gamma_2 &= -2\mu \frac{32(1-\nu)}{3(2-\nu)}, \qquad\qquad \Gamma_3 = 2\mu \frac{16\nu(1-\nu)}{3(2-\nu)}. \end{aligned} \tag{5.9}$$

The moduli fluctuations which have zero mean $\left(\left\langle \delta\overline{C} \right\rangle = 0\right)$ are given by

$$\delta\overline{\mathbf{C}} = \mathbf{C}^* - \mathbf{C}^{(s)} H(\mathbf{x}), \tag{5.10}$$

where the function $H(\mathbf{x})$ is defined in Eq. (3.40).

Wave propagation and scattering in heterogeneous and anisotropic media have been discussed in previous chapters using an anisotropic Green's function and employed to investigate the attenuations by uniaxially aligned cracks. The exact expressions of the attenuation for the three wave types were given in Eq. (2.13). In the next section, the attenuations are presented for perfectly aligned cracks.

5.3 Attenuations

To calculate the attenuations, the relevant inner products on the covariance of the effective moduli fluctuations are first determined. As discussed previously, for small concentrations of microcracks, the covariance can be written

$$\langle \delta C_{ijkl}(\mathbf{x}) \delta C_{\alpha\beta\gamma\delta}(\mathbf{y}) \rangle = \varepsilon \eta(r) \Xi_{ijkl}^{\alpha\beta\gamma\delta}. \tag{5.11}$$

The tensorial part of the covariance is represented by an eighth-rank tensor which is given in terms of four unit vectors by

$$\Xi\left(\mathbf{q}\right)_{\cdots\mathbf{\hat{u}}\mathbf{\hat{p}}\mathbf{\hat{s}}\mathbf{\hat{v}}}^{\cdots\cdots} = \Xi\left(\mathbf{q}\right)_{\alpha\beta\gamma\delta}^{ijkl} \hat{u}_\beta \hat{u}_k \hat{p}_\alpha \hat{p}_l \hat{s}_i \hat{s}_\delta \hat{v}_\gamma \hat{v}_j. \tag{5.12}$$

Averaging over all crack orientations, the tensorial part of the covariance is then given by performing the integration as

$$\begin{aligned}
\Xi_{ijkl}^{\alpha\beta\gamma\delta} \quad = \quad & \{b_1/2\left[\left(\hat{\mathbf{u}}\cdot\hat{\mathbf{s}}\right)\left(\hat{\mathbf{v}}\cdot\hat{\mathbf{p}}\right)+\left(\hat{\mathbf{p}}\cdot\hat{\mathbf{s}}\right)\left(\hat{\mathbf{v}}\cdot\hat{\mathbf{u}}\right)+b_2\left(\hat{\mathbf{p}}\cdot\hat{\mathbf{u}}\right)\left(\hat{\mathbf{v}}\cdot\hat{\mathbf{s}}\right)\right] \\
& +b_3\left(\hat{\mathbf{v}}\cdot\hat{\mathbf{s}}\right)\left(\hat{\mathbf{n}}\cdot\hat{\mathbf{u}}\right)\left(\hat{\mathbf{n}}\cdot\hat{\mathbf{p}}\right)+b_4\left(\hat{\mathbf{p}}\cdot\hat{\mathbf{u}}\right)\left(\hat{\mathbf{n}}\cdot\hat{\mathbf{s}}\right)\left(\hat{\mathbf{n}}\cdot\hat{\mathbf{v}}\right) \\
& +b_5/4\left[\left(\hat{\mathbf{p}}\cdot\hat{\mathbf{v}}\right)\left(\hat{\mathbf{n}}\cdot\hat{\mathbf{s}}\right)\left(\hat{\mathbf{n}}\cdot\hat{\mathbf{u}}\right)+\left(\hat{\mathbf{n}}\cdot\hat{\mathbf{s}}\right)\left(\hat{\mathbf{v}}\cdot\hat{\mathbf{u}}\right)\left(\hat{\mathbf{n}}\cdot\hat{\mathbf{p}}\right)\right. \\
& \left.+\left(\hat{\mathbf{p}}\cdot\hat{\mathbf{s}}\right)\left(\hat{\mathbf{n}}\cdot\hat{\mathbf{v}}\right)\left(\hat{\mathbf{n}}\cdot\hat{\mathbf{u}}\right)+\left(\hat{\mathbf{n}}\cdot\hat{\mathbf{v}}\right)\left(\hat{\mathbf{n}}\cdot\hat{\mathbf{p}}\right)\left(\hat{\mathbf{u}}\cdot\hat{\mathbf{s}}\right)\right] \\
& +b_6\left(\hat{\mathbf{n}}\cdot\hat{\mathbf{s}}\right)\left(\hat{\mathbf{n}}\cdot\hat{\mathbf{v}}\right)\left(\hat{\mathbf{n}}\cdot\hat{\mathbf{u}}\right)\left(\hat{\mathbf{n}}\cdot\hat{\mathbf{p}}\right)\}^2,
\end{aligned} \tag{5.13}$$

where the coefficients b_i are given by Eq. (5.4). The vectors $\hat{\mathbf{p}}$ and $\hat{\mathbf{s}}$, respectively, represent the incoming and outgoing propagation directions. The vectors $\hat{\mathbf{u}}$ and $\hat{\mathbf{v}}$ are vectors defining the polarization directions of the particular waves.

The attenuations will vary angularly only within the plane defined by the propagation direction and the symmetry direction. Therefore, without loss of generality, a reference

plane is defined as the $\hat{\mathbf{p}}-\hat{\mathbf{n}}$ plane as shown in Fig. 5.2. Thus, the vectors $\hat{\mathbf{n}}$, $\hat{\mathbf{p}}$ and $\hat{\mathbf{s}}$, and respective polarization directions $\hat{\mathbf{u}}$ and $\hat{\mathbf{v}}$ are defined with respect to a general coordinate system, which are given by Eqs. (4.21)-(4.23). Substituting these definitions of the relevant unit vectors into Eq. (5.13), the required inner products are for α_{SH},

$$\begin{aligned}
\Xi^{\cdots\hat{\mathbf{u}}_1\hat{\mathbf{p}}\hat{\mathbf{s}}\hat{\mathbf{v}}_1}_{\cdots\hat{\mathbf{u}}_1\hat{\mathbf{p}}\hat{\mathbf{s}}\hat{\mathbf{v}}_1} &= \frac{b_5^2}{16}\cos^2\Theta\cos^2\Theta'\sin^2\phi', \\
\Xi^{\cdots\hat{\mathbf{u}}_1\hat{\mathbf{p}}\hat{\mathbf{s}}\hat{\mathbf{v}}_2}_{\cdots\hat{\mathbf{u}}_1\hat{\mathbf{p}}\hat{\mathbf{s}}\hat{\mathbf{v}}_2} &= \frac{b_5^2}{16}\cos^2\Theta\sin^2\left(\Theta'+\gamma'\right)\cos^2\phi', \\
\Xi^{\cdots\hat{\mathbf{u}}_1\hat{\mathbf{p}}\hat{\mathbf{s}}\hat{\mathbf{v}}_3}_{\cdots\hat{\mathbf{u}}_1\hat{\mathbf{p}}\hat{\mathbf{s}}\hat{\mathbf{v}}_3} &= \frac{b_5^2}{16}\cos^2\Theta\cos^2\left(\Theta'+\gamma'\right)\cos^2\phi';
\end{aligned} \tag{5.14}$$

for α_{qP}

$$\begin{aligned}
\Xi^{\cdots\hat{\mathbf{u}}_2\hat{\mathbf{p}}\hat{\mathbf{s}}\hat{\mathbf{v}}_1}_{\cdots\hat{\mathbf{u}}_2\hat{\mathbf{p}}\hat{\mathbf{s}}\hat{\mathbf{v}}_1} &= \frac{b_5^2}{16}\sin^2\left(\Theta+\gamma\right)\cos^2\Theta'\cos^2\phi', \\
\Xi^{\cdots\hat{\mathbf{u}}_2\hat{\mathbf{p}}\hat{\mathbf{s}}\hat{\mathbf{v}}_2}_{\cdots\hat{\mathbf{u}}_2\hat{\mathbf{p}}\hat{\mathbf{s}}\hat{\mathbf{v}}_2} &= \Big\{b_2\cos\left(\gamma-\Theta\right)\cos\left(\gamma'-\Theta'\right)+b_3\cos\Theta\cos\gamma\cos\left(\gamma'-\Theta'\right) \\
&\quad +b_4\cos\left(\gamma-\Theta\right)\cos\Theta'\cos\gamma'+b_5/4\sin\left(\Theta+\gamma\right)\sin\left(\Theta'+\gamma'\right)\sin\phi' \\
&\quad +\left(b_4+b_5\right)\cos\Theta\cos\gamma\cos\Theta'\cos\gamma'\Big\}^2, \\
\Xi^{\cdots\hat{\mathbf{u}}_2\hat{\mathbf{p}}\hat{\mathbf{s}}\hat{\mathbf{v}}_3}_{\cdots\hat{\mathbf{u}}_2\hat{\mathbf{p}}\hat{\mathbf{s}}\hat{\mathbf{v}}_3} &= \Big\{b_2\cos\left(\gamma-\Theta\right)\sin\left(\gamma'-\Theta'\right)+b_3\cos\Theta\cos\gamma\sin\left(\gamma'-\Theta'\right) \\
&\quad +b_4\cos\left(\gamma-\Theta\right)\cos\Theta'\sin\gamma'-b_5/4\sin\left(\Theta+\gamma\right)\cos\left(\Theta'+\gamma'\right)\sin\phi' \\
&\quad +\left(b_4+b_5\right)\cos\Theta\cos\gamma\cos\Theta'\sin\gamma'\Big\}^2;
\end{aligned} \tag{5.15}$$

and, for α_{qSV}

$$\begin{aligned}
\Xi^{\cdots\hat{\mathbf{u}}_3\hat{\mathbf{p}}\hat{\mathbf{s}}\hat{\mathbf{v}}_1}_{\cdots\hat{\mathbf{u}}_3\hat{\mathbf{p}}\hat{\mathbf{s}}\hat{\mathbf{v}}_1} &= \frac{b_5^2}{16}\cos^2\left(\Theta+\gamma\right)\cos^2\Theta'\cos^2\phi', \\
\Xi^{\cdots\hat{\mathbf{u}}_3\hat{\mathbf{p}}\hat{\mathbf{s}}\hat{\mathbf{v}}_2}_{\cdots\hat{\mathbf{u}}_3\hat{\mathbf{p}}\hat{\mathbf{s}}\hat{\mathbf{v}}_2} &= \Big\{b_2\sin\left(\gamma-\Theta\right)\cos\left(\gamma'-\Theta'\right)+b_3\cos\Theta\sin\gamma\cos\left(\gamma'-\Theta'\right) \\
&\quad +b_4\sin\left(\gamma-\Theta\right)\cos\Theta'\cos\gamma'-b_5/4\cos\left(\Theta+\gamma\right)\sin\left(\Theta'+\gamma'\right)\sin\phi' \\
&\quad +\left(b_4+b_5\right)\cos\Theta\sin\gamma\cos\Theta'\cos\gamma'\Big\}^2,
\end{aligned} \tag{5.16}$$

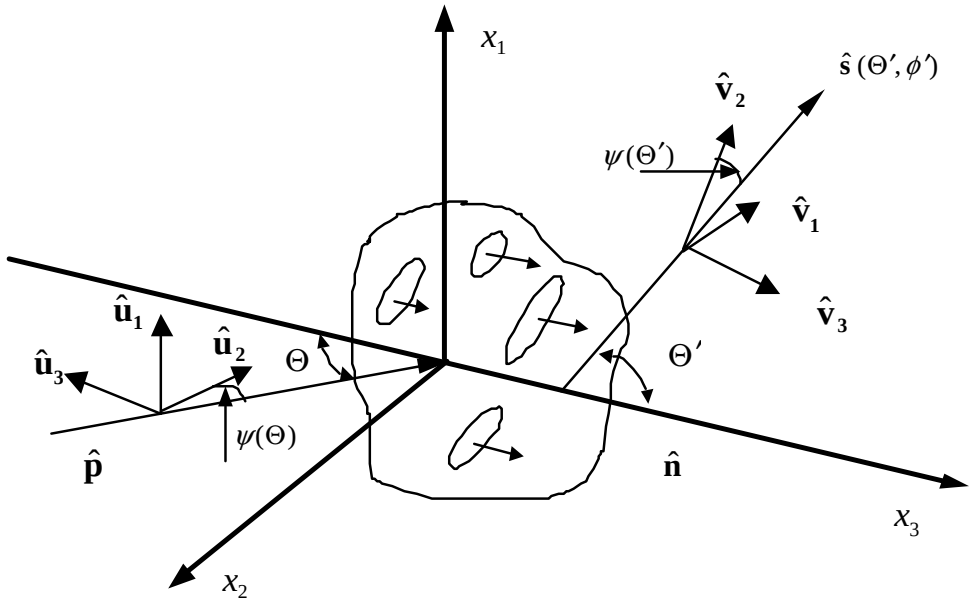

Figure 5.2: Geometry for the propagation direction $\hat{\mathbf{p}}$, the scattered direction $\hat{\mathbf{s}}$, and the respective polarization direction $\hat{\mathbf{u}}$ and $\hat{\mathbf{v}}$ in the local coordinate system for perfectly aligned cracks.

$$\begin{aligned}\Xi^{\cdots\hat{\mathbf{u}}_3\hat{\mathbf{p}}\hat{\mathbf{s}}\hat{\mathbf{v}}_3}_{\cdots\hat{\mathbf{u}}_3\hat{\mathbf{p}}\hat{\mathbf{s}}\hat{\mathbf{v}}_3} &= \left\{b_2 \sin(\gamma-\Theta)\sin\left(\gamma'-\Theta'\right) + b_3\cos\Theta\sin\gamma\sin\left(\gamma'-\Theta'\right)\right. \\ &\quad + b_4\sin(\gamma-\Theta)\cos\Theta'\sin\gamma' + b_5/4\cos(\Theta+\gamma)\cos\left(\Theta'+\gamma'\right)\sin\phi' \\ &\quad \left. + (b_4+b_5)\cos\Theta\sin\gamma\cos\Theta'\sin\gamma'\right\}^2 .\end{aligned}$$

In Eqs. (5.14)-(5.16), the coefficients are given in Eq. (5.4). As discussed previously, the tensorial and spatial components of the covariance are assumed independent. The correlation function η is assumed to have an exponential form as presented in Eq. (2.14). If three nondimensional frequencies are defined as $x_\beta = \omega L/c_\beta$, performing the spatial Fourier transform of the correlation function of the difference between two wave vectors, the functions $\tilde{\eta}(\hat{\mathbf{p}}, \hat{\mathbf{s}})$ are then expressed in terms of the above dimensionless frequencies by Eq. (2.16). The inner product $(\hat{\mathbf{p}} \cdot \hat{\mathbf{s}})$ is specified as $\hat{\mathbf{p}} \cdot \hat{\mathbf{s}} = \sin\Theta\sin\Theta'\sin\phi' + \cos\Theta\cos\Theta'$.

Substituting Eqs. (5.14)-(5.16) and Eq. (2.14) into Eq. (2.13), the resulting dimensionless attenuations are finally given in the form

$$\begin{aligned}\alpha_\beta(\hat{\mathbf{p}})\,L &= \frac{x_\beta^4 c_\beta(\hat{\mathbf{p}})\varepsilon}{2\rho^2}\times \\ &\left\{\int_{4\pi}\frac{\Xi^{\cdots\cdot\hat{\mathbf{u}}_K\hat{\mathbf{p}}\hat{\mathbf{s}}\hat{\mathbf{v}}_1}_{\cdots\cdot\hat{\mathbf{u}}_K\hat{\mathbf{p}}\hat{\mathbf{s}}\hat{\mathbf{v}}_1}}{\left(1+x_\beta^2(\hat{\mathbf{p}})+x_{SH}^2(\hat{\mathbf{s}})-2x_\beta(\hat{\mathbf{p}})\,x_{SH}(\hat{\mathbf{s}})\,\hat{\mathbf{p}}\cdot\hat{\mathbf{s}}\right)^2 c_{SH}^5(\hat{\mathbf{s}})}d^2\hat{s}\right. \\ &+\int_{4\pi}\frac{\Xi^{\cdots\cdot\hat{\mathbf{u}}_K\hat{\mathbf{p}}\hat{\mathbf{s}}\hat{\mathbf{v}}_2}_{\cdots\cdot\hat{\mathbf{u}}_K\hat{\mathbf{p}}\hat{\mathbf{s}}\hat{\mathbf{v}}_2}}{\left(1+x_\beta^2(\hat{\mathbf{p}})+x_{qP}^2(\hat{\mathbf{s}})-2x_\beta(\hat{\mathbf{p}})\,x_{qP}(\hat{\mathbf{s}})\,\hat{\mathbf{p}}\cdot\hat{\mathbf{s}}\right)^2 c_{qP}^5(\hat{\mathbf{s}})}d^2\hat{s} \\ &\left.+\int_{4\pi}\frac{\Xi^{\cdots\cdot\hat{\mathbf{u}}_K\hat{\mathbf{p}}\hat{\mathbf{s}}\hat{\mathbf{v}}_3}_{\cdots\cdot\hat{\mathbf{u}}_K\hat{\mathbf{p}}\hat{\mathbf{s}}\hat{\mathbf{v}}_3}}{\left(1+x_\beta^2(\hat{\mathbf{p}})+x_{qSV}^2(\hat{\mathbf{s}})-2x_\beta(\hat{\mathbf{p}})\,x_{qSV}(\hat{\mathbf{s}})\,\hat{\mathbf{p}}\cdot\hat{\mathbf{s}}\right)^2 c_{qSV}^5(\hat{\mathbf{s}})}d^2\hat{s}\right\},\end{aligned} \tag{5.17}$$

where K is defined as the polarization for the wave type β (1, 2,or 3 for wave types SH, qP and qSV, respectively). The density is now included in the final form of the attenuations. Equation (5.17) is the primary result of this chapter. The phase velocities c_β are given in the form of Eq. (4.15) and the corresponding coefficients are given in Eq. (5.9). In the long wavelength Rayleigh limit, $x_\beta \ll 1$, Eq. (5.17) can be simplified considerably and is given by

$$\begin{aligned}\frac{\alpha_\beta(\hat{\mathbf{p}})\,L}{x_\beta^4\varepsilon} &= \frac{c_\beta(\hat{\mathbf{p}})}{2\rho^2}\times\left\{\int_{4\pi}\frac{\Xi^{\cdots\cdot\hat{\mathbf{u}}_K\hat{\mathbf{p}}\hat{\mathbf{s}}\hat{\mathbf{v}}_1}_{\cdots\cdot\hat{\mathbf{u}}_K\hat{\mathbf{p}}\hat{\mathbf{s}}\hat{\mathbf{v}}_1}}{c_{SH}^5(\hat{\mathbf{s}})}d^2\hat{s}\right. \\ &\left.+\int_{4\pi}\frac{\Xi^{\cdots\cdot\hat{\mathbf{u}}_K\hat{\mathbf{p}}\hat{\mathbf{s}}\hat{\mathbf{v}}_2}_{\cdots\cdot\hat{\mathbf{u}}_K\hat{\mathbf{p}}\hat{\mathbf{s}}\hat{\mathbf{v}}_2}}{c_{qP}^5(\hat{\mathbf{s}})}d^2\hat{s}+\int_{4\pi}\frac{\Xi^{\cdots\cdot\hat{\mathbf{u}}_K\hat{\mathbf{p}}\hat{\mathbf{s}}\hat{\mathbf{v}}_3}_{\cdots\cdot\hat{\mathbf{u}}_K\hat{\mathbf{p}}\hat{\mathbf{s}}\hat{\mathbf{v}}_3}}{c_{qSV}^5(\hat{\mathbf{s}})}d^2\hat{s}\right\}.\end{aligned} \tag{5.18}$$

In Eq. (5.18), the dimensionless attenuations have been normalized by the fourth power of the dimensionless frequency and damage density for the respective wave type.

5.4 Numerical Results and Discussions

In this section, numerical results are now presented for a specific case, in which the observed transversely isotropy of the cracked material is entirely due to the presence of the perfectly aligned cracks. The material properties of the uncracked material used are Young's modulus $E = 2.0 \times 10^{11}$Pa, Poisson's ratio $\nu = 0.3$, and density $\rho = 7860\text{kg/m}^3$. First, the slowness surfaces are presented at the damage density $\varepsilon = 0.1$. The slowness is governed by Eq. (4.15), which is plotted in Fig. 5.3. The results given by Hudson [70], Eqs. (17) and (22-23), are shown as well. Exact agreement of the results for SH waves between the present model and Hudson's model is seen in Fig. 5.3. However, the slowness curves of the qP and qSV waves do not agree with each other well. This discrepancy is thought to be due to the assumption of non-varying polarization ($\psi = 0$) in the work of Hudson. Thus, if the polarization shift is neglected in the present analysis, the expressions of wave velocities are precisely the same for both models. However, it is generally known that the deviation angle of the polarization vector is not zero.

The attenuations within the Rayleigh limit are calculated using Eq. (5.18). It is seen that the attenuations are a function of the fourth power of frequency. Thus, the angular dependence of three attenuations is described by the quantity $\alpha_\beta L / \left(x_\beta^4 \varepsilon\right)$. Those parameters for each wave type are shown in Fig. 5.4, Fig. 5.5, and Fig. 5.6, respectively. The numerical integrations are performed by double integral function *dblquad* available in the software package Matlab [93]. The attenuations for SH waves for damage density $\varepsilon = 0.01$ and $\varepsilon = 0.05$ are presented first in Fig. 5.4. It is observed that the maximum attenuation of the SH wave is at $\Theta = 0°$, parallel to the normals of cracks, and at $\Theta = 90°$

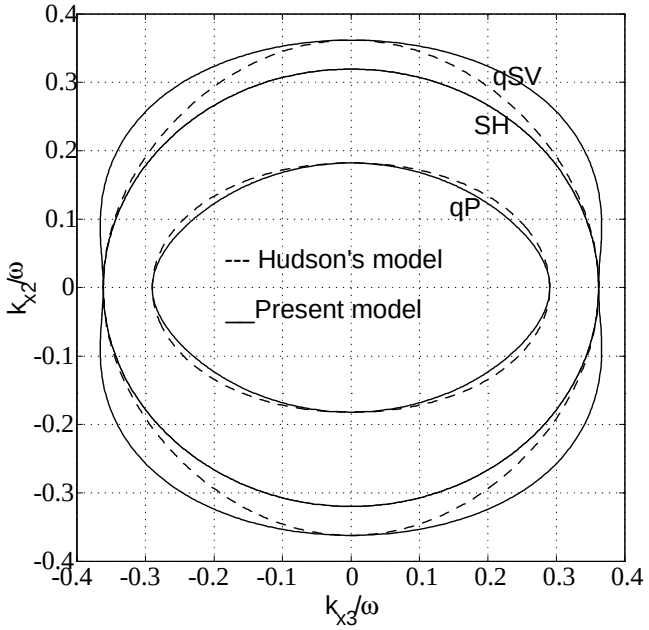

Figure 5.3: Slowness surfaces for damage density $\varepsilon = 0.1$.

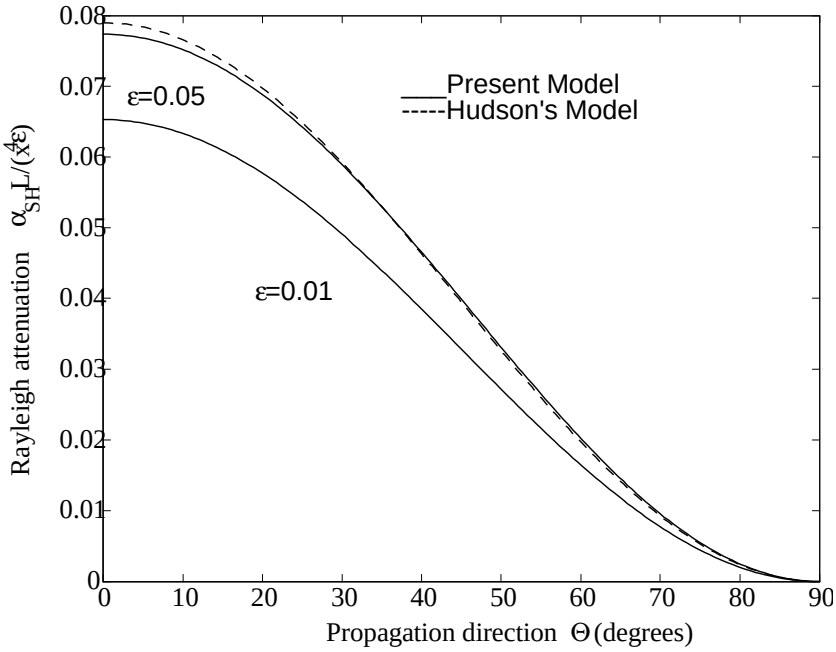

Figure 5.4: Rayleigh attenuation, $\alpha_{SH}L/\left(x_{SH}^4\varepsilon\right)$ as a function of direction.

there is the zero attenuation. In order to compare the present results with those studied by Hudson, the equivalent parameter is also shown in Fig. 5.4 (dashed line). It is seen from Fig. 5.4 that for two different damage densities, the attenuations of Hudson's model are exactly the same. This feature is easily seen from Eq. (5.18) presented here and Eq. (52) given by Hudson. In the work of Hudson [70], the velocities of uncracked solids are used to calculate the final attenuation, rather than the velocities of cracked solids used in the present study. Therefore, the attenuation is shown to scale linearly with the damage density, which is usually not the case for the anisotropic property in the Rayleigh limit. In addition, the correlation between the radiation fields of separate cracks is also neglected in Hudson's model. This assumption may in part result in the inaccurate results as well for the case discussed here. In Fig. 5.5, the Rayleigh attenuations of the qP wave are presented for both present model and Hudson's model. The difference between the two models is attributed to the same reasons as above discussed for SH waves. The maximum attenuation is also at $\Theta = 0°$, and at $\Theta = 90°$ the attenuation reaches the lowest value, but does not have the zero attenuation. The Rayleigh attenuations of the qSV wave are shown in Fig. 5.6. It is seen that the maximum value is about $\Theta = 45°$, and at $\Theta = 0°$ and $\Theta = 90°$ the attenuation is lowest, but it is not equal to zero. Also, an additional feature observed in Fig. 5.6 is the asymmetry that develops as damage density varies. The peak is around $\Theta = 45°$, but shifts as damage density changes as discussed in Chapter 4. This directional variation of the maximum attenuation is toward the crack alignment as the damage density increases. It is seen from Fig. 5.6, that the difference of Rayleigh attenuations of the qSV wave between the present model and Hudson's model is significant at damage density $\varepsilon = 0.05$. This

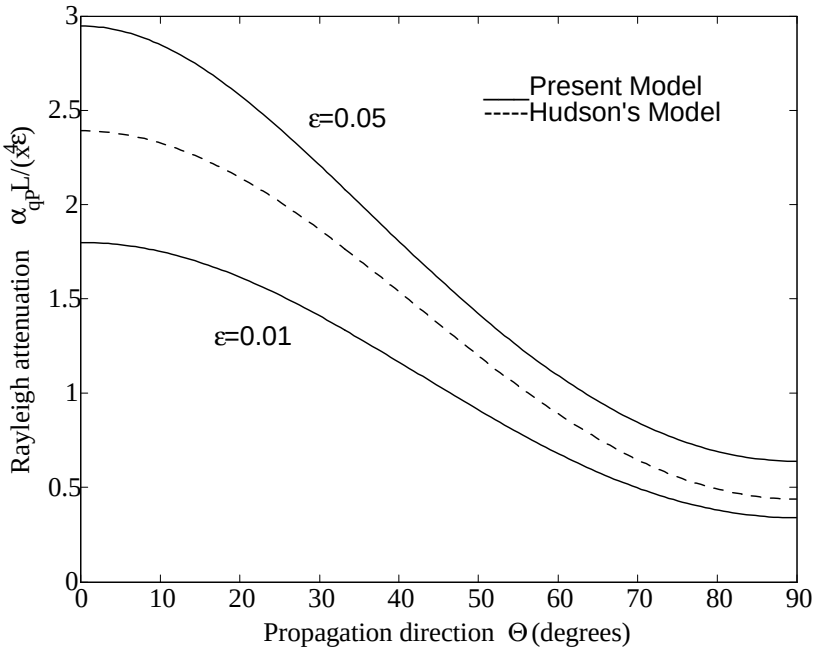

Figure 5.5: Rayleigh attenuation, $\alpha_{qP}L/\left(x_{qP}^4\varepsilon\right)$ as a function of direction.

phenomenon is thought to be the result of the assumptions made in Hudson's model as discussed above. Thus, one could conclude that the attenuation results of the three wave types presented by Hudson are more approximate than those determined here.

The results outside the Rayleigh regime are calculated using the complete integrals, Eq. (5.17). The directional dependence of the attenuation as a function of damage density is presented in terms of the single dimensionless frequency $x_{SH} = 1.0$. In Fig. 5.7, the attenuation of the SH wave, $\alpha_{SH}L$, is shown as a function of propagation direction for three damage densities $\varepsilon = 0.05$, $\varepsilon = 0.08$ and $\varepsilon = 0.1$, respectively. The attenuation for propagation parallel to the crack alignment direction is seen to increase more rapidly than other directions as the damage increases. This property was discussed for uniaxially aligned crack scattering [74] and for textured polycrystals by Hirsekorn [46], Ahmed and Thompson

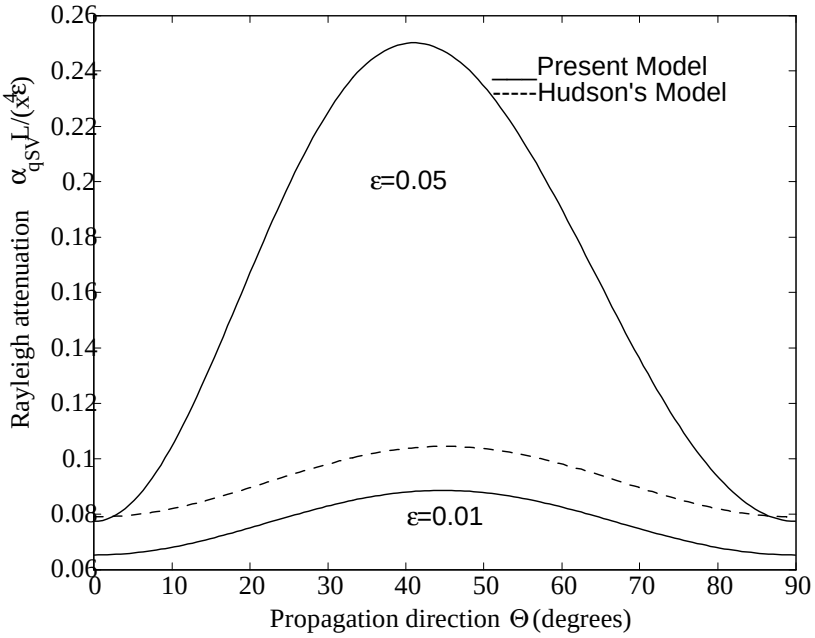

Figure 5.6: Rayleigh attenuation, $\alpha_{qSV}L/\left(x_{qSV}^4\varepsilon\right)$ as a function of direction.

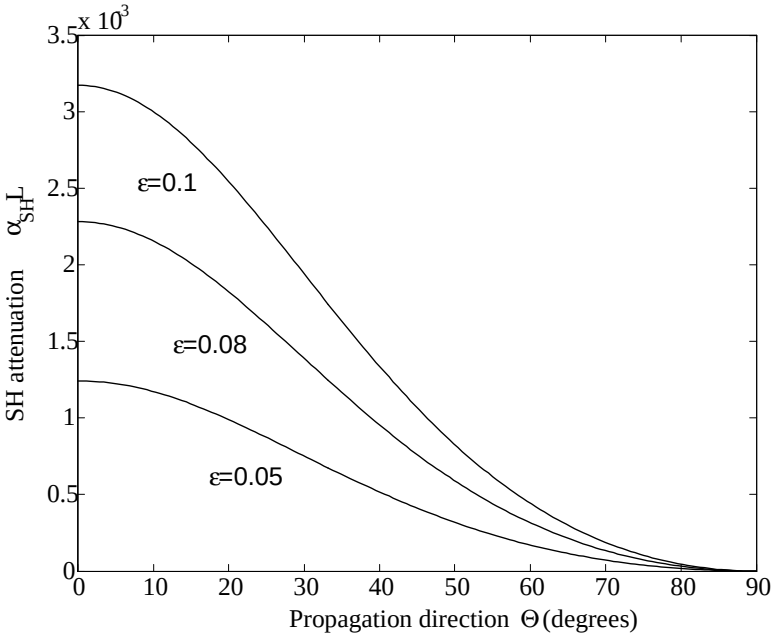

Figure 5.7: Angular dependence of the attenuation, $\alpha_{SH}L$, for various damage densities ε at frequency $x_{SH} = 1.0$.

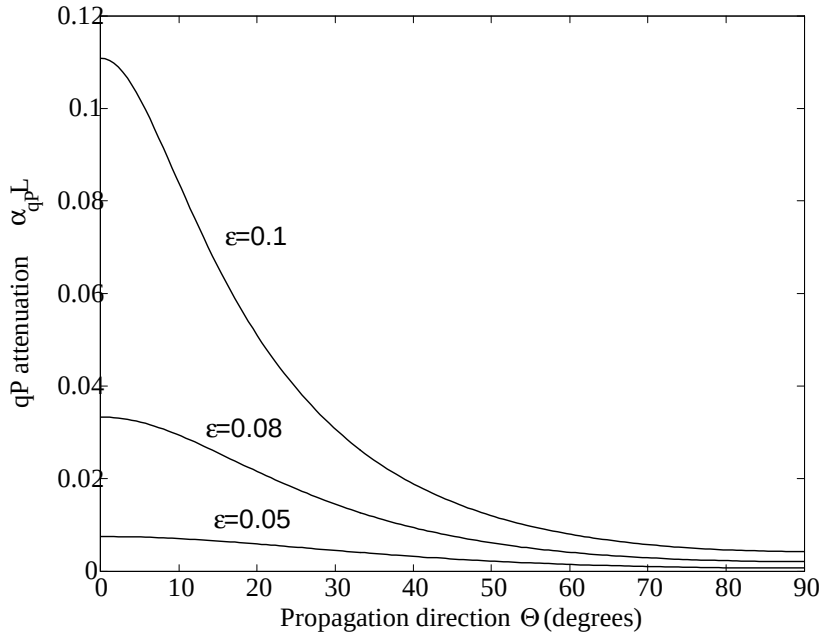

Figure 5.8: Angular dependence of the attenuation, $\alpha_{qP}L$, for various damage densities ε at frequency $x_{SH} = 1.0$.

[94], and Turner [57]. In Fig. 5.8, the results for the qP attenuation, $\alpha_{qP}L$, are presented. Similar behavior is seen upon increasing damage as discussed for the SH attenuation. The attenuation of the qSV wave is shown in Fig. 5.9 at the same damage densities as Figs. 5.7 and 5.8. As discussed for the Rayleigh limit results, the direction of maximum attenuation varies as the damage changes, and the shift from 45° to 0° is quite noticeable as shown in Fig. 5.9. This shift is thought to be the result of the induced anisotropy from the cracks. In general, the direction of the peak of the qSV attenuation is dependent on both frequency and damage.

Finally, the results are presented for the normalized attenuations of each wave type as a function of propagation direction for several different frequencies. These results could be contrasted with results in the Rayleigh limit. Figures 5.10 and 5.11 show the

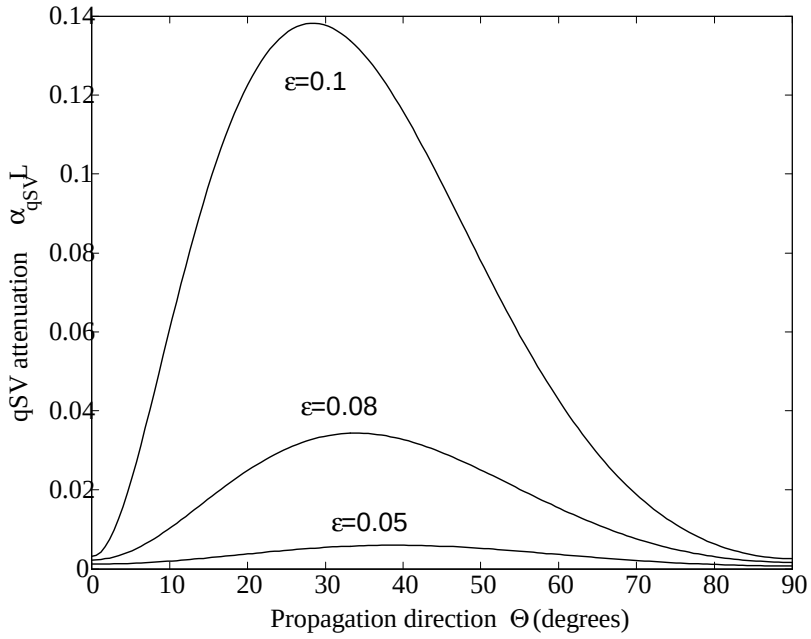

Figure 5.9: Angular dependence of the attenuation, $\alpha_{qSV}L$, for various damage densities ε at frequency $x_{SH} = 1.0$.

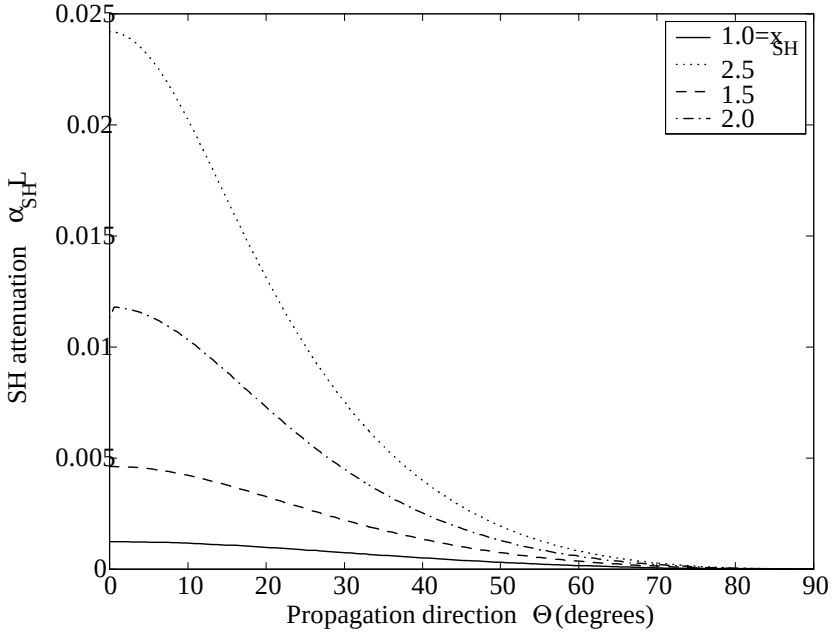

Figure 5.10: Angular dependence of the attenuation, $\alpha_{SH}L$, for various dimensionless frequencies x_{SH} at damage density $\varepsilon = 0.05$.

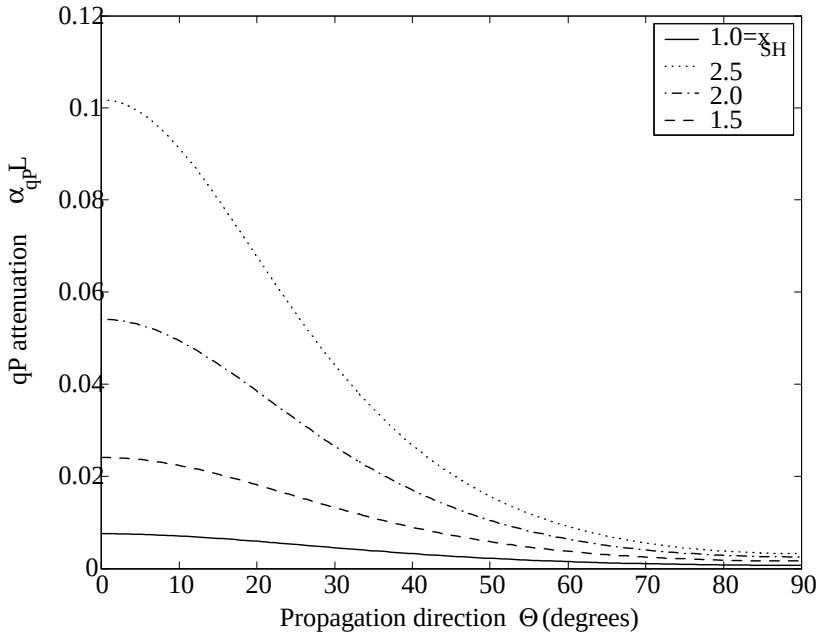

Figure 5.11: Angular dependence of the attenuation, $\alpha_{qP}L$, for various dimensionless frequencies x_{SH} at damage density $\varepsilon = 0.05$.

SH and qP attenuations versus the propagation direction Θ for normalized frequencies x_{SH} of $1.0, 1.5, 2.0, 2.5$. As the frequency increases it is seen that the attenuation in the alignment direction increases more than in other directions. In Fig. 5.12, the normalized qSV attenuation is plotted versus the propagation direction Θ for the same normalized frequencies as Figs. 5.10 and 5.11. It is seen that the peak of maximum attenuation shifts as the frequency increases. The asymmetry that develops as frequency increases is seen to be considerable in Fig. 5.12. This outcome is also attributed to the property of anisotropy from microcracking.

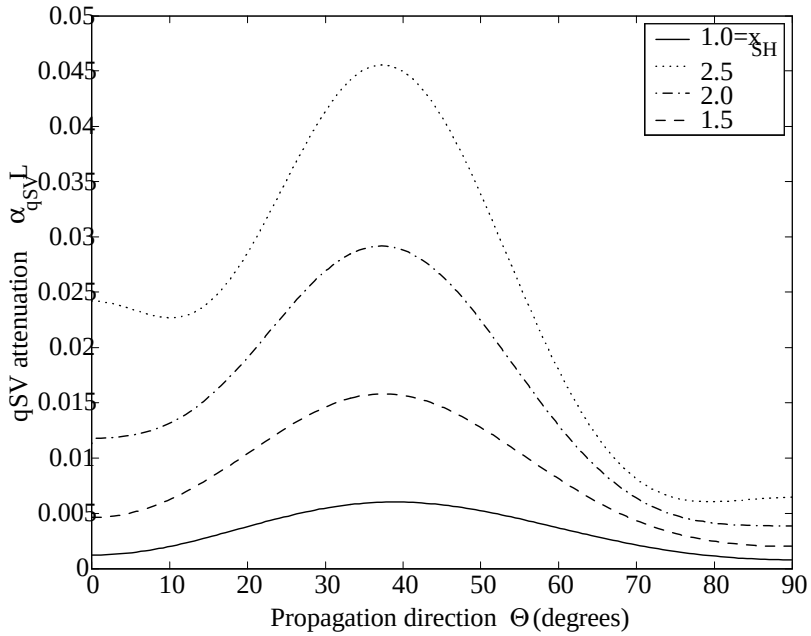

Figure 5.12: Angular dependence of the attenuation, $\alpha_{qSV}L$, for various dimensionless frequencies x_{SH} at damage density $\varepsilon = 0.05$.

5.5 Conclusions

The attenuations of elastic waves in solids with perfectly aligned cracks have been examined within limit of frequencies below the geometric optics limit. In the case of perfectly aligned cracks, these cracks have unit normals that are perpendicular to the plane of isotropy as first studied by Hudson. Approximate ensemble averaging of the elastic wave equation resulted in the Dyson equation, governing the mean field. Explicit expressions of the attenuation of each wave type, the shear horizontal, quasilongitudinal, quasishear vertical waves, were derived using the general Green's dyadic for a transversely isotropic medium. The final forms of the attenuations for the three wave types were expressed by simple integrations over the scattered direction. The general attenuations for each wave type are dependent on frequency, phase velocity, propagation direction, and damage den-

sity. In particular, the attenuations of each wave type were given in the long wavelength Rayleigh limit as presented by Hudson. Comparisons of the present model with Hudson's model in the Rayleigh limit show that the results presented here are more accurate than those presented by Hudson, due to the inclusion of the polarization direction. The general formulation is also directly related to backscattering problem. The simple form of the results makes them particularly useful for nondestructive testing and evaluation.

Chapter 6

Wave Velocity and Polarization in Textured Media

6.1 Introduction

Microstructural evolution during the heat treatment process has been a subject of research for the past several decades. The knowledge that the material microstructure directly affects the macroscopic material properties was a turning point in the field of material manufacturing. The specific types of manufacturing processes are to produce the corresponding microstructure in a controlled fashion. Many heat treatment processes, such as annealing, are used to relieve the internal stress state that develops during cold working, which allows the microstructure to rearrange to a state of lower energy. During such processing individual crystals in a polycrystalline aggregate submit to orientation changes. Often, the recrystallization process creates material texture, or preferred orientation of grains. The

orientation of the recrystallized grains together with the final grain size distribution determines the final properties of polycrystalline materials. The degree and type of texture are best described quantitatively by the orientation distribution function (ODF), which gives the probability of a particular crystallite in the sample having a specific orientation with respect to the sample axes. The subject of material texture is well developed by Roe [1],[2] and Bunge [3]. In general, most of these materials with preferred crystallographic orientation display anisotropy of physical properties. The anisotropic elastic response, which is strongly induced by texture, in turn influences the formability of a polycrystalline material [95], [96]. Ultrasonic techniques provide information about the interior microstructure due to the penetration of ultrasonic waves. In recent years, major advances in ultrasonic monitoring NDE demonstrate a potential to characterize the recrystallization process in metals because of their nondestructive nature. Thus, the texture of polycrystalline aggregates may be monitored by ultrasonic methods during the recrystallization process. However, the development of texture during recrystallization is not fully understood, in part due to a lack of quantitative measurements during recrystallization [97].

Measurements of the wave velocity and attenuation may be used to infer material texture in polycrystalline aggregates. Hence evaluation of wave phenomena in polycrystals is of importance for prediction of the materials microstructure. More recently, models of elastic wave propagation through polycrystalline materials with texture have typically focused on special cases of texture. For example, the wave velocity through cubic polycrystalline materials with one aligned axis has been studied using several different techniques [46],[56],[57]. These models were all based on appropriate averages of the stochastic elastic

wave equation. The Voigt averaging techniques, which have been applied previously for textured aggregates of crystals with particular symmetry [95],[98],[99],[100], [101], are used for calculating the average elastic constants here. The knowledge of wave velocity plays an important role in the explanation of a wide range of wave propagation behavior in polycrystalline materials. Ultrasonic velocities in polycrystalline aggregates have been analyzed by Sayers [98],[102], Thompson [103],[104], Hirsekorn [46] and others. Those results were most focused on the directional dependence of wave propagation along the symmetry axes. In the literature discussed by Crampin and Yedlin [105], Sayers [106], Pšenčík and Gajewski [107], Mensch and Rasolofosaon [108], and Farra [109], phase velocities were investigated in anisotropic geological media for the qP or qS wave modes. Although their discussions did not consider the texture effects, the analyses in anisotropic media provide a valuable insight with the texture characterization during processing.

In this chapter, wave velocity and polarization are analyzed for orthorhombic materials made up of cubic crystals. The single crystal elastic constants and the orientation distribution function of the constituent crystals are used for this work. In particular, the wave velocity of the three wave modes is examined during recrystallization, respectively. In polycrystals of cubic symmetry with rolling texture, the material is assumed to have three orthogonal axes, which are chosen as the normal direction (ND), transverse direction (TD), and rolling direction (RD). Upon moving through an anisotropic medium, three elastic waves, the quasilongitudinal (qP) and two quasishear ($qS1$ and $qS2$) waves, can propagate along any direction. The wavespeeds are dependent on the wave propagation direction, as are the polarization directions. Thus, the polarization directions are most

generally neither parallel nor perpendicular to the wave propagation direction. The wave velocities and their polarization directions correspond to the eigenvalues and eigenvectors of the so-called Christoffel matrix. Analytic expressions of the eigenvalues and the eigenvectors may be obtained only for special cases with simple symmetries. For example, the exact solutions can be derived upon propagation along any one of the three axes directions ND, TD and RD in a polycrystalline cubic sample. For more general cases, the eigenvalues and the eigenvectors must be found by numerical methods. Thus, the wave velocities and their corresponding polarization directions are calculated numerically. The angular deviations of the polarization vectors from the propagation directions are also discussed. It is shown that the maximum angular deviation is not too large relative to the propagation direction for waves propagating in different directions. Those results are then used to calculate the wave attenuations induced by grains of polycrystals with a certain distribution in the subsequent chapter.

This chapter is organized in the following manner. First, in Section 6.2 the orientation distribution function is discussed such that the general principle can be followed step by step. Discussion of the orientational averaging procedure and the general elastic tensor with orthorhombic symmetry follows in Section 6.3. In Section 6.4 an overview of the Christoffel equation is presented. In Section 6.5 analyses and numerical results of wave velocities and polarization vectors are presented. In Section 6.6 the wave velocity of the three wave types is discussed as related to the annealing process. Finally, conclusions are presented and discussed.

6.2 The Orientation Distribution Function

The best quantitative representation of texture of polycrystalline materials was developed by Roe [1],[2] and Bunge [3] in the 1960s. From a mathematical point of view, their mathematical formulation and terminology are equivalent although the notation is different. Here, Roe's notation will be adopted throughout. For textured materials, a detailed description of polycrystalline material properties in the sample requires a knowledge of the orientation distribution of all crystallites in the sample. The orientation of a given single crystallite is specified by the three Euler angles θ, ψ, and φ as shown in Fig. 6.1. The orientation distribution of crystalline grains with preferred directions in the sample can be described by the orientation distribution function (ODF) $w(\theta, \psi, \varphi)$, which is the probability density function in terms of the three Euler angles. To discuss the orientation of a grain, a set of crystallite-fixed axes X_i is chosen for a given grain, and one may clearly choose the sample-fixed axes x_i along the rolling, transverse, and normal directions of a rolled sheet, respectively. The relation between the crystallite axes X_i and the sample axes x_i can be transformed by a rotation matrix using the three Euler angles. The orientation of the crystallite with respect to the sample axes is then given by the transformation in the form

$$x_i = a_{ij} X_j, \tag{6.1}$$

where the components of the rotation matrix a_{ij} are given in terms of the Euler angles θ, ψ, and φ as

$$\begin{aligned} a_{11} &= -\sin\varphi\sin\psi + \cos\varphi\cos\psi\cos\theta, \\ a_{21} &= -\cos\varphi\sin\psi - \sin\varphi\cos\psi\cos\theta, \end{aligned}$$

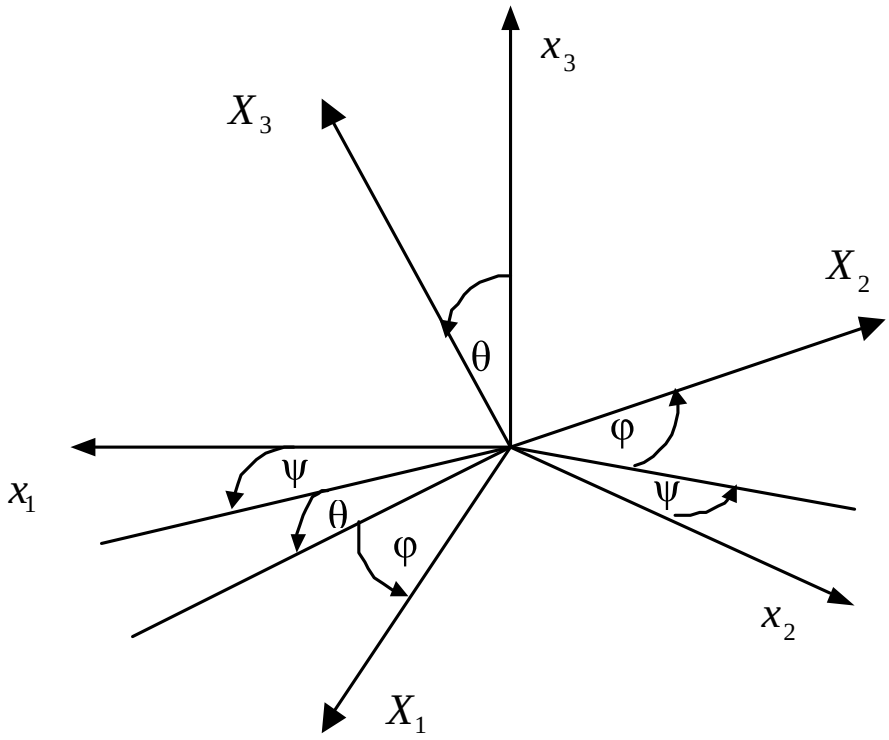

Figure 6.1: Roe's definition of Euler angles, ψ, θ, φ, describing the orientation of the crystallite coordinate system $0 - X_i$ with respect to the global coordinate system $o - x_i$.

$$
\begin{aligned}
a_{31} &= \cos\psi\sin\theta, \\
a_{12} &= \sin\varphi\cos\psi + \cos\varphi\sin\psi\cos\theta, \\
a_{22} &= \cos\varphi\cos\psi - \sin\varphi\sin\psi\cos\theta, \\
a_{32} &= \sin\psi\sin\theta, \\
a_{13} &= \cos\varphi\sin\theta, \\
a_{23} &= \sin\varphi\sin\theta, \\
a_{33} &= \cos\theta.
\end{aligned} \tag{6.2}
$$

As discussed above, an orientation distribution function (ODF) $w(\xi, \psi, \varphi)$, where $\xi = \cos\theta$, is introduced to represent uniquely the crystallite orientation distribution. Since $w(\xi, \psi, \varphi)$ is a probability density function, the integration of this density function over all possible directions must equal unity. That is,

$$
\int_0^{2\pi} \int_0^{2\pi} \int_{-1}^{+1} w(\xi, \psi, \varphi) d\xi d\psi d\varphi = 1. \tag{6.3}
$$

The ODF w may be expanded in a series of generalized spherical harmonics as

$$
w(\xi, \psi, \varphi) = \sum_{l=0}^{\infty} \sum_{m=-l}^{l} \sum_{n=-l}^{l} W_{lmn} Z_{lmn}(\xi) e^{-im\psi} e^{-in\varphi}, \tag{6.4}
$$

where Z_{lmn} is the generalized associated Legendre function, which can be expressed by the generalized Legendre function $P_l^{mn}(\xi)$ as [3]

$$
Z_{lmn} = i^{n-m} \sqrt{\frac{2l+1}{2}} P_l^{mn}(\xi), \tag{6.5}
$$

with

$$
\begin{aligned}
P_l^{mn}(\xi) &= \frac{(-1)^{l-m} i^{n-m}}{2^l (l-m)!} \left[\frac{(l-m)!(l+n)!}{(l+m)!(l-n)!} \right]^{\frac{1}{2}} \\
&\quad \times (1-\xi)^{-\frac{n-m}{2}} (1+\xi)^{-\frac{n+m}{2}} \frac{d^{l-n}}{d\xi^{l-n}} \left[(1-\xi)^{l-m} (1+\xi)^{l+m} \right].
\end{aligned}
$$

The expansion coefficients W_{lmn} are the orientation distribution coefficients (ODCs) in the polycrystalline aggregate and are determined by

$$W_{lmn} = \frac{1}{4\pi^2} \int_0^{2\pi} \int_0^{2\pi} \int_{-1}^{+1} w(\xi, \psi, \varphi) Z_{lmn}(\xi) e^{im\psi} e^{in\varphi} d\xi d\psi d\varphi. \tag{6.6}$$

Detailed results of the Z_{lmn} are discussed in the literature by Morris and Heckler [110]. The number of ODCs in Eq. (6.4) is actually much smaller than those expressed by the forms of the equation since for a particular aggregate the ODCs are dependent on the symmetry exhibited by the crystalline grains and the statistical symmetry of the sample as well. Here, our objective samples are assumed to have orthorhombic symmetry (rolling texture) made up of crystallites exhibiting cubic symmetry. In the assumption of orthorhombic-cubic symmetry, $W_{400}, W_{420}, W_{440}$ are the only three nonzero, independent coefficients which are necessary for determining the fourth-rank effective elastic stiffness tensor. For the calculation of the material covariance and attenuation, however, nine other nonzero, independent coefficients of interest, $W_{600}, W_{620}, W_{640}, W_{660}, W_{800}, W_{820}, W_{840}, W_{860}, W_{880}$, must be included. These details will be presented in the next chapter. The Z_{lmn} of interest here, for $l = 4, 6$, and 8, are calculated using Eq. (6.5).

Given the symmetry class of polycrystalline materials, for example aggregates with orthorhombic symmetry and crystal that is cubic, a number of investigations into the properties of the ODCs W_{lmn} and the generalized associated Legendre function Z_{lmn} are presented in the literature [1],[2],[3],[110]. In order to make this chapter complete, some properties corresponding to the W_{lmn} and Z_{lmn} are summarized here. For the ODCs W_{lmn} :

(a) The coefficients must adhere to the following relation

$$W_{lmn} = W_{l\bar{m}n} = W_{lm\bar{n}} = W_{l\bar{m}\bar{n}}, \tag{6.7}$$

where $\bar{m}$ or $\bar{n}$ denotes $-m$ or $-n$. W_{lmn} must equal zero unless l and m are even and $n = 4k, k = 0, \pm 1, \pm 2, \ldots$.

(b) The coefficients W_{lmn} are all real quantities. Therefore, it is often convenient to write the Eq. (6.4) as

$$w(\xi, \psi, \varphi) = \sum_{l=0}^{\infty} \sum_{m=-l}^{l} \sum_{n=-l}^{l} W_{lmn} Z_{lmn}(\xi) \cos(m\psi + n\varphi). \tag{6.8}$$

(c) The nonzero coefficients W_{lmn} are not all independent for the case discussed here. In particular, the following relations are shown by Roe [2]

$$\begin{aligned} W_{000} &= \frac{1}{4\sqrt{2}\pi^2}, \quad W_{2m0} = 0, \\ W_{4m4} &= \frac{5}{\sqrt{70}} W_{4m0}, \; W_{6m4} = -\frac{\sqrt{14}}{2} W_{6m0}, \\ W_{8m4} &= \frac{\sqrt{154}}{33} W_{8m0}, \; W_{8m8} = \frac{\sqrt{1430}}{66} W_{8m0}. \end{aligned} \tag{6.9}$$

For the generalized associated Legendre function Z_{lmn}, the following properties hold

$$\begin{aligned} \int_{-1}^{+1} Z_{lmn}(\xi) Z_{kmn}(\xi) d\xi &= \delta_{kl}, \\ Z_{l\bar{m}n}(\xi) = Z_{lm\bar{n}}(\xi) &= Z_{lmn}(-\xi), \\ Z_{lmn} = Z_{l\bar{m}\bar{n}} &= (-1)^{m+n} Z_{lnm}. \end{aligned} \tag{6.10}$$

In the next section, the generalized elastic stiffness tensor, $\mathbf{C}$, in an orthorhombic medium is presented. Then, the effective elastic constants for rolling texture with cubic crystal symmetry are estimated by employing a Voigt-type averaging procedure in which the stiffness tensor is averaged by integration over the ODF w.

6.3 The Average Elastic Stiffness for Rolling Texture

For a statistically orthorhombic medium, there are three mutually perpendicular planes of symmetry. Without loss of generality, the sample coordinate system x_i are chosen as those of the symmetry planes of anisotropy. Thus, for a rolled plate three axes are defined as RD, TD, ND, respectively, which are here represented as a, b, and c. The ensemble average polycrystalline media are characterized by the average elastic modulus tensor, $\langle \mathbf{C} \rangle$, which is determined by the integration of the single crystal over the ODF w. The orientation average of a single crystal tensorial property $f(\xi, \psi, \varphi)$ weighted by the ODF is then given by

$$\langle f \rangle = \int_0^{2\pi} \int_0^{2\pi} \int_{-1}^{+1} f(\xi, \psi, \varphi) w(\xi, \psi, \varphi) d\xi d\psi d\varphi. \tag{6.11}$$

For orthorhombic symmetry, the averaged elastic stiffness $\langle C_{ijkl} \rangle$ can be determined using Eq. (6.11) and Eq. (6.4). Therefore, the most general form for the elastic tensor is given in terms of two independent unit vectors b and c by

$$\begin{aligned}
\langle C_{ijkl} \rangle = {} & \Gamma_1 \delta_{ij}\delta_{kl} + \Gamma_2 \left(\delta_{ik}\delta_{jl} + \delta_{il}\delta_{jk}\right) + \Gamma_3 \left(\delta_{ij}c_k c_l + \delta_{kl}c_i c_j\right) \\
& + \Gamma_4 \left(\delta_{ik}c_j c_l + \delta_{il}c_j c_k + \delta_{jk}c_i c_l + \delta_{jl}c_i c_k\right) + \Gamma_5 \; c_i c_j c_k c_l \\
& + \Gamma_6 \left(\delta_{ij}b_k b_l + \delta_{kl}b_i b_j\right) + \Gamma_7 \left(\delta_{ik}b_j b_l + \delta_{il}b_j b_k + \delta_{jk}b_i b_l + \delta_{jl}b_i b_k\right) \\
& + \Gamma_8 \; b_i b_j b_k b_l + \Gamma_9 (b_i b_j c_k c_l + b_i b_k c_j c_l + b_i b_l c_j c_k \\
& + b_j b_k c_i c_l + b_j b_l c_i c_k + b_k b_l c_i c_j).
\end{aligned} \tag{6.12}$$

The nine independent coefficients in Eq. (6.12) are defined in the following as nine inde-

pendent elastic constants, C_{11}, C_{22}, C_{33}, C_{44}, C_{55}, C_{66}, C_{12}, C_{13}, C_{23}, respectively

$$\begin{aligned}
\Gamma_1 &= \frac{1}{3}\left(C_{11}+2C_{44}-2C_{55}-2C_{66}+2C_{12}+2C_{13}-2C_{23}\right), \\
\Gamma_2 &= \frac{1}{3}\left(C_{11}-C_{44}+C_{55}+C_{66}-C_{12}-C_{13}+C_{23}\right), \\
\Gamma_3 &= \frac{1}{3}\left(-C_{11}-2C_{44}+2C_{55}+2C_{66}-2C_{12}+C_{13}+2C_{23}\right), \\
\Gamma_4 &= \frac{1}{3}\left(-C_{11}+C_{44}+2C_{55}-C_{66}+C_{12}+C_{13}-C_{23}\right), \\
\Gamma_5 &= \left(C_{11}+C_{33}-4C_{55}-2C_{13}\right), \\
\Gamma_6 &= \frac{1}{3}\left(-C_{11}-2C_{44}+2C_{55}+2C_{66}+C_{12}-2C_{13}+2C_{23}\right), \\
\Gamma_7 &= \frac{1}{3}\left(-C_{11}+C_{44}-C_{55}+2C_{66}+C_{12}+C_{13}-C_{23}\right), \\
\Gamma_8 &= \left(C_{11}+C_{22}-4C_{66}-2C_{12}\right), \\
\Gamma_9 &= \frac{1}{3}\left(C_{11}+2C_{44}-2C_{55}-2C_{66}-C_{12}-C_{13}+C_{23}\right).
\end{aligned}$$

In the case of a transversely isotropic medium, it is known that $C_{11}=C_{22}, C_{44}=C_{55}, C_{13}=C_{23}$ and $2C_{66}=C_{11}-C_{12}$. Therefore, the coefficients Γ_6, Γ_7, Γ_8, and Γ_9 are equal to zero. Furthermore, the coefficients Γ_3, Γ_4 and Γ_5 will be zero under the assumption of statistical isotropy. In general, the elastic modulus tensor for a single cubic crystal is given by

$$C_{ijkl}=C_{12}^0\delta_{ij}\delta_{kl}+C_{44}^0\left(\delta_{ik}\delta_{jl}+\delta_{il}\delta_{jk}\right)+\kappa\sum_{n=1}^{3}a_{in}a_{jn}a_{kn}a_{ln}, \tag{6.13}$$

where the single crystal anisotropic factor $\kappa=C_{11}^0-C_{12}^0-2C_{44}^0$. The notation C_{ij}^0 represents the single crystal constants. The elements a_{kn} define the transformation matrix in term of the three Euler angles given in Eq. (6.2). If the differences of the elastic constants for each grain are only induced by a different orientation such that the grains are assumed to have

the same grain size, the averaged elastic tensor $\langle C_{ijkl} \rangle$ is given by Eq. (6.11) as follows:

$$\langle C_{ijkl} \rangle = C_{12}^0 \delta_{ij}\delta_{kl} + C_{44}^0 \left(\delta_{ik}\delta_{jl} + \delta_{il}\delta_{jk}\right) + \kappa \left\langle \sum_{n=1}^{3} a_{in}a_{jn}a_{kn}a_{ln} \right\rangle, \tag{6.14}$$

where the term within the bracket is expressed in detail as

$$\left\langle \sum_{n=1}^{3} a_{in}a_{jn}a_{kn}a_{ln} \right\rangle = \frac{1}{4\pi^2} \int_0^{2\pi} \int_0^{2\pi} \int_{-1}^{+1} \sum_{n=1}^{3} a_{in}a_{jn}a_{kn}a_{ln} w(\xi,\psi,\varphi) d\xi d\psi d\varphi. \tag{6.15}$$

For the case of rolling texture of orthorhombic-cubic symmetry, the nonzero averaged values in Eq. (6.15) are given by

$$\begin{aligned}
\left\langle \sum_{n=1}^{3} a_{n1}^4 \right\rangle &= \frac{3}{5} + \frac{12\sqrt{2}}{35}\pi^2 W_{400} - \frac{16\sqrt{5}}{35}\pi^2 W_{420} + \frac{8\sqrt{35}}{35}\pi^2 W_{440}, \\
\left\langle \sum_{n=1}^{3} a_{n2}^4 \right\rangle &= \frac{3}{5} + \frac{12\sqrt{2}}{35}\pi^2 W_{400} + \frac{16\sqrt{5}}{35}\pi^2 W_{420} + \frac{8\sqrt{35}}{35}\pi^2 W_{440}, \\
\left\langle \sum_{n=1}^{3} a_{n3}^4 \right\rangle &= \frac{3}{5} + \frac{32\sqrt{2}}{35}\pi^2 W_{400}, \\
\left\langle \sum_{n=1}^{3} a_{n2}^2 a_{n3}^2 \right\rangle &= \frac{1}{5} - \frac{16\sqrt{2}}{35}\pi^2 W_{400} - \frac{16\sqrt{5}}{35}\pi^2 W_{420}, \\
\left\langle \sum_{n=1}^{3} a_{n1}^2 a_{n3}^2 \right\rangle &= \frac{1}{5} - \frac{16\sqrt{2}}{35}\pi^2 W_{400} + \frac{16\sqrt{5}}{35}\pi^2 W_{420}, \\
\left\langle \sum_{n=1}^{3} a_{n1}^2 a_{n2}^2 \right\rangle &= \frac{1}{5} + \frac{4\sqrt{2}}{35}\pi^2 W_{400} - \frac{8\sqrt{35}}{35}\pi^2 W_{440}.
\end{aligned} \tag{6.16}$$

Using Eq. (6.14) and Eq. (6.16), the effective elastic constants in Eq. (6.12) can be written as the following explicit form in the Voigt compact notation:

$$\begin{aligned}
C_{11} &= C_{11}^0 - 2\kappa\Lambda_1, \quad C_{44} = C_{44}^0 + \kappa\Lambda_4, \quad C_{23} = C_{12}^0 + \kappa\Lambda_4, \\
C_{22} &= C_{11}^0 - 2\kappa\Lambda_2, \quad C_{55} = C_{44}^0 + \kappa\Lambda_5, \quad C_{13} = C_{12}^0 + \kappa\Lambda_5, \\
C_{33} &= C_{11}^0 - 2\kappa\Lambda_3, \quad C_{66} = C_{44}^0 + \kappa\Lambda_6, \quad C_{12} = C_{12}^0 + \kappa\Lambda_6,
\end{aligned} \tag{6.17}$$

with

$$
\begin{aligned}
\Lambda_1 &= \frac{1}{5} - \frac{6\sqrt{2}}{35}\pi^2\left[W_{400} - \frac{2\sqrt{10}}{3}W_{420} + \frac{\sqrt{70}}{3}W_{440}\right], \\
\Lambda_2 &= \frac{1}{5} - \frac{6\sqrt{2}}{35}\pi^2\left[W_{400} + \frac{2\sqrt{10}}{3}W_{420} + \frac{\sqrt{70}}{3}W_{440}\right], \\
\Lambda_3 &= \frac{1}{5} - \frac{16\sqrt{2}}{35}\pi^2 W_{400}, \\
\Lambda_4 &= \frac{1}{5} - \frac{16\sqrt{2}}{35}\pi^2\left[W_{400} + \frac{\sqrt{10}}{2}W_{420}\right], \\
\Lambda_5 &= \frac{1}{5} - \frac{16\sqrt{2}}{35}\pi^2\left[W_{400} - \frac{\sqrt{10}}{2}W_{420}\right], \\
\Lambda_6 &= \frac{1}{5} + \frac{4\sqrt{2}}{35}\pi^2\left[W_{400} - \sqrt{70}W_{420}\right].
\end{aligned}
\tag{6.18}
$$

These results are identical with the results presented in the literature [95],[98],[99],[101]. In the case of a statistically isotropic sample, that is, the grain orientation is randomly distributed, the ODCs W_{400},W_{420}, and W_{440} are equal to zero. As such, the ensemble averaged properties obviously lose their directional dependence. In the next section, the anisotropic Christoffel equation is presented.

6.4 Christoffel Equation

The propagation characteristics of elastic waves in an anisotropic medium are determined by the elastic stiffness of the materials. When elastic waves propagate through a homogeneous, anisotropic medium, the phase velocity V and the associated polarization vector $\mathbf{u}$ of plane waves must satisfy the Christoffel equation [73]:

$$
\left(T_{ik} - V^2\delta_{ik}\right)u_k = 0, \tag{6.19}
$$

where δ_{ik} is the Kronecker delta, and the notation $\mathbf{T}$ is the symmetric Christoffel tensor given by the relation

$$T_{ik} = \frac{1}{\rho} C_{ijkl}\ p_j p_l. \tag{6.20}$$

Here, ρ is the material density, and $\mathbf{p}$ is the unit vector in the propagation direction, which is often expressed by polar angle ϕ and azimuthal angle Θ as $\mathbf{p} = \mathbf{x}_1 \cos\Theta \sin\phi + \mathbf{x}_2 \sin\Theta \sin\phi + \mathbf{x}_3 \cos\phi$. The summation over repeated indices is implied. Because of the symmetry characteristics of the effective elastic tensor $\mathbf{C}$, the components of the Christoffel tensor are also symmetric. The tensor $\mathbf{T}$ therefore has six independent components. For the case of the orthorhombic system, those independent terms can be written in compact form as [72]

$$\begin{aligned}
\rho T_{11} &= C_{11} p_1^2 + C_{66} p_2^2 + C_{55} p_3^2, \\
\rho T_{22} &= C_{66} p_1^2 + C_{22} p_2^2 + C_{44} p_3^2, \\
\rho T_{33} &= C_{55} p_1^2 + C_{44} p_2^2 + C_{33} p_3^2, \\
\rho T_{12} &= (C_{12} + C_{66})\, p_1 p_2, \\
\rho T_{13} &= (C_{13} + C_{55})\, p_1 p_3, \\
\rho T_{23} &= (C_{23} + C_{44})\, p_2 p_3.
\end{aligned} \tag{6.21}$$

The effective elastic constants, Eq. (6.21), in the orthorhombic-cubic symmetry are given by Eq. (6.17). The Christoffel equation describes a standard eigenvalue $\left(V^2\right)$-eigenvector $(\mathbf{u})$ problem for the Christoffel tensor $\mathbf{T}$, which is exactly related to the wave velocity and polarization direction vectors. The detailed eigenvalue-eigenvector problem is discussed in the next section.

6.5 Wave Velocity and Polarization

In the case of a statistically orthorhombic sample made up of cubic crystallites, it is known that ultrasonic velocities depend on many factors within the polycrystal materials. The main effects are the single grain elastic constants and mass density, and especially the texture. Therefore, given the elastic constants and texture coefficients, and any chosen propagation direction, the wave velocities of the three wave types can be obtained by solving the Christoffel equation for that propagation direction. In general, the eigenvalues are calculated by

$$\det\ \left(T_{ik} - V^2\delta_{ik}\right) = 0. \tag{6.22}$$

The polarization vectors are equal to the eigenvectors of the Christoffel tensor $\mathbf{T}$ corresponding to the appropriate eigenvalue. When solving the system of equations, Eq. (6.22), for any given direction $\mathbf{p}$, three positive values of the squared phase velocity V^2 are obtained, which respectively represent the quasilongitudinal (qP),and two quasishear ($qS1$ and $qS2$) wave modes. After the eigenvalues are determined, the associated polarization vectors $\mathbf{u}$ of each corresponding mode can be obtained from Eq. (6.19). Since the Christoffel tensor $\mathbf{T}$ is symmetric, the polarization vectors of the three modes are always orthogonal to each other, but none of them is necessarily parallel or perpendicular to direction $\mathbf{p}$. In most cases, the above eigenvalues and the eigenvectors have to be solved by numerical methods. However, in some situations, for example waves propagating in the symmetry planes, analytic solutions may be found explicitly.

Given an orthorhombic model, there are always three mutually orthogonal planes of symmetry that coincide with the coordinate planes. While a plane wave propagating

in the $x_1 - x_2$ plane, the projection of direction $\mathbf{p}$ on the x_3 axis disappears, that is, $\mathbf{p} = \mathbf{x}_1 \cos\Theta + \mathbf{x}_2 \sin\Theta$. Therefore, the phase velocities of each wave type can be explicitly given in the form

$$\begin{aligned} \rho V_{qS1}^2 &= C_{44}\sin^2\Theta + C_{55}\cos^2\Theta, \\ 2\rho V_{qP}^2 &= Q + \sqrt{Q^2 - 4R}, \\ 2\rho V_{qS2}^2 &= Q - \sqrt{Q^2 - 4R}, \end{aligned} \tag{6.23}$$

where the quantities Q and R are defined by

$$\begin{aligned} Q &= C_{11}\cos^2\Theta + C_{22}\sin^2\Theta + C_{66}, \\ R &= \left(C_{11}\cos^2\Theta + C_{66}\sin^2\Theta\right)\left(C_{22}\sin^2\Theta + C_{66}\cos^2\Theta\right) \\ &\quad -(C_{12} + C_{66})^2 \sin^2\Theta\cos^2\Theta. \end{aligned} \tag{6.24}$$

The effective elastic constants are given in Eq. (6.17). In this case, the polarization direction of the quasishear ($qS1$) wave is perpendicular to the $x_1 - x_2$ plane, namely, $u_3 = x_3$. The polarization vectors of other two waves (qP and $qS2$) are to locate within the $x_1 - x_2$ plane. Given propagation along the x_1 axis, i.e. $\Theta = 0$, the phase velocities of each wave type in Eq. (6.23) are simplified as

$$\begin{aligned} \rho V_{qS1-13}^2 &= C_{44}^0 + \eta\left[\frac{1}{5} - \frac{16\sqrt{2}}{35}\pi^2\left(W_{400} - \frac{\sqrt{10}}{2}W_{420}\right)\right], \\ \rho V_{qP-11}^2 &= C_{11}^0 - 2\eta\left[\frac{1}{5} - \frac{6\sqrt{2}}{35}\pi^2\left(W_{400} - \frac{2\sqrt{10}}{3}W_{420} + \frac{\sqrt{70}}{3}W_{440}\right)\right], \\ \rho V_{qS2-12}^2 &= C_{44}^0 + \eta\left[\frac{1}{5} + \frac{4\sqrt{2}}{35}\pi^2\left(W_{400} - \sqrt{70}W_{420}\right)\right]. \end{aligned} \tag{6.25}$$

If propagation is along the x_2 axis, i.e. $\Theta = \pi/2$, the phase velocities of each wave type in

Eq. (6.23) are given by

$$\begin{aligned}
\rho V_{qS1-23}^2 &= C_{44}^0 + \eta\left[\frac{1}{5} - \frac{16\sqrt{2}}{35}\pi^2\left(W_{400} + \frac{\sqrt{10}}{2}W_{420}\right)\right], \\
\rho V_{qP-22}^2 &= C_{11}^0 - 2\eta\left[\frac{1}{5} - \frac{6\sqrt{2}}{35}\pi^2\left(W_{400} + \frac{2\sqrt{10}}{3}W_{420} + \frac{\sqrt{70}}{3}W_{440}\right)\right], \\
\rho V_{qS2-21}^2 &= C_{44}^0 + \eta\left[\frac{1}{5} + \frac{4\sqrt{2}}{35}\pi^2\left(W_{400} - \sqrt{70}W_{420}\right)\right].
\end{aligned} \tag{6.26}$$

When considering wave propagation in the $x_1 - x_3$ plane, the projection of direction $\mathbf{p}$ on the x_2 axis vanishes, that is $\mathbf{p} = \mathbf{x}_1 \cos\Theta + \mathbf{x}_3 \sin\Theta$. In this specific case, the phase velocities of the three wave types can be explicitly given in the form

$$\begin{aligned}
\rho V_{qS1}^2 &= C_{44}\sin^2\Theta + C_{66}\cos^2\Theta, \\
2\rho V_{qP}^2 &= P + \sqrt{P^2 - 4S}, \\
2\rho V_{qS2}^2 &= P - \sqrt{P^2 - 4S},
\end{aligned} \tag{6.27}$$

where the quantities P and S are defined as follows:

$$\begin{aligned}
P &= C_{11}\cos^2\Theta + C_{33}\sin^2\Theta + C_{55}, \\
S &= \left(C_{11}\cos^2\Theta + C_{55}\sin^2\Theta\right)\left(C_{33}\sin^2\Theta + C_{55}\cos^2\Theta\right) \\
&\quad -(C_{13} + C_{55})^2\sin^2\Theta\cos^2\Theta.
\end{aligned} \tag{6.28}$$

Again, the expression can be significantly simplified if one gives wave propagation along the directions of the x_1 and x_3 axes. For propagation along the x_1 axis, the same results are

given in Eq. (6.25). For propagation along the x_3 axis, the simplified results are given by

$$\begin{aligned}
\rho V_{qS1-32}^2 &= C_{44}^0 + \eta\left[\frac{1}{5} - \frac{16\sqrt{2}}{35}\pi^2\left(W_{400} + \frac{\sqrt{10}}{2}W_{420}\right)\right], \\
\rho V_{qP-33}^2 &= C_{11}^0 - 2\eta\left[\frac{1}{5} - \frac{16\sqrt{2}}{35}\pi^2 W_{400}\right], \\
\rho V_{qS2-31}^2 &= C_{44}^0 + \eta\left[\frac{1}{5} - \frac{16\sqrt{2}}{35}\pi^2\left(W_{400} - \frac{\sqrt{10}}{2}W_{420}\right)\right].
\end{aligned} \tag{6.29}$$

These results of the wave propagation along the three axes are identical with the results given by Sayers [98]. The notation $(-ij)$ denotes the wave propagation in the x_i direction and polarization in the x_j direction. It is shown that the values of these phase velocities are equal to each other for a wave propagating in the x_i direction and polarized in the x_j direction, with a wave propagating in the x_j direction and polarized in the x_i direction, $V_{ij} = V_{ji}$. This property is implied by the assumption of orthorhombic symmetry.

Finally, when considering wave propagation in the $x_2 - x_3$ plane, the projection of direction $\mathbf{p}$ on the x_1 axis vanishes, that is $\mathbf{p} = \mathbf{x}_2\cos\Theta + \mathbf{x}_3\sin\Theta$. In this case, the phase velocities of the three wave types are given by

$$\begin{aligned}
\rho V_{qS1}^2 &= C_{55}\sin^2\Theta + C_{66}\cos^2\Theta, \\
2\rho V_{qP}^2 &= M + \sqrt{M^2 - 4N}, \\
2\rho V_{qS2}^2 &= M - \sqrt{M^2 - 4N},
\end{aligned} \tag{6.30}$$

where the quantities M and N are defined by

$$\begin{aligned}
M &= C_{22}\cos^2\Theta + C_{33}\sin^2\Theta + C_{44}, \\
N &= \left(C_{22}\cos^2\Theta + C_{44}\sin^2\Theta\right)\left(C_{33}\sin^2\Theta + C_{44}\cos^2\Theta\right) \\
&\quad -(C_{23} + C_{44})^2\sin^2\Theta\cos^2\Theta.
\end{aligned} \tag{6.31}$$

Numerical results are now presented for a particular texture case. In 70% rolled steel, the single cubic grain constants and the texture coefficients of interest are given by [3],[45]

$$\begin{aligned} C_{11}^0 &= 2.37 \times 10^{11}\text{Pa}, \qquad C_{12}^0 = 1.41 \times 10^{11}\text{Pa}, \\ C_{44}^0 &= 1.16 \times 10^{11}\text{Pa}, \qquad \rho = 7850 \text{ kg/m}^3, \\ c_4^{00} &= -1.47, \qquad c_4^{20} = -0.46, \qquad c_4^{40} = 0.50. \end{aligned} \tag{6.32}$$

It should be pointed out that the ODCs' relation of the Bunge notation c_l^{mn} and the Roe notation W_{lmn} must be used for carrying out the calculation, that is

$$W_{lmn} = \frac{1}{8\pi^2}\sqrt{\frac{2}{2l+1}} \cdot (-1)^{m+n} c_l^{mn}. \tag{6.33}$$

If the propagation direction is defined by $\mathbf{p} = \mathbf{x}_1 \cos\Theta \sin\phi + \mathbf{x}_2 \sin\Theta \sin\phi + \mathbf{x}_3 \cos\phi$, where Θ is azimuthal angle and ϕ is polar angle, the phase velocities may be computed using Eq. (6.22). Since the orthorhombic symmetry has three mutually orthogonal planes of symmetry, all calculations are made for $0^\circ \leq \Theta \leq 90^\circ$,and $0^\circ \leq \phi \leq 90^\circ$. Figure 6.2 represents the quasilongitudinal (qP) wave velocity as a function of the azimuthal Θ at the given polar angle ϕ. At $\phi = 0^\circ$, the wave propagation direction is along the x_3 axis; for $\phi = 90^\circ$, wave propagation direction is within the $x_1 - x_2$ plane. It is observed from Fig. 6.2 that at $\phi = 0^\circ$ the quasilongitudinal wave velocity has a maximum. Figure 6.3 shows the phase velocities of two quasishear (qS) waves as a function of the azimuthal angle Θ at the given polar angle ϕ. The two quasishear waves are observed to have their minima at $\phi = 0^\circ$, respectively. The maximum variation of the phase velocity with respect to this specific model is at the polar angle $\phi = 90^\circ$, and $\phi = 0^\circ$ for wave propagation along the x_3

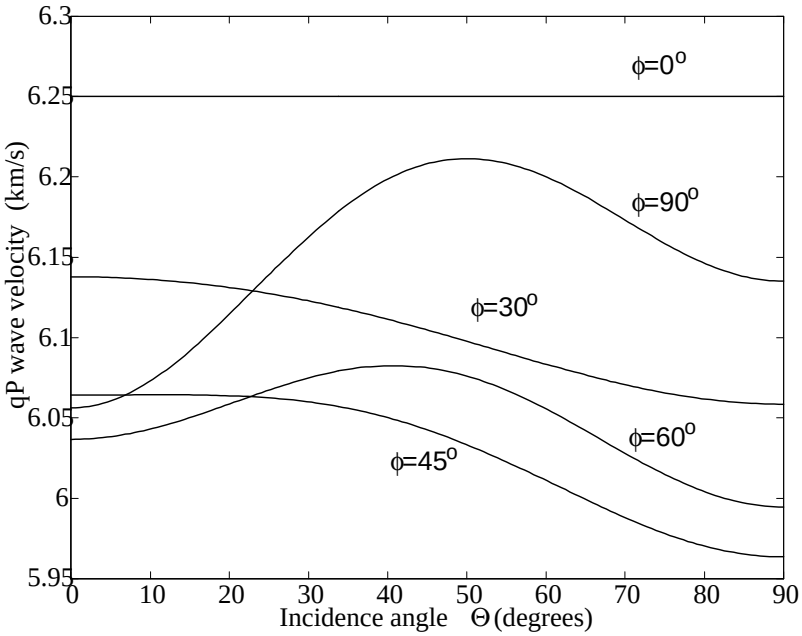

Figure 6.2: qP wave velocity as a function of the azimuthal angle Θ at the polar angle $\phi = 0°, 30°, 45°, 60°$ and $90°$.

axis, the velocities of the three wave modes are constants as shown in Eq. (6.29).

Because of their relation to the attenuation and experimental measurements, the angular deviations of the three wave polarization vectors must be discussed. Figure 6.4 shows the angular deviation of the qP wave polarization vector from the wave propagation direction $\mathbf{p}$. It is observed that the maximum deviation angle is about $3.5°$ at $\phi = 30°$ for this particular texture. At $\phi = 90°$, the wave propagation direction is within the $x_1 - x_2$ plane. Thus, when the wave propagates along the axes ($\Theta = 0°$ and $\Theta = 90°$), the qP wave polarization vectors are still along these axes such that the deviation angles are zero. In addition, an additional feature is observed in Fig. 6.4. There is a zero angular deviation for propagation between the azimuthal angle Θ at $0°$ and $90°$. In this situation, the polarization vector is the same as the wave propagation direction, that is, $u_1 = \mathbf{x}_1 \cos\Theta + \mathbf{x}_2 \sin\Theta$. Using

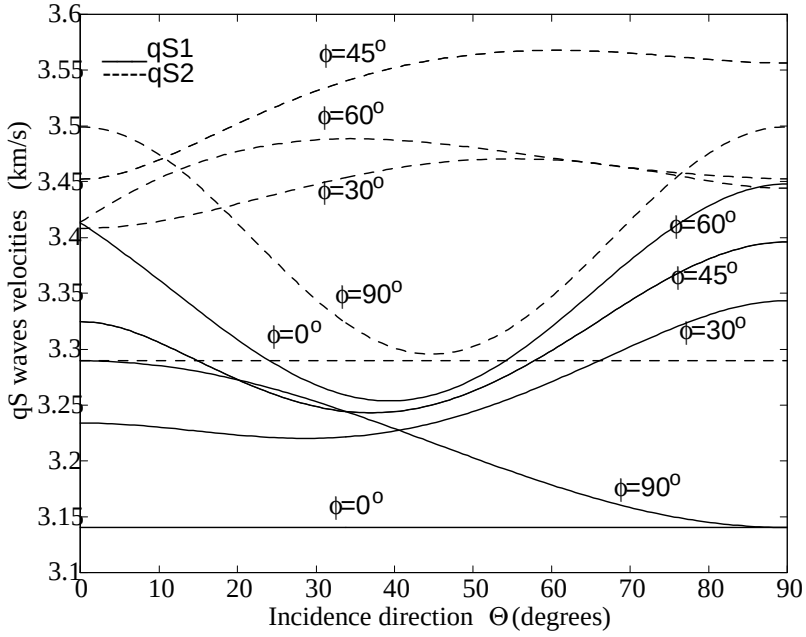

Figure 6.3: qS waves velocities as a function of the azimuthal angle Θ at the polar angle $\phi = 0°, 30°, 45°, 60°$ and $90°$.

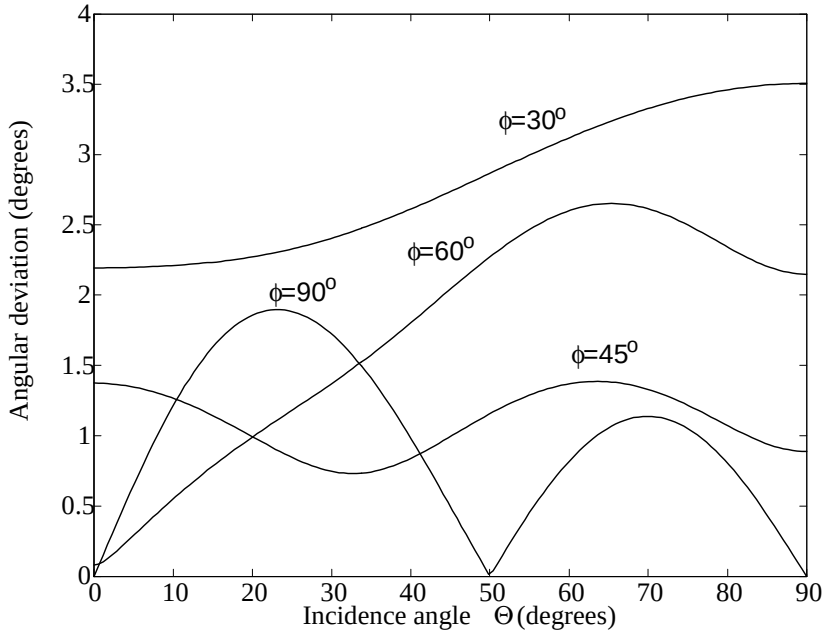

Figure 6.4: The angular deviation of the qP wave polarization vector from the propagation direction (degrees).

this relation and the Christoffel equation, Eq. (6.19), the azimuthal angles Θ are given by the relations:

$$\begin{aligned} \cos\Theta &= 0, \\ \sin\Theta &= 0, \\ \cos^2\Theta\left[1-2\Lambda_1-3\Lambda_6\right] &= \sin^2\Theta\left[1-2\Lambda_2-3\Lambda_6\right], \end{aligned} \tag{6.34}$$

where Λ_1 and Λ_2 are given in Eq. (6.18). From the first two equations, the values of Θ that are equal to 0° and 90° can be easily seen. Using the third equation, the azimuthal angle between 0° and 90°, which is dependent on the material texture, can be calculated if the texture coefficients are known. In this case, $\Theta = 50.03^\circ$. However, while propagating outside the symmetry plane, this feature shown in Fig. 6.4 does not exist. The result can be proved numerically. In Fig. 6.5, the deviation angles of the $qS1$ wave polarization vector from the propagation direction are presented. It is shown that at $\phi = 90^\circ$, the polarization vector is always perpendicular to the propagation plane ($x_1 - x_2$ plane). This physical property is implied in the wave propagation theory [111]. The results also show that as the polar angle increases gradually for propagation, there are some polarization vectors are perpendicular to the associated propagation plane. Due to the complexity of the expressions, however, closed-form can not be found. Figure 6.6 shows the angular deviation of the $qS2$ wave polarization vector from the propagation direction. Since the $qS2$ wave polarization vector is entirely within the same plane as that of the qP wave, the angular deviations are consistent with each other, which may be observed in Figs. 6.4 and 6.6.

In Fig. 6.7, the qP wave velocities are presented as a function of propagation direction within the $x_1 - x_2$, $x_1 - x_3$, and $x_2 - x_3$ planes, respectively. In the $x_1 - x_2$ plane,

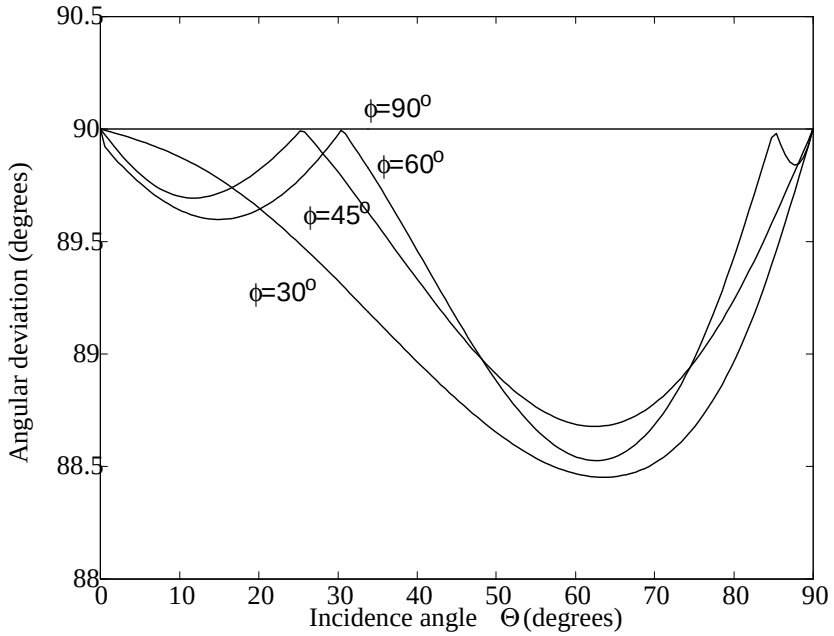

Figure 6.5: The angular deviation of the quasishear wave ($qS1$) polarization vector from the propagation direction (degrees).

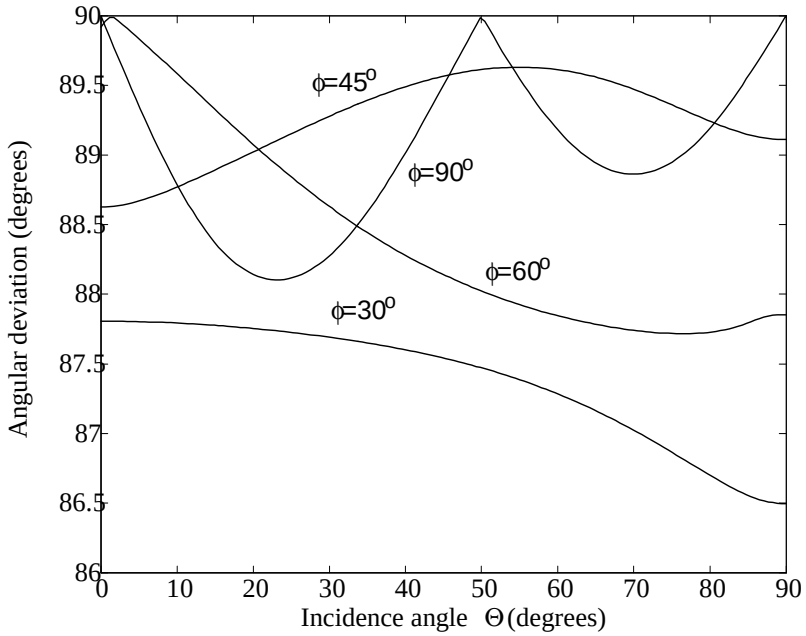

Figure 6.6: The angular deviation of the quasishear wave ($qS2$) polarization vector from the propagation direction (degrees).

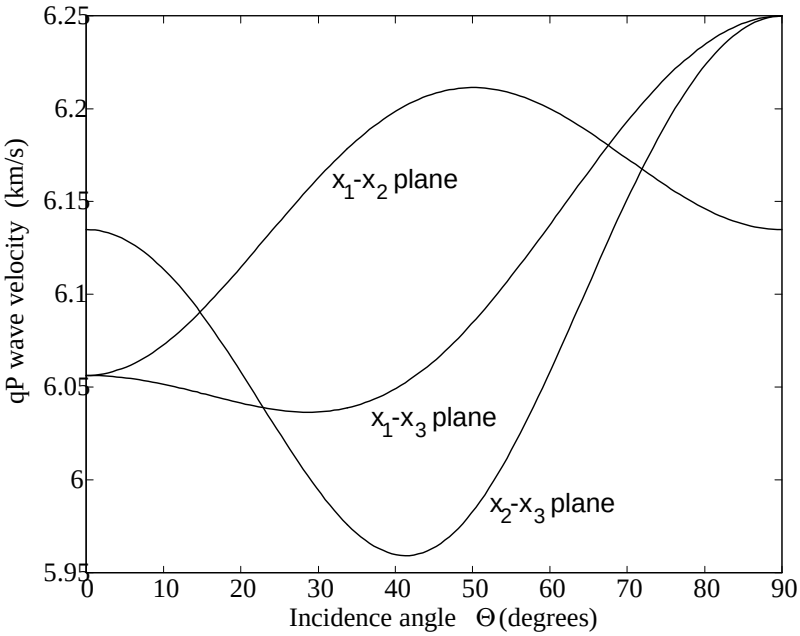

Figure 6.7: qP wave velocity upon wave propagation vector within three symmetry planes.

the wave velocity is seen to increase at the beginning and reach a maximum, then decrease as the azimuthal angle Θ increases. In contrast, the wave velocities in the $x_1 - x_3$ and $x_2 - x_3$ planes are observed to decrease first, then increase as the angle Θ increases for this particular texture. Upon propagation along the three axes, there are the same velocities as discussed previously. Figure 6.8 represents the two qS waves velocities when the wave propagation vector is located within the three symmetry planes. In the $x_1 - x_3$ and $x_2 - x_3$ planes, at the intersection points or singular points, the two quasishear waves have the same velocities. The singularity of the quasishear waves velocity is a basic feature in an anisotropic medium. Such a phenomenon was discussed for orthorhombic media in detail by Crampin [105] and Farra [109]. It is observed from Fig. 6.8 that the $qS1$ wave velocities have their maxima at $\Theta = 45^\circ$ when propagating within the $x_1 - x_3$ and $x_2 - x_3$ planes,

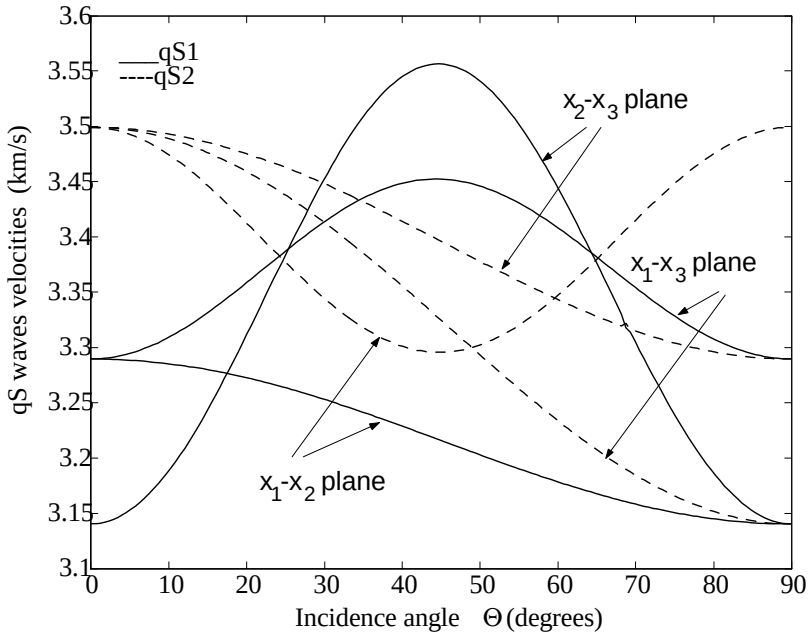

Figure 6.8: qS waves velocities upon wave propagation vector within three symmetry planes.

while the $qS2$ wave velocity has a minimum at $\Theta = 45°$ upon propagating in the $x_1 - x_2$ plane. The results also show that the $qS2$ wave velocities have their maxima at $\Theta = 0°$ and minima at $\Theta = 90°$ when propagating within the $x_1 - x_3$ and $x_2 - x_3$ planes, and the $qS1$ wave velocity has a maximum $\Theta = 0°$ and a minimum at $\Theta = 90°$ for propagation in the $x_1 - x_2$ plane. In the next section, the wave velocity during annealing is studied.

6.6 Phase Velocity during Annealing

To use ultrasonic techniques for monitoring texture during processing, the relationships between ultrasonic parameters, such as ultrasonic wave velocity and materials texture must be investigated. Liu and coworkers have presented a model to extract information about recrystallization from such ultrasonic measurements [112]. Here, their model is used

to discuss the ultrasonic wave velocity during annealing. It is noted that there are six ideal texture components which are generally assumed to be present in rolled and recrystallized aluminum [97]. In the model discussed by Liu, et al., those six ideal texture components are supposed to evolve in time following certain function forms with some constants to be determined. It is also assumed that the observed orientation distribution coefficients (ODCs), for example $W_{400}, W_{420}, W_{440}$, may be averagely weighted by the volume fraction of each component. Thus, for the case of rolled and recrystallized aluminum, the ODCs are given by [112]

$$\begin{aligned} W_{400} &= -0.0077 f_1(t) - 0.0309 f_2(t) - 0.0077 \left[f_3(t) + f_4(t) + f_5(t) \right], \\ W_{420} &= -0.0244 f_1(t) + 0.0081 f_2(t) - 0.0003 f_4(t) - 0.0081 f_5(t), \\ W_{440} &= 0.0134 f_1(t) + 0.0185 f_2(t) - 0.0108 f_3(t) - 0.0089 f_4(t) - 0.0108 f_5(t), \end{aligned} \tag{6.35}$$

where $f_i(t)$, $i = 1, 2, 3, 4, 5$, are the texture components evolving in time with functional form shown in Fig. 6.9. These respectively represent the Goss, Cube, Cu, S, B, and Random volume fractions. The detailed discussion was reviewed in the literature [97]. During annealing, the recrystallization texture, such as the Goss and Cube components, increases, while the rolling texture, the Cu, S, and B components, decreases. Thus, for this particular aluminum model the ODCs versus annealing time curves based on the texture shown in Fig. 6.9 are presented in Fig. 6.10. It is seen that during annealing the ODCs are to keep invariant at the beginning and the end of the process, while the ODCs are suddenly varied in the middle of the process.

Based on the above discussions, the wave velocity during annealing is presented. In this particular rolled and recrystallized aluminum, the elastic constants of the cubic crystal

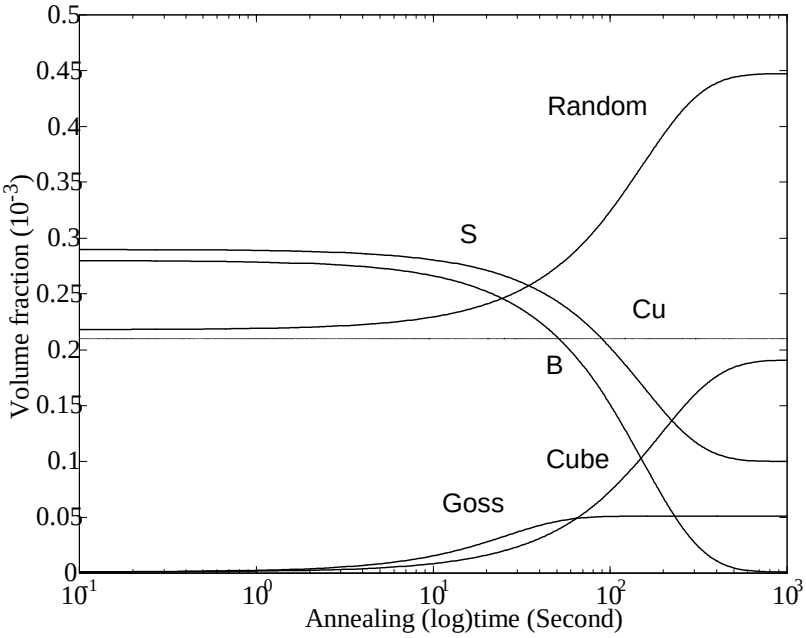

Figure 6.9: Texture components as a function of annealing (log)time.

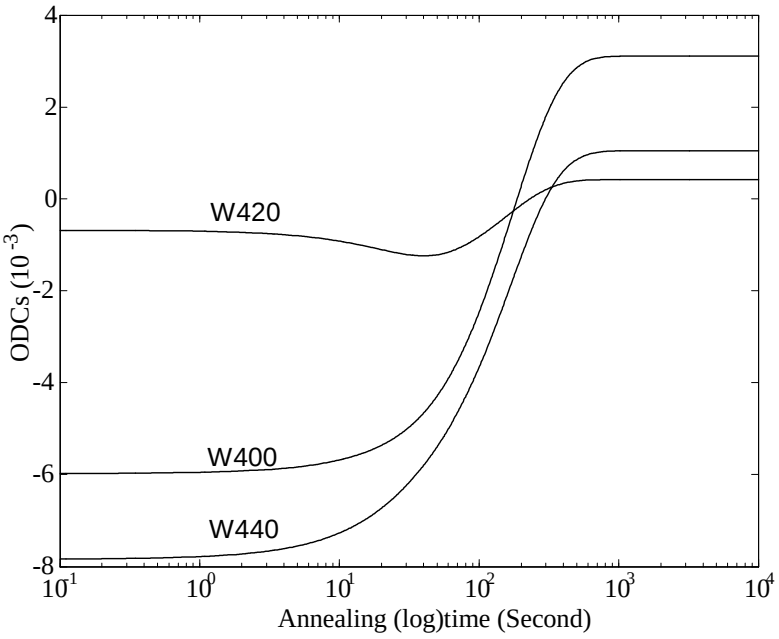

Figure 6.10: The ODCs versus annealing time.

grain used were: $C_{11}^0 = 1.08 \times 10^{11}$Pa, $C_{12}^0 = 0.61 \times 10^{11}$Pa, $C_{44}^0 = 0.29 \times 10^{11}$Pa, and density $\rho = 2700$ kg/m^3. In Fig. 6.11, the qP wave velocity is shown for propagation along the three orthogonal axes, i.e., ND, RD, and TD. The V_{ND}, V_{RD},and V_{TD} are quasilongitudinal wave velocities propagating in the normal direction, rolling direction, and transverse direction, respectively. The qP wave velocities decrease as the ODCs increase during annealing. Figure 6.12 represents one quasishear ($qS1$) wave velocity. V_{NT} is the wave velocity for propagation in the normal direction and polarization in the transverse direction and V_{TN} is the wave velocity for propagation in the transverse direction and polarization in the normal direction, and $V_{NT} = V_{TN}$, which is seen in Eqs. (6.29) and (6.26). The V_{RN} is the wave velocity for propagation in the rolling direction and polarization in the normal direction. In contrast, the $qS1$ wave velocities increase as the ODCs increase during annealing. Figure 6.13 shows the other quasishear ($qS2$) wave velocity. It is observed that the shear wave velocity of V_{RT} (V_{TR}) is dominated by the ODC W_{420}, which first decreases to reach the minimum, then increases to reach the initial value during annealing. Based on the information analyzed above, the texture of polycrystalline aggregates may be inferred as a function of annealing time. The ODCs, for example $W_{400}, W_{420}, W_{440}$, can be calculated from ultrasonic velocity measurements [112]. The ultrasonic velocities of sample specimens can be measured during annealing. Thus, the ODCs can be determined during such processing.

6.7 Conclusions

In this chapter, the wave velocity and polarization of ultrasonic waves in rolled and recrystallized materials have been discussed. The general elastic stiffness tensor in

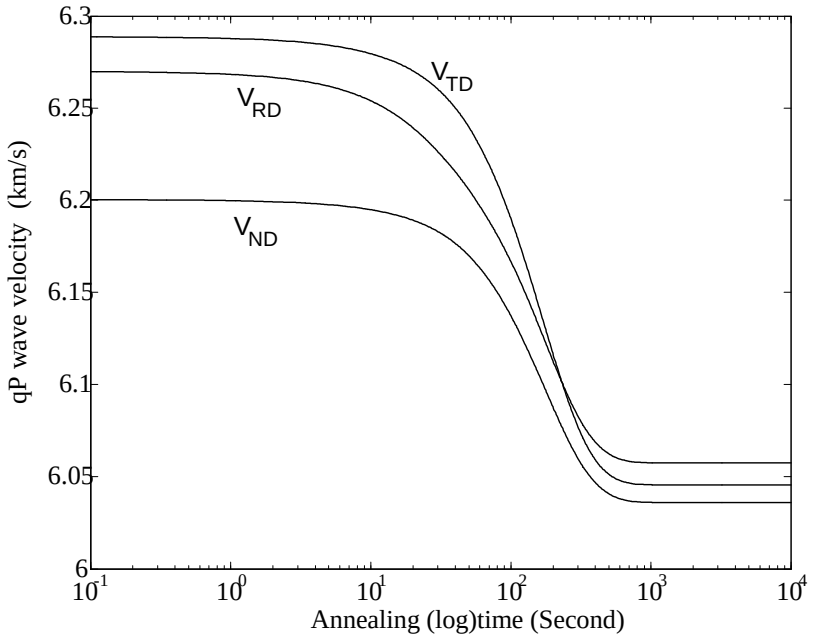

Figure 6.11: qP wave velocity versus annealing time when wave propagating in the ND, RD, TD, respectively.

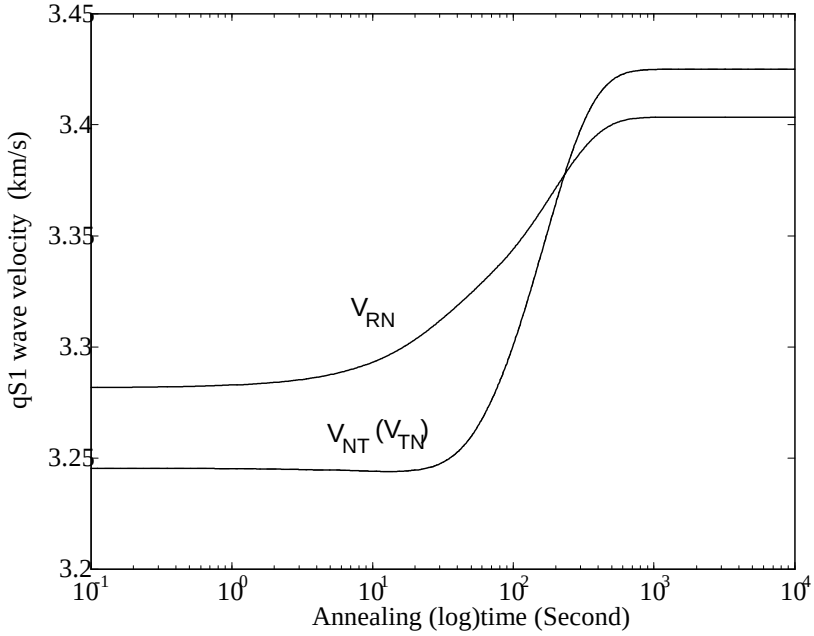

Figure 6.12: $qS1$ wave velocity versus annealing time when wave propagating in the ND, RD, TD, respectively.

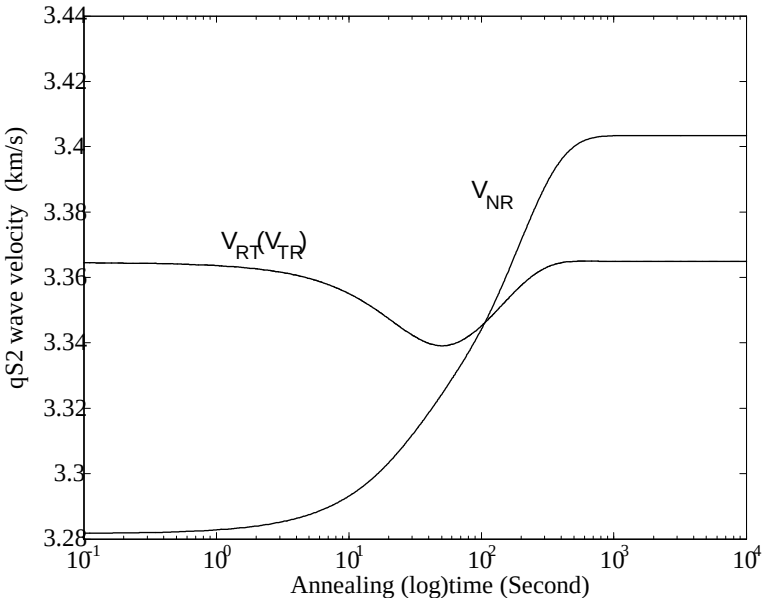

Figure 6.13: $qS2$ wave velocity versus annealing time when wave propagating in the ND, RD, TD, respectively.

orthorhombic media was presented. For the case of rolling texture of orthorhombic-cubic symmetry, the nine effective elastic constants were given in terms of the orientation distribution coefficients (ODCs). The coefficients are quantified by the orientation distribution function (ODF), the probability density function that is used to describe best the orientation of the grains or texture of a polycrystalline aggregate. The phase velocity V and the associated polarization vector $\mathbf{u}$ of plane waves are calculated by the Christoffel equation, which typically represents an eigenvalue and eigenvector problem. For the particular cases of wave propagation in the symmetry planes, analytic expressions of wave velocities for the quasilongitudinal and two quasishear waves were obtained. In general, the solutions are found using numerical methods. The angular deviations of the three waves, $qP, qS1$,and $qS2$, polarization vectors from the propagation direction were also examined. The example

results presented here show that the value of the angular deviations is not significant. The maximum deviation angle is about 3.5° for this particular texture. Finally, the wave velocities during the annealing process were discussed. The results analyzed show that the wave velocities and polarization vectors of the three wave modes can be considerably affected by texture. The results will be used to calculate the wave attenuations in the subsequent chapter. Those analyses will provide valuable information for modeling the microstructure during the recrystallization process, particularly for use with ultrasonic nondestructive techniques.

Chapter 7

Attenuations in Textured Media

7.1 Introduction

Metals and alloys are made of crystallite grains whose characteristics and arrangements can be changed by the application of heat processing, such as annealing. Microstructural parameters of metals that determine the macroscopic mechanical properties of a material include the grain size, grain shape, and the orientation of the grains or texture and their distribution in the microstructure. Ultrasonic waves propagating in such aggregates lose energy due to scattering from the granular microstructure of these materials. This scattering is generally characterized by the attenuation of the medium. In general, the attenuation and wave velocity are dependent on the grain size and shape, particularly on the orientation distribution of the grains. If the grains are randomly oriented such that the medium is statistically isotropic, these propagation properties are independent of direction. However, the scattering attenuation and wave velocity are a function of the propagation direction if the grains have a preferred orientation. The preferred orientation of grains,

or texture, is best quantitatively described by the orientation distribution function (ODF) defining as a probability density function, which is often expanded in a series generalized spherical harmonics [1],[2],[3]. The general description was given in Chapter 6. Often, most metallic materials with preferred orientation of grains display anisotropy of material properties. Therefore, knowledge of the anisotropic nature of the wave propagation and scattering in textured materials such as attenuation and velocity is critical for use with ultrasonic nondestructive techniques. Such information will then provide valuable insight for modeling the microstructure of such complex materials during processing.

The scattering of elastic waves by grains of polycrystals has received considerable attention. The most recent contributions for cubic symmetry with uniformly distributed orientations of grains were made by Hirsekorn [43],[44] and Weaver [50]. The problem of wave propagation and scattering in the case of polycrystalline grains with an aligned [001] axis have been examined by Ahmed and Thompson [56] and Turner [57]. In this particular case, the average medium is statistically transverse isotropy. Ahmed and Thompson also studied correlations defined by both equiaxed grains and grains with elongation. During the recrystallization process of metals such as annealing, the common microstructure may show the grains having the preferred crystallographic orientation. The material properties of this specific case are assumed to be orthorhombic due to the feature of the preferred orientation. For rolled texture, there are three orthogonal axes of symmetry which are defined as the rolling, transverse, and normal directions. Hirsekorn [45] also was one of the first to investigate the wave scattering in polycrystals of cubic symmetry with rolled texture as a function of frequency by using the perturbation approach. She then extended her theory to deter-

mine the directional dependence of the phase velocities and attenuations of the three wave types under the same assumption with fiber texture [46]. Her discussions were restricted to waves propagating in the direction of an axis of symmetry of the texture. The general formalism of the waves propagating in any direction through polycrystalline materials with rolled texture, however, has not yet been reported. In the previous chapter, the detailed wave velocities and polarizations of the three wave types, inclusive of the quasilongitudinal and two quasishear waves, have been discussed under the assumption of orthorhombic-cubic symmetry. A relationship between the phase velocity and the recrystallization characteristic variable (annealing time) was also studied for specific examples.

In this chapter, the more sensitive ultrasonic parameter, scattering attenuation, is studied for waves propagating in any direction through such textured media. The attenuations of the three wave types are calculated numerically as a function of dimensionless frequency and propagation direction, respectively, for given orientation distribution coefficients (ODCs). The resulting attenuations are shown to be directional dependent, frequency dependent, and dependent on the texture coefficients (ODCs) for the quasilongitudinal and two quasishear waves. The analysis of these expressions is restricted to frequencies below the high-frequency geometric optics limit. Those theoretical results may be used to improve the understanding of the microstructure during the recrystallization process. In addition, the present formulation may be used to study the backscattering problem in a straightforward manner. Although the present model is for the case of orthohombic-cubic symmetry, the formalism can be easily modified to apply to other given symmetry cases.

The preliminary elastodynamics of elastic wave propagation and scattering has

been introduced in terms of appropriate Green's dyadics in the previous chapters. Using the wave theory discussed, the formalism of the attenuations is developed for the anisotropic case of orthorhombic-cubic symmetry in the succeeding sections.

7.2 Covariance

To calculate the attenuations, the relevant inner products on the covariance of the effective moduli fluctuations are required. The covariance of the moduli fluctuations is represented by an eighth-rank tensor which is given explicitly by

$$\Xi\left(\mathbf{q}\right)_{\cdots\mathbf{\hat{u}\hat{p}\hat{s}\hat{v}}}^{\cdots\mathbf{\hat{u}\hat{p}\hat{s}\hat{v}}} = \Xi\left(\mathbf{q}\right)_{\alpha\beta\gamma\delta}^{ijkl}\,\hat{u}_\beta\hat{u}_k\hat{p}_\alpha\hat{p}_l\hat{s}_i\hat{s}_\delta\hat{v}_\gamma\hat{v}_j. \tag{7.1}$$

For polycrystals of cubic symmetry, the eighth-rank covariance, $\mathbf{\Xi}_{ijkl}^{\alpha\beta\gamma\delta}$, is written as

$$\begin{aligned}\mathbf{\Xi}_{ijkl}^{\alpha\beta\gamma\delta} &= \left\langle C_{ijkl}C_{\alpha\beta\gamma\delta}\right\rangle - \left\langle C_{ijkl}\right\rangle\left\langle C_{\alpha\beta\gamma\delta}\right\rangle \\ &= \kappa^2\left\langle\sum_{n=1}^{3}a_{in}a_{jn}a_{kn}a_{ln}\sum_{n=1}^{3}a_{\alpha n}a_{\beta n}a_{\gamma n}a_{\delta n}\right\rangle \\ &\quad -\kappa^2\left\langle\sum_{n=1}^{3}a_{in}a_{jn}a_{kn}a_{ln}\right\rangle\left\langle\sum_{n=1}^{3}a_{\alpha n}a_{\beta n}a_{\gamma n}a_{\delta n}\right\rangle,\end{aligned} \tag{7.2}$$

where the brackets, $< >$, denote an ensemble average over all orientations of grains, and $\kappa = C_{11}^0 - C_{12}^0 - 2C_{44}^0$ is the single crystal anisotropic factor. If the polycrystal considered here is of orthorhombic-cubic symmetry, the nonzero terms which are necessary for calculating the attenuations are determined in the following. For the second term in Eq. (7.2), the results have been given in the details of the previous chapter by Eq. (6.16). The first term

within the brackets in Eq. (7.2) is given as

$$
\begin{aligned}
&\left\langle \sum_{n=1}^{3} a_{in}a_{jn}a_{kn}a_{ln} \sum_{n=1}^{3} a_{\alpha n}a_{\beta n}a_{\gamma n}a_{\delta n} \right\rangle \\
= \;& \frac{1}{4\pi^2}\int_0^{2\pi}\int_0^{2\pi}\int_{-1}^{+1} \left(\sum_{n=1}^{3} a_{in}a_{jn}a_{kn}a_{ln}\right)\left(\sum_{n=1}^{3} a_{\alpha n}a_{\beta n}a_{\gamma n}a_{\delta n}\right) w(\xi,\psi,\varphi)d\xi d\psi d\varphi \\
= \;& 4\pi^2\Bigg\{ W_{000}T_{000} + W_{400}\left[T_{400} + \frac{5}{\sqrt{70}}\left(T_{404}+T_{40\bar{4}}\right)\right] \\
& + W_{420}\left[T_{420} + T_{42\bar{0}} + \frac{5}{\sqrt{70}}\left(T_{424}+T_{42\bar{4}}+T_{4\bar{2}4}+T_{4\bar{2}\bar{4}}\right)\right] \\
& + W_{440}\left[T_{440} + T_{44\bar{0}} + \frac{5}{\sqrt{70}}\left(T_{444}+T_{44\bar{4}}+T_{4\bar{4}4}+T_{4\bar{4}\bar{4}}\right)\right] \\
& + W_{600}\left[T_{600} - \frac{\sqrt{14}}{2}\left(T_{604}+T_{60\bar{4}}\right)\right] \\
& + W_{620}\left[T_{620} + T_{62\bar{0}} - \frac{\sqrt{14}}{2}\left(T_{624}+T_{62\bar{4}}+T_{6\bar{2}4}+T_{6\bar{2}\bar{4}}\right)\right] \\
& + W_{640}\left[T_{640} + T_{64\bar{0}} - \frac{\sqrt{14}}{2}\left(T_{644}+T_{64\bar{4}}+T_{6\bar{4}4}+T_{6\bar{4}\bar{4}}\right)\right] \\
& + W_{660}\left[T_{660} + T_{66\bar{0}} - \frac{\sqrt{14}}{2}\left(T_{664}+T_{66\bar{4}}+T_{6\bar{6}4}+T_{6\bar{6}\bar{4}}\right)\right] \\
& + W_{800}\left[T_{800} + \frac{\sqrt{154}}{33}\left(T_{804}+T_{80\bar{4}}\right) + \frac{\sqrt{1430}}{66}\left(T_{808}+T_{80\bar{8}}\right)\right] \\
& + W_{820}\Bigg[T_{820} + T_{82\bar{0}} + \frac{\sqrt{154}}{33}\left(T_{824}+T_{82\bar{4}}+T_{8\bar{2}4}+T_{8\bar{2}\bar{4}}\right) \\
& + \frac{\sqrt{1430}}{66}\left(T_{828}+T_{82\bar{8}}+T_{8\bar{2}8}+T_{8\bar{2}\bar{8}}\right)\Bigg] \\
& + W_{840}\Bigg[T_{840} + T_{84\bar{0}} + \frac{\sqrt{154}}{33}\left(T_{844}+T_{84\bar{4}}+T_{8\bar{4}4}+T_{8\bar{4}\bar{4}}\right) \\
& + \frac{\sqrt{1430}}{66}\left(T_{848}+T_{84\bar{8}}+T_{8\bar{4}8}+T_{8\bar{4}\bar{8}}\right)\Bigg] \\
& + W_{860}\Bigg[T_{860} + T_{86\bar{0}} + \frac{\sqrt{154}}{33}\left(T_{864}+T_{86\bar{4}}+T_{8\bar{6}4}+T_{8\bar{6}\bar{4}}\right) \\
& + \frac{\sqrt{1430}}{66}\left(T_{868}+T_{86\bar{8}}+T_{8\bar{6}8}+T_{8\bar{6}\bar{8}}\right)\Bigg]
\end{aligned}
\tag{7.3}
$$

$$+W_{880}\left[T_{880}+T_{8\bar{8}0}+\frac{\sqrt{154}}{33}\left(T_{884}+T_{8\bar{8}4}+T_{88\bar{4}}+T_{8\bar{8}\bar{4}}\right)\right.$$
$$\left.\left.+\frac{\sqrt{1430}}{66}\left(T_{888}+T_{8\bar{8}8}+T_{88\bar{8}}+T_{8\bar{8}\bar{8}}\right)\right]\right\},$$

where the w is orientation distribution function (ODF) as discussed in Chapter 6, which can be expanded in a series of generalized spherical harmonics. The W_{lmn} are the orientation distribution coefficients (ODCs). The terms T_{lmn} are defined as

$$\begin{aligned} T_{lmn} &= \frac{1}{4\pi^2}\int_0^{2\pi}\int_0^{2\pi}\int_{-1}^{+1}\left(\sum_{n=1}^{3}a_{in}a_{jn}a_{kn}a_{ln}\right)\left(\sum_{n=1}^{3}a_{\alpha n}a_{\beta n}a_{\gamma n}a_{\delta n}\right) \\ &\quad \times Z_{lmn}(\xi)e^{-im\psi}e^{-in\varphi}d\xi d\psi d\varphi. \end{aligned} \tag{7.4}$$

Within the assumption of orthorhombic-cubic symmetry, the nonzero terms which are required for calculating the attenuations, Eq. (7.3), are given as follows:

$$\begin{aligned} \left\langle\sum_{n=1}^{3}a_{n1}^4\sum_{m=1}^{3}a_{m1}^4\right\rangle &= \frac{41}{105}+\frac{2232\sqrt{2}\pi^2}{5005}W_{400}-\frac{2976\sqrt{5}\pi^2}{5005}W_{420}-\frac{1448\sqrt{35}\pi^2}{5005}W_{440} \\ &\quad -\frac{12\sqrt{26}\pi^2}{1001}W_{600}+\frac{64\sqrt{2730}\pi^2}{15015}W_{620}-\frac{128\sqrt{91}\pi^2}{5005}W_{640} \\ &\quad +\frac{64\sqrt{6006}\pi^2}{15015}W_{660}+\frac{56\sqrt{34}\pi^2}{7293}W_{800}-\frac{32\sqrt{1190}\pi^2}{12155}W_{820} \\ &\quad +\frac{32\sqrt{1309}\pi^2}{12155}W_{840}-\frac{32\sqrt{14586}\pi^2}{36465}W_{860}+\frac{16\sqrt{12155}\pi^2}{12155}W_{880}, \end{aligned}$$

$$\begin{aligned} \left\langle\sum_{n=1}^{3}a_{n2}^4\sum_{m=1}^{3}a_{m2}^4\right\rangle &= \frac{41}{105}+\frac{2232\sqrt{2}\pi^2}{5005}W_{400}+\frac{2976\sqrt{5}\pi^2}{5005}W_{420}+\frac{1448\sqrt{35}\pi^2}{5005}W_{440} \\ &\quad -\frac{12\sqrt{26}\pi^2}{1001}W_{600}-\frac{64\sqrt{2730}\pi^2}{15015}W_{620}-\frac{128\sqrt{91}\pi^2}{5005}W_{640} \\ &\quad +\frac{64\sqrt{6006}\pi^2}{15015}W_{660}+\frac{56\sqrt{34}\pi^2}{7293}W_{800}+\frac{32\sqrt{1190}\pi^2}{12155}W_{820} \\ &\quad +\frac{32\sqrt{1309}\pi^2}{12155}W_{840}+\frac{32\sqrt{14586}\pi^2}{36465}W_{860}+\frac{16\sqrt{12155}\pi^2}{12155}W_{880}, \end{aligned}$$

$$\left\langle\sum_{n=1}^{3}a_{n3}^4\sum_{m=1}^{3}a_{m3}^4\right\rangle = \frac{41}{105}+\frac{5952\sqrt{2}\pi^2}{5005}W_{400}+\frac{1024\sqrt{26}\pi^2}{15015}W_{600}+\frac{1024\sqrt{34}\pi^2}{36465}W_{800},$$

$$\left\langle \sum_{n=1}^{3} a_{n2}^4 \sum_{m=1}^{3} a_{m3}^4 \right\rangle = \frac{13}{35} + \frac{564\sqrt{2}\pi^2}{715} W_{400} + \frac{16\sqrt{5}\pi^2}{65} W_{420} + \frac{776\sqrt{35}\pi^2}{5005} W_{440} + \frac{128\sqrt{26}\pi^2}{5005} W_{600} - \frac{256\sqrt{91}\pi^2}{5005} W_{640} + \frac{128\sqrt{34}\pi^2}{12155} W_{800} + \frac{256\sqrt{1190}\pi^2}{85085} W_{820} + \frac{128\sqrt{1309}\pi^2}{85085} W_{840},$$

$$\left\langle \sum_{n=1}^{3} a_{n1}^4 \sum_{m=1}^{3} a_{m3}^4 \right\rangle = \frac{13}{35} + \frac{564\sqrt{2}\pi^2}{715} W_{400} - \frac{16\sqrt{5}\pi^2}{65} W_{420} + \frac{776\sqrt{35}\pi^2}{5005} W_{440} + \frac{128\sqrt{26}\pi^2}{5005} W_{600} - \frac{256\sqrt{91}\pi^2}{5005} W_{640} + \frac{128\sqrt{34}\pi^2}{12155} W_{800} - \frac{256\sqrt{1190}\pi^2}{85085} W_{820} + \frac{128\sqrt{1309}\pi^2}{85085} W_{840},$$

$$\left\langle \sum_{n=1}^{3} a_{n1}^4 \sum_{m=1}^{3} a_{m2}^4 \right\rangle = \frac{13}{35} + \frac{344\sqrt{2}\pi^2}{715} W_{400} + \frac{1392\sqrt{35}\pi^2}{5005} W_{440} + \frac{128\sqrt{26}\pi^2}{5005} W_{600} - \frac{256\sqrt{91}\pi^2}{5005} W_{640} + \frac{8\sqrt{34}\pi^2}{12155} W_{800} - \frac{32\sqrt{1309}\pi^2}{85085} W_{840} + \frac{16\sqrt{12155}\pi^2}{12155} W_{880},$$

$$\left\langle \sum_{n=1}^{3} a_{n1}^4 \sum_{m=1}^{3} a_{m1}^2 a_{m2}^2 \right\rangle = \frac{11}{105} + \frac{512\sqrt{2}\pi^2}{5005} W_{400} - \frac{272\sqrt{5}\pi^2}{5005} W_{420} - \frac{96\sqrt{35}\pi^2}{1001} W_{440} + \frac{32\sqrt{26}\pi^2}{3003} W_{600} - \frac{32\sqrt{2730}\pi^2}{15015} W_{620} + \frac{64\sqrt{91}\pi^2}{5005} W_{640} - \frac{32\sqrt{6006}\pi^2}{15015} W_{660} + \frac{8\sqrt{34}\pi^2}{7293} W_{800} - \frac{16\sqrt{1190}\pi^2}{85085} W_{820} - \frac{32\sqrt{1309}\pi^2}{85085} W_{840} - \frac{16\sqrt{14586}\pi^2}{36465} W_{860} - \frac{16\sqrt{12155}\pi^2}{12155} W_{880},$$

$$\left\langle \sum_{n=1}^{3} a_{n1}^4 \sum_{m=1}^{3} a_{m1}^2 a_{m3}^2 \right\rangle = \frac{11}{105} - \frac{1028\sqrt{2}\pi^2}{5005} W_{400} + \frac{192\sqrt{5}\pi^2}{1001} W_{420} + \frac{136\sqrt{35}\pi^2}{5005} W_{440} + \frac{32\sqrt{26}\pi^2}{3003} W_{600} - \frac{32\sqrt{2730}\pi^2}{15015} W_{620} + \frac{64\sqrt{91}\pi^2}{5005} W_{640} - \frac{32\sqrt{6006}\pi^2}{15015} W_{660} - \frac{64\sqrt{34}\pi^2}{7293} W_{800} + \frac{48\sqrt{1190}\pi^2}{17017} W_{820} - \frac{192\sqrt{1309}\pi^2}{85085} W_{840} + \frac{16\sqrt{14586}\pi^2}{36465} W_{860},$$

$$\left\langle \sum_{n=1}^{3} a_{n1}^4 \sum_{m=1}^{3} a_{m2}^2 a_{m3}^2 \right\rangle = \frac{13}{105} - \frac{172\sqrt{2}\pi^2}{715} W_{400} - \frac{288\sqrt{5}\pi^2}{715} W_{420} + \frac{232\sqrt{35}\pi^2}{5005} W_{440} - \frac{544\sqrt{26}\pi^2}{15015} W_{600} + \frac{32\sqrt{2730}\pi^2}{15015} W_{620} + \frac{192\sqrt{91}\pi^2}{5005} W_{640} + \frac{32\sqrt{6006}\pi^2}{15015} W_{660} - \frac{64\sqrt{34}\pi^2}{36465} W_{800} + \frac{16\sqrt{1190}\pi^2}{85085} W_{820} + \frac{64\sqrt{1309}\pi^2}{85085} W_{840} - \frac{16\sqrt{14586}\pi^2}{36465} W_{860},$$

$$\left\langle \sum_{n=1}^{3} a_{n2}^4 \sum_{m=1}^{3} a_{m1}^2 a_{m2}^2 \right\rangle = \frac{11}{105} + \frac{512\sqrt{2}\pi^2}{5005} W_{400} + \frac{272\sqrt{5}\pi^2}{5005} W_{420} - \frac{96\sqrt{35}\pi^2}{1001} W_{440} + \frac{32\sqrt{26}\pi^2}{3003} W_{600} + \frac{32\sqrt{2730}\pi^2}{15015} W_{620} + \frac{64\sqrt{91}\pi^2}{5005} W_{640} + \frac{32\sqrt{6006}\pi^2}{15015} W_{660} + \frac{8\sqrt{34}\pi^2}{7293} W_{800} + \frac{16\sqrt{1190}\pi^2}{85085} W_{820} - \frac{32\sqrt{1309}\pi^2}{85085} W_{840} - \frac{16\sqrt{14586}\pi^2}{36465} W_{860} - \frac{16\sqrt{12155}\pi^2}{12155} W_{880},$$

$$\left\langle \sum_{n=1}^{3} a_{n2}^4 \sum_{m=1}^{3} a_{m1}^2 a_{m3}^2 \right\rangle = \frac{13}{105} - \frac{172\sqrt{2}\pi^2}{715} W_{400} + \frac{288\sqrt{5}\pi^2}{715} W_{420} + \frac{232\sqrt{35}\pi^2}{5005} W_{440} - \frac{544\sqrt{26}\pi^2}{15015} W_{600} - \frac{32\sqrt{2730}\pi^2}{15015} W_{620} + \frac{192\sqrt{91}\pi^2}{5005} W_{640} - \frac{32\sqrt{6006}\pi^2}{15015} W_{660} - \frac{64\sqrt{34}\pi^2}{36465} W_{800} - \frac{16\sqrt{1190}\pi^2}{85085} W_{820} + \frac{64\sqrt{1309}\pi^2}{85085} W_{840} + \frac{16\sqrt{14586}\pi^2}{36465} W_{860},$$

$$\left\langle \sum_{n=1}^{3} a_{n2}^4 \sum_{m=1}^{3} a_{m2}^2 a_{m3}^2 \right\rangle = \frac{11}{105} - \frac{1028\sqrt{2}\pi^2}{5005} W_{400} - \frac{192\sqrt{5}\pi^2}{1001} W_{420} + \frac{136\sqrt{35}\pi^2}{5005} W_{440} + \frac{32\sqrt{26}\pi^2}{3003} W_{600} + \frac{32\sqrt{2730}\pi^2}{15015} W_{620} + \frac{64\sqrt{91}\pi^2}{5005} W_{640} + \frac{32\sqrt{6006}\pi^2}{15015} W_{660} - \frac{64\sqrt{34}\pi^2}{7293} W_{800} - \frac{48\sqrt{1190}\pi^2}{17017} W_{820} - \frac{192\sqrt{1309}\pi^2}{85085} W_{840} - \frac{16\sqrt{14586}\pi^2}{36465} W_{860},$$

$$\left\langle \sum_{n=1}^{3} a_{n3}^4 \sum_{m=1}^{3} a_{m1}^2 a_{m2}^2 \right\rangle = \frac{13}{105} + \frac{188\sqrt{2}\pi^2}{715} W_{400} - \frac{776\sqrt{35}\pi^2}{5005} W_{440} + \frac{128\sqrt{26}\pi^2}{15015} W_{600} + \frac{256\sqrt{91}\pi^2}{5005} W_{640} - \frac{128\sqrt{34}\pi^2}{36465} W_{800} - \frac{128\sqrt{1309}\pi^2}{85085} W_{840},$$

$$\left\langle \sum_{n=1}^{3} a_{n3}^4 \sum_{m=1}^{3} a_{m1}^2 a_{m3}^2 \right\rangle = \frac{11}{105} - \frac{688\sqrt{2}\pi^2}{5005} W_{400} + \frac{16\sqrt{5}\pi^2}{65} W_{420} - \frac{512\sqrt{26}\pi^2}{15015} W_{600} - \frac{512\sqrt{34}\pi^2}{36465} W_{800} + \frac{256\sqrt{1190}\pi^2}{85085} W_{820},$$

$$\left\langle \sum_{n=1}^{3} a_{n3}^4 \sum_{m=1}^{3} a_{m2}^2 a_{m3}^2 \right\rangle = \frac{11}{105} - \frac{688\sqrt{2}\pi^2}{5005} W_{400} - \frac{16\sqrt{5}\pi^2}{65} W_{420} - \frac{512\sqrt{26}\pi^2}{15015} W_{600} - \frac{512\sqrt{34}\pi^2}{36465} W_{800} - \frac{256\sqrt{1190}\pi^2}{85085} W_{820},$$

$$\left\langle \sum_{n=1}^{3} a_{n2}^2 a_{n3}^2 \sum_{m=1}^{3} a_{m2}^2 a_{m3}^2 \right\rangle = \frac{2}{35} - \frac{888\sqrt{2}\pi^2}{5005} W_{400} - \frac{96\sqrt{5}\pi^2}{455} W_{420} + \frac{48\sqrt{35}\pi^2}{5005} W_{440} - \frac{32\sqrt{26}\pi^2}{5005} W_{600} + \frac{64\sqrt{91}\pi^2}{5005} W_{640} + \frac{128\sqrt{34}\pi^2}{12155} W_{800} + \frac{256\sqrt{1190}\pi^2}{85085} W_{820} + \frac{128\sqrt{1309}\pi^2}{85085} W_{840},$$

$$\left\langle \sum_{n=1}^{3} a_{n2}^2 a_{n3}^2 \sum_{m=1}^{3} a_{m1}^2 a_{m3}^2 \right\rangle = \frac{4}{105} - \frac{712\sqrt{2}\pi^2}{5005} W_{400} - \frac{48\sqrt{35}\pi^2}{5005} W_{440} + \frac{608\sqrt{26}\pi^2}{15015} W_{600} - \frac{64\sqrt{91}\pi^2}{5005} W_{640} + \frac{128\sqrt{34}\pi^2}{36465} W_{800} - \frac{128\sqrt{1309}\pi^2}{85085} W_{840},$$

$$\left\langle \sum_{n=1}^{3} a_{n2}^2 a_{n3}^2 \sum_{m=1}^{3} a_{m1}^2 a_{m2}^2 \right\rangle = \frac{4}{105} - \frac{372\sqrt{2}\pi^2}{5005} W_{400} - \frac{272\sqrt{5}\pi^2}{5005} W_{420} - \frac{184\sqrt{35}\pi^2}{5005} W_{440} - \frac{64\sqrt{26}\pi^2}{15015} W_{600} - \frac{32\sqrt{2730}\pi^2}{15015} W_{620} - \frac{128\sqrt{91}\pi^2}{5005} W_{640} - \frac{32\sqrt{6006}\pi^2}{15015} W_{660} - \frac{64\sqrt{34}\pi^2}{36465} W_{800} - \frac{16\sqrt{1190}\pi^2}{85085} W_{820} + \frac{64\sqrt{1309}\pi^2}{85085} W_{840} + \frac{16\sqrt{14586}\pi^2}{36465} W_{860},$$

$$\left\langle \sum_{n=1}^{3} a_{n1}^2 a_{n2}^2 \sum_{m=1}^{3} a_{m1}^2 a_{m2}^2 \right\rangle = \frac{2}{35} - \frac{432\sqrt{2}\pi^2}{5005} W_{400} - \frac{96\sqrt{35}\pi^2}{1001} W_{440} - \frac{32\sqrt{26}\pi^2}{5005} W_{600} + \frac{64\sqrt{91}\pi^2}{5005} W_{640} + \frac{8\sqrt{34}\pi^2}{12155} W_{800} - \frac{32\sqrt{1309}\pi^2}{85085} W_{840} \frac{16\sqrt{12155}\pi^2}{12155} W_{880},$$

$$\left\langle \sum_{n=1}^{3} a_{n1}^2 a_{n2}^2 \sum_{m=1}^{3} a_{m1}^2 a_{m3}^2 \right\rangle = \frac{4}{105} - \frac{372\sqrt{2}\pi^2}{5005} W_{400} + \frac{272\sqrt{5}\pi^2}{5005} W_{420} - \frac{184\sqrt{35}\pi^2}{5005} W_{440} - \frac{64\sqrt{26}\pi^2}{15015} W_{600} + \frac{32\sqrt{2730}\pi^2}{15015} W_{620} - \frac{128\sqrt{91}\pi^2}{5005} W_{640} + \frac{32\sqrt{6006}\pi^2}{15015} W_{660} - \frac{64\sqrt{34}\pi^2}{36465} W_{800} + \frac{16\sqrt{1190}\pi^2}{85085} W_{820} + \frac{64\sqrt{1309}\pi^2}{85085} W_{840} - \frac{16\sqrt{14586}\pi^2}{36465} W_{860},$$

$$\left\langle \sum_{n=1}^{3} a_{n1}^2 a_{n3}^2 \sum_{m=1}^{3} a_{m1}^2 a_{m3}^2 \right\rangle = \frac{2}{35} - \frac{888\sqrt{2}\pi^2}{5005} W_{400} + \frac{96\sqrt{5}\pi^2}{455} W_{420} + \frac{48\sqrt{35}\pi^2}{5005} W_{440} - \frac{32\sqrt{26}\pi^2}{5005} W_{600} + \frac{64\sqrt{91}\pi^2}{5005} W_{640} + \frac{128\sqrt{34}\pi^2}{12155} W_{800} - \frac{256\sqrt{1190}\pi^2}{85085} W_{820} + \frac{128\sqrt{1309}\pi^2}{85085} W_{840},$$

$$\left\langle \sum_{n=1}^{3} a_{n1}^3 a_{n2} \sum_{m=1}^{3} a_{m1}^3 a_{m2} \right\rangle = \frac{2}{105} + \frac{174\sqrt{2}\pi^2}{5005} W_{400} - \frac{24\sqrt{5}\pi^2}{715} W_{420} - \frac{12\sqrt{35}\pi^2}{5005} W_{440} - \frac{40\sqrt{26}\pi^2}{3003} W_{600} + \frac{32\sqrt{2730}\pi^2}{15015} W_{620} - \frac{16\sqrt{91}\pi^2}{5005} W_{640} - \frac{32\sqrt{6006}\pi^2}{15015} W_{660} + \frac{8\sqrt{34}\pi^2}{7293} W_{800} - \frac{16\sqrt{1190}\pi^2}{85085} W_{820} - \frac{32\sqrt{1309}\pi^2}{85085} W_{840} + \frac{16\sqrt{14586}\pi^2}{36465} W_{860} - \frac{16\sqrt{12155}\pi^2}{12155} W_{880},$$

$$\left\langle \sum_{n=1}^{3} a_{n1} a_{n2}^3 \sum_{m=1}^{3} a_{m1} a_{m2}^3 \right\rangle = \frac{2}{105} + \frac{174\sqrt{2}\pi^2}{5005} W_{400} + \frac{24\sqrt{5}\pi^2}{715} W_{420} - \frac{12\sqrt{35}\pi^2}{5005} W_{440} - \frac{40\sqrt{26}\pi^2}{3003} W_{600} - \frac{32\sqrt{2730}\pi^2}{15015} W_{620} - \frac{16\sqrt{91}\pi^2}{5005} W_{640} + \frac{32\sqrt{6006}\pi^2}{15015} W_{660} + \frac{8\sqrt{34}\pi^2}{7293} W_{800} + \frac{16\sqrt{1190}\pi^2}{85085} W_{820} - \frac{32\sqrt{1309}\pi^2}{85085} W_{840} - \frac{16\sqrt{14586}\pi^2}{36465} W_{860} - \frac{16\sqrt{12155}\pi^2}{12155} W_{880},$$

$$\left\langle \sum_{n=1}^{3} a_{n1}^3 a_{n3} \sum_{m=1}^{3} a_{m1}^3 a_{m3} \right\rangle = \frac{2}{105} - \frac{6\sqrt{2}\pi^2}{455} W_{400} + \frac{24\sqrt{5}\pi^2}{5005} W_{420} + \frac{12\sqrt{35}\pi^2}{715} W_{440} + \frac{4\sqrt{26}\pi^2}{273} W_{600} - \frac{12\sqrt{2730}\pi^2}{5005} W_{620} + \frac{24\sqrt{91}\pi^2}{5005} W_{640} + \frac{4\sqrt{6006}\pi^2}{2145} W_{660} - \frac{64\sqrt{34}\pi^2}{7293} W_{800} + \frac{48\sqrt{1190}\pi^2}{17017} W_{820} - \frac{192\sqrt{1309}\pi^2}{85085} W_{840} + \frac{16\sqrt{14586}\pi^2}{36465} W_{860},$$

$$\left\langle \sum_{n=1}^{3} a_{n1} a_{n3}^3 \sum_{m=1}^{3} a_{m1} a_{m3}^3 \right\rangle = \frac{2}{105} + \frac{144\sqrt{2}\pi^2}{5005} W_{400} + \frac{192\sqrt{5}\pi^2}{5005} W_{420} - \frac{32\sqrt{26}\pi^2}{15015} W_{600} + \frac{64\sqrt{2730}\pi^2}{15015} W_{620} - \frac{512\sqrt{34}\pi^2}{36465} W_{800} + \frac{256\sqrt{1190}\pi^2}{85085} W_{820},$$

$$\left\langle \sum_{n=1}^{3} a_{n2}^3 a_{n3} \sum_{m=1}^{3} a_{m2}^3 a_{m3} \right\rangle = \frac{2}{105} - \frac{6\sqrt{2}\pi^2}{455} W_{400} - \frac{24\sqrt{5}\pi^2}{5005} W_{420} + \frac{12\sqrt{35}\pi^2}{715} W_{440} + \frac{4\sqrt{26}\pi^2}{273} W_{600} + \frac{12\sqrt{2730}\pi^2}{5005} W_{620} + \frac{24\sqrt{91}\pi^2}{5005} W_{640} - \frac{4\sqrt{6006}\pi^2}{2145} W_{660} - \frac{64\sqrt{34}\pi^2}{7293} W_{800} - \frac{48\sqrt{1190}\pi^2}{17017} W_{820} - \frac{192\sqrt{1309}\pi^2}{85085} W_{840} - \frac{16\sqrt{14586}\pi^2}{36465} W_{860},$$

$$\left\langle \sum_{n=1}^{3} a_{n2} a_{n3}^3 \sum_{m=1}^{3} a_{m2} a_{m3}^3 \right\rangle = \frac{2}{105} + \frac{144\sqrt{2}\pi^2}{5005} W_{400} - \frac{192\sqrt{5}\pi^2}{5005} W_{420} - \frac{32\sqrt{26}\pi^2}{15015} W_{600} - \frac{64\sqrt{2730}\pi^2}{15015} W_{620} - \frac{512\sqrt{34}\pi^2}{36465} W_{800} - \frac{256\sqrt{1190}\pi^2}{85085} W_{820},$$

$$\left\langle \sum_{n=1}^{3} a_{n1}^3 a_{n2} \sum_{m=1}^{3} a_{m1} a_{m2}^3 \right\rangle = -\frac{1}{70} - \frac{218\sqrt{2}\pi^2}{5005} W_{400} - \frac{12\sqrt{35}\pi^2}{5005} W_{440} + \frac{8\sqrt{26}\pi^2}{5005} W_{600} - \frac{16\sqrt{91}\pi^2}{5005} W_{640} + \frac{8\sqrt{34}\pi^2}{12155} W_{800} - \frac{32\sqrt{1309}\pi^2}{85085} W_{840} + \frac{16\sqrt{12155}\pi^2}{12155} W_{880},$$

$$\left\langle \sum_{n=1}^{3} a_{n1}^{3} a_{n3} \sum_{m=1}^{3} a_{m1} a_{m3}^{3} \right\rangle = -\frac{1}{70} - \frac{108\sqrt{2}\pi^2}{5005} W_{400} - \frac{8\sqrt{5}\pi^2}{455} W_{420} - \frac{8\sqrt{35}\pi^2}{715} W_{440} + \frac{8\sqrt{26}\pi^2}{5005} W_{600} - \frac{16\sqrt{91}\pi^2}{5005} W_{640} + \frac{128\sqrt{34}\pi^2}{12155} W_{800} - \frac{256\sqrt{1190}\pi^2}{85085} W_{820} + \frac{128\sqrt{1309}\pi^2}{85085} W_{840},$$

$$\left\langle \sum_{n=1}^{3} a_{n2}^{3} a_{n3} \sum_{m=1}^{3} a_{m2} a_{m3}^{3} \right\rangle = -\frac{1}{70} - \frac{108\sqrt{2}\pi^2}{5005} W_{400} + \frac{8\sqrt{5}\pi^2}{455} W_{420} - \frac{8\sqrt{35}\pi^2}{715} W_{440} + \frac{8\sqrt{26}\pi^2}{5005} W_{600} - \frac{16\sqrt{91}\pi^2}{5005} W_{640} + \frac{128\sqrt{34}\pi^2}{12155} W_{800} + \frac{256\sqrt{1190}\pi^2}{85085} W_{820} + \frac{128\sqrt{1309}\pi^2}{85085} W_{840}.$$

The W_{lmn} are the expansion coefficients of the orientation distribution function with respect to the generalized spherical functions.

7.3 Attenuations

As discussed previously, the tensorial and spatial components of the covariance are assumed independent. The correlation function η is assumed to have an exponential form given by Eq. (2.14). If three nondimensional frequencies are defined as $x_\beta = \omega L/c_\beta$, performing the spatial Fourier transform of the correlation function of the difference between two wave vectors, the functions $\tilde{\eta}(\hat{\mathbf{p}}, \hat{\mathbf{s}})$ are specified in terms of the above dimensionless frequencies in Eq. (2.16). The inner product $(\hat{\mathbf{p}} \cdot \hat{\mathbf{s}})$ is expressed as $\hat{\mathbf{p}} \cdot \hat{\mathbf{s}} = \sin\Theta \sin\Theta' \sin\phi \sin\phi' + \cos\Theta \cos\Theta' \sin\phi \sin\phi' + \cos\phi \cos\phi'$.

The forms of the attenuations presented in Eq. (2.13) require various inner products on the covariance tensor. These inner products have the general form of $\Xi^{\cdots\hat{\mathbf{u}}\hat{\mathbf{p}}\hat{\mathbf{s}}\hat{\mathbf{v}}}_{\cdots\hat{\mathbf{u}}\hat{\mathbf{p}}\hat{\mathbf{s}}\hat{\mathbf{v}}}$, where the vectors $\hat{\mathbf{p}}$ and $\hat{\mathbf{s}}$, respectively, represent the incoming and outgoing propagation direc-

tions. The vectors $\hat{\mathbf{u}}$ and $\hat{\mathbf{v}}$ are vectors defining the polarization directions of the particular waves. While waves propagate in arbitrary directions, the polarization vectors are generally solved by the Christoffel equation, Eq. (6.19). Substituting the correlation function, Eq. (2.16), and the inner products into Eq. (2.13), the resulting dimensionless attenuations are given in the form

$$\begin{aligned}
\alpha_\beta\left(\hat{\mathbf{p}}\right) L &= \frac{x_\beta^4 c_\beta(\hat{\mathbf{p}})}{2\rho^2} \times \\
&\left\{ \int_{4\pi} \frac{\Xi_{\cdots\hat{\mathbf{u}}_K\hat{\mathbf{p}}\hat{\mathbf{s}}\hat{\mathbf{v}}_1}^{\cdots\hat{\mathbf{u}}_K\hat{\mathbf{p}}\hat{\mathbf{s}}\hat{\mathbf{v}}_1}}{\left(1+x_\beta^2\left(\hat{\mathbf{p}}\right)+x_{qS1}^2\left(\hat{\mathbf{s}}\right)-2x_\beta\left(\hat{\mathbf{p}}\right)x_{qS1}\left(\hat{\mathbf{s}}\right)\hat{\mathbf{p}}\cdot\hat{\mathbf{s}}\right)^2 c_{qS1}^5\left(\hat{\mathbf{s}}\right)} d^2\hat{s} \right. \\
&+ \int_{4\pi} \frac{\Xi_{\cdots\hat{\mathbf{u}}_K\hat{\mathbf{p}}\hat{\mathbf{s}}\hat{\mathbf{v}}_2}^{\cdots\hat{\mathbf{u}}_K\hat{\mathbf{p}}\hat{\mathbf{s}}\hat{\mathbf{v}}_2}}{\left(1+x_\beta^2\left(\hat{\mathbf{p}}\right)+x_{qP}^2\left(\hat{\mathbf{s}}\right)-2x_\beta\left(\hat{\mathbf{p}}\right)x_{qP}\left(\hat{\mathbf{s}}\right)\hat{\mathbf{p}}\cdot\hat{\mathbf{s}}\right)^2 c_{qP}^5\left(\hat{\mathbf{s}}\right)} d^2\hat{s} \\
&\left. + \int_{4\pi} \frac{\Xi_{\cdots\hat{\mathbf{u}}_K\hat{\mathbf{p}}\hat{\mathbf{s}}\hat{\mathbf{v}}_3}^{\cdots\hat{\mathbf{u}}_K\hat{\mathbf{p}}\hat{\mathbf{s}}\hat{\mathbf{v}}_3}}{\left(1+x_\beta^2\left(\hat{\mathbf{p}}\right)+x_{qS2}^2\left(\hat{\mathbf{s}}\right)-2x_\beta\left(\hat{\mathbf{p}}\right)x_{qS2}\left(\hat{\mathbf{s}}\right)\hat{\mathbf{p}}\cdot\hat{\mathbf{s}}\right)^2 c_{qS2}^5\left(\hat{\mathbf{s}}\right)} d^2\hat{s} \right\},
\end{aligned} \tag{7.5}$$

where K is defined as the polarization for the wave type β (1, 2,or 3 for wave types $qS1, qP$ and $qS2$, respectively). It should be noted that these inner products have the units of κ^2. In the long wavelength Rayleigh limit, $x_\beta \ll 1$, Eq. (7.5) can be simplified as

$$\begin{aligned}
\alpha_\beta\left(\hat{\mathbf{p}}\right) L/x_\beta^4 &= \frac{c_\beta(\hat{\mathbf{p}})}{2\rho^2} \times \left\{ \int_{4\pi} \frac{\Xi_{\cdots\hat{\mathbf{u}}_K\hat{\mathbf{p}}\hat{\mathbf{s}}\hat{\mathbf{v}}_1}^{\cdots\hat{\mathbf{u}}_K\hat{\mathbf{p}}\hat{\mathbf{s}}\hat{\mathbf{v}}_1}}{c_{qS1}^5\left(\hat{\mathbf{s}}\right)} d^2\hat{s} \right. \\
&\left. + \int_{4\pi} \frac{\Xi_{\cdots\hat{\mathbf{u}}_K\hat{\mathbf{p}}\hat{\mathbf{s}}\hat{\mathbf{v}}_2}^{\cdots\hat{\mathbf{u}}_K\hat{\mathbf{p}}\hat{\mathbf{s}}\hat{\mathbf{v}}_2}}{c_{qP}^5\left(\hat{\mathbf{s}}\right)} d^2\hat{s} + \int_{4\pi} \frac{\Xi_{\cdots\hat{\mathbf{u}}_K\hat{\mathbf{p}}\hat{\mathbf{s}}\hat{\mathbf{v}}_3}^{\cdots\hat{\mathbf{u}}_K\hat{\mathbf{p}}\hat{\mathbf{s}}\hat{\mathbf{v}}_3}}{c_{qS2}^5\left(\hat{\mathbf{s}}\right)} d^2\hat{s} \right\}.
\end{aligned} \tag{7.6}$$

In Eq. (7.6), the dimensionless attenuation has been normalized by the fourth power of the dimensionless frequency for the respective wave type. It is known that in Eqs. (7.5) and (7.6) the inner products, $\Xi_{\cdots\hat{\mathbf{u}}\hat{\mathbf{p}}\hat{\mathbf{s}}\hat{\mathbf{v}}}^{\cdots\hat{\mathbf{u}}\hat{\mathbf{p}}\hat{\mathbf{s}}\hat{\mathbf{v}}}$, do not have general analytic expressions for arbitrary propagation directions in this orthorhombic-cubic case. Thus, these results must be calculated numerically. In the next section, example numerical results and discussions are

presented.

7.4 Numerical Results and Discussions

Numerical results are now presented for a 70% rolled steel plate. The material constants of a single crystal and the texture coefficients of the orientation distribution function with respect to the generalized spherical functions are given in the following [3]

$$\begin{aligned} C_{11}^0 &= 2.37 \times 10^{11}\text{Pa}, \quad C_{12}^0 = 1.41 \times 10^{11}\text{Pa}, \\ C_{44}^0 &= 1.16 \times 10^{11}\text{Pa}, \quad \rho = 7850\ \text{kg/m}^3, \end{aligned} \tag{7.7}$$

and

$$\begin{aligned} c_4^{00} &= -1.47, \quad c_4^{20} = -0.46, \\ c_4^{40} &= 0.50, \quad c_6^{00} = 2.69, \\ c_6^{20} &= -1.20, \quad c_6^{40} = 0.46, \\ c_6^{60} &= -0.14, \quad c_8^{00} = -0.07, \\ c_8^{20} &= 0.29, \quad c_8^{40} = -0.45, \\ c_8^{60} &= -0.47, \quad c_8^{80} = -0.22. \end{aligned} \tag{7.8}$$

Here, using Eq. (6.33), the orientation distribution coefficients (ODCs) in Bunge's notation c_l^{mn} must be converted into those in Roe's notation W_{lmn}, which are used in this discussion throughout. In order to carry out the expressions, Eq. (7.5), numerical methods have to be employed. The procedure of numerical methods for calculating the wave attenuations is described in details below. First, using the Christoffel equation, Eq.

(6.19), the eigenvalue-eigenvector problem is solved when the wave propagation direction and scattering direction are specified. Second, the covariance of the moduli fluctuations is calculated by Eq. (7.2). Next, using the known covariance and eigenvectors, the inner products of each wave type are calculated numerically. Finally, the double integration is implemented numerically by the extended trapezoidal method. In this presentation, a large number of examples are presented to describe important features of the wave attenuations. The examples are generated using the methods discussed above. Since the orthorhombic symmetry has three mutually orthogonal planes of symmetry, all calculations are made for $0° \leq \Theta \leq 90°$, and $0° \leq \phi \leq 90°$.

Before carrying out the attenuations, the convergence of the numerical integration is discussed. Without lose of generality, wave attenuations of each wave type are examined for waves propagating in the rolling direction, that is $\Theta = 0°$ and $\phi = 90°$, and at dimensionless frequency $x_{qS1} = 1.0$. The comparison of the different step sizes used to calculate the qP attenuation is shown in Table 7.1. Tables 7.2 and 7.3 show a comparison of the calculated attenuations for two quasishear waves, respectively. Here, N is the number of intervals used in the trapezoidal rule, and h is the uniform step size. The results given in Tables 7.1, 7.2, and 7.3 show fast convergence for each wave mode in numerical integrations using trapezoidal method. In order to make numerical programs efficient and less error, the number of intervals $N = 20$ is chosen for calculating the attenuations for each wave mode in the following results.

First, the attenuations within the Rayleigh limit are calculated using Eq. (7.6).

Table 7.1: Comparison of qP attenuations calculated in the rolling direction for different step sizes

N	h	qP attenuation	% difference from $N = 100$
6	$\pi/6$	0.004478642	0.20949
7	$\pi/7$	0.004476699	0.16602
10	$\pi/10$	0.004471528	0.050321
20	$\pi/20$	0.004469460	0.0040498
30	$\pi/30$	0.004469381	0.0022822
100	$\pi/100$	0.004469279	0

Table 7.2: Comparison of qS1 attenuations calculated in the rolling direction for different step sizes

N	h	$qS1$ attenuation	% difference from $N = 100$
6	$\pi/6$	0.01328883	0.049238
7	$\pi/7$	0.01328696	0.035159
10	$\pi/10$	0.01328393	0.012347
20	$\pi/20$	0.01328263	0.0025597
30	$\pi/30$	0.01328230	7.5288e-5
100	$\pi/100$	0.01328229	0

Table 7.3: Comparison of qS2 attenuations calculated in the rolling direction for different step sizes

N	h	$qS2$ attenuation	% difference from $N = 100$
6	$\pi/6$	0.01487709	0.50173
7	$\pi/7$	0.01481018	0.049720
10	$\pi/10$	0.01480339	0.0038506
20	$\pi/20$	0.01480312	0.0020266
30	$\pi/30$	0.01480284	1.3510e-4
100	$\pi/100$	0.01480282	0

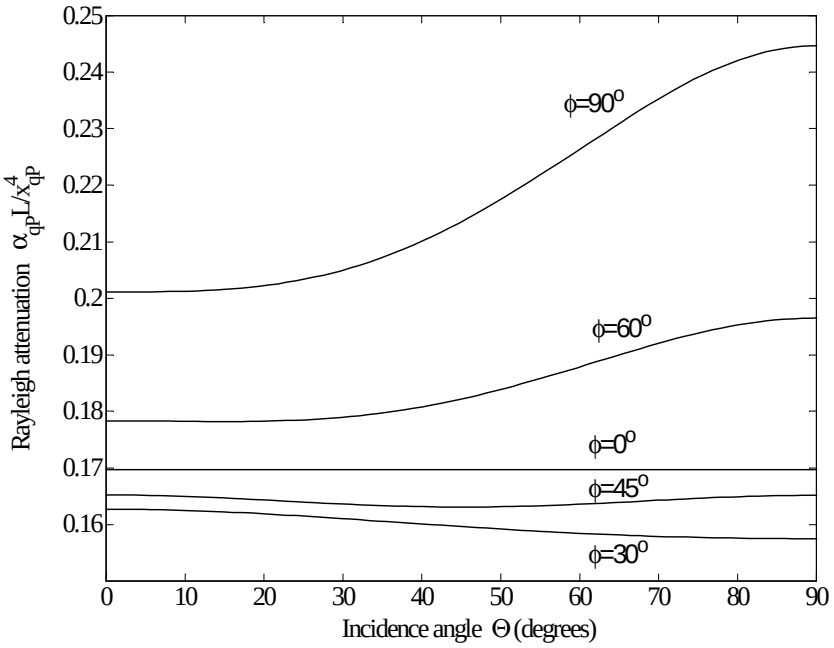

Figure 7.1: Rayleigh attenuation, $\alpha_{qP}L/x_{qP}^4$, as a function of propagation direction.

It is seen that the attenuations depend on the fourth power of frequency in the Rayleigh regime. Thus, the normalized Rayleigh attenuation $\alpha_\beta L/x_\beta^4$ of each wave mode is shown with the angular dependence in Figs. 7.1, 7.2, and 7.3 for various propagation directions, respectively. It is observed that in this specific case the attenuations of each wave mode is considerably dependent on the wave propagation direction. For waves propagating in different directions, the curves of the attenuations have smoothly changing shapes. In particular, at polar angle $\phi = 0$, as expected, the attenuations of the three wave modes are independent of azimuthal angle Θ.

Outside the Rayleigh regime, the attenuation results are calculated using the complete integrals, Eq. (7.5). The directional dependence of the attenuation is presented first for given dimensionless frequency, $x_{qS1} = 1.0$. Figure 7.4 shows the normalized quasilon-

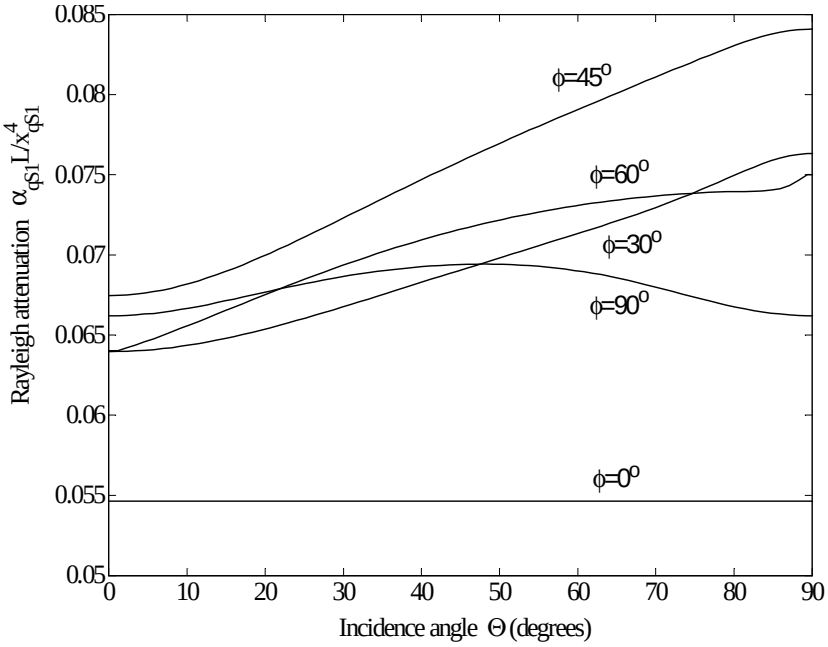

Figure 7.2: Rayleigh attenuation, $\alpha_{qS1}L/x_{qS1}^4$, as a function of propagation direction.

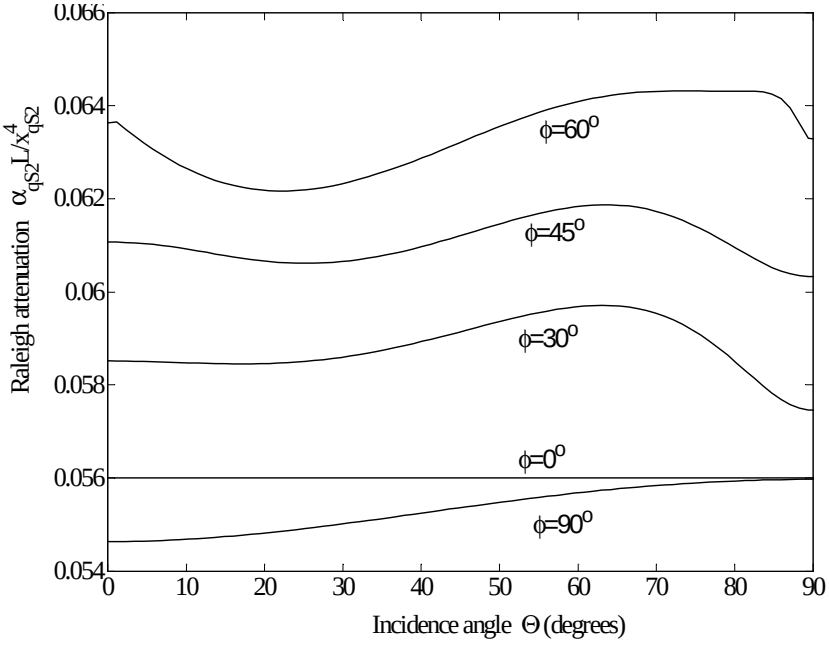

Figure 7.3: Rayleigh attenuation, $\alpha_{qS2}L/x_{qS2}^4$, as a function of propagation direction.

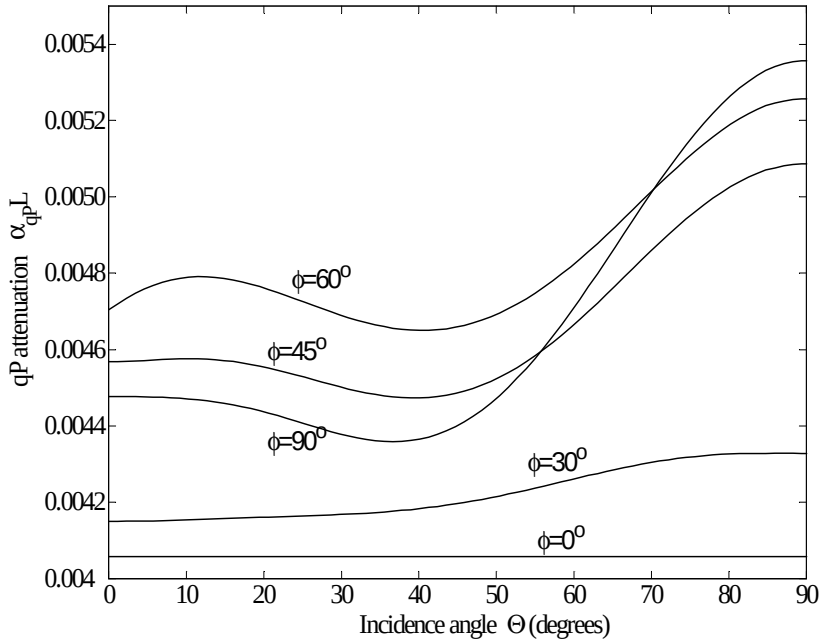

Figure 7.4: Directional dependence of the normalized qP attenuation, $\alpha_{qP}L$, for frequency $x_{qS1} = 1.0$.

gitudinal wave (qP) attenuation, $\alpha_{qP}L$, as a function of azimuthal direction Θ for various polar angles ϕ. It is seen that the attenuation is dramatically dependent on the propagation direction. The attenuation varies in different directions. The results for the normalized shear waves ($qS1$ and $qS2$) attenuations are presented in Figs. 7.5 and 7.6, respectively. The directional dependence on the propagation direction for the attenuations is also noticeable. These results may be contrasted with the results in the Rayleigh limit. Comparisons of the Rayleigh attenuations with attenuations outside the Rayleigh regime show that the tendency of variation is quite different with each other due to the effect of frequency. In Fig. 7.4, the qP wave attenuation is observed to have the maximum at $\Theta = 90°$ for given angles ϕ. In Fig. 7.5, the curves of the $qS1$ wave attenuation have smoothly changing shapes. Figure 7.6 shows that for propagation at polar angle $\phi = 30°$, $45°$ and $60°$, respectively, the

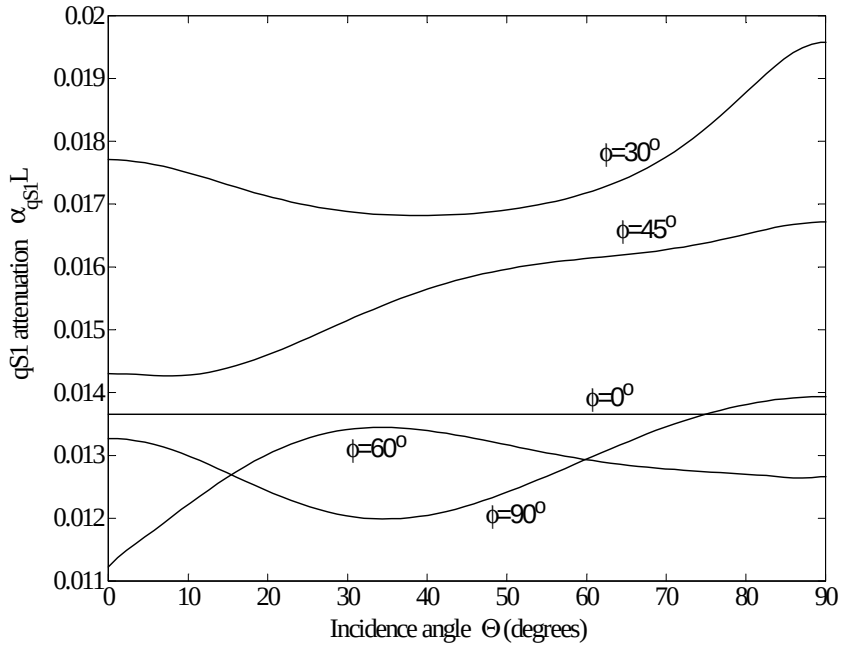

Figure 7.5: Directional dependence of the normalized $qS1$ attenuation, $\alpha_{qS1}L$, for frequency $x_{qS1} = 1.0$.

maximum attenuation is about $\Theta = 45°$, and at polar angle $\phi = 90°$, there is a minimum attenuation at $\Theta = 45°$. Furthermore, the asymmetry is observed in Fig. 7.6 for various polar angles.

Next, results are presented for the normalized attenuation as a function of azimuthal direction Θ for four different frequencies at given polar angle $\phi = 45°$ and $90°$, respectively. The normalized shear wave ($qS1$) attenuations, $\alpha_{qS1}L$, are shown in Figs. 7.7 and 7.8, respectively at $\phi = 45°$ and $90°$ for normalized frequency $x_{qS1} = 1.0, 1.5, 2.0$ and 2.5. It is seen that the attenuation curves show the similar shape as increasing the frequency for respective polar angle. The results for the normalized qP attenuations, $\alpha_{qP}L$, are shown in Figs. 7.9 and 7.10 at the same frequencies as above. Figures 7.11 and 7.12 show the normalized $qS2$ attenuations, $\alpha_{qS2}L$, as a function of propagation direction for the same

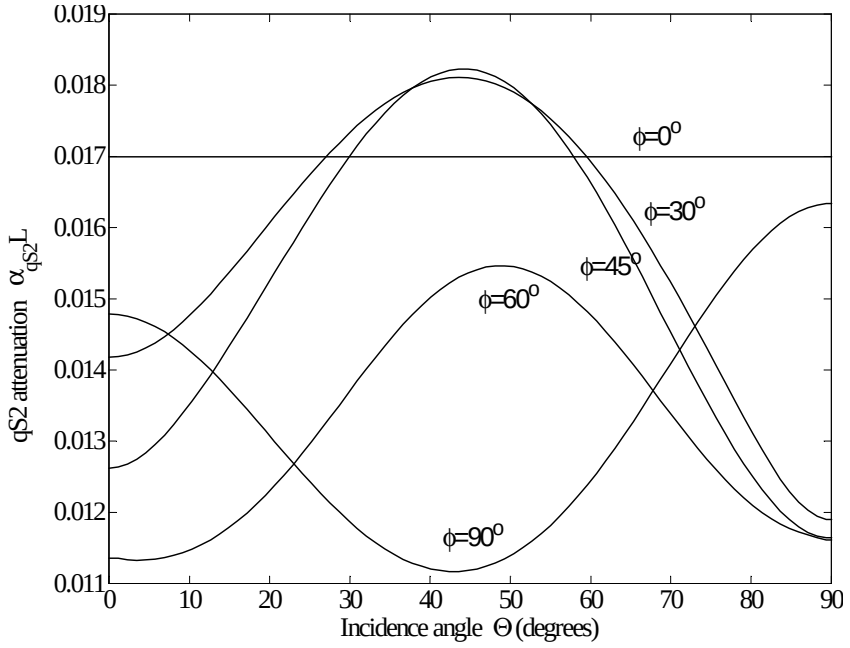

Figure 7.6: Directional dependence of the normalized $qS2$ attenuation, $\alpha_{qS2}L$, for frequency $x_{qS1} = 1.0$.

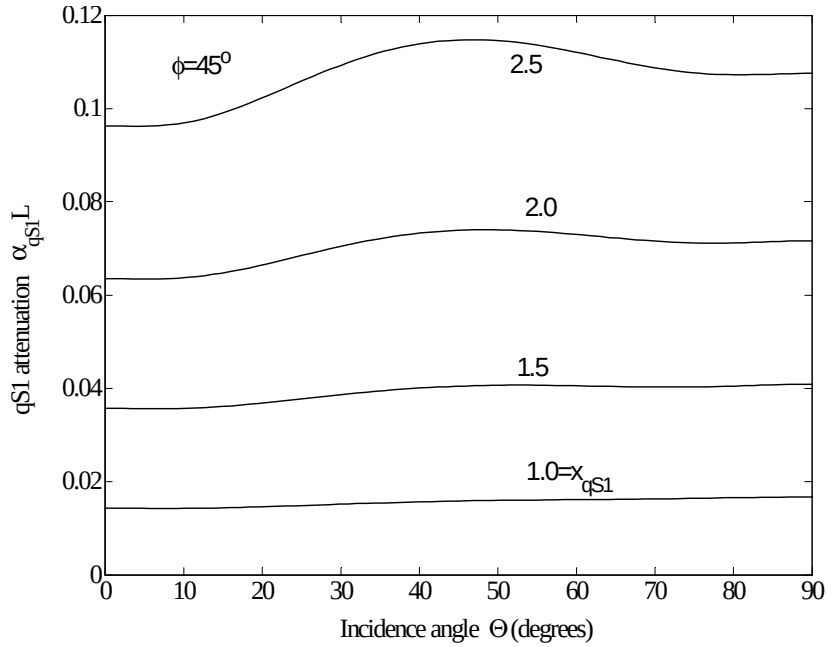

Figure 7.7: Angular dependence of the normalized $qS1$ attenuation, $\alpha_{qS1}L$, for various frequencies, x_{qS1}, at polar angle $\phi = 45°$.

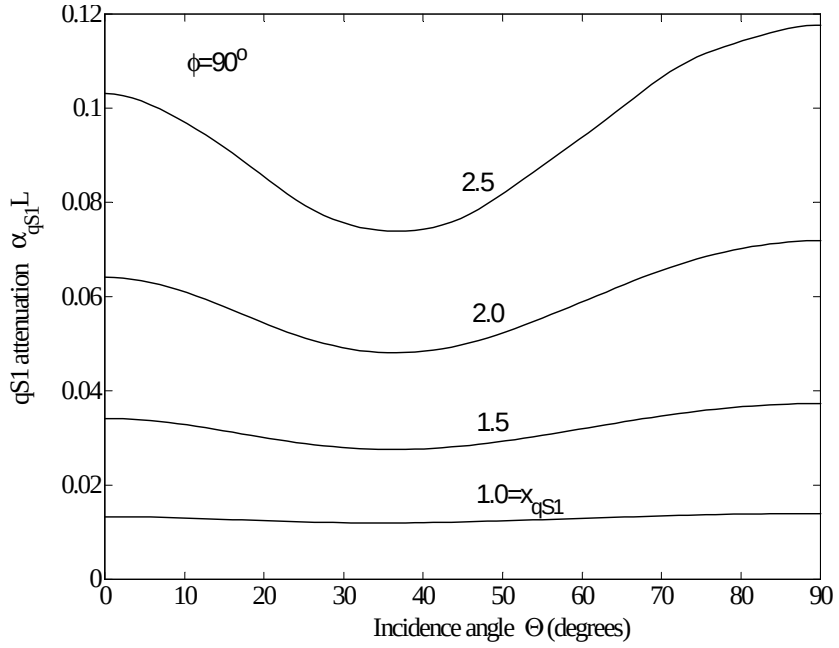

Figure 7.8: Angular dependence of the normalized $qS1$ attenuation, $\alpha_{qS1}L$, for various frequencies, x_{qS1}, at polar angle $\phi = 90°$.

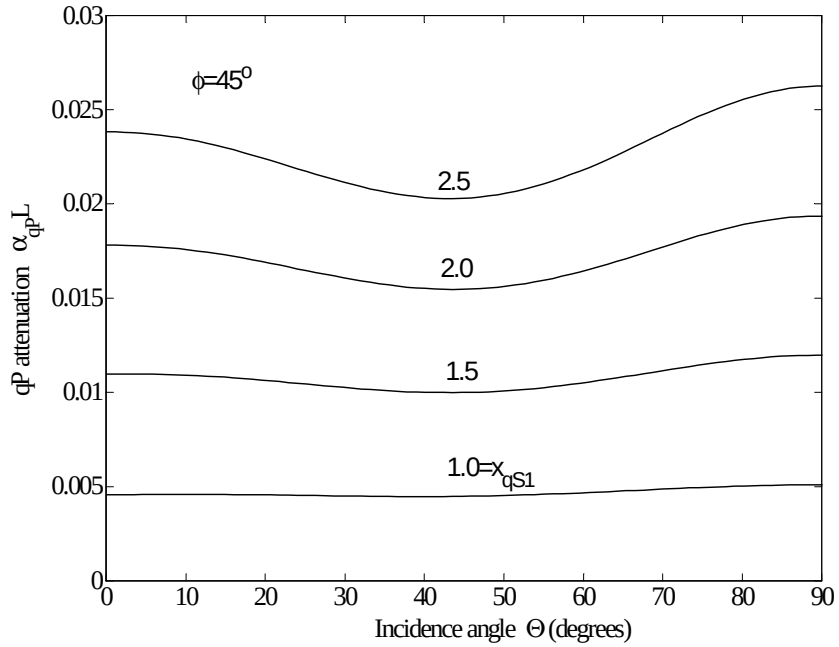

Figure 7.9: Angular dependence of the normalized qP attenuation, $\alpha_{qP}L$, for various frequencies, x_{qS1}, at polar angle $\phi = 45°$.

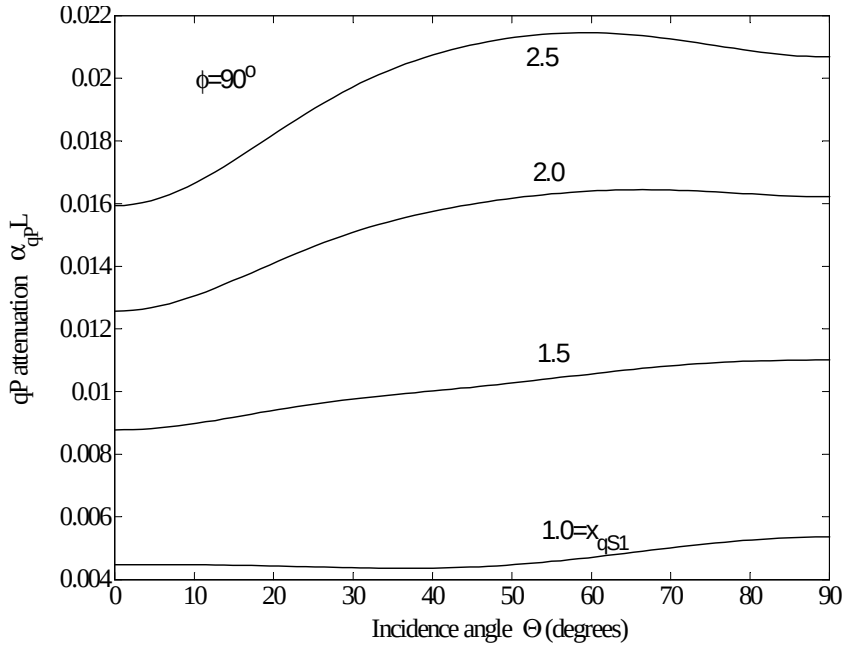

Figure 7.10: Angular dependence of the normalized qP attenuation, $\alpha_{qP}L$, for various frequencies, x_{qS1}, at polar angle $\phi = 90°$.

four different frequencies. It is observed that the attenuation curves show the similar shape as increasing the frequency for each wave type as well. All curves of the attenuations have smoothly changing shapes for various frequencies. In Fig. 7.11, it is seen that at polar angle $\phi = 45°$ the maximum attenuation is about $\Theta = 45°$ for four different frequencies. Figure 7.12 shows that at polar angle $\phi = 90°$ there is a minimum attenuation at $\Theta = 45°$ for various frequencies. There is no symmetry to be observed as increasing the frequency as well in Figs. 7.11 and 7.12.

Finally, results are presented for the normalized attenuations as a function of frequency for several propagation directions. In Figs. 7.13, 7.14, and 7.15, the normalized attenuations of the three wave modes are plotted versus dimensionless frequency, x_{qS1}, for propagation directions along rolling, normal and transverse directions, respectively. For

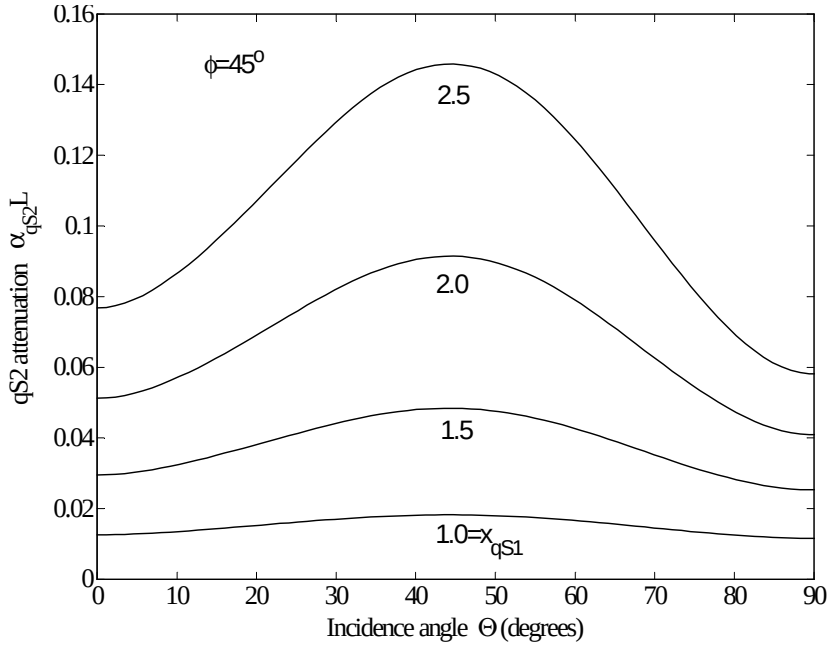

Figure 7.11: Angular dependence of the normalized $qS2$ attenuation, $\alpha_{qS2}L$, for various frequencies, x_{qS1}, at polar angle $\phi = 45°$.

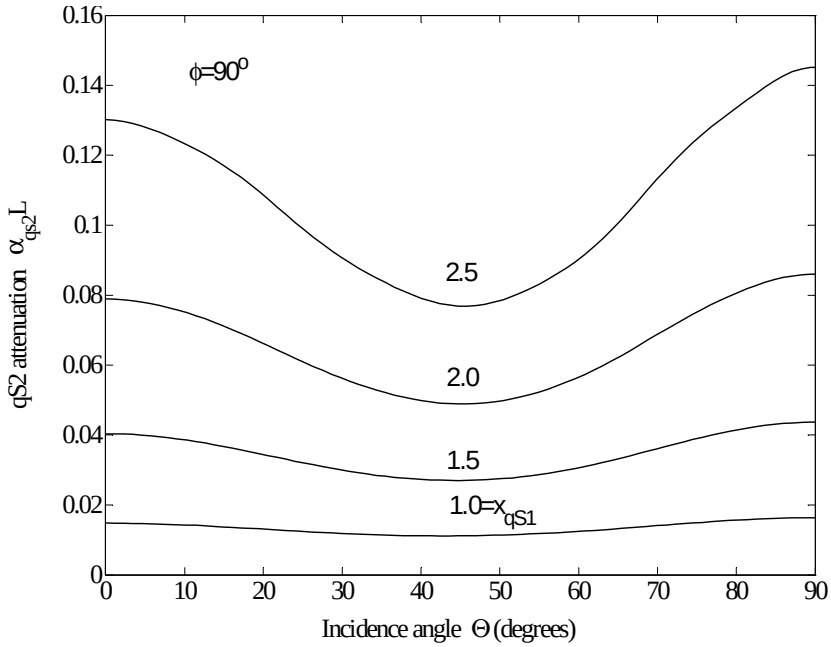

Figure 7.12: Angular dependence of the normalized $qS2$ attenuation, $\alpha_{qS2}L$, for various frequencies, x_{qS1}, at polar angle $\phi = 90°$.

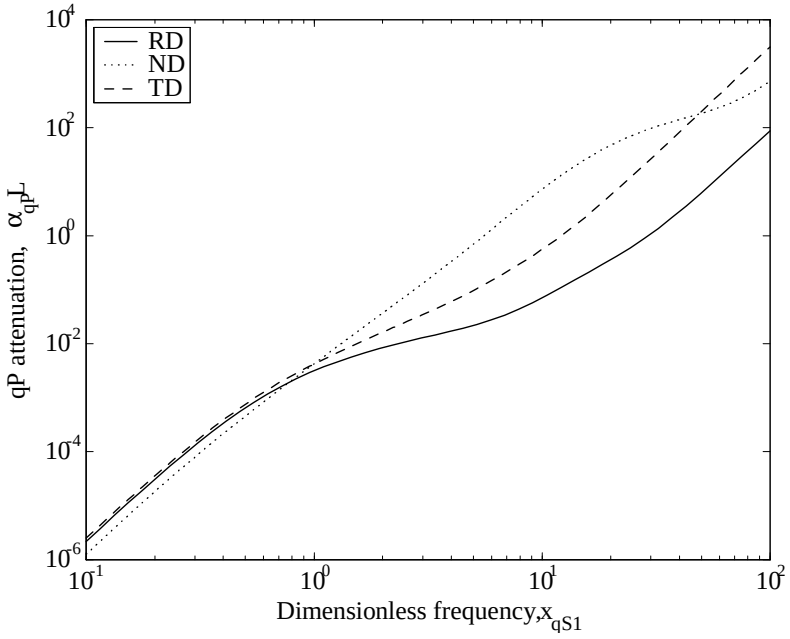

Figure 7.13: Normalized qP attenuation, $\alpha_{qP}L$, as a function of dimensionless frequency, x_{qS1},for propagating in rolling (RD), normal (ND) and transverse (TD) directions.

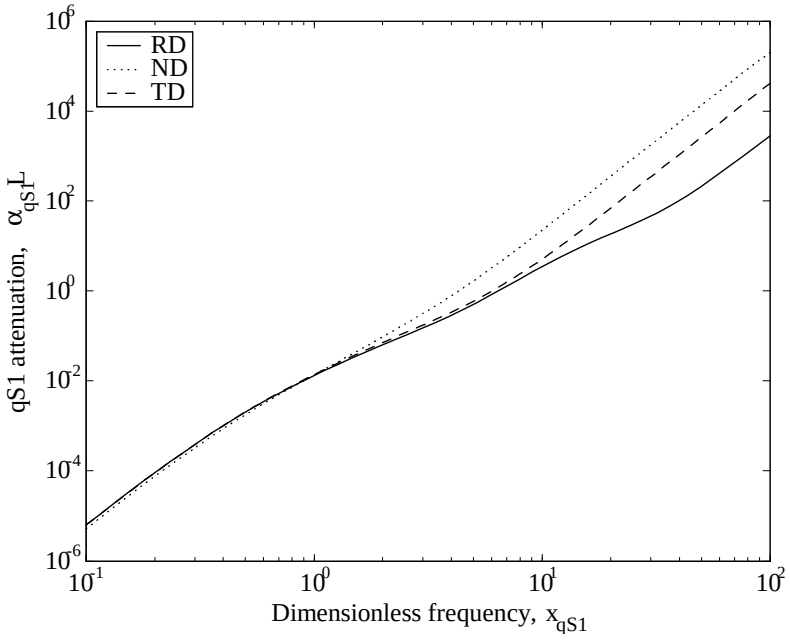

Figure 7.14: Normalized $qS1$ attenuation, $\alpha_{qS1}L$, as a function of dimensionless frequency, x_{qS1},for propagating in rolling (RD), normal (ND) and transverse (TD) directions.

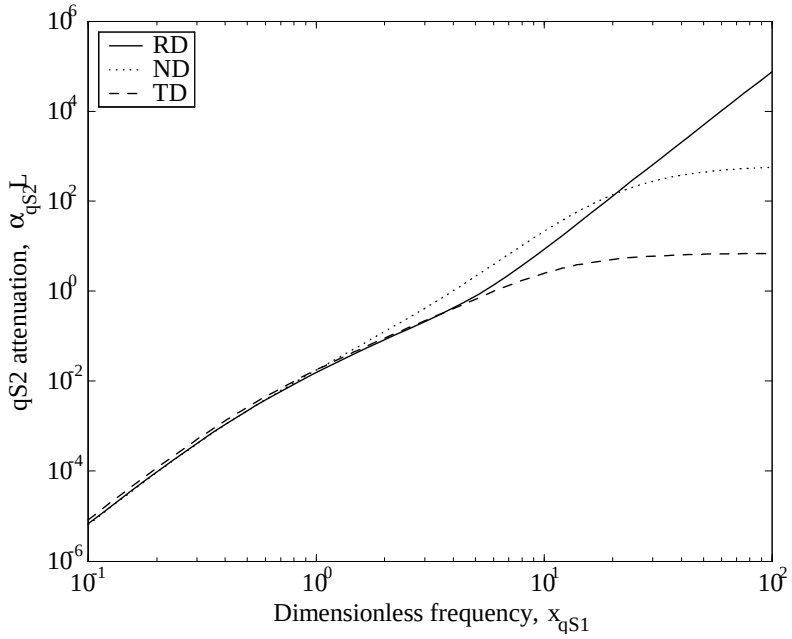

Figure 7.15: Normalized $qS2$ attenuation, $\alpha_{qS2}L$, as a function of dimensionless frequency, x_{qS1},for propagating in rolling (RD), normal (ND) and transverse (TD) directions.

the example considered here, Fig. 7.14 shows the $qS1$ wave attenuation propagated in the rolling, normal and transverse directions and polarized in the normal, transverse and rolling directions, respectively. Figure 7.15 shows the $qS2$ wave attenuation propagated in the rolling, normal and transverse directions and polarized in the transverse, rolling and normal directions, respectively. It is observed that there is a transition region as the dimensionless frequency increases. Thus, the order of the attenuation is switched in such a transition region for the three wave modes, respectively. The attenuations increase with the fourth power of frequency in the low frequency limit. After a transition region, the attenuations scale with the square of frequency as expected. Moreover, the normalized attenuation of each wave type is plotted versus normalized frequency, x_{qS1}, for propagation within the $x_1 - x_2$ plane for various azimuthal angles in Figs. 7.16, 7.17 and 7.18. It is

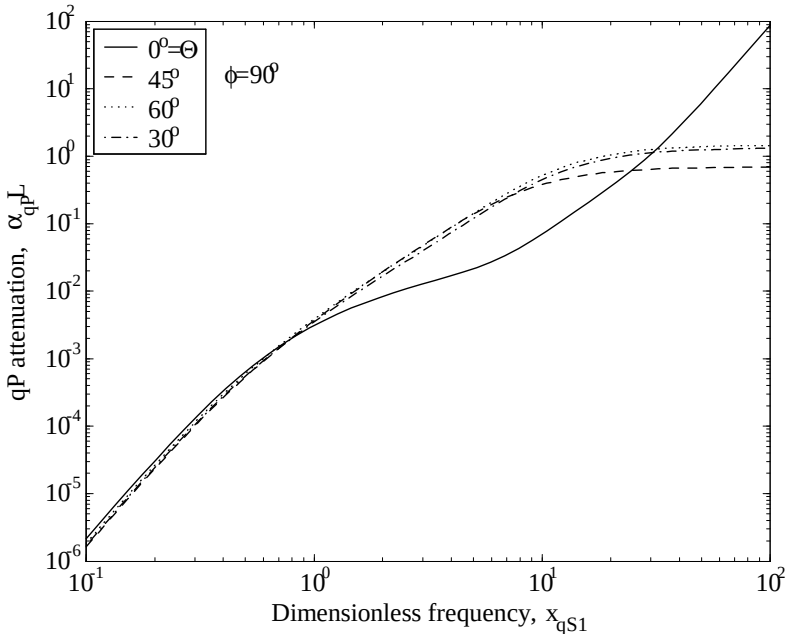

Figure 7.16: Normalized qP attenuation, $\alpha_{qP}L$, as a function of dimensionless frequency, x_{qS1},for propagating within $x_1 - x_2$ plane.

observed that the curves for each wave type mainly show the same shape except $\Theta = 0°$, which is to propagate in the rolling direction. For propagation at $\Theta = 30°$, $45°$ and $60°$, the attenuations of each wave mode are almost the same in the low frequency and slightly different in the high frequency. This feature is thought to be the result of the weak texture for the case discussed here.

7.5 Conclusions

In this chapter, the scattering of elastic waves in polycrystalline materials with texture was discussed. The ensemble averaging of the elastic wave response is governed by the Dyson equation within the limits of first-order smoothing approximation or Keller approximation. In order to calculate the attenuations, the relevant inner products on the

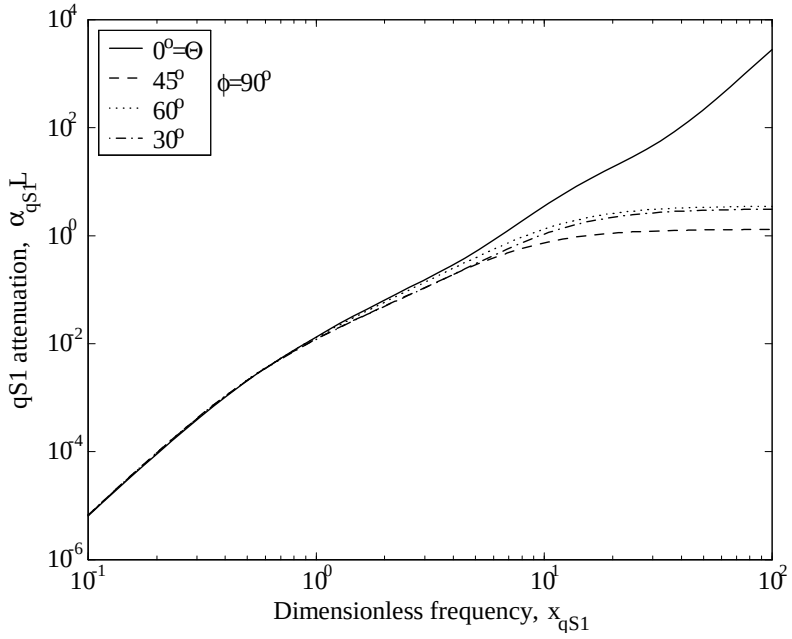

Figure 7.17: Normalized $qS1$ attenuation, $\alpha_{qS1}L$, as a function of dimensionless frequency, x_{qS1},for propagating within $x_1 - x_2$ plane.

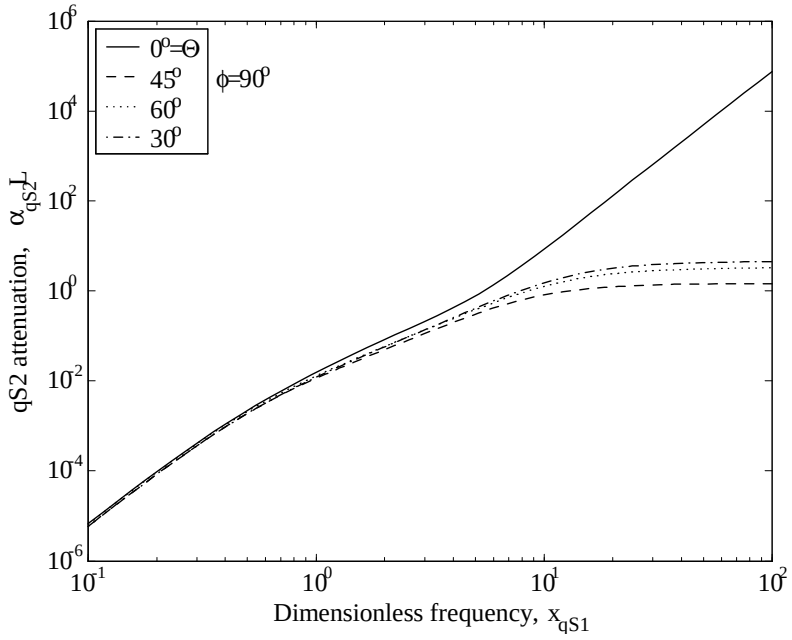

Figure 7.18: Normalized $qS2$ attenuation, $\alpha_{qS2}L$, as a function of dimensionless frequency, x_{qS1},for propagating within $x_1 - x_2$ plane.

covariance of the effective moduli fluctuations were derived in polycrystals of cubic symmetry with rolling texture. Compact expressions for the attenuations of the quasilongitudinal and two quasishear waves were then given in terms of integrations over the scattered directions. The derived expressions are limited to frequencies below the geometric optics limit. In particular, the Rayleigh attenuation was given by simplifying the integrals in the Rayleigh regime. The general attenuations for each wave type are dependent on frequency, wave velocity, wave propagation direction, and especially texture coefficients, which are the expansion coefficients of the orientation function with respect to the generalized spherical functions. Roe's notation was used throughout the discussion. Finally, numerical integration was performed by the extended trapezoidal method. The results show that the attenuations of each wave type can be comprehensively affected by those parameters. The general formulation is also directly related to backscattering problems. The simple form of the results makes them particularly useful for nondestructive testing and materials characterization research. To use ultrasonic techniques for monitoring texture during processing, the relationships between ultrasonic parameters, such as ultrasonic attenuation and materials texture must be investigated. If one knows the relationships between the ODCs and the ultrasonic attenuation, the texture coefficients might be able to be calculated from ultrasonic attenuation measurements. The ultrasonic attenuations of sample specimens can be measured during annealing. Therefore, the ODCs can be determined during processing.

Chapter 8

Conclusions

In this dissertation, the propagation and scattering of elastic waves have been presented for statistically anisotropic media. The research focus is on two important statistically anisotropic media, one of cracked media and one of textured media. This work is anticipated to have practical applications to quantitative nondestructive evaluation and materials characterization, particularly for ultrasonic techniques. The ensemble average elastic wave response was shown to be governed by the Dyson equation. The Dyson equation was then solved in the Fourier transform domain within the limits of the first-order smoothing approximation (FOSA), or Keller approximation. Compact expressions were derived for attenuations and wave velocities of the quasilongitudinal and two quasishear waves using stochastic wave theory in a generalized dyadic approach. The dyadic approach is convenient for making the results coordinate free. The analysis of expressions is limited to frequencies below the geometric optics limit. Thus, the final forms of the attenuations for the three wave modes were given directly by simple compact expressions involving inte-

grations over the scattered directions. In particular, the integrals simplify considerably in the long wavelength Rayleigh regime.

The derivation of explicit expressions of wave attenuation and velocities in a medium with damage from randomly distributed penny-shaped microcracks was first discussed. Under this assumption, the effective medium is assumed statistically isotropic. To model the ensemble effective material properties induced by a large number of microcracks, the effective compliance and stiffness due to a single penny-shaped crack embedded in an infinite elastic solids was investigated. The ensemble average moduli were then derived. The results of the effective Lamé constants are in agreement with those obtained in the literature. The moduli fluctuations were expressed relative to the average moduli. The ensemble average covariance of the moduli fluctuations, which is necessary for calculating the attenuations, was then derived for this isotropic case. The expressions of the dimensionless longitudinal and transverse attenuations were derived in compact form. As expected, the attenuations are shown to scale with the fourth power of frequency and linearly with damage density in the low frequency regime. After a transition region, the attenuations are dependent on the square of frequency. The results showed that the longitudinal attenuation is smaller than the transverse attenuation. The higher transverse attenuation is thought to be a combination of effects of wavelength and interaction with the cracks. The results also showed that the wave speed changes much less than the attenuation as has been observed experimentally in the literature for a given damage level.

Wave propagation and scattering by aligned penny-shaped cracks were then developed. The framework used to model the statistically isotropic situation was extended

to study the attenuations of elastic waves in two different types of aligned cracks, one of uniaxially aligned cracks and the other of perfectly aligned cracks. For uniaxially aligned cracks, the unit normals of all cracks were assumed to be coplanar, but random within the plane of isotropy. Thus, the uniaxial symmetry direction is perpendicular to this plane. The medium of uniaxially aligned cracks is then transversely isotropic. Explicit expressions for attenuations and wave speeds of the shear horizontal (SH), quasilongitudinal (qP), and quasishear vertical (qSV) waves were derived. The analysis is restricted to the limit of noninteraction approximation among individual cracks. The resulting attenuations were investigated in terms of the directional, frequency, and damage dependence. The results showed that the SH and qP attenuations have their maxima at the direction perpendicular to the crack alignment direction. The qSV attenuation has zero value for propagation along the symmetry axis and perpendicular to it. All wave types show zero attenuation along the symmetry axis because of the invariant material properties in that direction. Those results are qualitatively the same as previous work. In addition, the results showed that the peak of maximum qSV attenuation shifts slightly higher as the damage increases. This shift is thought to be the result of the induced anisotropy from microcracking.

The scattering of elastic waves by perfectly aligned cracks was also presented. For this case, the unit normals of all cracks are perpendicular to the plane of isotropy. Explicit expressions for attenuations and wave speeds of the three wave types were also obtained. For that development it is restricted to frequencies below the geometric optics limit. The results showed that the attenuations are directional, frequency, and damage dependence as well. Comparisons of the present model with Hudson's model in the Rayleigh limit showed

that the results presented here are more accurate than those presented in the literature due to the inclusion of the polarization direction. Since the interactions between individual microcracks are not considered, the present analysis is appropriate only for small crack densities.

Wave velocity and attenuation in polycrystalline materials with texture were also developed. For that modeling it was assumed that the polycrystal is an orthorhombic aggregate made up of cubic crystallites. For orthorhombic symmetry, the most general form for the elastic stiffness tensor was given. Wave velocities and their polarization directions correspond to the eigenvalues and eigenvectors of the Christoffel matrix. In general, these results must be obtained by numerical methods. For some special cases given here, analytic expressions of wave velocities were obtained. The angular deviation of the polarization vectors from the propagation directions was discussed. The results showed that the wave velocities and polarization directions are dependent on the wave propagation direction. The polarization directions are neither parallel nor perpendicular to the wave propagation direction as well. The maximum angular deviation is also not too large when waves propagate in different directions. Moreover, a relationship between the phase velocity and recrystallization variables, such as annealing time, was also investigated for specific examples.

The results obtained were then used to calculate the wave attenuations induced by grains of polycrystals. To model the attenuations, the relevant inner products on the covariance of the effective moduli fluctuations were derived in polycrystals of cubic symmetry with rolling texture in Roe's notation. Thus, compact expressions for the attenuations of the quasilongitudinal and two quasishear waves were given in terms of integrations over

the scattered directions. The attenuations of each wave type were performed numerically as a function of dimensionless frequency and wave propagation direction, respectively, for given orientation distribution coefficients (ODCs), which are, in essence, the coefficients of an expansion of crystallite of orientation distribution function (ODF) in terms of a series of generalized spherical harmonics. The results showed that the attenuations are dramatically dependent on the propagation direction and frequency. For waves propagating in different directions, the curves of attenuations mainly show the different shapes with each other. It is hoped that the new models may improve the understanding of the microstructure for polycrystalline materials. Moreover, the theory developed here is thought to have wide applications for a large number of materials in various fields.

The research work presented in this dissertation is considered to be just the theoretical part of the investigation of the materials microstructure in complex media by ultrasonic techniques. Once the models had been corroborated experimentally, the extensive applications of this work will be significant. Therefore, several topics which require further investigation, especially for the development of experiments are addressed in the following chapter.

Chapter 9

Future Work

9.1 Backscattering Model

In this dissertation, explicit formulae of the attenuations for the three wave modes have been presented in both cracked media and textured media. It is known that the scattering attenuation is the integration of the energy that scatters in all directions within the medium. As a result, the attenuations are calculated as integrals over all scattered angles. The backscatter coefficient, however, represents the amount of energy that scatters only in the backward direction. Therefore, using the models developed here and presented in the literature [52],[113],[114], expressions for the backscatter coefficient are anticipated to be obtained for both the assemblage of microcracks and for the textured microstructure in future research. The ability to detect damage is dependent on the amount of scattering due to the microcracks relative to the scattering from the heterogeneous background. The scattering from the microcracks is assumed independent of the microstructural scattering. Thus, the resulting models may provide a lower bound on damage detectability. It will

perhaps provide some valuable information for developing practical experiments.

9.2 Experimental Investigations

It is evident that theoretical analyses always contain certain limitations due to some types of assumptions. In general, a significant part of the experimental investigations have to be employed to corroborate the theoretical models developed. Therefore, the focus of the experimental research is expected to verify the theoretical models in subsequent research. Specific experiments will include measurements of wave speed and attenuation, and measurement of backscattered noise for both cracked media and textured media. It is anticipated that the ultrasonic parameters are measured experimentally over the frequency range of 0.1MHz-15MHz. Recently, many ultrasonic experiments have been conducted for investigating the scattering phenomena in concrete [114],[115],[116],[117],[118]. The measurements of damage in concrete have also been conducted using ultrasonic techniques [119],[120]. Experiments in polycrystalline materials have been investigated by many researchers as discussed in the first chapter. The experimental literature may provide helpful insights on future experimental investigations in cracked and textured media.

The first underlying objective of experimental investigations will be the corroboration of the theoretical research models presented in this dissertation. The microcracks or the heterogeneous microstructure of media cause the ultrasound to scatter significantly. Considering the ratio of the wavelength to the length scale of the microstructure grain, it is anticipated that the ultrasonic attenuation coefficients are measured in sample specimens such as concrete or aluminum as a function of frequency. Both longitudinal and

shear source/receiver transducers are expected to be used in the future experimental measurements. Often, longitudinal attenuation may be measured using immersion transducers within a water tank, while the shear attenuation is measured utilizing contact transducers. The raw data signal at various frequencies is saved to compute the attenuation for the specific samples. In addition, the respective wave speeds and material density are expected to be measured. The experimental results will be used to attest to the predictions of the theoretical analyses.

The next objective of the experimental research will focus on backscatter measurements. The works of Margetan et al. [65], Rose [64], and Turner and Weaver [53] demonstrate that the single scattering process (backscattering) provides important microstructure information about the specimens of interest. Those encouraging results motivate the possibility of backscattering investigations on cracked and textured materials. Generally, the backscatter signal will be acquired using an immersion-focused transducer, which is excited with a tone burst signal at various frequencies. The single backscatter signal will be recorded for various specimen material properties. The measurement noise level will depend on details of the materials properties, as well as on the measurement systems. To eliminate electronic noise from the backscattered response, spatial averaging performed at each transducer position is necessary. The required position averaging is done automatically using the current lab equipment, which is controlled with computer software. A root-mean-squared method discussed by Margetan et al. [65] will be used to quantify backscattered noise as a function of time. The backscattered noise depends on two sets of quantities, the physical properties of the measurement system such as the frequency, diameter and focal length of

the transducer, and a material parameters that describe the capacity of material to generate the noise. It is anticipated that the experimental results will provide significant insights into the detection of damage and the characterization of materials microstructure.

9.3 Other Issues

The research work contained here shows the models of wave propagation and scattering in two statistically anisotropic media. In the presentation, however, several theoretical issues which need future investigation have also arisen. First, the influence of grain shape should be included. In Chapter 2, the correlation function was always assumed to have the form appropriate for equiaxed grains, $\eta(r) = e^{-r/L}$. The correlation length, L, is typical of the order of the grain diameter. For the case of elongated grains, Ahmed and Thompson [121] introduced a correlation function of a slightly more complex form given by, $\eta(r) = e^{-r/L\sqrt{\sin^2\theta + b^2\cos^2\theta}}$. Here, b is the aspect ratio of the grains and θ defines the angle between the two points as measured from the direction of maximum elongation. In addition, the effects of other correlations should also be studied in subsequent research.

Second, the effect of microcrack interaction on the attenuation is not well understood. In this dissertation, the interactions between individual microcracks are not considered such that the present analyses are appropriate only for small crack densities. At larger concentrations of microcracks the probability of their interaction can become substantial. It becomes necessary to consider the effect of direct microcrack interaction on the attenuation, as well as the effective stiffness. Due to the complexity of this issue, analytic solutions may not be obtained. Therefore, numerical models must be employed to study

the effect of microcrack interaction.

Finally, models of more complicated distributions of microcracks may be necessary to be developed. It is known that although aligned cracks are often included in complex materials, the effective media may acquire orthotropy entirely due to the presence of microcracks for some situations. In this case, the microcrack distribution function may be expressed by

$$w(a,\theta,\varphi) = \sum_{l=0}^{\infty} \sum_{m=-l}^{l} \sum_{n=-l}^{l} W_{lmn} Z_{lmn}(\xi) e^{-im\theta} e^{-in\varphi}.$$

Under the assumption, the damage tensor must be introduced for describing the damage parameter. This topic is thought to be very complicated and challenging. More accurate theoretical models that take into account all the effects of the related problems are necessary for improved detection schemes. With continued advancements in these research areas, more techniques may be developed in only a few years.

Bibliography

[1] R.-J. Roe, "Description of Crystallite Orientation in Polycrystalline Materials. III. General Solution to Pole Figure Inversion," J. Appl. Phys. **36,** 2024–2031 (1965).

[2] R.-J. Roe, "Inversion of Pole Figures for Materials Having Cubic Crystal Symmetry," J. Appl. Phys. **37,** 2069–2072 (1966).

[3] H. J. Bunge, *Texture Analysis in Materials Science: Mathematical Methods* (Butterworths, London, 1982).

[4] W. Voigt, *Lehrbuch de Kristall Physik* (Leipzig, Teubner, 1928).

[5] A. Reuss, Z. Angew. Math. Mech. **9,** 49 (1924).

[6] R. Hill, "On Uniqueness and Stability in the Theory of Finite Elastic Strain," J. Mech. Phys. Solids **5,** 229–241 (1957).

[7] E. Kröner, Z. Phys. **151,** 504 (1958).

[8] A. K. Mal, "Dynamic Stress Intensity Factor for a Non-Axisymmetric Loading of the Penny Shaped Crack," Int. J. Eng. Sci. **6,** 725–733 (1968).

[9] A. K. Mal, "Dynamic Stress Intensity Factor for an Axisymmetric Loading of the Penny Shaped Crack," Int. J. Eng. Sci. **6,** 623–629 (1968).

[10] A. K. Mal, "Interaction of Elastic Waves with a Penny-Shaped Crack," Int. J. Eng. Sci. **8,** 381–388 (1968).

[11] A. K. Mal, "A Note on the Low Frequency Diffraction of Elastic Waves by a Griffith Crack," Int. J. Eng. Sci. **10,** 609–612 (1972).

[12] I. A. Robertson, "Diffraction of a Plane Longitudinal Wave by a Penny-Shaped Crack," Proc. Camb. Phil. Sol. **63,** 229–238 (1967).

[13] M. Piau, "Attenuation of a Plane Compressional Wave by a Random Distribution of Thin Circular Cracks," Int. J. Eng. Sci. **17,** 151–167 (1979).

[14] M. Piau, "Crack-Induced Anisotropic and Scattering in Stressed Rocks: Effective Elastic Moduli and Attenuation," Int. J. Eng. Sci. **18,** 549–568 (1980).

[15] A. Chatterjee, A. K. Mal, L. Knopoff, and J. Hudson, "Attenuation of Elastic Waves in a Cracked, Fluid-Saturated Solid," Math. Proc. Cambridge. Philos. Soc. **88,** 547–561 (1980).

[16] P. A. Martin, "Diffraction of Elastic Waves by a Penny-Shaped Crack," Proc. R. Soc. London A **378,** 263–285 (1981).

[17] S. Krenk and H. Schmidt, "Elastic Wave Scattering by a Circular Crack," Phil. Trans. R. Soc. London A **308,** 167–198 (1982).

[18] P. A. Martin and G. R. Wickham, "Diffraction of Elastic Waves by a Penny-Shaped Crack: Analytical and Numerical Results," Proc. R. Soc. London Ser. A **390,** 91–129 (1983).

[19] C. M. Sayers and R. L. Smith, "Ultrasonic Velocity and Attenuation in an Epoxy Matrix Containing Lead Inclusions," J. Phys. D: Appl. Phys. **16,** 1189–1194 (1983).

[20] D. E. Budreck and J. D. Achenbach, "Scattering from Three-Dimensional Planar Cracks by the Boundary Integral Equation Method," J. Appl. Mech. **55,** 405–412 (1988).

[21] H. J. Yang and D. B. Bogy, "Elastic Wave Scattering from an Interface Crack in a Layered Half Space," ASME J. Appl. Mech. **52,** 42–49 (1985).

[22] A. Boström, "Elastic Wave Scattering from an Interface Crack: Antiplane Strain," ASME J. Appl. Mech. **54,** 503–508 (1987).

[23] J. Qu, "Scattering of Plane Waves from an Interface Crack," Int. J. Eng. Sci. **33,** 179–194 (1994).

[24] D. A. Sotiropoulos and J. D. Achenbach, "Reflection of Elastic Waves by a Distribution of Coplanar Cracks," J. Acoust. Soc. Am. **84,** 752–759 (1988).

[25] C. Zhang and J. Achenbach, "Effective Wave Velocity and Attenuation in a Material with Distributed Penny-Shaped Cracks," Int. J. Solids Struct. **27,** 751–767 (1991).

[26] C. Zhang and D. Gross, "Wave Attenuation and Dispersion in Randomly Cracked Solids-I. Slit Cracks," Int. J. Eng. Sci. **31,** 841–858 (1993).

[27] C. Zhang and D. Gross, "Wave Attenuation and Dispersion in Randomly Cracked Solids-II. Penny-Shaped Cracks," Int. J. Engng. Sci. **31,** 859–872 (1993).

[28] C. Zhang and D. Gross, *On Wave Propagation in Elastic Solids with Cracks* (Computational Mechanics Incorporated, Southampton, 1997).

[29] V. P. Smyshlyaev and J. R. Willis, "Linear and Nonlinear Scattering of Elastic Waves by Microcracks," J. Mech. Phys. Solids **42,** 585–610 (1994).

[30] A. S. Eriksson, A. Boström, and S. K. Datta, "Ultrasonic Wave Propagation Through a Cracked Solid," Wave Motion **22,** 297–310 (1995).

[31] L. L. Foldy, "Multiple Scattering Theory of Waves," Phys. Rev. **67,** 107–119 (1945).

[32] A. Boström, "Review of Hypersingular Integral Equation Method for Crack Scattering and Application to Modeling of Ultrasonic Nondestructive Evaluation," Appl. Mech. Rev. **4,** 383–405 (2003).

[33] W. P. Mason and H. J. McSkimm, "Attenuation and Scattering of High Frequency Sound Waves in Metals and Glasses," J. Acoust. Soc. Am. **19,** 464–473 (1947).

[34] C. L. Pekeris, "Note on the Scattering of Radiation in an Inhomogeneous Medium," Phys. Rev. Lett. **71,** 268–269 (1947).

[35] W. Roth, "Scattering of Ultrasonic Radiation in Polycrystalline Metals," J. Appl. Phys. **19,** 901–910 (1948).

[36] H. B. Huntington, "On Ultrasonic Scattering by Polycrystals," J. Acoust. Soc. Am. **22,** 362–364 (1950).

[37] C. F. Ying and R. Truell, "Scattering of a Plane Longitudinal Wave by a Spherical Obstable in an Isotropically Elastic Solid," J. Appl. Phys. **27,** 1086–1097 (1956).

[38] N. G. Einspruch, E. J. Witterholt, and R. Truell, "Scattering of a Plane Transverse Wave by a Spherical Obstacle in an Elastic Medium," J. Appl. Phys. **31,** 806–818 (1960).

[39] A. B. Bhatia, "Scattering of High-Frequency Sound Waves in Polycrystalline Materials," J. Acoust. Soc. Am. **31,** 16–23 (1959).

[40] A. B. Bhatia and R. A. Moore, "Scattering of High-Frequency Sound Waves in Polycrystalline Materials II," J. Acoust. Soc. Am. **19,** 1140–1142 (1959).

[41] E. P. Papadakis, "Scattering in Polycrystalline Media," Meth. Exp. Phys **19,** 137–198 (1981).

[42] A. Vary, "Ultrasonic Measurement of Material Properties," In *Research Techniques in Nondestructive Testing*, R. S. Sharpe, ed., pp. 159–204 (1980).

[43] S. Hirsekorn, "The Scattering of Ultrasonic Waves by Polycrystals," J. Acoust. Soc. Am. **72,** 1021–1031 (1982).

[44] S. Hirsekorn, "The Scattering of Ultrasonic Waves by Polycrystals. II. Shear Waves," J. Acoust. Soc. Am. **73,** 1160–1163 (1983).

[45] S. Hirsekorn, "The Scattering of Ultrasonic Waves in Polycrystalline Materials with Texture," J. Acoust. Soc. Am. **77,** 832–843 (1985).

[46] S. Hirsekorn, "Directional Dependence of Ultrasonic Propagation in Textured Polycrystals," J. Acoust. Soc. Am. **79,** 1269–1279 (1986).

[47] F. E. Stanke and G. S. Kino, "A Unified Theory for Elastic Wave Propagation in Polycrystalline Materials," J. Acoust. Soc. Am. **75,** 665–681 (1984).

[48] F. C. Karal and J. B. Keller, "Elastic, Electromagnetic, and Other Waves in a Random Medium," J. Math. Phys. **5,** 537–547 (1964).

[49] S. Hirsekorn, "The Scattering of Ultrasonic Waves by Multiphase Polycrystals," J. Acoust. Soc. Am. **83,** 1231–1242 (1988).

[50] R. L. Weaver, "Diffusion of Ultrasound in Polycrystals," J. Mech. Phys. Solids **38,** 55–86 (1990).

[51] J. A. Turner and R. L. Weaver, "Radiative Transfer of Ultrasound," J. Acoust. Soc. Am. **96,** 3654–3674 (1994).

[52] J. A. Turner and R. L. Weaver, "Radiative Transfer and Multiple Scattering of Diffuse Ultrasound in Polycrystalline Media," J. Acoust. Soc. Am. **96,** 3675–3683 (1994).

[53] J. A. Turner and R. L. Weaver, "Time Dependence of Multiply Scattered Diffuse Ultrasound in Polycrystalline Media," J. Acoust. Soc. Am. **97,** 2639–2644 (1995).

[54] J. A. Turner and R. L. Weaver, "Ultrasonic Radiative Transfer Theory: Effects of a Fluid-Solid Interface," J. Acoust. Soc. Am. **98,** 2801–2808 (1995).

[55] J. A. Turner and R. L. Weaver, "Single Scattering and Diffusive Limits of the Ultra-

sonic Radiative Transfer Equation," In *Review of Progress in Quantitative NDE*, D. O. Thompson and D. E. Chimenti, eds.,**14,** 75–82 (Plenum Press, New York, 1995).

[56] S. Ahmed and R. B. Thompson, "Propagation of Elastic Waves in Equiaxed Stainless-Steel Polycrystals with Aligned [001] Axes," J. Acoust. Soc. Am. **99,** 2086–2096 (1996).

[57] J. A. Turner, "Elastic Wave Propagation and Scattering in Heterogeneous, Anisotropic Media: Textured Polycrystalline Materials," J. Acoust. Soc. Am. **106,** 541–552 (1999).

[58] M. Spies, "Elastic Waves in Homogeneous and Layered Transversely Isotropic Media: Plane Waves and Gaussian Wave Packets. A General Approach.," J. Acoust. Soc. Am. **95,** 1748–1760 (1994).

[59] M. Spies, "Elastic Wave Propagation in General Transversely Isotropic Media. I. Green's Functions and Elastodynamic Holography," J. Acoust. Soc. Am. **96,** 1144–1157 (1994).

[60] M. Spies, "Elastic Wave Propagation in Transversely Isotropic Media. II. The Generalized Rayleigh Function and an Integral Representation for the Transducer Field. Theory," J. Acoust. Soc. Am. **97,** 1–13 (1995).

[61] L. V. Ryzhik, G. C. Papanicolaou, and J. B. Keller, "Transport Equations for Elastic and Other Waves in Random Media," Wave Motion **24,** 327–370 (1996).

[62] K. Goebbels, "Ultrasonics for Microcrystalline Structure Examination," Philos. Trans. R. Soc. London A **320,** 161–169 (1986).

[63] J. Saniie and N. M. Bilgutay, "Quantitative Grain Size Evaluation Using Ultrasonic Backscattered Echoes," J. Acoust. Soc. Am. **80,** 1816–1824 (1986).

[64] J. H. Rose, "Ultrasonic Backscatter from Microstructure," In *Review of Progress in Quantitative NDE*, D. O. Thompson and D. E. Chimenti, eds.,**11,** 1677–1684 (Plenum Press, New York, 1992).

[65] F. J. Margetan, T. A. Gray, and R. B. Thompson, "A Technique for Quantitatively Measuring Microstructurally Induced Ultrasonic Noise," In *Review of Progress in Quantitative NDE*, D. O. Thompson and D. E. Chimenti, eds.,**10,** 1721–1728 (Plenum Press, New York, 1991).

[66] F. J. Margetan and R. B. Thompson, "Microstructural Noise in Titanium Alloys and its Influence on the Detectability of Hard-Alpha Inclusions," In *Review of Progress in Quantitative NDE*, D. O. Thompson and D. E. Chimenti, eds.,**11,** 1717–1724 (Plenum Press, New York, 1992).

[67] J. W. Littles, L. J. Jacobs, and J. Qu, "Experimental and Theoretical Investigation of Scattering from a Distribution of Cracks," Ultrasonics **33,** 37–43 (1995).

[68] R. B. Thompson, "A Generalized Model of the Effects of Microstructure on Ultrasonic Backscattering and Flaw Detection," In *Review of Progress in Quantitative NDE*, D. O. Thompson and D. E. Chimenti, eds.,**15,** 1471–1477 (Plenum Press, New York, 1996).

[69] K. Y. Han and R. B. Thompson, "Ultrasonic Backscattering in Duplex Microstructure: Theory and Application to Titanium Alloys," Metall. Trans. A **28,** 91 (1997).

[70] J. A. Hudson, "Wave Speeds and Attenuation of Elastic Waves in Material Containing Cracks," Geophys. J. Roy. Astron. Soc. **64,** 133–150 (1981).

[71] U. Frisch, "Wave Propagation in Random Media," In *Probabilistic Methods in Applied Mathematics*, A. T. Barucha-Reid, ed.,**1,** 75–198 (Academic Press, New York, 1968).

[72] F. I. Fedorov, *Theory of Elastic Waves in Crystals* (Plenum Press, New York, 1968).

[73] M. J. P. Musgrave, *Crystal Acoustics - Introduction to the Study of Elastic Waves and Vibrations in Crystals* (Holden-Day, San Francisco, 1970).

[74] L. Yang and J. A. Turner, "Elastic Wave Propagation and Scattering in Solids with Uniaxially Aligned Cracks," J. Acoust. Soc. Am. **114,** 591–600 (2003).

[75] F. E. Stanke, "Spatial Autocorrelation Functions for Calculations of Effective Propagation Constants in Polycrystalline Materials," J. Acoust. Soc. Am. **80,** 1479–1485 (1986).

[76] K. Z. Markov and J. R. Willis, "On the Two-Point Correlation Function for Dispersions of Nonoverlapping Spheres," Math. Models Methods Appl. Sci. **8,** 359–377 (1998).

[77] J. Achenbach, "Quantitative Nondestructive Evaluation," Int. J. Solids Struct. **Vol. 37,** 13–27 (2000).

[78] J. Lemaitre, *A Course on Damage Mechanics* (Springer-Verlag, Berlin, 1992).

[79] D. Krajcinovic, *Damage Mechanics* (North-Holland, Amsterdam, 1996).

[80] S. Nemat-Nasser and M. Hori, *Micromechanics: Overall Properties of Heterogeneous Materials* (North-Holland, Amsterdam, 1993).

[81] M. Kachanov, "Elastic Solids with Many Cracks and Related Problems," Adv. Appl. Mech. **29,** 259–445 (1993).

[82] Z. Hashin and S. Shtrikman, "A Variational Approach to the Theory of the Elastic Behavior of the Multiphase Materials," J. Mech. Phys. Solids **Vol.11,** 127–140 (1963).

[83] L. V. Gibiansky and S. Torquato, "Link Between the Conductivity and Elastic Moduli of Composite Materials," Phys. Rev. Lett. **Vol. 7,** 2927–2930 (1993).

[84] V. Lubarda and D. Krajcinovic, "Tensorial Representations of the Effective Elastic Properties of the Damaged Material," Int. J. Damage Mech. **Vol.3,** 38–56 (1994).

[85] H. Tada, *The Stress Analysis of Cracks* (Del. Res. Corp. Hellertown, PA, 1973).

[86] I. Kunin, *Elastic Media with Microstructure II* (Springer-Verlag, Berlin, 1983).

[87] J. Walsh, "The Effect of Cracks on Compressibility of Rocks," J. Geophys. Res. **70,** 381–389 (1965).

[88] B. Budiansky and R. J. O'Connell, "Elastic Moduli of a Cracked Solid," Int. J. Solid Struct. **12,** 81–97 (1976).

[89] M. Kachanov, I.Tsukrov, and B. Shafiro, "Effective Moduli of Solids with Cavities of Various Shapes," Appl. Mech. Rev. **Vol.47,** 151–174 (1994).

[90] R. Zimmerman, "The Effect of Microcracks on the Elastic Moduli of Brittle Materials," J. Mater. Sci. Lett. **Vol.4,** 1457–1460 (1985).

[91] S. F. Selleck, E. N. Landis, M. L. Peterson, S. P. Shah, and J. D. Achenbach, "Ultrasonic Investigation of Concrete with Distributed Damage," ACI Mater. J. **95,** 27–36 (1998).

[92] L. Yang and J. A. Turner, "Scattering of Elastic Waves in Damaged Media," J. Acoust. Soc. Am. **113,** 2992–3000 (2003).

[93] Matlab, *The Language of Technical Computing* (The Math Works, Inc., Natick, MA, 1996).

[94] S. Ahmed and R. B. Thompson, "Influence of Columnar Microstructure on Ultrasonic Backscattering," In *Review of Progress in QNDE*, D. O. Thompson and D. E. Chimenti, eds.,**14,** 1617–1624 (Plenum Press, New York, 1995).

[95] Y. Li and R. B. Thompson, "Relations Between Elastic Constants C_{ij} and Texture Parameters for Hexagonal Materials," J. Appl. Phys. **67,** 2663–2665 (1990).

[96] R. B. Thompson, S. S. Li, and C. M. Sayers, "Ultrasonic and Neutron Diffraction Characterization of Texture in an Inhomogeneously Rolled Titanium Plate," Mat. Sci. Eng. **A177,** 261–267 (1994).

[97] F. J. Humphreys and M. Hatherly, *Recrystallization and Related Annealing Phenomena* (Pergamon Press, New York, 1995).

[98] C. M. Sayers, "Ultrasonic Velocities in Anisotropic Polycrystalline Aggregates," J. Phys. D: Appl. Phys. **15,** 2157–2167 (1982).

[99] G. C. Johnson, "Acoustoelastic Response of a Polycrystalline Aggregate with Orthotropic Texture," J. Appl. Mech. **52,** 659–663 (1985).

[100] G. C. Johnson and H. R. Wenk, "Elastic Properties of Polycrystals with Trigonal Crystal and Orthorhombic Specimen Symmetry," J. Appl. Phys. **60,** 3868–3875 (1986).

[101] M. Hirao, K. Aoki, and H. Fukuoka, "Texture of Polycrystalline Metals Characterized by Ultrasonic Velocity Measurements," J. Acoust. Soc. Am. **81,** 1434–1440 (1987).

[102] C. M. Sayers, "Angular Dependent Ultrasonic Wave Velocities in Aggregates of Hexagonal Crystals," Ultrasonics **24,** 289–291 (1986).

[103] R. B. Thompson, S. S. Lee, and J. F. Smith, "Angular Dependence of Ultrasonic Wave Propagation in a Stressed, Orthorhombic Continuum: Theory and Application to the Measurement of Stress and Texture," J. Acoust. Soc. Am. **80,** 921–931 (1986).

[104] R. B. Thompson, S. S. Lee, and J. F. Smith, "Relative Anisotropies of Plane Waves and Guided Modes in Thin Orthorhombic Plates: Implication for Texture Characterization," Ultrasonics **25,** 133–137 (1987).

[105] S. Crampin and M. Yedlin, "Shear-Wave Singularities of Wave Propagation in Anisotropic Medium," J. Geophys. **49,** 43–46 (1981).

[106] C. M. Sayers, "P-Wave Propagation in Weakly Anisotropic Media," Geophys. J. Int. **116,** 799–805 (1994).

[107] I. Pšencík and D. Gajewski, "Polarization, Phase Velocity and NMO Velocity of qP Waves in Arbitrary Weakly Anisotropic Media," Geophysics **63,** 1754–1766 (1998).

[108] T. Mensch and V. Farra, "Computation of P-Wave Rays, Traveltimes and Slowness in Orthorhombic Media," Geophys. J. Int. **138,** 244–256 (1999).

[109] V. Farra, "Higher-Order Perturbations of the Phase Velocity and Polarization of qP and qS Waves in Anisotropic Media," Geophys. J. Int. **147,** 93–104 (2001).

[110] P. R. Morris and A. J. Heckler, "Crystallite Orientation Analysis for Rolled Cubic Materials," Adv. X-Ray Anal. **11,** 454–472 (1968).

[111] J. D. Achenbach, *Wave Propagation in Elastic Solids* (North-Holland, Amsterdam, 1973).

[112] G. Liu, D. K. Rehbein, J. C. Foley, and R. B. Thompson, *Review of Progress in Quantitative NDE, Edited by D. O. Thompson and D. E. Chimenti* (2000).

[113] J. A. Turner and P. Anugonda, "Scattering of Elastic Waves in Heterogeneous Media with Local Isotropy," J. Acoust. Soc. Am. **109,** 1787–1795 (2001).

[114] P. Anugonda, J. S. Wiehn, and J. A. Turner, "Diffusion of Ultrasound in Concrete," Ultrasonics **39,** 429–435 (2001).

[115] J. O. Owino and L. J. Jacobs, "Attenuation Measurements in Cement-Based Materials Using Laser Ultrasonics," J. Eng. Mechs. **125,** 637–647 (1999).

[116] L. J. Jacobs and R. W. Whitcomb, "Laser Generation and Detection of Ultrasound in Concrete," J. Nondestr. Eval. **16,** 57–65 (1997).

[117] K. Komlos, S. Popovics, T. Nurnbergerova, B. Babal, and J. S. Popovics, "Compar-

ison of Five Standards on Ultrasonic Pulse Velocity Testing of Concrete," Cement, Concrete, and Aggregates **18,** 42–48 (1996).

[118] J. S. Popovics and J. L. Rose, "A Survey of Developments in Ultrasonic NDE of Concrete," IEEE Transactions on Ultrasonics, Ferroelectrics, and Frequency Control **41,** 140–143 (1994).

[119] Y. Berthaud, "Damage Measurements in Concrete Via an Ultrasonic Technique. Part I Experiment," Cement and Concrete Research **21,** 73–82 (1991).

[120] W. Suaris and V. Fernando, "Ultrasonic Pulse Attenuation as a Measure of Damage Growth During Cyclic Loading of Concrete," ACI Materials Journal **84,** 185–193 (1987).

[121] S. Ahmed and R. B. Thompson, "Effects of Preferred Grain Orientation and Grain Elongation on Ultrasonic Wave Propagation in Stainless Steel," In *Review of Progress in Quantitative NDE*, D. O. Thompson and D. E. Chimenti, eds.,**11,** 1999–2006 (Plenum, New York, 1992).